Titre: Title:	Stability and Accuracy of Mesh-free Particle Methods for Free-surface and Multiphase Flows
Auteur: Author:	Faroogh Garoosi
Date:	2021
Type:	Mémoire ou thèse / Dissertation or Thesis
Référence: Citation:	Garoosi, F. (2021). Stability and Accuracy of Mesh-free Particle Methods for Free-surface and Multiphase Flows [Thèse de doctorat, Polytechnique Montréal]. PolyPublie. https://publications.polymtl.ca/6319/

URL de PolyPublie: PolyPublie URL:	https://publications.polymtl.ca/6319/
Directeurs de recherche: Advisors:	Ahmad Shakibaeinia
Programme: Program:	Génie civil

POLYTECHNIQUE MONTRÉAL

affiliée à l'Université de Montréal

Stability And Accuracy Of Mesh-free Particle Methods For Free-surface And Multiphase Flows

FAROOGH GAROOSI

Département de génies civil, géologique et des mines

Thèse présentée en vue de l'obtention du diplôme de *Philosophiae Doctor*

Génie Civil

Avril 2021

POLYTECHNIQUE MONTRÉAL

affiliée à l'Université de Montréal

Cette thèse intitulée:

Stability And Accuracy Of Mesh-free Particle Methods For Free-surface And Multiphase Flows

présentée par **Farоogh GAROOSI**

en vue de l'obtention du diplôme de *Philosophiae Doctor*

a été dûment acceptée par le jury d'examen constitué de :

Tew-Fik MAHDI, président
Ahmad SHAKIBAEINIA, membre et directeur de recherche
David VIDAL, membre
Elmira HASSANZADEH, membre
Vincent CHU, membre externe

DEDICATION

This thesis work is dedicated to my love, Hanife, who has been a perpetual source of support and motivation in my life. I also dedicate this work to my parents, Mohammad Amin and Tahereh, for their love and support.

ACKNOWLEDGEMENTS

I would like to thank my academic supervisors Professor Ahmad Shakibaeinia, for supporting me during these past four years and helping me to learn how to do research. I am also grateful to the funding received through the Merit scholarship pro- gram for foreign students (PBEEE) of the Ministère de l'Éducation et de l'Enseignement supérieur du Québec (MEES) and also Polytechnique Montreal's PIED program to undertake my PhD.

RÉSUMÉ

L'objectif principal de la thèse de doctorat actuelle est d'améliorer la cohérence et la précision de deux des méthodes de particules lagrangiennes sans maillage les plus largement utilisées, à savoir les modèles d'hydrodynamique des particules lissées (SPH) et les modèles semi-implicites de particules mobiles (MPS) pour simuler un large éventail de les écoulements multiphasiques et les problèmes de convection-diffusion impliquant un transfert de chaleur et de masse. À cette fin, quatre différents opérateurs gradient d'ordre élevé et laplaciens sont d'abord dérivés de l'expansion de la série de Taylor dans les contextes SPH et MPS et sont ensuite utilisés pour la discrétisation des termes de diffusion, l'équation de pression de Poisson (PPE) et la divergence de vitesse dans régir les équations. Afin de conserver la précision globale de la solution, un nouvel algorithme hybride de correction de prédicteur de pression est d'abord développé sur la base de la combinaison du schéma explicite TVD Runge-Kutta du troisième ordre et du modèle de projection en deux étapes, puis est utilisé pour le traitement. des termes transitoires dans les équations de Navier-stokes et de l'énergie et également la gestion du couplage pression-vitesse entre les équations de masse et de quantité de mouvement. Pour améliorer la stabilité des modèles, un nouveau schéma de régularisation des particules appelé Particle Shifting Technique (PST) est introduit dans le contexte du modèle MPS et est ensuite appliqué pour contourner le défaut associé au regroupement / regroupement de particules dans le cadre lagrangien. Cette technique est ensuite améliorée en incorporant le concept de collision de particules et la méthode des éléments discrets (DEM) pour traiter les écoulements violents à surface libre avec une grande déformation et une rupture d'interface et une coalescence. Pour améliorer encore la précision des modèles, quatre nouvelles fonctions de noyau sont construites par la combinaison des fonctions gaussiennes, polynomiales et cosinus pour les méthodologies SPH et MPS afin de créer la connectivité spatiale entre les particules en mouvement libre. En outre, une nouvelle technique de détection de surface libre est proposée basée sur la première et la deuxième dérivée de la fonction du noyau pour une imposition précise de la condition aux limites de pression de Dirichlet au niveau de la surface libre. La précision et la cohérence des modifications proposées sont vérifiées par rapport à une série de cas de référence difficiles, notamment: rupture de barrage avec et sans obstacle, rotation d'une plaque carrée de fluide, problèmes d'instabilité de Rayleigh-Taylor biphasés et triphasés (RTI), goutte circulaire concentrique oscillante, problème de tube de choc

de gazon 1D, analyse d'énergie et d'exergie du transfert de chaleur par convection naturelle dans la cavité chauffée différemment (DHC) et convection de Rayleigh-Bénard, transfert de chaleur par convection naturelle dans une cavité carrée avec obstacle chaud à l'intérieur, enceinte en forme de C, Boîtier en forme de L et boîtier carré contenant une paire de tuyaux horizontaux chauds et froids (échangeur de chaleur). Les résultats obtenus sont en excellent accord avec les données numériques et expérimentales disponibles sans maillage / basées sur un maillage.

ABSTRACT

The main objective of the current Ph.D. thesis is to enhance consistency and accuracy of two of the most widely used mesh-free Lagrangian particle methods namely Smoothed Particle Hydrodynamics (SPH) and Moving Particle Semi-implicit (MPS) models for simulating a wide range of multiphase flows and convection-diffusion problems involving heat and mass transfer. To this end, four different high-order gradient and Laplacian operators are first derived from the Taylor series expansion in both SPH and MPS contexts and are then employed for the discretization of diffusion terms, Pressure Poisson's equation (PPE), and divergence of velocity in governing equations. In order to retain the overall accuracy of the solution, a novel hybrid predictor-correction solution algorithm is first developed based on the combination of the explicit Third-order TVD Runge-Kutta scheme and two-step projection model and then is employed for the treatment of the transient terms in the Navier-stokes and energy equations and also handling the pressure-velocity coupling between the mass and momentum equations. To enhance the stability of the models, a novel particle regularization scheme so-called Particle Shifting Technique (PST) is introduced in the context of the MPS model and is then applied to circumvent the shortcoming associated with particle clustering/bunching in the Lagrangian framework. This technique is then further improved by incorporating the concept of the particle collision and Discrete Element Method (DEM) to deal with violent free-surface flows with large deformation and interface rupture and coalescence. To further enhance the accuracy of the models, four new Kernel functions are constructed by the combination of the Gaussian, polynomial, and cosine functions for both SPH and MPS methodologies and then are employed to create the spatial connectivity between freely moving particles. In addition, a novel free-surface detection technique is proposed based on the first and second derivatives of kernel function for the accurate imposition of Dirichlet pressure boundary condition at the free surface area. The accuracy and consistency of the proposed modifications are verified against a series of challenging benchmark cases including dam break with and without obstacle, rotation of a square patch of fluid, two-phase and three-phase Rayleigh-Taylor instability problems (RTI), oscillating concentric circular drop, 1D Sod shock tube problem, energy, and exergy analysis of natural convection heat transfer in Differentially Heated Cavity (DHC) and Rayleigh-Bénard convection, natural convection heat transfer in a square cavity with hot obstacle inside, C-shaped enclosure, L-shaped enclosure and a

square enclosure containing a pair of hot and cold horizontal pipes (heat exchanger). The obtained results are found to be in excellent agreement with available mesh-free/mesh-based numerical and experimental data.

Table of Contents

LIST OF TABLES

LIST OF FIGURES

LIST OF SYMBOLS AND ABBREVIATIONS

This list presents the symbols and abbreviations used in the thesis in alphabetical order, along with their meanings.

DHC Differentially Heated Cavity

FSI Fluid-Structure Interaction problems

HFD Hybrid Free-surface Detection technique

HPST Hybrid Particle Shifting Technique

ISPH Incompressible Smoothed Particle Hydrodynamics

KDF Kernel Derivative-Free

MPS Moving Particle Semi-implicit

MPG Modified Pressure Gradient operator

PST Particle Shifting Technique

PND Particle Number Density

RTI Rayleigh-Taylor Instability

RB Rayleigh-Bénard convection

TIC Tensile Instability Control

TVD Total Variation Diminishing

WCSPH Weakly Compressible Smoothed Particle Hydrodynamics

Chapter 1 INTRODUCTION

The study of multiphase flows with moving and deformable interfaces has received increasing attention because it is ubiquitous in our daily life and many industrial/engineering applications such as the bubble column reactors (Masterov, Baltussen, & Kuipers, 2020), petroleum engineering, solidification process of metals (Dou, Luo, Qi, Lian, & Hou, 2021), microfluidic devices (Chaves, Duarte, Coltro, & Santos, 2020), internal combustion engines (Xue et al., 2015), fluidized bed reactors (Liu et al., 2020) and cavitation in hydraulic power systems (Piscaglia, Giussani, Hèlie, Lamarque, & Aithal, 2021). However, due to limited understanding on the physics of gas-liquid two-phase flow there is an urgent need for more research in this area. In general, experimental, analytical, and numerical methods are three common approaches for the study of gas-liquid flow. The foundations of gas-liquid flow research can be found in many experimental and analytical studies (Tryggvason, Scardovelli, & Zaleski, 2011). However, it is not difficult to deduce that, the experimental methods are limited, due to the issues with the cost effectiveness, instrumental restrictions and uncontrolled environment. More importantly, in the case of experimental study, the laboratory model typically has a very different scale than the prototype, such that the results may not be generalizable to the larger scales (Ishii & Hibiki, 2010). In addition to that, the design and construction of one-off laboratory prototypes are expensive, time-consuming, and require sophisticated sensors and instruments to measure and monitor physical quantities (i.e. temperature, velocity, pressure, etc). On the other hand, the theoretical study is only restricted to extremely simple conditions and cannot be extended to many real-life applications with complex geometries and boundary conditions. Thanks to the rapid evolution of computer power, the application of CFD as the flexible and relatively inexpensive tool for study of multiphase flows has become more widespread and important. Over the past decade, extensive effort has been devoted towards the development of advanced numerical scheme to investigate the morphology and hydrodynamic behaviour of multiphase flow problems.

In general, the numerical modelling of multiphase flows can be accomplished through two primary frameworks, namely Eulerian and Lagrangian descriptions (Rebouillat & Liksonov, 2010). A comprehensive literature survey conducted by Yan et al. (Yan & Che, 2010) and Gibou et al. (Gibou, Fedkiw, & Osher, 2018) reveals that Volume-of-Fluid (VOF) (Hirt & Nichols,

1981) and Level-Set (LS) (Sussman, Smereka, & Osher, 1994) are two most commonly used interface-tracking/capturing models in Eulerian framework which have been widely used for the description and analysis of free-surface flows, particularly those involving large deformation, fragmentation and breaking. Although, the aforesaid methods have all been implemented in various multiphase problems, the results of the Ha et al. (Ha & Cleary, 2000) and Wu et al. (Wu et al., 2017) illustrate that the Eulerian mesh-based approaches have some innate drawbacks in determining the exact location of the flow front in multiphase phenomena. To overcome the aforementioned methodological problems and avoid difficulties in interface tracking, many scholars have adopted a newer generation of numerical technique so-called Mesh-free Lagrangian Particle method (i.e. SPH and MPS) (Khayyer, Gotoh, Falahaty, & Shimizu, 2018; Samulyak, Wang, & Chen, 2018), where particles in Lagrangian framework take the role of the grids in Eulerian one. Absence of the convection term in governing equations and free from constraints of the grids generation, make the SPH and MPS more efficient and robust models in dealing with the multiphase flows and fluid-structure interaction problems (FSI).

Historically, the Smoothed Particle Hydrodynamics (SPH) as a pure Lagrangian approach was introduced by Lucy (Lucy, 1977) and Gingold et al. (Gingold & Monaghan, 1977) to describe the evolution of planet-disk systems and became very popular in modelling of free-surface flows and thermal-hydraulics problems owing to its flexibility in adapting to complex geometries with curved boundary conditions (Hosain, Domínguez, Fdhila, & Kyprianidis, 2019). In the same context, the Moving Particle Semi-implicit (MPS) method was originally developed by Koshizuka et al. (Koshizuka & Oka, 1996) to simulate incompressible fluid flow. At the present, the existing SPH and MPS methods can be broadly classified into two sub-groups namely: (a) Weakly Compressible (WCSPH & WCMPS) and (b) truly Incompressible (ISPH & IMPS) models which have their own advantages and disadvantages (Daly, Grimaldi, & Bui, 2016b; Shakibaeinia & Jin, 2012; Tanaka, Cardoso, & Bahai, 2018a). A summary of the aforementioned particle methods with associated governing equations/operators is listed in tables 1-1 to 1-4. It is evident that, in the former approach, an algebraic thermodynamic pressure equation (Equation-Of-State) is used to determine the pressure field within the computational domain whereas in the second method the pressure term in the Navier-Stokes equation is computed implicitly by enforcing a divergence-free velocity field. Although computer programming of WCSPH and

WCMPS is conceptually straightforward, these models are characterized by spurious pressure oscillations, which can yield numerical instability. Another drawback associated with these models is that, they require a very small time step to meet the stability criterion for relaxing the solution towards the incompressible limit in low Mach number flows. On the other hand, although fully incompressible SPH and MPS benefit from smoother pressure field and high level of accuracy in terms of spatial discretization, they require the solution of a Pressure Poisson Equation (PPE) which are more complex to implement compared to the standard WCSPH and WCMPS models.

Table 1.1 The governing operators used in the classical WCSPH (X. Xu & Deng, 2016).

	WCSPH formulations	Governing operators
1:	$\frac{D\rho}{Dt}+\rho\nabla\cdot\mathbf{u}=0$	$\phi_i=\frac{\sum_j^N \phi_j W_{ij}\, m_j}{\sum_j^N W_{ij}\; m_j/\rho_j}$
2:	$\frac{D\mathbf{u}}{Dt}=-\frac{1}{\rho}\nabla P+\nu\nabla^2\mathbf{u}+\mathbf{g},$	$\nabla\cdot\mathbf{u}=\sum_j^N(\mathbf{u}_j-\mathbf{u}_i)\cdot\nabla W_{ij}\; m_j/\rho_j$
3:	$P=\frac{\rho_0 c_0^2}{\gamma}((\frac{\rho}{\rho_0})^{\lambda}-1)$	$\nabla P=\rho_i\sum_j^N(\frac{p_i}{\rho_i^2}+\frac{p_j}{\rho_j^2})\nabla W_{ij}\, m_j$
4:	$\frac{D\mathbf{r}}{Dt}=\mathbf{u},$	$\nabla^2\phi=\sum_j^N\frac{(\phi_j-\phi_i)\cdot(r_j-r_i)}{\lvert r_j-r_i\rvert^2+\eta^2}\nabla W_{ij}\; m_j/\rho_j$

During the past decade, many researchers have been motivated to employ some positive features of SPH and MPS models in solving a wide range of engineering and scientific problems (Shadloo, Oger, & Le Touzé, 2016; Z.-B. Wang et al., 2016). Modeling of capillary rise dynamics and bubble rising (Deng, Liu, Wang, Ge, & Li, 2013; X. Xu & Yu, 2019), simulation of tsunamis water waves generated by landslides and 3D dam-break flows with breaking waves (Tan & Chen, 2017; Zhang, Hu, & Adams, 2017), nuclear reactor design and dynamic analysis of landslide dam (Hosseini, Omidvar, Kheirkhahan, & Farzin, 2019; Kurowski & Spliethoff, 2016;

W. Wang, Chen, Zhang, Zheng, & Zhang, 2017; W. Wang et al., 2019), analysis of liquid droplet and liquid jet atomization (Li, Liu, Duan, Chong, & Yan, 2016; Lind, Stansby, & Rogers, 2016) are just a few examples of such studies in which particle methods such as SPH and MPS were adopted to solve complex flow and transport problems. However, despite the proven success of the SPH and MPS models in handling multi-fluid/multiphase systems with large interfacial deformation and discontinuities, these method have some key fundamental disadvantages in terms of accuracy and stability which may hinder its further application as a CFD tool for solving non-linear multiphase/multifluid flow problems.

Table 1.2 The governing operators used in the classical WCMPS (Shakibaeinia & Jin, 2012).

	WCMPS formulations	Governing operators
1:	$\frac{D\rho}{Dt}+\rho\nabla\cdot\mathbf{u}=0$	$\phi_i=\frac{\sum_j^N \phi_j W_{ij}\, m_j}{n_0}$, $n_i=\sum_j^N W_{ij}\ m_j/\rho_j$
2:	$\frac{D\mathbf{u}}{Dt}=-\frac{1}{\rho}\nabla P+\nu\nabla^2\mathbf{u}+\mathbf{g}$,	$\nabla\cdot\mathbf{u}=\frac{d}{n_0}\sum_j^N\frac{(\mathbf{u}_j-\mathbf{u}_i)}{(\mathbf{r}_j-\mathbf{r}_i)}\mathbf{e}_{ij}W_{ij}\ m_j/\rho_j$
3:	$P=\frac{\rho_0 c_0^2}{\gamma}((\frac{n_i}{n_0})^\lambda-1)$	$\nabla P=\frac{d}{n_0}\sum_j^N(\frac{p_j-p_i}{(\mathbf{r}_j-\mathbf{r}_i)})\mathbf{e}_{ij}W_{ij}\ m_j/\rho_j$
4:	$\frac{D\mathbf{r}}{Dt}=\mathbf{u}$,	$\nabla^2\phi=\frac{2d}{n_0}\sum_j^N\frac{(\phi_j-\phi_i)}{\lvert r_j-r_i\rvert^2+\eta^2}W_{ij}\ m_j/\rho_j$

Table 1.3 The governing operators used in the classical ISPH (Chow, Rogers, Lind, & Stansby).

	ISPH formulations	Governing operators
1:	$\nabla \cdot \mathbf{u} = 0$	$\phi_i = \dfrac{\sum_j^N \phi_j W_{ij}\, m_j}{\sum_j^N W_{ij}\ m_j/\rho_j}$,
2:	$\dfrac{D\mathbf{u}}{Dt} = -\dfrac{1}{\rho}\nabla P + \nu \nabla^2 \mathbf{u} + \mathbf{g},$	$\nabla \cdot \mathbf{u} = \sum_j^N (\mathbf{u}_j - \mathbf{u}_i) \cdot \nabla W_{ij}\ m_j/\rho_j$
3:	$\nabla^2 p = \dfrac{\rho \nabla \cdot \mathbf{u}}{\Delta t}$	$\nabla P = \rho_i \sum_j^N (\dfrac{p_i + p_j}{\rho_i \rho_j}) \nabla W_{ij}\, m_j$
4:	$\dfrac{D\mathbf{r}}{Dt} = \mathbf{u},$	$\nabla^2 \mathbf{u} = \sum_j^N \dfrac{(\mathbf{r}_j - \mathbf{r}_i) \cdot \nabla W_{ij}}{\lvert r_j - r_i \rvert^2 + \eta^2} \mathbf{u}_{ij}\, m_j/\rho_j$

Table 1.4 The governing operators used in the classical IMPS (Tanaka, Cardoso, & Bahai, 2018b).

	WCMPS formulations	Governing operators
1:	$\nabla \cdot \mathbf{u} = 0$	$\phi_i = \dfrac{\sum_j^N \phi_j W_{ij}\, m_j}{n_0}$, $n_i = \sum_j^N W_{ij}\ m_j/\rho_j$
2:	$\dfrac{D\mathbf{u}}{Dt} = -\dfrac{1}{\rho}\nabla P + \nu \nabla^2 \mathbf{u} + \mathbf{g},$	$\nabla \cdot \mathbf{u} = \dfrac{d}{n_0} \sum_j^N \dfrac{(\mathbf{u}_j - \mathbf{u}_i)}{(\mathbf{r}_j - \mathbf{r}_i)} \mathbf{e}_{ij} W_{ij}\ m_j/\rho_j$
3:	$\nabla^2 p = \dfrac{\rho \nabla \cdot \mathbf{u}}{\Delta t}$	$\nabla P = \dfrac{d}{n_0} \sum_j^N (\dfrac{p_j - p_{\min}}{\lvert \mathbf{r}_j - \mathbf{r}_i \rvert^2})(\mathbf{r}_j - \mathbf{r}_i) W_{ij}\ m_j/\rho_j$
4:	$\dfrac{D\mathbf{r}}{Dt} = \mathbf{u},$	$\nabla^2 \phi = \dfrac{2d}{\lambda_i n_0} \sum_j^N (\phi_j - \phi_i) W_{ij}\ m_j/\rho_j$ $\lambda_i = \sum_j^N (r_j - r_i)^2 W_{ij}\, m_j/\rho_j \Big/ \sum_j^N W_{ij}\, m_j/\rho_j$

Chapter 2 LITERATURE REVIEW

The use of mesh-free Lagrangian particle methods such as SPH and MPS as promising alternative approaches to conventional grid-based systems (e.g. FVM, FEM, etc) for modeling multi-fluid/multiphase problems has been a subject of interest in many research studies (Hammani, Marrone, Colagrossi, Oger, & Le Touzé, 2020; Li et al., 2020; Zheng, Sun, & Yu, n.d.). However, as highlighted before, these schemes face several crucial shortcomings including non-physical pressure oscillation (Molteni & Colagrossi, 2009), false detection of interfacial particles in multiphase and free-surface flows (Marrone, Colagrossi, Le Touzé, & Graziani, 2010), tensile instability caused by particle clustering (Sun, Colagrossi, Marrone, Antuono, & Zhang, 2019), low-order boundary treatment (Marrone et al., 2011), uncertainty in selecting the appropriate kernel function (Martinsson & Rokhlin, 2005), penetration of fluid particles into the boundaries walls (Daly, Grimaldi, & Bui, 2016a), low-order space and time discretization schemes used for calculating gradient, divergence and Laplacian operators (Oger, Doring, Alessandrini, & Ferrant, 2007; Schwaiger, 2008), false diffusion errors and density error accumulation (Lee et al., 2008) which can endanger the solution stability and even lead to premature termination of the calculations.

Over the past decade, substantial research efforts have been devoted to improve the precision and consistency of the SPH and MPS models. To address the problem of tensile instability and numerical inconsistency caused by particle clustering, Xu et al. (R. Xu, Stansby, & Laurence, 2009) suggested the use of particle rearranging technique where fluid particles are forced to travel from their streamlines to the region with low particle concentration, resulting in a notable improvement in the uniformity of particle arrangement. This technique was further extended and optimized by Lind et al. (Lind, Xu, Stansby, & Rogers, 2012) and Khayyer et al. (Khayyer, Gotoh, & Shimizu, 2017) for the simulation of water wave propagation. They numerically showed that, the implementation of PST can considerably enhance the homogeneity of particles dispersion and suppress the onset of tensile instability, accordingly. Another factor that causes tensile instability comes from the Lagrangian formulations of the SPH and MPS. Generally, the governing operators in the class of both SPH and MPS are derived by the hypothesis that particles are uniformly distributed across the whole computational domain whereas this assumption is not always valid for violent free surface flows where particle bunching is likely to

occur. To maintain regularity of particle distributions and improve the order of accuracy of gradient operator, Oger et al. (Oger et al., 2007) proposed a new renormalization technique based on the Taylor series expansion and concluded that renormalization of density and gradient operator can significantly enhance the consistency of the SPH model. To further suppress spurious void formation and pressure fluctuation, Schwaiger (Schwaiger, 2008) extended Oger's model (Oger et al., 2007) and developed higher-order Laplacian operator in the context of the SPH formulation. For elimination of non-physical pressure fluctuations, Sun et al. (Sun, Colagrossi, Marrone, Antuono, & Zhang, 2018) proposed a novel switching technique so-called Tensile Instability Control (TIC) that was achieved by altering Navier-Stokes equations into the non-conservative form. More precisely, in this technique, non-conservative form of the pressure gradient is utilized in the specific area with truncated kernel support (free-surface area) whereas the conservative one is applied on the interior particles. Antuono et al. (Antuono, Colagrossi, Marrone, & Molteni, 2010) invented an effective remedy to suppress the density error accumulation associated with the Weakly Compressible version of the SPH. They proposed a novel system of equations by inserting the additional diffusive term into the mass equation. Their results showed that, this extra term can significantly decrease the pressure oscillations in both time and spatial domain and named it as a Delta-SPH model (δ-SPH). Similar findings were also documented by Jandaghian and Shakibaeinia (Jandaghian & Shakibaeinia, 2020) who proposed the Delta version of the WCMPS model (δ-WCMPS) by inserting an artificial diffusive term into the continuity equation to eliminate the spurious high-frequency pressure fluctuations from the fluid domain. As stated before, another major source of instability can be traced back to the uncertainty in selecting the appropriate kernel function. Hongbin et al. (Hongbin & Xin, 2005) numerically proved that, the type of the kernel or weighting function as a heart of the Lagrangian particle method has a significant impact on the stability of the numerical solutions. They conducted a comparative study on ten different types of the kernel function and concluded that Gaussian and Q-spline can potentially generate more precise results for a benchmark one-dimensional shock tube problem as compared with the cubic-spline kernel function. Similar observation was also reported by Yang et al. (X. F. Yang, Peng, & Liu, 2014; X. Yang, Liu, & Peng, 2014) who constructed two different weighting functions and highlighted that, the smoothness and coherence of the first and second derivatives of kernel function have remarkable

impacts on the stability and consistency of the numerical simulations. Accurate detection of free-surface area for the imposition of Dirichlet boundary condition for the Pressure Poisson Equation (zero pressure) is another major challenge faced by the particle methods. To overcome this shortcoming and identify the position of the free-surface area, Marrone et al. (Marrone et al., 2010) proposed a novel scanning algorithm. In this technique, the specific scanning algorithm is employed to scan the local region around each target particle. If any gap is detected, the candidate particle will be labeled as a surface particle. However, the results of Haque et al. (Haque & Dilts, 2007) showed that the utilization of this technique for 3D free-surface problems or long-term simulations is computationally expensive.

In light of the above literature review, the main objectives of the present PhD thesis are to develop a robust and reliable high performance SPH and MPS models for the simulation of the multiphase and free-surface flows with low and high-density contrasts through addressing the aforementioned shortcomings associated with mesh-free Lagrangian particle methods.

Chapter 3 PROBLEM STATEMENT, OBJECTIVE, METHODOLOGY, STRUCTURE OF THE RESEARCH PROJECT

3.1 Problem statement

As highlighted before, multi-fluid/multiphase flows with severe interface deformation are found in a large number of industrial applications and CFD as a reliable, cost-effective, and powerful alternative or complement tool to experimental measurements have been widely applied to interpret the complex physics behind such phenomena. Generally, the morphology and hydrodynamic behaviours of the multi-fluid/multiphase flows can be examined using a method developed either in Eulerian or Lagrangian framework. However, despite the proven success of the Eulerian methods (i.e. VOF and Level-set) in dealing with free-surface flow with large interface deformation and discontinuities, these models are characterized by violation of local mass conservation and interface smearing which can immensely jeopardise the accuracy and reliability of the models. On the other hand, although the SPH and MPS models as truly Lagrangian methods have been shown to have the best overall performance over the traditional mesh-based methods in handling multiphase flows with sharp interface deformation and topological change, they have some major drawbacks in terms of numerical instability (i.e. the particles clustering and non-physical pressure oscillation) which can directly degrade the order of accuracy of the numerical scheme and often lead to premature termination of calculations. Based on the above explanation, the main aims of the current work are to introduce some possible solutions to improve the accuracy and consistency of existing SPH and MPS models.

3.2 Research objectives

The global objective of the proposed research is to develop a robust and high-performance mesh-free Lagrangian (particle) numerical method, based on the MPS and SPH formulations, for the simulation of multi-fluid/multiphase fluid flows with heat and mass transfer. In light of the above literature survey, the main objectives of the present research work may be summarized as follows:

1. Presenting a novel high-order kernel function to enhance the stability and accuracy of the particle methods,

2. Presenting a robust and accurate free-surface detection technique for the treatment of the free-surface flows and the enforcement of the Dirichlet boundary condition for the Pressure Poisson Equation (zero pressure),
3. Presenting a novel particle regularization technique to address the problems of particle clustering and tensile instability,
4. Implementing a mirror velocity technique to address the problems of particle penetration,
5. Presenting three novel high-order Laplacian, gradient and divergence operators in the context of the SPH and MPS for the elimination of unphysical pressure oscillation and void formation (tensile instability),
6. Evaluation of the validity and versatility of the proposed modifications in handling multi-fluid/multiphase problems through the simulations of several challenging benchmark test cases including dam break with and without obstacle, rotation of a square patch of fluid, two-phase and three-phase Rayleigh-Taylor instability problems (RTI), oscillating concentric circular drop, 1D Sod shock tube problem, energy, and exergy analysis of natural convection heat transfer in Differentially Heated Cavity (DHC) and Rayleigh-Bénard convection.

3.3 Methodology

In order to achieve the aforementioned goals, the methodology of the present research is divided into 8 steps as follows:

1. Implementing the explicit Third-order TVD Runge-Kutta scheme for discretization of transient terms in the governing equations,
2. Implementing a mirror velocity technique for the treatment of the rigid walls to prevent particle penetrations,
3. Developing a novel high-order gradient operator based on the Taylor series expansion for the discretization of pressure gradient and divergence of velocity for both SPH and MPS methods,
4. Developing a novel high-order Laplacian operator based on the Taylor series expansion for the discretization of Pressure Poisson Equation (PPE),

5. Developing a novel high-order Particle Shifting Technique (PST) based on the Taylor series expansion to supress the problem of tensile instability and particle clustering,
6. Improving the performance of the existing PST by incorporating the particle-collision technique into the method (i,e. Discrete Element Method) for the treatment of the free-surface area,
7. Developing a novel high-order smoothing operator based on the Taylor series expansion for the imposition of Neumann boundary conditions in both SPH and MPS frameworks,
8. Developing a robust and accurate free-surface detection technique based on the first and second derivatives of kernel function for the determination of the exact position of the interface,

3.4 Structure of the research project

As heighlited earlier, (1) unphysical pressure fluctuations, (2) tensile instability caused by particle clustering, (3) uncertainty in the selection of appropriate kernel function, (4) non-conservative form of pressure gradient operator, (5) false detection of interfacial particles in free-surface flows, (6) Low-order boundary treatment, (7) penetration of fluid particles into the boundaries walls and (8) low-order space and time discretization schemes used for calculating gradient, divergence and Laplacian operators are some crucial drawbacks associated with SPH and MPS models which can adversely influence the accuracy of the numerical solutions or even lead to the unwanted termination of the calculations. The aforementioned shortcomings have been systematically addressed within four scientific research articles. Based on the above explanation, the current PhD thesis is organized as follows:

In article 1, the Kernel Derivative-Free (KDF) version of the conventional Incompressible Smoothed Particle Hydrodynamics (ISPH) model is introduced for the simulation of the free-surface flows where no kernel gradient is required for the interpolation and particle approximation. To resolve the second shortcoming (tensile instability) and enhance the robustness of KDF-ISPH model, a novel Particle Shifting Technique (PST) is developed and then combined with the OPS scheme for the treatment of the free-surface area. To augment the order of the accuracy of the proposed model, a novel high-order Laplacian operator is derived based on the Taylor series expansion and is then utilized for the discretization of the Pressure Poisson

Equation (PPE) and diffusion terms in the governing equations. Moreover, a novel high-order kernel function is constructed through the combination of the cosine and signal functions and is then applied for the simulation of 1D Sod shock tube problem. The newly developed KDF-ISPH model is validated and evaluated against a series of challenging benchmark cases including dam break, stretching water drop, rotating square patch of fluid, and natural convection in square cavity. The results obtained from this article can give a deep insight into the process of the extracting of the governing operators in the context of the ISPH model and provide a necessary foundation and a numerical framework for the further development of the Lagrangian particle methods.

In article 2, the Kernel Derivative-Free (KDF) version of the conventional Weakly Compressible Smoothed Particle Hydrodynamics (WCSPH) model is introduced for the simulation of the free-surface flows and convection heat transfer problems where an explicit equation of state is employed for the calculation of the pressure field. However, as stated before, unlike the KDF-ISPH model, the traditional WCSPH method is characterized by spurious pressure fluctuation and density error accumulation which can immensely jeoparadise the accuracy and relaiability of the numerical solutions. In order to attenuate the unphysical pressure oscilation, a new additional diffusive term is derived and added into the continuity equation. A high-order Laplacian operator is also developed and then applied for the approximation of the diffusion terms (e.g., viscous term, thermal diffusion, and newly additional diffusion term in the continuity equation). Furthermore, a new high-order smoothing operator in the context of the MPS description (Moving Particle Semi-implicit) is also proposed and then applied for the treatment of the buoyancy force term in the natural convection heat transfer problems and also for the calculation of the pressure and temperature on the rigid walls. To further enhance the accuracy and stability of the model, a novel high-order kernel function is constructed and tested via simulation of the 1D Sod shock tube problem. A series of canonical test cases such as: dam break, stretching of a circular water drop, rotating square patch of fluid and natural convection heat transfer in a square enclosure are used to verify and assess the feasibility of the proposed modifications. The results obtained from this article can shed further light on the numerical performance and approximation properties of the Weakly Compressible version of the SPH.

In article 3, an improved version of the classical ISPH model is introduced where the Pressure Poisson Equation (PPE) is used for the prediction of the pressure field. To accomplish this, two

novel high-order gradient and Laplacian operators are derived based on the Taylor series expansion and are then implemented for the discretization of the Pressure Poisson Equation (PPE), gradient of pressure and the divergence of velocity in the governing equations. To enhance the regularity of the particles arrangment and circumvent the problem of tensile instability (particle clastering), the classical PST is combined by the Discrete Element Method (DEM) which results in more uniform particles distribution and stable numerical solution. Moreover, a roboust and efficient free-surface detection technique is developed for the accurate imposition of Dirichlet boundary condition (zero pressure) on the free surface area. To overcome the problem of density/viscousity discontinuity in the multiphase/multi-fluid flows, a novel high-order smoothing operator is also proposed based on the Taylor series expansion. The concept of mirror velocity technique is also incorporated into the method for the treatment of the rigid walls and the enforcement of the non-slip boundary condition. The results of this investigation can provide a deep insight into the ISPH model where derivatives of the kernel function are employed for the interpolation and particle approximation.

In article 4, an enhanced version of the classical MPS model is introduced for the modelling of multiphase/multi-fluid flows with high-density contrast. To this end, a set of high-order gradient and Laplacian operators are derived in the context of the MPS description and are then applied to the discretization of Navier-stokes and energy equations. Moreover, the combination of the explicit Third-order TVD Runge-Kutta scheme and two-step projection algorithm is employed for the discretization of the transient terms. A new high-order smoothing operator is also developed to circumvent the difficulties associated with physical discontinuities across the material interface. To solve the problem of uncertainty in the selection of appropriate kernel function, a new kernel function is constructed by merging the Gaussian and cosine functions and is succssesfully tested for the simulation of 1D Sod shock tube problem. The results of this study can provide a deep insight into the Lagrangian nature of the MPS model and its performance in handeling multiphase flow problems with high-density ratio.

3.5 Structure of the research project

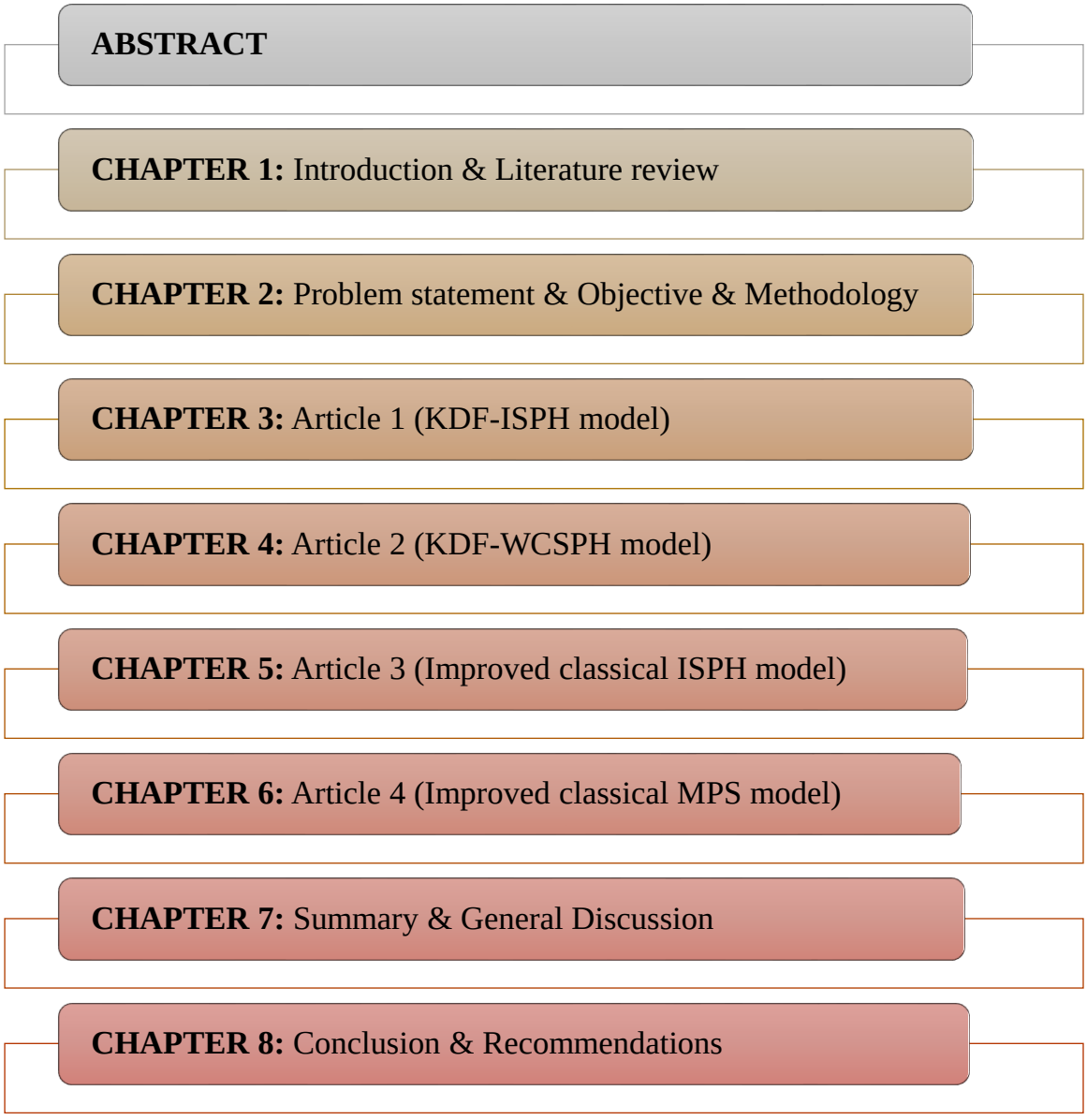

3.6 Novelties and modifications associated with each research article

Article 1 (KDF-ISPH model)	• New kernel function • New Laplacian operator • Modified the existing gradient operator • New Particle Shifting Technique (PST) • Implementing Mirror Velocity Technique • Implementing MLS technique
Article 2 (KDF-WCSPH model)	• New kernel function • New Laplacian operator • New smoothing operator • Modified the existing gradient operator • New additional diffusive term • Implementing Mirror Velocity Technique
Article 3 (Improved ISPH model)	• New kernel function • New gradient operator • New Laplacian operator • New hybrid PST+DEM • New free-surface detection technique • Implementing Mirror Velocity Technique
Article 4 (Improved MPS model)	• New kernel function • New gradient operator • New Laplacian operator • New smoothing operator • Implementing Mirror Velocity Technique • Implementing third-order TVD Runge-Kutta scheme

3.7 Publications

The results of the present research study have been published in four scientific journals as follows:

[1] Garoosi, Faroogh, and Ahmad Shakibaeinia. "Numerical simulation of entropy generation due to natural convection heat transfer using Kernel Derivative-Free (KDF) Incompressible Smoothed Particle Hydrodynamics (ISPH) model." *International Journal of Heat and Mass Transfer* 150 (2020): 119377.

[2] Garoosi, Faroogh, and Ahmad Shakibaeinia. "Numerical simulation of free-surface flow and convection heat transfer using a modified Weakly Compressible Smoothed Particle Hydrodynamics (WCSPH) method." *International Journal of Mechanical Sciences* 188 (2020): 105940.

[3] Garoosi, Faroogh, and Ahmad Shakibaeinia. "An improved high-order ISPH method for simulation of free-surface flows and convection heat transfer." *Powder Technology* 376 (2020): 668-696.

[4] Garoosi, Faroogh, and Ahmad Shakibaeinia. "Numerical simulation of Rayleigh-Bénard convection and three-phase Rayleigh-Taylor instability using a modified MPS method." *Engineering Analysis with Boundary Elements* 123 (2021): 1-35.

Chapter 4 ARTICLE 1: NUMERICAL SIMULATION OF ENTROPY GENERATION DUE TO NATURAL CONVECTION HEAT TRANSFER USING A KERNEL DERIVATIVE-FREE (KDF) INCOMPRESSIBLE SMOOTHED PARTICLE HYDRODYNAMICS (ISPH) MODEL

Faroogh Garoosi[*,a], Ahmad Shakibaeinia[a,b]

[a]Department of Civil, Geological and Mining Engineering, Polytechnique Montreal, Montreal, Quebec, Canada

[b]Canada Research Chair in Modeling of Complex Hydro-environmental Systems, Canada

Corresponding author: faroogh.garoosi@polymtl.ca,

Second author: ahmad.shakibaeinia@polymtl.ca

Abstract

This paper develops and applies a Kernel Derivative-Free (KDF) Incompressible Smoothed Particle Hydrodynamics (ISPH) model for analysis of entropy generation and heat transfer in fluid-structure coupling problems. A modified high order Laplacian operator is applied for the treatment of pressure-velocity coupling (Poisson's equation), while an explicit third-order TVD Runge-Kutta scheme is used for time integration of the momentum, energy and displacement equations. To improve the consistency and stability of the model, a new particle regularization technique based on the particle shifting is also introduced for simulating free-surface flows. The developed KDF-ISPH model is validated and evaluated for a series of challenging benchmark cases, including, dam break, stretching water drop, rotating square patch of fluid, and natural convection in square cavity. Accuracy and applicability of the method are further validated by analyzing entropy generation due to the natural convection heat transfer in three well-known geometries including: square cavity with hot obstacle inside, C-shaped enclosure, and square enclosure containing a pair of hot and cold horizontal pipes (heat exchanger). The results are found to be in good agreement with available numerical and experimental data. The accuracy of the developed KDF-ISPH with new Laplacian operator, for use in prediction of fluid flow and heat transfer characteristics is also proven. Finally, by combining the cosine and signal functions, a new high order smoothing kernel is constructed. The evaluation of this new kernel for the

propagation of shock wave in 1D tube demonstrates better global stability and consistency properties compared to two frequently used SPH kernels (i.e. cubic and quintic spline functions).

Keywords: KDF-ISPH, New Kernel Function, Particle Shifting Technique, Third-order TVD RK3, Convection Heat Transfer, Higher order Laplacian model

4.1 Introduction

Analysis of entropy generation and exergy efficiency due to natural convection phenomenon in closed enclosures (e.g., square or circular cavities) has received a great deal of research attention owing to its presence in the design of many heat transfer devices such as solar thermal receivers, cooling systems for electronic device, room ventilation, nuclear reactor design, and heat exchangers [1,2]. The natural convection in a semi-annulus enclosure containing several hot or cold obstacles is one of the fundamental and classical problems, which have been addressed by many researchers due to its application in heat exchangers [3–7]. Izadi et al. [8,9], Mohebbi [10,11] and Aghakhani et al. [12] investigated natural convection heat transfer in different geometries (L-shaped and C-shaped enclosures) and concluded that aspect ratio of the enclosure and Rayleigh number have a significant impact on the onset of the Rayleigh-Bénard convection and heat transfer rate within the enclosure. Similar observations were also reported by Li et al. [13], Biswal et al. [14,15] and Hassani et al. [16] who investigated the effects of the Rayleigh number and inclination angle of the enclosure on the entropy generation and pattern formation of the Rayleigh-Bénard convection using the Lattice Boltzmann model (LBM) and Galerkin weighted residual finite element method (GFEM). In the same context, Dutta et al. [17], Alnaqi et al. [18], Kefayati et al. [19], and Alkanhal et al. [20] implemented CVFDM, LBM and CVFEM methods to discretize the governing physical equations for modeling entropy generation rate during the natural convection heat transfer in the presence of transverse magnetic field. They showed that the MHD parameter reduces the flow intensity and causes average Nusselt number and overall entropy generation rate to attenuate accordingly. The problem of buoyancy-driven fluid flow with its corresponding exergy efficiency analysis inside closed enclosures has been investigated by several scholars utilizing various conventional CFD mesh-based approaches [21–28]. As remarked by Zainali et al. [29] most of the established CFD analysis tools rely heavily on an underlying lattice structures (mesh-based models) which may be fixed, or may be allowed to alter with rigid boundaries. This in turn may require specialized discretization techniques and

enhance computational cost. Recently, in a series of pioneering works, Hopp-Hirschler et al. [30], Aly et al. [31], Ng et al. [32], Yang et al. [33] and Zhang et al. [34] adopted Smoothed Particle Hydrodynamics (SPH) method to investigate natural convection heat transfer in complex geometries with curved boundaries. They stated that, SPH inherently can be considered as a robust alternative model in handling complex fluid-solid interaction (FSI) problems.

Historically, Smoothed Particle Hydrodynamics (SPH) was first proposed by Lucy [35] and Gingold et al. [36] as a fully Lagrangian particle technique to describe the evolution of planet-disk systems. During the past years, many researchers have been motivated to employ some positive features of SPH method in solving a wide range of engineering and scientific problems. Simulation of gas-solid fluidization and free surface flows during the injection molding [37,38], analysis of nuclear reactor safety and fuel drop impact on heated surfaces [39,40], liquid sloshing in a rectangular tank and bubble rising in a viscoelastic fluid [41–45], simulation of Rayleigh-Taylor Instability and fluid flow over the airfoil and square cylinder [46–49], analysis of free surface thermal flow and modeling of industrial processes involving heat transfer [50,51], simulation of tsunamis water waves generated by landslides and 3D dam-break flows with breaking waves [52,53], simulations of sediment transport and 2D dam break [54–56] are just a few examples of such applications which have been reported in the literature. A comprehensive and up-to-date review of recent applications and future prospects of the SPH method can be found in works of Wang et al. [57] and Shadloo et al. [58].

However, although the SPH as a truly mesh-free particle method has been shown to have the best overall performance over the traditional fixed grid methods in handling highly nonlinear multiphase flows with a free surface but it has some major drawbacks in terms of the numerical instability (i.e. the particles clustering and non-physical pressure oscillation) that can directly degrade the order of accuracy of the numerical scheme and often lead to premature termination of calculations. Until now, various attempts have been made to eliminate the occurrence of tensile instability and attenuate spurious fluctuations in pressure time history. Hongbin et al. [59] carried out a comparative study between ten different types of the kernel function in simulating one dimensional shock tube problem and pointed out that type of the smoothing functions has a significant influence on the accuracy and stability of the SPH. Similar results were reported by Yang et al. [60,61] who constructed two different kernel functions (cosine and hyperbolic shaped

kernel functions) and successfully applied to simulate dam break and viscous liquid drop benchmark cases. Aside from the role of kernel function on the numerical stability, another potential source of the inconsistency in the SPH is the negative pressure in the vicinity of the media interfaces which in turn leads to the formation of particle clusters in those areas. To overcome this shortcoming, Sun et al. [62] proposed a new technique called Tensile Instability Control (TIC) that was achieved by changing the momentum equation into the non-conservative form. Since, their scheme does not entirely respect the Taylor expansion, they suggested that, this technique should be only applied to areas with negative pressure values. Another factor that causes tensile instability comes from the Lagrangian formulation of the SPH itself. Generally, SPH is formulated by the hypothesis that particle distribution is uniform across the whole flow domain while this assumption is not always valid for violent free surface flows. To get a more uniform particle distribution and enhance the order of accuracy of gradient operator, Oger et al. [63,64] proposed a new renormalization procedure based on the Taylor series expansion and showed that renormalization of density and pressure gradient can successfully avoid any particle bunching and numerical fractures. Similar findings have been reported by Schwaiger [65] who established a new high-order Laplace operator in the framework of SPH for the treatment of pressure-Poisson equation. Another numerical scheme that can effectively redundant the excessive stretching and clustering of particles is through shifting the particles from higher concentration to the lower one. The idea of rearranging particles to prevent tensile instability came from Xu et al. [66] as a Particle Shifting Technique (PST) to solve the problem of heterogeneity in particle distributions. The PST was then extended and modified by Skillen et al. [67] and Sun et al. [68] based upon Fick's law of diffusion and Taylor expansion to control the total magnitude of particles displacement and its direction. Recently, Khayyer et al. [69] optimized particle shifting technique (OPS) and showed that by calculating the surface tangential vector and neglecting the movement of particles in the normal direction, PST can be straightforwardly applied to entire particles. Since, knowledge about the interface position and its nearby particles are also required for solving pressure Poisson equation (PPE) and enforcement of the Dirichlet boundary condition along the free-surface regions, during the last decade, many researchers have initiated studies on the particle labeling algorithms. Generally, a number of effective methods which have been proposed for free-surface detection can be classified into two different groups: kernel-based techniques (like PND [70]) and coverage detection methods (like

Scan Region Technique [71]). Duan et al. [72] and Zhang et al. [73] adopted the concept of the Particle Number Density (PND) proposed by Koshizuka et al. [70] for free-surface detection where a threshold value determines whether desired particle belongs to the free surface or not.

In light of the above literature survey, the objective of the present work is to introduce a new high-order Kernel Derivative-Free (KDF) incompressible smoothed particle hydrodynamic (ISPH) for analysis of entropy generation due to natural convection heat transfer and multiphase flows with free-surface. The spatial derivative approximation technique of proposed model is free from derivatives of kernel. In addition to increasing the SPH simplicity, this technique eliminates the differentiability condition from the kernel function, providing more freedom for the choice of kernel. For this purpose, a new high order smoothing kernel is first constructed and then applied for simulation of the propagation of shock wave in 1D tube. In the second step, higher order Laplacian operator proposed by Schwaiger [65] is reformulated according to the KDF model and then applied for the treatment of pressure-velocity coupling (Poisson's equation). To enhance the computational stability and accuracy of the method, a new Particle Shifting technique is also introduced for simulation of the violent flows. By conducting simulations of four different benchmark cases such as: dam break, stretching water drop, rotating square patch of fluid, and natural convection in square cavity, stability and accuracy of the proposed method (KDF-ISPH) have been verified. The results are presented in form of the streamlines, isotherms, velocity (u,v) field, local Bejan number, total entropy generation, average Nusselt number, related graph and chart.

4.2 Problem statement and governing equations

A schematic geometry of the eight different problems and their boundary conditions are shown in Fig. 4-1. Cases A1 to A5 are employed for validation of the proposed new model, while cases B1 to B3 are used for analysis of the entropy generation due to natural convection heat transfer. In all cases, the fluid flow ($\Pr = 0.71$ or 6.2) is considered as incompressible, Newtonian, two-dimensional and laminar. The only exception is the case A1, where fluid is compressible and subsequently the equation of state is used to estimate the pressure field. For the convection heat transfer part of the study, the thermo-physical properties of the fluid are assumed to be constant except for the density, which varies in accordance with the Boussinesq approximation. In cases A5, B1, B2 and B3, the temperatures $T_h = 304\,K$ and $T_c = 296\,K$ are uniformly imposed along

the hot and cold surfaces while other parts of the enclosure walls are all thermally insulated. The numerical simulations are performed using, an in-house CFD code written in a FORTRAN program.

For laminar and incompressible viscous hydrodynamic problems with convection heat transfer, the 2D continuity, momentum, energy and displacement equations in the Lagrangian frame are the ones that follow [74]:

$$\frac{\partial u}{\partial x}+\frac{\partial v}{\partial y}=0, \tag{4-1}$$

$$\frac{Du}{Dt}=-\frac{1}{\rho}\frac{\partial p}{\partial x}+\frac{\mu}{\rho}\left(\frac{\partial^2 u}{\partial x^2}+\frac{\partial^2 u}{\partial y^2}\right), \tag{4-2}$$

$$\frac{Dv}{Dt}=-\frac{1}{\rho}\frac{\partial p}{\partial y}+\frac{\mu}{\rho}\left(\frac{\partial^2 v}{\partial x^2}+\frac{\partial^2 v}{\partial y^2}\right)+F_b, \tag{4-3}$$

$$\frac{DT}{Dt}=\alpha\left(\frac{\partial^2 T}{\partial x^2}+\frac{\partial^2 T}{\partial y^2}\right), \tag{4-4}$$

$$\frac{D\mathbf{r}}{Dt}=\mathbf{u}, \tag{4-5}$$

where **u**: (*u*, *v*) and **r**: (*x*, *y*) are the velocity and position vectors. *D* is the material (Lagrangian) derivative and F_b is the body force, which is the gravitational ($F_b = g$) in the multi-phase flow or buoyancy force ($F_b = -g\,\beta\,(T - T_c)$) in natural convection heat transfer according to Boussinesq approximation with T_c being the reference fluid temperature. By combining local thermodynamic equilibrium and linear transport theory, the rate of local entropy generation for Newtonian flow can be expressed as [75]:

$$\begin{aligned} S_T &= \frac{k}{T_0^2}(\nabla T)^2 = \frac{k}{T_0^2}\left[\left(\frac{\partial T}{\partial x}\right)^2+\left(\frac{\partial T}{\partial y}\right)^2\right] \\ S_F &= \frac{\mu}{T_0}\phi = \frac{\mu}{T_0}\left[2\left(\frac{\partial u}{\partial x}\right)^2+2\left(\frac{\partial v}{\partial y}\right)^2+\left(\frac{\partial u}{\partial y}+\frac{\partial v}{\partial x}\right)^2\right] \end{aligned} \tag{4-6}$$

where S_T , S_F , *k* and T_0 are thermal dissipation, fluid friction irreversibility caused by velocity gradient, thermal conductivity of working fluid and bulk temperature, respectively. Eq. (4-6) can

be converted to the dimensionless form by introducing the following non-dimensional parameters:

$$X=\frac{x}{H},\qquad Y=\frac{y}{H},\qquad U=\frac{uH}{\alpha},\qquad V=\frac{vH}{\alpha},\qquad P=\frac{pH^2}{\rho\alpha^2},\qquad \theta=\frac{T-T_c}{T_h-T_c}.$$
$$t^*=\frac{t\alpha}{H^2},\qquad Ra=\frac{g\beta(T_h-T_c)H^3}{\alpha\nu},\qquad \Pr=\frac{\nu}{\alpha}. \tag{4-7}$$

$$S_T=\left[\left(\frac{\partial\theta}{\partial X}\right)^2+\left(\frac{\partial\theta}{\partial Y}\right)^2\right]$$
$$S_F=\varphi\left[2\left(\frac{\partial U}{\partial X}\right)^2+2\left(\frac{\partial V}{\partial Y}\right)^2+\left(\frac{\partial U}{\partial y}+\frac{\partial V}{\partial X}\right)^2\right] \tag{4-8}$$

In Eq. (4-8), φ is called irreversibility distribution ratio and taken as 10^{-4} similar to work of Ilis et al. [76]. The dimensionless total average entropy generation ($\overline{S}_{tot}$) is given by the summation of the entropy generation due to heat transfer and fluid friction, which can be calculated through the integration of the local entropy generation (S_{tot}) over the computational domain, as:

$$\overline{S}_T=\int_{dv}S_T\,dv,\qquad \overline{S}_F=\int_{dv}S_F\,dv,\qquad \overline{S}_{tot}=\overline{S}_T+\overline{S}_F \tag{4-9}$$

An alternative parameter to determine the relative importance of the heat transfer irreversibility is the Bejan number (Be) defined as [75]:

$$Be=\frac{S_T}{S_{tot}}\qquad \overline{Be}=\int_{dv}Be \tag{4-10}$$

Since, Bejan number ranges from 0 to 1, the condition of $Be<0.5$ implies that the irreversibility is dominated by fluid friction effects whereas $Be>0.5$is the case, in which irreversibilities due to the heat transfer dominate the processes. For the particular case of $Be=0.5$ entropy generation due to the viscous effects and the heat transfer are comparable.

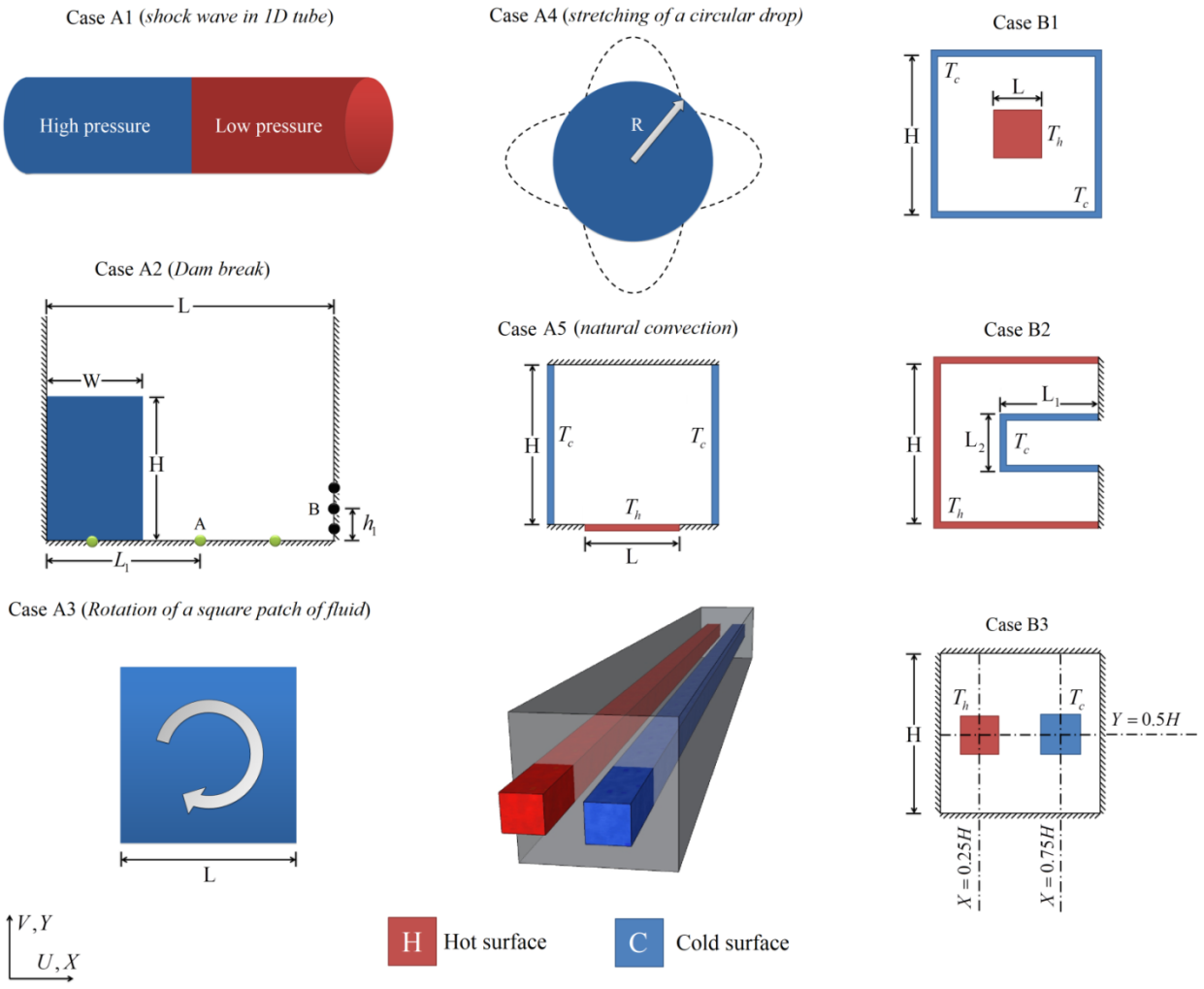

Figure 4-1 Schematical configuration of the considered problems with coordinate system and boundary conditions.

4.3 KDF-ISPH formulation and solution methodology

Here, a Kernel Derivative-Free (KDF) Incompressible Smoothed Particle Hydrodynamic (ISPH) model is employed to solve the flow and heat transfer governing equations. Similar to the meshfree particle methods [61], [66], [74], the governing equations are discretized using a set of free-to-move particles associated with physical properties of the system (e.g. density, viscosity, thermal conductivity and so forth). However, to approximate the spatial derivatives, the present

method uses the kernel function itself, instead of its derivatives. Appendix (A) explains the derivation of the relevant spatial operators (i.e. gradient, divergence, and Laplacian). A summary of operators used for approximation of the governing equations is listed in Table 4-1.

Table 4.1 List of the equations used for calculating gradient, divergence, and Laplacian operators.

Operator	Equation used
Divergence (for velocity) ($\mathbf{u}_x^{'}, \mathbf{u}_y^{'}$) Gradient (for temperature) ($\theta_x^{'}, \theta_y^{'}$)	Eq. (4-A4) is applied in the present work whereas Eq. (4-A2) can also be used.
Gradient (for pressure) ($p_x^{'}, p_y^{'}$)	Modified form of the Eq. (4-A4) is applied in the present work where $\chi = 1$ and $\chi = -1$ are used for internal and surface particles, respectively. (see Eq. (4-12))
Gradient (for concentration used in the PST)	Eqs. (4-A4) and (4-A5) without ($f_j - f_i$) is applied in the present work.
Buoyancy force in natural convection (θ_i)	Eq. (4-A3) is applied in the present work whereas Eq. (4-A2) can also be used.
Pressure on the solid walls (p_i) Temperature on the insulated walls (θ_i)	Eq. (4-A2) is applied in the present work whereas Eq. (4-A3) can also be used.
Laplacian (for pressure $\nabla^2 P$ and diffusion $\nabla^2\mathbf{u}, \nabla^2\theta$)	Eq. (4-A11) is applied in the present work whereas Eq. (4-A12) can also be used.

The solution method uses a combination of the third-order TVD Runge-kutta time integration scheme (TVD RK3) with a two-step projection method (proposed by Chorin [77]) for treatment of the velocity-pressure coupling. At first, a temporary particle velocity field without the pressure gradient is computed by solving the momentum balance equation as:

$$\frac{\mathbf{u}^* - \mathbf{u}^n}{\Delta t} = \upsilon \nabla^2 \mathbf{u}^n + \mathbf{F}_B \qquad (4\text{-}11)$$

where $\mathbf{u}$ and $\mathbf{F}_B$ are velocity components and body force vector, respectively. By considering the Quasi-Compressibility (Eq. (4-B13)), pressure at time level n^1 (first step of TVD RK3) is then evaluated implicitly by solving the pressure Poisson equation as:

$$\nabla^2 p^{(n+1)} = \frac{\rho^* \nabla \cdot \mathbf{u}^*}{\Delta t} + \lambda\left(\frac{\rho_0 - \rho^*}{\Delta t^2} + \frac{1}{\rho^*}\left[\frac{\partial \rho^*}{\partial x}\frac{\partial p^{(n+1)}}{\partial x} + \frac{\partial \rho^*}{\partial y}\frac{\partial p^{(n+1)}}{\partial y}\right]\right) \tag{4-12}$$

λ is constant coefficient (0 or 1) and used for stability analysis of the system (for further details refer to appendix B). After obtaining the pressure field and its gradient ($\frac{1}{\rho}\nabla p^{(1)}$), accelerations of the fluid particles ($D\mathbf{u}/Dt$) can be determined through Eqs. (4-2) and (4-3). To calculate ∇p across the whole particles (inner and surface particles), Eq. (4-A4) has been generalized according to *Tensile Instability Control (TIC)* suggested by Sun et al. [62] as follows:

$$\begin{bmatrix} \frac{\partial p}{\partial x} \\ \frac{\partial p}{\partial y} \end{bmatrix}_i = L \begin{bmatrix} \sum_{j=1}^{N} x_{ij}(p_j - \chi p_i) W_{ij} \frac{m_j}{\rho_j} \\ \sum_{j=1}^{N} y_{ij}(p_j - \chi p_i) W_{ij} \frac{m_j}{\rho_j} \end{bmatrix} \qquad L = \begin{bmatrix} \sum_{j=1}^{N} x_{ij}^2 W_{ij} \frac{m_j}{\rho_j} & \sum_{j=1}^{N} x_{ij} y_{ij} W_{ij} \frac{m_j}{\rho_j} \\ \sum_{j=1}^{N} x_{ij} y_{ij} W_{ij} \frac{m_j}{\rho_j} & \sum_{j=1}^{N} y_{ij}^2 W_{ij} \frac{m_j}{\rho_j} \end{bmatrix}^{-1} \tag{4-13}$$

where χ is equals to1 for internal (conservative form) and -1 for surface particles (non-conservative form). *m* is particle mass, W_{ij} is the kernel function, and i and j refer to the target particle and its neighbors, respectively. The Laplacian and divergence operators provided in Appendix A (by Eqs. (4-A11) and (4-A4)) are used to solve the PPE equation and calculate diffusion ($\nabla^2\mathbf{u}$), conduction ($\nabla^2 T$) and divergence ($\nabla\cdot\mathbf{u}$) terms. The temperature in the body force ($F_b = -g\beta(T - T_c)$) for convection heat transfer is treated by Shepard approximant (Eq. (4-A3)). After solving equations (4-2) to (4-4), the velocity vector ($\mathbf{u}^{(1)}$), position vector ($\mathbf{r}^{(1)}$) and temperature ($\theta^{(1)}$) of the particles can be updated using the first step of the Runge-Kutta method as:

$$\begin{aligned} \mathbf{u}^{(1)} &= \mathbf{u}^{(n)} + \Delta t \frac{D\mathbf{u}^{(n)}}{Dt} \\ \mathbf{r}^{(1)} &= \mathbf{r}^{(n)} + \Delta t\, \mathbf{u}^{(1)} \\ \theta^{(1)} &= \theta^{(n)} + \Delta t \frac{D\theta^{(n)}}{Dt} \end{aligned} \tag{4-14}$$

See also appendix C for details of TVD RK3. In the second step the above procedure is repeated using updated values of $\mathbf{u}^{(1)}$, $\mathbf{r}^{(1)}$ and $\theta^{(1)}$, obtained in the first step (instead of the $\mathbf{u}^n$, $\mathbf{r}^n$ and θ^n) to compute $\mathbf{u}^{(2)}$, $\mathbf{r}^{(2)}$ and $\theta^{(2)}$.

$$\mathbf{u}^{(2)} = \frac{3}{4}\mathbf{u}^{(n)} + \frac{1}{4}\mathbf{u}^{(1)} + \frac{1}{4}\Delta t \frac{D\mathbf{u}^{(1)}}{Dt}$$
$$\mathbf{r}^{(2)} = \frac{3}{4}\mathbf{r}^{(n)} + \frac{1}{4}\mathbf{r}^{(1)} + \frac{1}{4}\Delta t\, \mathbf{u}^{(2)} \qquad (4\text{-}15)$$
$$\theta^{(2)} = \frac{3}{4}\theta^{(n)} + \frac{1}{4}\theta^{(1)} + \frac{1}{4}\Delta t \frac{D\theta^{(1)}}{Dt}$$

This trend is continued for the third (last) step, where particles are displaced to the new position $\mathbf{r}^{(n+1)}$ with updated velocity $\mathbf{u}^{(n+1)}$ and temperature $\theta^{(n+1)}$ as:

$$\mathbf{u}^{(n+1)} = \frac{1}{3}\mathbf{u}^{(n)} + \frac{2}{3}\mathbf{u}^{(2)} + \frac{2}{3}\Delta t \frac{D\mathbf{u}^{(2)}}{Dt}$$
$$\mathbf{r}^{(n+1)} = \frac{1}{3}\mathbf{r}^{(n)} + \frac{2}{3}\mathbf{r}^{(2)} + \frac{2}{3}\Delta t\, \mathbf{u}^{(n+1)} \qquad (4\text{-}16)$$
$$\theta^{(n+1)} = \frac{1}{3}\theta^{(n)} + \frac{2}{3}\theta^{(2)} + \frac{2}{3}\Delta t \frac{D\theta^{(2)}}{Dt}$$

At the end of the process, the mean Nusselt number is determined by integrating the local Nusselt number over the hot and cold surfaces as:

$$\begin{bmatrix} \frac{\partial\theta}{\partial X} \\ \frac{\partial\theta}{\partial Y} \end{bmatrix} = L \begin{bmatrix} \sum_{j=1}^{N} x_{ij}(\theta_j - \theta_i) W_{ij} \frac{m_j}{\rho_j} \\ \sum_{j=1}^{N} y_{ij}(\theta_j - \theta_i) W_{ij} \frac{m_j}{\rho_j} \end{bmatrix} \qquad L = \begin{bmatrix} \sum_{j=1}^{N} x_{ij}^2 W_{ij} \frac{m_j}{\rho_j} & \sum_{j=1}^{N} x_{ij} y_{ij} W_{ij} \frac{m_j}{\rho_j} \\ \sum_{j=1}^{N} x_{ij} y_{ij} W_{ij} \frac{m_j}{\rho_j} & \sum_{j=1}^{N} y_{ij}^2 W_{ij} \frac{m_j}{\rho_j} \end{bmatrix}^{-1} \qquad (4\text{-}17)$$

On the active horizontal or vertical walls of the enclosure:

$$\overline{Nu} = \frac{1}{L}\int_0^L \frac{\partial\theta}{\partial X} dY, \quad \overline{Nu} = \frac{1}{H}\int_0^H \frac{\partial\theta}{\partial Y} dX \qquad (4\text{-}18)$$

On the walls of the obstacle:

$$\overline{Nu} = \frac{\int_{L_1}^{L_2} \frac{\partial\theta}{\partial X}\Big|_{Left} dY + \int_{L_1}^{L_2} \frac{\partial\theta}{\partial X}\Big|_{Right} dY + \int_{H_1}^{H_2} \frac{\partial\theta}{\partial Y}\Big|_{Bottom} dX + \int_{H_1}^{H_2} \frac{\partial\theta}{\partial Y}\Big|_{Top} dX}{A = 2(L_2 - L_1 + H_2 - H_1)}$$

where A is the non-dimensional effective surface area. At this stage, by having the velocity and temperature at the $\mathbf{u}^{n+1}, \theta^{n+1}$, entropy generation due to the viscous effects and the heat transfer can be computed using Eq. (4-8) and gradient operator presented by Eq. (4-A4).

Finally, by considering no slip condition and zero heat flux on the insulated walls, the boundary conditions would be adjusted as follows:

$$\begin{aligned}
&\frac{\partial \theta}{\partial \vec{n}} = 0 && \text{On the insulated walls of the enclosure}\\
&\theta = 1,\ \theta = 0 && \text{On the hot and cold surfaces}\\
&U = V = 0, && \text{On the solid-fluid interfaces}\\
&U_{ghost} = 2U_{solid-fluid\ \ interface} - U_{fluid} && \text{On the ghost particles (mirror velocity)}\\
&V_{ghost} = 2V_{solid-fluid\ \ interface} - V_{fluid} &&
\end{aligned} \qquad (4\text{-}19)$$

It should be noted that, in order to prevent the particles penetration and enforce no-slip conditions on the solid walls, Fixed Ghost Particles technique (dynamic boundary algorithm) proposed by Marrone et al. [78] is used to set up boundary conditions. More precisely, in this method solid-fluid interfaces are used as a reference point where mirror velocity of the fluid particles close to the solid boundary line (in active area) is interpolated on the other side of the rigid boundary. The pressure of the boundary particle (p_i) and temperature (θ_i) on the adiabatic walls of the enclosure are computed using Eq. (4-12) [79] such that at first, p_i or θ_i is calculated on the solid-fluid interface and then the obtained values are assigned to the corresponding ghost particles in the same rows or columns (see Fig. 4-2 and Eq. (4-A2) in appendix A).

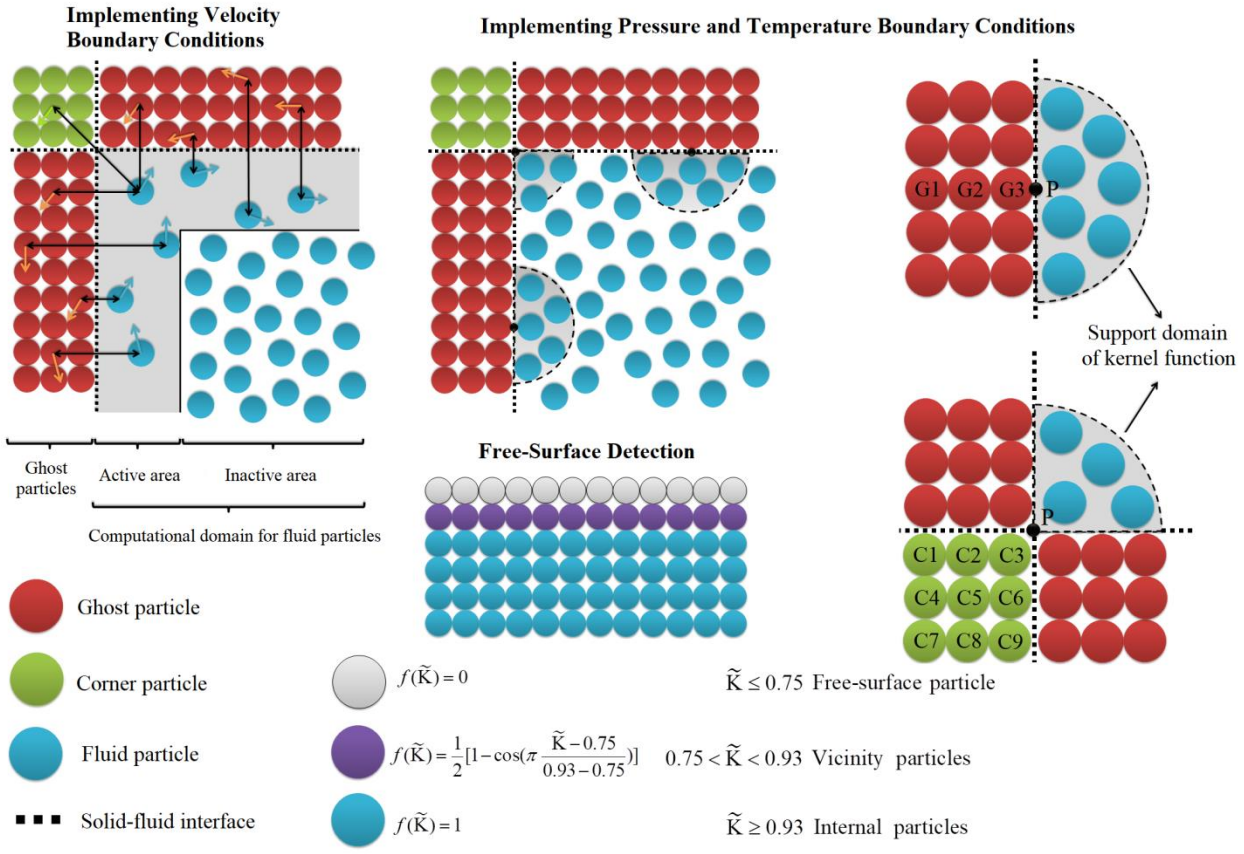

Figure 4-2Example of the Fixed Ghost Particles, free-surface detection techniques, calculation of pressure and temperature on the wall particles.

$$\begin{bmatrix} p_i \\ p'_{i,x} \\ p'_{i,y} \end{bmatrix} = L \begin{bmatrix} \sum_{j=1}^{N} p_j W_{ij} dV \\ \sum_{j=1}^{N} x_{ij} p_j W_{ij} dV \\ \sum_{j=1}^{N} y_{ij} p_j W_{ij} dV \end{bmatrix} \quad L = \begin{bmatrix} \sum_{j=1}^{N} W_{ij} dV & \sum_{j=1}^{N} x_{ij} W_{ij} dV & \sum_{j=1}^{N} y_{ij} W_{ij} dV \\ \sum_{j=1}^{N} x_{ij} W_{ij} dV & \sum_{j=1}^{N} x_{ij}^2 W_{ij} dV & \sum_{j=1}^{N} x_{ij} y_{ij} W_{ij} dV \\ \sum_{j=1}^{N} y_{ij} W_{ij} dV & \sum_{j=1}^{N} x_{ij} y_{ij} W_{ij} dV & \sum_{j=1}^{N} y_{ij}^2 W_{ij} dV \end{bmatrix}^{-1} \tag{4-20}$$

Note that above system of the equations can be solved using Gaussian elimination with partial pivoting.

4.4 New kernel function and Particle Shifting Technique (PST)

As mentioned before, the accuracy and consistency of the SPH and other mesh-free particle methods rely heavily on the type of the kernel function and uniformity of the particles within the computational domain. Thus, in this section a new kernel function and Particle shifting technique are introduced and discussed in details.

4.4.1 kernel function

Here a new smoothing kernel is constructed by combing cosine and signal functions, as:

$$W_{ij} = \alpha_D \begin{cases} \dfrac{\cos^3(\pi R/6)}{25+13R^2} & 0 \le R \le 3 \\ 0 & R > 3 \end{cases} \qquad (4\text{-}21)$$

$$\alpha_1 = \frac{12.9371393}{h},\ \alpha_2 = \frac{6.6067745}{h^2},\ \alpha_3 = \frac{3.3694114}{h^3},$$

where $R = \left|\mathbf{r}_{ij}\right| / h$ is relative distance between two particles *i* and *j*. h denotes a smoothing length and α_D is a constant number (*D*= 1, 2, 3 is the number of dimensions), which has been calculated using Simpson integration rule to satisfy the partition of unity criteria ($\sum_{j=1}^{N} W_{ij} dV = 1$). The efficiency and robustness of the newly proposed kernel function are demonstrated via numerical simulation of the shock-wave propagation in 1D tube, where two commonly used cubic (Eq. (4-22)) and quintic (Eq. (4-23)) spline functions [80] are considered for comparison purpose.

$$W_{ij} = \alpha \begin{cases} 2/3 - R^2 + R^3/2 & 0 \le R \le 1 \\ (2-R)^3/2 & 1 < R \le 2 \\ 0 & R > 2 \end{cases} \qquad (4\text{-}22)$$

$$\alpha_1 = \frac{1}{h},\ \alpha_2 = \frac{15}{7\pi h^2},\ \alpha_3 = \frac{3}{2\pi h^3},$$

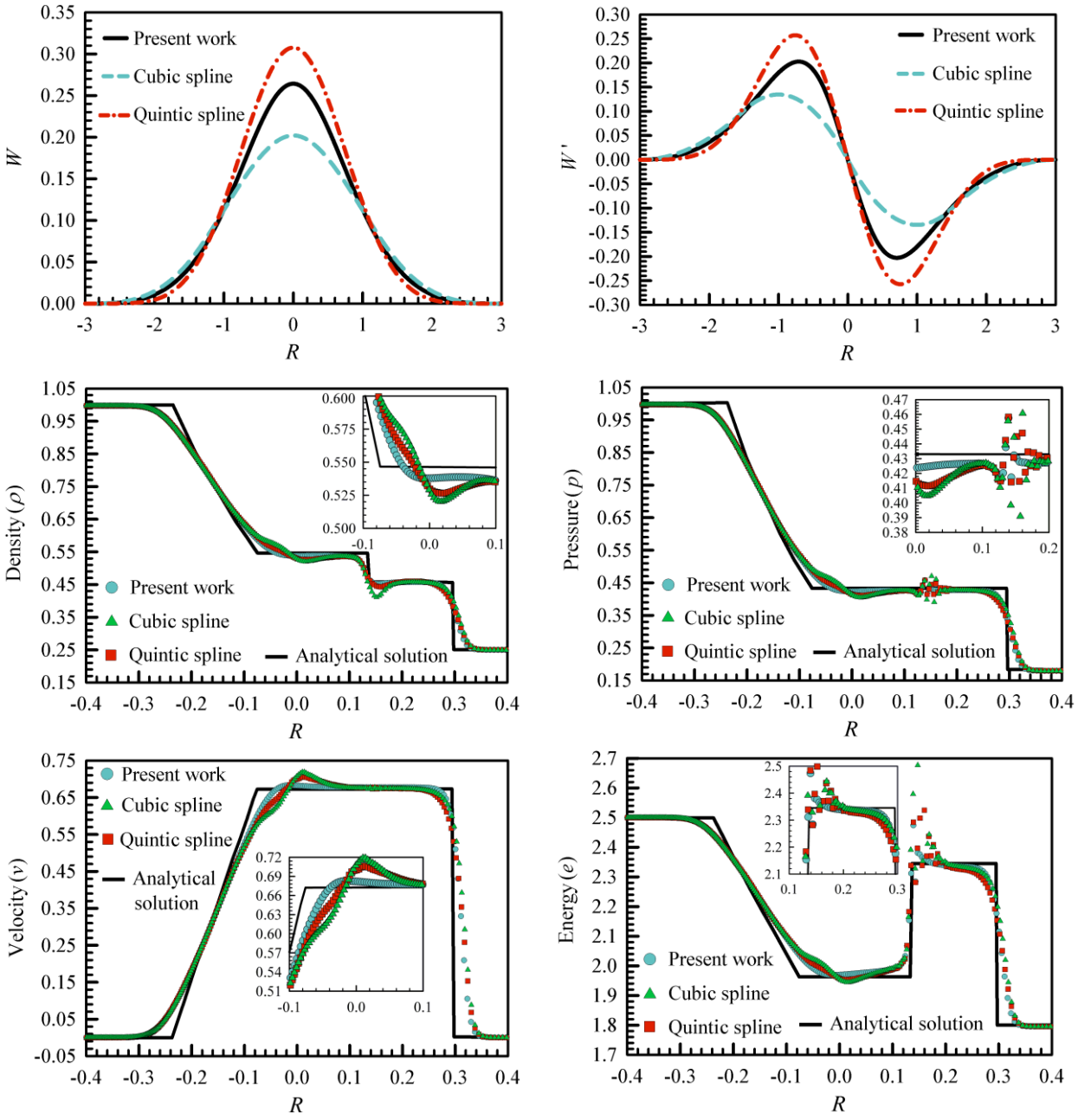

Figure 4-3 Comparison of the density, pressure, velocity and energy variations between present kernel function and those obtained by cubic and quintic spline functions in simulation of the shock tube at t=0.2s.

$$W_{ij}=\alpha\begin{cases}(3-R)^5-6(2-R)^5+15(1-R)^5 & 0\le R\le 1\\ (3-R)^5-6(2-R)^5 & 1<R\le 2\\ (3-R)^5 & 2<R\le 3\\ 0 & R>3\end{cases} \qquad (4\text{-}23)$$

$$\alpha_1=\frac{1}{120h},\ \alpha_2=\frac{7}{478\pi h^2},\ \alpha_3=\frac{1}{120\pi h^3},$$

The initial conditions of the shock tube (case A1) are similar to work of Gui-rong [80] i.e.:

$$\begin{array}{llllll} x\le 0, & \rho=1, & u=0, & e=2.5, & p=1, & \Delta x=0.001875,\ m=0.001875\\ x>0, & \rho=0.25, & u=0, & e=1.795, & p=0.1795, & \Delta x=0.0075,\ m=0.001875\end{array} \qquad (4\text{-}24)$$

The problem is simulated for $t=0.2s$ with Δt=0.005, where 320 particles are evenly located in the left half of the tube $[-0.6,0]$ with high-density and pressure while 80 particles are distributed in low-density area $[0,0.6]$ (see also appendix D). The proposed new kernel function itself and its first derivate (in 2D space) are depicted in Fig. 4-3. As the figure shows, the presented kernel function is located between cubic and quintic spline functions and declines rapidly with the increment of the distance. Due to intrinsic feature of the cosine function ($\cos^3(\pi R/6)$), it is sufficiently smooth and has a finite compact support even for the second derivative (compared to cubic spline function), leading to more stable numerical solutions. More importantly, unlike the piecewise quintic spline, which consists of three parts (requiring additional computational time), the developed kernel has only one piece and requires less number of the particles to reach the same level of the accuracy. Fig. 4-3 reveals that the new kernel function can successfully capture the positions of the shock ($x=0.3$) and rarefaction waves ($-0.25\le x\le 0$) with minimal fluctuation in the density, pressure and velocity profiles comparing to two other kernels. For instance, the estimated density, pressure and internal energy at the contact surface region ($x=0.135$) by proposed kernel function seems to be more accurate than those of the quintic kernels.

4.4.2 Particle Shifting Technique (PST)

Since, in Lagrangian framework, particles potentially have a tendency to move along the streamline trajectory, particle bunching is likely to happen within the computational domain. In order to preserve the uniformity of particles and enhance the robustness of KDF-ISPH model, a new particle shifting technique (PST) is developed to maintain homogeneity in the particle

distributions. In fact, under the effects of PST, particles are encouraged to deviate from their streamlines to the region with low particle concentration, resulting in a notable improvement in the uniformity of particle arrangement. By eliminating the term ($f_j - f_i$) from gradient operator (Eq. (4-A5)) and multiplying it by diffusion controller parameter ($D \le 0.5h^2$) [67], a particle shifting displacement vector ($\delta \mathbf{r}_i$) can be obtained as:

$$\nabla C_x = \frac{\sum_{j=1}^{N} x_{ij} W_{ij} \frac{m_j}{\rho_j}}{\sum_{j=1}^{N} x_{ij}^2 W_{ij} \frac{m_j}{\rho_j}}, \qquad \nabla C_y = \frac{\sum_{j=1}^{N} y_{ij} W_{ij} \frac{m_j}{\rho_j}}{\sum_{j=1}^{N} y_{ij}^2 W_{ij} \frac{m_j}{\rho_j}} \qquad \delta \mathbf{r}_i = -D \times \nabla C_i \tag{4-25}$$

$$\mathbf{r}_i^{(n+1)*} = \mathbf{r}_i^{(n+1)} + \delta \mathbf{r}_i^{(n+1)} \tag{4-26}$$

The terms ∇C_x and ∇C_y provide normal vector (normal to the interface points outside the dense area towards the dilute one with low particle concentration) on the each particles. Note that, particle shifting displacement obtained from Eq. (4-25) should be only applied on the inner particles whereas for free surface particles and their vicinity, the OPS scheme is used as:

$$\delta \mathbf{r}_{i,t} = -D \times (I - n_i \otimes n_i) \cdot \nabla C_i \tag{4-27}$$

where $\mathbf{n}_i$ is the corrected form of the $\delta \mathbf{r}_i$ near the interface which is calculated through Eq. (4-A4). $\delta \mathbf{r}_{i,t}$ is particle shifting displacement in tangential direction (for more details see work of Khayyer et al. [69]). After shifting the particles to the new position, the velocity field is modified accordingly by Taylor-series approximation as:

$$\begin{aligned} \phi_i^{(n+1)*} &= \phi_i^{(n+1)} + \nabla \phi_i^{(n+1)} \cdot \delta \mathbf{r}_i^{(n+1)} \\ \mathbf{u}_i^{(n+1)*} &= \mathbf{u}_i^{(n+1)} + \nabla \mathbf{u}_i^{(n+1)} \cdot \delta \mathbf{r}_i^{(n+1)} \end{aligned} \tag{4-28}$$

where $\nabla \mathbf{u}_i^{(n+1)}$ is gradient of velocity components. Prior to implementing particle regularization technique, an efficient free surface detection scheme should be applied to identify the type of each particle. In the current work, the combination of the Particle Number Density (PND) [70] and divergence of the displacement [67] is employed to track the position of the interface.

$$\mathrm{K}_1 = \sum_{j=1}^{N} W_{ij} \frac{m_j}{\rho_j}, \qquad \mathrm{K}_2 = \sum_{j=1}^{N} x_{ij} \nabla W_{ij,x} \frac{m_j}{\rho_j} + \sum_{j=1}^{N} y_{ij} \nabla W_{ij,y} \frac{m_j}{\rho_j} \tag{4-29}$$

In Eq. (4-29), the first and second terms are respectively PND (K_1) and divergence of the displacement ($\mathrm{K}_2 = \nabla \cdot \mathbf{r}$) which are ideally equal to unity and 2 when particle has a full kernel support (internal particles). Thus any deviation from these values indicates that kernel function is truncated and particle belongs to the interface area (see also Fig. 4-2).

$$\mathrm{K} = (\mathrm{K}_1 + \mathrm{K}_2)/3,$$

$$f(\mathrm{K}) = \begin{cases} 0 & \mathrm{K} \le 0.75 \quad \text{Free-surface particle} \\ \frac{1}{2}[1 - \cos(\pi \frac{\mathrm{K} - 0.75}{0.93 - 0.75})] & 0.75 < \mathrm{K} < 0.93 \quad \text{Vicinity particles} \\ 1 & \mathrm{K} \ge 0.93 \quad \text{Internal particles} \end{cases} \tag{4-30}$$

In Eq. (4-30), for intermediate particles ($0.75 < \mathrm{K} < 0.93$), smoothing function suggested by Skillen et al. [67] is employed to remove the discontinuity between $f(\mathrm{K}) = 1$ and $f(\mathrm{K}) = 0$. This equation has also been used to impose Dirichlet boundary conditions in solving Pressure Poisson equation in the form of the $[\mathbf{A}]\mathbf{x} = \mathbf{b}$ as follow:

$$a_{ii} p_i + \sum f(\mathrm{K}) a_{ij} p_j = f(\mathrm{K}) b_i \tag{4-31}$$

4.5 Validation

In this section, the accuracy and stability of developed model and the newly proposed kernel function, particle shifting technique and Laplacian operator are demonstrated through analysis of four different benchmark cases with various conditions. In all the simulations, ratio of smoothing length to particle spacing in kernel function (Eq. (4-21)) is taken as unity ($h = 1.0 d_p$), with d_p being the initial particle size. Time step size (Δt) is determined by a $CFL = 0.1$ (Courant number) condition based on the maximum velocity within the computational domain.

$$\Delta t_{convection} = CFL \frac{d_p}{|\mathbf{u}_{\max}|}$$

$$\Delta t_{viscous} = CFL \frac{d_p^2}{\nu} \tag{4-32}$$

$$\Delta t = \min(\Delta t_{convection}, \Delta t_{viscous})$$

4.5.1 Dam-break

The first test case (case A2) is classical dam-break flow and used to access the ability of the model in predicting a smooth pressure field and complex free surface features such as the return wave break. Numerical simulation is carried out in a two-dimensional rectangular enclosure with $L = 1.61m$, where a column of water ($\rho = 997\, kgm^{-3}, \nu = 8.9 \times 10^{-7}\, m^2 s^{-1}, p = 0, u = v = 0 ms^{-1}$) with initial depth and width of the $H = 0.3m$ and $W = 0.6m$ is installed on the right side of the enclosure. The time histories of the water level and pressure are monitored at three different points ($L_1 = 0.3m, 1.114m, 1.362m$ and $h_1 = 0.003m, 0.03m, 0.08m$), and obtained results are illustrated in Figs. 4-4 and 4-5. Generally, driven by the gravity, the water column collapses and flows downwards along a dry bed until the wave front reaches the downstream wall. After impinging on the left wall, it loses part of its kinetic energy such that the stagnation point starts to form on the corner of the enclosure which causes the velocity to attenuate accordingly. This event corresponds to the pressure peak in Fig. 4-5, first for the sensors 1 ($h_1 = 0.003m$) and 2 ($h_1 = 0.03m$) and later for the sensor 3 ($h_1 = 0.08m$). Thereafter the flow ascends upwards (forming a vertical jet on the wall), which is associated with continuous pressure signal recorded by the sensors. Under the gravity force, the vertical jet descends downwards and eventually collapses backward as a plunging wave leading to a second pressure jump (at around 0.63 sec. The new generated wave which has a less forward momentum moves to the right direction, forming a counterclockwise vortex in right half of the enclosure. Figs. 4-4 and 4-5 demonstrate that the developed KDF-ISPH model has successfully predicted a much smoother pressure field distribution with a well-detected free surface, particularly when the Particle Shifting is activated.

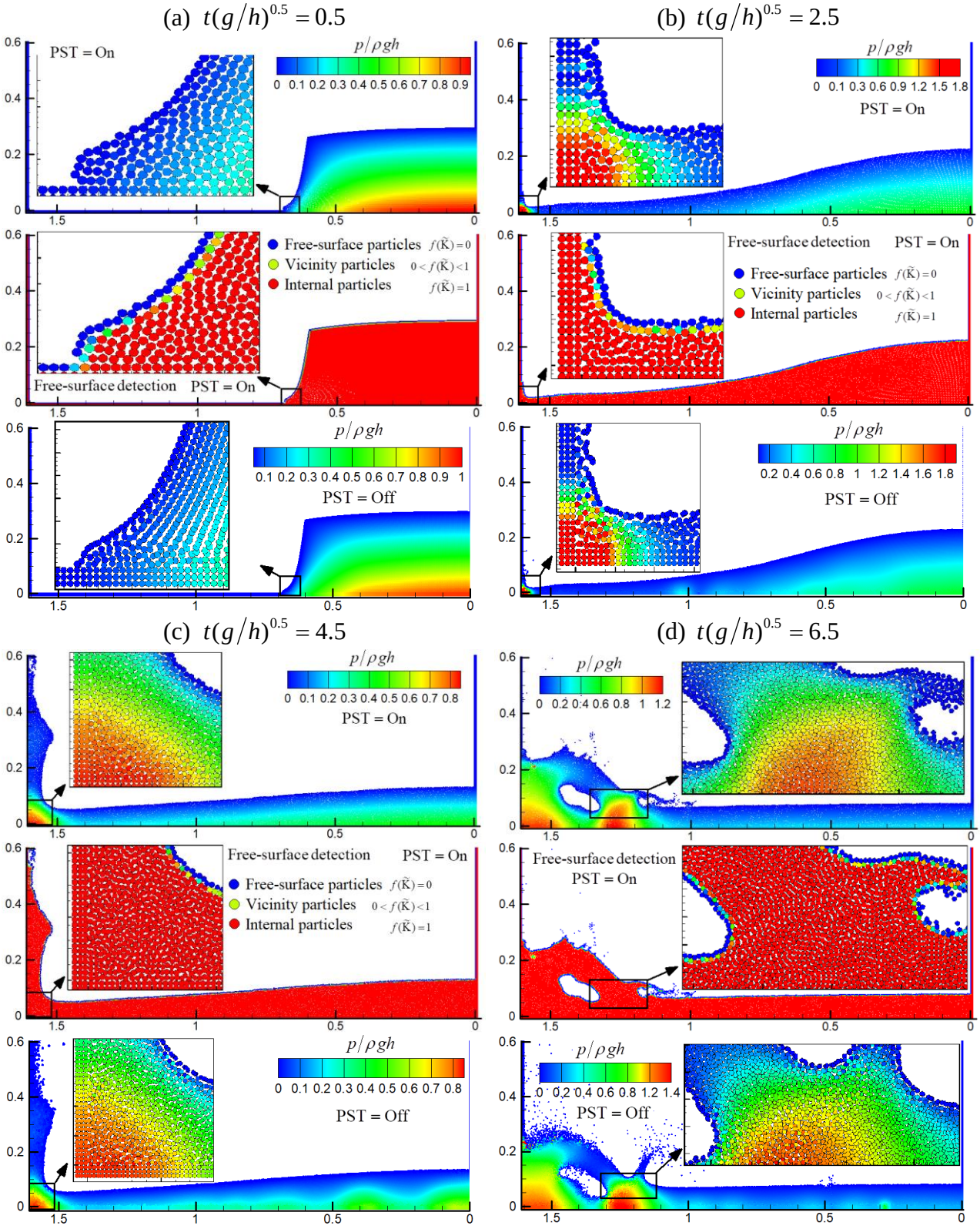

Figure 4-4Contours of the pressure field and free-surface area at different times. N_p=22050.

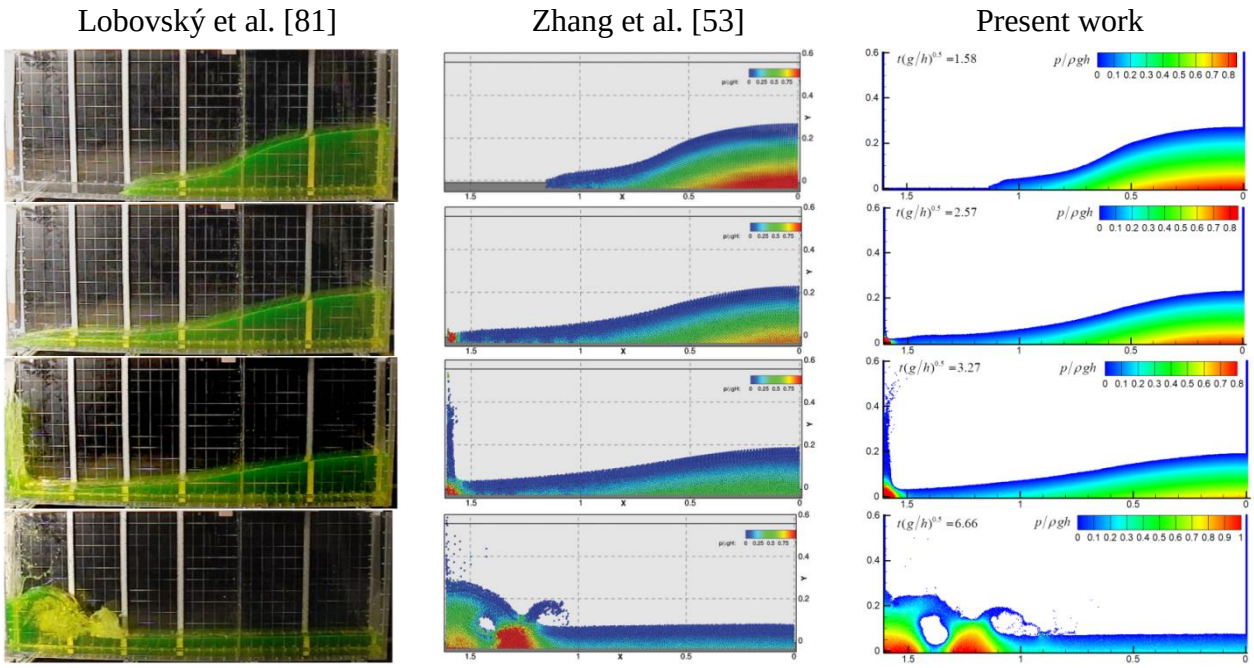

History of Water-level recorded at L_1, L_2 and L_3

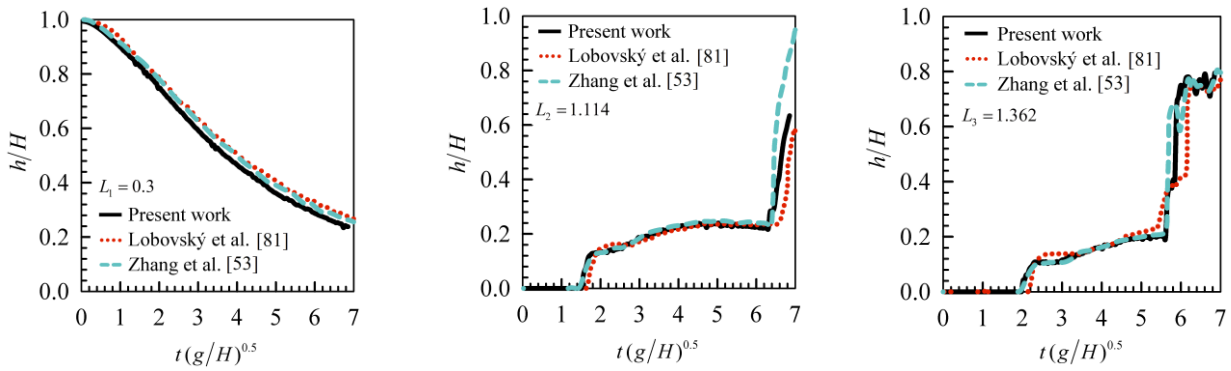

History of pressure signals recorded at h_1, h_2 and h_3

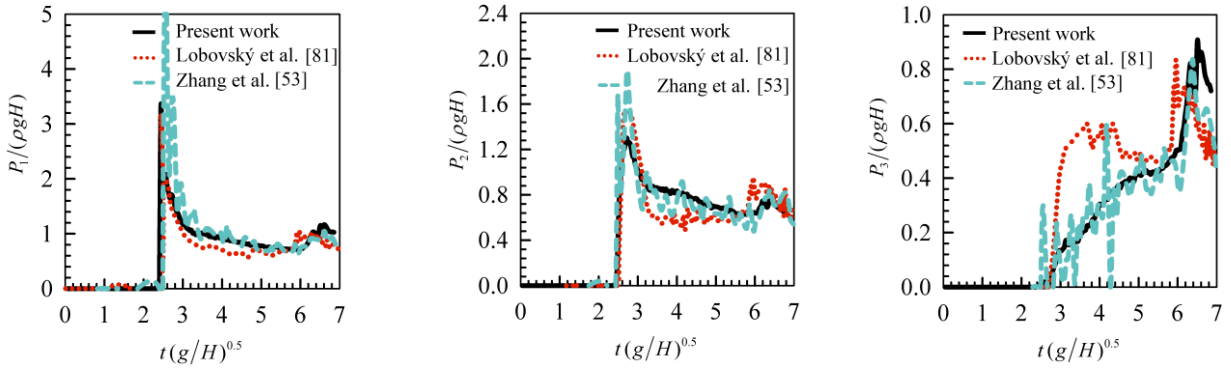

Figure 4-5 Validation of the present model against the numerical [53] and experimental results of Lobovský et al. [81] at different times $t^* = 1.58,\ 2.57,\ 3.27$ and 6.66 . $N_p = 22050$.

It can be seen from Fig. 4-5 that the water level and pressure time history are in satisfactory agreement with the experiment observations of Lobovský et al. [81]. Furthermore, less pressure fluctuations is observed, comparing to the numerical results of Zhang et al. [53] who used a classical Weakly-Compressible Smoothed Particle Hydrodynamics (WCSPH) with the assumption of inviscid flow. Another reason for such discrepancy can be attributed to implementation of the Particle Shifting Technique (PST) and new kernel function which in turn can immensely affect the solution accuracy and stability of the SPH predictions from the standpoint of less pressure fluctuations and particle consistency.

4.5.2 Rotating square patch of fluid

To demonstrate the capability of the KDF-ISPH model and PST in dealing with a negative pressure field, a hydrodynamic behavior of 2D square patch of fluid subjected to the clockwise eddy (in absence of external forces) is examined as the second benchmark case. In this problem, initial velocity and pressure fields are set as:

$$\begin{aligned} u_0(x,y) &= +y\omega \\ v_0(x,y) &= -x\omega \\ p_0(x,y) &= 0 \\ g(x,y,t) &= 0 \end{aligned} \tag{4-33}$$

where $L=1$ and $\omega = 1 s^{-1}$ are the length of the square patch and the initial angular velocity, respectively (see Fig. 4-1, case A3). Generally, due to centrifugal force, the corners of the square (with higher velocity) are elongated outward while its sides are dragged towards the center to satisfy the need for mass conservation as portrays in Fig. 4-6(a). It can be seen that in absence of PST (case of Fig. 4-6(b)), as the time goes on, the arms of the square patch began to grow and consequently magnitude of the negative pressure which is responsible for tensile instability intensifies, leading to the degradation of gradient interpolation, and occurrence of particle clustering ($t\omega < 0.1$). This structure ultimately destroys the particles interaction and compact support of the kernel function, resulting in the formation of unphysical discontinuity (numerical cavitation) and premature termination of calculations, accordingly.

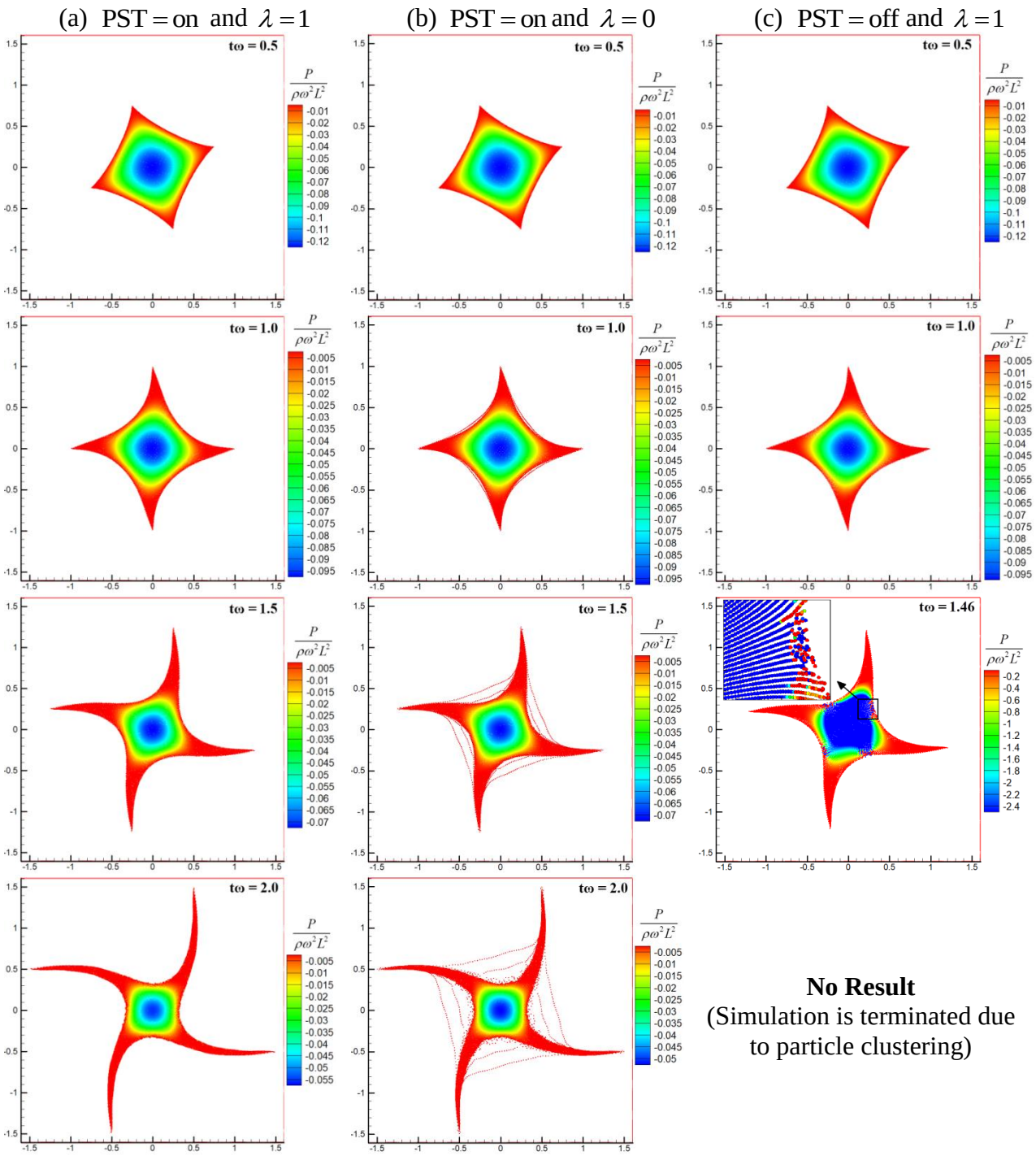

Figure 4-6The effects of the particle shifting technique and additional term in pressure Poisson equation on the evolution of rotating square patch of fluid at $t\omega = 0.5$, 1, 1.5 and 2($t\omega$ increases from top to bottom).

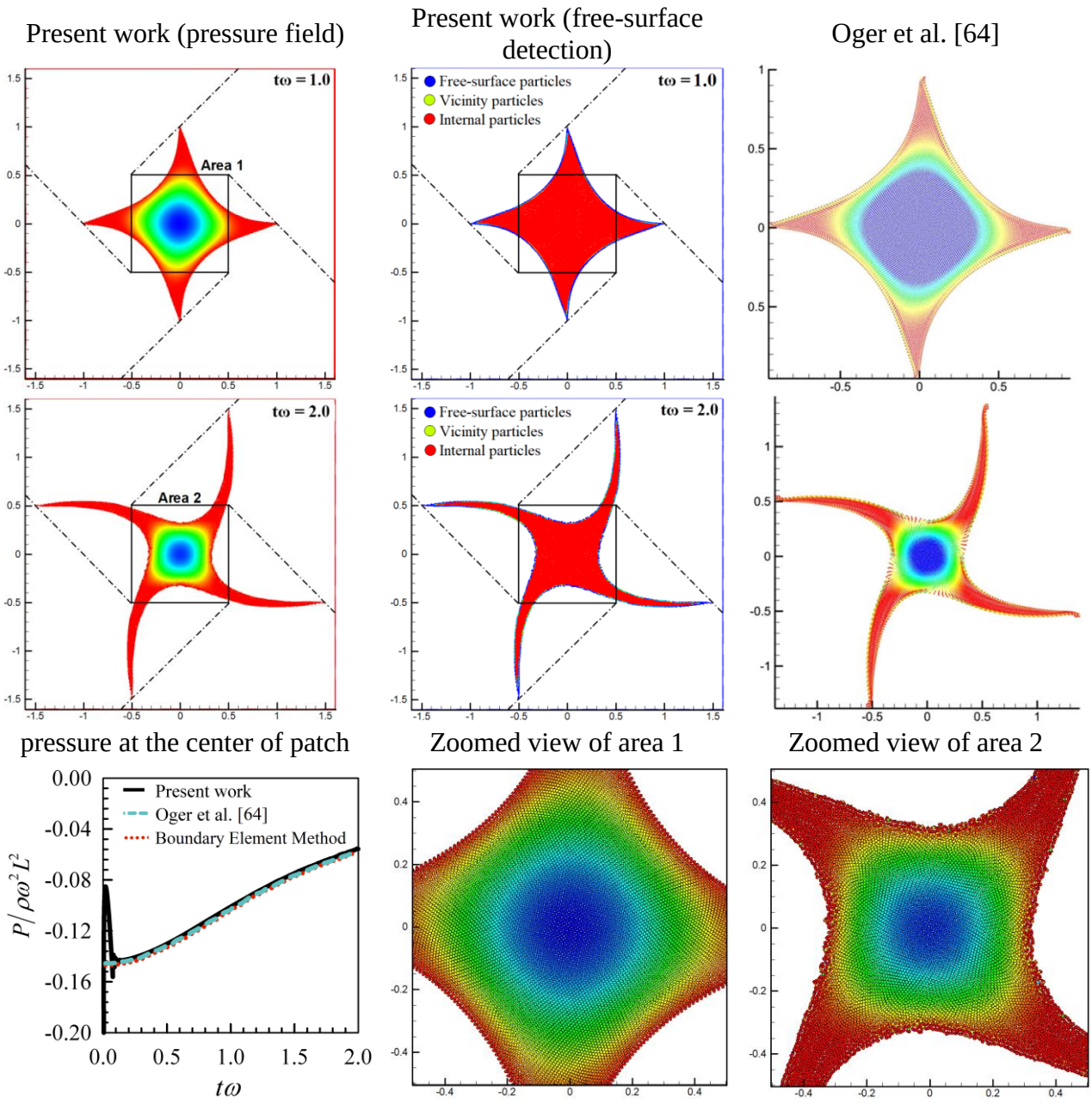

Figure 4-7Validation of the present model against the numerical results of Oger et al. [64] at $t\omega = 1$ and 2. $N_p = 12321$.

Similar observations were reported by Oger et al. [63], [64]. On the other hand, by eliminating the additional source term from the pressure Poisson equation ($\lambda = 0$ in Eq. (4-12)) a reverse trend occurs within the fluid domain. It can be seen from Fig. 4-6(c) that, due to the strong distortion of the fluid boundary, a thin layer of the surface particles is separated and moves

radially with constant velocity. This behavior can be explained by the fact that, assumption of incompressibility is valid only for inner particles and cannot be extended to the free-surface area where kernel support is truncated and particles are characterized by low density ratios ($\frac{\rho_{Surface}}{\rho_0} = \mathrm{K}_1 < 1$). Thus, it may be concluded that, implementing incompressibility condition ($\lambda = 0$) around the interface, can introduce an increasing error and leads to spurious segmentations of the interface. In other words, above discussion implies that, the hypothesis of the constant density and incompressible condition ($\nabla \cdot \mathbf{u}^{(n+1)} = 0$) are not valid and particle motion may be influenced by the density gradient. The time history of the pressure at the center of the fluid patch calculated using KDF-ISPH and newly proposed PST is shown in Fig. 4-7, together with the numerical results of Oger et al. [64]. Again, obtained results are found to be in reasonable agreement with the previously published data.

4.5.3 Stretching a circular drop

Behavioral analysis of stretching circular drop into an elliptical shape is considered here as the third benchmark case (case A4). The simulations are performed for the circular water drop ($\mu = 10^{-3}\ Pa\,s,\ \rho = 1000\ kgm^{-3}$) with radius of $R = 1m$ subjected to the following velocity field:

$$\begin{aligned} u_0(x,y) &= -100\,x \\ v_0(x,y) &= +100\,y \\ p_0(x,y) &= 0 \\ g(x,y,t) &= 0 \end{aligned} \qquad (4\text{-}34)$$

Unlike the previous case, the irrotational velocity field of this case generates a positive pressure field which encourages particle to stretch along the major axis in *y*-direction. Fig. 4-8 shows the effects of the PST on the particles position and pressure field. As mentioned before, in Lagrangian framework, particles typically tend to follow streamlines trajectory causing high level of heterogeneity in particle spacing, which in turn affects the stability of the mesh-free method. By comparing Figs. 4-8 (a) and (b), it is apparent that the PST has a notable impact on preserving particle uniformity through removing the voids between two different particles trajectory.

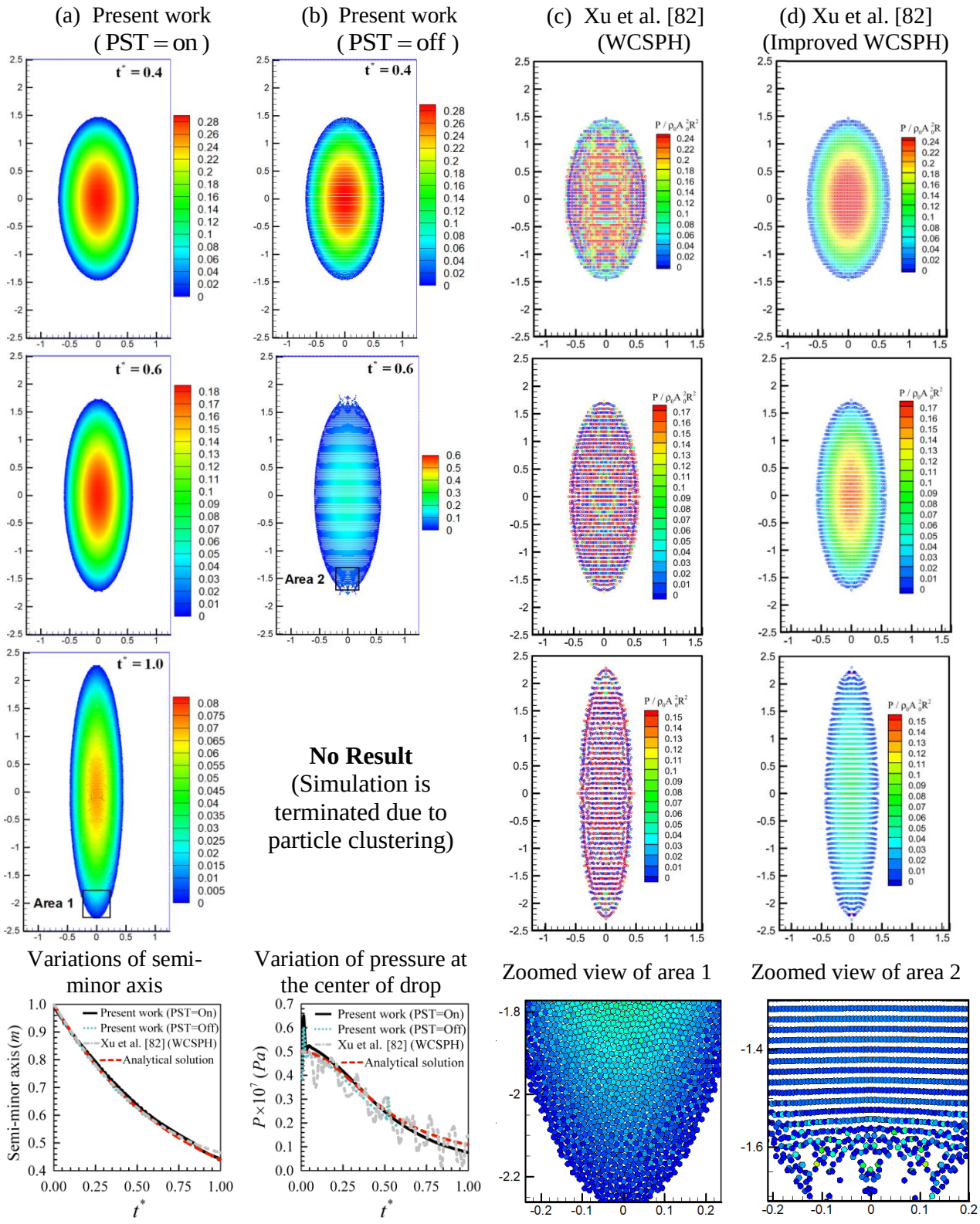

Figure 4-8 Evolution of an initially circular water drop: the comparison of particle positions and pressure contours obtained by present model against the numerical results of Xu et al. [82].

The accuracy of the KDF-ISPH model has been further proven by comparison with the analytical solution and numerical results of Xu et al. [82]. As shown in Figs. 4-8 (c) and (d), the proposed approach outperforms both classical and improved SPH schemes in terms of the pressure and semi-minor axis calculations. This superiority can be justified by the fact that, standard version of the SPH was derived based on the weakly compressibility hypothesis without any corrective matrixes, while current model benefits from high level of accuracy through implementing a set of the enhanced schemes. Absence of the PST in work of Xu et al. [82] (improved SPH) is another reason for such discrepancy which has led to particle clustering and non-physical gap within the fluid domain (compare Fig. 4-8 (a) with 8 (c)). Finally, Fig. 4-8 demonstrates that the obtained results by proposed model are in excellent agreement with the analytical solutions.

4.5.4 Natural convection heat transfer

Natural convection heat transfer in 2D square cavity with localized heating from below (T_h) is the last benchmark test case. As shown in Fig. 4-1 (case A5), the vertical walls of the enclosure are isothermally cooled at a constant low temperature (T_c), while the top wall and two unheated parts of the bottom wall are thermally insulated. Cavity is filled with air ($\mathrm{Pr} = 0.71$) with constant thermo-physical properties, except for the density, which varies linearly with the temperature according to Boussinesq approximation. Generally, due to the temperature difference between the hot and cold walls, the fluid adjacent to the heated surface ascends from the middle portion of the bottom wall, forming the curved shape thermal plume inside the enclosure. As the fluid moves upward and interacts with the colder particles, its temperature (energy) declines and consequently the fluid gets denser and descends more rapidly toward the bottom wall, resulting in appreciable enhancement in the size of the thermal plume. During repeated temperature cycle, the flow is shifted toward the corresponding vertical walls and cores of the two minor CW and CCW rotating vortices (which are separately located in the lower part of the cavity) moves up. This leads to the formation of the thermal boundary layers adjacent to the cold walls. The growth of the thermal boundary layers on the cold walls is in turn accompanied by augmentation of the temperature gradient and heat transfer rate within the enclosure.

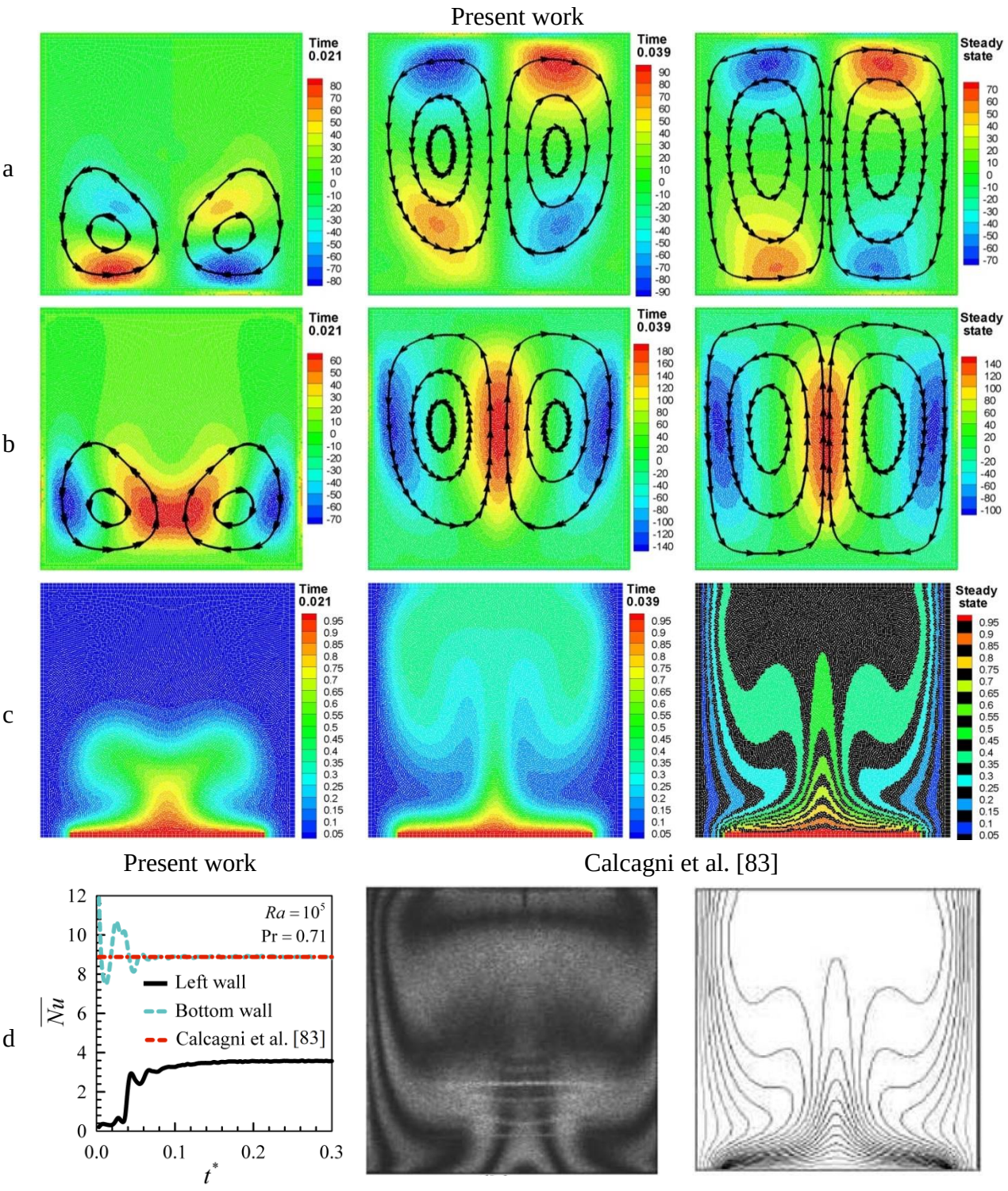

Figure 4-9 Validation of the present model against the numerical (mesh-based) and experimental results of Calcagni et al. [83] at $Ra = 10^5$. (a) contour of the velocity (u) in x-direction, (b) contour of the velocity (v) in y-direction, (c) isotherms. $L = 0.8H$. $N_p = 18225$.

As can be seen from Fig. 4-10, the present results are in excellent agreement with experimental and numerical data of Calcagni et al. [83], showing the capability of the proposed method in handling natural convection heat transfer. Finally, it worth mentioning that, besides the case A5, the entropy generation due to natural convection heat transfer in another benchmark case namely: Differentially Heated Cavity (DHC) has also been investigated and obtained results are compared with numerical data of Ilis et al. [76].

4.6 Results and discussion

Previous section vividly showed that the proposed models are robust and reliable for modeling a wide range of multiphase flows and convection heat transfer problems. In this section the proposed KDF-ISPH method is employed to investigate entropy generation due to natural convection heat transfer in three different geometries, (1) square cavity with hot obstacle inside (case B1), (2) C-shaped enclosure (case B2), and (3) square enclosure containing a pair of hot and cold horizontal pipes (case B3). Similar to traditional mesh-based methods, a particle independency test (grid study) at two different Rayleigh number was performed by considering seven sets of uniform particles size. It can be observed from table 4-2 that, a particle size of 139 ×139 ensures a particle independent solution.

Table 4.2 Effect of the grid size (particle independency test) on heat transfer rate ($\overline{Nu}$) for cases B1 to B3 at low and high Rayleigh number.

Number of particles (Case B1)							
Ra	39×39	59×59	79×79	99×99	119×119	139×139	159×159
10^3	1.1561	1.2009	1.2356	1.2423	1.2466	1.2472	1.2478
10^6	3.0412	3.6239	3.8374	3.9813	3.9881	3.9892	3.9897
Number of particles (Case B2)							
Ra	39×39	59×59	79×79	99×99	119×119	139×139	159×159
10^3	1.1428	1.6202	1.7771	1.7884	1.7953	1.7961	1.7966
10^6	3.2188	3.9074	4.2903	4.6638	4.8907	4.9022	4.9029
Number of particles (Case B3)							
Ra	39×39	59×59	79×79	99×99	119×119	139×139	159×159
10^3	2.0081	2.2102	2.2658	2.2893	2.3005	2.3069	2.3076
10^6	9.4573	10.4066	10.8251	10.8834	10.9078	10.9146	10.9155

Figs. 4-10 and 4-11 represents the effects of the Rayleigh number ($10^3 \le Ra \le 10^6$) on the isotherms and streamlines for cases B1 to B3 at different time instant. Generally, due to the temperature gradient and buoyancy induced by the hot surfaces, the fluid is heated and driven upward until it reaches the rigid top wall. The ascending hot fluid that gets blocked at the enclosure's upper wall travels horizontally toward the cold area, as it becomes gradually condensed and colder. After hitting the cold surfaces, the relatively heavier fluid comes down to lower part and ultimately returns back to the hot area and completes the recirculation pattern. This thermal mixing leads to the formation of some cellular structures inside the enclosure. Fig. 4-10 reveals that at low Rayleigh number ($Ra = 10^3$), the temperature field is nearly smooth and monotonic, which proves that the viscous force is dominant and energy transport is driven by the conduction. In this condition, due to weak buoyancy force, isotherms and streamlines are parallel to each other and basically take the shape of the enclosure.

Table 4.3The effects of the Rayleigh number on the heat transfer rate and entropy generation for cases B1 to B3 (steady-state condition).

Case B1										
Ra	$\overline{Nu}$	$\lvert U_{\max}\rvert$	$\lvert V_{\max}\rvert$	$\overline{Be}$	$\overline{S}_{tot}$	$S_{tot,\max}$	$\overline{S}_T$	$S_{T,\max}$	$\overline{S}_F$	$S_{F,\max}$
10^3	1.247	0.551	1.042	0.998	5.536	88.959	5.529	88.892	0.007	0.147
10^4	1.304	6.453	10.858	0.885	6.510	144.514	5.765	132.0414	0.745	16.659
10^5	2.281	55.726	75.954	0.218	46.456	1244.957	10.151	465.664	36.304	1094.520
10^6	3.989	199.952	324.550	0.027	659.249	24097.470	17.910	1144.494	641.338	23842.703
Case B2										
Ra	$\overline{Nu}$	$\lvert U_{\max}\rvert$	$\lvert V_{\max}\rvert$	$\overline{Be}$	$\overline{S}_{tot}$	$S_{tot,\max}$	$\overline{S}_T$	$S_{T,\max}$	$\overline{S}_F$	$S_{F,\max}$
10^3	1.796	0.613	1.169	0.999	6.809	85.514	6.804	85.445	0.005	0.157
10^4	1.834	6.772	11.851	0.930	7.456	139.551	6.935	125.108	0.521	16.666
10^5	2.937	52.022	77.660	0.264	41.800	1033.863	11.072	307.698	30.727	954.152
10^6	4.902	199.655	292.343	0.028	650.404	26780.951	18.491	656.526	631.912	26607.464
Case B3										
Ra	$\overline{Nu}$	$\lvert U_{\max}\rvert$	$\lvert V_{\max}\rvert$	$\overline{Be}$	$\overline{S}_{tot}$	$S_{tot,\max}$	$\overline{S}_T$	$S_{T,\max}$	$\overline{S}_F$	$S_{F,\max}$
10^3	2.307	1.114	1.378	0.995	2.436	53.922	2.424	53.827	0.011	0.222
10^4	2.934	9.098	11.859	0.781	3.944	99.623	3.089	91.529	0.855	17.637
10^5	6.267	30.891	45.196	0.297	22.851	677.567	6.798	298.047	16.052	393.814
10^6	10.915	85.317	1333.947	0.057	214.212	7967.239	12.275	696.920	201.937	7895.284

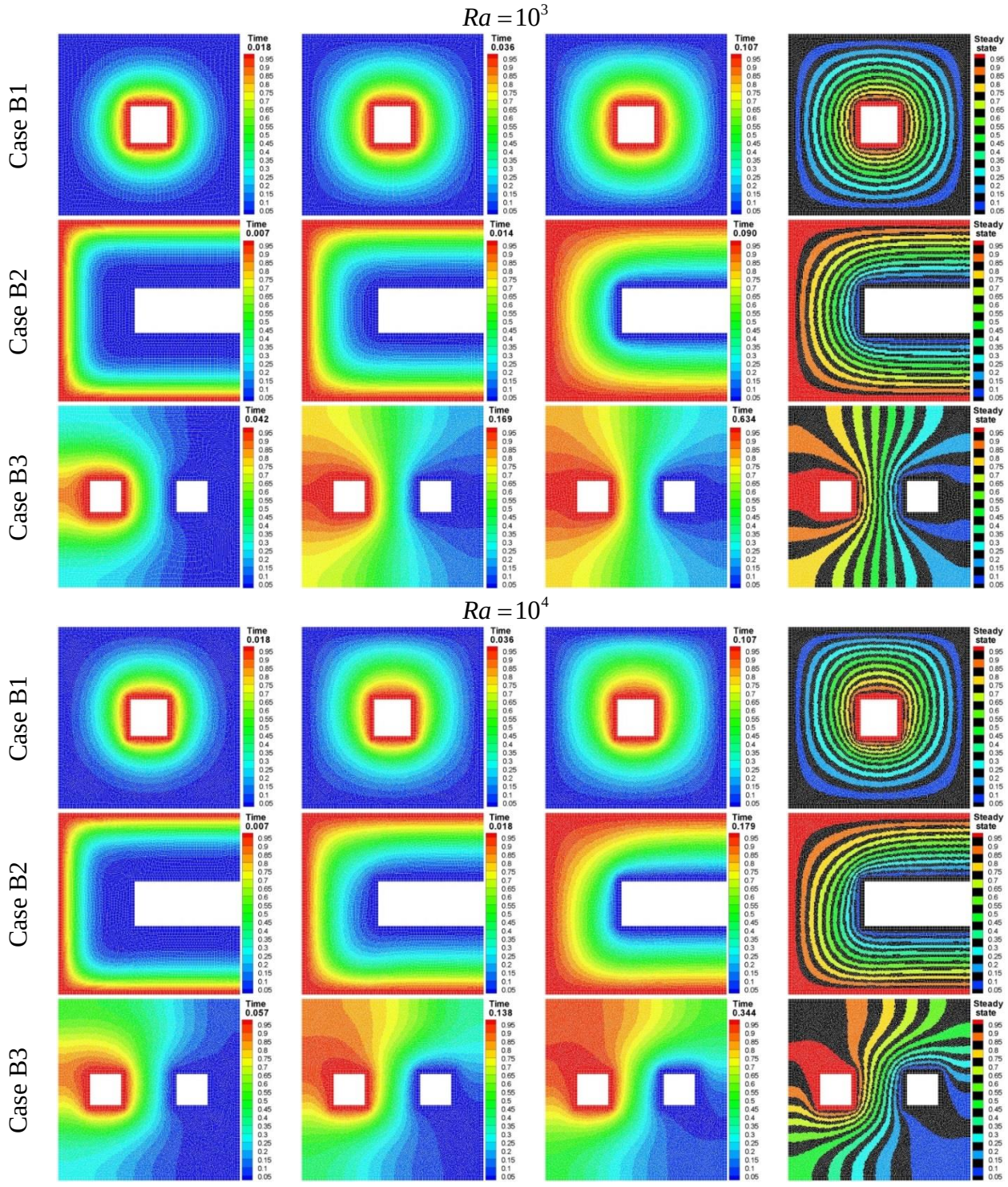

Figure 4-10 Isotherms for cases B1 to B3 at various Rayleigh numbers. $N_p = 139 \times 139 = 19321$. $d_p = 0.00724H$.

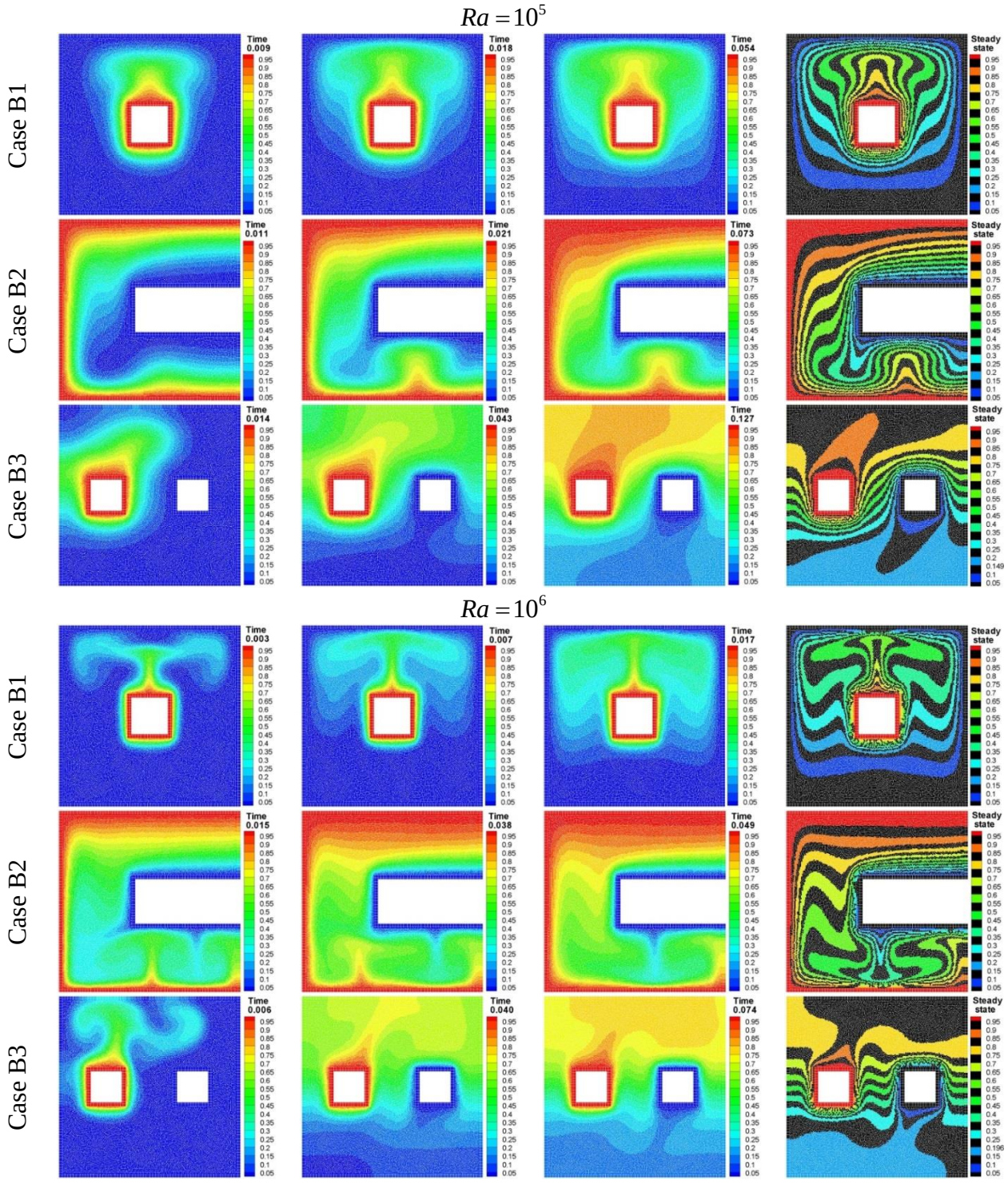

Figure 4-10 Isotherms for cases B1 to B3 at various Rayleigh numbers. $N_p = 139 \times 139 = 19321$. $d_p = 0.00724H$, (cont'd)

By increasing the *Ra* up to 10^4, the strength of the recirculating vortices augments and isotherms get slightly distorted and compressed by the flow pattern, showing the role of the convection mode in the heat transport. Indeed, it can be deduced that since strength of inertia forces in this situation is analogous with the viscous force, transition point from conduction to convection takes place at this *Ra*. With further increase of *Ra*, the effects of the buoyancy force become more dominant and the magnitude of the velocity field (u) increases. This increases the intensity vortices, causing the formation of the rising-sinking thermal plumes around the heated obstacles (for the sake of brevity, vertical velocity contours (v) are provided as a supplementary material). In this stage, flow structure (numbers and shape of eddies) and thermal pattern are remarkably affected by geometry configuration and type of the boundary condition. For example, in case B1, due to the symmetrical boundary conditions with respect to mid-plane of the enclosure, flow filed is characterized by the pair of the CW and CCW rotating loops in the left and right halves of the enclosure. By increasing the *Ra* up to 10^6, the cores of the vortices move upward and height of the thermal plume at the top portion of the annulus rises, indicating the establishment of the convection regime.

However, the different scenario occurs in C-shaped enclosure (case B2). Figs. 4-10 and 4-11 show that at low *Ra*, isotherms are evenly distributed and the single clockwise vortex is developed in the vertical part of the enclosure. By increasing *Ra* up to 10^5, buoyancy force dominates the viscous forces. Thus, the primary eddy in the horizontal part of the cavity gets segregated at the core and two counter rotating vortices are formed in that area. This flow structure, with regular thermal convective rolls, signifies the characteristics of Rayleigh-Bénard cells, where isotherms exhibit chaotic behavior and become more twisted and deformed due to existence of the primary ascending thermal plume under the cold rib. It can also be seen that owning to the presence of falling thermal plume on the corner of the cold rip, vertical flow cannot easily enter into the horizontal portion. This results in the formation of the three distinct recirculation zones, once the steady-state condition is achieved. Because of high momentum diffusivity at $Ra=10^6$, a third Bénard cell (which triggers onset of thermal instability) is formed as newly descending thermal plume. As time goes on, the counter-clockwise eddy which receives the incoming cold fluid grows in its size and pushes the clockwise eddy (ascending thermal plume) firmly towards the left wall of the enclosure.

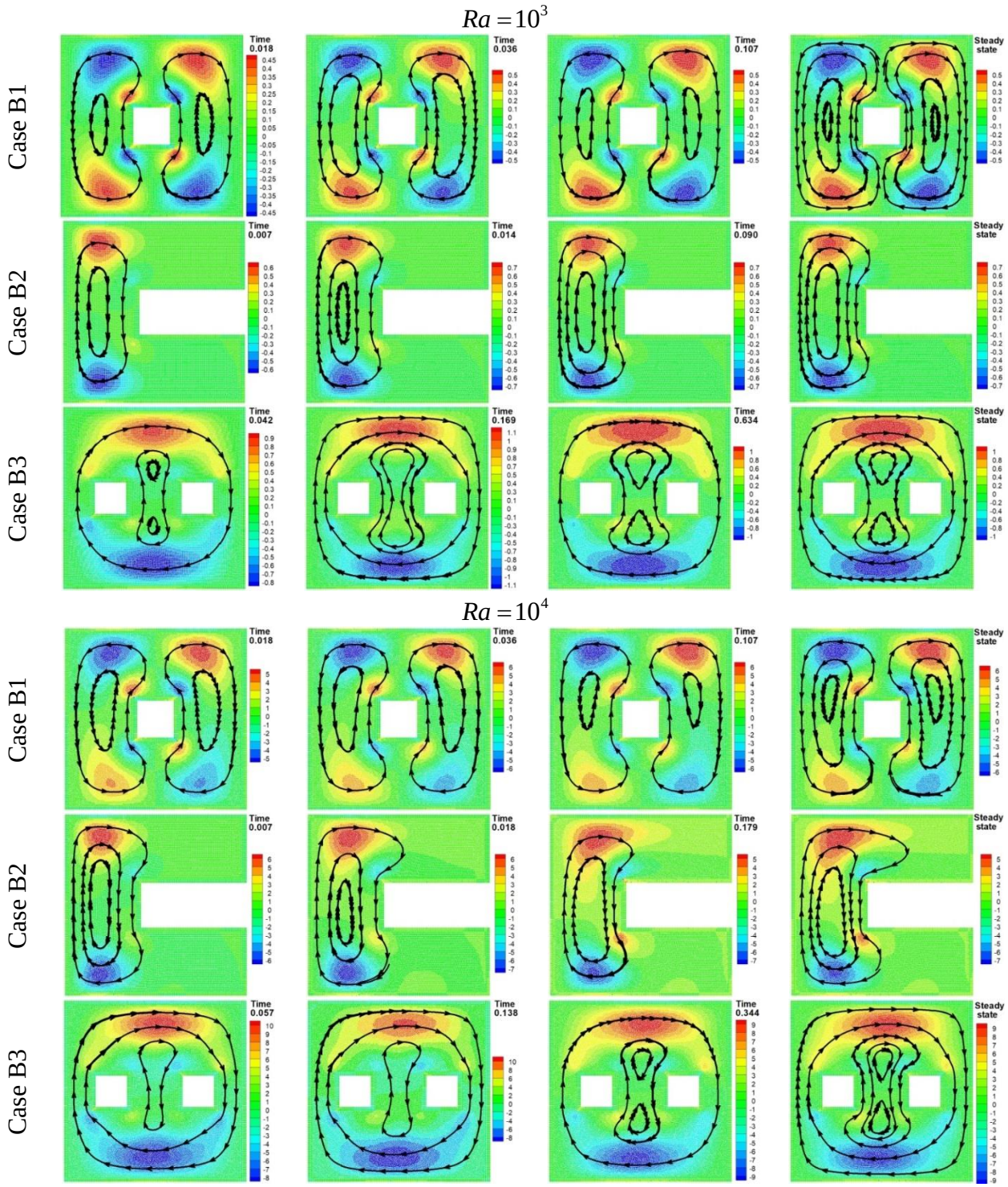

Figure 4-11 Streamlines and velocity in *x*-direction (*u*) for cases B1 to B3 at various Rayleigh numbers.

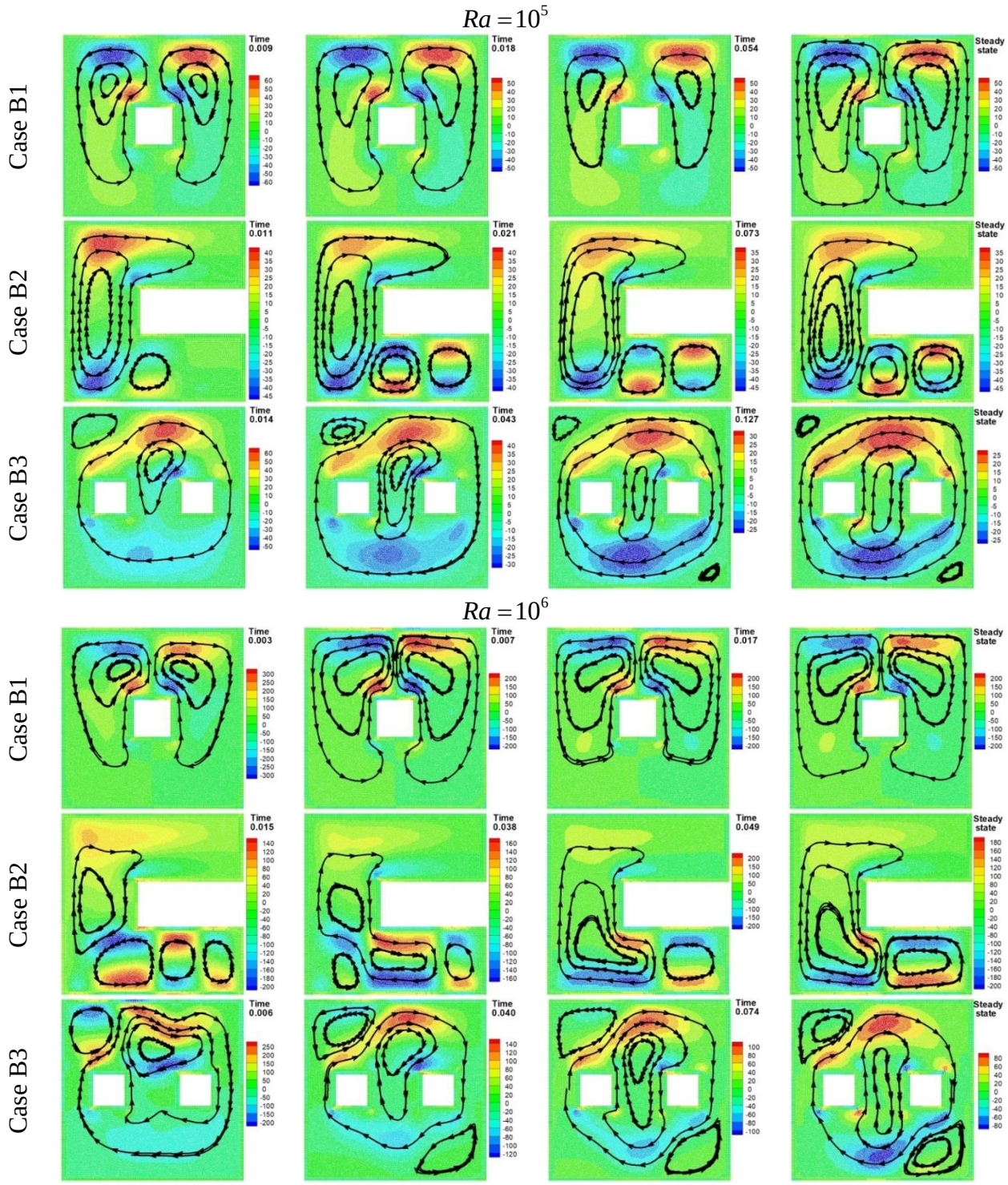

Figure 4-11 Streamlines and velocity in *x*-direction (*u*) for cases B1 to B3 at various Rayleigh numbers (cont'd).

Due to the interaction and expansion of these vortices, rising plume moves horizontally along the bottom wall and eventually vanishes owing to the caustic merging with the innermost vortex occupying the left side of the cavity. As shown in Figs. 4-10 and 4-11, when the flow enters a steady state condition, due to presence of the sinking thermal plum on the corner of the gap, two distinct regions are created in the enclosure, (1) vertical portion of the enclosure which is occupied by the strong clockwise eddy and (2) anti-clockwise elliptical eddy which is elongated and squeezed in horizontal section. This behavior is consistent with the findings of Saidi et al. [84] who investigated natural convection heat transfer in L-shaped enclosure.

Figs. 4-10 and 4-11 also display the flow structures and temperature patterns for case B3 (heat exchanger) where all walls of the enclosure are adiabatic and impermeable so that heat can only transfer from the hot pipe to the cold one. Similarly to what happens in cases B1 and B2, the working fluid first gets heated and rises up close to the hot pipe and flows down along the cold pipe, forming the pair of clockwise circulation vortexes inside the enclosure (outer recirculation zone which occupies about %75 of the enclosure together with an interior double-eddy which is elongated in *y*-direction). A close inspection of the magnitude of velocity component (*u*) in Fig. 4-11 and temperature distribution in Fig. 4-10 clearly show that due to dramatically larger hydraulic resistance and weak buoyancy force at $Ra=10^3$, conduction heat transfer is dominant. In fact, due to strong dominance of viscous force at this *Ra*, temperature field is practically unaffected by circulation pattern so that isotherms at the middle portion are smooth and vertically oriented. However, by increasing the *Ra*, flow initiates to penetrate within the enclosure which makes the isotherms to become parallel with the horizontal walls. In this circumstance ($Ra=10^6$), flow intensity and deformation of isotherms are severely elevated and sharp thermal boundary layer with steeper gradient is established around the differentially heated pipes. The decrement in the thermal boundary layer thickness and isotherm gathering, in turn, cause higher swirl flow in the annular space which leads to the significant rise in temperature gradient and heat transfer rate consequently. It is interesting to observe that, due to the dominance of convection mode and substantial augmentation in the fluid movement in the cavity, a pair of the upwelling and downwelling plumes is also generated on the top and bottom of the heated pipes. This results in in the development of two symmetric counter-clockwise eddies on the corners of the cavity.

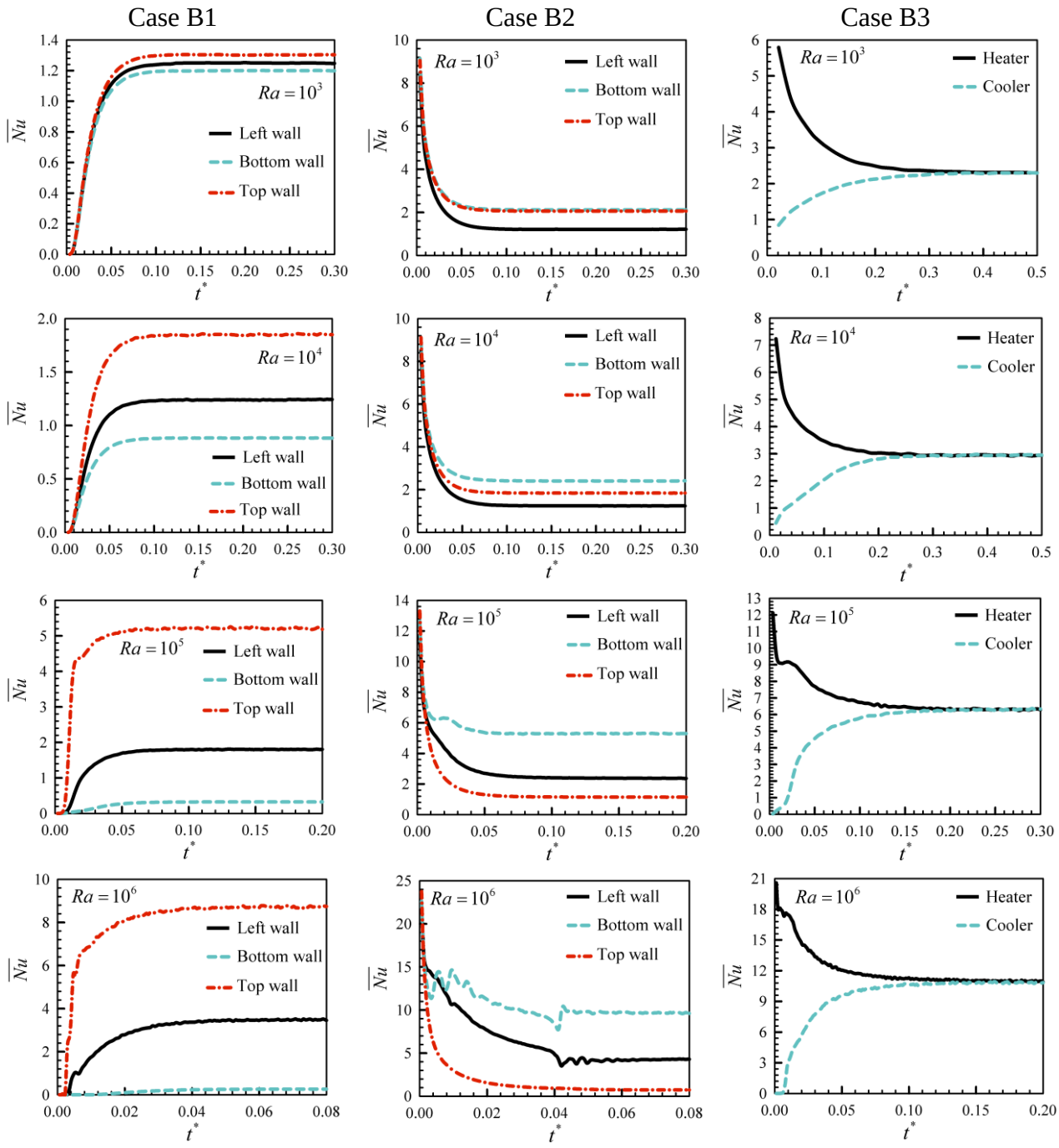

Figure 4-12 Variations of average Nusselt number as a function of the non-dimensional time for cases B1 to B3 at different Rayleigh numbers. Case B1 ($\mathrm{Pr}=0.71, L=0.25H$), case B2 ($\mathrm{Pr}=6.2, L_1=0.6H, L_2=0.3H$) and case B3 ($\mathrm{Pr}=6.2, L_c=L_h=0.225H$).

To better understand the effects of Rayleigh number on the heat transfer mechanism inside the enclosures, variations of average Nusselt number are elucidated in Fig. 4-12 and table 4-3. Fig. 4-12 demonstrates that in case B1 at low Rayleigh number, average Nusselt number along the cold walls of the enclosure are nearly identical while by increment of *Ra*, the difference between them enhances such that lowest and highest amount of the heat are transferred from the bottom and top walls, respectively. Take as an illustration, in steady state condition, the ratio of average Nusselt number between top and left walls ($\overline{Nu}_{top}/\overline{Nu}_{left}$) at $Ra=10^3$, 10^4, 10^5 and 10^6 are 1.04, 1.50, 2.88 and 2.48 while this trend is continued by 1.03, 1.39, 5.62 and 13.46 between the left and bottom walls ($\overline{Nu}_{left}/\overline{Nu}_{bottom}$). This behavior can be explained by the fact that in the conduction dominated regime ($Ra=10^3$) due to comparatively low momentum and penetration effect, heat spreads uniformly in all directions, leading to uniform temperature gradient near the heated surfaces. In this situation, averaged Nusselt number is heavily affected by reduction of the gap space between the hot and cold areas. Such a phenomenon occurs in case B2 where because of the relatively small space (low thermal resistance) available between horizontal walls of the enclosure and cold rip, averaged Nusselt number along the top and bottom walls is higher than that of the vertical one. By contrast, since at high *Ra* fluid tends to move upward with the assistance of the buoyancy force, higher heat transfer rate occurs in the upper region (top and left walls) while the bottom wall is practically inactive and has no contribution in the cooling process. This event is also accompanied by the occurrence of thermal stratification in the lower half of the enclosure. In fact, although at high Rayleigh number flow moves faster and convection mechanism is dominant but due to existence of the stagnant region in the lower part of the cavity in case B1, flow remains nearly motionless and consequently heat is transported through the conduction mode. Interestingly, this course of the event also occurs in case B2 but in reverse manner so that because of the heat trapping in upper half of the enclosure, $\overline{Nu}_{top}$ along the top wall declines and conduction mode becomes stronger as the *Ra* enhances. In fact, above discussion clearly suggests that locations of the hot and cold surfaces can be used as a control parameter for the heat and fluid flow. That is, maximum energy exchange can be attained when the hot surface is located lower than the cold one (and vice versa, for the lowest heat transfer rate). Similar finding were reported by Doo et al. [85], Izadi et al. [86] and Miroshnichenko et al. [87]. Another interesting feature at high *Ra*, is the transient oscillatory behavior in the values of

$\overline{Nu}$ along the bottom and left walls of the C-shaped (case B2) enclosure. In fact, the first fluctuation of $\overline{Nu}$ which occurs on the bottom wall ($0 \le t^* \le 0.02$) is related to the presence and movement of the rising-sinking plumes in the horizontal section while second oscillation which takes place simultaneously on both bottom and left walls of the enclosure ($0.04 \le t^* \le 0.05$) originates from merging of the rising plume with the primary CW eddy at the left half of the enclosure. Fig. 4-12 also reveals transient variations of the average Nusselt number around the hot and cold pipes in case B3. The results indicate that in steady-state condition, the average Nusselt number increases with increasing the *Ra*. However at each certain *Ra*, since initial temperature is taken as $T_c = 296K$ ($\theta = 0$), $\overline{Nu}_{hot\ pipe}$ around the heater declines whereas $\overline{Nu}_{cold\ pipe}$ increases until the thermal balance is established within the enclosure. It is worth to mention that, since sidewalls of the enclosure are totally adiabatic, the amount of the heat released by the hot pipe is entirely absorbed by the cold pipe which is another validation for the current work from the view point of first law of thermodynamics ($\overline{Nu}_{hot\ pipe} = \overline{Nu}_{cold\ pipe}$).

Figs. 4-13 and 4-14 illustrate local Bejan number and entropy generation due to heat transfer irreversibility at different *Ra* for case B1 to B3. As stated earlier, entropy generation stems from two main factors, namely, heat transfer irreversibility (temperature gradient) and viscous dissipation (velocity gradient). It can be seen from Fig. 4-13 that at $Ra=10^3$, the values of the local Bejan number in all cases are very close to unity which manifests thermal irreversibility is the major contributor of total entropy generation. This observation is compatible with maximum values of entropy generation provided in table 4-3. For instance at $Ra=10^3$, the maximum local entropy generation due to thermal dissipation ($S_{h,\max}$) for cases B1, B2 and B3 are respectively equal to 88.89, 85.44 and 53.82 while the maximum values of local entropy generation due to viscous dissipation ($S_{f,\max}$) are approximately 0.14, 0.15 and 0.22, which indicates that at low *Ra* where conduction heat transfer is dominant, fluid friction irreversibility is negligible. This behavior is also in agreement with results of Fig. 4-15 where time history of total entropy generation in all cases exhibits the peculiarity of heat transfer irreversibility ($S_{tot} \approx S_T$). As expected, by increasing the *Ra* up to 10^4, convection mechanism within the enclosures is

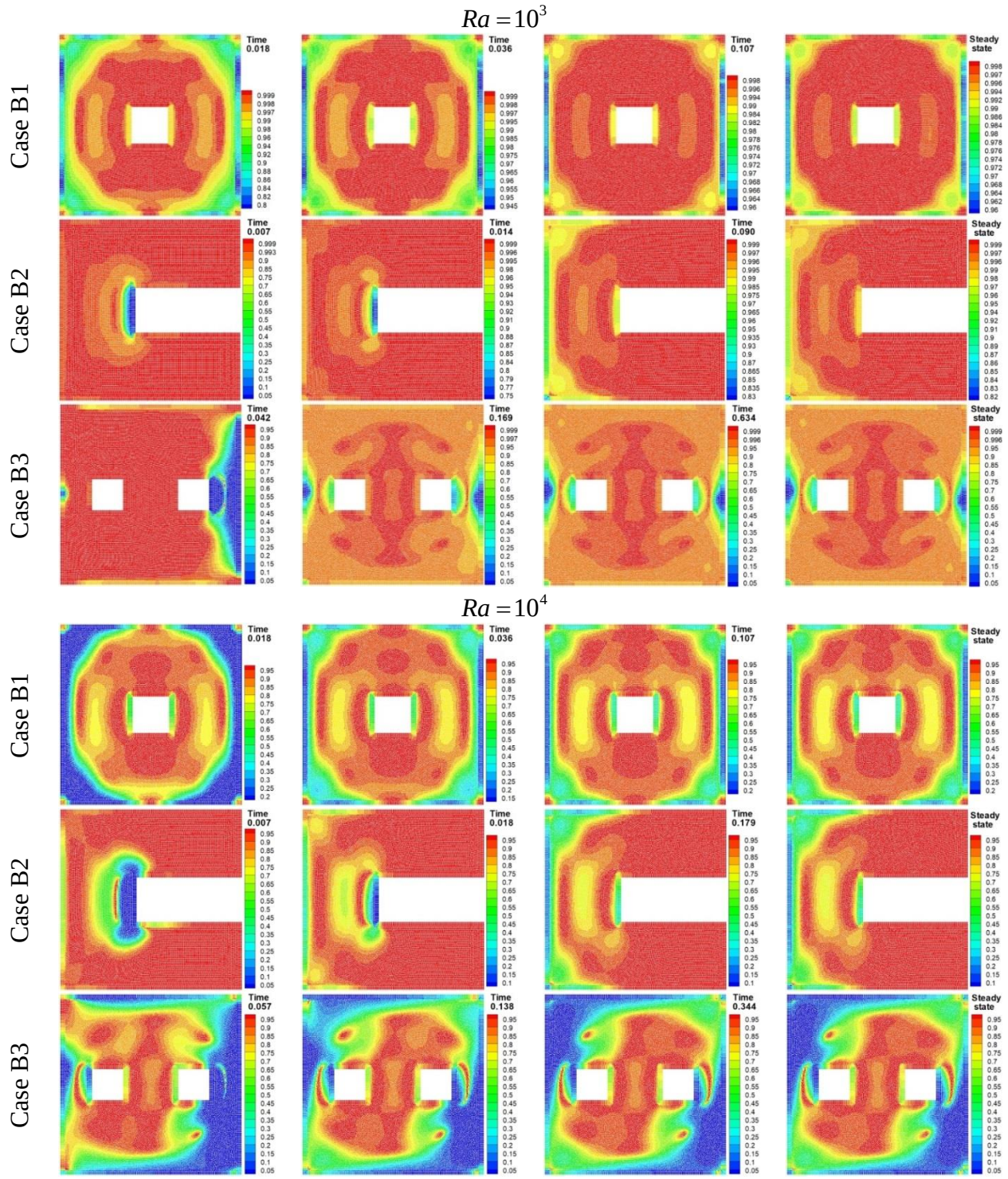

Figure 4-13 Contours of the local Bejan number for cases B1 to B3 at various Rayleigh numbers.

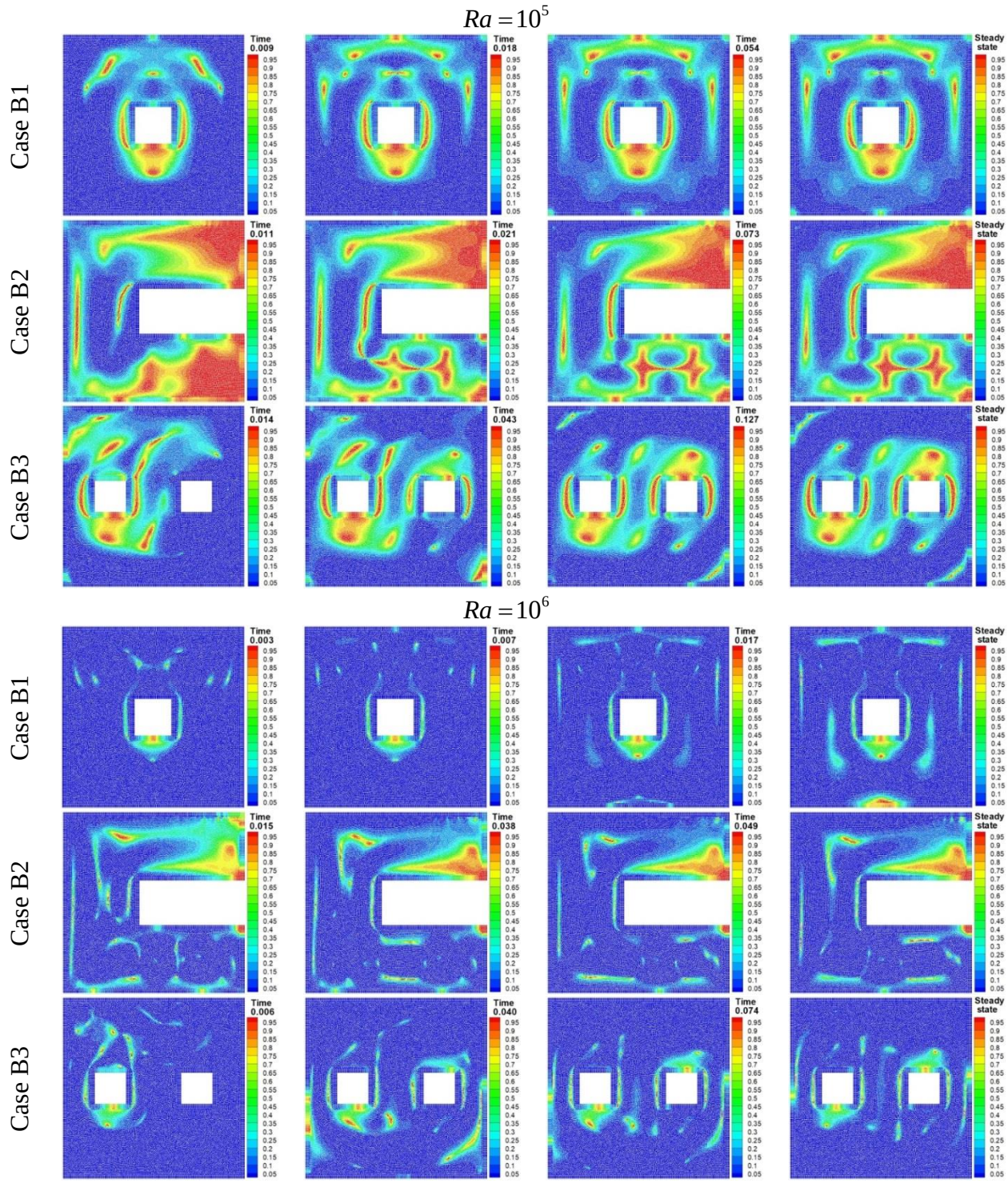

Figure 4-13 Contours of the local Bejan number for cases B1 to B3 at various Rayleigh numbers, (cont'd).

improved and hence temperature gradient and intensity of fluid flow increase, leading to the enhancement in total entropy generation. However, since onset of the convection heat transfer occurs at this *Ra* (transition from conduction to convection mode), buoyancy force is not sufficiently large to overcome hydraulic resistance, and hence entropy generation due to thermal dissipation is still more intense than that of the viscous dissipation ($S_T > S_F$). This is reflected in the local and average Bejan number values in Fig. 4-13 and table 4-3 where $\overline{Be} > 0.5$ clearly demonstrates that most of the exergy loss in all cases is still associated with the heat transfer irreversibility. It should be noted that in this condition, the entropy generation due to S_F is confined to the small region at the vicinity of the active walls where local Bejan number has a lower values compared with elsewhere within the computational domain (see Fig. 4-13). By increasing the *Ra* up to 10^5, a large temperature gradient is formed at the vicinity of the heated walls which causes fluid moves faster and velocity gradient to amplify accordingly. Increase in velocity and temperature gradients in turn is accompanied by concomitant loss of the available work and significant enhancement in overall rate of the entropy production. However, since augmentation in the entropy generation caused by viscous dissipation ($\overline{S}_F$) is slightly higher than that promoted by heat transfer irreversibility ($\overline{S}_T$), average Bejan number declines and becomes lower than half. This indicates that irreversibility due to fluid friction is coming into the picture. Variations of the average Bejan number ($0.218 \le \overline{Be} \le 0.297$) at $Ra=10^5$ in table 4-3 and Fig. 4-13 clearly demonstrate that $\overline{S}_T$ and $\overline{S}_F$ have the same order of magnitude and hence are analogous to each other. For instance, the ratio of $\overline{S}_F$ over that of the $\overline{S}_T$ in case B1, B2 and B3 are respectively 3.57, 2.77 and 2.36 which implies that $\overline{S}_F$ and $\overline{S}_T$ have a relatively equal contribution to overall entropy generation. This assertion is further supported by Fig. 4-13 where 40% of the enclosures in cases B1 to B3 is still covered by local Bejan number higher than 0.8. With further increment of Rayleigh number ($Ra=10^6$), total entropy generation rises while average Bejan number declines immensely and becomes less than $\overline{Be} < 0.08$, indicating the domination of fluid friction irreversibility (see also table 4-3 where $\overline{S}_T \ll \overline{S}_F$). In other words, it may be concluded that simultaneous increment of $\overline{S}_{tot}$ and attenuation of $\overline{Be}$ characterize the dynamical nature of the frictional entropy generation at high Rayleigh number where

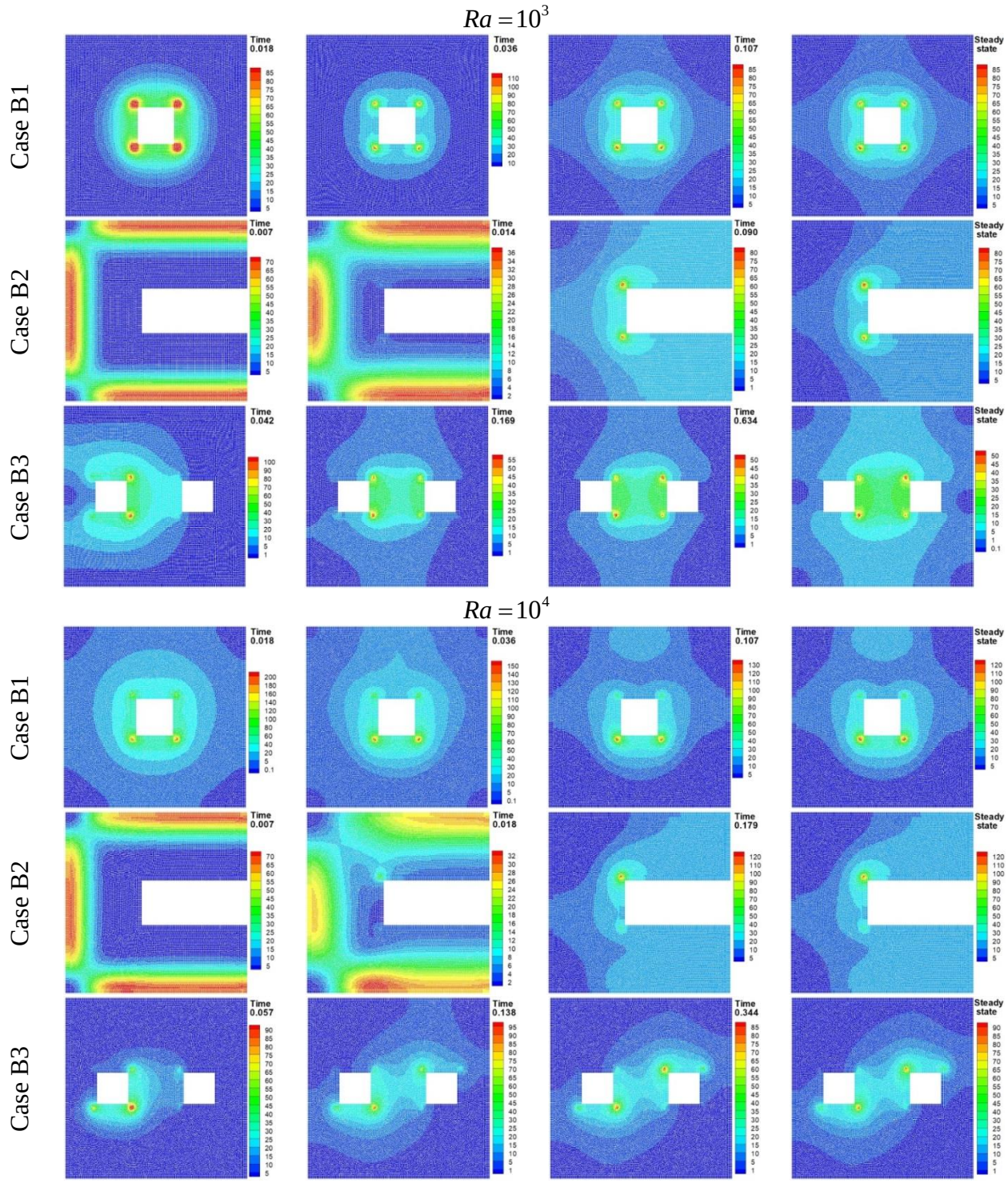

Figure 4-14 Contours of the local entropy generation due to heat transfer for cases B1 to B3 at various Ra.

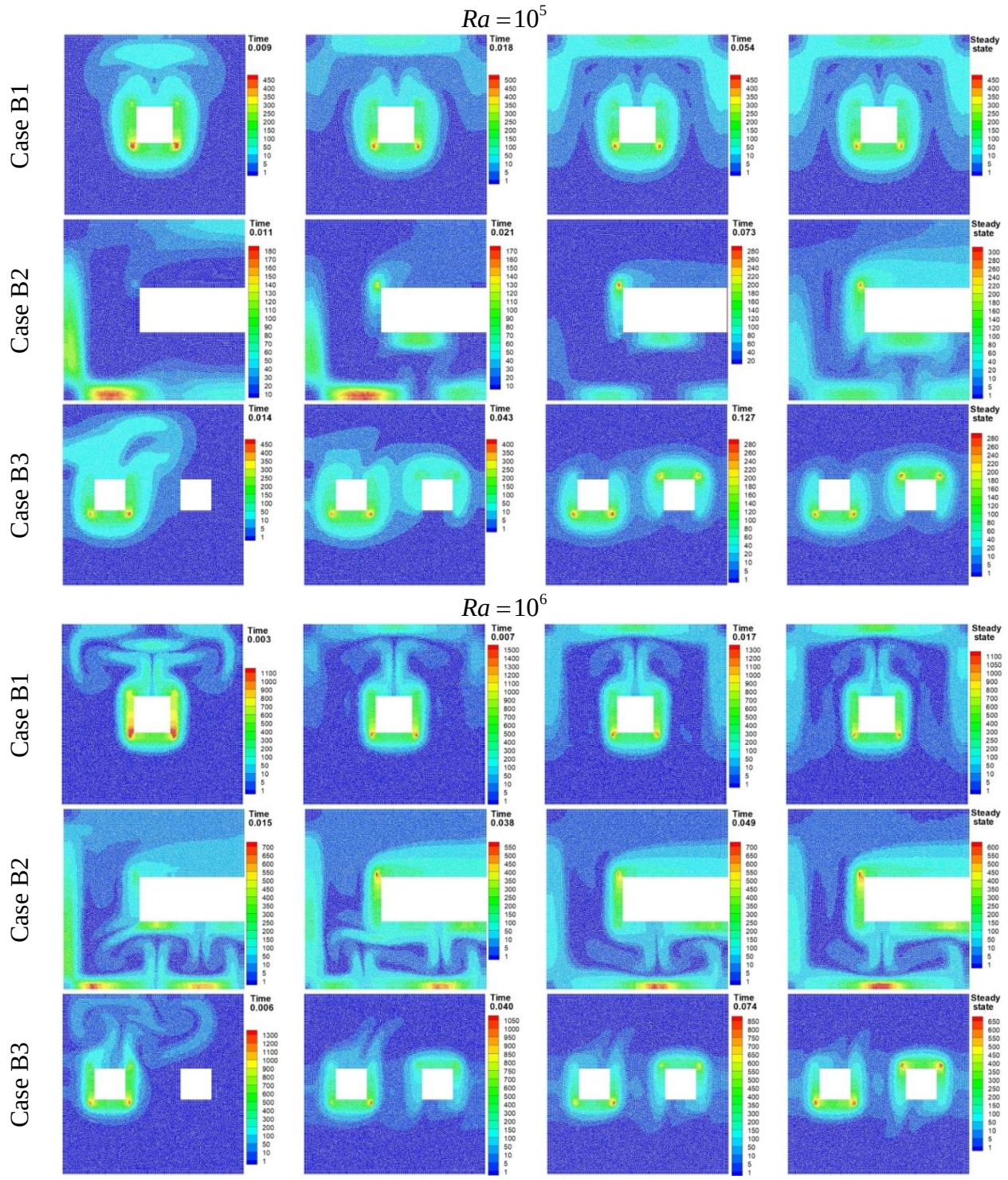

Figure 4-14 Contours of the local entropy generation due to heat transfer for cases B1 to B3 at various *Ra*, (cont'd).

convection heat transfer is dominant. However, besides the above results, some other interesting points can be drawn in this section. Generally, Fig. 4-14 illustrates that at all *Ra*, the source of entropy generation due to heat transfer (S_T) is concentrated near the active boundaries where higher temperature gradients occur within the enclosures. More precisely, it is evident from Fig. 4-15 that due to the weak convection effects at low *Ra*, local S_T in case B1 is uniformly distributed and maximum S_T occurs on the corners of the hot obstacle in the steady-state condition. Due to the steeper temperature gradient and compression of isotherms at high *Ra*, thickness of the thermal boundary layer near the bottom portion of the heater decreases and thereby lower-left and lower-right corners become the major sites of the maximum S_T. Furthermore, due to impingement of the single ascending thermal plume on the top wall, upper half of the enclosure experiences a moderate local S_T while lower one doesn't have any contribution to the S_T and acts as almost entropy free region owing to the presence of the stagnation region. Similar qualitatively trends also take place in case B2 such that at low *Ra*, S_T is found to be significant at the corners of the cold rip while in the rest of the domain, S_T is trivial due to low temperature gradient. By increasing the convective force via increase in the Rayleigh number, magnitude of S_T enhances and consequently left vertical and bottom horizontal parts of the enclosure become the prone zones of S_T. It is interesting to observe that, under this circumstance due to high level of thermal mixing and severe velocity gradients in lower half of the enclosure, S_F is markedly intensified and S_T starts to adopt the pattern of the isotherms.

Fig. 4-14 also demonstrates the local entropy generation due to heat transfer irreversibility for case B3. One of the interesting features related to this geometry is that, since hot and cold pipes are located in the same height, computational domain is completely free of the stagnation region, resulting in better and more efficient thermal mixing within the enclosure. It can be seen from Fig. 4-14 that at low *Ra*, maximum S_T occurs on the left and right corners of the differentially heated obstacles which have a lower distance with respect to each other. By increasing the *Ra*,

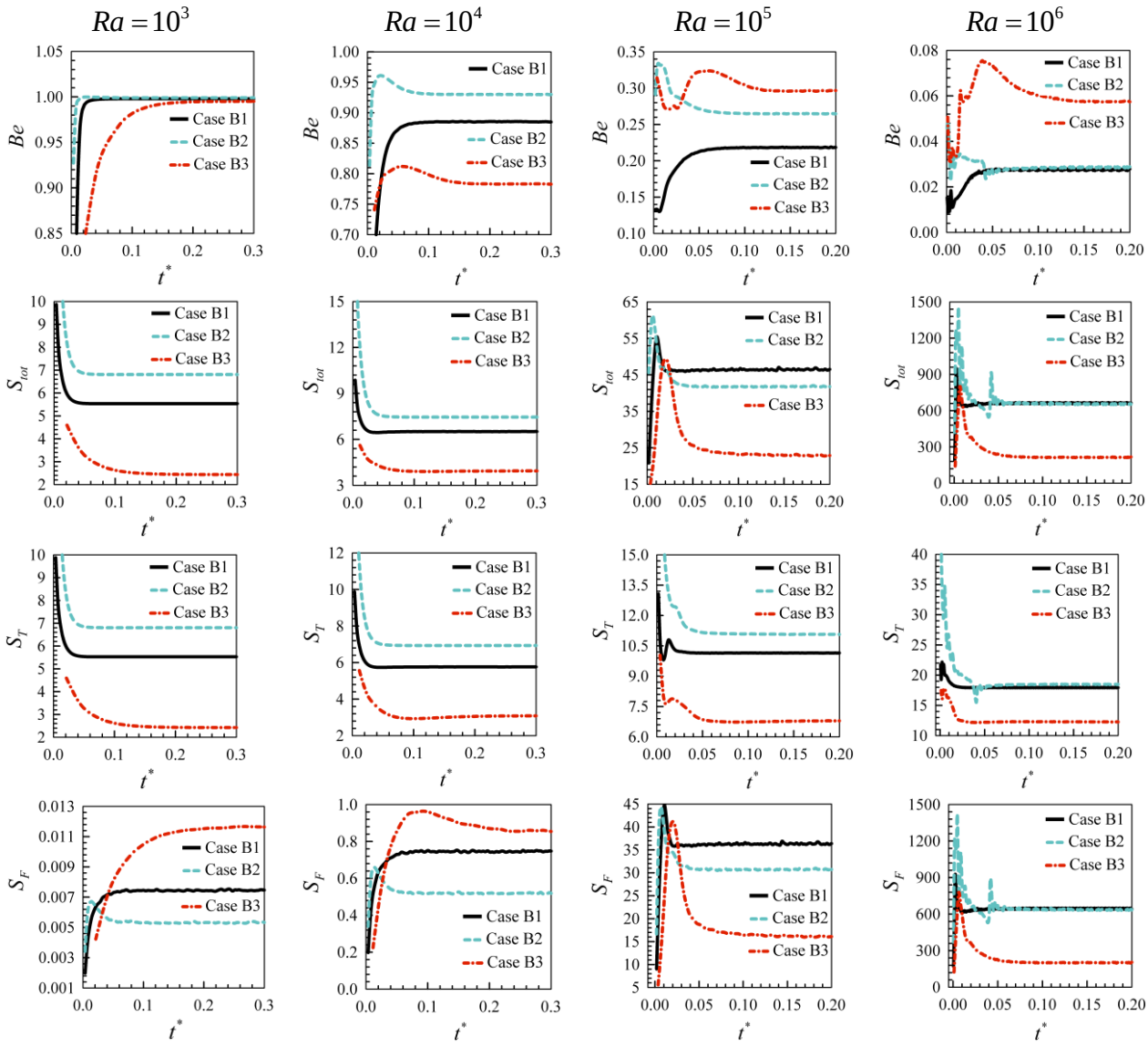

Figure 4-15 Variations of average Bejan number (Be), total average entropy generation (S_{tot}), average entropy generation due to thermal (S_T) and viscous (S_F) irreversibilities as a function of the non-dimensional time for cases B1 to B3 at different *Ra*. Case B1 ($\Pr = 0.71, L = 0.25H$), case B2 ($\Pr = 6.2, L_1 = 0.6H, L_2 = 0.3H$) and case B3 ($\Pr = 6.2, L_c = L_h = 0.225H$).

locations of maximum S_T are shifted to the bottom and top portions of the hot and cold cylinders respectively, where isotherms are densely packed and thermal stratification are formed in that areas. In fact, because of formation of thermal stratification and blockage effects of the heated pipes, lower and upper halves of the enclosure also experience a moderate heat transfer

irreversibility which is more visible in the corresponding local Bejan number (see Fig. 4-13 at $Ra \geq 10^5$ for case B3). In addition, by comparing Figs. 4-13 and 4-14 for case B3, one can conclude that, the region of low entropy generation corresponds to the middle of the enclosure where isotherms are horizontally oriented with lowest temperature gradients. Finally, Fig. 4-15 illustrates the time history of dimensionless entropy generation in the transient state for cases B1 to B3. It can be seen that although by increasing the *Ra* both $\overline{S}_F$ and $\overline{S}_T$ increase but at the certain value of Rayleigh number, $\overline{S}_F$ and $\overline{S}_T$ undergo the increasing and decreasing trends before reaching the steady-state condition. As mentioned before this behavior is attributed to the initial values which have been assigned for velocity ($\mathbf{u} = 0$) and temperature ($\theta = 0$) fields at the beginning of the simulations. By virtue of this fact, zero velocity results in lower velocity gradients which causes $\overline{S}_F$ to start from zero and increases as the time goes on. On the other hand, high level of the temperature gradients near the hot surfaces induces higher values of $\overline{S}_T$ at the start of the modeling ($t^* = 0$) in all cases. This observation is consistent with the results of Magherbi et al. [88] who numerically investigated transient natural convection and entropy generation in differentially heated cavity (DHC). They also stated that by increasing the *Ra*, a course of the fluctuations occurs in the total entropy generation on the basis of Prigogine's theory. This phenomenon is also observed in cases B1 to B3 where due to internal wave instability in the flow and temperature fields, instantaneous fluctuations are emerged in the $\overline{S}_F$ and $\overline{S}_T$. Note that since the temperature gradient is the underlying cause of the convection regime, this course of the oscillations also takes place in the values of average Nusselt number (see Fig. 4-12).

4.7 Conclusions

This paper introduced the Kernel Derivative-Free (KDF) Incompressible Smoothed Particle Hydrodynamic (ISPH) model for simulation of the multiphase flow and convection heat transfer problems. A new kernel function, Particle Shifting Technique (PST) and high order Laplacian and divergence operators are proposed to enhance the stability and accuracy of the numerical method. A wide range of the two-dimensional benchmark cases with different flow characteristics were used to verify the performance and its improvement for practical applications. The model was then applied to study the entropy generation due to natural

convection for different configurations. Based on the obtained results, the following points can be concluded:

4.7.1 KDF-ISPH method (development and evaluation, case A1 to A5)

- It is was found, the proposed new kernel function provided more accurate predictions compared to the cubic and quintic spline functions in modeling propagation of shock wave in 1D tube.
- The results indicated that proposed new Particle Shifting Technique (PST) has a significant impact on the stability of the mesh-free Lagrangian method, such that in its absence, particle clustering (tensile instability) is likely to happen.
- The model with the new Laplacian and divergence operators provided more accurate and smoother pressure field comparing to the traditional WCSPH in modeling of dam-breaking and rotating square patch of fluid.
- The capability of the new Laplacian and divergence operators was further verified by simulating natural convection heat transfer in a square cavity (case A5).
- It was found that, combination of the Particle Number Density (PND) and divergence of the displacement can successfully detect the position of the interface.
- The results showed that, the stability of the proposed method is significantly enhanced when non-conservative form of the momentum equation ($\chi = -1$) is used for free surface area (see Eq. (4-15)).
- Density error compensation term in PPE (additional term in Eq. (4-12)) was found to have a significant impact on the regularity of the particle distribution near the free-surface area such that in its absence, the particle inconsistency is likely to happen on the interface.

4.7.2 Entropy generation due to natural convection (case B1 to B3)

- The results indicated that, by increasing the *Ra* both average Nussent number and total entropy generation increase, while a downward trend is observed in average Bejan number.
- Entropy generation due to heat transfer (S_T), was found to be significant at low Rayleigh number ($Ra \leq 10^4$). In contrast, at the convection dominant regime ($Ra \geq 10^5$), most of the exergy loss in all cases was due to the viscous dissipation (S_F).

- It was found that the highest heat transfer rate is obtained when the hot surface is located lower than the cold one (and vice versa, for the lowest heat transfer rate).
- At low *Ra*, average Nusselt number and entropy generation due to all factors (S_T and S_F) alter asymptotically towards a certain value while at high *Ra* an oscillatory behavior occurs in the transient heat transfer rate and entropy generation before reaching the steady-state condition.
- It was found that due to low velocity gradients in the stagnation region, most of destruction of available work is due to the heat transfer irreversibility even at high *Ra* (corresponded to highest local Bejan number).

In future works, the energy conservation analysis of proposed model can be accomplished. Furthermore, the study can be extended for turbulent forced convection flow in complex geometries with curved boundaries. Simulation of standing wave, lid-driven differentially heated square cavity, dam break flow over a stationary obstacle, tank draining phenomena, and Rayleigh-Taylor Instability problem are some other benchmark cases that will be investigated in further work using proposed model.

4.8 Appendix A (gradient, Laplacian and divergence operators)

We take here a practical point of the view and derive three new gradient, Laplacian and divergence operators based on the KDF-ISPH in a form suitable for numerical solution. Using two-dimensional Taylor series expansion of a function at a nearby point (x_i,y_i) and multiplying it by W_{ij}, $x_{ij}W_{ij}$, $y_{ij}W_{ij}$ and integrating both sides of Eq. (4-A1) over the computational domain, particle approximation for the field function can be computed as follows:

$$f_j = f_i + f_x^{'}x_{ij} + f_y^{'}y_{ij} + \frac{1}{2}f_{xx}^{"}x_{ij}^2 + \frac{1}{2}f_{yy}^{"}y_{ij}^2 + f_{xy}^{"}x_{ij}y_{ij} + O(h^3) \tag{4-A1}$$

$$\begin{bmatrix} f_i \\ f_x^{'} \\ f_y^{'} \end{bmatrix} = L \begin{bmatrix} \sum_{j=1}^{N} f_j W_{ij} dV \\ \sum_{j=1}^{N} x_{ij} f_j W_{ij} dV \\ \sum_{j=1}^{N} y_{ij} f_j W_{ij} dV \end{bmatrix} \qquad L = \begin{bmatrix} \sum_{j=1}^{N} W_{ij} dV & \sum_{j=1}^{N} x_{ij} W_{ij} dV & \sum_{j=1}^{N} y_{ij} W_{ij} dV \\ \sum_{j=1}^{N} x_{ij} W_{ij} dV & \sum_{j=1}^{N} x_{ij}^2 W_{ij} dV & \sum_{j=1}^{N} x_{ij} y_{ij} W_{ij} dV \\ \sum_{j=1}^{N} y_{ij} W_{ij} dV & \sum_{j=1}^{N} x_{ij} y_{ij} W_{ij} dV & \sum_{j=1}^{N} y_{ij}^2 W_{ij} dV \end{bmatrix}^{-1} \tag{4-A2}$$

In the equation given above, f is a general variable such as velocity, temperature or pressure. $W_{ij} = W(\mathbf{r}_j - \mathbf{r}_i, h)$ is weight function and $dV = m_j / \rho_j$ represents the volume of particle i. $f_x^{'}$ and $f_y^{'}$ denote first derivatives of function $f(\mathbf{r}_j)$ while $x_{ij} = x_j - x_i$ and $y_{ij} = y_j - y_i$ are the distance between i-th particle to the j-th particle at positions $\mathbf{r}_i$ and $\mathbf{r}_j$ in x and y-directions, respectively. L is the corrective matrix which guarantees first-order accuracy in calculating field function (f_i). Eq. (4-A2) has also been documented by Colagrossi et al. [79] and known as a Moving Least-Squares method. However, when the kernel is fully supported by neighboring particles, the terms involving off-diagonal elements of the L matrix vanish ($\sum_{j=1}^{N} x_{ij} W_{ij} dV = \sum_{j=1}^{N} y_{ij} W_{ij} dV = \sum_{j=1}^{N} x_{ij} y_{ij} W_{ij} dV = 0$) such that inverse matrix L will be reduced to diagonal one. In this circumstance, field function can be computed through Shepard approximants at relatively low cost [89].

$$f_i = \frac{\sum_{j=1}^{N} f_j W_{ij} dV}{\sum_{j=1}^{N} W_{ij} dV} \qquad f_i = \sum_{j=1}^{N} f_j W_{ij}^S dV \qquad W_{ij}^S = \frac{W_{ij}}{\sum_{j=1}^{N} W_{ij} dV} \tag{4-A3}$$

Following the same argument, high-order particle approximation for the spatial derivative of the function can be obtained by subtracting Eq. (4-A1) from f_i and multiplying it by $x_{ij} W_{ij}$ and $y_{ij} W_{ij}$ as follows:

$$\begin{bmatrix} f_x^{'} \\ f_y^{'} \end{bmatrix} = L \begin{bmatrix} \sum_{j=1}^{N} x_{ij} (f_j - f_i) W_{ij} dV \\ \sum_{j=1}^{N} y_{ij} (f_j - f_i) W_{ij} dV \end{bmatrix} \quad L = \begin{bmatrix} \sum_{j=1}^{N} x_{ij}^2 W_{ij} dV & \sum_{j=1}^{N} x_{ij} y_{ij} W_{ij} dV \\ \sum_{j=1}^{N} x_{ij} y_{ij} W_{ij} dV & \sum_{j=1}^{N} y_{ij}^2 W_{ij} dV \end{bmatrix}^{-1} \tag{4-A4}$$

Eq. (4-A4) was originally introduced by Xu et al. [82] and known as a *mixed symmetric correction of kernel gradient*. From the above equations, it can be seen that in contrast to the standard SPH formulation, kernel gradient (∇W_{ij}) doesn't appear in Eq. (4-A4) and differential operation is only applied on the field function. Since the divergence operator is consisted of a series of gradient operators, the same procedure of the particle approximation with kernel normalisation can be adopted to compute ($\nabla \cdot \mathbf{f}$). Take as an illustration, for calculating

divergence of the velocity ($\nabla\cdot\mathbf{u}$), Eq. (4-A4) should be solved two times where sum of the velocity gradients in x ($f_x^{'}=\partial u/\partial x$) and y ($f_y^{'}=\partial v/\partial y$) directions can produce divergence operator. Similar to the field function (Eq. (4-A2)), when smoothing kernel has a compact support, gradient and divergence operators can be simplified into:

$$L=\begin{bmatrix}\sum_{j=1}^{N}x_{ij}^2W_{ij}dV & 0\\ 0 & \sum_{j=1}^{N}y_{ij}^2W_{ij}dV\end{bmatrix}^{-1}\qquad \nabla f=\begin{bmatrix}f_x^{'}\\ f_y^{'}\end{bmatrix}=\begin{cases}\sum_{j=1}^{N}x_{ij}(f_j-f_i)W_{ij}dV\Big/\sum_{j=1}^{N}x_{ij}^2W_{ij}dV\\ \sum_{j=1}^{N}y_{ij}(f_j-f_i)W_{ij}dV\Big/\sum_{j=1}^{N}y_{ij}^2W_{ij}dV\end{cases} \tag{4-A5}$$

By solving $\sum_{j=1}^{N}x_{ij}^2W_{ij}dV$ and $\sum_{j=1}^{N}y_{ij}^2W_{ij}dV$ in a polar coordinate system ($x_{ij}=r_{ij}\cos(\theta)$, $y_{ij}=r_{ij}\sin(\theta)$) in the case of the uniform particles distribution, Eq. (4-A5) can be simplified further and generalized into three-dimension as:

$$\begin{aligned}&\sum_{j=1}^{N}x_{ij}^2W_{ij}dV=\sum_{j=1}^{N}y_{ij}^2W_{ij}dV=\frac{1}{2}(\sum_{j=1}^{N}x_{ij}^2W_{ij}dV+\sum_{j=1}^{N}y_{ij}^2W_{ij}dV)=\\ &\frac{1}{3}(\sum_{j=1}^{N}x_{ij}^2W_{ij}dV+\sum_{j=1}^{N}y_{ij}^2W_{ij}dV+\sum_{j=1}^{N}z_{ij}^2W_{ij}dV)=\frac{1}{D_0}\sum_{j=1}^{N}r_{ij}^2W_{ij}dV\end{aligned} \tag{4-A6}$$

$$\nabla f=\frac{D_0\sum_{j=1}^{N}\mathbf{r}_{ij}(f_j-f_i)W_{ij}dV}{\sum_{j=1}^{N}\mathrm{r}_{ij}^2W_{ij}dV} \tag{4-A7}$$

$$\nabla\cdot\mathbf{f}=\frac{D_0\sum_{j=1}^{N}\mathbf{r}_{ij}\cdot(\mathbf{f}_j-\mathbf{f}_i)W_{ij}dV}{\sum_{j=1}^{N}\mathrm{r}_{ij}^2W_{ij}dV} \tag{4-A8}$$

where f, $\mathbf{f}$ and D_0 denote an arbitrary scalar, vector and spatial dimension. By retaining the second derivatives in Eq. (4-A1) (except $f_{xy}^{''}x_{ij}y_{ij}$) and multiplying it by W_{ij}, the discretization scheme for the Laplacian model can be written as follows:

$$\sum_{j=1}^{N}(f_j - f_i)W_{ij}dV = f_x^{'}\sum_{j=1}^{N}x_{ij}\,W_{ij}dV + f_y^{'}\sum_{j=1}^{N}y_{ij}\,W_{ij}dV + \frac{1}{2}\sum_{j=1}^{N}f_{xx}^{"}x_{ij}^2W_{ij}dV + \frac{1}{2}\sum_{j=1}^{N}f_{yy}^{"}y_{ij}^2\,W_{ij}dV \quad \text{(4-A9)}$$

To drive ($\nabla^2 f = f_{xx}^{"} + f_{yy}^{"}$) it is assumed that $\sum_{j=1}^{N}y_{ij}^2\,W_{ij}dV$ is equal to $\sum_{j=1}^{N}x_{ij}^2\,W_{ij}dV$. Although this hypothesis is only valid for regular particles arrangement and cannot be extended to free-surface area where kernel is truncated, but it is the only way in which $\nabla^2 f$ can be computed. Based on the above assumption, the third and fourth term in the right-hand side of Eq. (4-A9) can be rewritten as:

$$\begin{aligned}&\frac{1}{2}\sum_{j=1}^{N}f_{xx}^{"}x_{ij}^2W_{ij}dV + \frac{1}{2}\sum_{j=1}^{N}f_{yy}^{"}y_{ij}^2\,W_{ij}dV = \frac{1}{2}\sum_{j=1}^{N}f_{xx}^{"}x_{ij}^2W_{ij}dV + \frac{1}{2}\sum_{j=1}^{N}f_{yy}^{"}x_{ij}^2\,W_{ij}dV\\ &= \frac{1}{2}(f_{xx}^{"} + f_{yy}^{"})\sum_{j=1}^{N}x_{ij}^2W_{ij}dV = \frac{1}{2}(f_{xx}^{"} + f_{yy}^{"})\frac{1}{2}\sum_{j=1}^{N}(x_{ij}^2W_{ij}dV + y_{ij}^2\,W_{ij}dV) \quad \text{(4-A10)}\\ &= \frac{1}{2}(f_{xx}^{"} + f_{yy}^{"})\frac{1}{2}\sum_{j=1}^{N}r_{ij}^2W_{ij}dV \quad \textbf{for 2D}\end{aligned}$$

By substituting Eq. (4-A10) into Eq. (4-A9) a new Laplacian operator can be obtained:

$$\nabla^2 f = \frac{2\,D_0[\sum_{j=1}^{N}(f_j - f_i)W_{ij}dV - f_x^{'}\sum_{j=1}^{N}x_{ij}\,W_{ij}dV - f_y^{'}\sum_{j=1}^{N}y_{ij}\,W_{ij}dV - f_z^{'}\sum_{j=1}^{N}z_{ij}\,W_{ij}dV]}{\sum_{j=1}^{N}r_{ij}^2\,W_{ij}dV} \quad \text{(4-A11)}$$

where $f_x^{'}$ and $f_y^{'}$ are estimated by Eq. (4-A4). It is worthwhile mentioning that, the present model is very similar to the Schwaiger's model [65] who proposed high-order Laplacian operator discretization by taking gradient of kernel into account (∇W_{ij}). Finally, for the uniform particles arrangement ($\sum_{j=1}^{N}x_{ij}\,W_{ij}dV = \sum_{j=1}^{N}y_{ij}\,W_{ij}dV = \sum_{j=1}^{N}z_{ij}\,W_{ij}dV = 0$), Eq. (4-A10) can be reduced and expressed as:

$$\nabla^2 f = \frac{2 D_0 \sum_{j=1}^{N} (f_j - f_i) W_{ij} dV}{\sum_{j=1}^{N} r_{ij}^2 W_{ij} dV} \tag{4-A12}$$

This equation (Eq. (4-A12)) has also been derived independently by Koshizuka et al. [70] and Lei et al. [90] for simulation of the hydraulics problem and convection heat transfer, respectively.

4.9 Appendix B (Artificial term in Pressure Poisson Equation)

Generally, there are two types of the Pressure Poisson Equation which have been widely used in the context of the Lagrangian framework to estimate the pressure field namely: Divergence-Free (DF) velocity and Density Invariance (DI) models:

$$\nabla^2 P^{(n+1)} = \frac{\rho_0 \nabla \cdot \mathbf{u}^*}{\Delta t} \tag{4-B1}$$

$$\nabla \cdot (\frac{1}{\rho^*} \nabla P^{(n+1)}) = \frac{\rho_0 - \rho^*}{\rho_0 \Delta t^2} \tag{4-B2}$$

However, the results of Sun et al. [91] shown that the use of DF approach (Eq. (4-B1)) results in density error accumulation adjacent to free-surface area which in turn causes tensile instability and spurious numerical pressure vibration. On the other hand, Zheng et al. [92] reported that, solving Eq. (4-B2) alone leads to large density variation and particle explosion which subsequently attenuates stability of numerical simulation. To tackle this problem, Tanaka et al. [93], [94] suggested the use of hybrid model (Quasi-Compressibility) which benefits from both DF and DI source terms in PPE as given below:

$$\nabla^2 P^{(n+1)} = \frac{\rho_0 \nabla \cdot \mathbf{u}^*}{\Delta t} + \alpha \frac{\rho_0 - \rho^*}{\Delta t^2} \tag{4-B3}$$

where α is the relaxation coefficient of incompressibility which requires calibration in the range of $0 \le \alpha \le 1$. Based on the above brief description, along this appendix, the process of obtaining a new density error compensation term in Pressure Poisson Equation will be outlined and discussed in detail. By incorporating weak compressibility into the continuity equation ($\frac{D\rho}{\rho Dt}$), mass and momentum equations can be written as follows:

$$\frac{D\rho^{(n+1)}}{Dt}+\rho\nabla\cdot\mathbf{u}^{(n+1)}=0 \tag{4-B4}$$

$$\frac{\mathbf{u}^{(n+1)}-\mathbf{u}^{n}}{\Delta t}=-\frac{\nabla p^{(n+1)}}{\rho}+\upsilon\nabla^{2}\mathbf{u}^{n}+\mathbf{F}_{B} \tag{4-B5}$$

By inserting the intermediate velocity ($\mathbf{u}^{*}$) into the left-hand side of Eq. (4-B5) and implementing two-step projection method given by Chorin [77], momentum equation can be splitted into two successive parts as:

$$\frac{\mathbf{u}^{(n+1)}-\mathbf{u}^{*}+\mathbf{u}^{*}-\mathbf{u}^{n}}{\Delta t}=-\frac{\nabla p^{(n+1)}}{\rho}+\upsilon\nabla^{2}\mathbf{u}^{n}+\mathbf{F}_{B} \tag{4-B6}$$

$$\frac{\mathbf{u}^{*}-\mathbf{u}^{n}}{\Delta t}=\upsilon\nabla^{2}\mathbf{u}^{n}+\mathbf{F}_{B} \tag{4-B7}$$

$$\frac{\mathbf{u}^{(n+1)}-\mathbf{u}^{*}}{\Delta t}=-\frac{\nabla p^{(n+1)}}{\rho} \tag{4-B8}$$

The divergence of Eq. (4-B8) reads:

$$\nabla\cdot\mathbf{u}^{(n+1)}-\nabla\cdot\mathbf{u}^{*}=\nabla\cdot(-\frac{\Delta t}{\rho}\nabla p^{(n+1)}) \tag{4-B9}$$

Accordingly, by substituting equation (4-B9) into Eq. (4-B4), one obtains:

$$\frac{D\rho^{(n+1)}}{Dt}+\rho\nabla\cdot\mathbf{u}^{*}-\rho\nabla\cdot(\frac{\Delta t}{\rho}\nabla p^{(n+1)})=0 \tag{4-B10}$$

Taking into account that the third term can be expressed as:

$$\rho\nabla\cdot(\frac{\Delta t}{\rho}\nabla p^{(n+1)})=\Delta t\rho[-\frac{1}{\rho^{2}}\frac{\partial\rho}{\partial x}\frac{\partial p}{\partial x}-\frac{1}{\rho^{2}}\frac{\partial\rho}{\partial y}\frac{\partial p}{\partial y}]+\Delta t\rho(\frac{1}{\rho}\nabla^{2}p) \tag{4-B11}$$

we can establish an alternative form of the PPE as:

$$\nabla^{2}p=\frac{\rho\nabla\cdot\mathbf{u}^{*}}{\Delta t}+\frac{D\rho^{(n+1)}}{\Delta t Dt}+\frac{1}{\rho}[\frac{\partial\rho}{\partial x}\frac{\partial p}{\partial x}+\frac{\partial\rho}{\partial y}\frac{\partial p}{\partial y}] \tag{4-B12}$$

By defining parameters λ_1, λ_2 and λ_3, Eq. (4-B12) can be rewritten in a general form as:

$$\nabla^{2}p=\lambda_{1}\frac{\rho^{*}\nabla\cdot\mathbf{u}^{*}}{\Delta t}+\lambda_{2}\frac{\rho_{0}-\rho^{*}}{\Delta t^{2}}+\lambda_{3}\frac{1}{\rho^{*}}[\frac{\partial\rho^{*}}{\partial x}\frac{\partial p}{\partial x}+\frac{\partial\rho^{*}}{\partial y}\frac{\partial p}{\partial y}] \tag{4-B13}$$

Note that for $\lambda_1 = 1, \lambda_2 = 0, \lambda_3 = 0$, the expression reduces to the frequently used ISPH form (Eq. (4-B1)) while for $\lambda_1 = 0, \lambda_2 = 1, \lambda_3 = 0$ it turns into Eq. (4-B2). For the particular case of the $\lambda_1 = 1, \lambda_2 = 1, \lambda_3 = 0$, the hybrid DF-DI model (Eq. (4-B3)) can be obtained. The third term in Eq. (4-B13) is the new additional term which takes the spatial gradient of density into account. Finally, the values of $\rho^*, \frac{\partial \rho^*}{\partial x}$ and $\frac{\partial \rho^*}{\partial y}$ can be simultaneously obtained through gradient operator provided by Eq. (4-A2). Note that, the terms $\frac{\partial p}{\partial x}$ and $\frac{\partial p}{\partial y}$ (pressure gradient) in Eq. (4-B13) can be considered as a source term in the discretization process.

4.10 Appendix C (third-order TVD Runge-Kutta)

In the current work, a three-stage TVD Runge-Kutta (RK3) scheme with third-order accuracy proposed by Shu et al. [95] is adopted to discretize the physical transient term as follows:

$$\frac{du}{dt} = L_h(u) \qquad \frac{dr}{dt} = R_h(u) \qquad \frac{d\theta}{dt} = T_h(\theta) \tag{4-C1}$$

$$\begin{aligned} u^{(1)} &= \alpha_1 u^{(n)} + \beta_1 \Delta t\, L_h(u^{(n)}) \\ r^{(1)} &= \alpha_1 r^{(n)} + \beta_1 \Delta t\, R_h(u^{(1)}) \\ \theta^{(1)} &= \alpha_1 \theta^{(n)} + \beta_1 \Delta t\, T_h(\theta^{(n)}) \end{aligned} \tag{4-C2}$$

$$\begin{aligned} u^{(2)} &= \alpha_2 u^{(n)} + \beta_2 u^{(1)} + \beta_2 \Delta t\, L_h(u^{(1)}) \\ r^{(2)} &= \alpha_2 r^{(n)} + \beta_2 r^{(1)} + \beta_2 \Delta t\, R_h(u^{(2)}) \\ \theta^{(2)} &= \alpha_2 \theta^{(n)} + \beta_2 \theta^{(1)} + \beta_2 \Delta t\, T_h(\theta^{(1)}) \end{aligned} \tag{4-C3}$$

$$\begin{aligned} u^{(n+1)} &= \alpha_3 u^{(n)} + \beta_3 u^{(2)} + \beta_3 \Delta t\, L_h(u^{(2)}) \\ r^{(n+1)} &= \alpha_3 r^{(n)} + \beta_3 r^{(2)} + \beta_3 \Delta t\, R_h(u^{(n+1)}) \\ \theta^{(n+1)} &= \alpha_3 \theta^{(n)} + \beta_3 \theta^{(2)} + \beta_3 \Delta t\, T_h(\theta^{(2)}) \end{aligned} \tag{4-C4}$$

where $\alpha_1 = 1,\ \alpha_2 = 3/4,\ \alpha_3 = 1/3,\ \beta_1 = 1,\ \beta_2 = 1/4$ and $\beta_3 = 2/3$. $\mathbf{u}^n$ and $\mathbf{u}^{n+1}$ are the velocity at n^{th} and $(n+1)$ time step, respectively.

4.11 Appendix D (propagation of shock wave in 1D tube)

The Lagrangian form of the momentum, energy and continuity equations for simulation of the propagation of shock waves are given as [80]:

$$\frac{D\mathbf{u}}{Dt} = -\sum_{J=1}^{N} m_j \left(\frac{p_i + p_j}{\rho_i \rho_j} + \Pi_{ij}\right)\nabla W_{ij} \tag{4-D1}$$

$$\frac{De}{Dt} = -\frac{1}{2}\sum_{J=1}^{N} m_j \left(\frac{p_i}{\rho_i^2} + \frac{p_j}{\rho_j^2}\right)(\mathbf{u}_{ij} \cdot \nabla W_{ij}) \tag{4-D2}$$

$$\rho = \sum_{J=1}^{N} m_j W_{ij} \tag{4-D3}$$

$$\begin{aligned} \mathbf{u}^{(n+1)} &= \mathbf{u}^{(n)} + \Delta t \frac{D\mathbf{u}^{(n)}}{Dt} \\ \mathbf{r}^{(n+1)} &= \mathbf{r}^{(n)} + \Delta t\, \mathbf{u}^{(n+1)} \\ e^{(n+1)} &= e^{(n)} + \Delta t \frac{De^{(n)}}{Dt} \end{aligned} \tag{4-D4}$$

$$p = \rho(\gamma - 1)e, \quad c = \sqrt{\frac{\gamma p}{\rho}}, \tag{4-D5}$$

The symbols e, c and ∇W_{ij} denotes internal energy, speed of the sound and gradient of the kernel function, respectively. γ is a constant number equals to 1.4. The typical procedure to solve above equations consists of two steps. First, Eqs. (4-D1) to (4-D3) are solved to calculate material derivatives and density ($\frac{D\mathbf{u}}{Dt}, \frac{De}{Dt}, \rho$) and then particles are advected to new positions with updated velocity and energy according to Eq. (4-D4). Once the density and energy are found, pressure and sound speed are modified by Eq. (4-D5) and process will be repeated for the next time step. It should be noted that, artificial viscosity proposed by Monaghan [96] is frequently employed to prevent non-physical pressure oscillation and particles clustering near the shock as follows:

$$\begin{aligned} \Pi_{ij} &= \begin{cases} \dfrac{-\alpha \bar{c}_{ij}\phi_{ij} + \beta\phi_{ij}^2}{\bar{\rho}_{ij}} & \mathbf{u}_{ij} \cdot \mathbf{r}_{ij} < 0 \\ 0 & \mathbf{u}_{ij} \cdot \mathbf{r}_{ij} > 0 \end{cases} \\ \phi_{ij} &= \frac{h_{ij}(\mathbf{u}_{ij} \cdot \mathbf{r}_{ij})}{\left|r_{ij}\right|^2 + \varphi^2} \\ \bar{c}_{ij} &= \frac{c_i + c_j}{2}, \ \bar{\rho}_{ij} = \frac{\rho_i + \rho_j}{2}, \ \varphi = 0.01h_{ij}, \ \alpha = \beta = 1 \end{aligned} \tag{4-D6}$$

4.12 References

[1] P. Biswal, T. Basak, Entropy generation vs energy efficiency for natural convection based energy flow in enclosures and various applications: a review, Renew. Sustain. Energy Rev. 80 (2017) 1412–1457.

[2] D. Das, M. Roy, T. Basak, Studies on natural convection within enclosures of various (non-square) shapes – A review, Int. J. Heat Mass Transf. 106 (2017) 356–406. doi:10.1016/j.ijheatmasstransfer.2016.08.034.

[3] Y. Ma, R. Mohebbi, M.M. Rashidi, Z. Yang, Effect of hot obstacle position on natural convection heat transfer of MWCNTs-water nanofluid in U-shaped enclosure using lattice Boltzmann method, Int. J. Numer. Methods Heat Fluid Flow. 29 (2019) 223–250.

[4] Y. Ma, R. Mohebbi, M.M. Rashidi, Z. Yang, Simulation of nanofluid natural convection in a U-shaped cavity equipped by a heating obstacle: Effect of cavity's aspect ratio, J. Taiwan Inst. Chem. Eng. 93 (2018) 263–276. doi:10.1016/j.jtice.2018.07.026.

[5] Y. Ma, R. Mohebbi, M.M. Rashidi, Z. Yang, M.A. Sheremet, Numerical study of MHD nanofluid natural convection in a baffled U-shaped enclosure, Int. J. Heat Mass Transf. 130 (2019) 123–134.

[6] M. Afrand, S. Rostami, M. Akbari, S. Wongwises, M.H. Esfe, A. Karimipour, Effect of induced electric field on magneto-natural convection in a vertical cylindrical annulus filled with liquid potassium, Int. J. Heat Mass Transf. 90 (2015) 418–426.

[7] M. Afrand, D. Toghraie, A. Karimipour, S. Wongwises, A numerical study of natural convection in a vertical annulus filled with gallium in the presence of magnetic field, J. Magn. Magn. Mater. 430 (2017) 22–28.

[8] M. Izadi, R. Mohebbi, A. Chamkha, I. Pop, Effects of cavity and heat source aspect ratios on natural convection of a nanofluid in a C-shaped cavity using lattice Boltzmann method, Int. J. Numer. Methods Heat Fluid Flow. 28 (2018) 1930–1955.

[9] M. Izadi, R. Mohebbi, D. Karimi, M.A. Sheremet, Numerical simulation of natural convection heat transfer inside a$^{\perp}$ shaped cavity filled by a MWCNT-Fe3O4/water hybrid nanofluids using LBM, Chem. Eng. Process. Intensif. 125 (2018) 56–66.

[10] R. Mohebbi, M.M. Rashidi, Numerical simulation of natural convection heat transfer of a nanofluid in an L-shaped enclosure with a heating obstacle, J. Taiwan Inst. Chem. Eng. 72 (2017) 70–84.

[11] R. Mohebbi, M. Izadi, A.J. Chamkha, Heat source location and natural convection in a C-shaped enclosure saturated by a nanofluid, Phys. Fluids. 29 (2017) 122009.

[12] S. Aghakhani, A.H. Pordanjani, A. Karimipour, A. Abdollahi, M. Afrand, Numerical investigation of heat transfer in a power-law non-Newtonian fluid in a C-Shaped cavity with magnetic field effect using finite difference lattice Boltzmann method, Comput. Fluids. 176 (2018) 51–67.

[13] Y. Li, M. Firouzi, A. Karimipour, M. Afrand, Effect of an inclined partition with constant thermal conductivity on natural convection and entropy generation of a nanofluid under magnetic field inside an inclined enclosure: Applicable for electronic cooling, Adv. Powder Technol. (2019).

[14] P. Biswal, T. Basak, Role of differential vs Rayleigh-Benard heating at curved walls for efficient processing via entropy generation approach, Int. J. Heat Mass Transf. 124 (2018) 390–413.

[15] P. Biswal, T. Basak, Role of thermal and flow characteristics on entropy generation during natural convection in porous enclosures with curved walls subjected to Rayleigh-Bénard heating, Int. J. Heat Mass Transf. 109 (2017) 1261–1280.

[16] M. Hassani, A. Karimipour, Discrete ordinates simulation of radiative participating nanofluid natural convection in an enclosure, J. Therm. Anal. Calorim. 134 (2018) 2183–2195.

[17] S. Dutta, N. Goswami, A.K. Biswas, S. Pati, Numerical investigation of magnetohydrodynamic natural convection heat transfer and entropy generation in a rhombic enclosure filled with Cu-water nanofluid, Int. J. Heat Mass Transf. 136 (2019) 777–798.

[18] A.A. Alnaqi, S. Aghakhani, A.H. Pordanjani, R. Bakhtiari, A. Asadi, M.-D. Tran, Effects of magnetic field on the convective heat transfer rate and entropy generation of a nanofluid in an inclined square cavity equipped with a conductor fin: Considering the radiation effect, Int. J. Heat Mass Transf. 133 (2019) 256–267.

[19] G.H.R. Kefayati, H. Tang, MHD thermosolutal natural convection and entropy generation of Carreau fluid in a heated enclosure with two inner circular cold cylinders, using LBM, Int. J. Heat Mass Transf. 126 (2018) 508–530.

[20] T.A. Alkanhal, M. Sheikholeslami, A. Arabkoohsar, R. Haq, A. Shafee, Z. Li, I. Tlili, Simulation of convection heat transfer of magnetic nanoparticles including entropy generation using CVFEM, Int. J. Heat Mass Transf. 136 (2019) 146–156.

[21] A.I. Alsabery, F. Selimefendigil, I. Hashim, A.J. Chamkha, M. Ghalambaz, Fluid-structure interaction analysis of entropy generation and mixed convection inside a cavity with flexible right wall and heated rotating cylinder, Int. J. Heat Mass Transf. 140 (2019) 331–345.

[22] A.A.A.A. Al-Rashed, A. Shahsavar, O. Rasooli, M.A. Moghimi, A. Karimipour, M.D. Tran, Numerical assessment into the hydrothermal and entropy generation characteristics of biological water-silver nano-fluid in a wavy walled microchannel heat sink, Int. Commun. Heat Mass Transf. 104 (2019) 118–126.

[23] M. Esfandiary, B. Mehmandoust, A. Karimipour, H.A. Pakravan, Natural convection of Al2O3–water nanofluid in an inclined enclosure with the effects of slip velocity mechanisms: Brownian motion and thermophoresis phenomenon, Int. J. Therm. Sci. 105 (2016) 137–158.

[24] M.R. Safaei, A. Karimipour, A. Abdollahi, T.K. Nguyen, The investigation of thermal radiation and free convection heat transfer mechanisms of nanofluid inside a shallow cavity by lattice Boltzmann method, Phys. A Stat. Mech. Its Appl. 509 (2018) 515–535.

[25] S.M. Seyyedi, A.S. Dogonchi, M. Hashemi-Tilehnoee, Z. Asghar, M. Waqas, D.D. Ganji, A computational framework for natural convective hydromagnetic flow via inclined cavity: an analysis subjected to entropy generation, J. Mol. Liq. 287 (2019) 110863.

[26] S.M. Seyyedi, A.S. Dogonchi, M. Hashemi-Tilehnoee, M. Waqas, D.D. Ganji, Investigation of entropy generation in a square inclined cavity using control volume finite element method with aided quadratic Lagrange interpolation functions, Int. Commun. Heat Mass Transf. 110 (2020) 104398.

[27] X. Shi, Y. Wang, X. Huai, K. Cheng, Influence of geometrical parameters on thermal-hydraulic performance and entropy generation in cross-wavy channels with variable air properties, Appl. Therm. Eng. 157 (2019) 113714.

[28] K.M. Rabbi, M. Sheikholeslami, A. Karim, A. Shafee, Z. Li, I. Tlili, Prediction of MHD flow and entropy generation by Artificial Neural Network in square cavity with heater-sink for nanomaterial, Phys. A Stat. Mech. Its Appl. (2019) 123520.

[29] A. Zainali, N. Tofighi, M.S. Shadloo, M. Yildiz, Numerical investigation of Newtonian and non-Newtonian multiphase flows using ISPH method, Comput. Methods Appl. Mech. Eng. 254 (2013) 99–113.

[30] M. Hopp-Hirschler, M.S. Shadloo, U. Nieken, A Smoothed Particle Hydrodynamics approach for thermo-capillary flows, Comput. Fluids. 176 (2018) 1–19.

[31] A.M. Aly, Z.A.S. Raizah, Incompressible smoothed particle hydrodynamics (ISPH) method for natural convection in a nanofluid-filled cavity including rotating solid structures, Int. J. Mech. Sci. 146 (2018) 125–140.

[32] K.C. Ng, Y.L. Ng, T.W.H. Sheu, A. Mukhtar, Fluid-solid conjugate heat transfer modelling using weakly compressible smoothed particle hydrodynamics, Int. J. Mech. Sci. 151 (2019) 772–784.

[33] X. Yang, S.-C. Kong, Numerical study of natural convection in a horizontal concentric annulus using smoothed particle hydrodynamics, Eng. Anal. Bound. Elem. 102 (2019) 11–20.

[34] Z.L. Zhang, K. Walayat, C. Huang, J.Z. Chang, M.B. Liu, A finite particle method with particle shifting technique for modeling particulate flows with thermal convection, Int. J. Heat Mass Transf. 128 (2019) 1245–1262.

[35] L.B. Lucy, A numerical approach to the testing of the fission hypothesis, Astron. J. 82 (1977) 1013–1024.

[36] R.A. Gingold, J.J. Monaghan, Smoothed particle hydrodynamics: theory and application to non-spherical stars, Mon. Not. R. Astron. Soc. 181 (1977) 375–389.

[37] X. Xu, P. Yu, Extension of SPH to simulate non-isothermal free surface flows during the injection molding process, Appl. Math. Model. (2019).

[38] L. Deng, Y. Liu, W. Wang, W. Ge, J. Li, A two-fluid smoothed particle hydrodynamics (TF-SPH) method for gas-solid fluidization, Chem. Eng. Sci. 99 (2013) 89–101. doi:10.1016/j.ces.2013.05.047.

[39] Z. Wang, F. Hu, G. Duan, K. Shibata, S. Koshizuka, Numerical modeling of floating bodies transport for flooding analysis in nuclear reactor building, Nucl. Eng. Des. 341 (2019) 390–405.

[40] X. Yang, M. Ray, S.-C. Kong, C.-B.M. Kweon, SPH simulation of fuel drop impact on heated surfaces, Proc. Combust. Inst. 37 (2019) 3279–3286.

[41] X. Zheng, Q. Ma, W. Duan, Comparison of different iterative schemes for ISPH based on Rankine source solution, Int. J. Nav. Archit. Ocean Eng. 9 (2017) 390–403.

[42] A. Khayyer, H. Gotoh, Enhancement of stability and accuracy of the moving particle semi-implicit method, J. Comput. Phys. 230 (2011) 3093–3118.

[43] A. Khayyer, H. Gotoh, Enhancement of performance and stability of MPS mesh-free particle method for multiphase flows characterized by high density ratios, J. Comput. Phys. 242 (2013) 211–233.

[44] A. Khayyer, H. Gotoh, A higher order Laplacian model for enhancement and stabilization of pressure calculation by the MPS method, Appl. Ocean Res. 32 (2010) 124–131.

[45] H. Gotoh, A. Khayyer, H. Ikari, T. Arikawa, K. Shimosako, On enhancement of Incompressible SPH method for simulation of violent sloshing flows, Appl. Ocean Res. 46 (2014) 104–115.

[46] R. Fatehi, A. Rahmat, N. Tofighi, M. Yildiz, M.S. Shadloo, Density-based smoothed particle hydrodynamics methods for incompressible flows, Comput. Fluids. 185 (2019) 22–33.

[47] H. Nasiri, M.Y.A. Jamalabadi, R. Sadeghi, M.R. Safaei, T.K. Nguyen, M.S. Shadloo, A smoothed particle hydrodynamics approach for numerical simulation of nano-fluid flows, J. Therm. Anal. Calorim. 135 (2019) 1733–1741.

[48] M.S. Shadloo, A. Zainali, M. Yildiz, Simulation of single mode Rayleigh–Taylor instability by SPH method, Comput. Mech. 51 (2013) 699–715.

[49] M.S. Shadloo, A. Zainali, M. Yildiz, A. Suleman, A robust weakly compressible SPH method and its comparison with an incompressible SPH, Int. J. Numer. Methods Eng. 89 (2012) 939–956.

[50] E.O. Reséndiz-Flores, F.R. Saucedo-Zendejo, Meshfree numerical simulation of free surface thermal flows in mould filling processes using the Finite Pointset Method, Int. J. Therm. Sci. 127 (2018) 29–40.

[51] M.L. Hosain, J.M. Domínguez, R.B. Fdhila, K. Kyprianidis, Smoothed particle hydrodynamics modeling of industrial processes involving heat transfer, Appl. Energy. 252 (2019) 113441.

[52] H. Tan, S. Chen, A hybrid DEM-SPH model for deformable landslide and its generated surge waves, Adv. Water Resour. 108 (2017) 256–276.

[53] C. Zhang, X.Y. Hu, N.A. Adams, A weakly compressible SPH method based on a low-dissipation Riemann solver, J. Comput. Phys. 335 (2017) 605–620.

[54] E. Harada, H. Gotoh, H. Ikari, A. Khayyer, Numerical simulation for sediment transport using MPS-DEM coupling model, Adv. Water Resour. 129 (2019) 354–364.

[55] A. Khayyer, N. Tsuruta, Y. Shimizu, H. Gotoh, Multi-resolution MPS for incompressible fluid-elastic structure interactions in ocean engineering, Appl. Ocean Res. 82 (2019) 397–414.

[56] L. Wang, A. Khayyer, H. Gotoh, Q. Jiang, C. Zhang, Enhancement of pressure calculation in projection-based particle methods by incorporation of background mesh scheme, Appl. Ocean Res. 86 (2019) 320–339.

[57] Z.-B. Wang, R. Chen, H. Wang, Q. Liao, X. Zhu, S.-Z. Li, An overview of smoothed particle hydrodynamics for simulating multiphase flow, Appl. Math. Model. 40 (2016) 9625–9655.

[58] M.S. Shadloo, G. Oger, D. Le Touzé, Smoothed particle hydrodynamics method for fluid flows, towards industrial applications: Motivations, current state, and challenges, Comput. Fluids. 136 (2016) 11–34.

[59] J. Hongbin, D. Xin, On criterions for smoothed particle hydrodynamics kernels in stable field, J. Comput. Phys. 202 (2005) 699–709.

[60] X. Yang, M. Liu, S. Peng, Smoothed particle hydrodynamics modeling of viscous liquid drop without tensile instability, Comput. Fluids. 92 (2014) 199–208.

[61] X.F. Yang, S.L. Peng, M.B. Liu, A new kernel function for SPH with applications to free surface flows, Appl. Math. Model. 38 (2014) 3822–3833.

[62] P.N. Sun, A. Colagrossi, S. Marrone, M. Antuono, A.M. Zhang, Multi-resolution Delta-plus-SPH with tensile instability control: Towards high Reynolds number flows, Comput. Phys. Commun. 224 (2018) 63–80.

[63] G. Oger, M. Doring, B. Alessandrini, P. Ferrant, An improved SPH method: Towards higher order convergence, J. Comput. Phys. 225 (2007) 1472–1492.

[64] G. Oger, S. Marrone, D. Le Touzé, M. De Leffe, SPH accuracy improvement through the combination of a quasi-Lagrangian shifting transport velocity and consistent ALE formalisms, J. Comput. Phys. 313 (2016) 76–98.

[65] H.F. Schwaiger, An implicit corrected SPH formulation for thermal diffusion with linear free surface boundary conditions, Int. J. Numer. Methods Eng. 75 (2008) 647–671.

[66] R. Xu, P. Stansby, D. Laurence, Accuracy and stability in incompressible SPH (ISPH) based on the projection method and a new approach, J. Comput. Phys. 228 (2009) 6703–6725.

[67] A. Skillen, S. Lind, P.K. Stansby, B.D. Rogers, Incompressible smoothed particle hydrodynamics (SPH) with reduced temporal noise and generalised Fickian smoothing applied to body–water slam and efficient wave–body interaction, Comput. Methods Appl. Mech. Eng. 265 (2013) 163–173.

[68] P.N. Sun, A. Colagrossi, S. Marrone, M. Antuono, A.-M. Zhang, A consistent approach to particle shifting in the δ-Plus-SPH model, Comput. Methods Appl. Mech. Eng. 348 (2019) 912–934.

[69] A. Khayyer, H. Gotoh, Y. Shimizu, Comparative study on accuracy and conservation properties of two particle regularization schemes and proposal of an optimized particle shifting scheme in ISPH context, J. Comput. Phys. 332 (2017) 236–256.

[70] S. Koshizuka, Y. Oka, Moving-particle semi-implicit method for fragmentation of incompressible fluid, Nucl. Sci. Eng. 123 (1996) 421–434.

[71] S. Marrone, A. Colagrossi, D. Le Touzé, G. Graziani, Fast free-surface detection and level-set function definition in SPH solvers, J. Comput. Phys. 229 (2010) 3652–3663. doi:10.1016/j.jcp.2010.01.019.

[72] G. Duan, B. Chen, X. Zhang, Y. Wang, A multiphase MPS solver for modeling multi-fluid interaction with free surface and its application in oil spill, Comput. Methods Appl. Mech. Eng. 320 (2017) 133–161.

[73] Y. Zhang, D. Wan, MPS-FEM coupled method for sloshing flows in an elastic tank, Ocean Eng. 152 (2018) 416–427.

[74] S.J. Lind, R. Xu, P.K. Stansby, B.D. Rogers, Incompressible smoothed particle hydrodynamics for free-surface flows: A generalised diffusion-based algorithm for stability and validations for impulsive flows and propagating waves, J. Comput. Phys. 231 (2012) 1499–1523.

[75] A. Bejan, Entropy generation through heat and fluid flow, Wiley, 1982.

[76] G.G. Ilis, M. Mobedi, B. Sunden, Effect of aspect ratio on entropy generation in a rectangular cavity with differentially heated vertical walls, Int. Commun. Heat Mass Transf. 35 (2008) 696–703.

[77] A.J. Chorin, Numerical solution of the Navier-Stokes equations, Math. Comput. 22 (1968) 745–762.

[78] S. Marrone, M. Antuono, A. Colagrossi, G. Colicchio, D. Le Touzé, G. Graziani, δ-SPH model for simulating violent impact flows, Comput. Methods Appl. Mech. Eng. 200 (2011) 1526–1542.

[79] A. Colagrossi, M. Landrini, Numerical simulation of interfacial flows by smoothed particle hydrodynamics, J. Comput. Phys. 191 (2003) 448–475.

[80] L. Gui-rong, Smoothed particle hydrodynamics: a meshfree particle method, World Scientific, 2003.

[81] L. Lobovský, E. Botia-Vera, F. Castellana, J. Mas-Soler, A. Souto-Iglesias, Experimental investigation of dynamic pressure loads during dam break, J. Fluids Struct. 48 (2014) 407–434.

[82] X. Xu, X.-L. Deng, An improved weakly compressible SPH method for simulating free surface flows of viscous and viscoelastic fluids, Comput. Phys. Commun. 201 (2016) 43–62.

[83] B. Calcagni, F. Marsili, M. Paroncini, Natural convective heat transfer in square enclosures heated from below, Appl. Therm. Eng. 25 (2005) 2522–2531.

[84] M. Saidi, G. Karimi, Free convection cooling in modified L-shape enclosures using copper–water nanofluid, Energy. 70 (2014) 251–271.

[85] J.H. Doo, G.S. Mun, M.Y. Ha, S.Y. Seong, Thermo-dynamic irreversibility induced by natural convection in square enclosure with inner cylinder. Part-II: Effect of vertical position of inner cylinder, Int. J. Heat Mass Transf. 97 (2016) 1120–1139. doi:10.1016/j.ijheatmasstransfer.2016.02.054.

[86] M. Izadi, S. Sinaei, S.A.M. Mehryan, H.F. Oztop, N. Abu-Hamdeh, Natural convection of a nanofluid between two eccentric cylinders saturated by porous material: Buongiorno's two phase model, Int. J. Heat Mass Transf. 127 (2018) 67–75. doi:10.1016/j.ijheatmasstransfer.2018.07.066.

[87] I. V Miroshnichenko, M.A. Sheremet, Turbulent natural convection combined with thermal surface radiation inside an inclined cavity having local heater, Int. J. Therm. Sci. 124 (2018) 122–130. doi:10.1016/j.ijthermalsci.2017.09.023.

[88] M. Magherbi, H. Abbassi, A. Ben Brahim, Entropy generation at the onset of natural convection, Int. J. Heat Mass Transf. 46 (2003) 3441–3450.

[89] T. Belytschko, Y. Krongauz, J. Dolbow, C. Gerlach, On the completeness of meshfree particle methods, Int. J. Numer. Methods Eng. 43 (1998) 785–819.

[90] J.-M. Lei, X.-Y. Peng, Improved kernel gradient free-smoothed particle hydrodynamics and its applications to heat transfer problems, Chinese Phys. B. 25 (2015) 20202.

[91] Z. Sun, K. Djidjeli, J.T. Xing, Modified MPS method for the 2D fluid structure interaction problem with free surface, Comput. Fluids. 122 (2015) 47–65.

[92] X. Zheng, Q.W. Ma, W.Y. Duan, Incompressible SPH method based on Rankine source solution for violent water wave simulation, J. Comput. Phys. 276 (2014) 291–314.

[93] M. Tanaka, T. Masunaga, Stabilization and smoothing of pressure in MPS method by quasi-compressibility, J. Comput. Phys. 229 (2010) 4279–4290.

[94] M. Tanaka, R. Cardoso, H. Bahai, Multi-resolution MPS method, J. Comput. Phys. 359 (2018) 106–136.

[95] C.-W. Shu, S. Osher, Efficient implementation of essentially non-oscillatory shock-capturing schemes, J. Comput. Phys. 77 (1988) 439–471.

[96] J.J. Monaghan, SPH without a tensile instability, J. Comput. Phys. 159 (2000) 290–311.

Chapter 5 ARTICLE 2: NUMERICAL SIMULATION OF FREE-SURFACE FLOW AND CONVECTION HEAT TRANSFER USING A MODIFIED WEAKLY COMPRESSIBLE SMOOTHED PARTICLE HYDRODYNAMICS (WCSPH) METHOD

Faroogh Garoosi*, Ahmad Shakibaeinia

Department of Civil, Geological and Mining Engineering, Polytechnique Montreal, Montreal, Quebec, Canada

Corresponding author: faroogh.garoosi@polymtl.ca,

Second author: ahmad.shakibaeinia@polymtl.ca

Abstract

A novel Kernel Derivative-Free (KDF) Weakly-Compressible Smoothed Particle Hydrodynamics (WCSPH) model is developed for simulation of free-surface flows and convection heat transfer. A high-order Laplacian operator is developed and then applied for the approximation of the diffusion terms (e.g., viscous term, thermal diffusion, and newly additional diffusion term in the continuity equation). The transient term in Navier–Stokes equation is discretized using the third-order TVD Runge-Kutta scheme, while a stiff equation of state is employed to predict pressure field. To increase numerical accuracy, a new high-order smoothing operator in the context of the MPS description (Moving Particle Semi-implicit) is also proposed and then applied for the treatment of the buoyancy force term in the momentum equation. Furthermore, a new high-order smoothing kernel is constructed and tested via simulation of the 1D Sod shock tube problem. A series of numerical benchmark cases such as: dam break, stretching of a circular water drop, rotating square patch of fluid and natural convection heat transfer in a square enclosure are used to verify and evaluate the feasibility of the proposed models. It is found that all simulation results are in excellent agreement with the available experimental and numerical data. Capability and performance of KDF-WCSPH method in handling particulate flows with thermal convection are further demonstrated through analysis of entropy generation due to natural convection heat transfer in the three different well-known geometries including: Differentially Heated Cavity, L-shaped enclosure and horizontal annuli. Comparison with the past Finite-Volume results

demonstrates that the present model can maintain stability and accuracy, which makes it a very useful tool for simulation of thermo-hydraulic problems.

Keywords: KDF-WCSPH, Kernel Function, Smoothing operator, Laplacian operator, Entropy generation, Natural Convection,

5.1 Introduction

Natural convection heat transfer driven by buoyancy force is of a significant scientific issue which has attracted much attention in the recent years because of its wide range of applications in industrial and engineering systems such as: cooling of electronic component [1], solar collectors [2], heat exchangers [3], nuclear reactor cooling [4], thermal design of buildings [5] and etc. From an academic perspective, the problems of buoyancy-induced heat transfer in L-shaped enclosure and in the annulus between two horizontal concentric cylinders are of great interest and practical importance due to their unique application as a heat exchanger. Works of Saravanan et al. [6], Garoosi et al. [7], Hooshmand et al. [8] and Pordanjani et al. [9] can be mentioned as a few examples of such studies, in which they numerically simulated natural convection heat transfer in closed enclosure containing the hot obstacles. They discussed the effects of the length and location of the hot blocks on the heat transfer rate and found that flow field, temperature pattern and average Nusselt number are strongly dependent on the size and position of the hot pipe. Similar observations were reported by Mohebbi et al. [10], Saidi et al. [11], Elshehabey et al. [12] and Gawas et al. [13] who numerically investigated natural convection heat transfer in L-shaped enclosures.

In the last few decades, the significant effort has been devoted to optimize process parameters in enhancing the thermal design of the industrial and domestic systems which operate under natural convection mode. The concept of the entropy generation minimization was first introduced by Bejan [14] who mathematically demonstrated that, the generation of entropy or exergy loss leads to the reduction in the available work and consequently decreases the energy efficiency of the system [15]. During the past several years, many researchers have been motivated to apply the second law analysis to design thermal industrial systems with desirable characteristics [16]. Sivaraj et al. [17], Kefayati [18], Siavashi et al. [19] and Arun et al. [20] investigated the effects of the magnetic field on the heat transfer rate and entropy generation in the square enclosure with an inner hot obstacle. They found that, presence of the magnetic field minimizes the entropy

generation. Followed by the aforementioned studies, a few earlier works were also carried out by Liu et al. [21], Zhang et al. [22] and Astanina et al. [23] to optimize natural convection process in the closed cavities filled with a porous medium. They implemented EGM approach and demonstrated that by the increment of Rayleigh number, both heat transfer rate and irreversibilities of the thermal system increase. A comprehensive review of latest first and second law analysis of natural convection mechanism in closed enclosures with various practical applications can be found in works of the Biswal et al. [24] and Das et al. [25].

Besides the analysis of entropy generation and heat transfer, simulation of the multiphase flows involving complex interfaces is another most challenging topic in fluid mechanics which is difficult to represent by CFD tools. A literature review conducted by Pan et al. [26] shows that Volume-of-Fluid (VOF) [27] and Level-Set (LS) [28] are two most commonly used interface-tracking/capturing approaches in an Eulerian framework for modeling free-surface flows. However, although, the aforesaid methods have all been implemented in various multiphase problems, but the results of the Ha et al. [29] and Wu et al. [30] illustrate that the Eulerian mesh-based approaches have some innate drawbacks in determining the exact location of the flow front in multiphase phenomena.

To overcome aforementioned methodological problems and avoid difficulties in interface tracking, many scholars have adopted a newer generation of numerical techniques called Smoothed Particle Hydrodynamics (SPH), where particles in Lagrangian framework take the role of the grids in Eulerian one. Absence of the convection term in governing equations and free from constraints of the grids generation, make the SPH more efficient and robust method in dealing with the free-surface flow with large deformation or breaking. The SPH was initially introduced by Gingold and Monaghan [31] for describing the evolution of astrophysical phenomena. After its initial appearance, it was extensively applied in many research areas such as: simulation of liquid jet impinging on a flat plate and jet formation from a high pressure nozzle [32], [33], modeling of capillary rise dynamics and bubble rising [34], [35], simulation of convection heat transfer [36]–[39], simulation of droplet impact, gas-liquid two-phase flow and granular flow [40]–[42], respectively. The state-of-the-art review of recent applications of SPH and its future prospects can be found in works of Wang et al. [43] and Shadloo et al. [44].

However, although the above-cited studies vividly demonstrate the ability of Smoothed Particle Hydrodynamics (SPH) in modeling fluid-structure interaction problems (FSI) but this method has some key fundamental disadvantages in terms of accuracy and stability [45]. Non-physical pressure oscillation [46], [47], particle clustering (tensile instability) [48], low-order boundary treatment [49], false diffusion and density error accumulation [50], instability due to selection of the unsuitable kernel function to build the connection between the particles [51], penetration of particles into the boundaries walls [52], and low-order space and time discretization schemes for computing gradient, divergence and Laplacian operators [53], [54], are some major flaws related to this model which can endanger the solution stability and even lead to premature termination of the calculations. Over the last few years, substantial attempts were made to modify some of the shortcomings associated with the standard SPH model. For elimination of non-physical pressure fluctuations, Sun et al. [55], [56] proposed a new scheme called Tensile Instability Control (TIC) that was based on the altering the momentum equation to a non-conservative form. They suggested that this treatment should be only applied in some certain areas with unstable flow regime. Antuono et al. [57] invented an effective remedy to suppress the density error accumulation associated with the Weakly Compressible version of the SPH. They proposed a novel system of equations by inserting the additional diffusive term into the mass equation. Their results showed that, this extra term can significantly decrease the pressure oscillations in both time and spatial domain and named it as a Delta-SPH model ($\delta - SPH$). Particle Shifting Technique (PST) was first introduced by Xu [58] to overcome the instability caused by particle clustering. This technique was further extended and implemented by Lind et al. [59] and Khayyer et al. [60] for modeling of water wave propagation. They concluded that PST improves the homogeneity of particles dispersion and prevent the onset of tensile instability and particle bunching. Another possible source of the tensile instability can be traced back to the classical formulation of the SPH model. Originally, the governing equations of the SPH were derived by the fact that, particles are uniformly distributed within the computational domain. Thus, it is obvious that any heterogeneity among the particles can jeopardise the consistency of the simulation through inaccurate estimation of the governing operators. In a pioneering work, Oger et al. [54] suggested the use of renormalization technique to enhance the consistency of the gradient operator. They found that, reproducing the derivatives of kernel function using the corrective matrix can considerably increase the accuracy of particle approximations and

guarantee convergence properties of the method. In a similar work, Schwaiger [53] adopted Oger's technique [54] and proposed a new high-order Laplacian operator by eliminating the gradient terms from the Taylor-series expansion. Penetration of particles into the rigid walls is another major challenge faced with the SPH which causes numerical oscillations and termination of all computations. To prevent this phenomenon and reduce the boundary errors, Marrone et al. [49] suggested the use of Mirror Particles technique and concluded that this technique can provide significant improvement on the boundary condition and meanwhile prevent the unphysical particle penetration. Hongbin et al. [61] showed that kernel or weighting function as a heart of the SPH method plays a vital role on the stability of the numerical simulation. They performed a comparative study on ten different types of the kernel function and pointed out that Gaussian and Q-spline can potentially generate more precise results for a benchmark one-dimensional shock tube problem over the cubic-spline kernel function.

In light of the above discussion, the main objective of the present study is to introduce a novel Kernel-Derivative Free (KDF) Weakly Compressible Smoothed Particle Hydrodynamics (WCSPH) model for simulation of free-surface flows and convection heat transfer. Unlike the conventional WCSPH, in the proposed method the approximation of special derivatives has been accomplished based on the direct application of the kernel function (not its derivatives). A new kernel function is first constructed and then applied for simulation of propagation of shock wave in 1D tube. Moreover, a new high-order Laplace operator in the context of the MPS model (Moving Particle Semi-implicit method proposed by Koshizuka [62], [63]) is also formulated and then applied for discretization of the diffusion terms. Accuracy and performance of the proposed method (KDF-WCSPH) are verified against the existing results for free-surface flows and convection heat transfer problems such as: dam break, stretching of circular water drop, rotating square patch of fluid and natural convection heat transfer in square cavity heated from below. Finally, the verified KDF-WCSPH model is applied to study entropy generation due to natural convection heat transfer in three different geometries such as: Differentially Heated Cavity, L-shaped enclosure and horizontal annuli. To the best of the authors' knowledge and from the above literature survey, numerical simulation of entropy generation due to natural convection heat transfer using mesh-free particle method has never been reported in the literature so far.

5.1 Problem statement and governing equations

The coordinate system and geometrical configuration of physical models under consideration are presented in Fig. 5-1. Four different benchmark cases (A1 to A4) are used for verification of the proposed models whereas cases B1 to B3 are employed to demonstrate the capability of the enhanced KDF-WCSPH model in dealing with the natural convection heat transfer with special emphasis on the exergy aspects of the systems. The fluid flow in all cases ($\mathrm{Pr} = 0.71$ or 6.2) is assumed to be Newtonian, unsteady, laminar and two-dimensional with constant properties except for the density which varies linearly according to Boussinesq approximation in natural convection problems. To induce the buoyancy force in cases A4, B1, B2 and B3, the temperature difference is uniformly imposed on the hot ($T_h = 304\,K$) and cold ($T_c = 296\,K$) walls while the remaining parts of the cavity walls are thermally adiabatic. The numerical simulations are performed using, an in-house CFD code written in a FORTRAN program.

Under the assumption of constant thermo-physical properties of working fluid, the Lagrangian form of the continuity, momentum, energy and displacement equations for unsteady laminar flow can be written as follows [39]:

$$\frac{D\rho}{\rho Dt} + \nabla \cdot \mathbf{u} = 0 \tag{5-1}$$

$$\frac{D\mathbf{u}}{Dt} = -\frac{1}{\rho}\nabla P + \nu \nabla^2 \mathbf{u} + \frac{\mathbf{F_B}}{\rho}, \tag{5-2}$$

$$\frac{DT}{Dt} = \frac{1}{\rho C_P}\nabla \cdot (k \nabla T), \tag{5-3}$$

$$\frac{D\mathbf{r}}{Dt} = \mathbf{u}, \tag{5-4}$$

where **u** is the velocity vector, (with *u* and *v* components in 2D space), **r** is the position vector (with *x* and *y* components in 2D space). The terms ρ, μ, T, k and C_p are respectively density, dynamic viscosity, temperature, heat conductivity and specific heat. $\mathbf{F_B}$ represents the body forces per unit volume which is set as $F_b = \rho g$ (gravitational force) in the multi-phase flow or $F_b = -\rho g \beta (T - T_c)$ (buoyancy force) in natural convection heat transfer problems (with T_c being

the reference fluid temperature). After obtaining velocity and temperature fields, the rate of local entropy generation for Newtonian flow can be computed as follow [14]:

$$\dot{S}_{tot} = \dot{S}_T + \dot{S}_F \tag{5-5}$$

$$\dot{S}_{tot} = \frac{k}{T_0^2}(|\nabla T|)^2 + \frac{\bar{\bar{\tau}} : \bar{\bar{\nabla}}\mathbf{u}}{T_0}\phi = \frac{k}{T_0^2}\left[\left(\frac{\partial T}{\partial x}\right)^2 + \left(\frac{\partial T}{\partial y}\right)^2\right] + \frac{\mu}{T_0}\left[2\left(\frac{\partial u}{\partial x}\right)^2 + 2\left(\frac{\partial v}{\partial y}\right)^2 + \left(\frac{\partial u}{\partial y} + \frac{\partial v}{\partial x}\right)^2\right] \tag{5-6}$$

The first term in Eq. (5-6) represents the dimensional entropy generation caused by thermal dissipation while the second term is fluid friction irreversibility. By using the following dimensionless parameters, Eq. (5-6) can be converted to the non-dimensional form as:

$$X = \frac{x}{H}, \quad Y = \frac{y}{H}, \quad U = \frac{uH}{\alpha}, \quad V = \frac{vH}{\alpha}, \quad P = \frac{pH^2}{\rho\alpha^2}, \quad t^* = \frac{t\alpha}{H^2}, \quad \theta = \frac{T - T_c}{T_h - T_c}.$$
$$Ra = \frac{g\beta(T_h - T_c)H^3}{\alpha\nu}, \qquad \Pr = \frac{\nu}{\alpha}. \tag{5-7}$$

$$\dot{S}_{tot} = \dot{S}_T + \dot{S}_F = \left[\left(\frac{\partial \theta}{\partial X}\right)^2 + \left(\frac{\partial \theta}{\partial Y}\right)^2\right] + \varphi\left[2\left(\frac{\partial U}{\partial X}\right)^2 + 2\left(\frac{\partial V}{\partial Y}\right)^2 + \left(\frac{\partial U}{\partial Y} + \frac{\partial V}{\partial X}\right)^2\right]$$
$$\varphi = \frac{\mu T_0 \alpha^2}{kH^2(T_h - T_c)^2}, \qquad T_0 = \frac{T_h + T_c}{2} \tag{5-8}$$

In Eq. (5-8), φ is known as irreversibility distribution ratio which represents the ratio of the viscous dissipation to thermal entropy generation. The value of φ in the current work, is constant and taken as 10^{-4} similar to work of Ilis et al. [64]. The total volumetric entropy generation can be obtained via integrating the local entropy generation as follows:

$$\bar{S}_T = \frac{1}{\bar{\bar{V}}}\int S_T \, d\bar{V}, \qquad \bar{S}_F = \frac{1}{\bar{\bar{V}}}\int S_F \, d\bar{V}, \qquad \bar{S}_{tot} = \bar{S}_T + \bar{S}_F \tag{5-9}$$

Contribution of the heat transfer irreversibility to the total generated entropy can be determined by computing Bejan number as:

$$Be = \frac{S_T}{S_T + S_F} \qquad \overline{Be} = \frac{1}{\bar{\bar{V}}}\int Be \, d\bar{V} \tag{5-10}$$

Since Bejan number ranges from $0 \le Be \le 1$, $Be < 0.5$ indicates the relative dominance of the fluid friction irreversibility whereas $Be > 0.5$ implies that the irreversibility due to heat transfer is dominant. It is obvious that in case of $Be = 0.5$, thermal irreversibility and viscous dissipation are comparable.

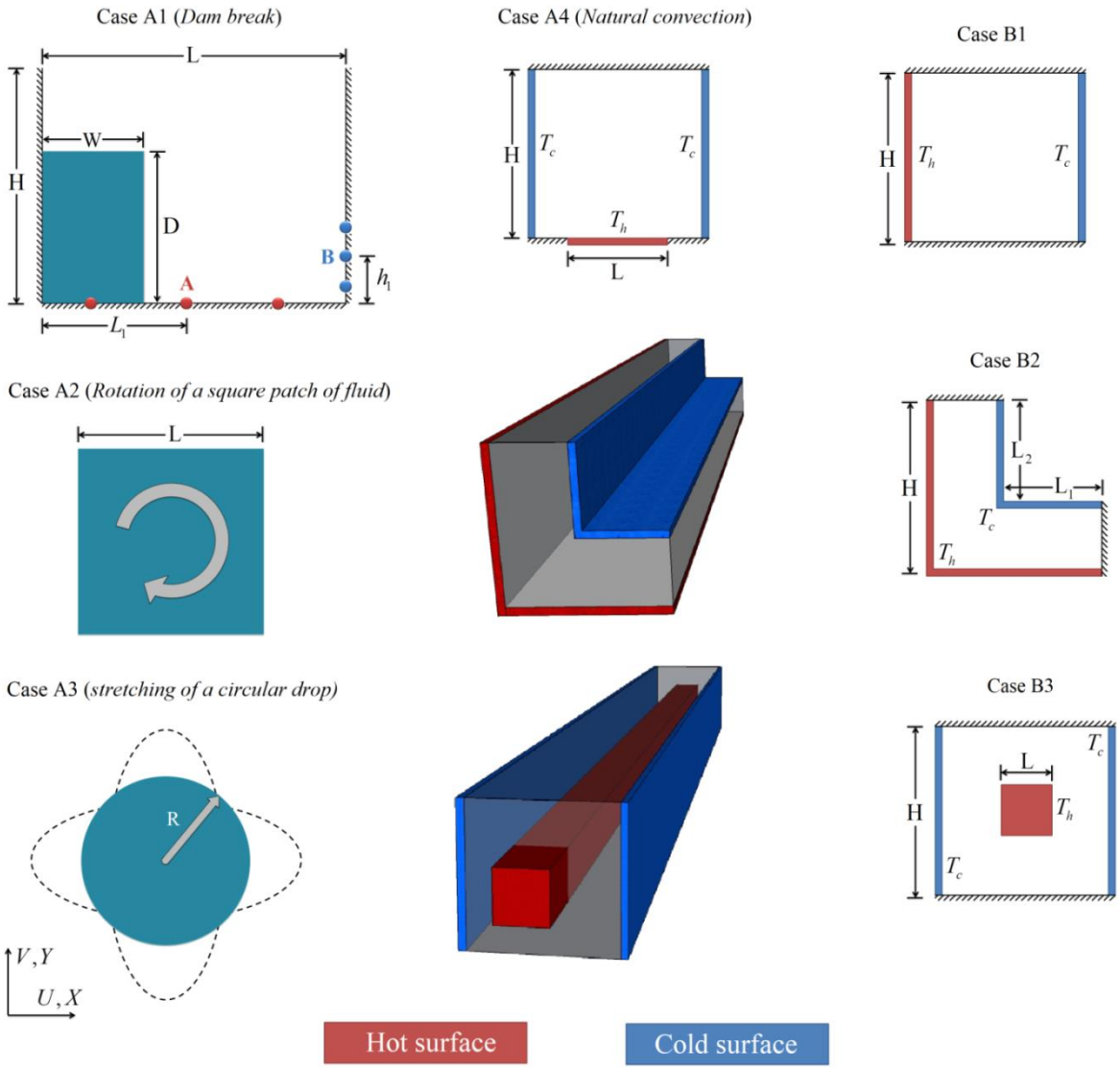

Figure 5-1 Schematical configuration of the considered problems with coordinate system and boundary conditions.

5.2 KDF-WCSPH formulation and solution methodology

Here, a Kernel Derivative-Free (KDF) form of the Weakly Compressible Smoothed Particle Hydrodynamics (WSPH) method with numerical diffusion term is developed and employed to solve the governing equations (5-1) to (5-5). Similar to the conventional SPH method [48], [57], [65], the entire domain including both fluid and boundary regions are spatially discretized using a set of the mobile particles. The proposed model is completely free from the derivative of kernel and uses the kernel function itself to approximate the special derivatives. Appendix (A) presents the derivation procedure of relevant governing operators (i.e. gradient, divergence, and Laplacian) for this newly developed model. The list of equations used to approximate the spatial derivatives of quantities (e.g., p, T and ρ) and vectors (e.g., $\mathbf{u}$) is summarized in Table 5-1.

Table 5.1 List of the equations used for calculating gradient, divergence, and Laplacian operators.

Operator	Equation used
Divergence (for velocity) ($\mathbf{u}_x^{'}, \mathbf{u}_y^{'}$) Gradient (for temperature) ($\theta_x^{'}, \theta_y^{'}$) Gradient (for density) ($\rho_x^{'}, \rho_y^{'}$)	Eq. (5-A2) is applied in the present work whereas Eq. (5-A3) with $\chi = 1$ can also be used.
Gradient (for pressure) ($p_x^{'}, p_y^{'}$)	Modified form of the Eq. (5-A3) is applied in the present work where $\chi = 1$ and $\chi = -1$ are used for internal and surface particles, respectively. (see Eq. (5-15))
Laplacian (for additional δ-term, ($\nabla^2 \rho$) and diffusion terms ($\nabla^2 \mathbf{u}, \nabla^2 \theta$))	Eq. (5-A11) is applied in the present work whereas Eq. (5-A12) can also be used.
Buoyancy force in natural convection (θ_i)	Eq. (5-A6) is applied in the present work whereas Eq. (5-A2) can also be used.
Pressure on the solid walls (p_i) Temperature on the insulated walls (θ_i)	Eq. (5-A2) is applied in the present work whereas Eq. (5-A6) can also be used.

5.2.1 Discretization of governing equation

To approximate solutions, the combination of two-step projection method given by Chorin [66] and third-order TVD Runge-kutta scheme is used (see also Appendix B). The first step involves calculation of the intermediate velocity at position x^n and y^n without the pressure term from the momentum balance equation as:

$$\frac{\mathbf{u}^* - \mathbf{u}^n}{\Delta t} = \upsilon \nabla^2 \mathbf{u}^n + \mathbf{F}_B \tag{5-11}$$

where **u** and $\mathbf{F_B}$ are velocity components and body force vector, respectively. By considering the weakly compressible condition, density at time level n^1 (first stage of TVD RK3) is calculated through the continuity equation as:

$$\frac{D\rho^{(n)}}{Dt} = -\rho^{(n)} \nabla \cdot \mathbf{u}^* + \lambda \Delta t \, c_0^2 \nabla^2 \rho \tag{5-12}$$

$$\rho^{(1)} = \rho^{(n)} + \Delta t \frac{D\rho^{(n)}}{Dt} \tag{5-13}$$

where variables c_0 and ρ_0 are artificial sound speed and reference density of particle *i*. The first term on the right-hand-side of Eq. (5-12) is the divergence of intermediate velocity ($\mathbf{u}^*$) while the second term is the Laplacian of density ($\nabla^2 \rho$), known as a Delta term (δ) [57]. This term is related to the density diffusion and is added to compensate the false diffusion errors (see also Appendix C). Here λ=0 or 1 is an on/off switch, to investigate the impact of this term. Note that unlike the δ-WCSPH method [57], here the newly diffusion term is totally free from the tuning parameter δ. Once the temporary density ($\rho^{(1)}$) is computed during the first stage of Runge-kutta, pressure and its gradient can be calculated. More precisely, allowing a slight compressibility, the pressure can be estimated explicitly through an equation of state (EOS) given by:

$$p^{(1)} = c_0^2 (\rho^{(1)} - \rho_0) \tag{5-14}$$

The pressure gradient can then be calculated as:

$$\nabla p^{(1)} = \begin{bmatrix} \dfrac{\partial p^{(1)}}{\partial x} \\ \dfrac{\partial p^{(1)}}{\partial y} \end{bmatrix} = L \begin{bmatrix} \displaystyle\sum_{j=1}^{N} x_{ij} \frac{(p_j^{(1)} - \chi p_i^{(1)})}{r_{ij}^2} W_{ij} \frac{m_j}{\rho_j} \\ \displaystyle\sum_{j=1}^{N} y_{ij} \frac{(p_j^{(1)} - \chi p_i^{(1)})}{r_{ij}^2} W_{ij} \frac{m_j}{\rho_j} \end{bmatrix} \quad L = \begin{bmatrix} \displaystyle\sum_{j=1}^{N} \frac{x_{ij}^2 W_{ij}}{r_{ij}^2} dV & \displaystyle\sum_{j=1}^{N} \frac{x_{ij} y_{ij} W_{ij}}{r_{ij}^2} dV \\ \displaystyle\sum_{j=1}^{N} \frac{x_{ij} y_{ij} W_{ij}}{r_{ij}^2} dV & \displaystyle\sum_{j=1}^{N} \frac{y_{ij}^2 W_{ij}}{r_{ij}^2} dV \end{bmatrix}^{-1} \tag{5-15}$$

To remove the spurious high-frequency noise near the free surface area, Eq. (5-15) is modified and generalized by inserting control parameter (χ) according to *Tensile Instability Control* (TIC) [55], [56] where conservative form of the pressure gradient ($\chi = 1$) is used for interior particles ($p_j^{(1)} - p_i^{(1)}$) while non-conservative one ($\chi = -1$) is applied on the interface particles ($p_j^{(1)} + p_i^{(1)}$). The corrected pressure gradient ($\nabla p^{(1)}$) is subsequently used to calculate accelerations of the fluid particles ($D\mathbf{u}/Dt$) through Eqs. (5-2) and (5-3). After solving equations (5-2) to (5-4), the velocity ($\mathbf{u}^{(1)}$), position ($\mathbf{r}^{(1)}$) and temperature ($\theta^{(1)}$) of the particles can be updated using the first step of the Runge-Kutta scheme as follows:

$$\begin{aligned} \mathbf{u}^{(1)} &= \mathbf{u}^{(n)} + \Delta t \frac{D\mathbf{u}^{(n)}}{Dt} \\ \mathbf{r}^{(1)} &= \mathbf{r}^{(n)} + \Delta t\, \mathbf{u}^{(1)} \\ \theta^{(1)} &= \theta^{(n)} + \Delta t \frac{D\theta^{(n)}}{Dt} \end{aligned} \tag{5-16}$$

By replacing $\mathbf{u}^{(1)}$, $\mathbf{r}^{(1)}$, $\theta^{(1)}$ with the corresponding variables $\mathbf{u}^n$, $\mathbf{r}^n$, θ^n and repeating the same procedure described above, the second step of the Runge-Kutta method can be accomplished as:

$$\frac{\mathbf{u}^{*}-\mathbf{u}^{(1)}}{\Delta t}=\upsilon\nabla^{2}\mathbf{u}^{(1)}+\mathbf{F}_{B}$$
$$\frac{D\rho^{(1)}}{Dt}=-\rho^{(1)}\nabla\cdot\mathbf{u}^{*}+\lambda\Delta t\,c_{0}^{2}\nabla^{2}\rho$$
$$\rho^{(2)}=\frac{3}{4}\rho^{(n)}+\frac{1}{4}\rho^{(1)}+\frac{1}{4}\Delta t\frac{D\rho^{(1)}}{Dt}$$
$$p^{(2)}=c_{0}^{2}(\rho^{(2)}-\rho_{0}) \qquad (5\text{-}17)$$
$$\mathbf{u}^{(2)}=\frac{3}{4}\mathbf{u}^{(n)}+\frac{1}{4}\mathbf{u}^{(1)}+\frac{1}{4}\Delta t\frac{D\mathbf{u}^{(1)}}{Dt}$$
$$\mathbf{r}^{(2)}=\frac{3}{4}\mathbf{r}^{(n)}+\frac{1}{4}\mathbf{r}^{(1)}+\frac{1}{4}\Delta t\,\mathbf{u}^{(2)}$$
$$\theta^{(2)}=\frac{3}{4}\theta^{(n)}+\frac{1}{4}\theta^{(1)}+\frac{1}{4}\Delta t\frac{D\theta^{(1)}}{Dt}$$

This procedure is continued for the last stage where particles are shifted to the new position $\mathbf{r}^{(n+1)}$ with updated velocity $\mathbf{u}^{(n+1)}$ and temperature $\theta^{(n+1)}$ as:

$$\frac{\mathbf{u}^{*}-\mathbf{u}^{(2)}}{\Delta t}=\upsilon\nabla^{2}\mathbf{u}^{(2)}+\mathbf{F}_{B}$$
$$\frac{D\rho^{(2)}}{Dt}=-\rho^{(2)}\nabla\cdot\mathbf{u}^{*}+\lambda\Delta t\,c_{0}^{2}\nabla^{2}\rho$$
$$\rho^{(n+1)}=\frac{1}{3}\rho^{(n)}+\frac{2}{3}\rho^{(2)}+\frac{2}{3}\Delta t\frac{D\rho^{(2)}}{Dt}$$
$$p^{(n+1)}=c_{0}^{2}(\rho^{(n+1)}-\rho_{0}) \qquad (5\text{-}18)$$
$$\mathbf{u}^{(n+1)}=\frac{1}{3}\mathbf{u}^{(n)}+\frac{2}{3}\mathbf{u}^{(2)}+\frac{2}{3}\Delta t\frac{D\mathbf{u}^{(2)}}{Dt}$$
$$\mathbf{r}^{(n+1)}=\frac{1}{3}\mathbf{r}^{(n)}+\frac{2}{3}\mathbf{r}^{(2)}+\frac{2}{3}\Delta t\,\mathbf{u}^{(n+1)}$$
$$\theta^{(n+1)}=\frac{1}{3}\theta^{(n)}+\frac{2}{3}\theta^{(2)}+\frac{2}{3}\Delta t\frac{D\theta^{(2)}}{Dt}$$

It should be noted that, in the above equations, Laplacian operator provided by Eq. (5-A11) have been used to calculate Delta (δ), diffusion ($\nabla^{2}\mathbf{u}$) and conduction ($\nabla^{2}\theta$) terms while Eq. (5-A3) is used to estimate divergence of the velocity field ($\nabla\cdot\mathbf{u}^{*}$). The temperature in the body force term ($F_{b}=-g\,\beta(T-T_{c})$) for convection heat transfer is computed by *Smoothing operator* according to Eq. (5-A2).

At the end of the above process, by integrating the local Nusselt number along the hot and cold surfaces, the average Nusselt number can be determined as:

$$\begin{bmatrix} \theta_i \\ \theta'_{i,x} \\ \theta'_{i,y} \end{bmatrix} = L \begin{bmatrix} \sum_{j=1}^{N} \frac{\theta_j^{(n+1)} W_{ij}}{r_{ij}^2} dV \\ \sum_{j=1}^{N} \frac{x_{ij} \theta_j^{(n+1)} W_{ij}}{r_{ij}^2} dV \\ \sum_{j=1}^{N} \frac{y_{ij} \theta_j^{(n+1)} W_{ij}}{r_{ij}^2} dV \end{bmatrix} \qquad L = \begin{bmatrix} \sum_{j=1}^{N} \frac{W_{ij}}{r_{ij}^2} dV & \sum_{j=1}^{N} \frac{x_{ij} W_{ij}}{r_{ij}^2} dV & \sum_{j=1}^{N} \frac{y_{ij} W_{ij}}{r_{ij}^2} dV \\ \sum_{j=1}^{N} \frac{x_{ij} W_{ij}}{r_{ij}^2} dV & \sum_{j=1}^{N} \frac{x_{ij}^2 W_{ij}}{r_{ij}^2} dV & \sum_{j=1}^{N} \frac{x_{ij} y_{ij} W_{ij}}{r_{ij}^2} dV \\ \sum_{j=1}^{N} \frac{y_{ij} W_{ij}}{r_{ij}^2} dV & \sum_{j=1}^{N} \frac{x_{ij} y_{ij} W_{ij}}{r_{ij}^2} dV & \sum_{j=1}^{N} \frac{y_{ij}^2 W_{ij}}{r_{ij}^2} dV \end{bmatrix}^{-1} \tag{5-19}$$

Over the heated walls of the enclosure:

$$\overline{Nu} = \frac{1}{L} \int_0^L \frac{\partial \theta}{\partial X} dY, \quad \overline{Nu} = \frac{1}{H} \int_0^H \frac{\partial \theta}{\partial Y} dX$$

On the walls of the hot obstacle:

$$\overline{Nu} = \frac{\int_{L_1}^{L_2} \left. \frac{\partial \theta}{\partial X} \right|_{Left} dY + \int_{L_1}^{L_2} \left. \frac{\partial \theta}{\partial X} \right|_{Right} dY + \int_{H_1}^{H_2} \left. \frac{\partial \theta}{\partial Y} \right|_{Bottom} dX + \int_{H_1}^{H_2} \left. \frac{\partial \theta}{\partial Y} \right|_{Top} dX}{A = 2(L_2 - L_1 + H_2 - H_1)} \tag{5-20}$$

where A is the non-dimensional effective surface area. With the knowledge of the temperature ($\theta'_{i,x} = \partial\theta/\partial x$, $\theta'_{i,y} = \partial\theta/\partial y$) and velocity gradients ($u'_{i,x}$, $u'_{i,y}$, $v'_{i,x}$, $v'_{i,y}$), entropy generation due to both factors (S_T, S_F) can be determined through Eq. (5-8) with the help of Eq. (5-A3).

5.2.2 Implementing boundary condition

By considering no-slip condition on the structure walls and zero heat flux on the insulated surfaces, dimensionless boundary conditions can be expressed as:

$\frac{\partial \theta}{\partial \vec{n}} = 0$	On the insulated surfaces
$\theta = 1, \ \theta = 0$	On the hot and cold walls
$U = V = 0,$	On the solid-fluid interfaces
$U_{ghost} = 2U_{solid-fluid\ \ interface} - U_{fluid}$	On the ghost particles (mirror velocity)
$V_{ghost} = 2V_{solid-fluid\ \ interface} - V_{fluid}$	

(5-21)

To enforce the non-slip and Neumann-boundary condition on the rigid wall, dynamic boundary algorithm (mirror particle) suggested by Marrone et al. [49] is employed to set up the ghost particles outside the fluid domain. In this technique mirrored velocity of the fluid particles in active zone is interpolated on the other side of the fluid-solid interface where corresponding ghost particle is located. The pressure (p_i) and temperature (θ_i on the insulated surfaces) of the ghost particle are calculated using Eq. (5-22). In this process at first, field function (p_i or θ_i) is estimated on the solid-fluid interface and then allocated to the corresponding ghost particles in the same rows or columns (see Fig. 5-2 and Eq. (5-A2) in appendix A).

$$\begin{bmatrix} p_i \\ p'_{i,x} \\ p'_{i,y} \end{bmatrix} = L \begin{bmatrix} \sum_{j=1}^{N} \frac{p_j W_{ij}}{r_{ij}^2} dV \\ \sum_{j=1}^{N} \frac{x_{ij} p_j W_{ij}}{r_{ij}^2} dV \\ \sum_{j=1}^{N} \frac{y_{ij} p_j W_{ij}}{r_{ij}^2} dV \end{bmatrix} \qquad L = \begin{bmatrix} \sum_{j=1}^{N} \frac{W_{ij}}{r_{ij}^2} dV & \sum_{j=1}^{N} \frac{x_{ij} W_{ij}}{r_{ij}^2} dV & \sum_{j=1}^{N} \frac{y_{ij} W_{ij}}{r_{ij}^2} dV \\ \sum_{j=1}^{N} \frac{x_{ij} W_{ij}}{r_{ij}^2} dV & \sum_{j=1}^{N} \frac{x_{ij}^2 W_{ij}}{r_{ij}^2} dV & \sum_{j=1}^{N} \frac{x_{ij} y_{ij} W_{ij}}{r_{ij}^2} dV \\ \sum_{j=1}^{N} \frac{y_{ij} W_{ij}}{r_{ij}^2} dV & \sum_{j=1}^{N} \frac{x_{ij} y_{ij} W_{ij}}{r_{ij}^2} dV & \sum_{j=1}^{N} \frac{y_{ij}^2 W_{ij}}{r_{ij}^2} dV \end{bmatrix}^{-1} \tag{5-22}$$

Note that the above symmetric linear system can be solved using Gaussian elimination with partial pivoting.

5.2.3 Particle Shifting Technique and free surface detection

To address the tensile instability and unphysical discontinuity within the fluid domain, Particle Shifting technique (PST) based on the Fick's law proposed by Lind et al. [59] is adopted here as:

$$\delta \mathbf{r}_{shift}^{(n+1)} = -D \times \nabla C_i \tag{5-23}$$

$$\nabla C_i = \sum_{j=1}^{N} \left[1 + R_{ij}\right] \nabla W_{ij} \frac{m_j}{\rho_j} \tag{5-24}$$

$$R_{ij} = 0.2 \left(\frac{W_{ij}}{W_{ij}(d_p)}\right)^4 \tag{5-25}$$

$$\mathbf{r}_i^{(n+1)*} = \mathbf{r}_i^{(n+1)} + \delta \mathbf{r}_{shift}^{(n+1)} \tag{5-26}$$

where D denotes a diffusion controller parameter ($D \le 0.5h^2$) and the term ∇C_i is the gradient of particle concentration which provide normal vector on the target particle *i*. R_{ij} is the artificial

repulsive force described by Monaghan [67] and $\delta\mathbf{r}_{shift}^{(n+1)}$ is the particle shifting distance which triggers particles migrate from region of high concentration to the lower one. $\mathbf{r}_i^{(n+1)*}$ is the particle's new position after applying PST. However, to avoid the problem of separating particle from the interface, optimized particle shifting (OPS) model suggested by Khayyer [60] is employed. In this procedure, for interfacial particles, normal direction of $\delta\mathbf{r}_{shift}^{(n+1)}$ is nullified whereas tangential component ($\delta\mathbf{r}_{shift,t}^{(n+1)}$) is kept unaltered as:

$$\delta\mathbf{r}_{shift,t}^{(n+1)} = -D\times(I - n_i \otimes n_i)\cdot\nabla C_i \tag{5-27}$$

$$\mathbf{r}_{i,t}^{(n+1)*} = \mathbf{r}_i^{(n+1)} + \delta\mathbf{r}_{shift,t}^{(n+1)} \tag{5-28}$$

where $\mathbf{n}_i$ is the corrected form of the $\delta\mathbf{r}_{shift}^{(n+1)}$ near the interface (for more details see work of Khayyer et al. [60]). Based on the above discussion, one may find that prior to implementing PST, the particle labeling scheme should be applied to determine the position of the interface. In the current work, the combination of Particle Number Density (PND) [68] and divergence of the displacement [59] is used as a hybrid kernel-based technique to capture the free-surface area as:

$$\mathrm{K}_1 = \sum_{j=1}^{N} W_{ij}\frac{m_j}{\rho_j}, \tag{5-29}$$

$$\mathrm{K}_2 = \sum_{j=1}^{N} x_{ij}\nabla W_{ij,x}\frac{m_j}{\rho_j} + \sum_{j=1}^{N} y_{ij}\nabla W_{ij,y}\frac{m_j}{\rho_j} \tag{5-30}$$

$$\mathrm{K} = (\mathrm{K}_1 + \mathrm{K}_2)/3, \tag{5-31}$$

$$f(\mathrm{K}) = \begin{cases} 0 & \mathrm{K} \le 0.75 \quad \text{Free-surface particle} \\ \frac{1}{2}[1-\cos(\pi\frac{\mathrm{K}-0.75}{0.93-0.75})] & 0.75 < \mathrm{K} < 0.93 \quad \text{Vicinity particles} \\ 1 & \mathrm{K} \ge 0.93 \quad \text{Internal particles} \end{cases} \tag{5-32}$$

Ideally, for a given particle, K_1 (PND) and K_2 ($\nabla\cdot\mathbf{r}$) would be equal to unity and 2, respectively. As a result, any deviation of K_1 and K_2 from their threshold values signifies that kernel function is truncated which subsequently gives an indication of the free-surface area. Finally, to identify the vicinity particles ($0.75 < \mathrm{K} < 0.93$) and eliminate the discontinuity between interface

($K \le 0.75$) and interior region ($K \ge 0.93$) in this process, cosine function (Eq. (5-32)) suggested by Skillen et al. [69] is used for smoothing purpose.

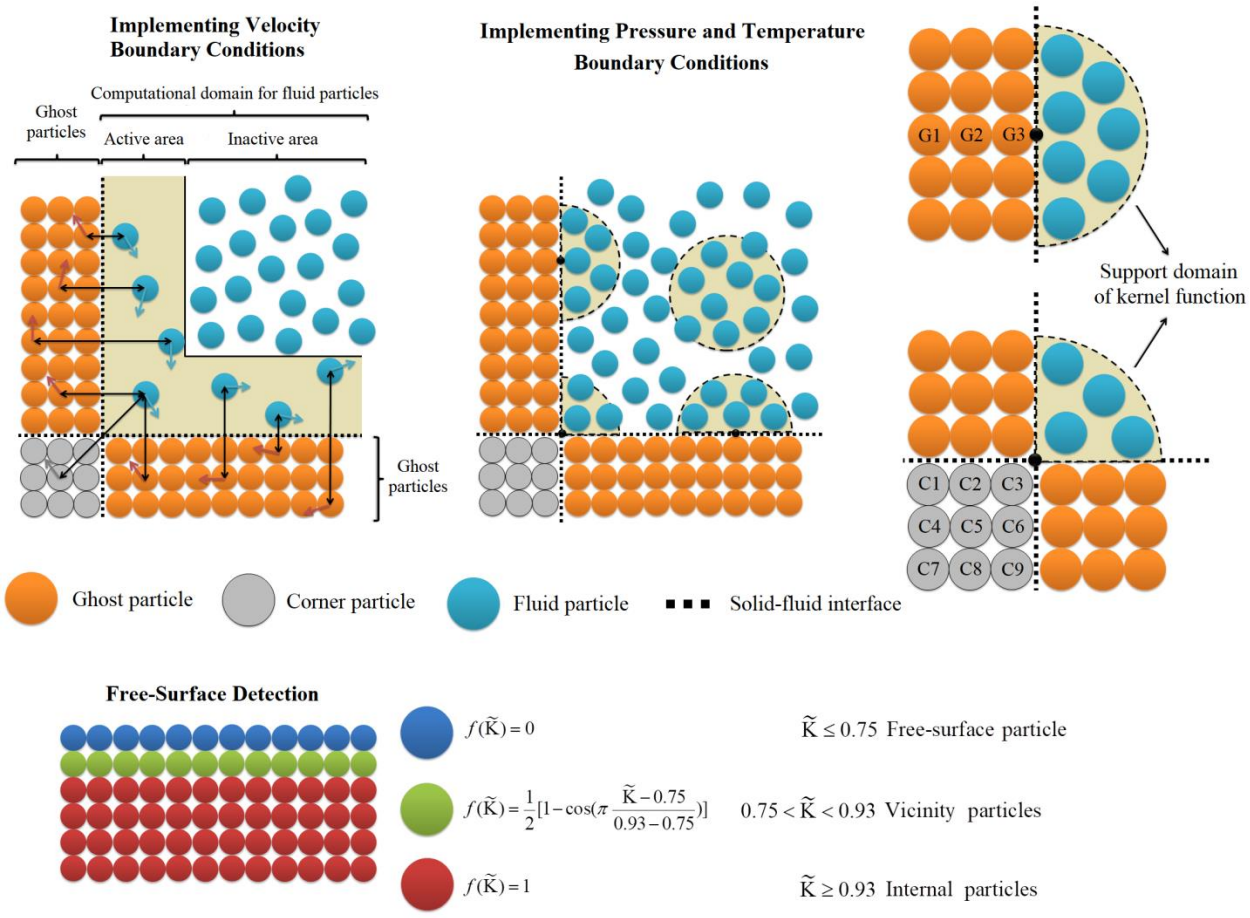

Figure 5-2 Example of the Fixed Ghost Particles, free-surface detection techniques, calculation of pressure and temperature on the wall particles.

5.3 New kernel function

Motivated by work of Hongbin et al. [61], in order to enhance the stability and accuracy of the particle method, a new high-order smoothing kernel is constructed by combing cosine and polynomial functions as:

$$W_{ij} = \alpha_D \begin{cases} \cos^{2.25}(\pi R/6)(3-R)^3(1+R) & 0 \le R \le 3 \\ 0 & R > 3 \end{cases}$$
$$\alpha_{1D} = \frac{0.019505894}{h},\ \alpha_{2D} = \frac{0.010373313}{h^2},\ \alpha_{3D} = \frac{0.005612838}{h^3}, \tag{5-33}$$

where h and $R = \left|\mathbf{r_{ij}}\right| / h$ denote smoothing length and relative distance between two interacting particle *i* and *j*, respectively. Since, analytical integration doesn't exist for Eq. (5-33), Simpson's rule is implemented to calculate constant coefficient α_D and satisfy unity condition ($\sum_{j=1}^{N} W_{ij} dV = 1$). The accuracy and consistency of newly proposed kernel function are demonstrated through numerical simulation of 1D Sod shock tube problem where two most frequently used kernel function namely: cubic Eq. (5-34) and quintic Eq. (5-35) spline functions are considered for comparison purpose [70].

$$W_{ij} = \alpha \begin{cases} 2/3 - R^2 + R^3/2 & 0 \le R \le 1 \\ (2-R)^3/2 & 1 < R \le 2 \\ 0 & R > 2 \end{cases}$$
$$\alpha_{1D} = \frac{1}{h},\ \alpha_{2D} = \frac{15}{7\pi h^2},\ \alpha_{3D} = \frac{3}{2\pi h^3}, \tag{5-34}$$

$$W_{ij} = \alpha \begin{cases} (3-R)^5 - 6(2-R)^5 + 15(1-R)^5 & 0 \le R \le 1 \\ (3-R)^5 - 6(2-R)^5 & 1 < R \le 2 \\ (3-R)^5 & 2 < R \le 3 \\ 0 & R > 3 \end{cases}$$
$$\alpha_{1D} = \frac{1}{120h},\ \alpha_{2D} = \frac{7}{478\pi h^2},\ \alpha_{3D} = \frac{1}{120\pi h^3}, \tag{5-35}$$

The initial conditions and material parameters of Sod shock tube (case A1) are similar to work of Gui-rong [70] where 320 particles with high pressure and density are uniformly located in the

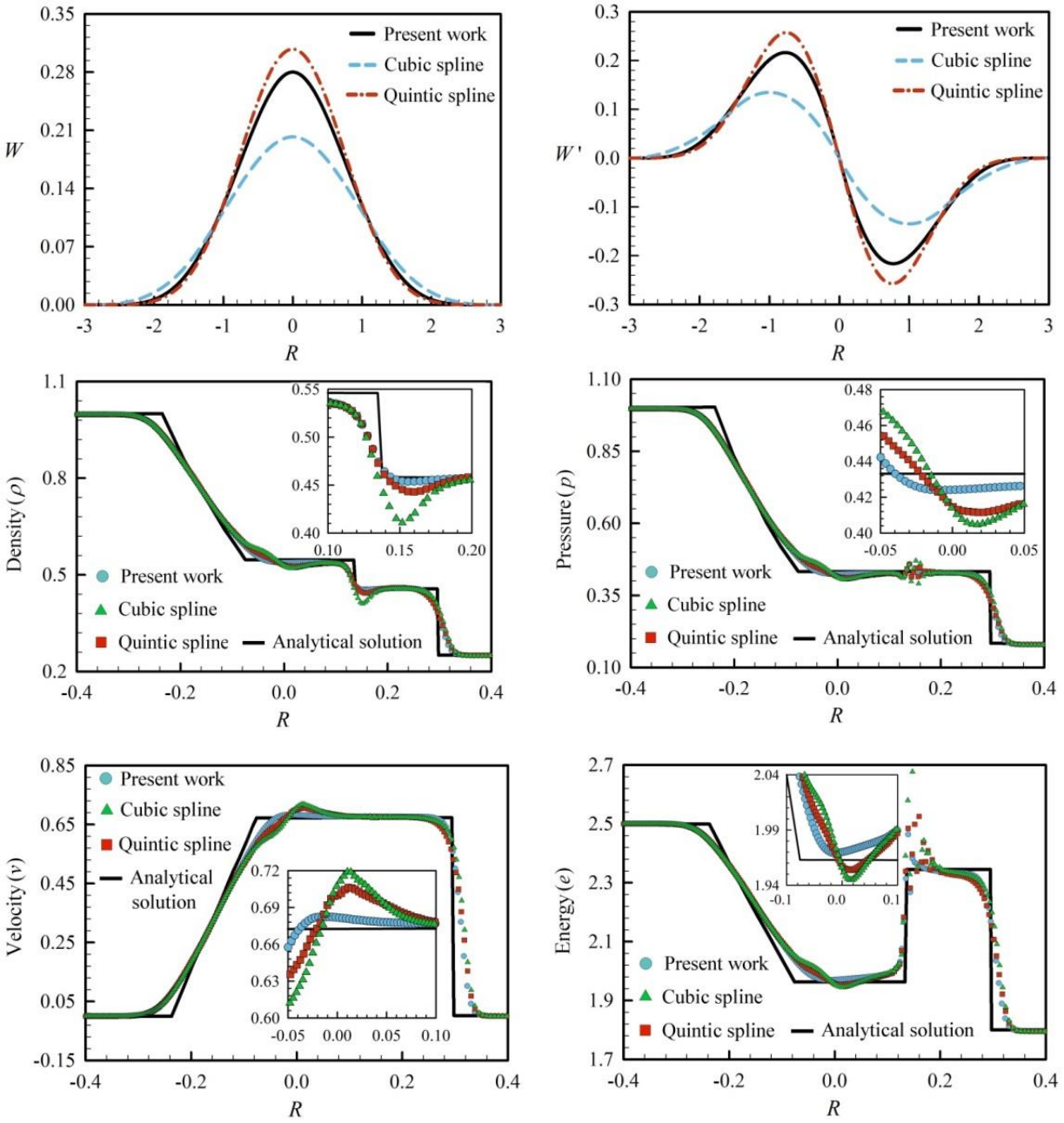

Figure 5-3 Comparison of the density, pressure, velocity and energy profiles between proposed kernel function and those obtained by cubic and quintic spline functions in simulation of the 1D Sod shock tube at t=0.2s.

left half of the tube $[-0.6, 0]$whereas 80 particles with low-density are evenly dispersed at low pressure region$[0, 0.6]$ (see also appendix D).

$$\begin{array}{llllll} x \le 0, & \rho = 1, & u = 0, & e = 2.5, & p = 1, & \Delta x = 0.001875, \quad m = 0.001875 \\ x > 0, & \rho = 0.25, & u = 0, & e = 1.795, & p = 0.1795, & \Delta x = 0.0075, \quad m = 0.001875 \end{array} \tag{5-36}$$

Simulation runs for $t = 0.2s$ with time step of $\Delta t = 0.005$ and numerical outcomes in terms of the velocity, pressure, density and energy profiles are plotted in Fig. 5-3. It can be seen that, the presented smoothing kernel is very close to the quintic spline function with the relatively same center peak value of 0.28 and lessens monotonically as the relative distance (*R*) augments. Unlike the cubic spline kernel which has a piecewise linear derivative with narrower compact support ($R = 2$), the present kernel is sufficiently smooth and has a finite compact support of $R = 3$ even for third derivative, resulting in more stable numerical solutions. Moreover, unlike the cubic and quintic kernels which are comprised of two and three pieces, the proposed kernel has only one piece which makes it more cost-effective from low computational cost and ease of use viewpoints. The obtained results in Fig. 5-3 show that, the new kernel can successfully identify and resolve the locations of the shock wave ($x = 0.3$), contact discontinuity ($x = 0.135$) and internal energy profiles of the rarefaction wave ($-0.25 \le x \le 0$) with minimal oscillation. As can be observed from Fig. 5-3 that, the proposed weight function demonstrates reasonably good agreement with analytical solutions and provides better predictions compared to the cubic and quintic kernel functions.

5.4 Validation

In this section, accuracy and performance of the new kernel function and Laplacian operator are demonstrated through a set of numerical and experimental benchmark cases including, dam break, stretching of circular water drop, rotating square patch of fluid and natural convection heat transfer in a square cavity. In all cases, smoothing length in kernel function (Eq. (5-33)) is taken as $h = 1.0\Delta x$ where $\Delta x = \Delta y$ is initial particle size. Time step (Δt) is chosen according to the $CFL = 0.1$ (Courant number) condition based on the maximum velocity within the computational domain as:

$$\Delta t_{convection} = CFL \frac{\Delta x}{c_0}, \; c_0 = 10 \left| \mathbf{u}_{\max} \right| \tag{5-37}$$

$$\Delta t_{viscous} = CFL \frac{\Delta x^2}{\nu}$$

$$\Delta t = \min(\Delta t_{convection}, \Delta t_{viscous})$$

5.4.1 Dam break

To assess the efficiency and reliability of the proposed KDF-WCSPH model in dealing with the large deformation and fragmentation of the multiphase flows in engineering applications, numerical modeling of the classical dam break on the dry bed has been chosen as a first benchmark case (case A1). Simulation is conducted in a two-dimensional enclosure ($H = 1.0\,m$ and $L = 1.61m$) where the rectangular water column ($D = 0.3\,m$ and $W = 0.6\,m$) with zero initial velocity ($u_0 = v_0 = 0 ms^{-1}$) and pressure ($p_0 = 0$) is stored on the left side of the reservoir as sketched in Fig. 5-1. Snapshots of pressure field together with the time evolutions of the dynamic pressure on the downstream wall and liquid levels at three different sampling points are plotted in Figs. 5-4 and 5-5. Generally, transient flow induced by failure of a dam can be divided into three stages. The first step involves collapsing and spreading of the water volume under the influence of the gravity force. It is evident that as the fluid propagates along the dry horizontal bed, the initial water level at the dam site ($L_1 = 0.3m$) declines monotonically until the water front toe reaches the right side of the reservoir with high celerity. The second step takes into account the impact of the front flow against the end wall where a vertical run-up jet and subsequent splash-up process are generated in that area. This stage is also accompanied by the first pressure shock as recorded by sensors 1 ($h_1 = 0.003m$) and 2 ($h_2 = 0.03m$) at $t^* = 2.43$ and $t^* = 2.68$, respectively. As the created surface wave moves upward, due to the restoring action of the gravity force, its velocity and kinetic energy decrease and subsequently the stagnation point is formed in the bottom right portion of the enclosure. This phenomenon causes continuous suppression of the dynamic pressure near the sampling points 1 and 2 ($h_1 = 0.003m, h_2 = 0.03m,\ 2.7 \le t^* \le 6$) while the ascending trend is observed at sensor 3 ($h_3 = 0.08m$). Under this circumstance, the strength of the impact force gradually drops and consequently the crest of the jet becomes thicker and starts to come down into the underlying fluid, resulting in the development of an avalanche-like motion

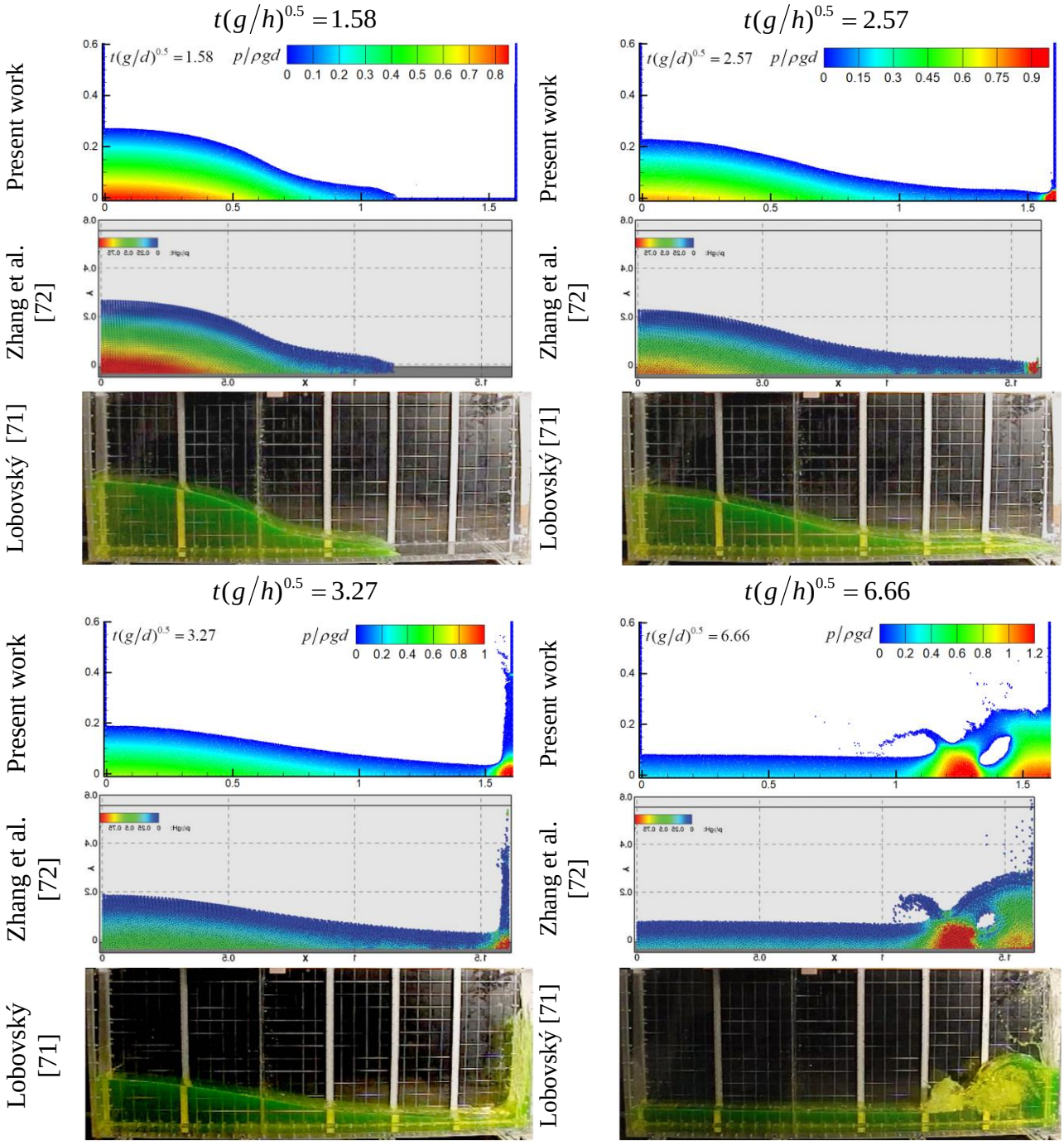

Figure 5-4 A qualitative comparison of present results with the existing numerical solution and experimental data of Zhang et al. [72] and Lobovský [71] for the case of dam break at different non-dimensional times ($t(g/h)^{0.5} = 1.58,\ 2.57,\ 3.27$ and 6.66).

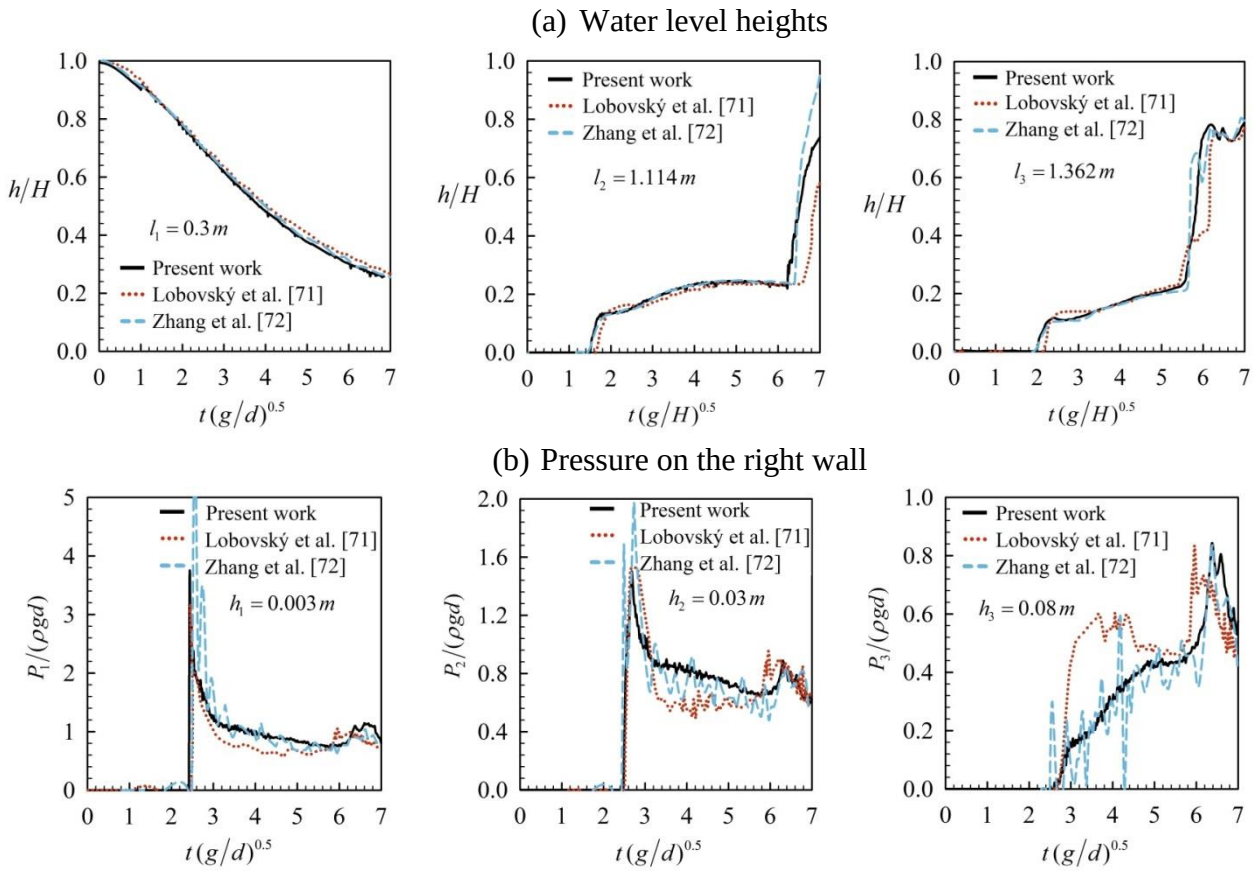

Figure 5-5 A quantitative comparison of present model with the numerical [72] and experimental results of Lobovský et al. [71] in terms of the (a) water level heights and pressure variations on the right wall. (a) History of Water-level recorded at L_1=0.3m, L_2=1.1 and L_3=1.362m $L_3 = 1.362m$. (b) History of pressure signals recorded at h_1=0.003m, h_2=0.03m and h_3=0.08m, N_p=22050.

(plunging breaker) and second sudden bulge in pressure time history. It can be seen from Fig. 5-5 that, duration and values of second peak impact pressure at the marked points h_1 ($t^* = 6.28,\ p_1 = 2640.7\,N/m^2$), h_2 ($t^* = 6.3,\ p_2 = 2582.1 N/m^2$) and h_3 ($t^* = 6.28,\ p_3 = 2464.7\,N/m^2$) are in quantitative agreement with the experimental measured data and numerical results of Lobovský et al. [71] and Zhang et al. [72], respectively. In the last stage,

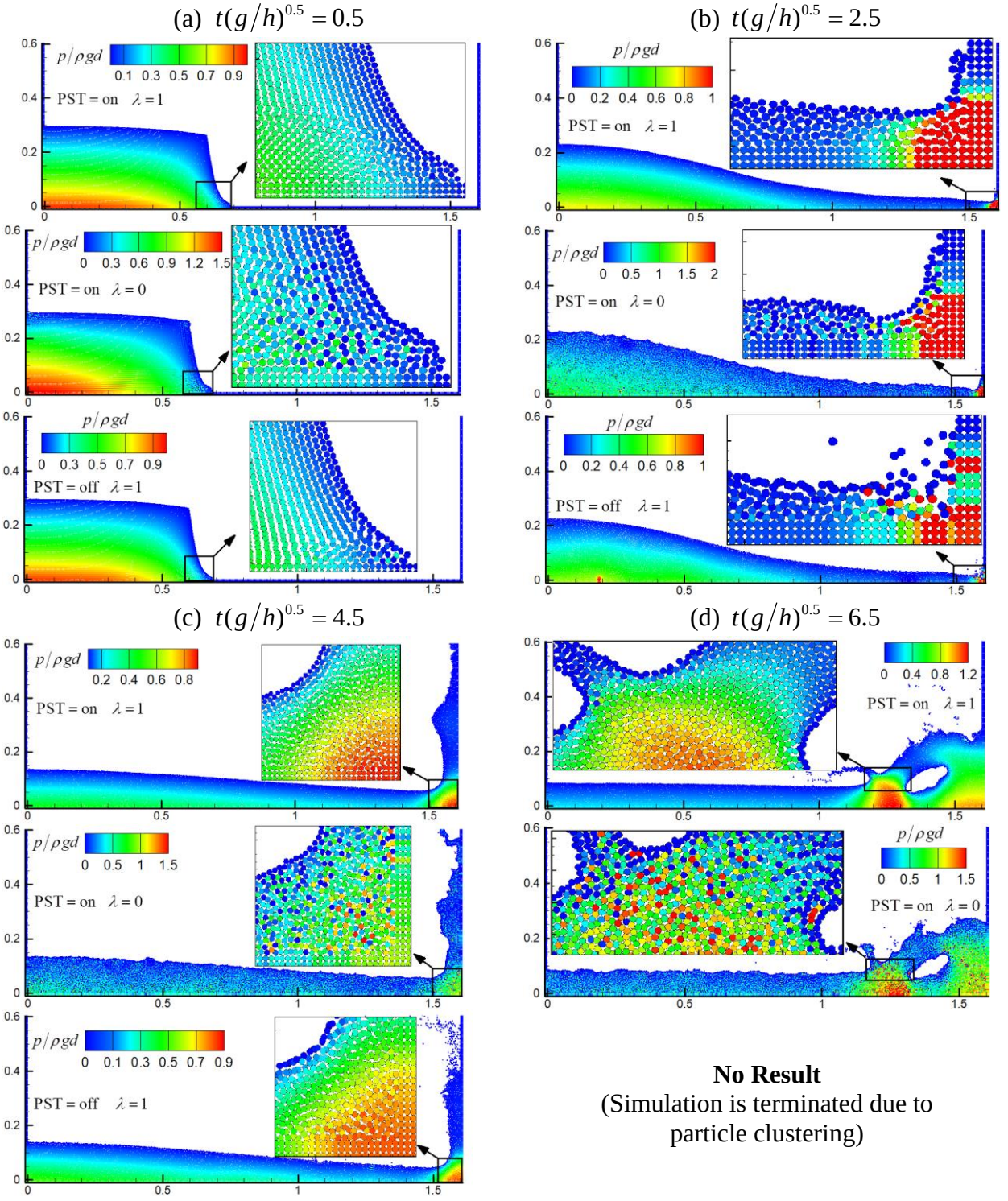

Figure 5-6 The effects of the particle shifting technique (PST) and additional diffusive term (λ) on the pressure field for the case of the dam break at different time intervals. $\rho = 997\,kgm^{-3}, \nu = 8.9\times10^{-7}\,m^2s^{-1}, g = -9.81ms^{-2}$.

the backward plunging jet travels toward the left part of the reservoir as a surge wave with the second splash-up scenario where some surface particles are separated from the bulk fluid, and freely aviated along the wet bed with moderate velocity. It is evident that both the pressure contour and configuration of the coalescence and rolling down of the interface (water tongue) are successfully predicted which signify the capability of the present method in handling complex solid-fluid interactions. To better understand the roles of the above mentioned factors, a sensitive analysis has been accomplished and obtained results are depicted in Fig. 5-6. It can be seen that by turning particle shifting off ($\mathrm{PST} = \mathrm{off}$), particle clustering takes place within the fluid domain (especially on the free-surface area) which ultimately leads to unexpected termination of the simulation. On the other hand, absence of the $\delta - \mathrm{term}$ ($\lambda = 0$) leads to spurious staggered pressure noise which dramatically affects the accuracy of the method. These observations are consistent with the findings of Antuono et al. [57] and Khayyer et al. [60] who investigated the effects of the PST and additional diffusive term on the stability of the Lagrangian particle method.

5.4.2 Rotating square patch of fluid

To check the capability of the proposed model and performance of the PST in handling negative pressure field, the evolution of 2D square patch of fluid subjected to the clockwise vortex is chosen here as a second benchmark case (case A2). The initial velocity field is given as the same manner introduced by Sun et al. [55] and Khayyer et al. [60]:

$$\begin{aligned} u_0(x,y) &= +y\,\omega \qquad -L/2 \le y \le L/2 \\ v_0(x,y) &= -x\omega \qquad -L/2 \le x \le L/2 \\ p_0(x,y) &= 0 \\ g(x,y,t) &= 0 \end{aligned} \tag{5-38}$$

where $\omega = 1\,s^{-1}$ and $L = 1$ are angular velocity and length of the fluid patch, respectively. Generally, hydrodynamic behavior of the square patch under the influence of the negative pressure field is characterized by the isotropic shrinkage of the medium sides where due to the centrifugal force, the middle parts of the patch are dragged towards the center of the vortex. Meanwhile, its corners gradually start to grow in the opposite direction to satisfy the continuity condition as shown in Fig. 5-7 (a). As the time progresses, four distinct arms of the patch becomes more visible which

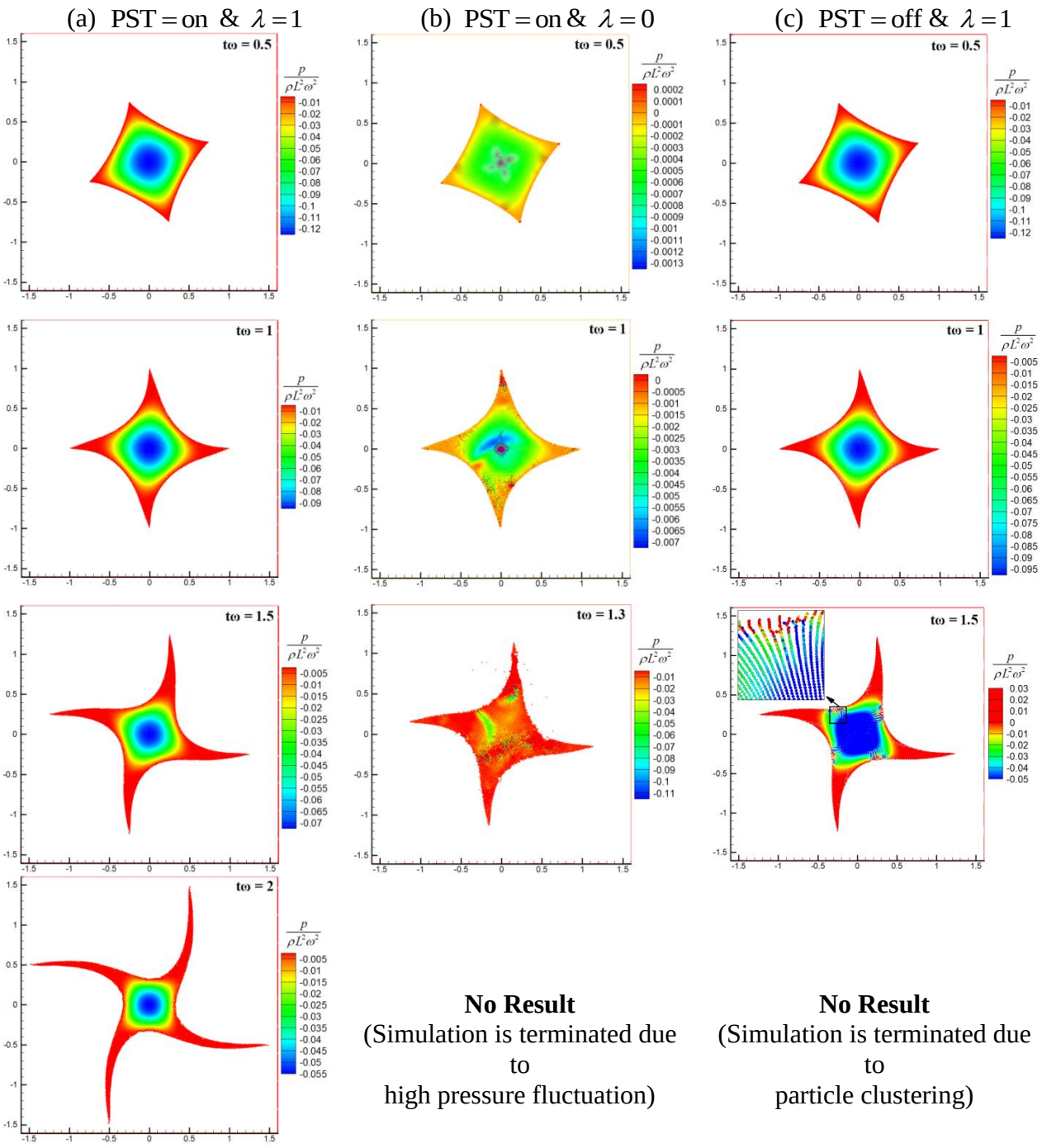

Figure 5-7 The effects of the particle shifting technique (PST) and additional diffusive term (λ) on the evolution of rotating square patch of fluid at for different time instants ($t\omega = 0.5$, 1, 1.5 and 2).($t\omega$ increases from top to bottom).

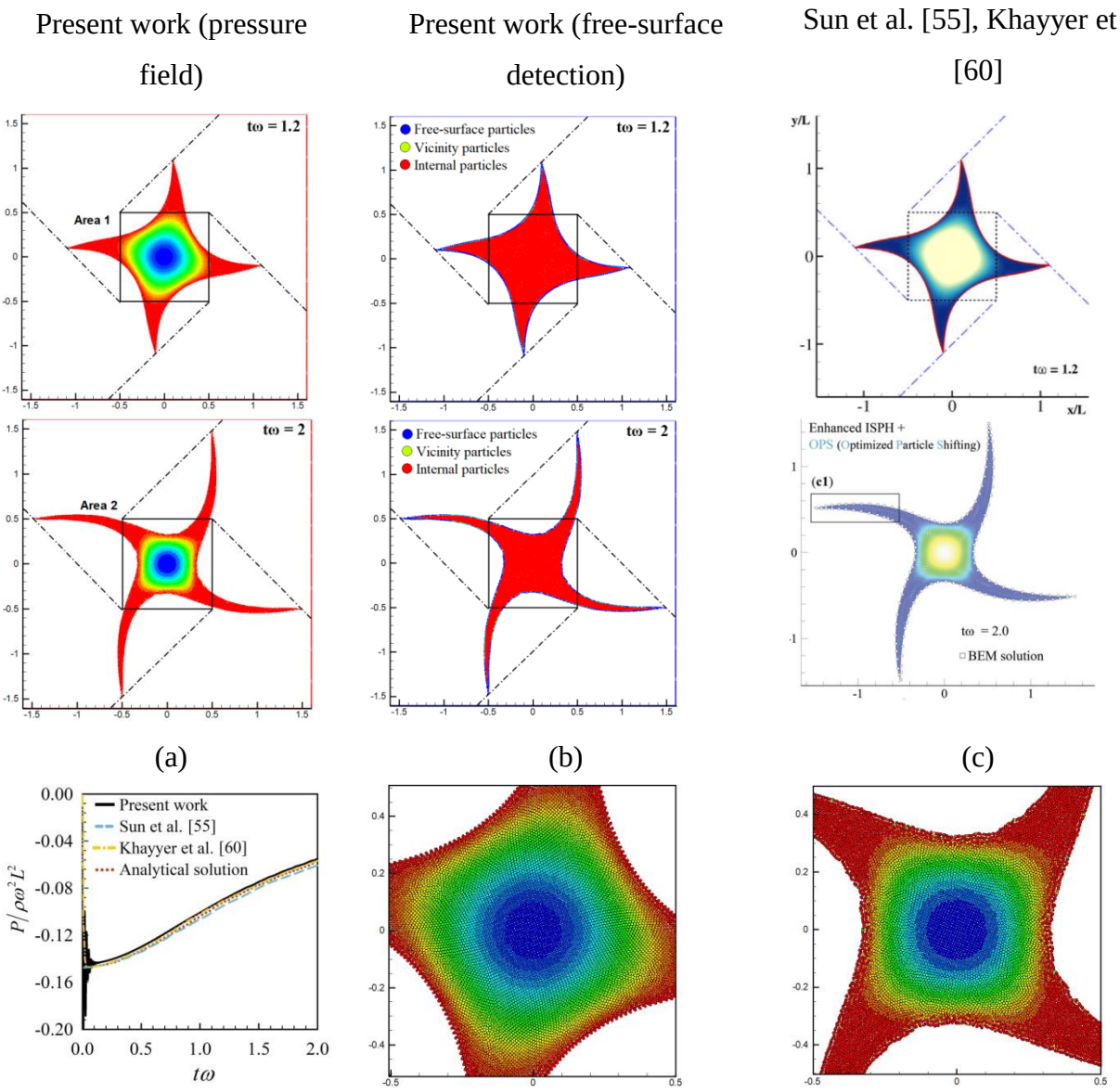

Figure 5-8 Validation of the present model against the numerical results of Sun et al. [55] and Khayyer et al. [60] at two different time instants ($t\omega = 1$ and 2). $N_p = 12321$. (a) History of non-dimensional pressure variation at the center of the fluid patch as a function of the dimensionless time ($t\omega$). Zoomed view of areas 1 (b) and 2 (c) depicted in the first column.

indicates that tensile instability is coming into the picture. This event is reflected in Fig. 5-7(a) where adoption of the PST as a means of particle regularization, provides much uniform particle distribution while in the absence of it, due to large particles deformation, the solution gets unstable, resulting in the occurrence of the numerical cavitation and degradation of the free

surface area (see Fig. 5-7(c)). By comparing Figs. 5-7(b) and 5-7(c), one can deduce that, the presence of the $\delta-\text{term}\,(\lambda=1)$ helps to remove spurious high-frequency oscillations (which is typical of the traditional SPH) from the density field and provide much smoother pressure distribution, accordingly. The time history of pressure at the center of the patch and snapshots of computed free surface area are plotted in Fig. 5-8. The comparisons reveal an excellent agreement with analytical solution and previous numerical results [55], [60].

5.4.3 Stretching of circular water drop

Deformation of the weightless circular water drop ($\mu=10^{-3}\,Pa\,s$, $\rho=1000\;kgm^{-3}$, $R=1m$, $g=0\,ms^{-2}$) into an elliptical shape is considered as the third benchmark test (case A3). In general, due to irrotational velocity field ($\mathbf{u}=-100x\hat{i}+100y\,j$), left and right parts of the water drop begins to shorten in the longitudinal direction whereas bottom and top portions elongate transversally. This process results in formation of the positive pressure field as revealed in Fig. 5-9. Similarly to what observed in previous cases, prototypes of the flow without the PST is unstable and characterized by undesirable effects of the tensile instability and unphysical discontinuity. On the other hand, the occurrence of the density error accumulation is attributed to the elimination of the $\delta-\text{term}\,(\lambda=0)$ which eventually destroys pressure field and drives the numerical calculation to the wrong evolution. This event is confirmed by zoomed view of area 2 in Fig. 5-10 where due to the high level of the particles interaction in *x*-direction, particle stratification and unphysical void regions are horizontally established within the fluid domain. Furthermore, it is discernible from Figs. 5-9(c) and 5-9(d) that the flow patterns generated by both conventional WCSPH [47] and present model without the $\delta-\text{term}\,(\lambda=0)$ suffer from unphysical pressure oscillations (staggered noise) and particle inconsistency. This event implies that traditional WCSPH formulations cannot sufficiently guarantee the conservation of total mass. Time history of the horizontal semi-axis movement and pressure variations at the center of the drop are illustrated in Fig. 5-10. Despite the small discrepancy that may come from assigning zero initial value for pressure ($p_0=0$), numerical outcomes of the present work are in good overall agreement with analytical solution [47].

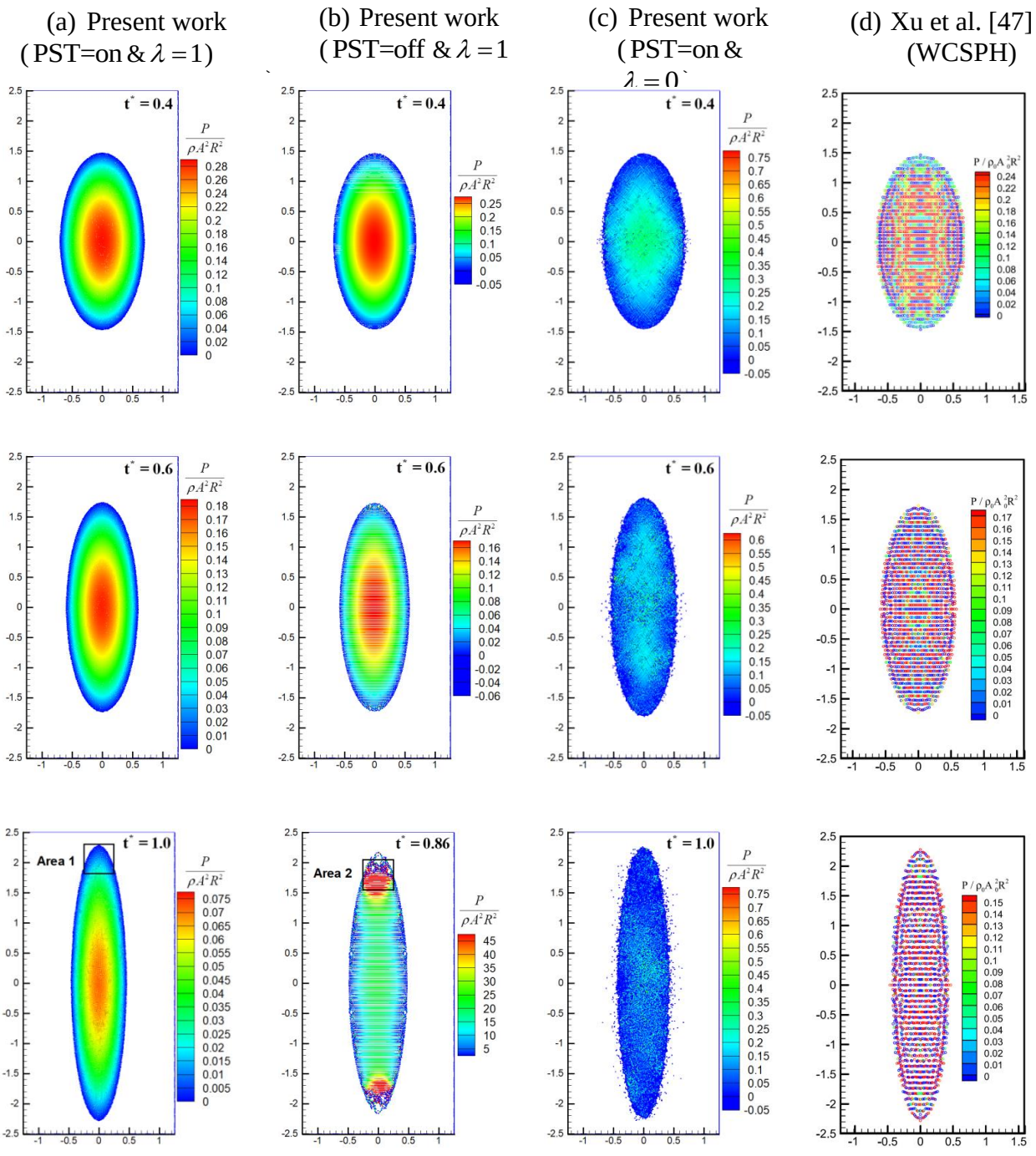

Figure 5-9 A quantitative comparison of calculated results with the numerical data of Xu et al. [47] in terms of particles distribution and pressure contours for the case of stretching circular water drop (case A3). (a-c) the impacts of Particle Shifting Technique (PST=On & PST=Off) and additional diffusive term ($\lambda = 0$ & $\lambda = 1$) on the particles behavior. $N_p = 15388, R = 1m$.

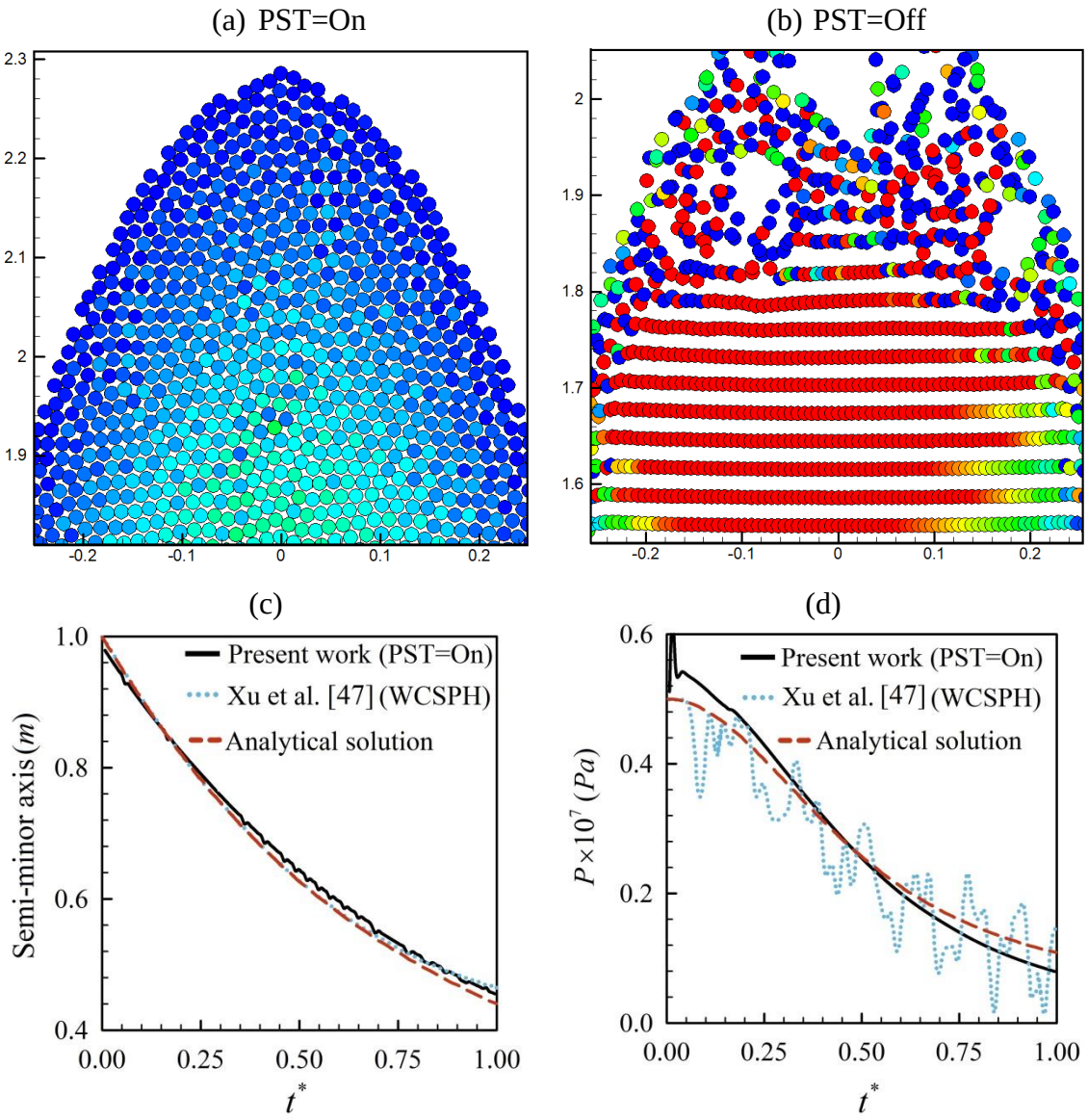

Figure 5-10 Zoomed view of areas 1 (a) and 2 (b) under the influences of Particle Shifting Technique (PST) (see also first and second columns in Fig. 9). Comparison of (c) semi-minor axis variations and time history of non-dimensional pressure at the center of drop (d) obtained from the present model and those reported by Xu et al. [47].

5.4.1 Natural convection heat transfer

In order to verify the model ability to handle buoyancy-driven flow, analysis of natural convection heat transfer in the two-dimensional square cavity with localized heating from below is considered as a last benchmark test. The schematic diagram of the enclosure along with its boundary conditions is presented in Fig. 5-1 (case A4). As shown, the bottom wall is partially heated with uniform high temperature (T_h) whereas vertical sidewalls of the enclosure are maintained at a constant but low temperature (T_c). The remaining parts of the horizontal walls are insulated and impermeable to mass transfer. Fig. 5-11 illustrates the streamlines, isotherms, and contours of the velocity components (u,v) at $Ra = 10^5, \Pr = 0.71$. Generally, due to the thermally-induced buoyancy effect, the heated fluid adjacent to the bottom wall ascends along the centerline of the enclosure until it hits the isolated top wall. Then, it changes its direction and moves horizontally towards the vertical cavity walls where, due to interaction with surrounding cold particles, it becomes gradually denser and heavier. The relatively cold fluid which has lost a portion of its energy descends downwards along the lateral sidewalls and ultimately enters the thermal boundary layer of the hot surface with minimal energy. This cycle results in a formation of the mushroom-like temperature pattern and two circulating cells within the enclosure. As the simulation goes on, isotherms become more distorted at the core and distinct thermal boundary layer is developed near the active walls, indicating convection dominant mode of the heat transfer at $Ra = 10^5$. Again, it is evident that the thermal characteristics of the air-flow in terms of the average Nusselt number and temperature distribution are well in accordance with the recent experimental measurements and numerical data of Calcagni et al. [73] and Sheikholeslami et al. [74].

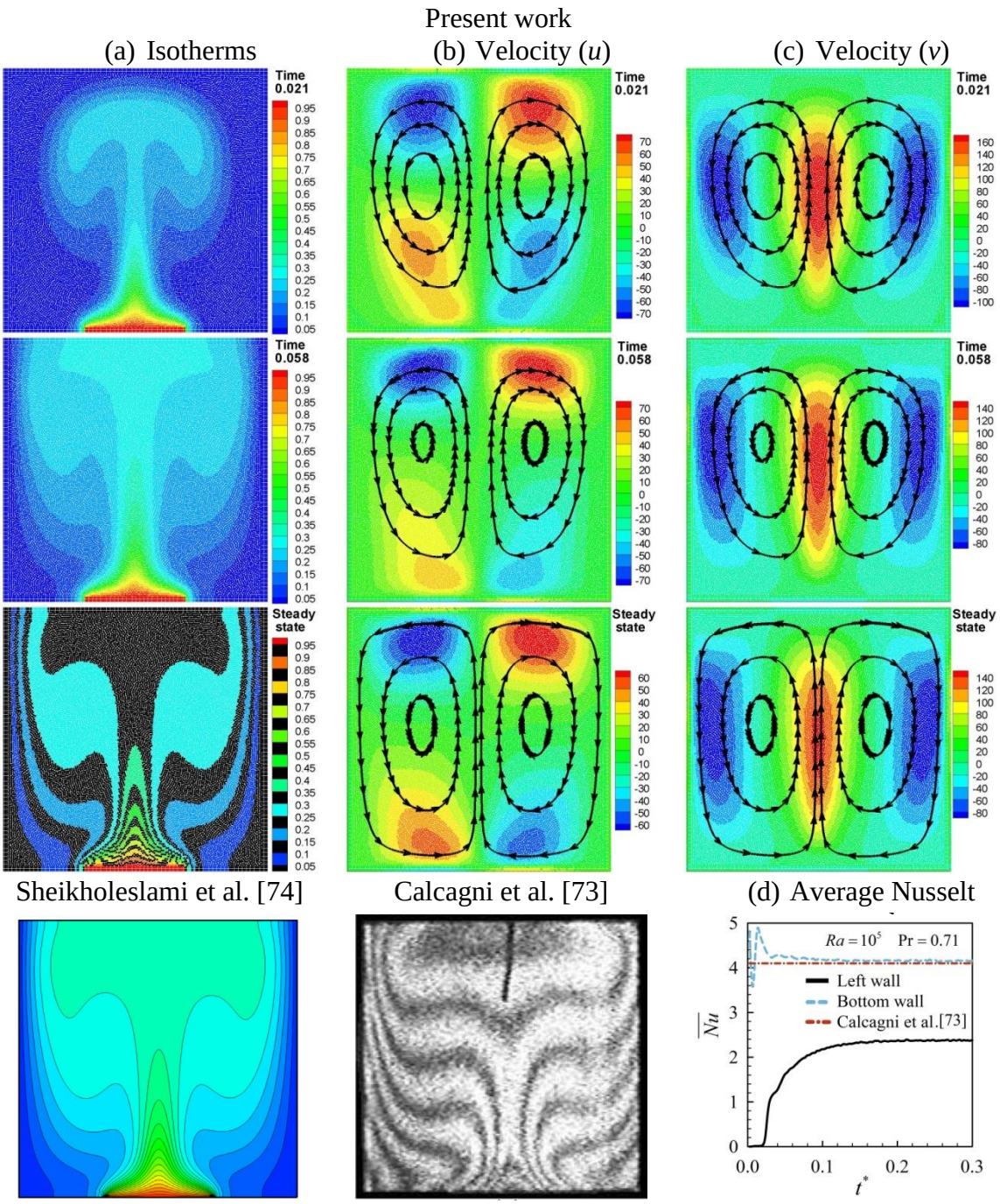

Figure 5-11 Validation of the present model against the numerical (mesh-based) and experimental results of Sheikholeslami et al. [74] and Calcagni et al. [73] for case A4 in terms of the (a) isotherms, (b-c) velocity contours in the x and y-directions, and (d) average Nusselt number. $L = 0.4H$. $N_p = 18225$. Ra=10^5 and Pr=0.71.

5.5 Results and discussion

Previous section clearly demonstrated that KDF-WCSPH model together with proposed new operators are robust and reliable for modeling a wide range of particulate flows with thermal convection and complex interface scenarios. Thus, in this section entropy generation due to natural convection heat transfer in three different geometries is examined using KDF-WCSPH.

Figs. 5-12 and 5-13 present the streamlines and isotherms for case B1 ($\mathrm{Pr}=0.71$), case B2 ($\mathrm{Pr}=6.2, L_1=L_2=0.6H$) and case B3 ($\mathrm{Pr}=0.71, L=0.3H$) at different Rayleigh number ($10^3 \le Ra \le 10^6$) and time instants. Generally, in all cases the buoyancy force induced by the density difference and temperature gradient within the enclosure causes the working fluid to rise up along the hot surface and migrates toward the cold area to exchange its high level of energy. After impinging on the cold walls, the lighter fluid becomes more and more squeezed and denser as its internal energy alleviates. Subsequently, it gets heavier and falls down at the vicinity of the cold wall and turns back to the hot area to complete the thermal cycle and satisfy the mass continuity. This process is repeated until the steady-state condition is attained within the computational domain where no improvement occurs in the macroscopic behavior of the heat transfer rate ($\overline{Nu}$). Based on the above mechanism, it can be seen that due to dominant conduction mode of the heat transfer at $Ra=10^3$, the flow field in case B1 is characterized by a weak clockwise circulation which occupies the entire enclosure. As expected, corresponding isotherms are smooth and undistorted, signifying poor transportation of heat from left to right cold wall. As *Ra* increases to 10^4, prevalent effect of buoyancy force becomes more discernible such that isotherms gradually get shifted towards the sidewalls and strength of the flow circulation enhances. In this circumstance, due to onset of convection, the core of the primary vortex is found to be slightly elongated in *x*-direction and distinct thermal boundary layer starts to establish near the vertical walls. With the further increase in *Ra*, the main vortex breaks down diagonally into two small eddies at the core and absolute values of velocity components which represent the intensity of the flow enhances (see also $|U_{\max}|$ and $|V_{\max}|$ in table 5-2). It is evident that, the corresponding isotherms get more condensed under twisting effects of flow pattern in the middle portion and the thickness of the thermal boundary layer reduces.

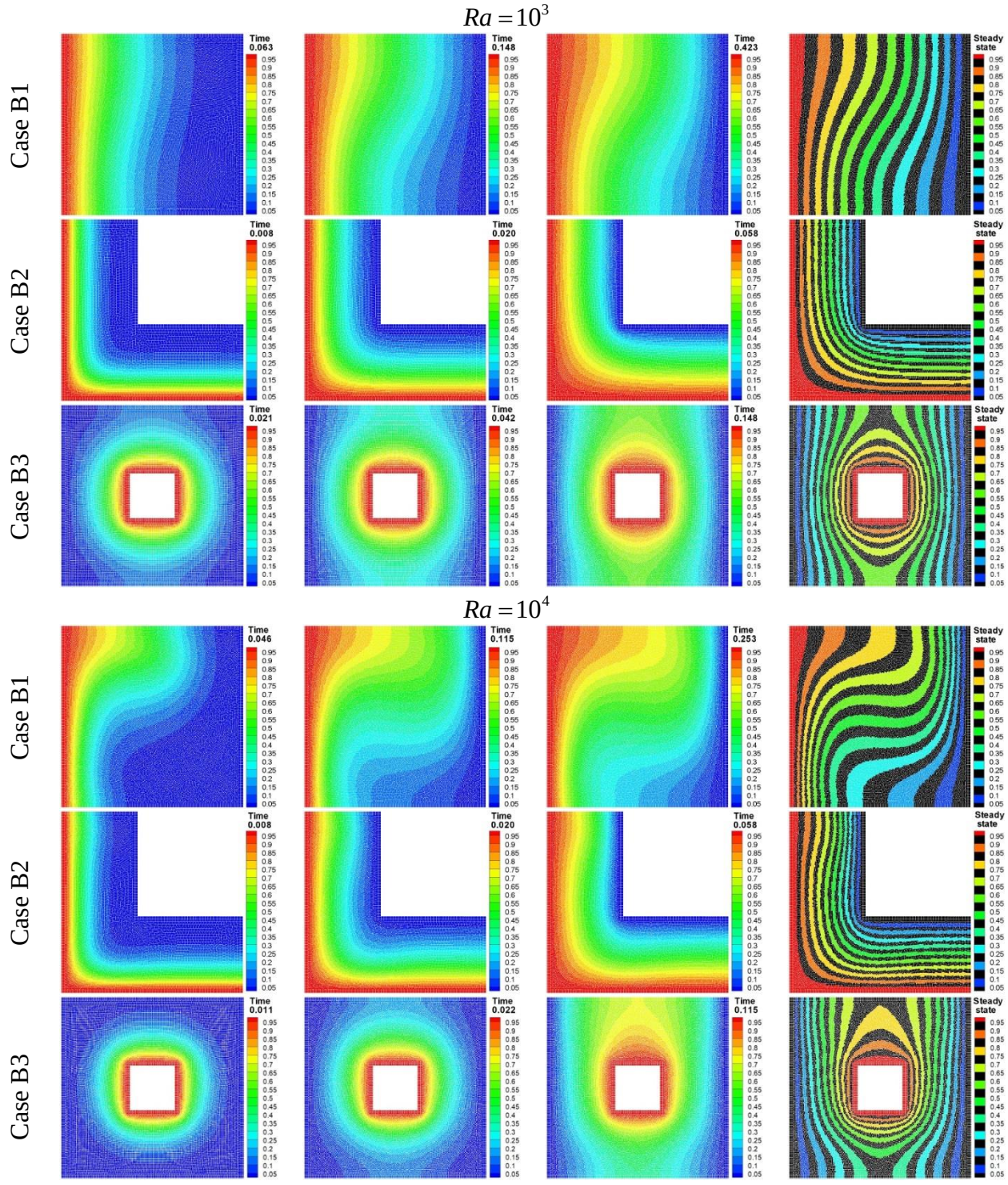

Figure 5-12 Transient variations of isotherms (temperature field) as a function of the non-dimensional time for cases B1 to B3 at different Rayleigh numbers.

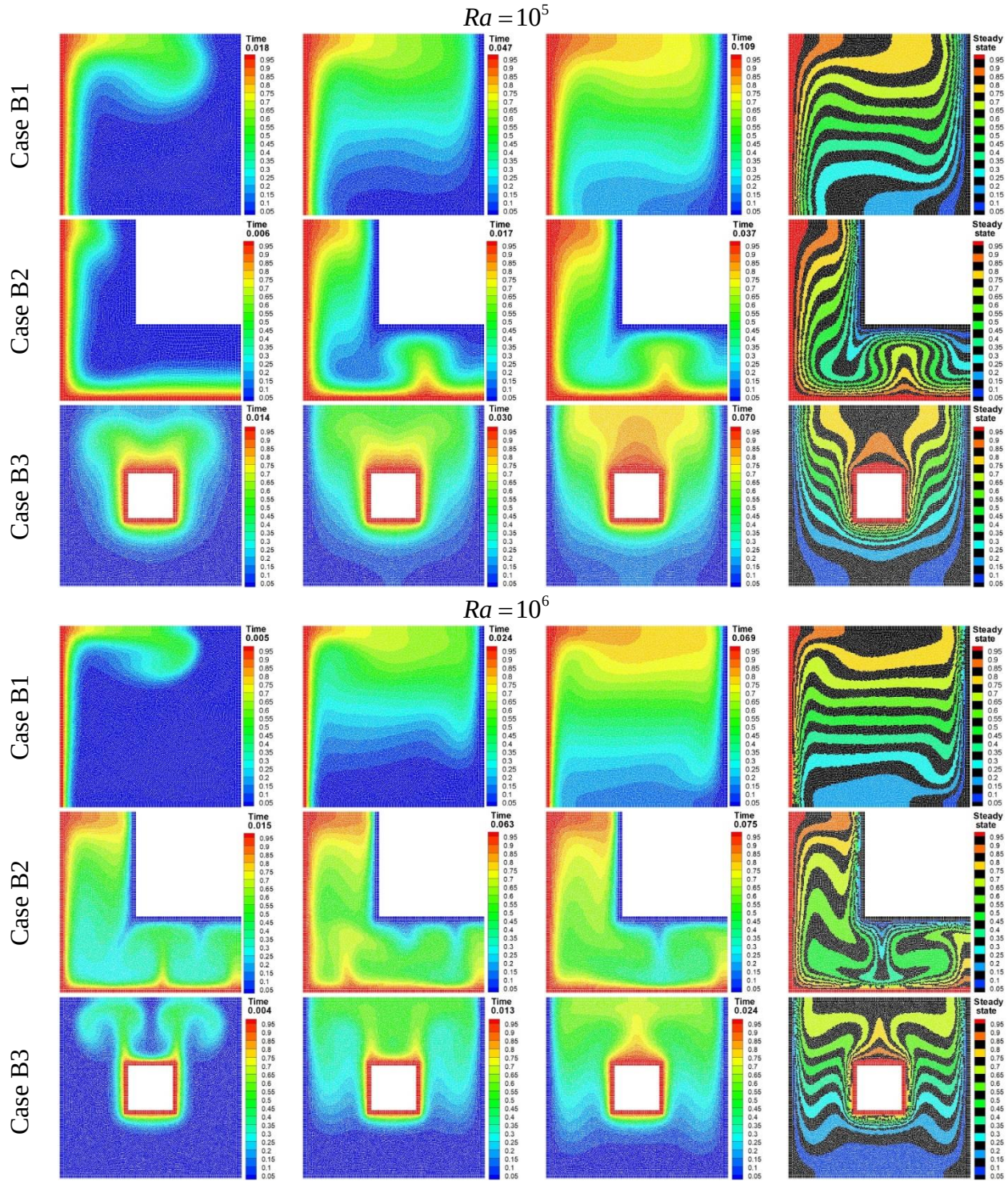

Figure 5-12 Transient variations of isotherms (temperature field) as a function of the non-dimensional time for cases B1 to B3 at different Rayleigh numbers (cont'd).

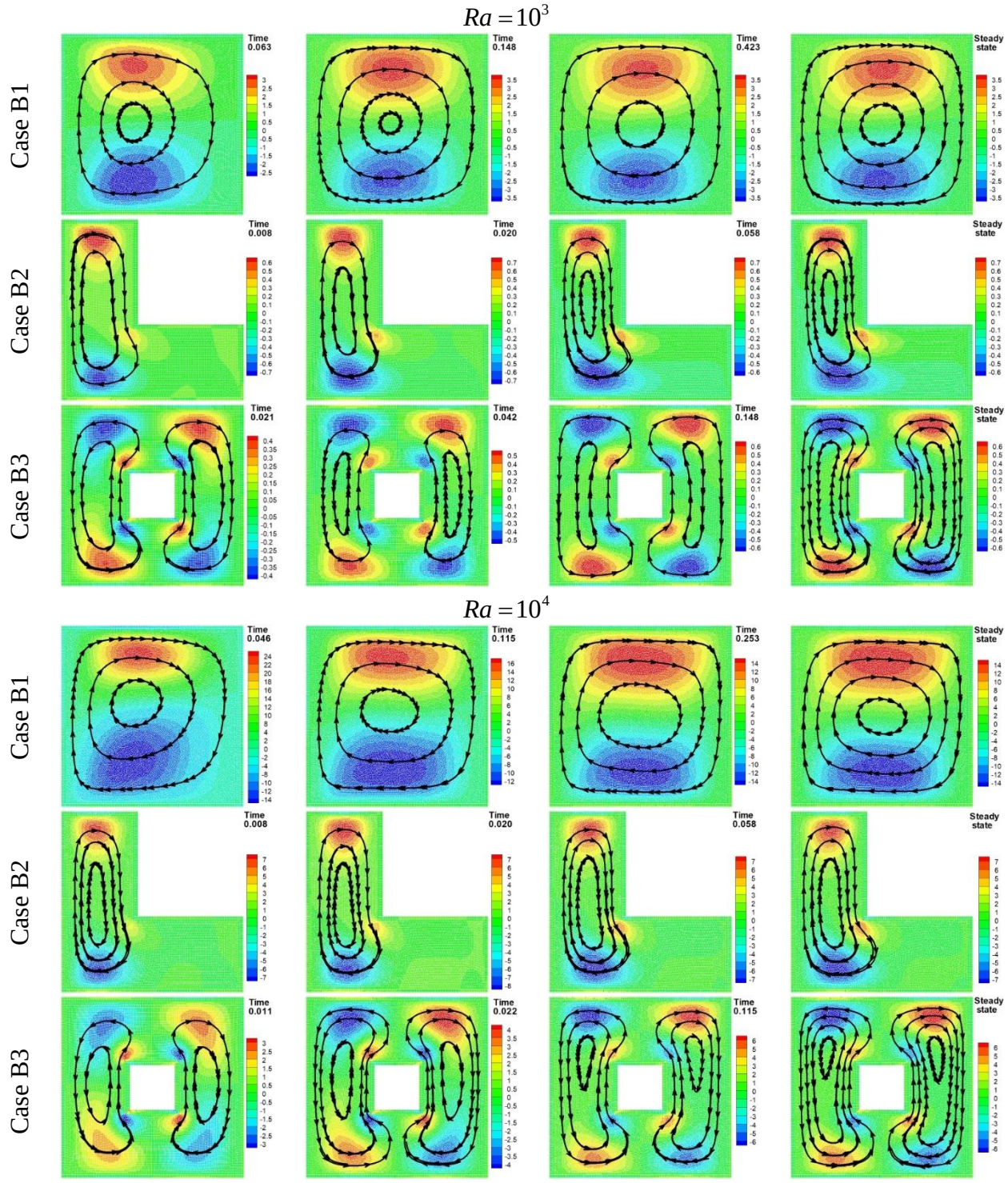

Figure 5-13 Transient variations of streamlines and velocity in x-direction (u) as a function of the non-dimensional time for cases B1 to B3 at various Rayleigh numbers.

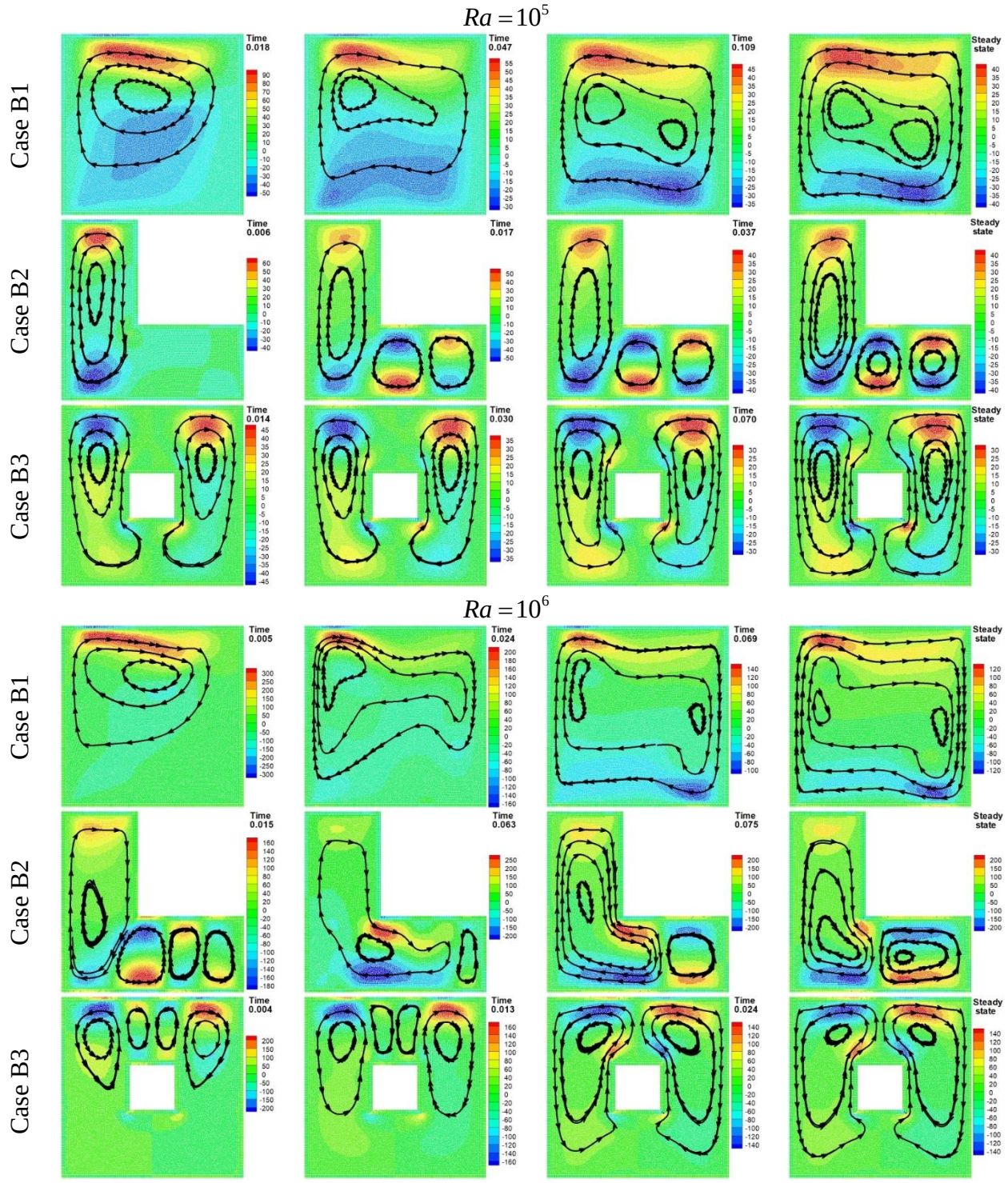

Figure 5-13 Transient variations of streamlines and velocity in x-direction (u) as a function of the non-dimensional time for cases B1 to B3 at various Rayleigh numbers (cont'd).

This implies that the convection regime is dominant and viscous effects are no more in the flow. As *Ra* enhances to 10^6, due to high momentum diffusivity and increasing effects of convection, velocity contours are highly stretched and isotherms become more concentrated near the differentially heated walls, resulting in a much larger temperature gradient and thermal mixing inside the enclosure. It is also evident that, due to strong upward and downward flow movement in the close vicinity of the heated walls, two egg-shaped cores are dragged toward the lateral walls and subsequently middle zone becomes broadly stagnated which is concordant with horizontal thermal stratification in that area. However, a different scenario occurs in the L-shaped enclosure (case 2B). It can be seen that at $Ra = 10^3$ a single clockwise eddy is formed in the vertical part of the enclosure and isotherms are smooth curves and uniformly distributed throughout the enclosure.

Table 5.2 The effects of the Rayleigh number on the heat transfer rate and entropy generation for cases B1 to B3 (steady-state condition).

Case A										
Ra	$\overline{Nu}$	$\lvert U_{\max}\rvert$	$\lvert V_{\max}\rvert$	$\overline{Be}$	$\overline{S}_{tot}$	$S_{tot,\max}$	$\overline{S}_T$	$S_{T,\max}$	$\overline{S}_F$	$S_{F,\max}$
10^3	1.120	3.633	3.681	0.970	1.149	2.291	1.115	2.274	0.034	0.242
10^4	2.249	16.179	19.569	0.684	3.243	25.210	2.220	12.584	1.023	16.113
10^5	4.548	43.476	68.597	0.194	22.831	590.975	4.450	60.563	18.381	557.458
10^6	8.957	123.011	221.395	0.025	335.159	15877.138	8.630	320.876	326.529	15754.411
Case B										
Ra	$\overline{Nu}$	$\lvert U_{\max}\rvert$	$\lvert V_{\max}\rvert$	$\overline{Be}$	$\overline{S}_{tot}$	$S_{tot,\max}$	$\overline{S}_T$	$S_{T,\max}$	$\overline{S}_F$	$S_{F,\max}$
10^3	1.82	0.757	1.216	0.998	5.898	68.668	5.889	68.490	0.008	0.177
10^4	1.911	7.324	12.664	0.874	7.048	66.348	6.165	46.668	0.882	19.679
10^5	4.1225	48.045	80.680	0.207	64.890	976.628	13.450	116.445	51.440	921.250
10^6	7.302	213.197	347.404	0.022	1085.504	28548.838	24.324	536.187	1061.180	28399.721
Case C										
Ra	$\overline{Nu}$	$\lvert U_{\max}\rvert$	$\lvert V_{\max}\rvert$	$\overline{Be}$	$\overline{S}_{tot}$	$S_{tot,\max}$	$\overline{S}_T$	$S_{T,\max}$	$\overline{S}_F$	$S_{F,\max}$
10^3	2.193	0.676	0.990	0.998	4.978	58.721	4.969	58.576	0.009	0.147
10^4	2.334	6.854	10.016	0.859	6.140	101.420	5.277	88.428	0.862	14.873
10^5	4.116	32.885	64.247	0.228	41.131	907.241	9.383	345.404	31.747	679.228
10^6	7.245	116.523	205.969	0.034	490.809	21709.545	16.737	835.338	474.072	21567.823

One can observe that unlike the case B1 ($\Pr = 0.71, V_{B1} = H^2$), by increasing the *Ra* up to 10^4, the flow pattern remains invariant and isotherms still tend to follow the geometry profile of the

enclosure. These observations can be attributed to the small gap between the active walls and high Prandtl number used in case B2 ($\Pr = 6.2, V_{B2} = H^2 - L_1 L_2 = 0.64H^2$) which leads to the significant reduction of the flow intensity and thereby postponement of the convection initiation to higher values of Rayleigh number ($Ra > 10^4$). This feature can also be verified by examination of absolute values of maximum velocities in table 5-2 where $|U_{\max}|$ and $|V_{\max}|$ in case B1 are approximately twice as those of case B2. With subsequent increase in Rayleigh number (Ra=10^5), the role of convection in heat transfer becomes more accentuated which causes the unicellular rotating vortex to turn slowly into a multi-cellular eddies. This trend is accompanied by appearance of the rising thermal plume (Ω-shaped plum) in horizontal section and the other gigantic sinking thermal plume close to the convex corner of the cold rip. Traditionally, this physical model with regular thermal convective rolls is referred to as Rayleigh-Bénard cells which in turn can triggers the onset of thermal instability in horizontal part of the enclosure. As expected, by increasing the Ra up to 10^6, fluid motion inside the enclosure is accelerated and therefore Rayleigh-Bénard instability becomes more prominent. It can be seen that in this condition, the third Bénard cell is established as newly falling cold plum at t^*=0.015. As time progresses, the descending plume which receives the incoming cold fluid, starts to grow and push the rising plume unremittingly towards the vertical part of the enclosure. During the interaction and expansion of these thermal plumes, the isotherms are distorted incessantly and thereby some secondary rolls of less importance are developed and vanished within the enclosure. As the rising plume moves horizontally along the bottom wall, it becomes wavy and twisted. It eventually penetrates into the vertical side and merges with the innermost eddy occupying that area.

Flow transitions for case B3 (annulus) is also depicted in Figs. 5-12 and 5-13 where the working fluid is confined between two-square concentric duct annuli. It can be seen that due to the symmetric placement of the heat source and boundary conditions of the problem, the flow undergoes a bifurcation and consequently a pair of counter rotating vortices with circular-shaped cores is established within the enclosure. Similar to previous cases, at low Rayleigh number (Ra=10^3) isotherms are parallel to each other and symmetrically dispersed with respect to center of the enclosure which indicates that heat transfer rate is primarily controlled by diffusion and temperature field is totally decoupled from the flow field. Slight distortion in the trend of isotherms at Ra=10^4 is consistent with a mode so-called transition regime (convection initiation)

where heat is conveyed by simultaneous conduction and convection. This stage is also accompanied by appearance of very weak ascending plume over the hot obstacle and formation of the thermal boundary layer near the cold walls. By increasing the *Ra* to 10^5, the height of the rising plum enhances and isotherms become more confused. In fact, significant twisting of the isotherms together with the development of the hotspot (hot stagnant fluid) adjacent to the top wall of the heater clearly exhibit characteristics of the convection-dominated regime. With further increase in Rayleigh number, convection mechanism is substantially improved so that the eyes of the two counter-rotating cells move upward and meet each other at the top portion of the annulus while streamlines in bottom half become more diverge. A close inspection of the horizontal velocity contour (*u*) in Fig. 5-13 vividly demonstrates that at $Ra=10^6$, due to increasing effects of convection and impingement of the ascending plume on the top wall, streamlines are densely concentrated in upper half of the annulus while a reverse trend occurs in the lower one. Furthermore, it is interesting to observe that, thermal boundary layer thickness in close proximity to the cold walls progressively declines from bottom to top portion.The substantial reduction of thermal boundary layer thickness and elongation of the velocity components together with streamlines clustering indicate that most of the heat removal rate and much of the fluid motion take place in the upper region while the cold heavy fluid in the lower region is practically stagnant. These observations indicate that, heat transfer in bottom of the annulus takes place primarily as a result of diffusion even at high Rayleigh number. This behaviour is also compatible with the streamlines diverging and smoothness of the isotherms in the lower half of the enclosure. Similar findings were also reported by Saravanan et al. [6] and Hooshmand et al. [8] who investigated natural convection heat transfer in the annulus.

Figs. 5-14 and 5-15 illustrate contours of the local Bejan number (*Be*) and entropy generation due to heat transfer irreversibilities (S_T) at different *Ra* and time instants for cases B1 to B3. Overall evaluation of Figs. 5-14 and 5-15 illustrate that, because of weak buoyancy force and constant thermal gradient at low Rayleigh number ($Ra = 10^3$), local S_T is spaced uniformly throughout the domain and consequently local *Be* in all cases approaches unity ($Be \approx 1$) which indicates that contribution of viscous dissipation ($S_F \approx 0$) on total entropy generation ($S_{tot} \approx S_T$) is trivial.

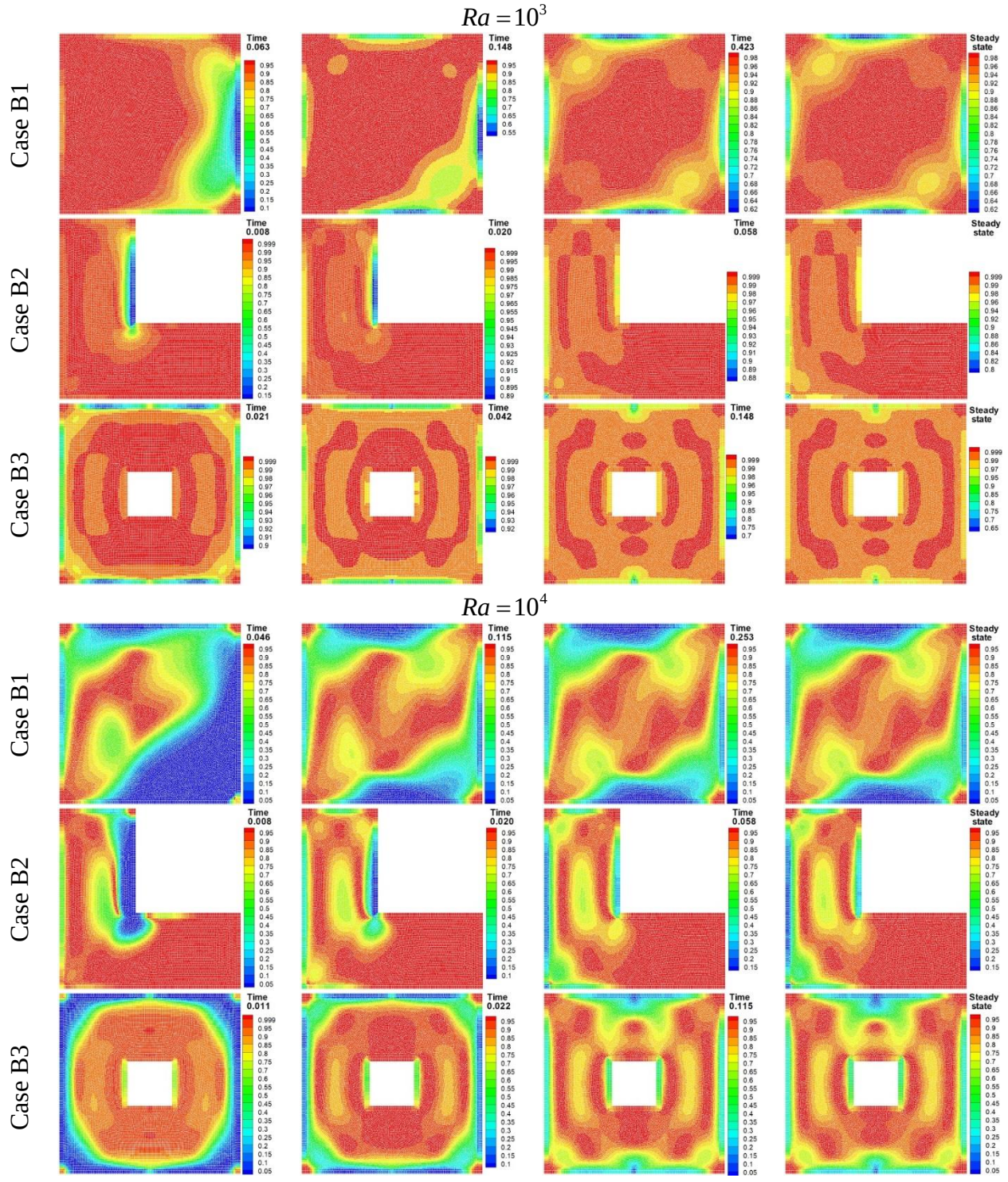

Figure 5-14 Transient variations of local Bejan number as a function of the non-dimensional time for cases B1 to B3 at various Rayleigh numbers.

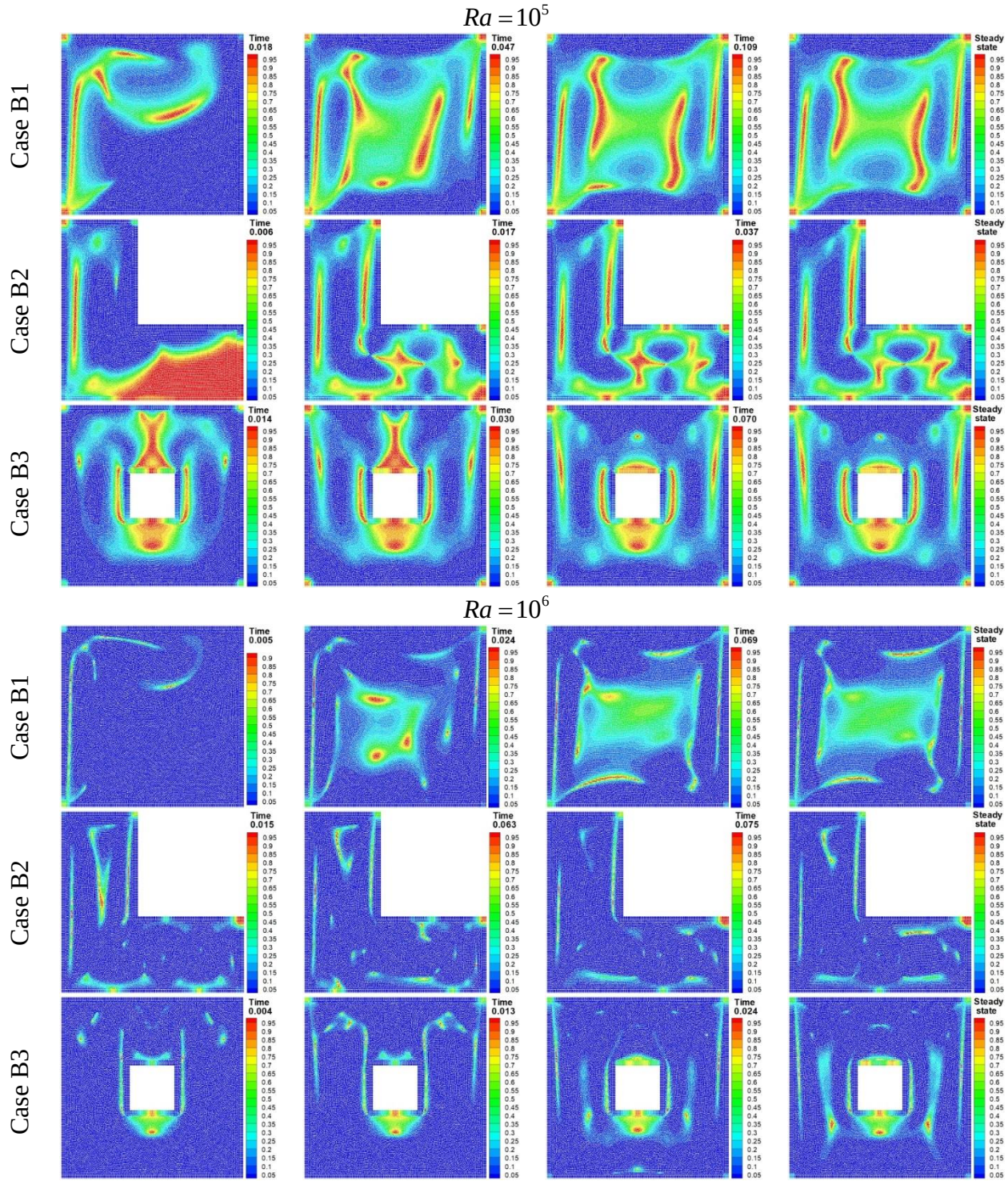

Figure 5-14 Transient variations of local Bejan number as a function of the non-dimensional time for cases B1 to B3 at various Rayleigh numbers (cont'd).

Since at this stage, entropy generation due to viscous dissipation is sufficiently small to be negligible ($S_F \ll S_T$), contours of total entropy generation would be identical to thermal dissipation map (see also Fig. 5-13). However, as discussed earlier, by increasing the *Ra*, the conduction mechanism gradually shifts to the convection mode, leading to the greater thermal smearing (higher temperature gradient) and flow penetration depth (higher velocity gradient) within the enclosures. Hence, according to Eq. (5-8), total entropy generation due to both factors (S_T, S_F) augments. Interestingly, table 5-2 shows that although by increasing the *Ra* both S_T and S_F increase but the increment of S_F is remarkably higher than that of the S_T, resulting in the deterioration of average Bejan number. However, since buoyancy force at $Ra=10^4$ has a same order of magnitude of the hydraulic resistance (quasi-conduction regime), *Be* still remains higher than 0.5 ($0.68 \le \overline{Be} \le 1$) which indicates that the large amount of the exergy loss in all cases is still associated with the thermal dissipation. This assertion is well reflected in the local Bejan number values in Fig. 5-14 where entropy generation due to fluid friction is confined only to the small zone in close vicinity of the heated walls. This trend persists and even intensifies as the convective transport strengthens. By increasing the *Ra*, fluid motion in all cases is considerably invigorated and consequently the viscous dissipation (S_F) becomes the major contributor to the total entropy generation rise. As stated before, since irreversibility due to fluid friction augments much faster than that of the heat transfer, local and average Bejan number decline rapidly and approach zero especially near the lateral walls. This finding indicates that at high *Ra*, only the small amount of the available work is utilized to compensate the irreversibilities due to the heat transfer (see also table 5-2 at $Ra=10^6$ where $\overline{S}_T \ll \overline{S}_F$). It can be seen that, in case B1 at $Ra=10^6$, due to comparatively lesser velocity gradients and weak convective flow in the middle portion, fluid becomes nearly stagnant and thermal stratification is generated in that area. This in turn results in the higher values of local Bejan number which subsequently manifests the relative dominance of S_T. A similar configuration also occurs in the vertical and horizontal parts of the L-shaped enclosure (case B2) especially in proximity of the upwelling and down-welling thermal plumes. It is evident from Fig. 5-14 that, the values of the local Bejan number near the thermal plumes are greater than 0.5 ($Be > 0.5, S_T > S_F$), which indicates that the formation of thermal plume has a negative impact on the exergy efficiency (destruction of the available work) and can be considered as a major source of the energy consumption and thermal dissipation. Interestingly, this physical model is more pronounced at $Ra=10^5$ where moderate thermal and flow

perturbations occur within the enclosure. This scenario is further verified in case B3 where due to existence of the rising plume (hotspot) and less velocity gradient in the bottom of the annulus, insignificant S_F is observed in those areas ($S_T > S_F$) which in turn is responsible for the enhancement of local Bejan number ($Be > 0.5$). The corresponding local entropy generation due to the heat transfer irreversibility in Fig. 5-15 also reveals that at high Rayleigh number, the maximum values of S_T take place in close vicinity of the thermal surfaces where isotherms are densely packed and thin thermal boundary layer is developed. Moreover, by making detailed comparisons between Figs. 5-12 and 5-15, one can observe that entropy generation due to heat transfer irreversibility intrinsically has a tendency to follow morphological characteristics of the temperature field. For instance, it can be seen that compression of isotherms near the heated walls (in case B1), formation and movement of the ascending thermal plume along the bottom wall (in case B2), presence of the hotspot and stagnation point in the top and bottom portions of the annulus (in case B3) are well reflected in the contour of the thermal dissipation in Fig. 5-15. In fact, from the above discussion, one can conclude that, the results from the second-law of thermodynamics might be superior to the isotherms and streamlines (first-law of thermodynamics) in determining the regime of the fluid flow and heat transfer in the thermal systems involving bifurcation, thermal plumes, hotspot, stagnation point, and thermal stratification. For getting further insight into the influence of Rayleigh number on the heat transfer rate and exergy destruction within the enclosures, transient variation of the average Nusselt number ($\overline{Nu}$), $\overline{S}_{tot}$, $\overline{S}_T$, $\overline{S}_F$ and ($\overline{Be}$) are depicted in Fig. 5-16. It can be seen that by increasing the *Ra*, the average Nusselt number, $\overline{S}_T$ and $\overline{S}_F$ increase while a downward trend occurs in the values of $\overline{Be}$. As stated before, at low *Ra* due to weak fluid motion and low velocity gradients, the significant amount of entropy generation in all cases takes place as a result of the thermal dissipation. However, due to augmented convective motion of the working fluid at high *Ra*, $\overline{S}_{tot}$ enhances drastically and begins to follow the pattern of $\overline{S}_F$ in the majority with minor impacts of $\overline{S}_T$. These results are to be expected at high *Ra* where fluidity and gradients of velocity are considerably intensified due to stronger buoyancy-driven flow.

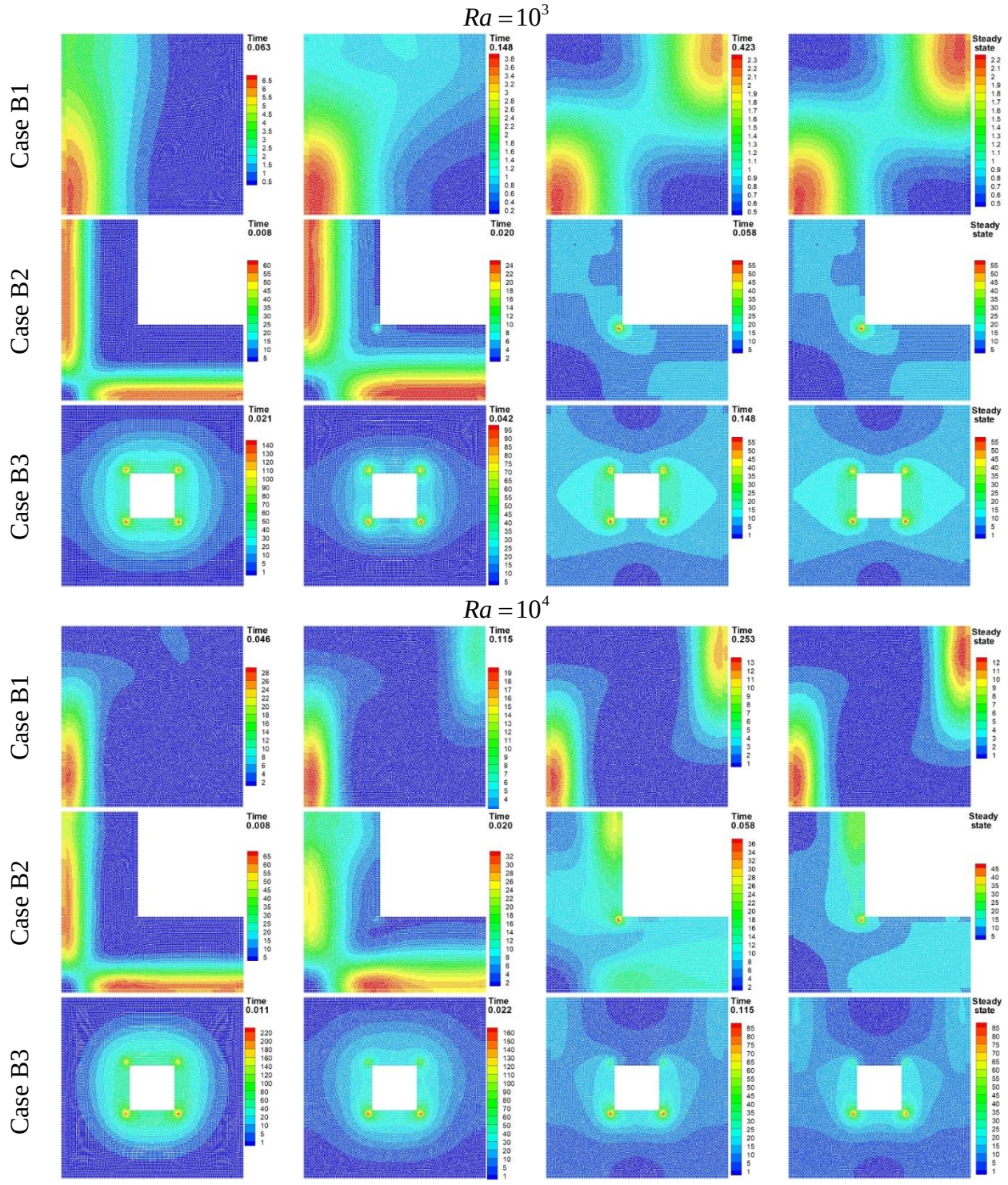

Figure 5-15Transient variations of local entropy generation due to heat transfer as a function of the non-dimensional time for cases B1 to B3 at various Rayleigh numbers.

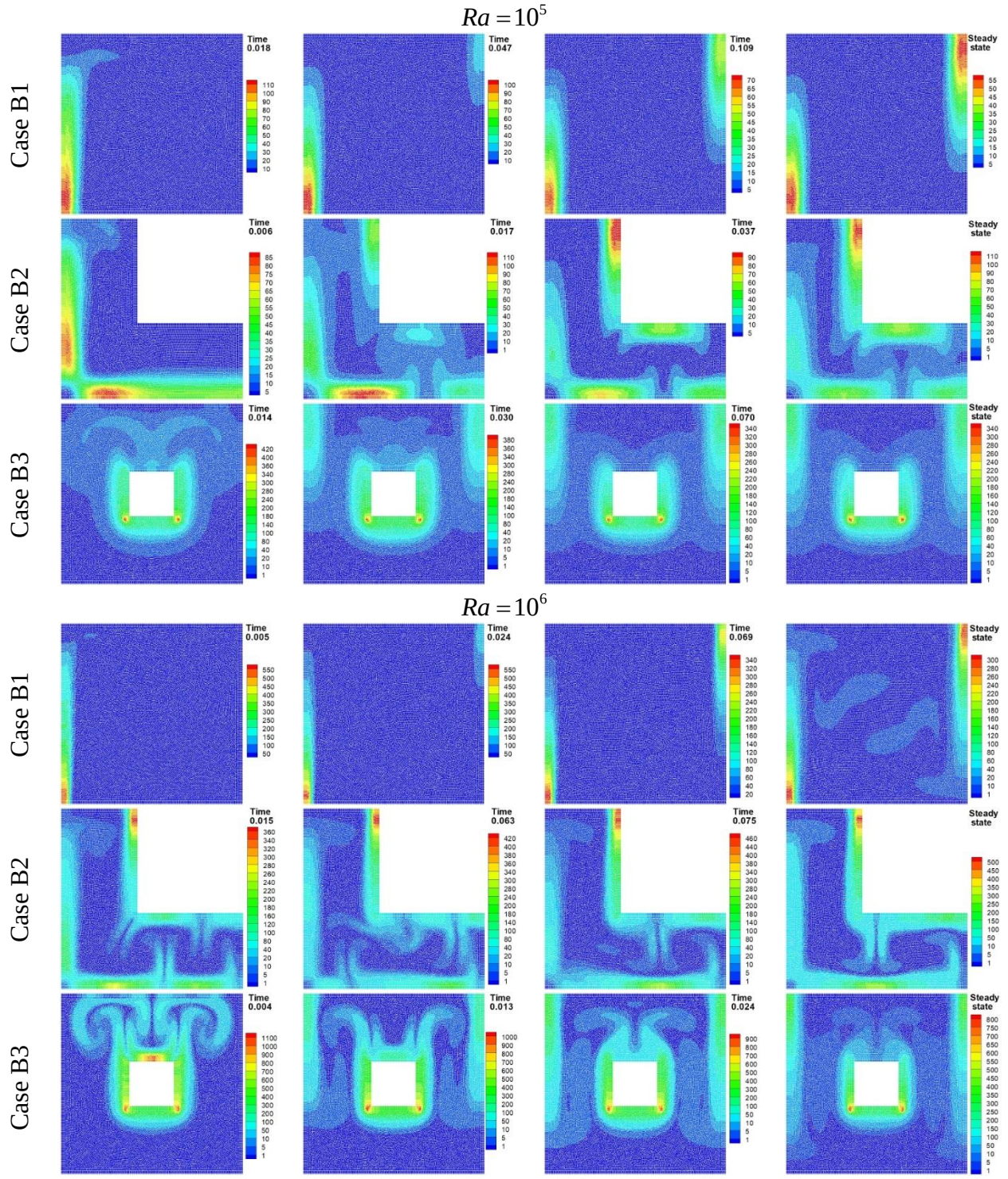

Figure 5-15 Transient variations of local entropy generation due to heat transfer as a function of the non-dimensional time for cases B1 to B3 at various Rayleigh numbers (cont'd).

Fig. 5-16 also reveals that at low Rayleigh number ($Ra = 10^3$), due to conduction dominant mode of the heat transfer, all the above-mentioned pertinent parameters ($\overline{Nu}$, $\overline{S}_{tot}$, $\overline{S}_T$, $\overline{S}_F$ and $\overline{Be}$) converge to the constant value asymptotically, while at relatively high Rayleigh numbers ($Ra > 10^4$), an oscillatory behavior emerges within the computational domain prior to reaching the steady-state condition. This phenomenon can be attributed to the significant movement of the temperature perturbation generated by the buoyancy force at high *Ra*. For example, in case B2 at $Ra=10^6$, the first fluctuation in the values of $\overline{Nu}$ and $\overline{S}_{tot}$ at $0 \le t^* \le 0.02$ is associated with the formation of the ascending thermal plume in the horizontal part of the enclosure whereas the second fluctuation at $0.06 \le t^* \le 0.09$ takes place due to the displacement of the rising plume toward the vertical section. Similar observation were reported by Magherbi et al. [75] who investigated entropy generation due to natural convection heat transfer within the differentially heated cavity. Finally, it is worth mentioning that, since entropy generation during the natural convection heat transfer has been well-documented in the literature, the results of the case B1 can be considered as a further validation in the present work (see Figs. 3 and 4 in work of Ilis et al. [64]).

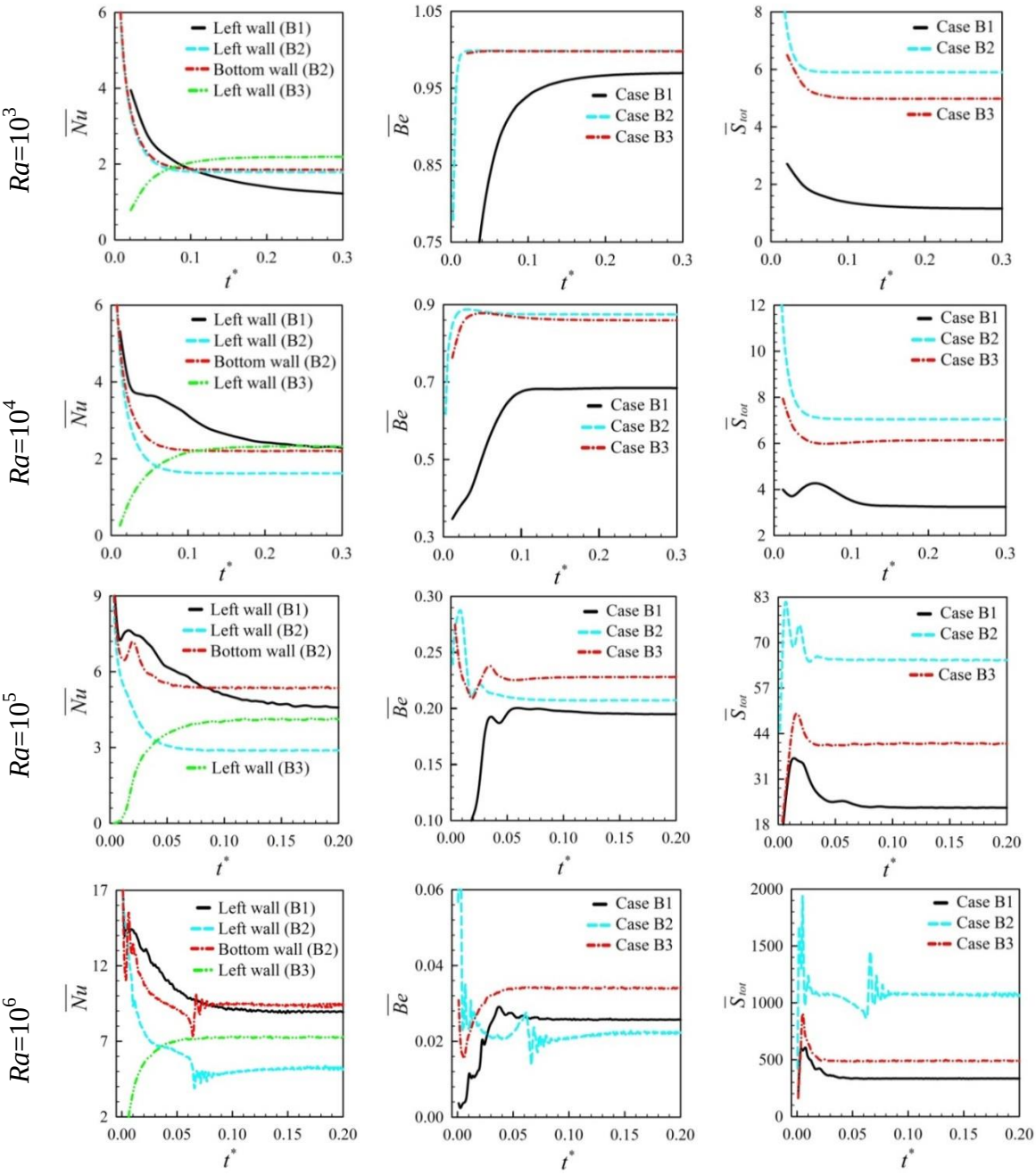

Figure 5-16 Variations of average Nusselt number ($\overline{Nu}$), average Bejan number ($\overline{Be}$), total entropy generation ($\overline{S}_{tot}$), entropy generation due to thermal ($\overline{S}_T$) and viscose ($\overline{S}_F$) irreversibilities as a function of the non-dimensional time for cases B1 to B3 at different Rayleigh numbers. Case B1 ($\mathrm{Pr}=0.71$), case B2 ($\mathrm{Pr}=6.2, L_1=L_2=0.6H$) and case B3 ($\mathrm{Pr}=0.71$, $L=0.3H$).

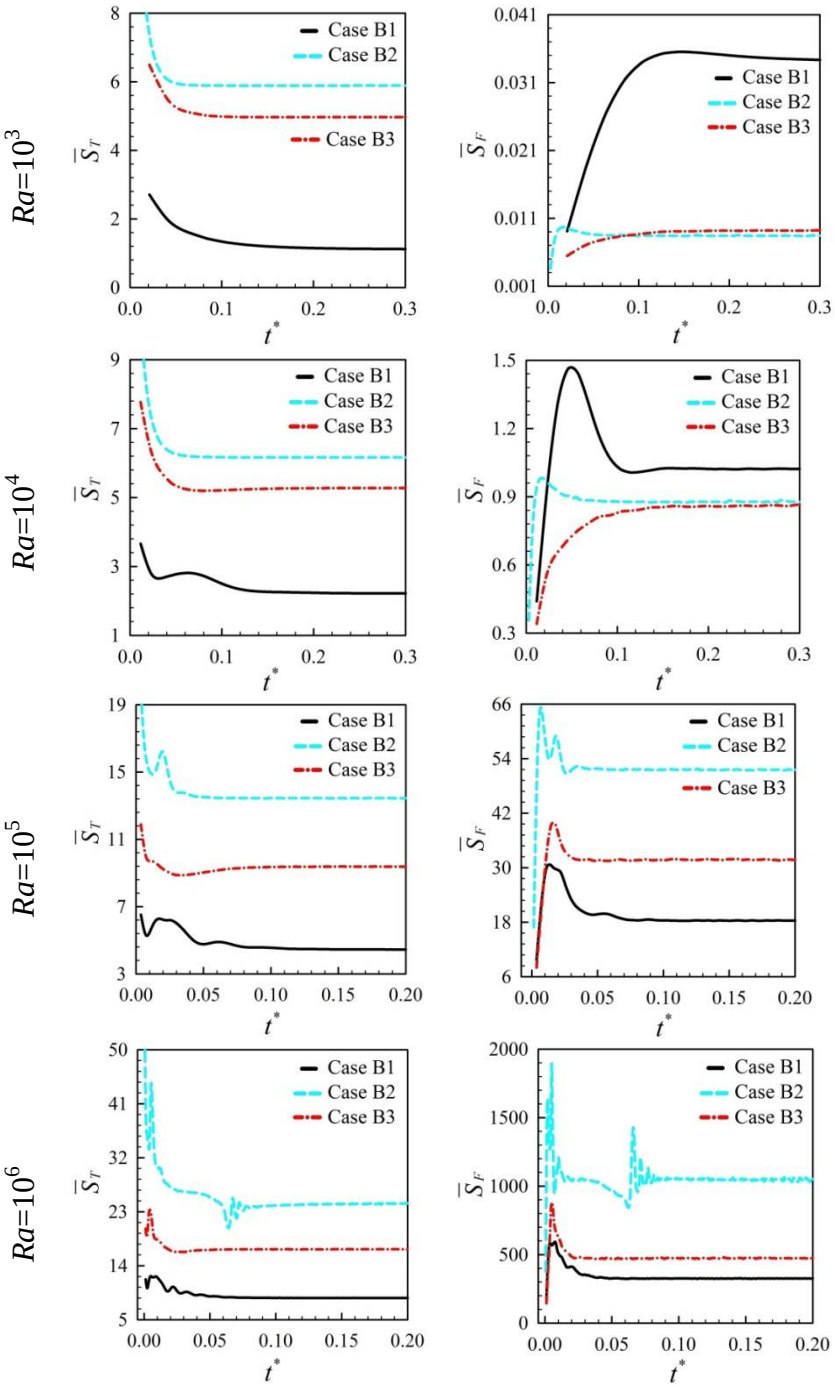

Figure 5-16 Variations of average Nusselt number ($\overline{Nu}$), average Bejan number ($\overline{Be}$), total entropy generation ($\overline{S}_{tot}$), entropy generation due to thermal ($\overline{S}_T$) and viscose ($\overline{S}_F$) irreversibilities as a function of the non-dimensional time for cases B1 to B3 at different Rayleigh numbers. Case B1 ($\mathrm{Pr}=0.71$), case B2 ($\mathrm{Pr}=6.2, L_1=L_2=0.6H$) and case B3 ($\mathrm{Pr}=0.71$, $L=0.3H$), (cont'd).

5.6 Conclusions

In the current work, a new Kernel Derivative-Free (KDF) version of the Weakly Compressible Smoothed Particle Hydrodynamics model (WCSPH) has been introduced for simulation of free-surface flows and natural convection heat transfer problems. A wide range of the two-dimensional benchmark cases in various fields of engineering and science has been employed to demonstrate the capability and performance of the proposed model (KDF-WCSPH). The outcomes of the numerical simulations drawn from this study support the following major conclusions:

- The results showed that the proposed new kernel function significantly outperformed two commonly used kernel functions (i.e. cubic and quintic spline functions) in modeling 1D Sod shock tube problem.
- The results showed that the proposed Laplacian operator provides more accurate results compared to traditional WCSPH method in modeling breaking dam flow, stretching of circular water drop, rotating square patch of fluid and natural convection heat transfer in a square enclosure.
- The results showed that combination of the Particle Number Density (PND) and divergence of the displacement as the particle labeling scheme can successfully identify the location of the free-surface and its vicinity particles.
- It was found that traditional formulations of SPH model are prone to tensile instability whereas the proposed model (KDF-WCSPH) benefit from high level of accuracy and consistency.
- It was found that implementing Particle Shifting Technique (PST) has a marked impact on the stability and accuracy of the mesh-free particle methods.
- It was found that inserting additional diffusive term into the continuity equation can considerably suppress (or remove) high-frequency oscillations noise from the pressure field (unfavorable check-board pressure field), leading to more accurate results as compared to conventional WCSPH.
- It was found that, the proposed smoothing operator can successfully interpolate values of the field function (in the current work the smoothing operator has been used to calculate the temperature values in the buoyancy force term $F_b = -g\,\beta\,(T - T_c)$).

- The results showed that, with the increment of Rayleigh number, both heat transfer rate ($\overline{Nu}$) and overall entropy generation rate augment whereas a reverse trend occurs in the values of average Bejan number.
- The obtained results showed that, exergy analysis as an effective tool outperformed first-law analysis of thermodynamics in determining regime of fluid flow and heat transfer in the thermal systems involving bifurcation, thermal plumes, hotspot, stagnation point, and thermal stratification.

5.7 Appendix A (Gradient, Laplacian and divergence operators)

Along this appendix three main operators including: gradient, Laplacian and divergence will be derived based on the Taylor series expansion. By multiplying Eq. (5-A1) with W_{ij}/r_{ij}^2 , $x_{ij}W_{ij}/r_{ij}^2$, $y_{ij}W_{ij}/r_{ij}^2$ and integrating over the computational domain, particle approximation for the field function (smoothing operator) can be computed as follows:

$$f_j = f_i + f_x^{'}x_{ij} + f_y^{'}y_{ij} + \frac{1}{2}f_{xx}^{''}x_{ij}^2 + \frac{1}{2}f_{yy}^{''}y_{ij}^2 + f_{xy}^{''}x_{ij}y_{ij} + O(h^3) \tag{5-A1}$$

$$\begin{bmatrix} f_i \\ f_{i,x}^{'} \\ f_{i,y}^{'} \end{bmatrix} = L\begin{bmatrix} \sum_{j=1}^{N}\frac{f_j W_{ij}}{r_{ij}^2}dV \\ \sum_{j=1}^{N}\frac{x_{ij}f_j W_{ij}}{r_{ij}^2}dV \\ \sum_{j=1}^{N}\frac{y_{ij}f_j W_{ij}}{r_{ij}^2}dV \end{bmatrix} \qquad L = \begin{bmatrix} \sum_{j=1}^{N}\frac{W_{ij}}{r_{ij}^2}dV & \sum_{j=1}^{N}\frac{x_{ij}W_{ij}}{r_{ij}^2}dV & \sum_{j=1}^{N}\frac{y_{ij}W_{ij}}{r_{ij}^2}dV \\ \sum_{j=1}^{N}\frac{x_{ij}W_{ij}}{r_{ij}^2}dV & \sum_{j=1}^{N}\frac{x_{ij}^2W_{ij}}{r_{ij}^2}dV & \sum_{j=1}^{N}\frac{x_{ij}y_{ij}W_{ij}}{r_{ij}^2}dV \\ \sum_{j=1}^{N}\frac{y_{ij}W_{ij}}{r_{ij}^2}dV & \sum_{j=1}^{N}\frac{x_{ij}y_{ij}W_{ij}}{r_{ij}^2}dV & \sum_{j=1}^{N}\frac{y_{ij}^2W_{ij}}{r_{ij}^2}dV \end{bmatrix}^{-1} \tag{5-A2}$$

In above equation, f_i is a general variable such as velocity, temperature or pressure. $W_{ij} = W(\mathbf{r}_j - \mathbf{r}_i, h)$ and $dV = m_j/\rho_j$ denote kernel function and volume of particle *i*, respectively. $x_{ij} = x_j - x_i$ and $y_{ij} = y_j - y_i$ represent the distance between *i*-th particle to the *j*-th particle at positions $\mathbf{r}_i$ and $\mathbf{r}_j$. *L* is the corrective matrix which allows the method to fulfill the first-order accuracy. By subtracting f_i from both sides of Eq. (5-A1) and multiplying it by $x_{ij}W_{ij}/r_{ij}^2$ and $y_{ij}W_{ij}/r_{ij}^2$, the gradient operator can be derived as follow:

$$\begin{bmatrix} f_x^{'} \\ f_y^{'} \end{bmatrix} = L \begin{bmatrix} \sum_{j=1}^{N} \frac{x_{ij}(f_j - f_i)}{r_{ij}^2} W_{ij} dV \\ \sum_{j=1}^{N} \frac{y_{ij}(f_j - f_i)}{r_{ij}^2} W_{ij} dV \end{bmatrix} \qquad L = \begin{bmatrix} \sum_{j=1}^{N} \frac{x_{ij}^2 W_{ij}}{r_{ij}^2} dV & \sum_{j=1}^{N} \frac{x_{ij} y_{ij} W_{ij}}{r_{ij}^2} dV \\ \sum_{j=1}^{N} \frac{x_{ij} y_{ij} W_{ij}}{r_{ij}^2} dV & \sum_{j=1}^{N} \frac{y_{ij}^2 W_{ij}}{r_{ij}^2} dV \end{bmatrix}^{-1} \tag{5-A3}$$

Eq. (5-A3) was originally introduced by Khayyer et al. [33] and known as a *corrected gradient model of original MPS method*. Note that, Eq. (5-A3) can be modified and generalized by inserting control parameter (χ) on the basis of the *Tensile Instability Control* (TIC) [55], [56] as follows

$$\begin{bmatrix} f_x^{'} \\ f_y^{'} \end{bmatrix} = L \begin{bmatrix} \sum_{j=1}^{N} \frac{x_{ij}(f_j - \chi f_i)}{r_{ij}^2} W_{ij} dV \\ \sum_{j=1}^{N} \frac{y_{ij}(f_j - \chi f_i)}{r_{ij}^2} W_{ij} dV \end{bmatrix} \qquad L = \begin{bmatrix} \sum_{j=1}^{N} \frac{x_{ij}^2 W_{ij}}{r_{ij}^2} dV & \sum_{j=1}^{N} \frac{x_{ij} y_{ij} W_{ij}}{r_{ij}^2} dV \\ \sum_{j=1}^{N} \frac{x_{ij} y_{ij} W_{ij}}{r_{ij}^2} dV & \sum_{j=1}^{N} \frac{y_{ij}^2 W_{ij}}{r_{ij}^2} dV \end{bmatrix}^{-1} \tag{5-A4}$$

where the conservative form of the gradient operator ($\chi = 1$) is used for inner particles ($f_j - f_i$) whereas non-conservative form ($\chi = -1$) should be applied on the interface ($f_j + f_i$). Again, it is worthwhile to mention that, Eq. (5-A3) is utilized to calculate the divergence and gradient of velocity ($\nabla \cdot \mathbf{u}$, $\nabla \mathbf{u}$) and temperature ($\nabla \theta$) across the whole computational domain whereas Eq. (5-A4) should be implemented for calculating the pressure gradient. However, for a uniform particle distribution, off-diagonal elements of the corrective matrix in Eqs. (5-A2) to (5-A4) can be neglected, resulting in the following approximations:

$$\begin{aligned} &\sum_{j=1}^{N} \frac{x_{ij} W_{ij}}{r_{ij}^2} dV = \sum_{j=1}^{N} \frac{y_{ij} W_{ij}}{r_{ij}^2} dV = \sum_{j=1}^{N} \frac{x_{ij} y_{ij} W_{ij}}{r_{ij}^2} dV = 0 \\ &\sum_{j=1}^{N} \frac{x_{ij}^2}{r_{ij}^2} W_{ij} dV = \sum_{j=1}^{N} \frac{y_{ij}^2}{r_{ij}^2} W_{ij} dV = \frac{1}{2} \left(\sum_{j=1}^{N} \frac{x_{ij}^2}{r_{ij}^2} W_{ij} dV + \sum_{j=1}^{N} \frac{y_{ij}^2}{r_{ij}^2} W_{ij} dV \right) = \frac{1}{2} \left(\sum_{j=1}^{N} W_{ij} dV \right) \\ &\frac{1}{3} \left(\sum_{j=1}^{N} \frac{x_{ij}^2}{r_{ij}^2} W_{ij} dV + \sum_{j=1}^{N} \frac{y_{ij}^2}{r_{ij}^2} W_{ij} dV + \sum_{j=1}^{N} \frac{z_{ij}^2}{r_{ij}^2} W_{ij} dV \right) = \frac{1}{D_0} \sum_{j=1}^{N} W_{ij} dV, \quad \text{where} \quad x_{ij}^2 + y_{ij}^2 = r_{ij}^2 \end{aligned} \tag{5-A5}$$

$$f_i = \frac{\sum_{j=1}^{N} \frac{f_j W_{ij}}{r_{ij}^2} dV}{\sum_{j=1}^{N} \frac{W_{ij}}{r_{ij}^2} dV} \tag{5-A6}$$

$$\nabla f = \frac{D_0 \sum_{j=1}^{N} \frac{\mathbf{r}_{ij}(f_j - f_i)}{r_{ij}^2} W_{ij} dV}{\sum_{j=1}^{N} W_{ij} dV} \tag{5-A7}$$

$$\nabla \cdot \mathbf{f} = \frac{D_0 \sum_{j=1}^{N} \frac{\mathbf{r}_{ij} \cdot (\mathbf{f}_j - \mathbf{f}_i) W_{ij}}{r_{ij}^2} dV}{\sum_{j=1}^{N} W_{ij} dV} \tag{5-A8}$$

where f, $\mathbf{f}$ and D_0 denote an arbitrary scalar, vector and spatial dimension. Eq. (5-A6) is the MPS form of the Shepard approximant [76] while Eqs. (5-A7) and (5-A8) are gradient and divergence operators in the classical MPS formulation that were initially introduced by Koshizuka [62], [63]. Note that, Eq. (5-A5) can be proved by solving $\sum_{j=1}^{N} \frac{x_{ij}^2 W_{ij}}{r_{ij}^2} dV$ and $\sum_{j=1}^{N} \frac{y_{ij}^2 W_{ij}}{r_{ij}^2} dV$ in a polar coordinate system $(x_{ij} = r_{ij}\cos(\theta),\ y_{ij} = r_{ij}\sin(\theta))$. By ignoring the term $f_{xy}^{"} x_{ij} y_{ij}$ in Eq. (5-A1) and multiplying it by $\frac{W_{ij}}{r_{ij}^2}$ and integrating over the computational domain, the following Laplacian operator can be obtained:

$$\begin{aligned} \sum_{j=1}^{N} (f_j - f_i) \frac{W_{ij}}{r_{ij}^2} dV &= f_x^{'} \sum_{j=1}^{N} x_{ij} \frac{W_{ij}}{r_{ij}^2} dV + f_y^{'} \sum_{j=1}^{N} y_{ij} \frac{W_{ij}}{r_{ij}^2} dV \\ &+ \frac{1}{2} \sum_{j=1}^{N} f_{xx}^{"} \frac{x_{ij}^2 W_{ij}}{r_{ij}^2} dV + \frac{1}{2} \sum_{j=1}^{N} f_{yy}^{"} \frac{y_{ij}^2 W_{ij}}{r_{ij}^2} dV \end{aligned} \tag{5-A9}$$

To drive $(\nabla^2 f = f_{xx}^{"} + f_{yy}^{"})$ it is assumed that $\sum_{j=1}^{N} \frac{y_{ij}^2 W_{ij}}{r_{ij}^2} dV$ is equal to $\sum_{j=1}^{N} \frac{x_{ij}^2 W_{ij}}{r_{ij}^2} dV$. Although this assumption is not valid for irregular particles arrangement and free surface region where kernel is truncated but it is the only way in which $\nabla^2 f$ can be computed. Under the aforementioned hypothesis, the third and fourth terms in Eq. (5-A9) can be written as:

$$\frac{1}{2}\sum_{j=1}^{N} f_{xx}^{"}\frac{x_{ij}^2 W_{ij}}{r_{ij}^2}dV+\frac{1}{2}\sum_{j=1}^{N} f_{yy}^{"}\frac{y_{ij}^2 W_{ij}}{r_{ij}^2}dV=\frac{1}{2}\sum_{j=1}^{N} f_{xx}^{"}\frac{x_{ij}^2 W_{ij}}{r_{ij}^2}dV+\frac{1}{2}\sum_{j=1}^{N} f_{yy}^{"}\frac{x_{ij}^2 W_{ij}}{r_{ij}^2}dV$$

$$=\frac{1}{2}(f_{xx}^{"}+f_{yy}^{"})\sum_{j=1}^{N}\frac{x_{ij}^2 W_{ij}}{r_{ij}^2}dV=\frac{1}{2}(f_{xx}^{"}+f_{yy}^{"})\frac{1}{2}\sum_{j=1}^{N}(\frac{x_{ij}^2 W_{ij}}{r_{ij}^2}dV+\frac{y_{ij}^2 W_{ij}}{r_{ij}^2}dV) \quad (5\text{-A10})$$

$$=\frac{1}{2}(f_{xx}^{"}+f_{yy}^{"})\frac{1}{2}\sum_{j=1}^{N}W_{ij}dV \qquad where \quad x_{ij}^2+x_{ij}^2=r_{ij}^2$$

By substituting Eq. (5-A10) into Eq. (5-A9), the new Laplacian operator can be expressed as:

$$\nabla^2 f=\frac{2D_0[\sum_{j=1}^{N}\frac{(f_j-f_i)W_{ij}}{r_{ij}^2}dV-f_x^{'}\sum_{j=1}^{N}\frac{x_{ij}W_{ij}}{r_{ij}^2}dV-f_y^{'}\sum_{j=1}^{N}\frac{y_{ij}W_{ij}}{r_{ij}^2}dV-f_z^{'}\sum_{j=1}^{N}\frac{z_{ij}W_{ij}}{r_{ij}^2}dV]}{\sum_{j=1}^{N}W_{ij}dV} \quad (5\text{-A11})$$

where $f_x^{'}$ and $f_y^{'}$ are gradient of arbitrary scalar or vector function (f_i) (i.e. velocity, temperature, density or pressure, etc) which can be computed through Eqs. (5-A3) or (5-A4). It is worthwhile mentioning that, the present model is similar to work of Schwaiger [53] who proposed high-order Laplacian operator by taking gradient of kernel into account ($\nabla W_{ij,x}, \nabla W_{ij,y}$). However, since gradient of kernel doesn't appear in Eqs. (5-A1) to (5-A11), the current model could thus be referred to as a Kernel Derivative-Free (KDF) version of the WCSPH model (KDF-WCSPH). Similar to gradient operators, for the uniform particles distribution ($\sum_{j=1}^{N}\frac{x_{ij}W_{ij}}{r_{ij}^2}dV=\sum_{j=1}^{N}\frac{y_{ij}W_{ij}}{r_{ij}^2}dV=\sum_{j=1}^{N}\frac{z_{ij}W_{ij}}{r_{ij}^2}dV=0$), Eq. (5-A11) can be reduced to the relatively simple expression as:

$$\nabla^2 f=\frac{2D_0\sum_{j=1}^{N}\frac{(f_j-f_i)W_{ij}}{r_{ij}^2}dV}{\sum_{j=1}^{N}W_{ij}dV} \quad (5\text{-A12})$$

It is also possible to derive the second Laplacian operator directly, without considering any additional assumptions. This is achieved by subtracting f_i from both sides of Eq. (5-A1) and decomposing it into *x* and *y* directions as follow:

$$f_j - f_i = f_x^{'} x_{ij} + f_y^{'} y_{ij} + \frac{1}{2} f_{xx}^{"} x_{ij}^2 + \frac{1}{2} f_{yy}^{"} y_{ij}^2 \tag{5-A13}$$

$$\frac{1}{2}(f_j - f_i) = f_x^{'} x_{ij} + \frac{1}{2} f_{xx}^{"} x_{ij}^2 \tag{5-A14}$$

$$\frac{1}{2}(f_j - f_i) = f_y^{'} y_{ij} + \frac{1}{2} f_{yy}^{"} y_{ij}^2 \tag{5-A15}$$

By multiplying Eqs. (5-A14) and (5-A15) by $\frac{W_{ij}}{r_{ij}^2}$ and integrating over the computational domain, the second derivatives of shape function ($f_{xx}^{"}, f_{yy}^{"}$) can be obtained as:

$$\sum_{j=1}^{N} \frac{1}{2}(f_j - f_i)\frac{W_{ij}}{r_{ij}^2} dV = f_x^{'} \sum_{j=1}^{N} x_{ij} \frac{W_{ij}}{r_{ij}^2} dV + f_{xx}^{"} \sum_{j=1}^{N} \frac{1}{2} x_{ij}^2 \frac{W_{ij}}{r_{ij}^2} dV,$$

$$f_{xx}^{"} = \frac{\sum_{j=1}^{N} \frac{1}{2}(f_j - f_i)\frac{W_{ij}}{r_{ij}^2} dV - f_x^{'} \sum_{j=1}^{N} x_{ij} \frac{W_{ij}}{r_{ij}^2} dV}{\sum_{j=1}^{N} \frac{1}{2} \frac{x_{ij}^2}{r_{ij}^2} W_{ij} dV}, \tag{5-A16}$$

$$\sum_{j=1}^{N} \frac{1}{2}(f_j - f_i)\frac{W_{ij}}{r_{ij}^2} dV = f_y^{'} \sum_{j=1}^{N} y_{ij} \frac{W_{ij}}{r_{ij}^2} dV + f_{yy}^{"} \sum_{j=1}^{N} \frac{1}{2} y_{ij}^2 \frac{W_{ij}}{r_{ij}^2} dV,$$

$$f_{yy}^{"} = \frac{\sum_{j=1}^{N} \frac{1}{2}(f_j - f_i)\frac{W_{ij}}{r_{ij}^2} dV - f_y^{'} \sum_{j=1}^{N} y_{ij} \frac{W_{ij}}{r_{ij}^2} dV}{\sum_{j=1}^{N} \frac{1}{2} \frac{y_{ij}^2}{r_{ij}^2} W_{ij} dV}, \tag{5-A17}$$

By directly summing the terms $f_{xx}^{"}$ and $f_{yy}^{"}$ in above equations, the second Laplacian operator can be written as:

$$\nabla^2 f = f''_{yy} + f''_{xx} = \frac{\sum_{j=1}^{N} \frac{1}{2}(f_j - f_i)\frac{W_{ij}}{r_{ij}^2} dV - f'_x \sum_{j=1}^{N} x_{ij} \frac{W_{ij}}{r_{ij}^2} dV}{\sum_{j=1}^{N} \frac{1}{2} \frac{x_{ij}^2}{r_{ij}^2} W_{ij} dV} + \frac{\sum_{j=1}^{N} \frac{1}{2}(f_j - f_i)\frac{W_{ij}}{r_{ij}^2} dV - f'_y \sum_{j=1}^{N} y_{ij} \frac{W_{ij}}{r_{ij}^2} dV}{\sum_{j=1}^{N} \frac{1}{2} \frac{y_{ij}^2}{r_{ij}^2} W_{ij} dV}, \quad \text{(5-A18)}$$

Finally, it is interesting to note that, similar to previous equations for the case of the fully supported kernel, Eq. (5-A18) will eventually turn into Eq. (5-A12).

5.8 Appendix B (Third-order TVD Runge-Kutta)

In the current work, transient term in Navier-Stoks and energy equations is discretized in time using third-order total-variation-diminishing (TVD) Runge–Kutta scheme as follows [77]:

$$\frac{du}{dt} = L_h(u) \qquad \frac{dr}{dt} = R_h(u) \qquad \frac{d\theta}{dt} = T_h(\theta) \qquad \frac{d\rho}{dt} = \Phi_h(\rho) \quad \text{(5-B1)}$$

$$\begin{aligned} \rho^{(1)} &= \alpha_1 \rho^{(n)} + \beta_1 \Delta t \, \Phi_h(\rho^{(n)}) \\ u^{(1)} &= \alpha_1 u^{(n)} + \beta_1 \Delta t \, L_h(u^{(n)}) \\ r^{(1)} &= \alpha_1 r^{(n)} + \beta_1 \Delta t \, R_h(u^{(1)}) \\ \theta^{(1)} &= \alpha_1 \theta^{(n)} + \beta_1 \Delta t \, T_h(\theta^{(n)}) \end{aligned} \quad \text{(5-B2)}$$

$$\begin{aligned} \rho^{(2)} &= \alpha_2 \rho^{(n)} + \beta_2 \rho^{(1)} + \beta_2 \Delta t \, \Phi_h(\rho^{(1)}) \\ u^{(2)} &= \alpha_2 u^{(n)} + \beta_2 u^{(1)} + \beta_2 \Delta t \, L_h(u^{(1)}) \\ r^{(2)} &= \alpha_2 r^{(n)} + \beta_2 r^{(1)} + \beta_2 \Delta t \, R_h(u^{(2)}) \\ \theta^{(2)} &= \alpha_2 \theta^{(n)} + \beta_2 \theta^{(1)} + \beta_2 \Delta t \, T_h(\theta^{(1)}) \end{aligned} \quad \text{(5-B3)}$$

$$\begin{aligned} \rho^{(n+1)} &= \alpha_3 \rho^{(n)} + \beta_3 \rho^{(2)} + \beta_3 \Delta t \, \Phi_h(\rho^{(2)}) \\ u^{(n+1)} &= \alpha_3 u^{(n)} + \beta_3 u^{(2)} + \beta_3 \Delta t \, L_h(u^{(2)}) \\ r^{(n+1)} &= \alpha_3 r^{(n)} + \beta_3 r^{(2)} + \beta_3 \Delta t \, R_h(u^{(n+1)}) \\ \theta^{(n+1)} &= \alpha_3 \theta^{(n)} + \beta_3 \theta^{(2)} + \beta_3 \Delta t \, T_h(\theta^{(2)}) \end{aligned} \quad \text{(5-B4)}$$

where $\alpha_1 = 1$, $\alpha_2 = 3/4$, $\alpha_3 = 1/3$, $\beta_1 = 1$, $\beta_2 = 1/4$ and $\beta_3 = 2/3$.

5.9 Appendix C (Additional Delta term (δ) in continuity equation)

Generally, there are two different approaches in the context of the weakly compressible SPH for predicting pressure domain namely: Number Density (Eq. (5-C1)) [78], [79] and mass conservation law (Eq. (5-C2)) [80], [81] as given below:

$$\begin{cases} \rho = \sum_{j=1}^{N} \rho_j W_{ij} dV \\ p = c_0^2 (\rho - \rho_0) \end{cases} \tag{5-C1}$$

$$\begin{cases} \dfrac{D\rho}{Dt} = -\rho \nabla \cdot \mathbf{u} \\ p = c_0^2 (\rho - \rho_0) \end{cases} \tag{5-C2}$$

The former estimates the density through summation over all particles in the kernel support without the need of velocity divergence. Nevertheless, the results of Monaghan [82] shown that, although Eq. (5-C1) requires less computational effort than Eq. (5-C2) but due to kernel truncation error, it causes significant density drop adjacent to the free-surface area. On the other hand, Lee et al. [50] have questioned the accuracy of the standard WCSPH and highlighted that on the coarser resolutions and high Reynolds number, pressure field predicted by Eq. (5-C2) is unreliable and noisy. To deal with this shortcoming and avoid spurious high-frequency density/pressure oscillations, Antuono et al. [57] modified the classical WCSPH by introducing the new additional diffusive term in the continuity equation. This method which is known as $\delta-$WCSPH, has been widely used in the literature to solve the practical hydraulics problems such as: 2D oscillating water chamber [83], simulation of violent impact flow [49] and flow past a circular cylinder [55], [56]. Based on the above brief literature review, along this appendix, the process of deriving Fully-Kernel Based version of the density diffusive term (δ) will be presented and discussed in detail. The transient governing equations of mass and momentum for a weakly compressible fluid in Lagrangian framework are the ones that follow:

$$\frac{D\rho^{(n+1)}}{Dt} + \rho \nabla \cdot \mathbf{u}^{(n+1)} = 0 \tag{5-C3}$$

$$\frac{\mathbf{u}^{(n+1)} - \mathbf{u}^{n}}{\Delta t} = -\frac{\nabla p^{(n+1)}}{\rho} + \upsilon \nabla^2 \mathbf{u}^{n} + \mathbf{F}_B \tag{5-C4}$$

By adding and subtracting the temporary velocity ($\mathbf{u}^*$) into the left-hand side of Eq. (5-C4) and employing two-step projection algorithm for velocity-pressure coupling [66], momentum equation can be divided into two successive parts as given below:

$$\frac{\mathbf{u}^{(n+1)}-\mathbf{u}^*+\mathbf{u}^*-\mathbf{u}^n}{\Delta t}=-\frac{\nabla p^{(n+1)}}{\rho}+\upsilon\nabla^2\mathbf{u}^n+\mathbf{F}_B \tag{5-C5}$$

$$\frac{\mathbf{u}^*-\mathbf{u}^n}{\Delta t}=\upsilon\nabla^2\mathbf{u}^n+\mathbf{F}_B \tag{5-C6}$$

$$\frac{\mathbf{u}^{(n+1)}-\mathbf{u}^*}{\Delta t}=-\frac{\nabla p^{(n+1)}}{\rho} \tag{5-C7}$$

The divergence of Eq. (5-C7) reads:

$$\nabla\cdot\mathbf{u}^{(n+1)}-\nabla\cdot\mathbf{u}^*=\nabla\cdot(-\frac{\Delta t}{\rho}\nabla p^{(n+1)}) \tag{5-C8}$$

By substituting equation (5-C8) into Eq. (5-C3), one obtains:

$$\frac{D\rho^{(n+1)}}{Dt}+\rho\nabla\cdot\mathbf{u}^*-\rho\nabla\cdot(\frac{\Delta t}{\rho}\nabla p^{(n+1)})=0 \tag{5-C9}$$

Using the first-order state equation, the third term in Eq. (5-C9) can be expressed in the form of the density as:

$$p=c_0^2(\rho-\rho_0) \tag{5-C10}$$

$$\rho\nabla\cdot(\frac{\Delta t}{\rho}\nabla p)=\rho\nabla\cdot(\frac{\Delta t\,c_0^2}{\rho}\nabla\rho)=\Delta t\,c_0^2(\nabla^2\rho) \tag{5-C11}$$

By substituting equation (5-C11) into Eq. (5-C9), an alternative form of the continuity equation can be obtained as:

$$\frac{D\rho}{Dt}=-\rho\nabla\cdot\mathbf{u}^*+\Delta t\,c_0^2(\nabla^2\rho) \tag{5-C12}$$

The second term in the right-hand side of the above equation is the additional diffusive term ($\Delta t\,c_0^2(\nabla^2\rho)$). One of the most notable features of Eq. (5-C12) is that unlike the conventional $\delta-$WCSPH [57], the present model does not contain any tunable parameter to control the

density diffusive term. Finally, it should be noted that similar to the viscous term Eq. (5-A11) or (5-A18) can be used to calculate the Laplacian of density ($\nabla^2\rho$).

5.10 Appendix D (1D Sod shock tube)

The dimensional governing equations including momentum, energy, continuity and displacement in a Lagrangian framework for 1D Sod shock tube problem are shown as follows:

$$\frac{D\mathbf{u}}{Dt} = -\sum_{J=1}^{N} m_j \left(\frac{p_i + p_j}{\rho_i \rho_j} + \Pi_{ij}\right)\nabla W_{ij} \tag{5-D1}$$

$$\frac{De}{Dt} = -\frac{1}{2}\sum_{J=1}^{N} m_j \left(\frac{p_i}{\rho_i^{\,2}} + \frac{p_j}{\rho_j^{\,2}}\right)(\mathbf{u}_{ij}\cdot\nabla W_{ij}) \tag{5-D2}$$

$$\rho = \sum_{J=1}^{N} m_j W_{ij} \tag{5-D3}$$

$$\begin{aligned} \mathbf{u}^{(n+1)} &= \mathbf{u}^{(n)} + \Delta t \frac{D\mathbf{u}^{(n)}}{Dt} \\ \mathbf{r}^{(n+1)} &= \mathbf{r}^{(n)} + \Delta t\, \mathbf{u}^{(n+1)} \\ e^{(n+1)} &= e^{(n)} + \Delta t \frac{De^{(n)}}{Dt} \end{aligned} \tag{5-D4}$$

$$p = \rho(\gamma - 1)e, \quad c = \sqrt{\frac{\gamma p}{\rho}}, \tag{5-D5}$$

where e and ∇W_{ij} are internal energy and gradient of kernel function, respectively. The symbols c and $\gamma = 1.4$ denotes artificial sound speed and heat capacity ratio. The typical procedure for solving the above equations is detailed in [70] and illustrated above. First, material derivatives and density ($\frac{D\mathbf{u}}{Dt}, \frac{De}{Dt}, \rho$) are computed using Eqs. (5-D1) to (5-D3) and subsequently particles are advected to the new positions with updated velocity and energy according to the forward Euler time integration scheme (Eq. (5-D4)). Having obtained the density and energy fields, pressure and sound speed are estimated by Eq. (5-D5) and process will be repeated for the next time step. To stabilise the simulation and dampen non-physical fluctuations appearing near the shock waves, artificial viscosity (Π_{ij}) proposed by Monaghan [67] is frequently added in the momentum equation as follows:

$$\Pi_{ij} = \begin{cases} \dfrac{-\alpha \bar{c}_{ij} \phi_{ij} + \beta \phi_{ij}^2}{\bar{\rho}_{ij}} & \mathbf{u}_{ij} \cdot \mathbf{r}_{ij} < 0 \\ 0 & \mathbf{u}_{ij} \cdot \mathbf{r}_{ij} > 0 \end{cases}$$

$$\phi_{ij} = \frac{h_{ij} (\mathbf{u}_{ij} \cdot \mathbf{r}_{ij})}{\left| r_{ij} \right|^2 + \varphi^2} \tag{5-D6}$$

$$\bar{c}_{ij} = \frac{c_i + c_j}{2}, \ \bar{\rho}_{ij} = \frac{\rho_i + \rho_j}{2}, \ \varphi = 0.01 h_{ij}, \ \alpha = \beta = 1$$

5.11 References

[1] S. Banerjee, A. Mukhopadhyay, S. Sen, and R. Ganguly, "Natural convection in a bi-heater configuration of passive electronic cooling," Int. J. Therm. Sci., vol. 47, no. 11, pp. 1516–1527, 2008.

[2] S. Phiraphat, R. Prommas, and W. Puangsombut, "Experimental study of natural convection in PV roof solar collector," Int. Commun. Heat Mass Transf., vol. 89, pp. 31–38, 2017.

[3] S.-Y. Tan, J. Liu, and W.-Q. Lu, "Numerical investigation on natural convection heat transfer of the annular structure in heat exchangers and solenoids," Appl. Therm. Eng., vol. 150, pp. 674–685, 2019.

[4] J. Liu et al., "Flow characteristics in the containment cooling pools of small modular reactors," Int. J. Heat Mass Transf., vol. 133, pp. 445–460, 2019.

[5] H. M. Elshehabey, F. M. Hady, S. E. Ahmed, and R. A. Mohamed, "Numerical investigation for natural convection of a nanofluid in an inclined L-shaped cavity in the presence of an inclined magnetic field," Int. Commun. Heat Mass Transf., vol. 57, pp. 228–238, 2014.

[6] S. Saravanan and C. Sivaraj, "Combined thermal radiation and natural convection in a cavity containing a discrete heater: effects of nature of heating and heater aspect ratio," Int. J. Heat Fluid Flow, vol. 66, pp. 70–82, 2017.

[7] F. Garoosi, F. Hoseininejad, and M. M. Rashidi, "Numerical study of natural convection heat transfer in a heat exchanger filled with nanofluids," Energy, vol. 109, 2016.

[8] P. Hooshmand, H. Khakrah, M. Y. A. Jamalabadi, and D. Ross, “Natural convection heat transfer in a circle-square annulus using lattice Boltzmann method-Treatment of curved boundary conditions,” Int. J. Mech. Sci., vol. 161, p. 105086, 2019.

[9] A. H. Pordanjani, A. Jahanbakhshi, A. A. Nadooshan, and M. Afrand, “Effect of two isothermal obstacles on the natural convection of nanofluid in the presence of magnetic field inside an enclosure with sinusoidal wall temperature distribution,” Int. J. Heat Mass Transf., vol. 121, pp. 565–578, 2018.

[10] R. Mohebbi and M. M. Rashidi, “Numerical simulation of natural convection heat transfer of a nanofluid in an L-shaped enclosure with a heating obstacle,” J. Taiwan Inst. Chem. Eng., vol. 72, pp. 70–84, 2017.

[11] M. Saidi and G. Karimi, “Free convection cooling in modified L-shape enclosures using copper–water nanofluid,” Energy, vol. 70, pp. 251–271, 2014.

[12] H. M. Elshehabey, F. M. Hady, S. E. Ahmed, and R. A. Mohamed, “Numerical investigation for natural convection of a nanofluid in an inclined L-shaped cavity in the presence of an inclined magnetic field,” Int. Commun. Heat Mass Transf., vol. 57, pp. 228–238, 2014.

[13] A. S. Gawas and D. V Patil, “Rayleigh-Bénard type natural convection heat transfer in two-dimensional geometries,” Appl. Therm. Eng., vol. 153, pp. 543–555, 2019.

[14] A. Bejan, Entropy generation through heat and fluid flow. Wiley, 1982.

[15] A. Bejan, “Entropy generation minimization: The new thermodynamics of finite-size devices and finite-time processes,” J. Appl. Phys., vol. 79, no. 3, pp. 1191–1218, 1996.

[16] X. Chen, T. Zhao, M.-Q. Zhang, and Q. Chen, “Entropy and entransy in convective heat transfer optimization: A review and perspective,” Int. J. Heat Mass Transf., vol. 137, pp. 1191–1220, 2019.

[17] C. Sivaraj and M. A. Sheremet, “MHD natural convection and entropy generation of ferrofluids in a cavity with a non-uniformly heated horizontal plate,” Int. J. Mech. Sci., vol. 149, pp. 326–337, 2018.

[18] G. H. R. Kefayati and H. Tang, “Double-diffusive laminar natural convection and entropy generation of Carreau fluid in a heated enclosure with an inner circular cold cylinder (Part II: Entropy generation),” Int. J. Heat Mass Transf., vol. 120, pp. 683–713, 2018.

[19] M. Siavashi, R. Yousofvand, and S. Rezanejad, “Nanofluid and porous fins effect on natural convection and entropy generation of flow inside a cavity,” Adv. Powder Technol., vol. 29, no. 1, pp. 142–156, 2018.

[20] S. Arun and A. Satheesh, “Mesoscopic analysis of MHD double diffusive natural convection and entropy generation in an enclosure filled with liquid metal,” J. Taiwan Inst. Chem. Eng., vol. 95, pp. 155–173, 2019.

[21] W. Liu, A. Shahsavar, A. A. Barzinjy, A. A. A. A. Al-Rashed, and M. Afrand, “Natural convection and entropy generation of a nanofluid in two connected inclined triangular enclosures under magnetic field effects,” Int. Commun. Heat Mass Transf., vol. 108, p. 104309, 2019.

[22] D. Zhang, H. Peng, and X. Ling, “Lattice Boltzmann method for thermomagnetic convection and entropy generation of paramagnetic fluid in porous enclosure under magnetic quadrupole field,” Int. J. Heat Mass Transf., vol. 127, pp. 224–236, 2018.

[23] M. S. Astanina, M. A. Sheremet, H. F. Oztop, and N. Abu-Hamdeh, “MHD natural convection and entropy generation of ferrofluid in an open trapezoidal cavity partially filled with a porous medium,” Int. J. Mech. Sci., vol. 136, pp. 493–502, 2018.

[24] P. Biswal and T. Basak, “Entropy generation vs energy efficiency for natural convection based energy flow in enclosures and various applications: A review,” Renew. Sustain. Energy Rev., vol. 80, pp. 1412–1457, 2017.

[25] D. Das, M. Roy, and T. Basak, “Studies on natural convection within enclosures of various (non-square) shapes–A review,” Int. J. Heat Mass Transf., vol. 106, pp. 356–406, 2017.

[26] H. Pan, X. Z. Chen, X. F. Liang, L. T. Zhu, and Z. H. Luo, “CFD simulations of gas-liquid-solid flow in fluidized bed reactors - A review,” Powder Technol., vol. 299, pp. 235–258, 2016.

[27] C. W. Hirt and B. D. Nichols, “Volume of fluid (VOF) method for the dynamics of free boundaries,” J. Comput. Phys., vol. 39, no. 1, pp. 201–225, 1981.

[28] M. Sussman, P. Smereka, and S. Osher, “A level set approach for computing solutions to incompressible two-phase flow,” J. Comput. Phys., vol. 114, no. 1, pp. 146–159, 1994.

[29] J. Ha and P. W. Cleary, “Comparison of SPH simulations of high pressure die casting with the experiments and VOF simulations of Schmid and Klein,” Int. J. Cast Met. Res., vol. 12, no. 6, pp. 409–418, 2000.

[30] B. Wu, M. Firouzi, T. Mitchell, T. E. Rufford, C. Leonardi, and B. Towler, “A critical review of flow maps for gas-liquid flows in vertical pipes and annuli,” Chem. Eng. J., vol. 326, pp. 350–377, 2017.

[31] R. A. Gingold and J. J. Monaghan, “Smoothed particle hydrodynamics: theory and application to non-spherical stars,” Mon. Not. R. Astron. Soc., vol. 181, no. 3, pp. 375–389, 1977.

[32] G. G. Pereira, P. W. Cleary, and Y. Serizawa, “Prediction of fluid flow through and jet formation from a high pressure nozzle using Smoothed Particle Hydrodynamics,” Chem. Eng. Sci., vol. 178, pp. 12–26, 2018.

[33] A. Khayyer and H. Gotoh, “Enhancement of stability and accuracy of the moving particle semi-implicit method,” J. Comput. Phys., vol. 230, no. 8, pp. 3093–3118, 2011.

[34] P. Nair and T. Pöschel, “Dynamic capillary phenomena using Incompressible SPH,” Chem. Eng. Sci., vol. 176, pp. 192–204, 2018.

[35] S. Natsui, R. Nashimoto, H. Takai, T. Kumagai, T. Kikuchi, and R. O. Suzuki, “SPH simulations of the behavior of the interface between two immiscible liquid stirred by the movement of a gas bubble,” Chem. Eng. Sci., vol. 141, pp. 342–355, 2016.

[36] M. Hopp-Hirschler, M. S. Shadloo, and U. Nieken, “A Smoothed Particle Hydrodynamics approach for thermo-capillary flows,” Comput. Fluids, vol. 176, pp. 1–19, 2018.

[37] K. C. Ng, Y. L. Ng, T. W. H. Sheu, and A. Mukhtar, “Fluid-solid conjugate heat transfer modelling using weakly compressible smoothed particle hydrodynamics,” Int. J. Mech. Sci., vol. 151, pp. 772–784, 2019.

[38] X. Yang and S.-C. Kong, “Numerical study of natural convection in a horizontal concentric annulus using smoothed particle hydrodynamics,” Eng. Anal. Bound. Elem., vol. 102, pp. 11–20, 2019.

[39] Z. L. Zhang, K. Walayat, C. Huang, J. Z. Chang, and M. B. Liu, “A finite particle method with particle shifting technique for modeling particulate flows with thermal convection,” Int. J. Heat Mass Transf., vol. 128, pp. 1245–1262, 2019.

[40] J.-Y. Chen, F.-S. Lien, C. Peng, and E. Yee, “GPU-accelerated smoothed particle hydrodynamics modeling of granular flow,” Powder Technol., 2019.

[41] X. Dong, X. Huang, and J. Liu, “Modeling and simulation of droplet impact on elastic beams based on SPH,” Eur. J. Mech., vol. 75, pp. 237–257, 2019.

[42] P. Nair and G. Tomar, “Simulations of gas-liquid compressible-incompressible systems using SPH,” Comput. Fluids, vol. 179, pp. 301–308, 2019.

[43] Z.-B. Wang, R. Chen, H. Wang, Q. Liao, X. Zhu, and S.-Z. Li, “An overview of smoothed particle hydrodynamics for simulating multiphase flow,” Appl. Math. Model., vol. 40, no. 23–24, pp. 9625–9655, 2016.

[44] M. S. Shadloo, G. Oger, and D. Le Touzé, “Smoothed particle hydrodynamics method for fluid flows, towards industrial applications: Motivations, current state, and challenges,” Comput. Fluids, vol. 136, pp. 11–34, 2016.

[45] J. W. Swegle, D. L. Hicks, and S. W. Attaway, “Smoothed particle hydrodynamics stability analysis,” J. Comput. Phys., vol. 116, no. 1, pp. 123–134, 1995.

[46] D. Molteni and A. Colagrossi, “A simple procedure to improve the pressure evaluation in hydrodynamic context using the SPH,” Comput. Phys. Commun., vol. 180, no. 6, pp. 861–872, 2009.

[47] X. Xu and X.-L. Deng, “An improved weakly compressible SPH method for simulating free surface flows of viscous and viscoelastic fluids,” Comput. Phys. Commun., vol. 201, pp. 43–62, 2016.

[48] P. N. Sun, A. Colagrossi, S. Marrone, M. Antuono, and A.-M. Zhang, “A consistent approach to particle shifting in the δ-Plus-SPH model,” Comput. Methods Appl. Mech. Eng., vol. 348, pp. 912–934, 2019.

[49] S. Marrone, M. Antuono, A. Colagrossi, G. Colicchio, D. Le Touzé, and G. Graziani, “δ-SPH model for simulating violent impact flows,” Comput. Methods Appl. Mech. Eng., vol. 200, no. 13–16, pp. 1526–1542, 2011.

[50] E.-S. Lee, C. Moulinec, R. Xu, D. Violeau, D. Laurence, and P. Stansby, “Comparisons of weakly compressible and truly incompressible algorithms for the SPH mesh free particle method,” J. Comput. Phys., vol. 227, no. 18, pp. 8417–8436, 2008.

[51] X. F. Yang, S. L. Peng, and M. B. Liu, “A new kernel function for SPH with applications to free surface flows,” Appl. Math. Model., vol. 38, no. 15–16, pp. 3822–3833, 2014.

[52] N. Nomeritae, E. Daly, S. Grimaldi, and H. Bui, “Explicit incompressible SPH algorithm for free-surface flow modelling: A comparison with weakly compressible schemes,” Adv. Water Resour, vol. 97, pp. 156–167, 2016.

[53] H. F. Schwaiger, “An implicit corrected SPH formulation for thermal diffusion with linear free surface boundary conditions,” Int. J. Numer. Methods Eng., vol. 75, no. 6, pp. 647–671, 2008.

[54] G. Oger, M. Doring, B. Alessandrini, and P. Ferrant, “An improved SPH method: Towards higher order convergence,” J. Comput. Phys., vol. 225, no. 2, pp. 1472–1492, 2007.

[55] P. N. Sun, A. Colagrossi, S. Marrone, and A. M. Zhang, “The δplus-SPH model: simple procedures for a further improvement of the SPH scheme,” Comput. Methods Appl. Mech. Eng., vol. 315, pp. 25–49, 2017.

[56] P. N. Sun, A. Colagrossi, S. Marrone, M. Antuono, and A. M. Zhang, “Multi-resolution Delta-plus-SPH with tensile instability control: Towards high Reynolds number flows,” Comput. Phys. Commun., vol. 224, pp. 63–80, 2018.

[57] M. Antuono, A. Colagrossi, S. Marrone, and D. Molteni, “Free-surface flows solved by means of SPH schemes with numerical diffusive terms,” Comput. Phys. Commun., vol. 181, no. 3, pp. 532–549, 2010.

[58] R. Xu, P. Stansby, and D. Laurence, “Accuracy and stability in incompressible SPH (ISPH) based on the projection method and a new approach,” J. Comput. Phys., vol. 228, no. 18, pp. 6703–6725, 2009.

[59] S. J. Lind, R. Xu, P. K. Stansby, and B. D. Rogers, “Incompressible smoothed particle hydrodynamics for free-surface flows: A generalised diffusion-based algorithm for stability and validations for impulsive flows and propagating waves,” J. Comput. Phys., vol. 231, no. 4, pp. 1499–1523, 2012.

[60] A. Khayyer, H. Gotoh, and Y. Shimizu, “Comparative study on accuracy and conservation properties of two particle regularization schemes and proposal of an optimized particle shifting scheme in ISPH context,” J. Comput. Phys., vol. 332, pp. 236–256, 2017.

[61] J. Hongbin and D. Xin, “On criterions for smoothed particle hydrodynamics kernels in stable field,” J. Comput. Phys., vol. 202, no. 2, pp. 699–709, 2005.

[62] M. Tanaka, R. Cardoso, and H. Bahai, “Multi-resolution MPS method,” J. Comput. Phys., vol. 359, pp. 106–136, 2018.

[63] S. Koshizuka, “A particle method for incompressible viscous flow with fluid fragmentation,” Comput. Fluid Dyn. J., vol. 4, p. 29, 1995.

[64] G. G. Ilis, M. Mobedi, and B. Sunden, “Effect of aspect ratio on entropy generation in a rectangular cavity with differentially heated vertical walls,” Int. Commun. Heat Mass Transf., vol. 35, no. 6, pp. 696–703, 2008.

[65] Y. Lin, G. R. Liu, and G. Wang, “A particle-based free surface detection method and its application to the surface tension effects simulation in smoothed particle hydrodynamics (SPH),” J. Comput. Phys., vol. 383, pp. 196–206, 2019.

[66] A. J. Chorin, “Numerical solution of the Navier-Stokes equations,” Math. Comput., vol. 22, no. 104, pp. 745–762, 1968.

[67] J. J. Monaghan, “SPH without a Tensile Instability,” J. Comput. Phys., vol. 159, no. 2, pp. 290–311, 2000.

[68] G. Duan, B. Chen, X. Zhang, and Y. Wang, “A multiphase MPS solver for modeling multi-fluid interaction with free surface and its application in oil spill,” Comput. Methods Appl. Mech. Eng., vol. 320, pp. 133–161, 2017.

[69] A. Skillen, S. Lind, P. K. Stansby, and B. D. Rogers, “Incompressible smoothed particle hydrodynamics (SPH) with reduced temporal noise and generalised Fickian smoothing applied to body–water slam and efficient wave–body interaction,” Comput. Methods Appl. Mech. Eng., vol. 265, pp. 163–173, 2013.

[70] L. Gui-rong, Smoothed particle hydrodynamics: a meshfree particle method. World Scientific, 2003.

[71] L. Lobovský, E. Botia-Vera, F. Castellana, J. Mas-Soler, and A. Souto-Iglesias, “Experimental investigation of dynamic pressure loads during dam break,” J. Fluids Struct., vol. 48, pp. 407–434, 2014.

[72] C. Zhang, X. Y. Hu, and N. A. Adams, “A weakly compressible SPH method based on a low-dissipation Riemann solver,” J. Comput. Phys., vol. 335, pp. 605–620, 2017.

[73] B. Calcagni, F. Marsili, and M. Paroncini, “Natural convective heat transfer in square enclosures heated from below,” Appl. Therm. Eng., vol. 25, no. 16, pp. 2522–2531, 2005.

[74] M. Sheikholeslami and R. Ellahi, “Three dimensional mesoscopic simulation of magnetic field effect on natural convection of nanofluid,” Int. J. Heat Mass Transf., vol. 89, pp. 799–808, 2015.

[75] M. Magherbi, H. Abbassi, and A. Ben Brahim, “Entropy generation at the onset of natural convection,” Int. J. Heat Mass Transf., vol. 46, no. 18, pp. 3441–3450, 2003.

[76] D. Shepard, “A two-dimensional interpolation function for irregularly-spaced data,” in Proceedings of the 1968 23rd ACM national conference, 1968, pp. 517–524.

[77] C.-W. Shu and S. Osher, “Efficient implementation of essentially non-oscillatory shock-capturing schemes,” J. Comput. Phys., vol. 77, no. 2, pp. 439–471, 1988.

[78] M. S. Shadloo and M. Yildiz, “Numerical modeling of Kelvin–Helmholtz instability using smoothed particle hydrodynamics,” Int. J. Numer. Methods Eng., vol. 87, no. 10, pp. 988–1006, 2011.

[79] S. Adami, X. Y. Hu, and N. A. Adams, “A transport-velocity formulation for smoothed particle hydrodynamics,” J. Comput. Phys., vol. 241, pp. 292–307, 2013.

[80] P. Wittek, G. G. Pereira, M. A. Emin, V. Lemiale, and P. W. Cleary, “Accuracy analysis of SPH for flow in a model extruder with a kneading element,” Chem. Eng. Sci., vol. 187, pp. 256–268, 2018.

[81] D. F. Gunn, M. Rudman, and R. C. Z. Cohen, “Wave interaction with a tethered buoy: SPH simulation and experimental validation,” Ocean Eng., vol. 156, pp. 306–317, 2018.

[82] J. J. Monaghan, “Smoothed particle hydrodynamics,” Annu. Rev. Astron. Astrophys., vol. 30, no. 1, pp. 543–574, 1992.

[83] H. Wen, B. Ren, and X. Yu, “An improved SPH model for turbulent hydrodynamics of a 2D oscillating water chamber,” Ocean Eng., vol. 150, pp. 152–166, 2018.

Chapter 6 ARTICLE 3: AN IMPROVED HIGH-ORDER ISPH METHOD FOR SIMULATION OF FREE-SURFACE FLOWS AND CONVECTION HEAT TRANSFER

Faroogh Garoosi[*,a], Ahmad Shakibaeinia[a,b]

[a]Department of Civil, Geological and Mining Engineering, Polytechnique Montreal, Montreal, Quebec, Canada

[b]Canada Research Chair in Modeling Complex Hydro-environmental Systems, Canada

Corresponding author: faroogh.garoosi@polymtl.ca,

Second author: ahmad.shakibaeinia@polymtl.ca

Abstract

The present work introduces a modified Incompressible Smoothed Particle Hydrodynamics (ISPH) model for simulation of free-surface flows and convection heat transfer. First, two new gradient and Laplacian models are proposed based on the Taylor series expansion and then used for discretization of the diffusion terms, Pressure Poisson's equation (PPE), and divergence of velocity. To maintain overall high-order accuracy, an explicit third-order TVD Runge-Kutta scheme is employed for discretization of the transient terms in Navier-Stokes and energy equations. Moreover, a new Hybrid Particle Shifting Technique (HPST) is developed by combining the classical PST and a collision model. A new kernel function is developed by combination of the Gaussian and polynomial functions and is then applied to the simulation of classical 1D Sod shock tube. Furthermore, a novel Hybrid Free-surface Detection (HFD) technique is proposed for accurate imposition of Dirichlet pressure boundary condition at the free surface area. The validity and applicability of proposed numerical schemes are verified against the several challenging benchmark cases including: dam-break flows with/without an obstacles, stretching water drop, rotating square patch of fluid, Rayleigh-Taylor instability, energy and exergy analysis of natural convection heat transfer in differentially heated cavity. The results show that, the newly constructed kernel function can successfully guarantee the stability and convergence of the numerical solution. Furthermore, it is found that, the proposed Hybrid Particle

Shifting Technique (HPST) can efficiently resolve the unphysical discontinuity and suppress spurious pressure fluctuations.

Keywords: New Kernel Function; Hybrid Particle Shifting Technique; New free-surface detection technique; New gradient operator; New Laplacian operator; Improved ISPH;

6.1 Introduction

The Smoothed Particle Hydrodynamics (SPH) approach as a truly Lagrangian particle model was originally proposed by Gingold and Monaghan [1] to describe the evolution of astrophysical systems and migration of giant planets. Unlike the Eulerian models (e.g. FDM, FEM, FVM) [2]–[5], in the SPH description, the computational domain is discretized by set of the moving particles where the specific smoothing kernel is used to establish the spatial relationships between field variables. Free from false diffusion associated with convection terms and absence of severe mesh distortions and element entanglement make the SPH more reliable and useful tool for modeling multiphase flows involving severe interfacial deformation, stretching, breaking, and splashing [6]. Due to its inherent mesh-less features and superiority over traditional Eulerian methods in tracking the evolution of interfacial areas and moving boundaries, the SPH has been extensively applied to various industrial and engineering applications such as: simulation of granular material [7]–[11], natural and forced convection heat transfer in the complex geometries [12]–[18], nuclear reactor design and dynamic analysis of landslide dam [19]–[22], simulation of Rayleigh-Taylor instability and bubble rising [23]–[25], modeling violent free-surface flows and droplet collision and coalescence [26]–[29], simulations of multiphase flows and fluidized beds [30]–[35], analysis of liquid sloshing and fluid flow over the airfoil and circular cylinder [36]–[40]. A comprehensive literature survey concerning the potential application of the SPH in many fields of engineering and science can be found in works of Wang et al. [41] and Shadloo et al. [42]. Despite the fact that, the SPH has been proved to be an efficient approach for analysis of fluid-structure interaction (FSI) problems, it still faces several crucial shortcomings including the occurrence of tensile instability caused by particle clustering [24], [43]–[45], spurious checkerboard pressure in both time and spatial domains [46], [47], non-conservative form of pressure gradient operator [37], [48], uncertainty in selecting the appropriate kernel function [49]–[51], and false detection of interfacial particles in multiphase flows [52]–[57] which can immensely jeopardize the stability and accuracy of the numerical simulation. Over the past

decade, substantial research efforts have been devoted to enhance the precision and consistency of the SPH. In a pioneering work, Xu et al. [43] introduced the concept of the Particle Shifting Technique (PST) to resolve the problem of particle bunching and void formation. The PST was then modified and implemented by Skillen et al. [44] and Shadloo et al. [24] to solve the problem of particle clustering in modeling of circular Couette flow and Rayleigh-Taylor instability. Recently, Khayyer et al. [45] introduced a novel improved and optimized version of the PST for consistent and accurate treatment of the free-surface area. In another work, Lee et al. [58] adopted the principle of Lennard-Jones molecular force [6] and introduced the idea of using collision model to control the regularity and arrangement of moving particles. This technique was then employed by Chen et al. [59], Xu et al. [60] and Shakibaeinia et al. [61] for simulation of dam break, Rayleigh-Taylor and Kelvin-Helmholtz instability problems. Another potential source of instability can be traced back quantitatively to the classical SPH operators. Ideally, the SPH was formulated for particles with uniform distribution while this assumption is not valid in the zones with incomplete kernel support. To overcome this shortcoming, Oger et al. [47] suggested the use of the kernel derivative correction technique and concluded that, reproducing kernel function and related gradient operators through renormalization technique can significantly suppress non-physical pressure fluctuations and minimize particle perturbations. To further eliminate unphysical void formation and pressure oscillations, Schwaiger [46] extended Oger's model [47] and proposed higher-order Laplacian operator based on the Taylor series expansion. To enhance the conservation properties of classical SPH formulations and eliminate tensile instability, Sun et al. [37], [48] proposed a new switching technique so-called Tensile Instability Control (TIC). In this technique, non-conservative form of the pressure gradient is used in the specific area with truncated kernel support. Recently, Hongbin et al. [49] conducted a comparative study to investigate the effects of the type of the kernel function on the performance of the SPH model. They stated that, type of the kernel function has a remarkable impact on the consistency and accuracy of the mesh-free particle methods. In the same context, Yang et al. [50], [51] constructed two different kernels and highlighted that, the smoothness and coherence of the first and second derivatives of kernel function play a major role in the stability of the numerical simulations. Despite the success of these efforts, selecting the reliable and efficient kernel function is still a subject of controversy [62]–[64]. Accurate detection of boundary surface to impose Dirichlet boundary condition for the Pressure Poisson Equation (zero pressure) is another

major challenge faced with the ISPH model. Generally, the existing boundary recognition algorithms can be classified into two categories: (a) coverage detection techniques [52], [53], [56], [57] and (b) kernel-based algorithms [54], [55], [65]. In the former, the specific scanning algorithm is utilized to scan the local region around each target particle. If any gap is found, the candidate particle will be labeled as a surface particle. However, the results of Haque et al. [56] revealed that the implementation of the aforementioned technique for 3D free-surface problems or long-term simulations is not computationally affordable. The second method takes the advantages of kernel summation (PND) [55] and its derivatives (Divergence of Particle Position) [54], [65], [66] to determine which particles belong to interface or interior area. However, in spite of being computationally inexpensive, this technique is sensitive to regularity and uniformity of particles distribution such that the occurrence of particle clustering can lead to erroneous predictions of interface position.

In light of the above literature review, the main aim of the current work is to introduce a novel high-order Mesh-free Particle Model (MPM) in the context of the ISPH for simulation of the free-surface flows and convection heat transfer. For this purpose, the governing operators (i.e. gradient, divergence and Laplacian) are first reformulated based on the Taylor series expansion and then applied for discretization of governing equations. To further enhance the stability and accuracy of the method, a new high-order kernel function is constructed by combination of the Gaussian and polynomial functions. Furthermore, a novel Hybrid Particle Shifting Technique (HPST) is proposed to remove tensile instability and particle clustering. Moreover, a novel Hybrid Free-surface Detection (HFD) technique is proposed for accurate imposition of Dirichlet pressure boundary condition at the free surface area. Detailed description of the methodology with associated higher-order schemes proposed in the current work can establish a wide panorama of promising alternative treatment on the improvements of Lagrangian Particle Models.

6.2 Problem statement and governing equations

Schematic diagram of various configurations under study together with associated boundary conditions and coordinate system are depicted in Fig. 6-1. Six different benchmark test cases have been simulated to demonstrate the promising potential of the proposed models in handling wide range of free-surface flow and convection heat transfer problems. In all the simulations, the

flow is assumed to be two-dimensional and laminar and the working fluid is considered as incompressible and Newtonian except for the case of 1D Sod shock tube problem where density is linked to pressure via a stiff equation of state (EOS).

The governing equations describing the 2D incompressible, Newtonian and laminar flow in the Lagrangian framework is given by [67]:

$$\frac{\partial u}{\partial x}+\frac{\partial v}{\partial y}=0, \tag{6-1}$$

$$\frac{D\rho u}{Dt}=-\frac{\partial p}{\partial x}+\mu\left(\frac{\partial^2 u}{\partial x^2}+\frac{\partial^2 u}{\partial y^2}\right), \tag{6-2}$$

$$\frac{D\rho v}{Dt}=-\frac{\partial p}{\partial y}+\mu\left(\frac{\partial^2 v}{\partial x^2}+\frac{\partial^2 v}{\partial y^2}\right)+F_b, \tag{6-3}$$

$$\frac{D\rho C_p T}{Dt}=k\left(\frac{\partial^2 T}{\partial x^2}+\frac{\partial^2 T}{\partial y^2}\right), \tag{6-4}$$

$$\frac{D\mathbf{r}}{Dt}=\mathbf{u}, \tag{6-5}$$

where **u**: (u, v), **r**: (x, y), k and T denote velocity and position vectors, thermal conductivity and temperature. ρ, C_p and μ are density, specific heat capacity and dynamic viscosity of the fluid, respectively. D is the substantial derivative and F_b represents body force acting on the fluid which is gravity force ($F_b=\rho g$) in the free-surface flows or buoyancy force ($F_b=-\rho g\,\beta(T-T_c)$) in the natural convection heat transfer according to Boussinesq approximation.

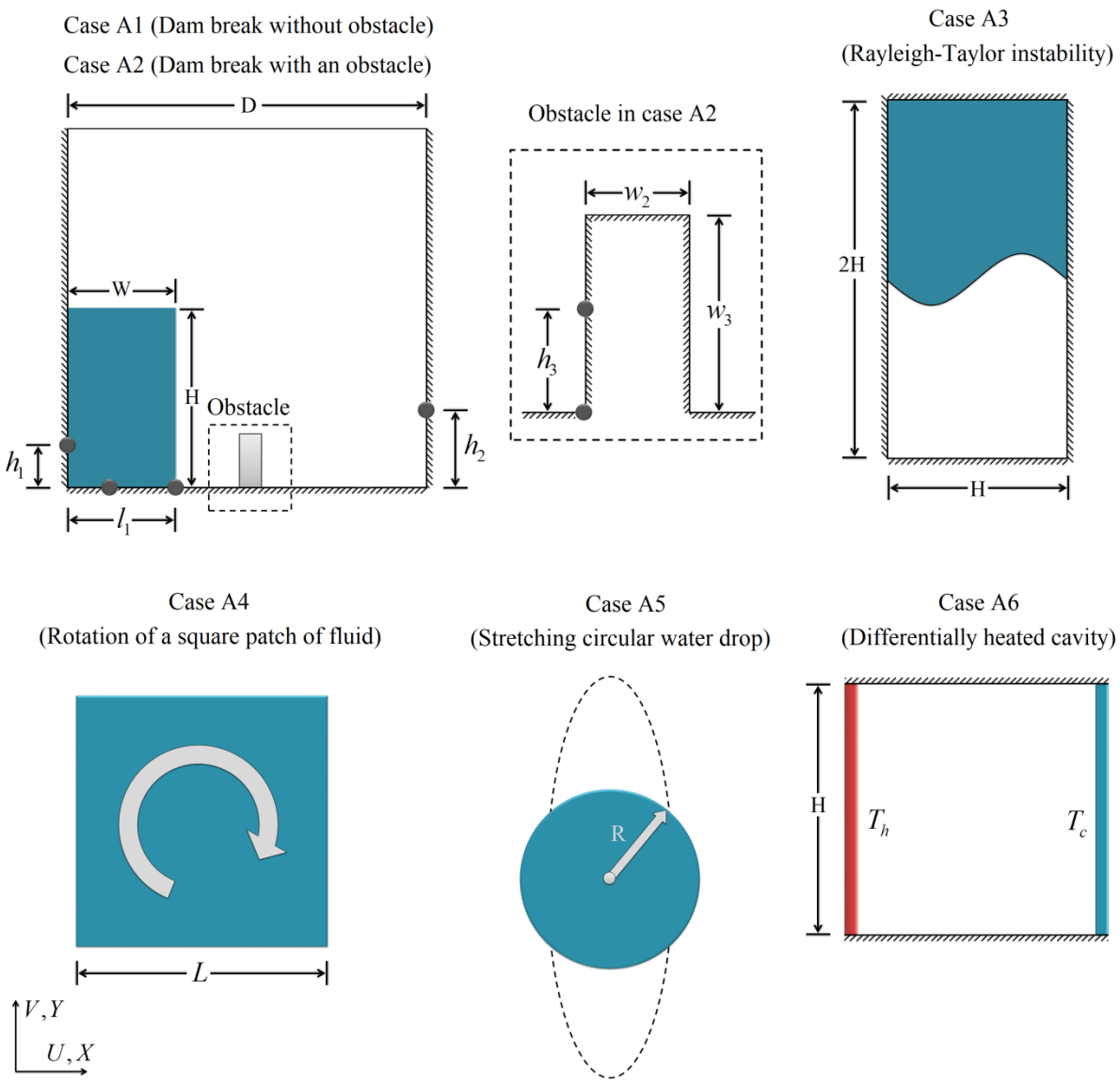

Figure 6-1 Schematic description of the physical models with associated boundary conditions and coordinate system.

As described by Bejan [68], the total volumetric entropy generation rate (S_{tot}) due to thermal dissipation (S_T) and fluid friction irreversibility (S_F) for 2D problems can be computed by the following expression:

$$S_{tot} = S_T + S_F \tag{6-6}$$

$$S_T = \frac{k(\nabla T \cdot \nabla T)}{T_0^2} = \frac{k}{T_0^2}\left[\left(\frac{\partial T}{\partial x}\right)^2 + \left(\frac{\partial T}{\partial y}\right)^2\right] \tag{6-7}$$

$$S_F = \frac{\mu}{T_0}\left(\frac{\partial \mathbf{u}_i}{\partial \mathbf{r}_j} + \frac{\partial \mathbf{u}_j}{\partial \mathbf{r}_i}\right)\frac{\partial \mathbf{u}_i}{\partial \mathbf{r}_j} = \frac{\mu}{T_0}\left[2\left(\frac{\partial u}{\partial x}\right)^2 + 2\left(\frac{\partial v}{\partial y}\right)^2 + \left(\frac{\partial u}{\partial y} + \frac{\partial v}{\partial x}\right)^2\right] \tag{6-8}$$

where $T_0 = (T_h + T_c)/2$ is a bulk temperature [69]. The dimensionless form of the governing equations for entropy generation can be obtained by introducing the following non-dimensional parameters:

$$\begin{aligned} &X = \frac{x}{H}, \quad Y = \frac{y}{H}, \quad U = \frac{uH}{\alpha}, \quad V = \frac{vH}{\alpha}, \quad P = \frac{pH^2}{\rho\alpha^2}, \quad \theta = \frac{T - T_c}{T_h - T_c}. \\ &t^* = \frac{t\alpha}{H^2}, \quad Ra = \frac{g\beta(T_h - T_c)H^3}{\alpha\nu}, \quad \mathrm{Pr} = \frac{\nu}{\alpha}. \end{aligned} \tag{6-9}$$

By substituting above pertinent parameters in Eqs. (6-6) to (6-8), one can obtain non-dimensional form of the entropy generation as follows:

$$\begin{aligned} S_T &= \left[\left(\frac{\partial \theta}{\partial X}\right)^2 + \left(\frac{\partial \theta}{\partial Y}\right)^2\right] \\ S_F &= \varphi\left[2\left(\frac{\partial U}{\partial X}\right)^2 + 2\left(\frac{\partial V}{\partial Y}\right)^2 + \left(\frac{\partial U}{\partial y} + \frac{\partial V}{\partial X}\right)^2\right] \end{aligned} \tag{6-10}$$

φ is a constant parameter which represents the ratio of the viscous dissipation to the heat transfer irreversibility, defined as [70], [71]:

$$\varphi = \frac{\mu T_0 \alpha^2}{kH^2(T_h - T_c)^2}, \tag{6-11}$$

In the current work, the value of φ in case A6 is taken as 10^{-4} similar to work of Ilis et al. [72]. The total entropy generation can be computed via integrating the local entropy generation rate with respect to *X* and *Y* coordinates:

$$\overline{S}_T = \frac{1}{V}\int S_T dX\, dY \qquad \overline{S}_F = \frac{1}{V}\int S_F dX\, dY \qquad \overline{S}_{tot} = \overline{S}_T + \overline{S}_F \tag{6-12}$$

The relative dominance of thermal dissipation to total irreversibility can be mathematically expressed by computing local and average Bejan numbers as:

$$Be = \frac{S_T}{S_T + S_F} \qquad \overline{Be} = \frac{1}{\overline{V}} \int Be \, dX \, dY \tag{6-13}$$

According to the above definition, $0 \le Be < 0.5$ indicates the relative dominance of the viscous dissipation ($S_F > S_T$) while thermal irreversibility ($S_F < S_T$) is dominant when $0.5 < Be \le 1$. For $Be = 0.5$, the entropy generation due to the viscous dissipation and heat transfer irreversibility are equal. Once the temperature field is obtained, the rate of the heat transfer on the active walls can be computed through the average Nusselt numbers as follows:

$$Nu = \frac{hH}{k} = -\frac{\partial \theta}{\partial \vec{n}} \qquad \overline{Nu} = \frac{1}{H} \int_0^H \frac{\partial \theta}{\partial X} dY \tag{6-14}$$

As shown in Fig. 6-1, no-slip and impermeable boundary conditions are imposed on the rigid walls for cases A1, A2, A3 and A6 as follows:

$$U = V = 0, \tag{6-15}$$

For the specific case of convection heat transfer (case A6), zero heat flux condition is imposed on the horizontal walls while left and right walls of the cavity are maintained at different constant temperatures:

$$\begin{aligned} &\theta = 1, \ \theta = 0 && \text{On the isothermal vertical walls} \\ &\frac{\partial \theta}{\partial \vec{n}} = 0 && \text{On the insulated walls} \end{aligned} \tag{6-16}$$

6.3 Implementing boundary condition in a Lagrangian framework

In the current study, the combination of the fixed ghost particles and mirror velocity technique suggested by Marrone et al. [73] is used to enforce no-slip boundary conditions on the solid walls. Fig. 6-2 vividly illustrates that in this technique, the solid-fluid interface is used as a reference point to reflect the mirror velocity of the fluid particles (in active zone) on the corresponding ghost particles. However, to enforce the Neumann boundary condition for pressure (p_i) and temperature (θ_i on the adiabatic walls), the value of the target variable is calculated

first on the solid boundary ling using Eq. (6-17), and then the computed results are assigned to the corresponding ghost particles on the other side of the fluid domain.

$$\begin{bmatrix} p_i \\ p_x^{'} \\ p_y^{'} \end{bmatrix} = L \begin{bmatrix} \sum_{j=1}^{N} p_j W_{ij} dV \\ \sum_{j=1}^{N} p_j \nabla W_{ij,x} dV \\ \sum_{j=1}^{N} p_j \nabla W_{ij,y} dV \end{bmatrix} \qquad \begin{bmatrix} \theta_i \\ \theta_x^{'} \\ \theta_y^{'} \end{bmatrix} = L \begin{bmatrix} \sum_{j=1}^{N} \theta_j W_{ij} dV \\ \sum_{j=1}^{N} \theta_j \nabla W_{ij,x} dV \\ \sum_{j=1}^{N} \theta_j \nabla W_{ij,y} dV \end{bmatrix} \tag{6-17}$$

In the above equation, L is the corrective matrix which satisfies first-order derivative completeness condition. W_{ij} and ∇W_{ij} are the kernel function and its derivative which will be discussed in the next section (see also Fig. 6-2 and Eq. (6-A2) in appendix A).

6.4 New kernel function

Motivated by works of Hongbin et al. [49] and Yang et al. [50], [51], in this section a new high-order kernel function is proposed through combination of the Gaussian and polynomial functions as follows:

$$W_{ij} = \alpha_D \begin{cases} e^{\left(\frac{-R^2}{1.125\sqrt{\pi}}\right)} (9 - R^2)^3 & 0 \le R \le 3 \\ 0 & R > 3 \end{cases} \tag{6-18}$$

$$\alpha_{1D} = \frac{0.723176 \times 10^{-3}}{h},\ \alpha_{2D} = \frac{0.38735 \times 10^{-3}}{h^2},\ \alpha_{3D} = \frac{0.210907 \times 10^{-3}}{h^3},$$

where h and $R = \left|\mathbf{r_{ij}}\right| / h$ represents smoothing length and support domain of the kernel function, respectively. Since, Eq. (6-18) doesn't have any analytical integration, Simpson's rule is employed to estimate constant coefficient α_D and satisfy normalization condition ($\sum_{j=1}^{N} W_{ij} dV = 1$) for all three dimensions. The accuracy and stability of the newly constructed kernel function are verified via numerical modeling of one dimensional shock tube problem. The obtained results in terms of the density, energy, velocity and pressure profiles together with the kernel behavior (W_{ij}) and its first derivative (∇W_{ij}) are also compared with two frequently used smoothing kernels (i.e. Cubic spline function [74] and Wendland [75]) and exact solutions.

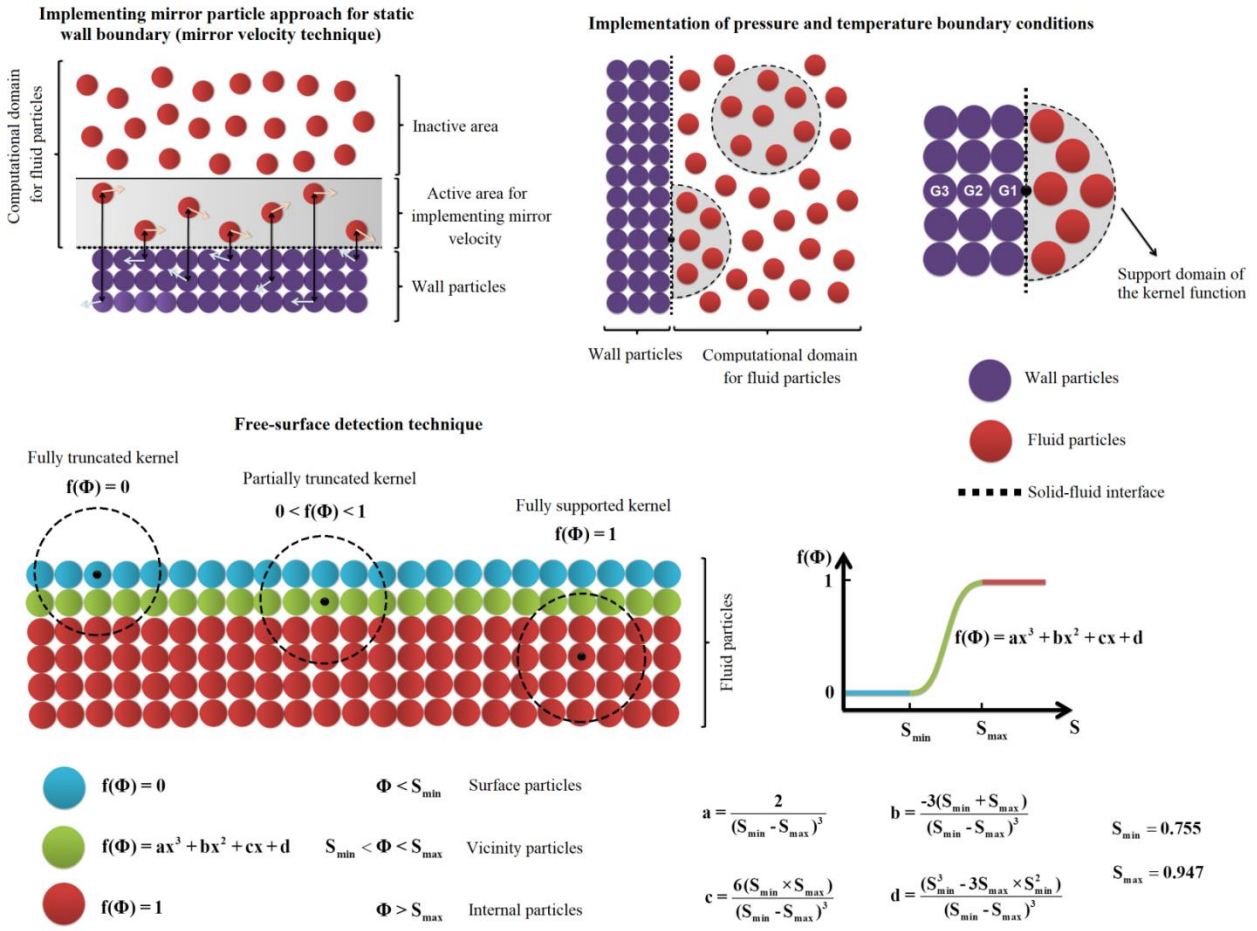

Figure 6-2 Examples of implementing Neumann boundary condition for pressure and temperature, mirror velocity technique and surface particle tracking and related techniques used in the current work.

It can be seen from Fig. 6-3 that, the proposed kernel function is even (*Symmetric property*) and positive (*Positivity*) and declines monotonically as the relative distance (R) increases. Furthermore, due to simultaneous presence of the Gaussian ($Exp(\frac{-R^2}{1.125\sqrt{\pi}})$ and polynomial ($(9-R^2)^3$) terms, it is extremely smooth and has a compact support of $R=3$ even for the third derivative (*Smoothness property*). The new kernel also fulfills the Dirac delta function condition as the smoothing length gets closer to zero (*Delta function property*) [6].

$$\lim_{h\to 0} W_{ij}(r_{ij},h)=\delta \tag{6-19}$$

The obtained results in Fig. 6-3 illustrate that, the proposed kernel function can efficiently delineate two distinct regions of the shock-wave system (i.e. shock ($x=0.3$) and contact ($0.1<x<0.15$) discontinuities) and predict the correct pressure and velocity profiles of the rarefaction wave ($-0.3<x<0$) with minimal fluctuations. It is also evident that, the newly kernel function provides more accurate results than the cubic and Wendland functions in capturing rarefaction wave region and shock position. Fig. 6-3 also reveals that, a very good agreement exist between the calculated results and analytical solutions (for more details see appendix B).

6.5 New Hybrid Free-surface Detection technique (HFD)

As mentioned in the introduction section, Dirichlet pressure condition ($p=0$) must be applied on the free-surface region. This highlights the need of proper identification of the interface position and its vicinity particles. Thus, in this section a new Hybrid Free-surface Detection (HFD) technique is proposed by introducing two additional criteria besides the ones suggested by Koshizuka [55] and Lee et al. [66] as follows:

$$\Phi_1=\sum_{j=1}^{N} W_{ij}\frac{m_j}{\rho_j}, \tag{6-20}$$

$$\Phi_2=\nabla\cdot\mathbf{r}=\sum_{j=1}^{N} x_{ij}\nabla W_{ij,x}\frac{m_j}{\rho_j}+\sum_{j=1}^{N} y_{ij}\nabla W_{ij,y}\frac{m_j}{\rho_j} \tag{6-21}$$

$$\Phi_3=\nabla^2\mathbf{r}=\frac{1}{2}\sum_{j=1}^{N} x_{ij}^2\nabla^2 W_{ij,xx}\frac{m_j}{\rho_j}+\frac{1}{2}\sum_{j=1}^{N} y_{ij}^2\nabla^2 W_{ij,yy}\frac{m_j}{\rho_j} \tag{6-22}$$

$$\Phi_4=\sum_{j=1}^{N} x_{ij}y_{ij}\nabla^2 W_{ij,xy}\frac{m_j}{\rho_j} \tag{6-23}$$

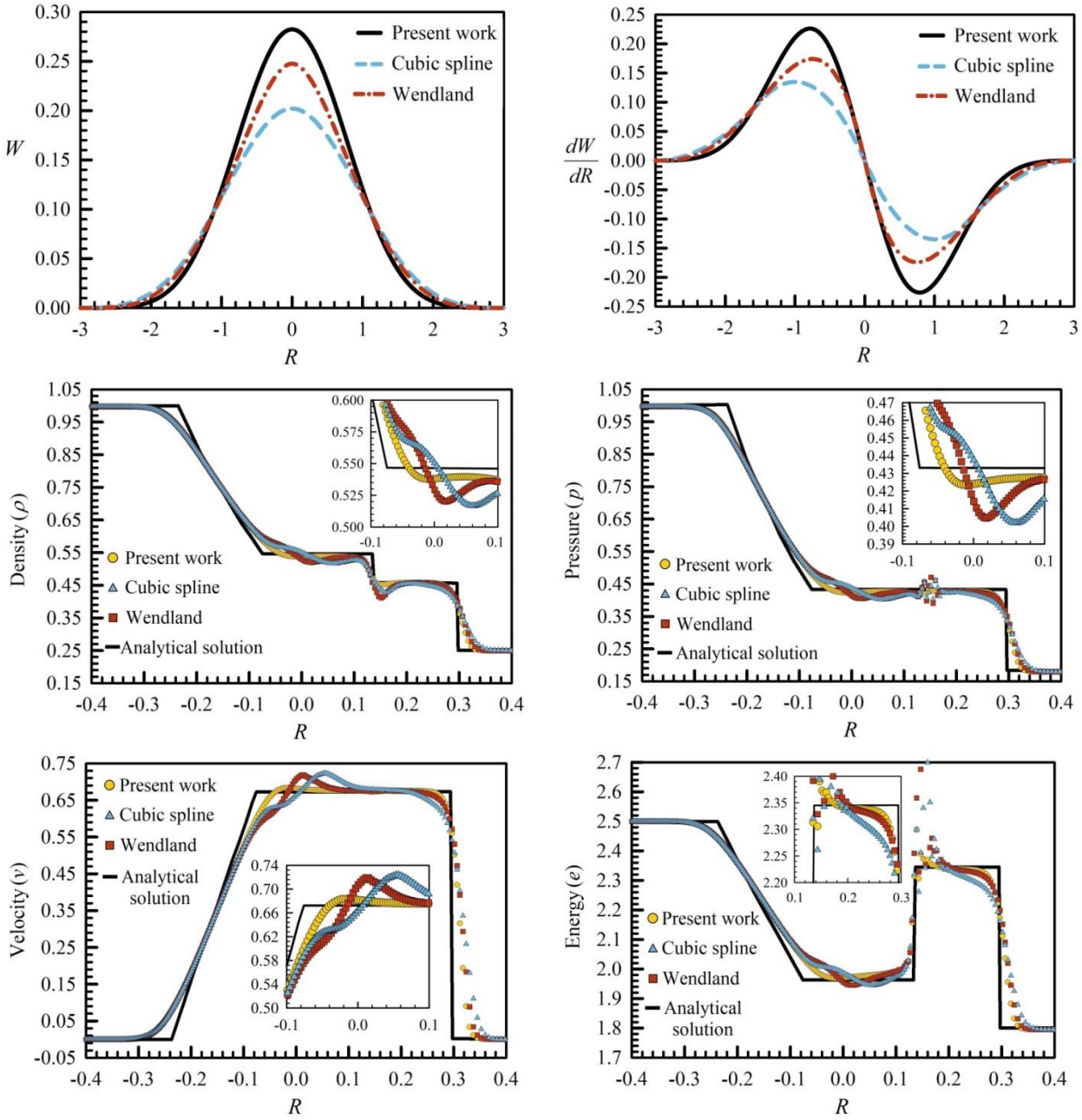

Figure 6-3 The effects of the type of kernel function on the spatial evolution of density, pressure, velocity and energy profiles for the Sod shock tube problem at t=0.2s.

The variables Φ_1 and Φ_2 are known as a Particle Number Density (PND) [55] and divergence of particle displacement [66] while Φ_3 and Φ_4 are two new complementary conditions which can be simply referred to as Laplacian of particle displacement and mixed partial derivative of kernel

function, respectively. Ideally, in the case of fully supported kernel, the values of Φ_1, Φ_2, Φ_3 and Φ_4 are equal to unity, 2, 2 and unity. Any deviation from the aforementioned characteristic values indicates that the kernel function may be truncated and consequently the candidate particle belongs to surface area. By defining the threshold values of $S_{\min} = 0.755$ and $S_{\max} = 0.947$, the fluid domain can be segregated into three distinct zones as:

$$\overline{\Phi} = (\Phi_1 + \Phi_2 + \Phi_3 + \Phi_4)/6, \tag{6-24}$$

$$f(\overline{\Phi}) = \begin{cases} 0 & \overline{\Phi} \le S_{\min} \quad \text{Free-surface particle} \\ ax^3 + bx^2 + cx + d & S_{\min} < \overline{\Phi} < S_{\max} \quad \text{Vicinity particles} \\ 1 & \overline{\Phi} \ge S_{\max} \quad \text{Internal particles} \end{cases} \tag{6-25}$$

$$a = \frac{2}{(S_{\min} - S_{\max})^3},\ b = \frac{-3(S_{\min} + S_{\max})}{(S_{\min} - S_{\max})^3},$$
$$c = \frac{6(S_{\min} \times S_{\max})}{(S_{\min} - S_{\max})^3}, d = \frac{S_{\min}^3 - 3S_{\max} \times S_{\min}^2}{(S_{\min} - S_{\max})^3} \tag{6-26}$$

It should be noted that, the cubic polynomial function in Eq. (6-25) is used to remove the discontinuity between free-surface ($f(\overline{\Phi}) = 0$) and internal ($f(\overline{\Phi}) = 1$) particles (see also Fig. 6-2).

6.6 New Hybrid Particle Shifting Technique (HPST)

Inspired by works of Skillen et al. [44], Lee et al. [58] and Shakibaeinia et al. [61], a novel hybrid particle regularization scheme is proposed by combining Particle Shifting Technique and a pairwise collision model. In this technique, PST is applied only to the interior particles whereas collision model is used for treatment of the interface and its nearby particles. A more detailed mathematical description of present model is given in appendix C. As mentioned in previous section, prior to implementing HPST, the robust and efficient particle labeling scheme (free-surface detection technique) is needed to determine the role of each particle (i.e. inner, vicinity or surface particle). Given the assumption that this technique has been accomplished, the process of implementing HPST can be summarized as follows:

$$\delta r_{i,x,PST} = \frac{-\beta}{\lambda} \sum_{j=1}^{N} x_{ij} W_{ij} \frac{m_j}{\rho_j}$$

$$\delta r_{i,y,PST} = \frac{-\beta}{\lambda} \sum_{j=1}^{N} y_{ij} W_{ij} \frac{m_j}{\rho_j}$$

$$\lambda = \frac{1}{2} \sum_{j=1}^{N} r_{ij}^2 W_{ij} \frac{m_j}{\rho_j} \qquad (6\text{-}27)$$

$$\beta = 0.5 \alpha h^2$$

$$\mathbf{r}_i^{(n+1)*} = \mathbf{r}_i^{(n+1)} + \delta \mathbf{r}_{i,PST}^{(n+1)}$$

In the current work, the value of α is taken as 0.1. The variable *h* is the smoothing length in kernel function (Eq. (6-18)) which is equal to the initial particle spacing ($h = 1.0\Delta x = 1.0\Delta y$). As mentioned in appendix C, Lambda (λ) is the constant coefficient which should be computed at the initial arrangement of particles (*t*=0) where kernel has a fully compact support. Eq. (6-27) is applied only to the inner particles. Therefore, the interface and vicinity particles still require a re-arrangement technique to avoid clustering and tensile stability. In the proposed technique, this is accomplished by applying a pairwise collision technique, adapted from the Discrete Element Method (DEM) that displaces the interface and vicinity particles as:

$$\delta r_{i,x,DEM} = (dt)^2 \, f_{i,x} / m_i$$

$$\delta r_{i,y,DEM} = (dt)^2 \, f_{i,y} / m_i$$

$$f_{i,x} = -\sum_{j=1}^{N} k_n \delta_{x,ij} \qquad (6\text{-}28)$$

$$f_{i,y} = -\sum_{j=1}^{N} k_n \delta_{y,ij}$$

$$\mathbf{r}_{i,t}^{(n+1)*} = \mathbf{r}_i^{(n+1)} + \delta \mathbf{r}_{i,DEM}^{(n+1)}$$

where $\mathbf{r}_i^{(n+1)*}$ is the new position of the particle after applying the HPST. δ_{ij} is the corresponding overlap of two particles. k_n denotes stiffness coefficient in normal direction which is taken as $5 \times 10^4 \, Kg \, ms^{-2}$. It should be noted that, unlike the classical DEM formulations [76], in order to preserve the global conservation of momentum and kinetic energy, the collision force in the

current work ($f_{i,x}$, $f_{i,y}$) is directly applied to particle position ($\delta r_{i,x,DEM}$ and $\delta r_{i,y,DEM}$) instead of particle velocity. Finally, it is worth to mention that, although in the current work, the DEM is only applied on the free-surface area but our experience shows that, the DEM model ($\delta \mathbf{r}_{i,DEM}$) can also be used for both interior and surface areas in conjunction with particle shifting technique ($\delta \mathbf{r}_{i,PST}$). However, implementing it on the interior particles will impose the stiff/strict condition on the motion of particles especially in the multiphase flow problems where the primary phase should has a chance to move freely within the secondary phase (the best example is the splashing and the falling of the water particles into the air phase generated by the breaking of a dam).

6.7 Discretization of governing equations and solution algorithm

The ISPH discretization of the governing equations over a set of mobile particles is conducted by high-order differential gradient, divergence and Laplacian operators. The combination of the third-order TVD Runge-Kutta scheme [77] and two-step projection model [78] is utilized to handle transient terms and velocity-pressure coupling. The first calculation step is an explicit prediction one where an intermediate velocity field is calculated through Navier-Stokes equations without the pressure gradient as:

$$\mathbf{u}^* = \mathbf{u}^n + (\upsilon \nabla^2 \mathbf{u}^n + \mathbf{F}_B / \rho)\Delta t \tag{6-29}$$

The second step is an implicit correction one where pressure is computed by solving the Poisson equation as:

$$\nabla^2 p^1 = \frac{\rho^* \nabla \cdot \mathbf{u}^*}{\Delta t} \tag{6-30}$$

Once the PPE is solved, the material derivatives of velocity ($D\mathbf{u}/Dt$) and energy (DT/Dt) can be determined through Eqs. (6-2) to (6-4) as follows:

$$\frac{D\mathbf{u}^n}{Dt} = -\frac{\nabla p^1}{\rho} + \frac{\mu}{\rho}\nabla^2 \mathbf{u}^n + \frac{\mathbf{F}_B}{\rho} \tag{6-31}$$

$$\frac{DT^n}{Dt} = \frac{k}{\rho C_p}\nabla^2 T^n \tag{6-32}$$

After solving equations (6-31) and (6-32), the velocity ($\mathbf{u}^{(1)}$), position ($\mathbf{r}^{(1)}$) and temperature ($\theta^{(1)}$) of each particle can be determined through the first step of the Runge-Kutta scheme as:

$$\begin{aligned}\mathbf{u}^{(1)} &= \mathbf{u}^{(n)} + \Delta t \frac{D\mathbf{u}^{(n)}}{Dt} \\ \mathbf{r}^{(1)} &= \mathbf{r}^{(n)} + \Delta t\, \mathbf{u}^{(1)} \\ \theta^{(1)} &= \theta^{(n)} + \Delta t \frac{D\theta^{(n)}}{Dt}\end{aligned} \tag{6-33}$$

By repeating the above process with updated values of $\mathbf{u}^{(1)}$, $\mathbf{r}^{(1)}$ and $\theta^{(1)}$ (instead of $\mathbf{u}^{n}$, $\mathbf{r}^{n}$ and θ^{n}), the second step of the Runge-Kutta method can be written as:

$$\begin{aligned}\mathbf{u}^{(2)} &= \frac{3}{4}\mathbf{u}^{(n)} + \frac{1}{4}\mathbf{u}^{(1)} + \frac{1}{4}\Delta t \frac{D\mathbf{u}^{(1)}}{Dt} \\ \mathbf{r}^{(2)} &= \frac{3}{4}\mathbf{r}^{(n)} + \frac{1}{4}\mathbf{r}^{(1)} + \frac{1}{4}\Delta t\, \mathbf{u}^{(2)} \\ \theta^{(2)} &= \frac{3}{4}\theta^{(n)} + \frac{1}{4}\theta^{(1)} + \frac{1}{4}\Delta t \frac{D\theta^{(1)}}{Dt}\end{aligned} \tag{6-34}$$

The last stage of the Runge-Kutta method can be obtained by replacing new data $\mathbf{u}^{(2)}$, $\mathbf{r}^{(2)}$ and $\theta^{(2)}$ with old ones ($\mathbf{u}^{(1)}$, $\mathbf{r}^{(1)}$ and $\theta^{(1)}$) as follows:

$$\begin{aligned}\mathbf{u}^{(n+1)} &= \frac{1}{3}\mathbf{u}^{(n)} + \frac{2}{3}\mathbf{u}^{(2)} + \frac{2}{3}\Delta t \frac{D\mathbf{u}^{(2)}}{Dt} \\ \mathbf{r}^{(n+1)} &= \frac{1}{3}\mathbf{r}^{(n)} + \frac{2}{3}\mathbf{r}^{(2)} + \frac{2}{3}\Delta t\, \mathbf{u}^{(n+1)} \\ \theta^{(n+1)} &= \frac{1}{3}\theta^{(n)} + \frac{2}{3}\theta^{(2)} + \frac{2}{3}\Delta t \frac{D\theta^{(2)}}{Dt}\end{aligned} \tag{6-35}$$

where $\mathbf{r}^{(n+1)}$, $\mathbf{u}^{(n+1)}$ and $\theta^{(n+1)}$ are new position, velocity and temperature of the particles at (*n+1*)-*th* time step. As mentioned before, particles in Lagrangian description have a natural tendency to cluster along the streamline trajectory. Thus, to reduce the error generated by tensile-instability and alleviate unfavorable effects of particle clustering, the proposed Hybrid Particle Shifting Technique is applied to underlying position of particles as follows (see also section 6):

$$\begin{aligned}\mathbf{r}_i^{(n+1)*} &= \mathbf{r}_i^{(n+1)} + \delta\mathbf{r}_{i,PST}^{(n+1)} \quad \text{for inner particles} \\ \mathbf{r}_{i,t}^{(n+1)*} &= \mathbf{r}_i^{(n+1)} + \delta\mathbf{r}_{i,DEM}^{(n+1)} \quad \text{for surface and vicinity particles}\end{aligned} \tag{6-36}$$

At the end of the process, the average Nusselt number and entropy generation due to both factors (S_T and S_F) can be calculated through Eqs. (6-10) to (6-14) particularly for case A6.

Table 6.1 List of the equations used for estimating gradient, divergence, and Laplacian operators.

Operator	Equation used
Divergence (for velocity) ($\mathbf{u}_x^{'}, \mathbf{u}_y^{'}$) Gradient (for temperature) ($\theta_x^{'}, \theta_y^{'}$)	Eq. (6-A6) is implemented in the present study whereas Eq. (6-A3) or Eq. (6-A5) can also be used.
Gradient (for pressure) ($p_x^{'}, p_y^{'}$)	Revised form of the Eq. (6-A6) is applied in the current work where $\chi = 1$ and $\chi = -1$ are used for inner and surface particles, respectively. (see also Eq. (6-37))
Hybrid Particle Shifting Technique (HPST)	Eq. (6-27) is applied on the inner particles while Eq. (6-28) is used for surface and its nearby particles (see also appendix C).
Kernel function	Eq. (6-18) is used for all simulations (cases A1 to A6)
Hybrid Free-surface Detection technique (HFD)	Eqs. (6-20) to (6-26) are used for particle-labeling process
Buoyancy force in natural convection (θ_i) Density smoothing process in Rayleigh Taylor instability ($\rho_{\text{interface}}$)	Eq. (6-A2) is used to calculate field functions (θ_i and $\rho_{\text{interface}}$).
Pressure on the solid walls (p_i) Temperature on the insulated walls (θ_i)	Eq. (6-A2) is applied to calculate field functions on the solid walls (p_i and θ_i)
Laplacian (for pressure $\nabla^2 P$ and diffusion $\nabla^2\mathbf{u}, \nabla^2\theta$)	Eq. (6-A12) is applied in the present work whereas Eqs. (6-A13), (6-A14) or (6-A15) can also be used.

Note that, the proposed high-order Laplacian operator (Eq. (6-A12)) has been used to calculate diffusion terms ($\nabla^2\mathbf{u}, \nabla^2 T$) and PPE ($\nabla^2 p$) while Eq. (6-A6) is employed to estimate temperature gradient ($\nabla T, \nabla\theta$), velocity gradient ($\partial u/\partial x, \partial v/\partial y$) and divergence of velocity

components ($\nabla\cdot\mathbf{u}$). Moreover, Eq. (6-A2) is applied as a high-order *smoothing operator* to calculate temperature (T) in the buoyancy force ($F_b=-\rho g\,\beta(T-T_c)$) and density of the interface ($\rho_{\text{interface}}$) in transient natural-convection and Rayleigh-Taylor instability problems, respectively. However, to calculate pressure gradient (∇p), a multi-technique approach should be adopted to handle both interior and interface particles. For this purpose, Eq. (6-A6) is modified according to *Tensile Instability Control* (TIC) suggested by Sun et al. [37], [48] as follows:

$$\begin{bmatrix}\frac{\partial p}{\partial x}\\ \frac{\partial p}{\partial y}\end{bmatrix}=L\begin{bmatrix}\sum_{j=1}^{N}\frac{(p_j-\chi p_i)}{r_{ij}^2}\nabla W_{ij,x}dV\\ \sum_{j=1}^{N}\frac{(p_j-\chi p_i)}{r_{ij}^2}\nabla W_{ij,y}dV\end{bmatrix}\qquad L=\begin{bmatrix}\sum_{j=1}^{N}\frac{x_{ij}\nabla W_{ij,x}}{r_{ij}^2}dV & \sum_{j=1}^{N}\frac{y_{ij}\nabla W_{ij,x}}{r_{ij}^2}dV\\ \sum_{j=1}^{N}\frac{x_{ij}\nabla W_{ij,y}}{r_{ij}^2}dV & \sum_{j=1}^{N}\frac{y_{ij}\nabla W_{ij,y}}{r_{ij}^2}dV\end{bmatrix}^{-1}\tag{6-37}$$

χ is an integer valued parameter which varies between 1 and -1 for internal and interface particles, respectively. More precisely, in order to prevent the inception of the tensile-instability, the non-conservative form ($\chi=-1$) of the momentum equation (p_j+p_i) is used for the free-surface area and its nearby particles whereas the conservative one ($\chi=1$) is applied on the interior particles (p_j-p_i). In fact, Eq. (6-37) takes the advantages of both first-order consistency and linear momentum conservation. Hereafter, Eq. (6-37) will be referred to as a *Modified Pressure Gradient* operator (MPG). The summary of equations used in the current work is provided in table 6-1.

6.8 Results and discussion

The applicability and robustness of newly proposed kernel function, Hybrid Particle Shifting Technique (HPST), free-surface detection technique together with high-order governing operators are demonstrated here through simulation of wide variety of challenging benchmark cases including: dam break with/without an obstacle (cases A1 and A2), Rayleigh-Taylor instability (cases A3), rotation of square patch of fluid (case A4), stretching circular water drop (case A5) and entropy generation due to natural convection heat transfer. In all the simulations, the value of smoothing length in the kernel function (Eq. (6-18)) is equal to initial particle size ($h=\Delta x=\Delta y$). The time step (Δt) is governed based on two stability criteria (diffusion condition and maximum velocity of fluid flow) as:

$$\Delta t_{convection} = CFL \frac{\Delta x}{|\mathbf{u}_{\max}|}$$

$$\Delta t_{viscous} = CFL \frac{\Delta x^2}{2\nu} \tag{6-38}$$

$$\Delta t = \min(\Delta t_{convection}, \Delta t_{viscous})$$

In the current work, minimum and maximum values of Courant number are taken as $\mathrm{CFL}_{\min} = 0.05$ and $\mathrm{CFL}_{\max} = 0.15$ for cases A1 and A6, respectively. The simulations have been carried out using, an in-house CFD code written in the Intel® Visual FORTRAN Compiler.

6.8.1 Dam break with and without obstacle (Cases A1 and A2)

Numerical simulation of classical dam break with/without an obstacle are presented in this subsection to demonstrate superiority of the proposed models over the conventional SPH method in handling violent free-surface flows involving high-pressure shock wave generated by impact. The model set-up for 2D dam break (case A1) is shown in Fig. 6-1 where a rectangular water column ($H = 0.5m, W = 0.25m, \rho = 10^3 Kg\, m^{-3}$, $\mu = 10^{-3} Kg\, m^{-1} s^{-1}$) is initially confined in the left half of the square reservoir ($D = 1m$). In general, once the virtual gate is removed, the gravitational force causes the water column to collapse and flow out along a rigid horizontal plane with low level of kinetic energy. Fig. 6-4 shows that as the time proceeds, the generated surface wave propagates along the deck while its kinetic energy enhances. The velocity of water front toe progressively enhances until the flow front reaches the vertical wall, producing a great impact pressure and vigorous vertical water jet adjacent to the downstream wall. The impact of the water front against the vertical wall at $t^* = t(g/H)^{0.5} = 1.54$ is also accompanied by irreversible destruction of kinetic energy and formation of the first pressure shock ($P^* = p/\rho gH = 2.35$) as recorded by sensor 2 ($h_2 = 0.025m$).

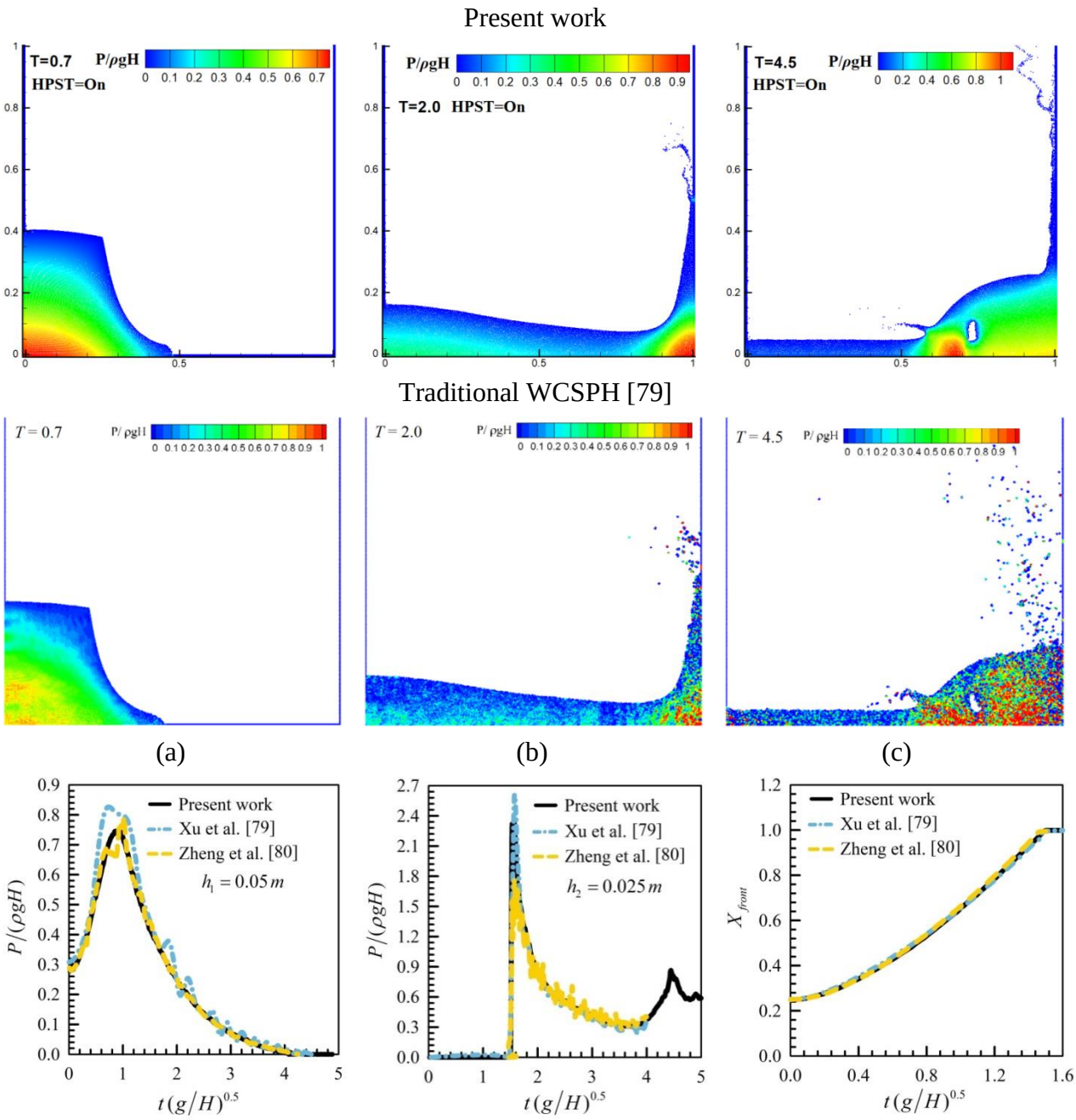

Figure 6-4 Qualitative and quantitative comparison between calculated results and those reported by Xu et al. [79] and Zheng et al. [80] for case A1. Time history of pressure variations on the left (a) and right (b) walls. Time history of water front toe represented by X_{front}. $N_p = 17672$.

It can be seen that after impinging water tongue onto the right wall, due to the presence of inertia force, the fluid deviates upward and reaches the maximum position at $t(g/H)^{0.5} = 3.1$. However, after $3.1 < t^*$ because of restoring action of gravity force, the fluid acceleration reduces and subsequently thickness of the ascending water jet increases, which indicates that the adverse pressure gradient is coming into the picture.

As time goes on, the intensity of inertia force gradually weakens and motion of the upward-moving jet slows down. Finally, the water jet overturns back as a plunging wave onto the underlying wet bed, leading to the formation of second impact pressure and sudden rise in pressure time history ($P^* = 0.95,\ t^* = 4.44$). It is interesting to note that during the above run up/run down cycle, the quasi-hydrostatic pressure region is developed on the bottom-right corner of the enclosure where flow is nearly stagnant and characterized by quasi-static and shock loading. In contrast, the right and bottom walls experience dynamic shock pressures, due to the development of up-going and down-going waves (for more details see animation 1 in the supplementary material). As shown in Fig. 6-4, the proposed models provide more accurate results in terms of the smoother pressure field (noise-free pressures) and less splashing rate compared to the original SPH model used by Xu et al. [79] and Zheng et al. [80]. It is worth to mention that, the experimental measurements for this canonical test case are also available in the literature which can be used for further validation of the current work [55], [81].

To provide deeper insight into the effectiveness of proposed Hybrid Particle Shifting Technique (HPST) and free-surface detection scheme, contours of the pressure field with associated close-up snapshots are provided in Fig. 6-5. It can be seen from Fig. 6-5 (a) that, when the HPST is active (HPST=On), particles are uniformly arranged without any noticeable unphysical particle overlapping, spurious interface fragmentation and water spray, leading to the smoother pressure field across the whole computational domain. However, as mentioned before, in the absence of HPST (HPST=Off), particles start to cluster along the streamline, resulting in the rapid emergence of void space and density error accumulation. The effects of this event can be clearly seen in Fig. 6-5(b) where destructive effects of particle clumping caused by high-pressure gradients lead to the spurious pressure fluctuations and non-physical water spray during the flow evolution.

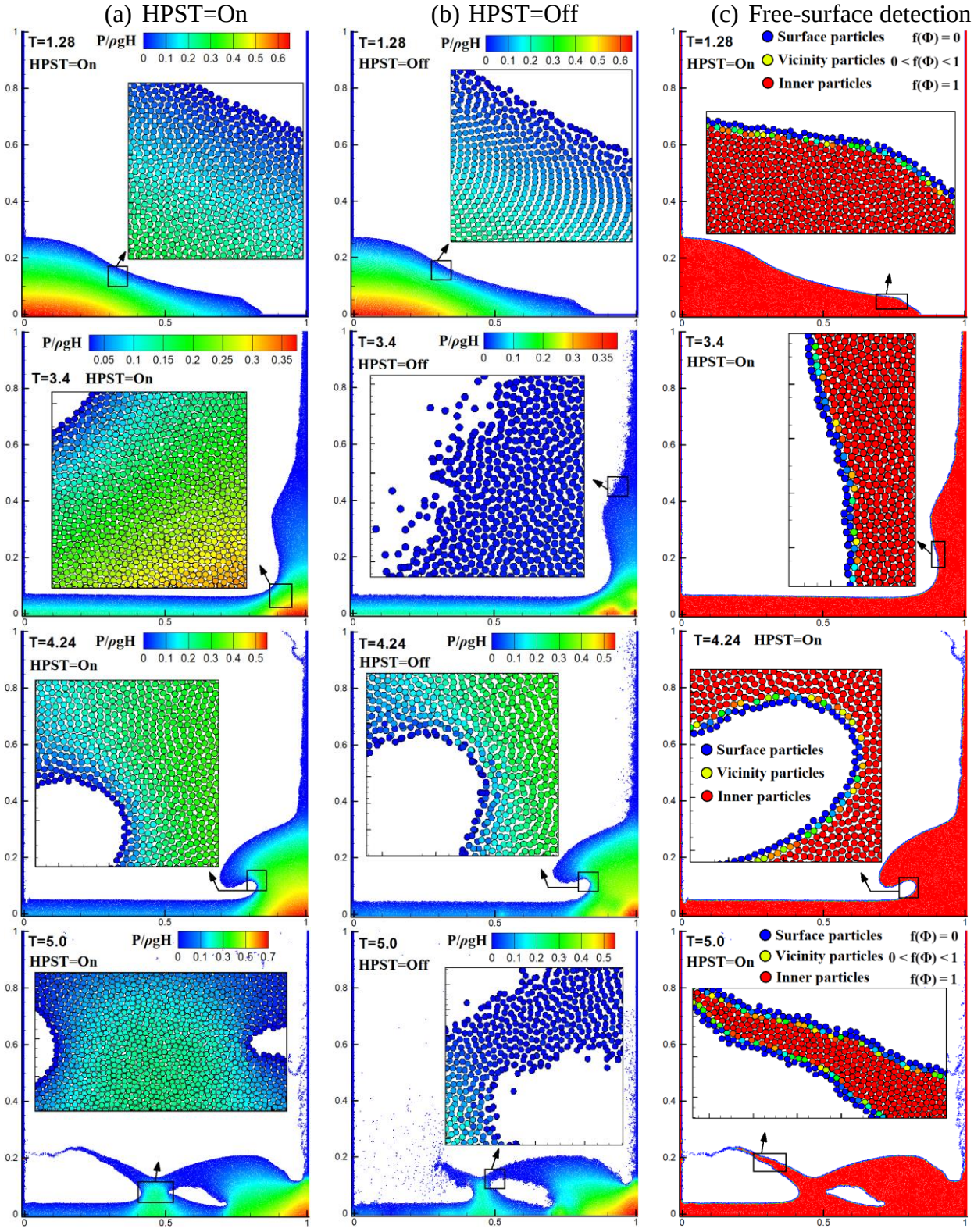

Figure 6-5 (a) and (b) the effects of the PST on the pressure field. (c) Contours of the free-surface area for case A1.

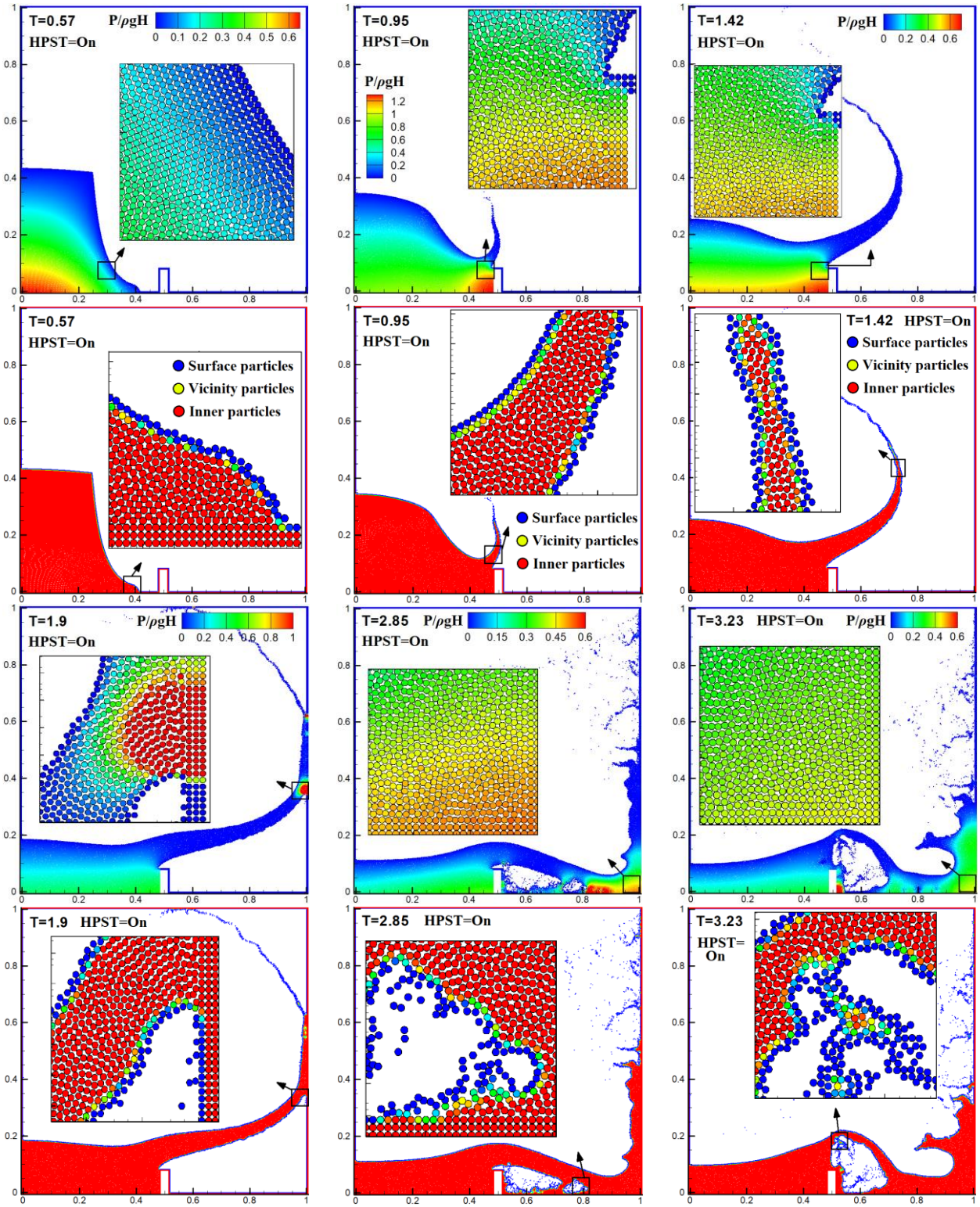

Figure 6-6 Contour maps of pressure field and surface particles detection for case A2 at different time instants.

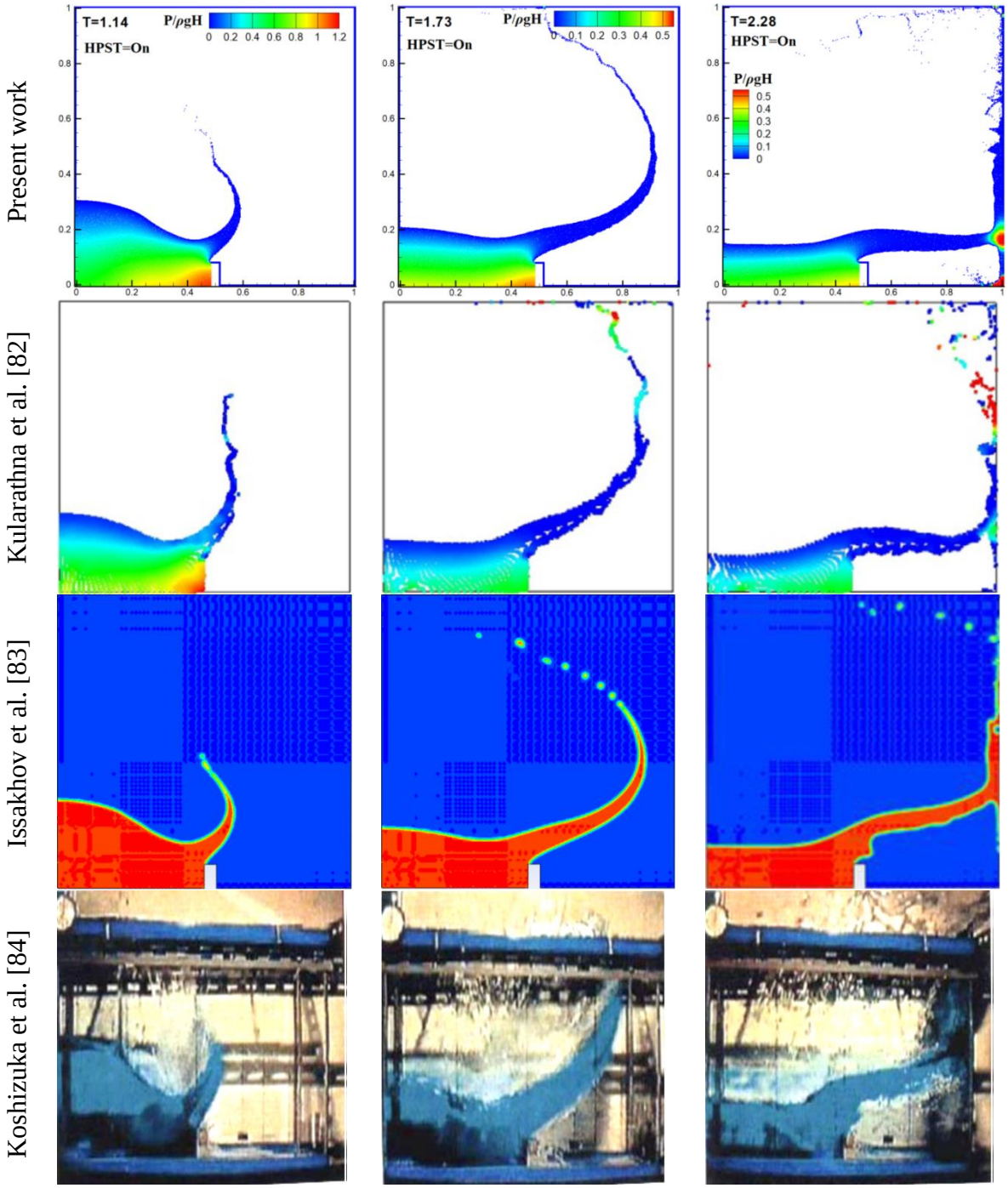

Figure 6-7 Qualitative comparison of the predicted results with numerical and experimental data of Kularathna et al. [82] (MPM model), Issakhov et al. [83] (VOF model) and Koshizuka et al. [84] for case A2. $N_p = 22155$.

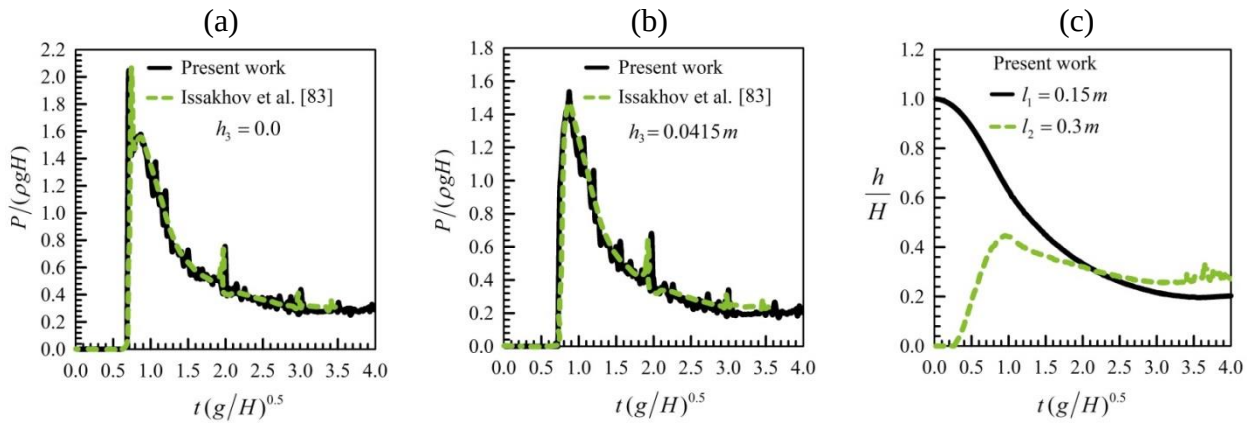

Figure 6-8 Quantitative comparison of the predicted results with numerical data of Issakhov et al. [83] (VOF model) for case A2. (a) pressure variations on the left-bottom corner of the obstacle, (b) pressure variations on the middle-left side of the obstacle, (c) variations of water level height at two different sections ($l_1 = 0.15m$, $l_2 = 0.3m$). $N_p = 22155$ $\mathbf{g} = 9.81 m\,s^{-2}$, $\rho = 997\,kg\,m^{-3}$, $\mu = 855\times10^{-6}\ N\cdot sm^{-2}$.

Furthermore, Fig. 6-5 (c) reveals that for the case of HPST=On, the proposed free-surface tracking scheme can correctly determine the position of the interface (blue color) and its nearby particles (colorful particles) without any misidentification in the particle labeling process. The transient evolution of the breaking dam in the presence of an obstacle (case A2) is plotted in Figs. 6-6 to 6-8 where a rectangular water column ($H = 0.5m, W = 0.25m$) is installed in the left part of the square tank ($D = 1m$). Qualitatively, short-term dynamics and morphological peculiarities of dam break with an obstacle are very similar to the former case where conversion of potential energy into kinetic energy takes place primarily when the virtual gate is eliminated. It can be seen that the water column descends downward under the gravity force and travels horizontally along the dry bed. However due to presence of the stationary obstacle in middle portion of the bottom wall ($W_2 = 0.041m, W_3 = 0.082m$), the fluid flow changes its direction and moves vertically along the left side of the obstacle. In fact, due to barrier effects of obstacle and abrupt change in flow direction, the first pressure peak occurs on the left side of the block where sensors 1 ($h_3 = 0, t^* = 0.70$ and $p^* = 2.04$) and 2 ($h_3 = 0.041, t^* = 0.85$ and $p^* = 1.62$) are located. The rest of the fluid which escapes from the shock region travels slantwise in form of the water jetpack

until it hits the downstream vertical wall where the second wave impact and splash-up scenario occur. Despite the geometrical complexity of this physical model, it can be seen that hydrodynamics characteristics of flying jet are well predicted by proposed models and the obtained results are in good agreement with numerical and experimental data of Kularathna et al. [82], Issakhov et al. [83] and Koshizuka et al. [84].

6.8.2 Rayleigh-Taylor instability (Cases A3)

The versatility and robustness of the proposed models in handling moving interface problem with large deformation and stretching are demonstrated by simulating the Rayleigh-Taylor instability problem where Eq. (6-A2) is employed to circumvent discontinuities in the physical parameters at the interface.

$$\begin{bmatrix} \rho_s \\ \rho'_{s,x} \\ \rho'_{s,y} \end{bmatrix} = L \begin{bmatrix} \sum_{j=1}^{N} \rho_j W_{ij} dV \\ \sum_{j=1}^{N} \rho_j \nabla W_{ij,x} dV \\ \sum_{j=1}^{N} \rho_j \nabla W_{ij,y} dV \end{bmatrix} \qquad \begin{bmatrix} \mu_s \\ \mu'_{s,x} \\ \mu'_{s,y} \end{bmatrix} = L \begin{bmatrix} \sum_{j=1}^{N} \mu_j W_{ij} dV \\ \sum_{j=1}^{N} \mu_j \nabla W_{ij,x} dV \\ \sum_{j=1}^{N} \mu_j \nabla W_{ij,y} dV \end{bmatrix} \tag{6-39}$$

In the above equation, ρ_s and μ_s are smoothed density and viscosity, respectively. As illustrated in Fig. 6-1, the simulation is carried out in a rectangular enclosure with dimensions of $H \times 2H$ where two immiscible fluids ($\rho_H = 1.8$, $\rho_L = 1$) are separated by an initial interface perturbation located at $y = 1 - 0.15 \times \sin(2\pi x)$. The instability is characterized by the Atwood number ($At = (\rho_H - \rho_L)/(\rho_H + \rho_L)$) equals to $2/7$ which represents the density ratio between two different fluids. The Reynolds number is defined as $\mathrm{Re} = H\sqrt{Hg}/\upsilon$ where $H = 1$, $\mathbf{g} = 17.64$, and $\upsilon_H = \upsilon_L = 0.01$ denote the characteristic length (width of the enclosure), gravity acceleration and kinematic viscosity, respectively. The computational domain is discretized over a set of the uniform particle ($N_p = 250 \times 500$) and obtained results are depicted in Figs. 6-9 and 6-10 at different time instants. In general, the evolution of RTI can be divided into three distinct stages namely: linear, weakly non-linear and fully non-linear stages.

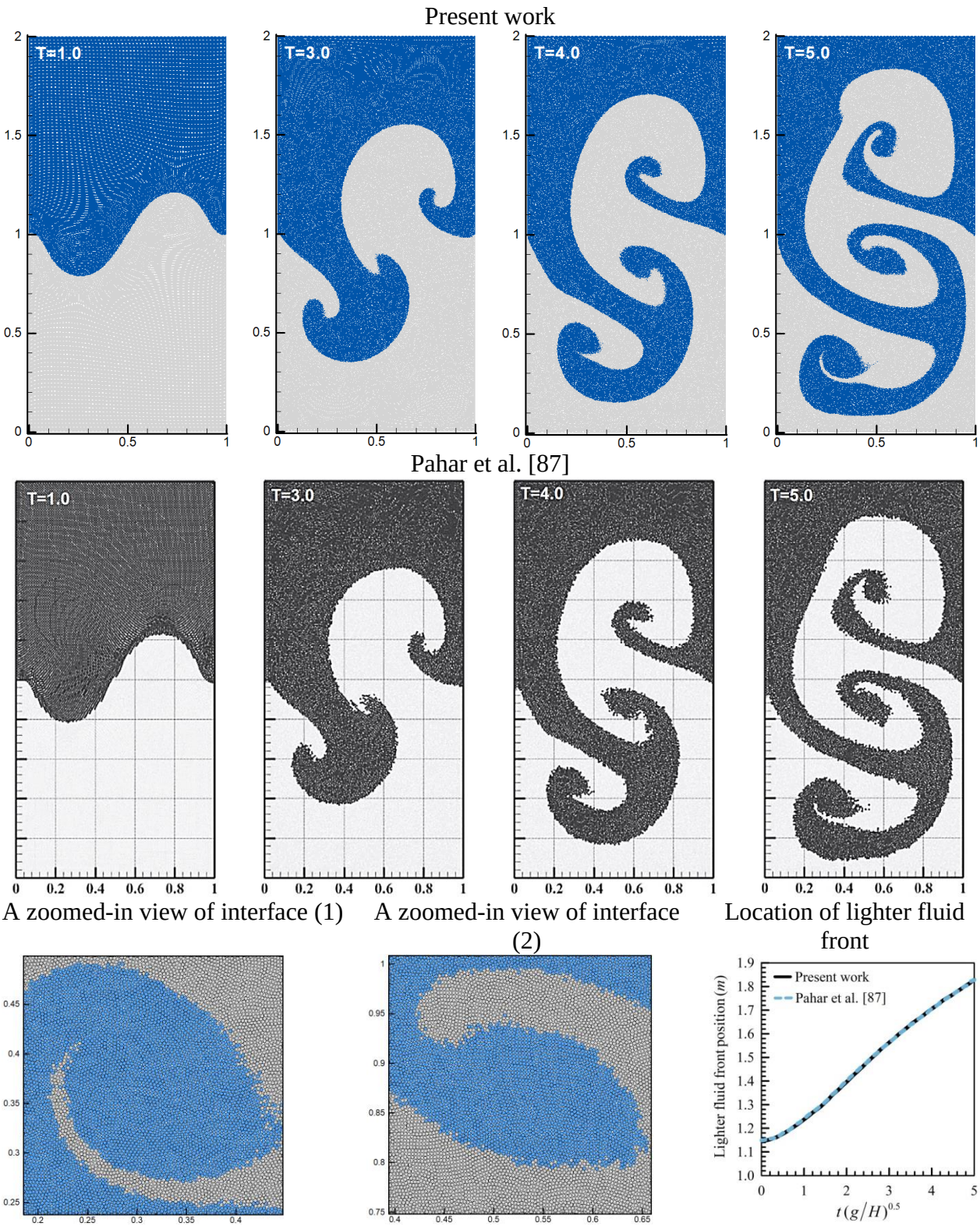

Figure 6-9 Comparisons of the predicted results with numerical data of Pahar et al. [87] for Rayleigh–Taylor instability problem (case A3).

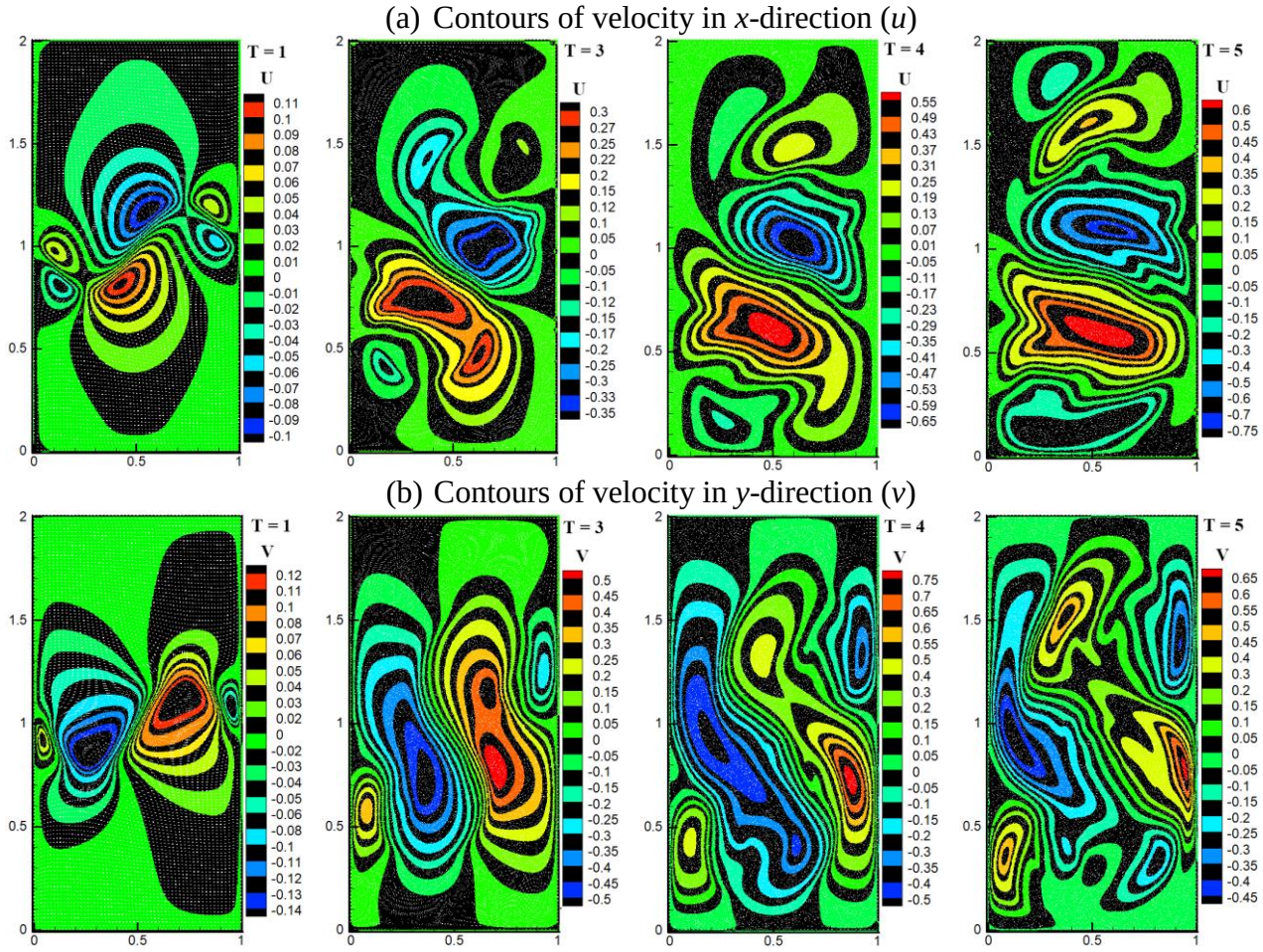

Figure 6-10 Non-dimensional velocity contours in the x and y-directions ($\mathbf{U} = \mathbf{u}/(\mathbf{g}H)^{0.5}$) for Rayleigh-Taylor instability problem at various non-dimensional time.

During the first stage of development, the buoyant force induced by density gradient across the interface causes the denser fluid to move downward along the left wall while the relatively lighter fluid rises up, leading to the formation of the clockwise vortex at the center of the enclosure. It is evident from Figs. 6-9 and 6-10 that until T= 1, the amplitudes of the interface wave and velocity components in the x and y-directions are almost symmetrical with respect to the center of the enclosure which indicates that the Rayleigh-Taylor instability (RTI) development follows the linear theory [85], [86]. However, as time progressed ($1 \le T \le 3$), intensity of recirculating flow enhances and consequently the RTI development enters into the semi-nonlinear growth stage. In this circumstance, the flow pattern starts to deviate from its symmetrical state and subsequently a

pair of asymmetric mushroom-shaped structure in form of the descending spike and ascending bubble is generated within the enclosure (T=3). This trend persists and even accelerates in the last stage where the shear force causes the interface to roll-up/down, producing some secondary vortexes within the enclosure (see also Fig. 6-10). Inspection of Fig. 6-9 reveals that, the calculated results are qualitatively and quantitatively in an excellent agreement with numerical data of Pahar et al. [87]. Finally, the smoothness of the interface and uniformity of particle distribution in the zoomed-in views in Fig. 6-9 clearly demonstrate the robustness and potential capability of the proposed algorithm in modeling multiphase problems involving large deformations and physical discontinuities.

6.8.3 Rotation of a square patch of fluid and stretching circular water drop (Cases A4 and A5)

The effectiveness and performance of the newly proposed Hybrid Particle Shifting Technique (HPST) are highlighted in this section through modeling of rotating square patch of fluid (case A4) and stretching circular liquid drop (case A5) where due to unfavorable effects of concomitant negative pressure gradient and high velocity field, particle bunching and void formation are inevitable. As sketched in Fig. 6-1, case A4 consists of a weightless square patch of water ($\mathbf{g}=0$) subjected to the following clockwise-rotating eddy:

$$\begin{aligned} u_0(x,y) &= +y\,\omega \qquad -L/2 \le y \le L/2 \\ v_0(x,y) &= -x\omega \qquad -L/2 \le x \le L/2 \\ p_0(x,y) &= 0 \end{aligned} \tag{6-40}$$

where $\omega = 1\,s^{-1}$ and $L = 1$ denote angular velocity and length of the square patch, respectively. In general, hydrodynamic behavior of rotating square patch of fluid is characterized by the formation of the negative pressure field and severe particle migration towards the core region of the vortex. This mechanism leads to large free boundary deformations and substantial accumulation of particles in the vortex core which are responsible for onset and progression of tensile instability problem. More precisely, during the earliest stages of growth, the centrifugal force causes the middle parts to drag towards the center of the vortex while patch corners propagate radially outward to satisfy local mass continuity.

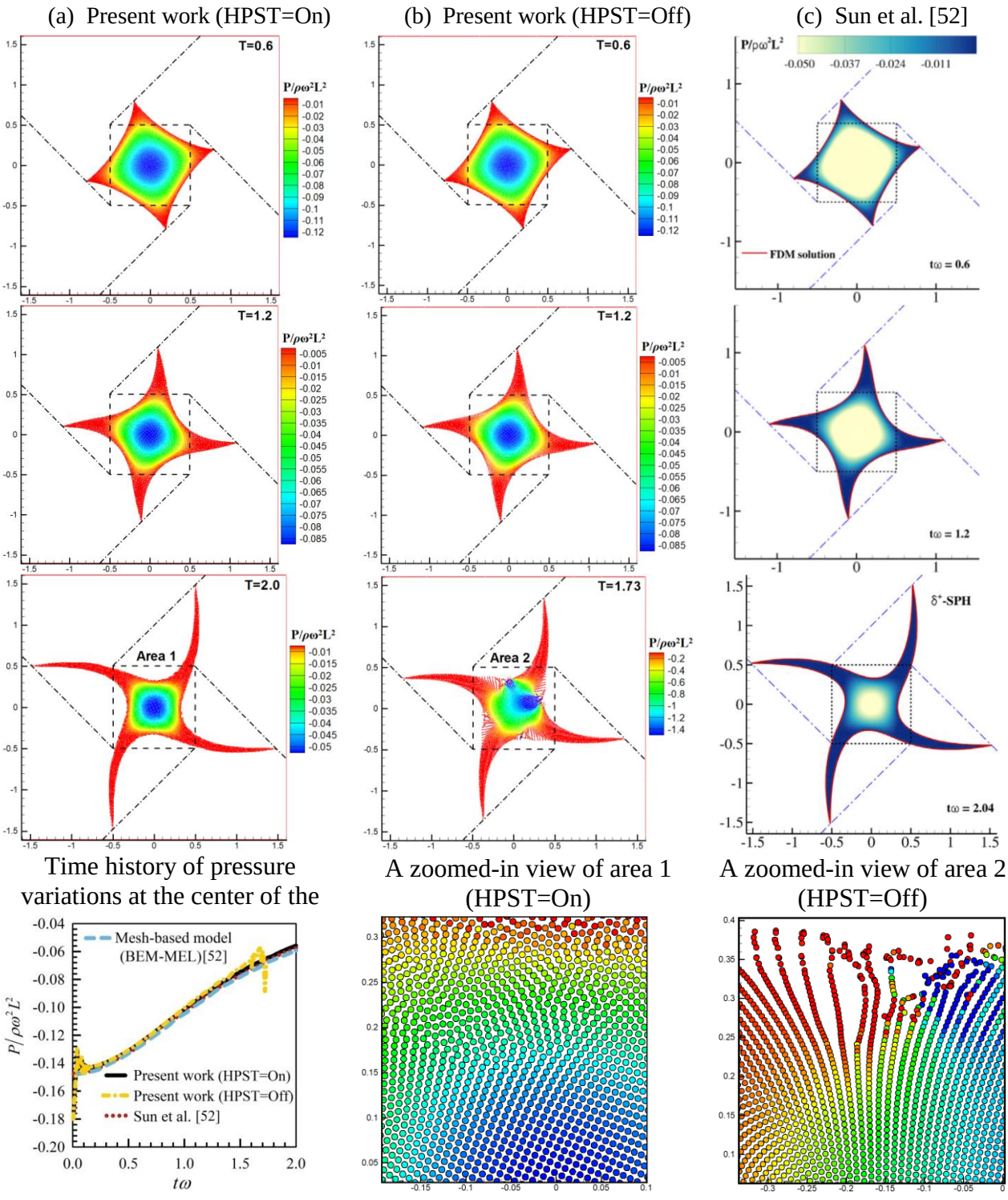

Figure 6-11 Comparison between the results of present work (a) and those reported by Sun et al. [52] (c) for the case of rotating square patch of fluid (case A4). The effects of the particle shifting technique on the particle distributions: (a) HPST=On and (b) HPST=Off.

Fig. 6-11 (a) shows that as time goes on, the size of the sidewalls lessens and arms of the patch start to grow, resulting in a formation of star-shaped structure within the fluid domain. However, as expected, in the case of HPST=Off, particles begin to follow the pattern of streamlines while gradually approaching the center of the circulation, resulting in simultaneous formation of unphysical gap (branch-like structures) and numerical cavitation. Particle overlapping and non-physical fragmentation of the fluid domain are, in turn, accompanied by concomitant density error accumulation ($\sum_{j=1}^{N} W_{ij} dV > 1$) and violation of mass and momentum conservation. These progressive unphysical behaviors eventually jeopardize the stability and accuracy of the method, leading to the premature failure of calculations (see Fig. 6-11 (b) and zoomed-in view of area 2). Fig. 6-11 also portrays qualitative and quantitative comparisons between obtained results and numerical data of Sun et al. [52]. As can be seen, a very good agreement exists between two solutions.

To shed further light onto the HPST performance and its impacts on the particle regularization, stretching of an initially circular water drop (case A5) is simulated where due to imposition of a strong shear field and rapid shrinkage of the matrix, the fluid domain is prone to extreme stratification and topological changes. As sketched in Fig. 6-1, the problem configuration consists of a weightless circular water patch ($\mathbf{g} = 0, \mu = 10^{-3}\ Pa\,s$ and $\rho = 1000\ kgm^{-3}$) subjected to the following irrotational velocity field:

$$\begin{aligned} u_0(x,y) &= -100\,x \qquad -R/2 \le x \le R/2 \\ v_0(x,y) &= +100\,y \qquad -R/2 \le x \le R/2 \\ p_0(x,y) &= 0 \end{aligned} \tag{6-41}$$

Fig. 6-12 shows that, due to large values of strain rate generated by irrotational velocity field, the circular water drop undergoes striking morphological changes (i.e. elongation in the longitudinal direction) during its development. Generally, extreme strain rate has a manifest tendency to keep the drop compact, leading to the establishment of positive pressure field and high degree of particle-particle interactions. Fig. 6-illustrates that as the drop evolves further into the oval or ellipsoidal shape, magnitude of pressure at the core region decreases which indicates that rate of particles bunching starts to decay as the time proceeds.

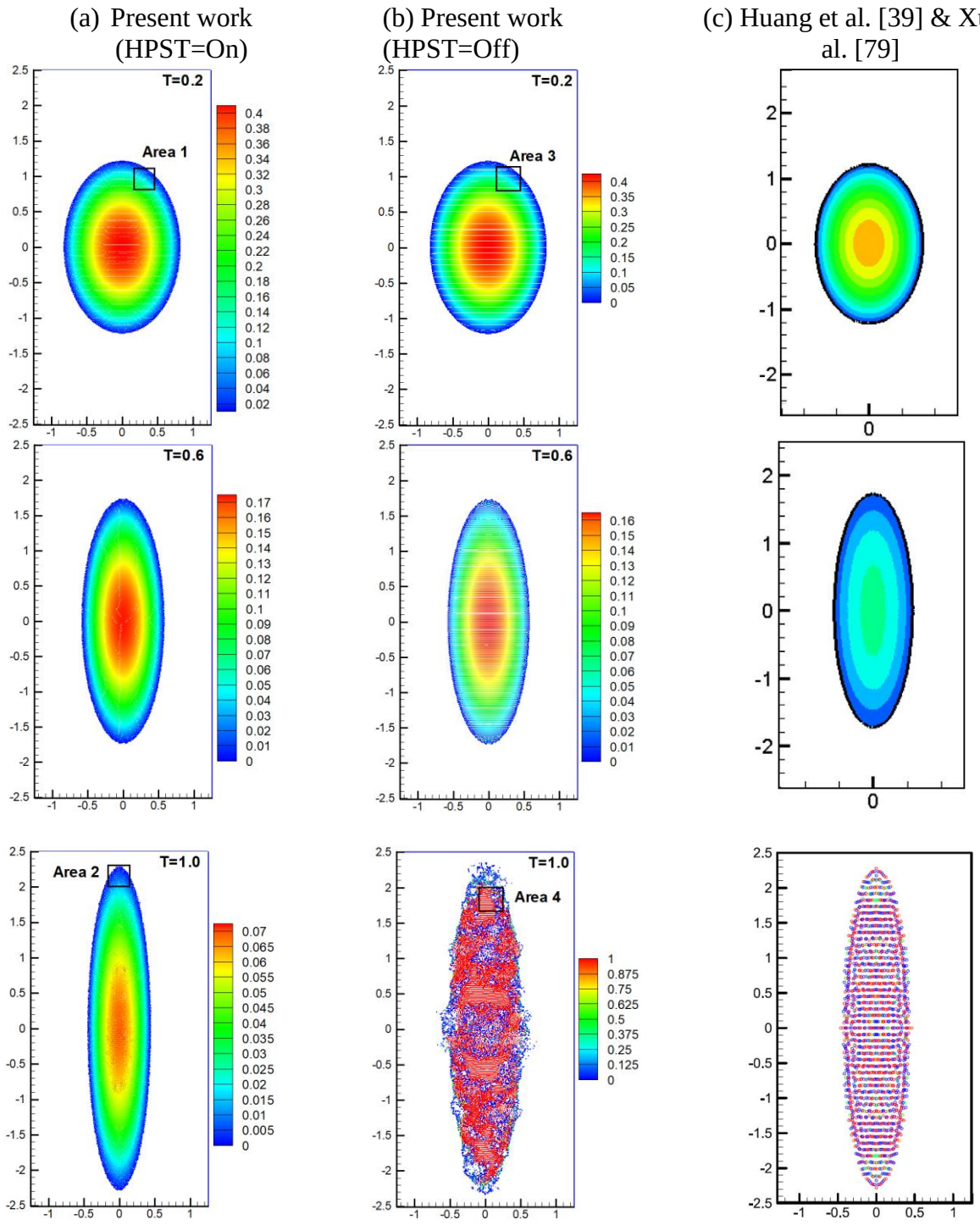

Figure 6-12 Comparison of calculated results (a) with numerical data of Huang et al. [39] and Xu et al. [79] (c) for the case of stretching circular drop (case A5). The effects of the HPST on the particles distributions (a) and (b).

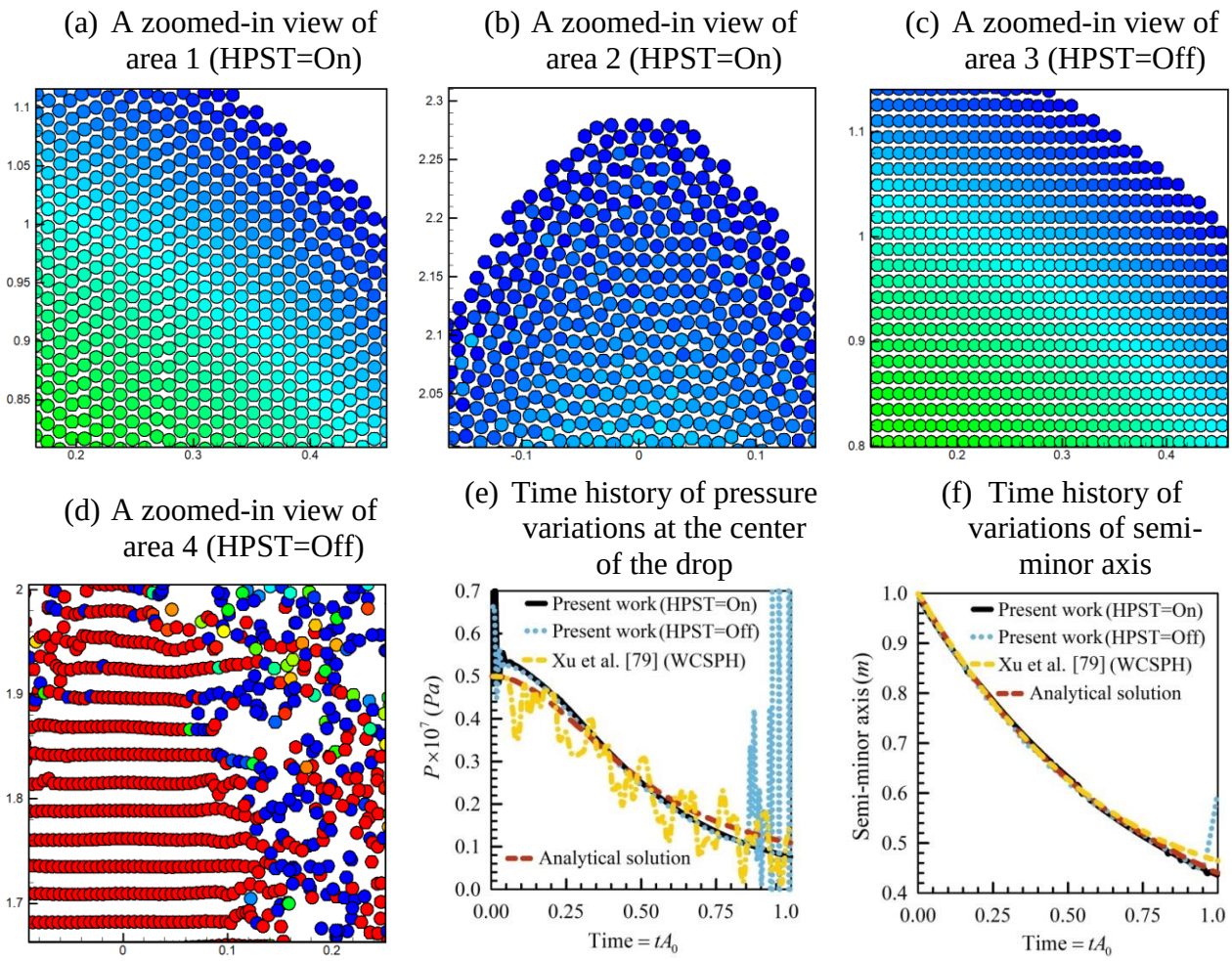

Figure 6-13 (a) to (d) the snapshots of four different zoomed-in view of particles distributions under the influence of the hybrid particle shifting technique. (e) and (f) time history of variations of semi-minor axis and pressure at the center of the drop for case A5.

Not surprisingly, similar to previous benchmark case, the prototype of the flow pattern in the absence of the HPST is manifested by detrimental influence of the particle clustering and void formation. It is evident from Figs. 6-13 (a) and 6-13 (b) that, in the presence of HPST (=On), particles are hexagonally distributed without any unphysical gap which clearly demonstrate the performance of the proposed HPST in handling tensile instability. However, when HPST is turned off, the particle stratification and numerical fractures as undesirable effects of tensile instability start to appear within the fluid domain which damages the interpolation accuracy in the free boundary area. These progressively deteriorate the interpolation procedure and consequently

direct the numerical simulation to a non-physical solution. The effects of this event are well reflected in Figs. 6-13 (c) and (d) where the occurrence of particles stratification and coherent structures ultimately lead to the unwanted termination of the calculation. By scrutinizing Figs. 6-13 (a) and (b) one can conclude that, the PST causes particles to migrate from the area with high concentration to the lower one, resulting in a rapid particle rearrangement within the computational domain. The time histories of the pressure variations at the center of the drop together with horizontal semi-axis movement are plotted in Fig. 6-13. As it is shown in this figure, a reasonable good agreement is achieved between analytical solutions and those predicted by present ISPH scheme. Furthermore, it can be seen from Figs. 6-12 and 6-13 that, the enhanced ISPH model produces much smoother pressure distributions compared to previously published conventional WCSPH results [39], [79]. The marked discrepancies between two numerical outcomes can be attributed to the implementation of the higher-order discretization schemes and consistent kernel function in the current work. The absence of the particle regularization technique and employing non-conservative form of the governing operators especially in work of Xu et al. [79] are two other major factors which can immensely affect the accuracy and reliability of the SPH computations.

6.8.4 Entropy generation due to natural convection heat transfer (Case A6)

As a further verification, the entropy generation due to natural convection heat transfer (case A6) is examined in this section where the *smoothing operator* (Eq. (6-A2)) is employed to estimate temperature value (T) in the buoyancy force ($F_b = -\rho g \beta (T - T_c)$) according to the Boussinesq approximation. As depicted in Fig. 6-1, the horizontal walls of the cavity are thermally insulated while vertical ones are maintained at different constant temperatures ($T_h > T_c$). Similar to convectional Eulerian methods, a particle independency test (grid study) was conducted using seven different particle distributions to ensure sustained accuracy. Table 6-2 reveals that, a uniform particle size of 139 ×139 ensures a particle-independent solution.

Table 6.2 Effect of the grid size (particle independency test) on $\overline{Nu}$ for case A6 at low and high Rayleigh number.

	Number of particles (Case A6)						
Ra	39×39	59×59	79×79	99×99	119×119	139×139	159×159
10^3	1.0885	1.0964	1.1048	1.1117	1.1183	1.1201	1.1205
10^6	8.4317	8.6536	8.7804	8.8605	8.9181	8.9222	8.9231

Generally, due to the presence of density gradient within the cavity, the working fluid in the immediate vicinity of the left wall ascends upwards and gets lighter as its level of energy enhances. Since the insulated top wall is impermeable, the expanded fluid turns its direction and moves horizontally toward the right wall. After impinging onto the cold wall, it exchanges its high level of energy and descends downward as it becomes gradually denser and heavier. The condensed working fluid eventually travels horizontally outward in contact with the bottom wall until it encounters the thermal boundary layer of hot area and completes its thermal cycle. Hence, the clockwise vortex is developed inside the enclosure. It can be seen from Figs. 6-14 and 6-15 that at *Ra*= 10^3, flow field is characterized by weak circulation pattern and corresponding isotherms are almost parallel and evenly distributed, indicating that the temperature field is totally decoupled from the flow field and conduction is the dominant mode of energy transport within the enclosure. It is evident from Fig. 6-16 that the corresponding local Bejan number is very close to unity ($Be \approx 1$) which signifies the strong dominance of thermal dissipation over the viscous irreversibility ($S_T \gg S_F$). This observation is in accordance with the maximum and average values of entropy generation due to heat transfer ($S_{T,\max} = 2.277$ and $\overline{S}_T = 1.119$) and fluid friction irreversibility ($S_{F,\max} = 0.244$ and $\overline{S}_F = 0.035$) provided in table 6-3. However, by increasing the Rayleigh number up to 10^4, the effect of buoyancy force gets more prominent and consequently intensity of the recirculation inside the cavity enhances. This effect is dynamically characterized by the horizontal elongation of main vortex core and the appearance of distinct thermal boundary layer adjacent to the heated and cooled walls.

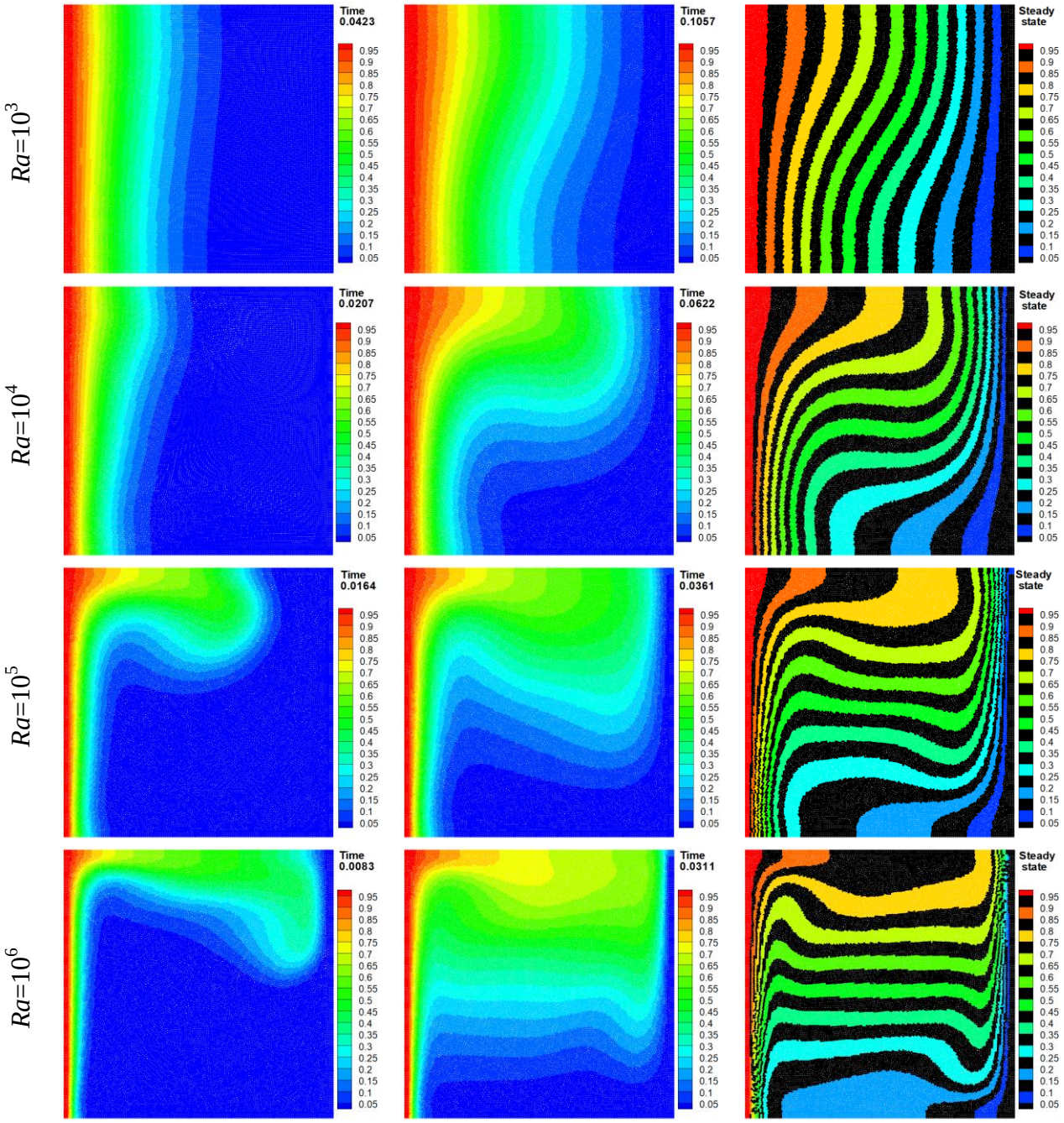

Figure 6-14 Transient variations of isotherms as a function of the non-dimensional time at different Rayleigh numbers for case A6.

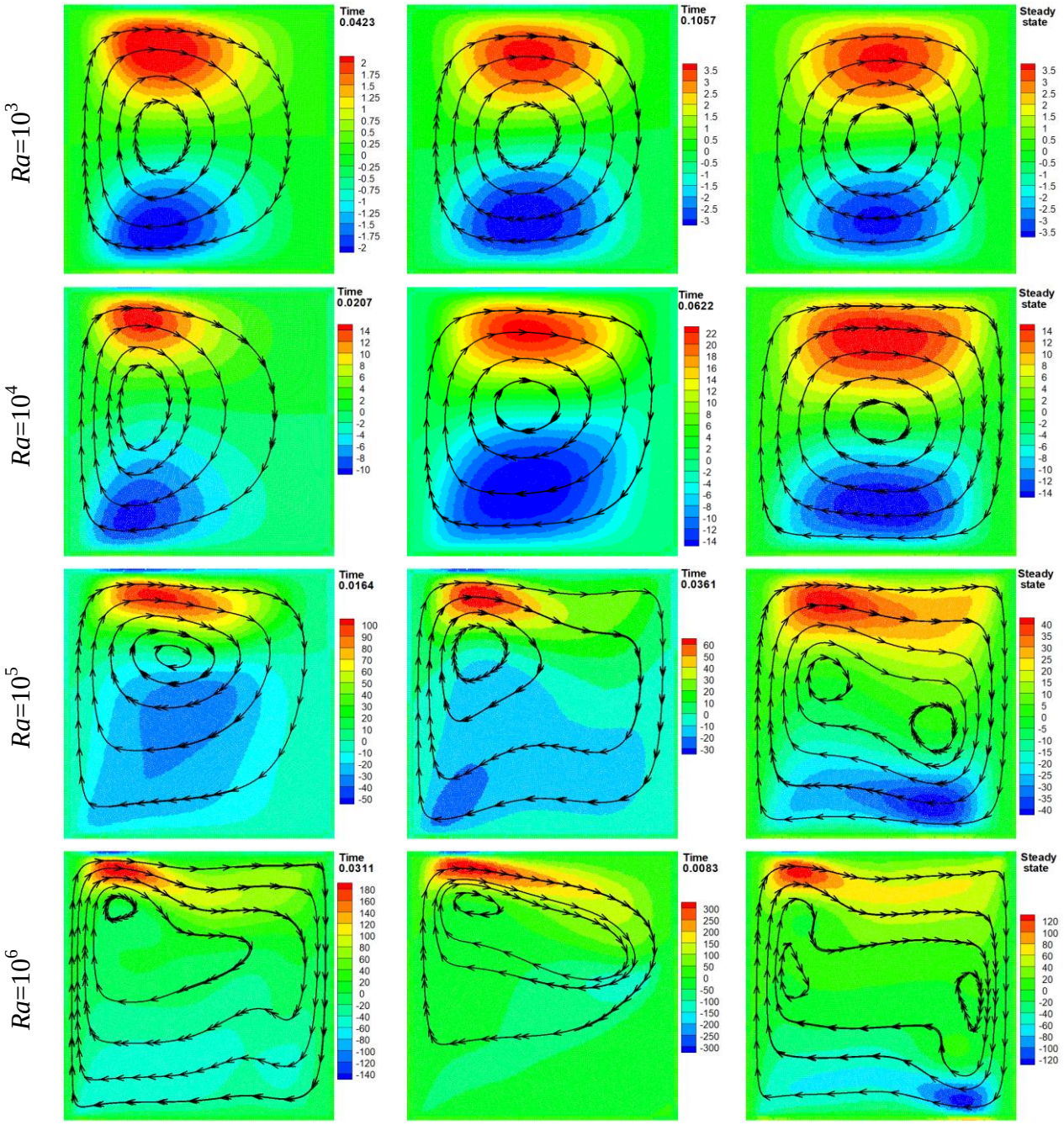

Figure 6-15 Transient variations of streamlines and velocity component in x-direction as a function of the non-dimensional time at different Rayleigh numbers for case A6.

The enhancement in the flow intensity is also accompanied by a significant increase in velocity and temperature gradients, resulting in a remarkable augmentation of both heat transfer rate and total entropy generation according to Eqs. (6-10) to (6-14). Note that, the slightly slanting

isotherms and weak compression of streamlines along the vertical walls also imply that the inception of the convection regime takes place at this *Ra* where viscous and buoyancy forces are comparable. The comparison of average entropy generation due to both factors ($\overline{S}_T > \overline{S}_F$) in table 6-3 reveals that the thermal dissipation is still the major source of irreversibility within the enclosure. This observation is also compatible with Fig. 6-16 where local Bejan number with values greater than half ($Be > 0.5$) occupies the major part of the enclosure. Fig. 6-17 illustrates that in this circumstance ($Ra=10^4$) , the active zones of entropy generation due to thermal dissipation are confined in the lower and upper halves of the isothermal walls where maximum temperature gradient occurs (compatible with the characteristics of isotherms). This trend is accentuated by increasing the Rayleigh number up to 10^5. It is evident from Figs. 6-14 and 6-15 that due to strong convective motion and buoyancy force, isotherms are dragged towards the vertical wall and streamlines become more twisted. In this condition, velocity components undergo stretching and the clockwise circulation vortex is segregated at the core and consequently two CW small eddies are developed within the enclosure. The horizontally oriented isotherms in the middle portion and sudden decrement in the thickness of the thermal boundary layer clearly confirm that heat is transferred primarily due to convection mode and viscous force is no more in the flow. As displayed in table 6-3, by increasing the *Ra*, the contribution of S_F to the total entropy generation augments such that average Bejan number declines rapidly and becomes less than half ($\overline{Be} = 0.197 < 0.5$). In fact, from the viewpoint of sensitivity analysis one can deduce that, entropy generation due to viscous dissipation (S_F) is much more sensitive than the heat transfer irreversibility (S_T) to any alteration in Rayleigh number and flow intensity. However, by increasing the *Ra*, heat transfer irreversibility enhances marginally and becomes more pronounced at the lower and upper portions of the left and right sidewalls with a local maxima of $S_{T,\max} = 60.56$. As expected, for higher values of Rayleigh number ($Ra=10^6$), the primary source of exergy destruction (or irreversibility) in the cavity turns out to be viscous dissipation. It is obvious from Fig. 6-16 that, the active zone of local Bejan number is restricted to a relatively small portion of the middle zone where fluid is nearly stagnant and characterized by an elongated uni-cellular motion and thermal stratification.

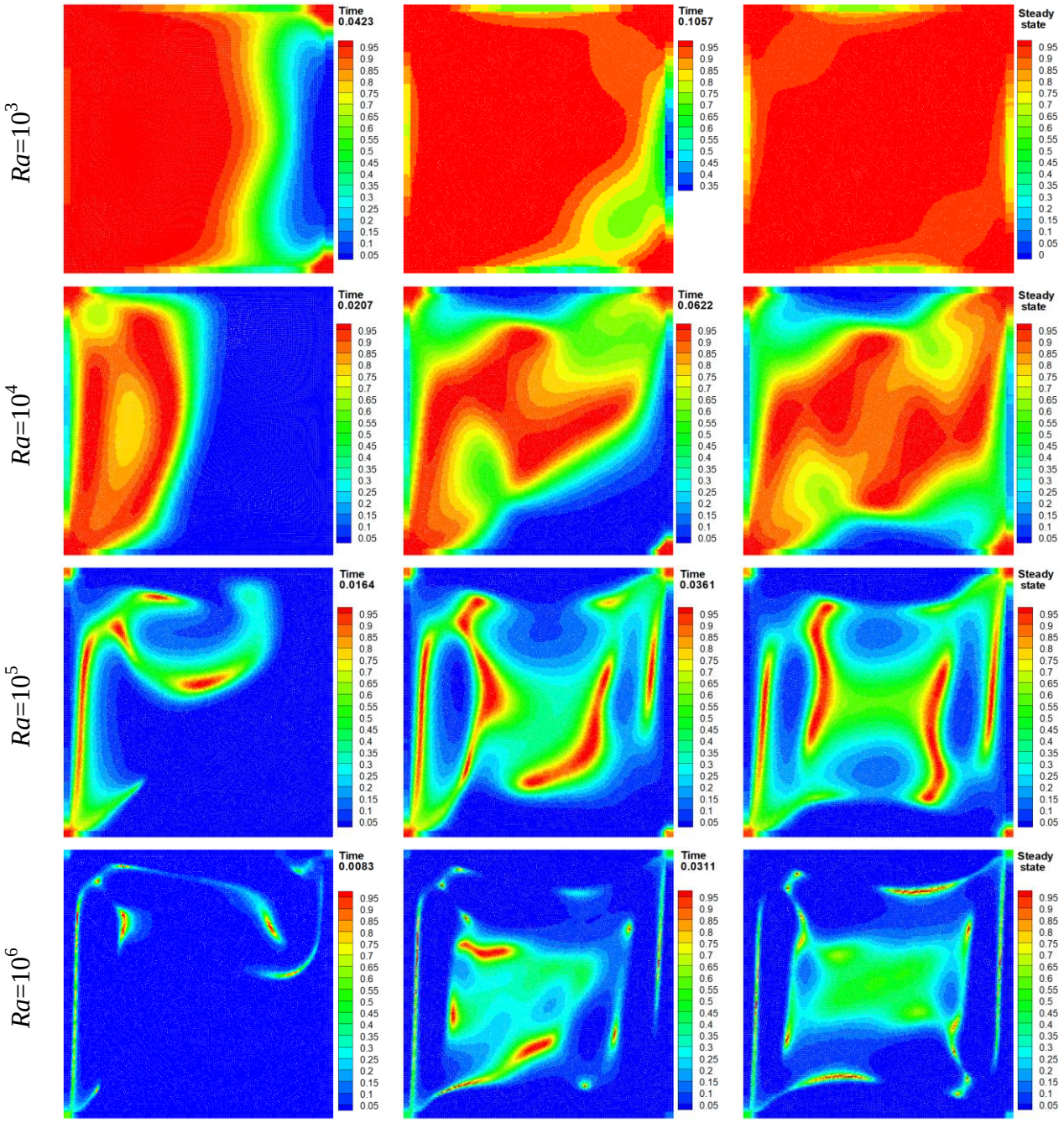

Figure 6-16 Transient variations of local Bejan number (Be) as a function of the non-dimensional time at different Rayleigh numbers for case A6.

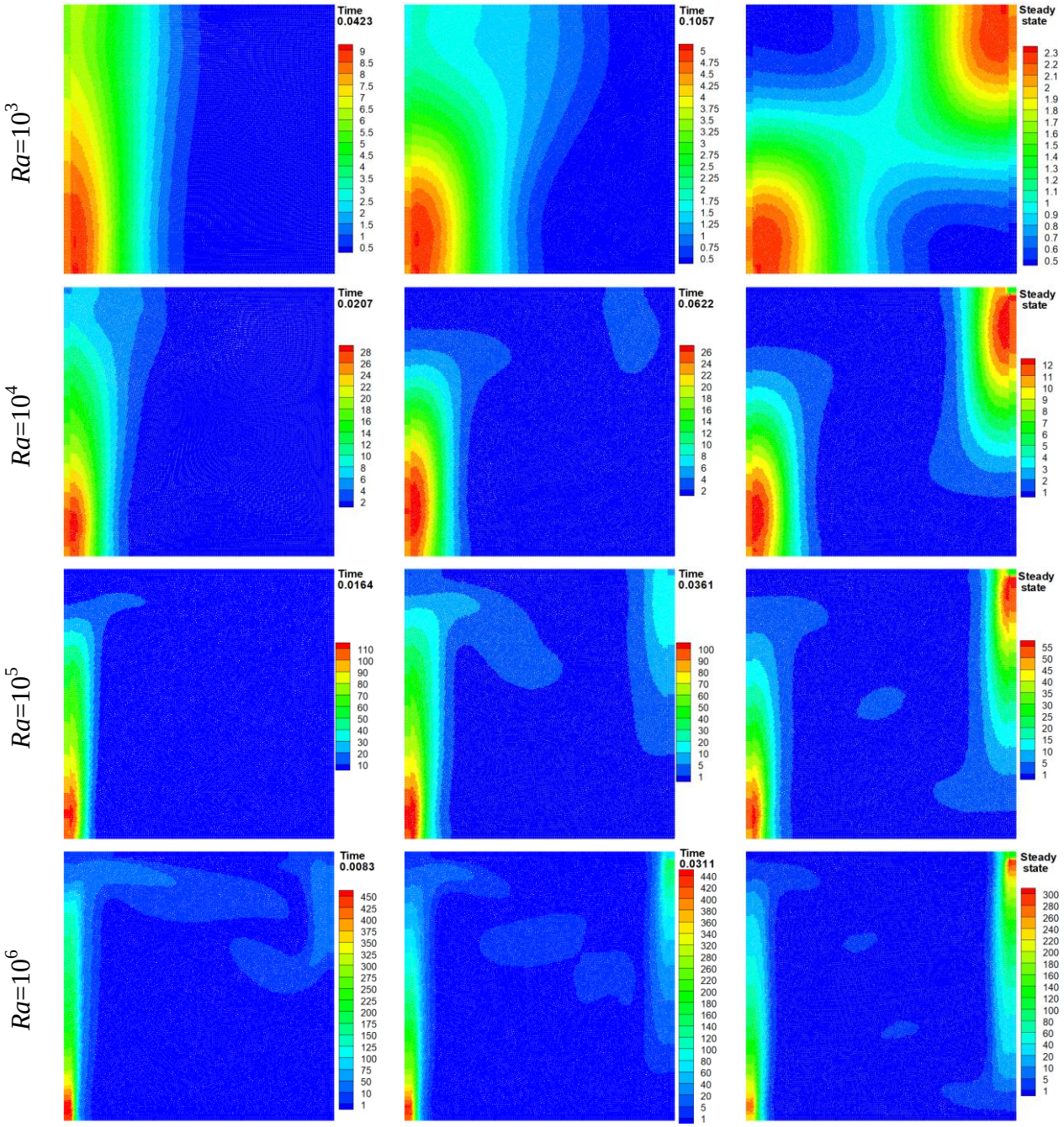

Figure 6-17 Transient variations of local entropy generation due to heat transfer (S_T) as a function of the non-dimensional time at different Rayleigh numbers for case A6.

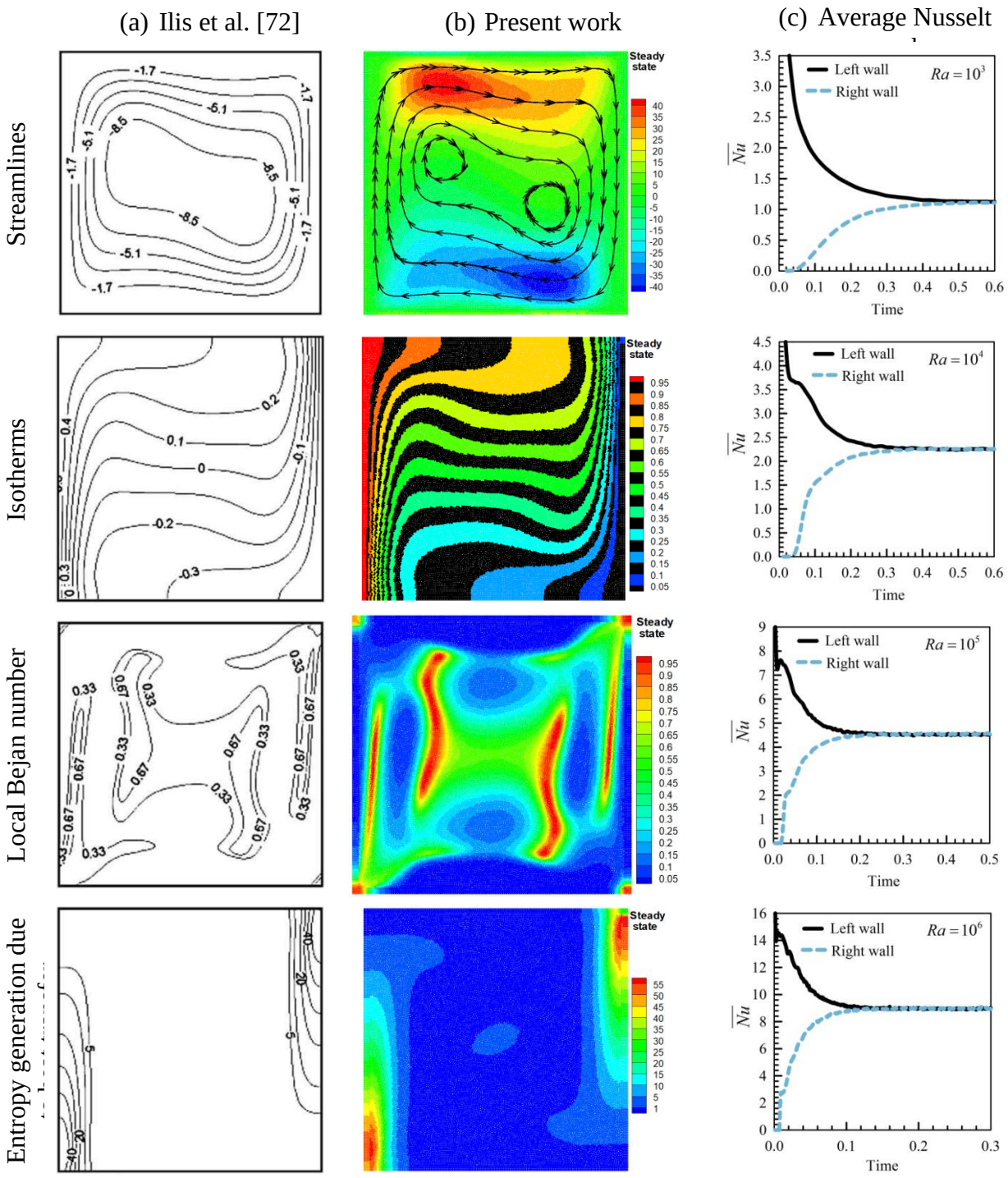

Figure 6-18Comparison of isotherms, streamlines, local Bejan number (*Be*) and local entropy generation due to heat transfer (S_T) contours obtained from the present work (b) with those reported by Ilis et al. [72] (a) in steady-state condition at Ra=10^5 for case A6.

Table 6.3 The effects of the Rayleigh number on the maximum velocity components, average Nusselt number and entropy generation for case A6 (steady-state condition).

Case A6										
Ra	$\overline{Nu}$	$\lvert U_{\max}\rvert$	$\lvert V_{\max}\rvert$	$\overline{Be}$	$\overline{S}_{tot}$	$S_{tot,\max}$	$\overline{S}_T$	$S_{T,\max}$	$\overline{S}_F$	$S_{F,\max}$
10^3	1.130	3.620	3.692	0.972	1.146	2.280	1.119	2.277	0.035	0.244
10^4	2.247	16.181	19.584	0.685	3.240	25.213	2.224	12.579	1.024	16.115
10^5	4.544	43.473	68.583	0.197	22.836	590.981	4.455	60.567	18.379	558.463
10^6	8.973	123.006	221.389	0.026	335.163	15877.142	8.628	320.880	326.532	15754.417

By comparing the local Be and S_T in Figs. 6-16 and 6-17 one can conclude that, although the active zones of S_T are concentrated adjacent to the vertical walls but they are comparatively trivial compared to S_F, resulting in a substantial reduction in the values of local Bejan number ($Be \ll 0.5$) in those regions. The foregoing discussion implies that at this stage, only negligible amount of the available work is exploited to overcome the irreversibility due to heat transfer ($S_T \ll S_F$). Similar findings were also documented by Basak et al. [88] and Das et al. [89], [90] who investigated entropy generation during the natural convection in square, triangular and trapezoidal enclosures. Comparison with previously published work in terms of streamlines, isotherms, local Bejan number, entropy generation due to heat transfer and average Nusselt number is depicted in Fig. 6-18. It can be seen that, there is an excellent agreement between the present calculations and those reported by Ilis et al. [72]. It is necessary to note that for sake of the brevity, transient variations of $\overline{S}_{tot}, \overline{S}_T, \overline{S}_F, \overline{Be}$ together with the velocity contour in the *y*-direction are provided as a supplementary material.

6.9 Conclusions

The present study introduced two novel gradient and Laplacian operators in the Lagrangian framework for analysis of free-surface flows and thermal characteristics of convection heat transfer problems. Moreover, a novel hybrid particle regularization scheme is developed to improve the consistency and accuracy of the numerical model. In addition, a new free-surface detection technique has been proposed for the treatment of free-surface particles and the enforcement of the Dirichlet boundary condition for the Pressure Poisson Equation. Feasibility

and performance of the developed models have been verified through various challenging test cases and experiments. Based on the results obtained from the present investigation, the following major conclusions can be drawn:

- The results show that, the newly developed smoothing kernel (W_{ij}) remarkably outperformed the existing kernel functions (i.e. Cubic and Wendland) in modeling of shockwave propagation and multiphase flow with physical discontinuities.
- It is found that, the proposed Hybrid Free-surface Detection (HFD) technique can successfully identify the position of interface and its nearby particles.
- It is found that, the proposed Hybrid Particle Shifting Technique (HPST) can efficiently eliminate spurious pressure fluctuation caused by tensile instability (particle clustering) from the computational domain.
- The results show that, particles in Lagrangian framework have a natural tendency to cluster along the streamline, resulting in a significant void formation and density error accumulation.
- The results show that, implementing an efficient particle regularization technique (HPST) can significantly enhance the accuracy and stability of the numerical solution.
- The results show that, the combination of the third-order TVD Runge-Kutta scheme and two-step projection model provides more accurate and reliable results than the classical SPH model.
- The results show that, implementing high-order discretization schemes for gradient, Laplacian and divergence operators can immensely enhance the accuracy and consistency of the ISPH method.
- The results show that, the proposed high-order gradient and Laplacian operators produce a much smoother pressure field than the conventional WCSPH formulations.
- The obtained results vividly demonstrate the broad applicability of proposed models for simulating free-surface flows and particulate flows with thermal convection.
- The results show that, the proposed Modified Pressure Gradient operator (MPG) can successfully resolve the problem of particle clumping on the interface while retaining the conservation properties of momentum.

- The results show that, the proposed *smoothing operator* can efficiently handle density discontinuities in the multiphase flow problems (e.g. Rayleigh-Taylor instability).
- The results show that, by increasing the Rayleigh number, average Nusselt number and entropy generation due to both factors (S_T, S_F) augment while a reverse trend occurs in the values of local and average Bejan numbers.

As a future investigation, the proposed models will be extended to explore multiphase flow with high density ratio such as bubble rising, two-phase dam break and water droplet falling in air where undesirable particle scattering/clustering is likely to occur on the interface. It would be a future challenge to investigate turbulent natural convection heat transfer in porous enclosure which has many important applications ranging from electronic packaging to solar collector technology.

6.10 CRediT authorship contribution statement

Faroogh Garoosi: Conceptualization, Investigation, Methodology, Software, Validation, Visualization, Writing-original draft, Writing-review & editing.

Ahmad Shakibaeinia: Supervision, Funding acquisition, Writing-review & editing.

6.11 Appendix A (gradient, Laplacian and divergence operators)

Detailed description of the derivation of governing operators including gradient, divergence and Laplacian is presented here for a general class of Lagrangian framework. Generally, for 2D space, by multiplying both sides of Eq. (6-A1) by $W_{ij}, \nabla W_{ij,x}, \nabla W_{ij,y}$ and then integrating it over point (x_i,y_i), the numerical approximations of a field function (f_i) and its derivatives can be obtained as follows:

$$f_j = f_i + f_x^{'} x_{ij} + f_y^{'} y_{ij} + \frac{1}{2} f_{xx}^{"} x_{ij}^2 + \frac{1}{2} f_{yy}^{"} y_{ij}^2 + f_{xy}^{"} x_{ij} y_{ij} + O(h^3) \quad \text{(6-A1)}$$

$$\begin{bmatrix} f_i \\ f_x^{'} \\ f_y^{'} \end{bmatrix} = L \begin{bmatrix} \sum_{j=1}^{N} f_j W_{ij} dV \\ \sum_{j=1}^{N} f_j \nabla W_{ij,x} dV \\ \sum_{j=1}^{N} f_j \nabla W_{ij,y} dV \end{bmatrix} \qquad L = \begin{bmatrix} \sum_{j=1}^{N} W_{ij} dV & \sum_{j=1}^{N} x_{ij} W_{ij} dV & \sum_{j=1}^{N} y_{ij} W_{ij} dV \\ \sum_{j=1}^{N} \nabla W_{ij,x} dV & \sum_{j=1}^{N} x_{ij} \nabla W_{ij,x} dV & \sum_{j=1}^{N} y_{ij} \nabla W_{ij,x} dV \\ \sum_{j=1}^{N} \nabla W_{ij,y} dV & \sum_{j=1}^{N} x_{ij} \nabla W_{ij,y} dV & \sum_{j=1}^{N} y_{ij} \nabla W_{ij,y} dV \end{bmatrix}^{-1} \tag{6-A2}$$

In above equations, $W_{ij}, \nabla W_{ij,x}$ and $\nabla W_{ij,y}$ are kernel function and its first spatial derivatives in x and y-directions. $dV = m_j / \rho_j$ is the volume of the particle while $x_{ij} = x_j - x_i$ and $y_{ij} = y_j - y_i$ denote the distance between target particle i and its neighboring particle j, respectively. L is a corrective matrix which satisfies the first-order completeness condition for the kernel function. It is interesting to note that, Eq. (6-A2) is equivalent to the MLS approximation proposed by Nayroles et al. [91]. In the present work, Eq. (6-A2) will be referred to as *smoothing operator* henceforth.

By subtracting f_i from both sides of Eq. (6-A1) and multiplying it by $\nabla W_{ij,x}$ and $\nabla W_{ij,y}$, the gradient operator can be obtained as follows:

$$\begin{bmatrix} f_x^{'} \\ f_y^{'} \end{bmatrix} = L \begin{bmatrix} \sum_{j=1}^{N} (f_j - f_i) \nabla W_{ij,x} dV \\ \sum_{j=1}^{N} (f_j - f_i) \nabla W_{ij,y} dV \end{bmatrix} \qquad L = \begin{bmatrix} \sum_{j=1}^{N} x_{ij} \nabla W_{ij,x} dV & \sum_{j=1}^{N} y_{ij} \nabla W_{ij,x} dV \\ \sum_{j=1}^{N} x_{ij} \nabla W_{ij,y} dV & \sum_{j=1}^{N} y_{ij} \nabla W_{ij,y} dV \end{bmatrix}^{-1} \tag{6-A3}$$

Eq. (6-A3) was initially proposed by Krongauz et al. [92] and was then successfully implemented by Oger et al. [93] to solve the dam-break problem. However, in the case of kernel with compact support, all off-diagonal elements of matrix L vanish, forming the symmetric diagonal matrix ($\sum_{j=1}^{N} y_{ij} \nabla W_{ij,x} dV = \sum_{j=1}^{N} x_{ij} \nabla W_{ij,y} dV = 0$) as follows:

$$L = \begin{bmatrix} \sum_{j=1}^{N} x_{ij} \nabla W_{ij,x} dV & 0 \\ 0 & \sum_{j=1}^{N} y_{ij} \nabla W_{ij,y} dV \end{bmatrix}^{-1} \tag{6-A4}$$

In this circumstance, gradients of the field function can be estimated with the lowest computational cost as follows:

$$f_x^{'} = \frac{\partial f}{\partial x} = \frac{\sum_{j=1}^{N}(f_j - f_i)\nabla W_{ij,x}dV}{\sum_{j=1}^{N} x_{ij}\nabla W_{ij,x}dV}, \qquad f_y^{'} = \frac{\partial f}{\partial y} = \frac{\sum_{j=1}^{N}(f_j - f_i)\nabla W_{ij,y}dV}{\sum_{j=1}^{N} y_{ij}\nabla W_{ij,y}dV} \tag{6-A5}$$

The above equation is known as a *Modified Version of the Conventional SPH derivatives* pioneered by Johnson et al. [94] which has been frequently used to express the rate of deformation. It should be noted that, Eq. (6-A5) cannot guarantee a linear exactness adjacent to the interface where the kernel function is truncated with insufficient number of the particles.

It is also possible to derive the second gradient operator by subtracting f_i from both sides of Eq. (6-A1) and multiplying it by $\nabla W_{ij,x}/r_{ij}^2$ and $\nabla W_{ij,y}/r_{ij}^2$ instead of $\nabla W_{ij,x}$ and $\nabla W_{ij,y}$. This gives:

$$\begin{bmatrix} f_x^{'} \\ f_y^{'} \end{bmatrix} = L \begin{bmatrix} \sum_{j=1}^{N} \frac{(f_j - f_i)}{r_{ij}^2}\nabla W_{ij,x}dV \\ \sum_{j=1}^{N} \frac{(f_j - f_i)}{r_{ij}^2}\nabla W_{ij,y}dV \end{bmatrix} \qquad L = \begin{bmatrix} \sum_{j=1}^{N} \frac{x_{ij}\nabla W_{ij,x}}{r_{ij}^2}dV & \sum_{j=1}^{N} \frac{y_{ij}\nabla W_{ij,x}}{r_{ij}^2}dV \\ \sum_{j=1}^{N} \frac{x_{ij}\nabla W_{ij,y}}{r_{ij}^2}dV & \sum_{j=1}^{N} \frac{y_{ij}\nabla W_{ij,y}}{r_{ij}^2}dV \end{bmatrix}^{-1} \tag{6-A6}$$

By subtracting Eq. (6-A1) from f_i and decomposing it into two separate equations in x and y directions, the Taylor series approximation can be written as follows:

$$f_j - f_i = f_x^{'}x_{ij} + f_y^{'}y_{ij} + \frac{1}{2}f_{xx}^{''}x_{ij}^2 + \frac{1}{2}f_{yy}^{''}y_{ij}^2 \tag{6-A7}$$

$$\frac{1}{2}(f_j - f_i) = f_x^{'}x_{ij} + \frac{1}{2}f_{xx}^{''}x_{ij}^2 \tag{6-A8}$$

$$\frac{1}{2}(f_j - f_i) = f_y^{'}y_{ij} + \frac{1}{2}f_{yy}^{''}y_{ij}^2 \tag{6-A9}$$

The SPH stencil for the second derivatives of f_i can be calculated by multiplying Eqs. (6-A8) and (6-A9) by $x_{ij}\nabla W_{ij,x}$ and $y_{ij}\nabla W_{ij,y}$, and integrating it over all neighbor particles j as follows:

$$\sum_{j=1}^{N}\frac{1}{2}(f_j-f_i)\,x_{ij}\nabla W_{ij,x}dV=f_x^{'}\sum_{j=1}^{N}x_{ij}^2\nabla W_{ij,x}dV+f_{xx}^{"}\sum_{j=1}^{N}\frac{1}{2}x_{ij}^3\nabla W_{ij,x}dV,$$

$$f_{xx}^{"}=\frac{\sum_{j=1}^{N}\frac{1}{2}(f_j-f_i)\,x_{ij}\nabla W_{ij,x}dV-f_x^{'}\sum_{j=1}^{N}x_{ij}^2\nabla W_{ij,x}dV}{\sum_{j=1}^{N}\frac{1}{2}x_{ij}^3\nabla W_{ij,x}dV}, \tag{6-A10}$$

$$\sum_{j=1}^{N}\frac{1}{2}(f_j-f_i)\,y_{ij}\nabla W_{ij,y}dV=f_y^{'}\sum_{j=1}^{N}y_{ij}^2\nabla W_{ij,y}dV+f_{yy}^{"}\sum_{j=1}^{N}\frac{1}{2}y_{ij}^3\nabla W_{ij,y}dV,$$

$$f_{yy}^{"}=\frac{\sum_{j=1}^{N}\frac{1}{2}(f_j-f_i)\,y_{ij}\nabla W_{ij,y}dV-f_y^{'}\sum_{j=1}^{N}y_{ij}^2\nabla W_{ij,y}dV}{\sum_{j=1}^{N}\frac{1}{2}y_{ij}^3\nabla W_{ij,y}dV}, \tag{6-A11}$$

Finally, by summing the terms $f_{xx}^{"}$ and $f_{yy}^{"}$ expressed in Eqs. (6-A10) and (6-A11), the Laplacian operator can be obtained as follows:

$$\nabla^2 f=f_{xx}^{"}+f_{yy}^{"}=\frac{\sum_{j=1}^{N}\frac{1}{2}(f_j-f_i)\,x_{ij}\nabla W_{ij,x}dV-f_x^{'}\sum_{j=1}^{N}x_{ij}^2\nabla W_{ij,x}dV}{\sum_{j=1}^{N}\frac{1}{2}x_{ij}^3\nabla W_{ij,x}dV}+$$
$$\frac{\sum_{j=1}^{N}\frac{1}{2}(f_j-f_i)\,y_{ij}\nabla W_{ij,y}dV-f_y^{'}\sum_{j=1}^{N}y_{ij}^2\nabla W_{ij,y}dV}{\sum_{j=1}^{N}\frac{1}{2}y_{ij}^3\nabla W_{ij,y}dV} \tag{6-A12}$$

where $f_x^{'}$ and $f_y^{'}$ are the first derivatives of the shape function (f_i) which can be computed through Eq. (6-A3) or (6-A6). It is worth mentioning that, by comparing the Eqs. (6-A5) and (6-A12), one can conclude that, the aforementioned equations are analogous to the approximations used in the finite difference method where partial derivative in the *x*-direction (*x* or *y*) is totally independent of other directions.

However, similar to gradient operator, in the case of uniform particle arrangements ($\sum_{j=1}^{N} x_{ij}^2 \nabla W_{ij,x} dV = \sum_{j=1}^{N} y_{ij}^2 \nabla W_{ij,y} dV = 0$ and $\sum_{j=1}^{N} \frac{1}{2} x_{ij}^3 \nabla W_{ij,x} dV = \sum_{j=1}^{N} \frac{1}{2} y_{ij}^3 \nabla W_{ij,y} dV$) the discretization of the Laplacian operator can be simplified to the following expression:

$$\nabla^2 f = f_{xx}^{"} + f_{yy}^{"} = \frac{2\sum_{j=1}^{N} (f_j - f_i) x_{ij} \nabla W_{ij,x} dV + 2\sum_{j=1}^{N} (f_j - f_i) y_{ij} \nabla W_{ij,y} dV}{\sum_{j=1}^{N} x_{ij}^3 \nabla W_{ij,x} dV + \sum_{j=1}^{N} y_{ij}^3 \nabla W_{ij,y} dV} \tag{6-A13}$$

Note that, the expression of $\sum_{j=1}^{N} \frac{1}{2} x_{ij}^3 \nabla W_{ij,x} dV = \sum_{j=1}^{N} \frac{1}{2} y_{ij}^3 \nabla W_{ij,y} dV$ can be proved by solving $\int \frac{1}{2} x_{ij}^3 \nabla W_{ij,x} dV$ and $\int \frac{1}{2} y_{ij}^3 \nabla W_{ij,y} dV$ in a polar coordinate system ($x_{ij} = r_{ij} \cos\varphi$, $y_{ij} = r_{ij} \sin\varphi$).

It is worth mentioning that, by multiplying Eqs. (6-A8) and (6-A9) by $x_{ij} \nabla W_{ij,x} / r_{ij}^2$ and $y_{ij} \nabla W_{ij,y} / r_{ij}^2$ instead of $x_{ij} \nabla W_{ij,x}$ and $y_{ij} \nabla W_{ij,y}$, the second Laplacian operator can be obtained as follows:

$$\nabla^2 f = f_{xx}^{"} + f_{yy}^{"} = \frac{\sum_{j=1}^{N} \frac{1}{2} (f_j - f_i) \frac{x_{ij} \nabla W_{ij,x}}{r_{ij}^2} dV - f_x^{'} \sum_{j=1}^{N} \frac{x_{ij}^2 \nabla W_{ij,x}}{r_{ij}^2} dV}{\sum_{j=1}^{N} \frac{1}{2} \frac{x_{ij}^3 \nabla W_{ij,x}}{r_{ij}^2} dV} + \frac{\sum_{j=1}^{N} \frac{1}{2} (f_j - f_i) \frac{y_{ij} \nabla W_{ij,y}}{r_{ij}^2} dV - f_y^{'} \sum_{j=1}^{N} \frac{y_{ij}^2 \nabla W_{ij,y}}{r_{ij}^2} dV}{\sum_{j=1}^{N} \frac{1}{2} \frac{y_{ij}^3 \nabla W_{ij,y}}{r_{ij}^2} dV} \tag{6-A14}$$

Similar to previous approach, for regular particle distributions, Eq. (6-A14) can be reduced to a simpler form as follows:

$$\nabla^2 f = f_{xx}^{"} + f_{yy}^{"} = 2\sum_{j=1}^{N}(f_j - f_i)\frac{x_{ij}\nabla W_{ij,x}}{r_{ij}^2}dV + 2\sum_{j=1}^{N}(f_j - f_i)\frac{y_{ij}\nabla W_{ij,y}}{r_{ij}^2}dV,$$
$$\nabla^2 f = f_{xx}^{"} + f_{yy}^{"} = 2\sum_{j=1}^{N}(f_j - f_i)\frac{\mathbf{r_{ij}}\cdot\nabla W_{ij}}{r_{ij}^2}dV \quad \text{(6-A15)}$$

Eq. (6-A15) was initially introduced by Cummins et al. [95] for discretization of PPE operator and then modified by Lo and Shao [96] for treatment of the viscous term in Navier-Stokes equation.

6.12 Appendix B (1D Sod shock tube)

The governing equations (momentum, energy and continuity) in a Lagrangian framework along with the classical numerical procedure for solving 1D Sod shock tube problem is detailed here [6].

$$\frac{D\mathbf{u}}{Dt} = -\sum_{J=1}^{N} m_j\left(\frac{p_i + p_j}{\rho_i\rho_j} + \Pi_{ij}\right)\nabla W_{ij} \quad \text{(6-B1)}$$

$$\frac{De}{Dt} = -\frac{1}{2}\sum_{J=1}^{N} m_j\left(\frac{p_i}{\rho_i^{\,2}} + \frac{p_j}{\rho_j^{\,2}}\right)(\mathbf{u}_{ij}\cdot\nabla W_{ij}) \quad \text{(6-B2)}$$

$$\rho = \sum_{J=1}^{N} m_j W_{ij} \quad \text{(6-B3)}$$

$$\mathbf{u}^{(n+1)} = \mathbf{u}^{(n)} + \Delta t\frac{D\mathbf{u}^{(n)}}{Dt}$$
$$e^{(n+1)} = e^{(n)} + \Delta t\frac{De^{(n)}}{Dt} \quad \text{(6-B4)}$$
$$\mathbf{r}^{(n+1)} = \mathbf{r}^{(n)} + \Delta t\,\mathbf{u}^{(n+1)}$$

$$p = \rho(\gamma - 1)e, \quad c = \sqrt{\frac{\gamma p}{\rho}}, \quad \text{(6-B5)}$$

In above equations, e , c, $\gamma = 1.4$ and $\mathbf{u}$ represent internal energy, artificial sound speed, heat capacity ratio and velocity of the gas, respectively. Similar to work of Liu et al. [6], 320 particles with high level of pressure and energy are uniformly spaced in the high-density area $[-0.6, 0]$ while 80 particles are uniformly spaced at low density region $[0, 0.6]$.

$$\begin{aligned} &x \le 0, \quad \rho = 1, \quad u = 0, \quad e = 2.5, \quad p = 1, \quad \Delta x = 0.001875, \quad m = 0.001875 \\ &x > 0, \quad \rho = 0.25, \quad u = 0, \quad e = 1.795, \quad p = 0.1795, \quad \Delta x = 0.0075, \quad m = 0.001875 \end{aligned} \tag{6-B6}$$

Δx and Δt are particle spacing and time step, respectively. Simulation has been conducted for 40 time step with Δt being $0.005s$. The arrangement of equations given above clearly show the solution steps for programing in which first, Eqs. (6-B1) to (6-B3) are solve and then particles are shifted to the new positions with updated velocity and internal energy using first order Euler forward time discretization scheme (Eq. (6-B4)). In the last step, pressure and artificial sound speed for each particle are updated using Eq. (6-B5). This procedure is repeated until $t = 0.2s$. In resolving the shock, the artificial viscosity (Π_{ij}) suggested by Monaghan [97] is typically used to prevent particle bunching and enhance the stability of the method as follows:

$$\begin{aligned} &\Pi_{ij} = \begin{cases} \dfrac{-\alpha \bar{c}_{ij} \phi_{ij} + \beta \phi_{ij}^2}{\bar{\rho}_{ij}} & \mathbf{u}_{ij} \cdot \mathbf{r}_{ij} < 0 \\ 0 & \mathbf{u}_{ij} \cdot \mathbf{r}_{ij} > 0 \end{cases} \\ &\phi_{ij} = \frac{h_{ij} (\mathbf{u}_{ij} \cdot \mathbf{r}_{ij})}{\left| r_{ij} \right|^2 + \varphi^2} \\ &\bar{c}_{ij} = \frac{c_i + c_j}{2}, \ \bar{\rho}_{ij} = \frac{\rho_i + \rho_j}{2}, \ \varphi = 0.01 h_{ij}, \ \alpha = \beta = 1 \end{aligned} \tag{6-B7}$$

Finally, Cubic [74] and Wendland [75] kernel functions which have been used for comparison purposes in section 3 are provided below:

$$\begin{aligned} &W_{ij} = \alpha \begin{cases} 2/3 - R^2 + R^3/2 & 0 \le R \le 1 \\ (2-R)^3/2 & 1 < R \le 2 \\ 0 & R > 2 \end{cases} \\ &\alpha_{1D} = \frac{1}{h}, \ \alpha_{2D} = \frac{15}{7\pi h^2}, \ \alpha_{3D} = \frac{3}{2\pi h^3}, \end{aligned} \tag{6-B8}$$

$$\begin{aligned} &W_{ij} = \alpha \begin{cases} (1 - R/2)^4 (2R+1) & 0 \le R < 2 \\ 0 & 2 \le R \end{cases} \\ &\alpha_{1D} = \frac{3}{4h}, \ \alpha_{2D} = \frac{7}{4\pi h^2}, \ \alpha_{3D} = \frac{21}{16\pi h^3}, \end{aligned} \tag{6-B9}$$

6.13 Appendix C (Hybrid Particle Shifting Technique)

Motivated by works of Xu et al. [43] and Lee et al. [58], along this appendix a novel Hybrid Particle Shifting Technique (HPST) is developed by the combination of the PST and collision models. The model consists of two separate parts namely: deriving new PST through Taylor series expansion and constructing a novel collision model based on the concept of the Discrete Element Method (DEM) [76]. By subtracting f_i from both sides of the Eq. (6-A1) and multiplying it first by $x_{ij}W_{ij}$ and then by $y_{ij}W_{ij}$ the following equations can be obtained:

$$(f_j - f_i)x_{ij}W_{ij} = f_x^{'}x_{ij}^2W_{ij} + f_y^{'}y_{ij}x_{ij}W_{ij} \tag{6-C1}$$

$$(f_j - f_i)y_{ij}W_{ij} = f_x^{'}x_{ij}y_{ij}W_{ij} + f_y^{'}y_{ij}^2W_{ij} \tag{6-C2}$$

By integrating both sides of Eqs. (6-C1) and (6-C2) over the neighbor particles and imposing the assumption of homogeneous particles distribution ($\sum_{j=1}^{N} x_{ij}y_{ij}W_{ij}dV = 0$), the first partial derivatives of shape function read as:

$$f_x^{'} = \frac{\sum_{j=1}^{N} x_{ij}(f_j - f_i)W_{ij}dV}{\sum_{j=1}^{N} x_{ij}^2W_{ij}dV} \qquad f_y^{'} = \frac{\sum_{j=1}^{N} y_{ij}(f_j - f_i)W_{ij}dV}{\sum_{j=1}^{N} y_{ij}^2W_{ij}dV} \tag{6-C3}$$

By eliminating the term (f_j-f_i) from Eq. (6-C3) and defining (λ) as a constant parameter, the final form of the PST can be written as:

$$\delta r_{i,x,PST} = \frac{-\beta}{\lambda}\sum_{j=1}^{N} x_{ij}W_{ij}dV \qquad \delta r_{i,y,PST} = \frac{-\beta}{\lambda}\sum_{j=1}^{N} y_{ij}W_{ij}dV \tag{6-C4}$$

$\beta = 0.5\alpha h^2$ is a shifting coefficient which controls the magnitude of particle displacement with $0 \le \alpha \le 1$. h and N denote the smoothing length and number of neighbor particles, respectively. The constant coefficient Lambda ($\lambda = \sum_{j=1}^{N} x_{ij}^2W_{ij}dV = \sum_{j=1}^{N} y_{ij}^2W_{ij}dV = \frac{1}{2}\sum_{j=1}^{N} r_{ij}^2W_{ij}dV$) should be calculated at the initial arrangement of particles (initial time step, t=0) where kernel has a fully

compact support (inner particles). In fact, in order to keep magnitude of particle shifting constant (δr_i), the parameter Lambda (λ) should remain unaltered during the simulation.

To derive the collision model, it is assumed that each fluid element is circular (in 2D space) or spherical (in 3D space) in shape with radii R_i. In the case of the physical contact ($\delta_{n,ij} = (R_j + R_i - \left|\vec{r}_j - \vec{r}_i\right|) > 0$), the normal collision forces ($f_{i,x}$ and $f_{i,y}$) with associated particle displacements ($\delta r_{i,x,DEM}$ and $\delta r_{i,y,DEM}$) can be calculated as follows:

$$\delta_{n,xij} = (R_j + R_i - \left|\vec{r}_j - \vec{r}_i\right|)\vec{n}_x \qquad \vec{n}_x = (\vec{x}_j - \vec{x}_i)\Big/\left|\vec{r}_{ij}\right| \tag{6-C5}$$

$$\delta_{n,yij} = (R_j + R_i - \left|\vec{r}_j - \vec{r}_i\right|)\vec{n}_y \qquad \vec{n}_y = (\vec{y}_j - \vec{y}_i)\Big/\left|\vec{r}_{ij}\right| \tag{6-C6}$$

$$f_{i,x} = -\sum_{j=1}^{N}(k_n\delta_{n,xij} + \gamma_n v_{n,xij}) \qquad \delta r_{i,x,DEM} = (dt)^2\ f_{i,x}/m_i \tag{6-C7}$$

$$f_{i,y} = -\sum_{j=1}^{N}(k_n\delta_{n,yij} + \gamma_n v_{n,yij}) \qquad \delta r_{i,y,DEM} = (dt)^2\ f_{i,y}/m_i \tag{6-C8}$$

where, k_n, $\vec{n}_{ij}$ and m_i denote normal spring stiffness of linear spring, normal unit vector and mass of particle. $\delta_{n,xij}$ and $\delta_{n,yij}$ are normal overlap distance between two contacting particles *i* and *j* with position vector $\vec{r}_{ij} = r_j - r_i$. $f_{i,x}$ and $f_{i,y}$ are sum of all contact forces from neighbor particles in *x* and y-directions. γ_n and $\vec{v}_n$ denote the normal damping and the normal velocity components in the x and y-directions ($v_{n,xij}, v_{n,yij}$) which can be computed as follows:

$$\vec{v}_{n,ij} = (\vec{v}_{ij} \cdot \vec{n}_{ij})\vec{n}_{ij} \tag{6-C9}$$

However, in order to preserve liner momentum, the value of γ_n is taken as zero in the current work.

6.14 References

[1] R. A. Gingold and J. J. Monaghan, “Smoothed particle hydrodynamics: theory and application to non-spherical stars,” Mon. Not. R. Astron. Soc., vol. 181, no. 3, pp. 375–389, 1977.

[2] K. W. Chu et al., “Understand solids loading effects in a dense medium cyclone: Effect of particle size by a CFD-DEM method,” Powder Technol., vol. 320, pp. 594–609, 2017.

[3] K. W. Chu, B. Wang, A. B. Yu, and A. Vince, “CFD-DEM modelling of multiphase flow in dense medium cyclones,” Powder Technol., vol. 193, no. 3, pp. 235–247, 2009.

[4] Q. Liu and Z.-H. Luo, “CFD-VOF-DPM simulations of bubble rising and coalescence in low hold-up particle-liquid suspension systems,” Powder Technol., vol. 339, pp. 459–469, 2018.

[5] H. Ma, Y. Zhao, and Y. Cheng, “CFD-DEM modeling of rod-like particles in a fluidized bed with complex geometry,” Powder Technol., vol. 344, pp. 673–683, 2019.

[6] G.-R. Liu and M. B. Liu, Smoothed particle hydrodynamics: a meshfree particle method. World Scientific, 2003.

[7] W.-J. Xu, X.-Y. Dong, and W.-T. Ding, “Analysis of fluid-particle interaction in granular materials using coupled SPH-DEM method,” Powder Technol., vol. 353, pp. 459–472, 2019.

[8] Z. Wu, F. Yu, P. Zhang, and X. Liu, “Micro-mechanism study on rock breaking behavior under water jet impact using coupled SPH-FEM/DEM method with Voronoi grains,” Eng. Anal. Bound. Elem., vol. 108, pp. 472–483, 2019.

[9] R. Tayeb, Y. Mao, and Y. Zhang, “Smoothed particle hydrodynamics simulation of granular system under cyclic compressions,” Powder Technol., vol. 353, pp. 84–97, 2019.

[10] J.-Y. Chen, F.-S. Lien, C. Peng, and E. Yee, “GPU-accelerated smoothed particle hydrodynamics modeling of granular flow,” Powder Technol., 2019.

[11] J. Chen, O. Orozovic, K. Williams, J. Meng, and C. Li, “A coupled DEM-SPH model for moisture migration in unsaturated granular material under oscillation,” Int. J. Mech. Sci., vol. 169, p. 105313, 2020.

[12] Z. L. Zhang, K. Walayat, C. Huang, J. Z. Chang, and M. B. Liu, “A finite particle method with particle shifting technique for modeling particulate flows with thermal convection,” Int. J. Heat Mass Transf., vol. 128, pp. 1245–1262, 2019.

[13] X. Yang and S.-C. Kong, “Numerical study of natural convection in a horizontal concentric annulus using smoothed particle hydrodynamics,” Eng. Anal. Bound. Elem., vol. 102, pp. 11–20, 2019.

[14] K. C. Ng, Y. L. Ng, T. W. H. Sheu, and A. Mukhtar, “Fluid-solid conjugate heat transfer modelling using weakly compressible smoothed particle hydrodynamics,” Int. J. Mech. Sci., vol. 151, pp. 772–784, 2019.

[15] K. C. Ng, Y. L. Ng, T. W. H. Sheu, and A. Alexiadis, “Assessment of Smoothed Particle Hydrodynamics (SPH) models for predicting wall heat transfer rate at complex boundary,” Eng. Anal. Bound. Elem., vol. 111, pp. 195–205, 2020.

[16] M. Hopp-Hirschler, M. S. Shadloo, and U. Nieken, “A Smoothed Particle Hydrodynamics approach for thermo-capillary flows,” Comput. Fluids, vol. 176, pp. 1–19, 2018.

[17] A. M. Aly and Z. A. S. Raizah, “Incompressible smoothed particle hydrodynamics (ISPH) method for natural convection in a nanofluid-filled cavity including rotating solid structures,” Int. J. Mech. Sci., vol. 146, pp. 125–140, 2018.

[18] R. Fatehi, A. Rahmat, N. Tofighi, M. Yildiz, and M. S. Shadloo, “Density-based smoothed particle hydrodynamics methods for incompressible flows,” Comput. Fluids, vol. 185, pp. 22–33, 2019.

[19] W. Wang, K. Yin, G. Chen, B. Chai, Z. Han, and J. Zhou, “Practical application of the coupled DDA-SPH method in dynamic modeling for the formation of landslide dam,” Landslides, vol. 16, no. 5, pp. 1021–1032, 2019.

[20] W. Wang, G. Chen, Y. Zhang, L. Zheng, and H. Zhang, “Dynamic simulation of landslide dam behavior considering kinematic characteristics using a coupled DDA-SPH method,” Eng. Anal. Bound. Elem., vol. 80, pp. 172–183, 2017.

[21] M.-P. Kurowski and H. Spliethoff, “Deposition and slagging in an entrained-flow gasifier with focus on heat transfer, reactor design and flow dynamics with SPH,” Fuel Process. Technol., vol. 152, pp. 147–155, 2016.

[22] K. Hosseini, P. Omidvar, M. Kheirkhahan, and S. Farzin, “Smoothed particle hydrodynamics for the interaction of Newtonian and non-Newtonian fluids using the μ (I) model,” Powder Technol., vol. 351, pp. 325–337, 2019.

[23] Q. Yang, J. Yao, Z. Huang, and M. Asif, “A comprehensive SPH model for three-dimensional multiphase interface simulation,” Comput. Fluids, vol. 187, pp. 98–106, 2019.

[24] M. S. Shadloo, A. Zainali, and M. Yildiz, “Simulation of single mode Rayleigh–Taylor instability by SPH method,” Comput. Mech., vol. 51, no. 5, pp. 699–715, 2013.

[25] E. A. Patino-Narino, A. F. Galvis, P. Sollero, R. Pavanello, and S. A. Moshkalev, “A consistent multiphase SPH approximation for bubble rising with moderate Reynolds numbers,” Eng. Anal. Bound. Elem., vol. 105, pp. 1–19, 2019.

[26] M. Hirschler, G. Oger, U. Nieken, and D. Le Touzé, “Modeling of droplet collisions using Smoothed Particle Hydrodynamics,” Int. J. Multiph. Flow, vol. 95, pp. 175–187, 2017.

[27] M. Ozbulut, M. Yildiz, and O. Goren, “A numerical investigation into the correction algorithms for SPH method in modeling violent free surface flows,” Int. J. Mech. Sci., vol. 79, pp. 56–65, 2014.

[28] G. Zhang, S. Wang, Z. Sui, L. Sun, Z. Zhang, and Z. Zong, “Coupling of SPH with smoothed point interpolation method for violent fluid-structure interaction problems,” Eng. Anal. Bound. Elem., vol. 103, pp. 1–10, 2019.

[29] A. Rahmat and M. Yildiz, “A multiphase ISPH method for simulation of droplet coalescence and electro-coalescence,” Int. J. Multiph. Flow, vol. 105, pp. 32–44, 2018.

[30] Q. Xiong, L. Deng, W. Wang, and W. Ge, “SPH method for two-fluid modeling of particle–fluid fluidization,” Chem. Eng. Sci., vol. 66, no. 9, pp. 1859–1865, 2011.

[31] M. Rezavand, C. Zhang, and X. Hu, “A weakly compressible SPH method for violent multi-phase flows with high density ratio,” J. Comput. Phys., vol. 402, p. 109092, 2020.

[32] P. Nair and G. Tomar, “Simulations of gas-liquid compressible-incompressible systems using SPH,” Comput. Fluids, vol. 179, pp. 301–308, 2019.

[33] T. Douillet-Grellier, F. De Vuyst, H. Calandra, and P. Ricoux, “Simulations of intermittent two-phase flows in pipes using smoothed particle hydrodynamics,” Comput. Fluids, vol. 177, pp. 101–122, 2018.

[34] L. Deng, Y. Liu, W. Wang, W. Ge, and J. Li, “A two-fluid smoothed particle hydrodynamics (TF-SPH) method for gas–solid fluidization,” Chem. Eng. Sci., vol. 99, pp. 89–101, 2013.

[35] A. Zainali, N. Tofighi, M. S. Shadloo, and M. Yildiz, “Numerical investigation of Newtonian and non-Newtonian multiphase flows using ISPH method,” Comput. Methods Appl. Mech. Eng., vol. 254, pp. 99–113, 2013.

[36] U. O. Ünal, G. Bilici, and H. Akyıldız, “Liquid sloshing in a two-dimensional rectangular tank: A numerical investigation with a T-shaped baffle,” Ocean Eng., vol. 187, p. 106183, 2019.

[37] P. N. Sun, A. Colagrossi, S. Marrone, M. Antuono, and A. M. Zhang, “Multi-resolution Delta-plus-SPH with tensile instability control: Towards high Reynolds number flows,” Comput. Phys. Commun., vol. 224, pp. 63–80, 2018.

[38] P. N. Sun, A. Colagrossi, S. Marrone, M. Antuono, and A.-M. Zhang, “A consistent approach to particle shifting in the δ-Plus-SPH model,” Comput. Methods Appl. Mech. Eng., vol. 348, pp. 912–934, 2019.

[39] C. Huang, T. Long, S. M. Li, and M. B. Liu, “A kernel gradient-free SPH method with iterative particle shifting technology for modeling low-Reynolds flows around airfoils,” Eng. Anal. Bound. Elem., vol. 106, pp. 571–587, 2019.

[40] M. S. Shadloo, A. Zainali, M. Yildiz, and A. Suleman, “A robust weakly compressible SPH method and its comparison with an incompressible SPH,” Int. J. Numer. Methods Eng., vol. 89, no. 8, pp. 939–956, 2012.

[41] Z.-B. Wang, R. Chen, H. Wang, Q. Liao, X. Zhu, and S.-Z. Li, “An overview of smoothed particle hydrodynamics for simulating multiphase flow,” Appl. Math. Model., vol. 40, no. 23–24, pp. 9625–9655, 2016.

[42] M. S. Shadloo, G. Oger, and D. Le Touzé, “Smoothed particle hydrodynamics method for fluid flows, towards industrial applications: Motivations, current state, and challenges,” Comput. Fluids, vol. 136, pp. 11–34, 2016.

[43] R. Xu, P. Stansby, and D. Laurence, “Accuracy and stability in incompressible SPH (ISPH) based on the projection method and a new approach,” J. Comput. Phys., vol. 228, no. 18, pp. 6703–6725, 2009.

[44] A. Skillen, S. Lind, P. K. Stansby, and B. D. Rogers, “Incompressible smoothed particle hydrodynamics (SPH) with reduced temporal noise and generalised Fickian smoothing applied to

body–water slam and efficient wave–body interaction," Comput. Methods Appl. Mech. Eng., vol. 265, pp. 163–173, 2013.

[45] A. Khayyer, H. Gotoh, and Y. Shimizu, "Comparative study on accuracy and conservation properties of two particle regularization schemes and proposal of an optimized particle shifting scheme in ISPH context," J. Comput. Phys., vol. 332, pp. 236–256, 2017.

[46] H. F. Schwaiger, "An implicit corrected SPH formulation for thermal diffusion with linear free surface boundary conditions," Int. J. Numer. Methods Eng., vol. 75, no. 6, pp. 647–671, 2008.

[47] G. Oger, M. Doring, B. Alessandrini, and P. Ferrant, "An improved SPH method: Towards higher order convergence," J. Comput. Phys., vol. 225, no. 2, pp. 1472–1492, 2007.

[48] P. N. Sun, D. Le Touzé, and A.-M. Zhang, "Study of a complex fluid-structure dam-breaking benchmark problem using a multi-phase SPH method with APR," Eng. Anal. Bound. Elem., vol. 104, pp. 240–258, 2019.

[49] J. Hongbin and D. Xin, "On criterions for smoothed particle hydrodynamics kernels in stable field," J. Comput. Phys., vol. 202, no. 2, pp. 699–709, 2005.

[50] X. Yang, M. Liu, and S. Peng, "Smoothed particle hydrodynamics modeling of viscous liquid drop without tensile instability," Comput. Fluids, vol. 92, pp. 199–208, 2014.

[51] X. F. Yang, S. L. Peng, and M. B. Liu, "A new kernel function for SPH with applications to free surface flows," Appl. Math. Model., vol. 38, no. 15–16, pp. 3822–3833, 2014.

[52] P. N. Sun, A. Colagrossi, S. Marrone, and A. M. Zhang, "The δplus-SPH model: simple procedures for a further improvement of the SPH scheme," Comput. Methods Appl. Mech. Eng., vol. 315, pp. 25–49, 2017.

[53] S. Marrone, A. Colagrossi, D. Le Touzé, and G. Graziani, "Fast free-surface detection and level-set function definition in SPH solvers," J. Comput. Phys., vol. 229, no. 10, pp. 3652–3663, 2010.

[54] S. J. Lind, R. Xu, P. K. Stansby, and B. D. Rogers, "Incompressible smoothed particle hydrodynamics for free-surface flows: A generalised diffusion-based algorithm for stability and

validations for impulsive flows and propagating waves," J. Comput. Phys., vol. 231, no. 4, pp. 1499–1523, 2012.

[55] S. Koshizuka and Y. Oka, "Moving-particle semi-implicit method for fragmentation of incompressible fluid," Nucl. Sci. Eng., vol. 123, no. 3, pp. 421–434, 1996.

[56] A. Haque and G. A. Dilts, "Three-dimensional boundary detection for particle methods," J. Comput. Phys., vol. 226, no. 2, pp. 1710–1730, 2007.

[57] Y. Lin, G. R. Liu, and G. Wang, "A particle-based free surface detection method and its application to the surface tension effects simulation in smoothed particle hydrodynamics (SPH)," J. Comput. Phys., vol. 383, pp. 196–206, 2019.

[58] B.-H. Lee, J.-C. Park, M.-H. Kim, and S.-C. Hwang, "Step-by-step improvement of MPS method in simulating violent free-surface motions and impact-loads," Comput. Methods Appl. Mech. Eng., vol. 200, no. 9–12, pp. 1113–1125, 2011.

[59] X. Chen, G. Xi, and Z.-G. Sun, "Improving stability of MPS method by a computational scheme based on conceptual particles," Comput. Methods Appl. Mech. Eng., vol. 278, pp. 254–271, 2014.

[60] T. Xu and Y.-C. Jin, "Improvement of a projection-based particle method in free-surface flows by improved Laplacian model and stabilization techniques," Comput. Fluids, vol. 191, p. 104235, 2019.

[61] A. Shakibaeinia and Y.-C. Jin, "MPS mesh-free particle method for multiphase flows," Comput. Methods Appl. Mech. Eng., vol. 229, pp. 13–26, 2012.

[62] R. M. Cabezón, D. García-Senz, and A. Relaño, "A one-parameter family of interpolating kernels for smoothed particle hydrodynamics studies," J. Comput. Phys., vol. 227, no. 19, pp. 8523–8540, 2008.

[63] D. A. Fulk and D. W. Quinn, "An analysis of 1-D smoothed particle hydrodynamics kernels," J. Comput. Phys., vol. 126, no. 1, pp. 165–180, 1996.

[64] M. B. Liu, G. R. Liu, and K. Y. Lam, "Constructing smoothing functions in smoothed particle hydrodynamics with applications," J. Comput. Appl. Math., vol. 155, no. 2, pp. 263–284, 2003.

[65] A. Khayyer, H. Gotoh, and Y. Shimizu, “A projection-based particle method with optimized particle shifting for multiphase flows with large density ratios and discontinuous density fields,” Comput. Fluids, vol. 179, pp. 356–371, 2019.

[66] E.-S. Lee, C. Moulinec, R. Xu, D. Violeau, D. Laurence, and P. Stansby, “Comparisons of weakly compressible and truly incompressible algorithms for the SPH mesh free particle method,” J. Comput. Phys., vol. 227, no. 18, pp. 8417–8436, 2008.

[67] A. M. Aly and S. E. Ahmed, “ISPH simulations for a variable magneto-convective flow of a ferrofluid in a closed space includes open circular pipes,” Int. Commun. Heat Mass Transf., vol. 110, p. 104412, 2020.

[68] A. Bejan, Entropy generation through heat and fluid flow. Wiley, 1982.

[69] G. H. R. Kefayati, “Simulation of double diffusive MHD (magnetohydrodynamic) natural convection and entropy generation in an open cavity filled with power-law fluids in the presence of Soret and Dufour effects (part II: entropy generation),” Energy, vol. 107, pp. 917–959, 2016.

[70] P. Biswal and T. Basak, “Bejan’s heatlines and numerical visualization of convective heat flow in differentially heated enclosures with concave/convex side walls,” Energy, vol. 64, pp. 69–94, 2014.

[71] S. Bhardwaj, A. Dalal, and S. Pati, “Influence of wavy wall and non-uniform heating on natural convection heat transfer and entropy generation inside porous complex enclosure,” Energy, vol. 79, pp. 467–481, 2015.

[72] G. G. Ilis, M. Mobedi, and B. Sunden, “Effect of aspect ratio on entropy generation in a rectangular cavity with differentially heated vertical walls,” Int. Commun. Heat Mass Transf., vol. 35, no. 6, pp. 696–703, 2008.

[73] S. Marrone, M. Antuono, A. Colagrossi, G. Colicchio, D. Le Touzé, and G. Graziani, “δ-SPH model for simulating violent impact flows,” Comput. Methods Appl. Mech. Eng., vol. 200, no. 13–16, pp. 1526–1542, 2011.

[74] J. J. Monaghan and J. C. Lattanzio, “A refined particle method for astrophysical problems,” Astron. Astrophys., vol. 149, pp. 135–143, 1985.

[75] H. Wendland, “Piecewise polynomial, positive definite and compactly supported radial functions of minimal degree,” Adv. Comput. Math., vol. 4, no. 1, pp. 389–396, 1995.

[76] H. R. Norouzi, R. Zarghami, R. Sotudeh-Gharebagh, and N. Mostoufi, Coupled CFD-DEM modeling: formulation, implementation and application to multiphase flows. John Wiley & Sons, 2016.

[77] C.-W. Shu and S. Osher, “Efficient implementation of essentially non-oscillatory shock-capturing schemes,” J. Comput. Phys., vol. 77, no. 2, pp. 439–471, 1988.

[78] A. J. Chorin, “Numerical solution of the Navier-Stokes equations,” Math. Comput., vol. 22, no. 104, pp. 745–762, 1968.

[79] X. Xu and X.-L. Deng, “An improved weakly compressible SPH method for simulating free surface flows of viscous and viscoelastic fluids,” Comput. Phys. Commun., vol. 201, pp. 43–62, 2016.

[80] X. Zheng, Q. W. Ma, and W. Y. Duan, “Incompressible SPH method based on Rankine source solution for violent water wave simulation,” J. Comput. Phys., vol. 276, pp. 291–314, 2014.

[81] C. F. Janßen, S. T. Grilli, and M. Krafczyk, “On enhanced non-linear free surface flow simulations with a hybrid LBM–VOF model,” Comput. Math. with Appl., vol. 65, no. 2, pp. 211–229, 2013.

[82] S. Kularathna and K. Soga, “Implicit formulation of material point method for analysis of incompressible materials,” Comput. Methods Appl. Mech. Eng., vol. 313, pp. 673–686, 2017.

[83] A. Issakhov, Y. Zhandaulet, and A. Nogaeva, “Numerical simulation of dam break flow for various forms of the obstacle by VOF method,” Int. J. Multiph. Flow, vol. 109, pp. 191–206, 2018.

[84] S. Koshizuka, Y. Oka, and H. Tamako, “A particle method for calculating splashing of incompressible viscous fluid,” American Nuclear Society, Inc., La Grange Park, IL (United States), 1995.

[85] J. W. Jacobs and I. Catton, “Three-dimensional Rayleigh-Taylor instability Part 1. Weakly nonlinear theory,” J. Fluid Mech., vol. 187, pp. 329–352, 1988.

[86] K. Guo, R. Chen, Y. Li, W. Tian, G. Su, and S. Qiu, “Numerical simulation of Rayleigh-Taylor Instability with periodic boundary condition using MPS method,” Prog. Nucl. Energy, vol. 109, pp. 130–144, 2018.

[87] G. Pahar and A. Dhar, “Mixed miscible-immiscible fluid flow modelling with incompressible SPH framework,” Eng. Anal. Bound. Elem., vol. 73, pp. 50–60, 2016.

[88] T. Basak, R. Anandalakshmi, P. Kumar, and S. Roy, “Entropy generation vs energy flow due to natural convection in a trapezoidal cavity with isothermal and non-isothermal hot bottom wall,” Energy, vol. 37, no. 1, pp. 514–532, 2012.

[89] D. Das and T. Basak, “Role of distributed/discrete solar heaters for the entropy generation studies in the square and triangular cavities during natural convection,” Appl. Therm. Eng., vol. 113, pp. 1514–1535, 2017.

[90] D. Das, L. Lukose, and T. Basak, “Role of multiple discrete heaters to minimize entropy generation during natural convection in fluid filled square and triangular enclosures,” Int. J. Heat Mass Transf., vol. 127, pp. 1290–1312, 2018.

[91] B. Nayroles, G. Touzot, and P. Villon, “Generalizing the finite element method: diffuse approximation and diffuse elements,” Comput. Mech., vol. 10, no. 5, pp. 307–318, 1992.

[92] Y. Krongauz and T. Belytschko, “Consistent pseudo-derivatives in meshless methods,” Comput. Methods Appl. Mech. Eng., vol. 146, no. 3–4, pp. 371–386, 1997.

[93] G. Oger, M. Doring, B. Alessandrini, and P. Ferrant, “An improved SPH method : Towards higher order convergence,” vol. 225, pp. 1472–1492, 2007.

[94] G. R. Johnson and S. R. Beissel, “Normalized smoothing functions for SPH impact computations,” Int. J. Numer. Methods Eng., vol. 39, no. 16, pp. 2725–2741, 1996.

[95] S. J. Cummins and M. Rudman, “An SPH projection method,” J. Comput. Phys., vol. 152, no. 2, pp. 584–607, 1999.

[96] E. Y. M. Lo and S. Shao, “Simulation of near-shore solitary wave mechanics by an incompressible SPH method,” Appl. Ocean Res., vol. 24, no. 5, pp. 275–286, 2002.

[97] J. J. Monaghan, “Smoothed particle hydrodynamics,” Annu. Rev. Astron. Astrophys., vol. 30, no. 1, pp. 543–574, 1992.

Chapter 7 ARTICLE 4: NUMERICAL SIMULATION OF RAYLEIGH-BÉNARD CONVECTION AND THREE-PHASE RAYLEIGH-TAYLOR INSTABILITY USING A MODIFIED MPS METHOD

Faroogh Garoosi[*,a], Ahmad Shakibaeinia[a,b]

[a]Department of Civil, Geological and Mining Engineering, Polytechnique Montreal, Montreal, Quebec, Canada

[b]Canada Research Chair in Computational Hydrosystems, Canada

Corresponding author: faroogh.garoosi@polymtl.ca,

Second author: ahmad.shakibaeinia@polymtl.ca

Abstract

The main objective of the current work is to enhance consistency and capabilities of Moving Particle Semi-implicit (MPS) method for simulating a wide range of free-surface flows and convection heat transfer. For this purpose, two novel high-order gradient and Laplacian operators are derived from the Taylor series expansion and are applied for the discretization of governing equations. Furthermore, the combination of the explicit Third-order TVD Runge-Kutta scheme and two-step projection algorithm is employed to approximate transient terms in the Navier-stokes and energy equations. To further improve the accuracy and performance of the method, a new kernel function is constructed by a combination of the Gaussian and cosine functions and then implemented for modeling the 1D Sod shock tube problem. Validation and verification of the proposed model are conducted through the simulations of several canonical test cases such as: dam break, rotation of a square patch of fluid, two-phase Rayleigh-Taylor instability, oscillating concentric circular drop and good agreement are achieved. The proposed model is then employed to simulate three-phase Rayleigh-Taylor instability and entropy generation due to natural convection heat transfer (Differentially Heated Cavity and Rayleigh-Bénard convection). The obtained results reveal that, the newly constructed kernel function provides more reliable results in comparison with two frequently used kernel functions namely; quartic spline and Wendland. Furthermore, it is found that, the enhanced MPS model is capable of handling multiphase flow problems with low and high density contrast.

Keywords: New Kernel Function; New gradient operator; New Laplacian operator; Third-order TVD Runge-Kutta; High-order MPS; Natural convection

7.1 Introduction

The Moving Particle Semi-implicit (MPS) method belongs to a group of truly Lagrangian mesh-free (particle) methods for continuum modelling, which was originally pioneered in the work of Koshizuka et al. [1] to investigate incompressible fluid flow with free surfaces. Contrary to conventional Eulerian methods with topological constraints (mesh distortion) [2], [3], the MPS takes the advantages of being Lagrangian and free from any mesh system, which make it fairly natural in modeling of violent free-surface flows, particularly those involving large deformation, fragmentation and breaking. Similar to other particle methods like Smoothed Particle Hydrodynamics (SPH), MPS represents the continuum fluid by a finite set of "discrete particles" where the interaction of freely-moving particles is determined by means of specific smoothing or kernel function. In view of its flexibility and potential effectiveness in handling highly nonlinear multi-physical interaction problem and convection-dominated transport phenomena, applications have been extended to various engineering and science problems [4]. Simulation of wave-structure interaction [5], analysis of natural/forced convection heat transfer and Arc welding [6], [7], nuclear reactor design and dynamic analysis of landslide [8], [9], modeling of violent free-surface flows [10], simulation of multiphase flows and solid-liquid phase change process [11]–[13], analysis of liquid droplet and liquid jet atomization [14], [15] are just a few examples of such studies in which particle methods such as MPS were adopted to solve complex flow and transport problems. An up-to-date comprehensive literature review concerning recent applications and future prospects of the meshless particle methods can be found in works of Wang et al. [16] and Shadloo et al. [17].

Despite several advantages, similar to other particle methods, MPS has several drawbacks including unphysical pressure fluctuations and particle clustering [18]–[21], uncertainty in the selection of appropriate kernel function, implementing discretization schemes with low order of accuracy in space and time [22]–[26] and non-conservative form of pressure gradient operator [27]–[29]. Over the past decade, substantial research efforts have been devoted to enhancing the accuracy and stability of particle methods such as MPS. As pointed out in [4], one of the major factors for the loss of accuracy in the particle methods comes from the inconsistency in governing

operators. MPS (and SPH) are formulated based on the hypothesis that particles are distributed evenly across the whole computational domain whereas this assumption is not valid in certain regions characterized by truncated kernel function or unphysical particle accumulation (depletion) [30]. To overcome this shortcoming and reduce the truncation error associated with low order discretization schemes, Oger et al. [22] introduced the concept of Renormalization technique based on a Taylor series expansion. This technique was then adopted by Khayyer et al. [24] and Xu et al. [26] in the context of the MPS to establish the high-order gradient operator. They showed that, reproducing the gradient operator through implementing corrective matrix can significantly minimize the spurious pressure oscillations and provide more homogeneous particle distributions, accordingly. Similar observations were reported by Liu et al. [23] and Duan et al. [25] who developed two novel high-order Laplacian models by eliminating the first-order partial derivatives from the Taylor-series expansion. They reported that, the corrected Laplacian model can effectively reduce the solution fluctuations and provide more accurate results than the classical MPS formulations. To decrease numerical discretization errors generated by solving non-conservative form of momentum equation, Sun et al. [27], [28] presented a novel switching technique so-called Tensile Instability Control (TIC) that was achieved by altering Navier-Stokes equations into the non-conservative form in the specific regions characterized by numerical cavitation and particle bunching. To fulfil the conservation law while preserving the first-order completeness, Garoosi et al. [29] proposed a new hybrid pressure gradient operator (for a kernel-derivative-free SPH, which mimics the characteristics of MPS) based on Renormalization technique [26] and Tensile Instability Control (TIC) [27], [28] and showed that, the newly-hybrid method can efficiently remove the particle clustering and undesirable pressure noise from the free-surface area. As stated before, another major source of instability can be traced back to the Lagrangian nature of the MPS model. Generally, particles in the Lagrangian framework have a tendency to travel along the streamline trajectory, resulting in the occurrence of void formation or particle stratification within the fluid domain. This inconsistency leads to a serious degradation of interpolation procedure and loss of accuracy [31], [32]. To attenuate adverse effects of tensile instability and maintain nearly uniform particle distribution, in a pioneering works, Xu et al. [18] and Shadloo et al. [19] suggested the use of rearranging the particle position (artificial particle displacement) that was achieved by slightly deflecting particles across streamlines, thereby avoiding the substantial stretching and clumping of particles. They found that, implementing

particle shifting/reordering scheme can help achieving more reliable, stable and noise-free solutions even at high Reynolds numbers without sacrificing precision. However, the results of Lind et al. [21] showed that, the PST causes particles to escape from free-surface area, resulting in an unrealistic particle scattering (particle separation) within the computational domain. To address this limitation, Khayyer et al. [20] proposed an optimized version of the Particle Shifting Technique (OPS) via a careful elimination of the normal shifting from the free-surface area and its nearby particles. Uncertainty in the selection of appropriate kernel function is another factor which can immensely influence the performance of the particles methods [33]. Hongbin et al. [34] conducted a comparative investigation on various types of the kernel functions and concluded that, Gaussian and Q-spline kernels considerably outperformed the existing Cubic and Quartic kernels in modeling one dimensional shock tube problem. Liu et al. [35] presented a general approach for constructing an efficient kernel function and demonstrated that, the smoothness of the first and second derivatives of kernel function has a significant impact on the accuracy and stability of the numerical simulations. Similar findings were documented by Yang et al. [36], [37] who constructed two new kernel functions (hyperbolic-shaped and double cosine kernels) for modeling viscous liquid drop and water entry of a horizontal circular cylinder. Despite the success of these attempts, choosing an efficient smoothing function is still a subject of controversy [38]–[40].

In light of the above literature review, the primary objective of the present work is to introduce two new higher-order gradient and Laplacian operators to enhance the accuracy and convergence performance of the original MPS approach in modeling free-surface flows and convection heat transfer. For this purpose, the classical governing operators are first reformulated based on the Taylor series expansion and are then employed for discretization of diffusion terms, Pressure Poisson's equation (PPE) and divergence of velocity. To further suppress the error caused by irregular particle distribution, a novel high-order kernel function is constructed by combination of the Gaussian and cosine functions. To maintain overall high-order accuracy, the combination of the third-order TVD Runge-Kutta scheme and two-step projection method is used for the treatment of the transient terms in the Navier-stokes and energy equations. The feasibility and validity of the proposed models are verified via simulation of four different challenging benchmark cases including dam break, rotation of a square patch of fluid, two-phase Rayleigh-Taylor instability and oscillating concentric circular drop.

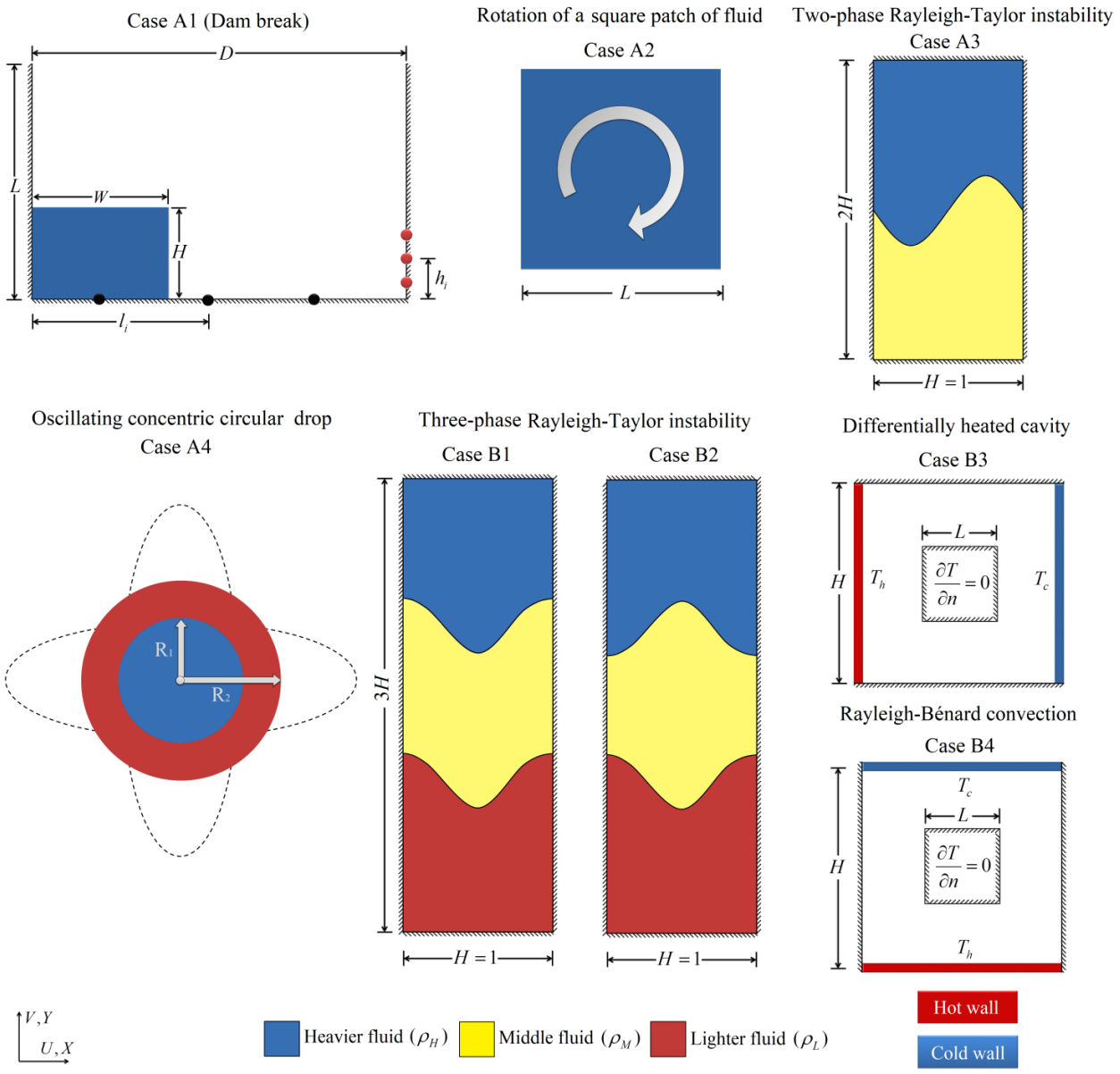

Figure 7-1 Schematic diagram of eight different canonical test cases with associated boundary conditions and coordinate system.

7.2 Problem statement and governing equations

Schematic representation of eight different canonical test cases with associated boundary conditions and coordinate system are sketched in Fig. 7-1. In all the simulations, the flow is considered to be laminar, two-dimensional, Newtonian and incompressible except for the case of 1D Sod shock tube problem where the gas is compressed isentropically in accordance with a stiff

equation of state (EOS). The thermo-physical properties of the fluid are assumed to be constant except for the density in cases B3 and B4 which varies linearly according to the Oberbeck-Boussinesq approximation.

Based on the aforementioned assumptions, the continuity, momentum, energy and displacement equations in the Lagrangian description read as follows [41]:

$$\frac{\partial u}{\partial x}+\frac{\partial v}{\partial y}=0, \tag{7-1}$$

$$\frac{D\rho u}{Dt}=-\frac{\partial p}{\partial x}+\mu\left(\frac{\partial^2 u}{\partial x^2}+\frac{\partial^2 u}{\partial y^2}\right), \tag{7-2}$$

$$\frac{D\rho v}{Dt}=-\frac{\partial p}{\partial y}+\mu\left(\frac{\partial^2 v}{\partial x^2}+\frac{\partial^2 v}{\partial y^2}\right)+F_b, \tag{7-3}$$

$$\frac{D\rho C_p T}{Dt}=k\left(\frac{\partial^2 T}{\partial x^2}+\frac{\partial^2 T}{\partial y^2}\right), \tag{7-4}$$

$$\frac{D\mathbf{r}}{Dt}=\mathbf{u}, \tag{7-5}$$

where **u**: (u, v) and **r**: (x, y) represent fluid velocity and position vectors. ρ, μ, k and C_p are fluid density, dynamic viscosity, thermal conductivity and specific heat capacity, respectively. D denotes the substantial derivative and t is time. The flow motion is mainly governed by the external body force per unit mass (F_b) exerted on the particle which would be gravity force ($F_b=\rho g$) in the multiphase flows or buoyancy force ($F_b=-\rho g\,\beta(T-T_c)$) in the natural convection heat transfer. By introducing following non-dimensional parameters:

$$\begin{gathered} X=\frac{x}{H},\qquad Y=\frac{y}{H},\qquad U=\frac{uH}{\alpha},\qquad V=\frac{vH}{\alpha},\qquad P=\frac{pH^2}{\rho\alpha^2},\qquad \theta=\frac{T-T_c}{T_h-T_c}. \\ t^*=\frac{t\alpha}{H^2},\qquad Ra=\frac{g\beta(T_h-T_c)H^3}{\alpha\nu},\qquad \mathrm{Pr}=\frac{\nu}{\alpha}. \end{gathered} \tag{7-6}$$

Eqs. (7-1) to (7-5) can be converted to the following non-dimensional forms for the case of natural convection heat transfer:

$$\frac{\partial U}{\partial X}+\frac{\partial V}{\partial Y}=0, \tag{7-7}$$

$$\frac{DU}{Dt^*}=-\frac{\partial P}{\partial X}+\Pr\,(\frac{\partial^2 U}{\partial X^2}+\frac{\partial^2 U}{\partial Y^2}), \tag{7-8}$$

$$\frac{DV}{Dt^*}=-\frac{\partial P}{\partial Y}+\Pr(\frac{\partial^2 V}{\partial X^2}+\frac{\partial^2 V}{\partial Y^2})+Ra\,\Pr\theta, \tag{7-9}$$

$$\frac{D\theta}{Dt^*}=(\frac{\partial^2 \theta}{\partial X^2}+\frac{\partial^2 \theta}{\partial Y^2}), \tag{7-10}$$

$$\frac{D\mathbf{r}}{Dt^*}=\mathbf{U}, \tag{7-11}$$

where *Pr* and *Ra* are Prandtl number and Rayleigh number, respectively. As described by Bejan [42], dimensionless form of the entropy generation rate (S_{tot}) due to heat transfer (S_T) and fluid friction irreversibility (S_F) for 2D problems can be expressed as:

$$S_T=\left[\left(\frac{\partial\theta}{\partial X}\right)^2+\left(\frac{\partial\theta}{\partial Y}\right)^2\right] \tag{7-12}$$

$$S_F=\varphi\left[2\left(\frac{\partial U}{\partial X}\right)^2+2\left(\frac{\partial V}{\partial Y}\right)^2+\left(\frac{\partial U}{\partial y}+\frac{\partial V}{\partial X}\right)^2\right] \tag{7-13}$$

φ is called irreversibility factor which represents the ratio of the fluid friction to the thermal dissipation. It is given as [43], [44]:

$$\varphi=\frac{\mu T_0\alpha^2}{kH^2(T_h-T_c)^2}, \tag{7-14}$$

In the present work, the value of φ in cases B3 and B4 is considered as 10^{-4} similar to previous works of Ilis et al. [45] and Biswal et al. [46]. The global average entropy generation ($\overline{S}_{tot}$) due to both factors (S_T , S_F) can be calculated via integrating the local entropy generation rates over the whole domain:

$$\overline{S}_T=\frac{1}{V}\int S_T dX\,dY \qquad \overline{S}_F=\frac{1}{V}\int S_F dX\,dY \qquad \overline{S}_{tot}=\overline{S}_T+\overline{S}_F \tag{7-15}$$

The relative contribution of heat transfer irreversibility to the total entropy generation rate can be mathematically defined by calculating local and average Bejan numbers as [47]:

$$Be = \frac{S_T}{S_T + S_F} \qquad \overline{Be} = \frac{1}{V}\int Be\, dX\, dY \tag{7-16}$$

According to the above definition, $0 \le Be < 0.5$ implies the relative dominance of the viscous dissipation (S_F) whereas $0.5 < Be \le 1$ indicates that heat transfer irreversibility (S_T) is dominant. However, for the case of $Be = 0.5$, entropy generation due to the viscous effects and heat transfer have the same order of magnitude.

Once the temperature distribution is calculated, the net rate of heat transfer within the enclosure can be quantified by means of the average Nusselt number as follows:

$$Nu = \frac{hH}{k} = -\frac{\partial \theta}{\partial \vec{n}} \qquad \overline{Nu} = \frac{1}{H}\int_0^H \frac{\partial \theta}{\partial X} dY \qquad \overline{Nu} = \frac{1}{H}\int_0^H \frac{\partial \theta}{\partial Y} dX \tag{7-17}$$

As shown in Fig. 7-1, no-slip boundary condition is imposed on the impermeable surfaces as follows:

$$U = V = 0, \tag{7-18}$$

For the specific case of the convection heat transfer (cases B3 and B4), the energy equation (Eq. (7-10)) is subjected to the following boundary conditions;

$$\begin{aligned} &\theta = 1,\ \theta = 0 && \text{On the heated and cooled walls} \\ &\frac{\partial \theta}{\partial \vec{n}} = 0 && \text{On the adiabatic walls} \end{aligned} \tag{7-19}$$

7.3 Implementing boundary condition in a Lagrangian framework

As highlighted before, unlike the conventional Eulerian mesh-based methods, addressing the influence of the solid walls in the purely Lagrangian mesh-free models such as MPS and SPH is not often as straightforward as it seemed. In the present work, the dynamic ghost particle technique suggested by Marrone et al. [48] is employed to satisfy no-slip and no-penetration conditions on the rigid walls. Fig. 7-2 reveals that, in this technique, both tangential and normal

component of fluid velocity with opposite sign (no-slip) is extrapolated on the corresponding wall particles outside of the flow domain. However, to impose the Neumann boundary condition, the target variable (i.e. pressure (p_i) or temperature (θ_i) on the isolated walls) is first computed on the solid boundary line using Eq. (7-20), and then the predicted values are assigned to the corresponding ghost particles in the same row, column (i.e *W1*,*W2* and *W3*) or corner (*C1* to *C9*). Note that, as schematically shown in Fig. 7-2, only the fluid particles in the support domain of the kernel function are utilized to approximate the pressure or temperature on the fixed ghost particles.

$$\begin{bmatrix} p_i \\ p_{i,x} \\ p_{i,y} \end{bmatrix} = L \begin{bmatrix} \sum_{j=1}^{N} \frac{p_j W_{ij}}{|r_{ij}|} dV \\ \sum_{j=1}^{N} \frac{p_j x_{ij} W_{ij}}{|r_{ij}|} dV \\ \sum_{j=1}^{N} \frac{p_j y_{ij} W_{ij}}{|r_{ij}|} dV \end{bmatrix} \qquad \begin{bmatrix} \theta_i \\ \theta_{i,x} \\ \theta_{i,y} \end{bmatrix} = L \begin{bmatrix} \sum_{j=1}^{N} \frac{\theta_j W_{ij}}{|r_{ij}|} dV \\ \sum_{j=1}^{N} \frac{\theta_j x_{ij} W_{ij}}{|r_{ij}|} dV \\ \sum_{j=1}^{N} \frac{\theta_j y_{ij} W_{ij}}{|r_{ij}|} dV \end{bmatrix} \tag{7-20}$$

In above equation, *L* denotes renormalized matrix defined by

$$L = \begin{bmatrix} \sum_{j=1}^{N} \frac{W_{ij}}{|r_{ij}|} dV & \sum_{j=1}^{N} \frac{x_{ij} W_{ij}}{|r_{ij}|} dV & \sum_{j=1}^{N} \frac{y_{ij} W_{ij}}{|r_{ij}|} dV \\ \sum_{j=1}^{N} \frac{x_{ij} W_{ij}}{|r_{ij}|} dV & \sum_{j=1}^{N} \frac{x_{ij}^2 W_{ij}}{|r_{ij}|} dV & \sum_{j=1}^{N} \frac{x_{ij} y_{ij} W_{ij}}{|r_{ij}|} dV \\ \sum_{j=1}^{N} \frac{y_{ij} W_{ij}}{|r_{ij}|} dV & \sum_{j=1}^{N} \frac{x_{ij} y_{ij} W_{ij}}{|r_{ij}|} dV & \sum_{j=1}^{N} \frac{y_{ij}^2 W_{ij}}{|r_{ij}|} dV \end{bmatrix}^{-1} \tag{7-21}$$

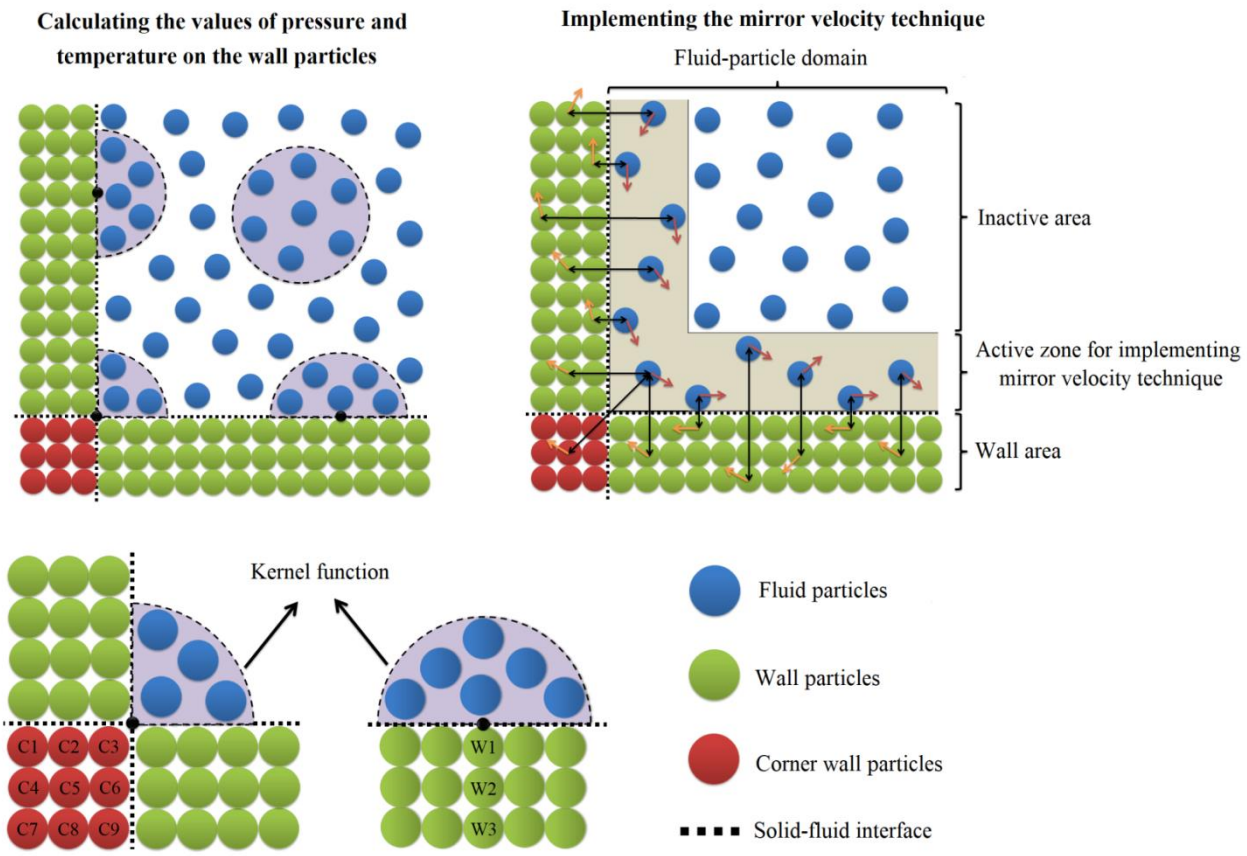

Figure 7-2 The conceptual illustrations of implementing Neumann ($\partial p/\partial n = 0,\ \partial \theta/\partial n = 0$) and Dirichlet (mirror velocity technique, $\mathbf{u} = 0$) boundary conditions in the context of the Lagrangian particle method.

For more details see also Eq. (7-A2) in appendix A. It is worth to mention that, the enhanced version of the imposition of the Neumann boundary condition can be found in works of Matsunaga et al. [49] and Duan et al. [50].

7.4 New kernel function

Inspired by works of Hongbin et al. [51] and Yang et al. [36], [37], in this section, a novel high-order smoothing kernel is constructed by merging the Gaussian and cosine functions as follows:

$$W_{ij} = \alpha_D \begin{cases} \cos^{3.5}(\frac{\pi R}{6}) \times e^{(\frac{-R^2}{\pi})} & 0 \le R \le 3 \\ 0 & R > 3 \end{cases} \qquad (7\text{-}22)$$

$$\alpha_{1D} = \frac{0.518442932}{h},\ \alpha_{2D} = \frac{0.274031624}{h^2},\ \alpha_{3D} = \frac{0.147708163}{h^3},$$

In above equation, h and $R = \left|\mathbf{r_{ij}}\right| / h$ are smoothing length and support domain of the kernel function, respectively. α_D is the *dimension-dependent normalization constant* [35] which satisfies an essential requirement of being unity ($\sum_{j=1}^{N} W_{ij} dV = 1$) in all the three dimensions. It is evident from Fig. 7-3 that, the newly constructed kernel function is non-negative ($W_{ij}(0 \le R \le 3) \ge 0$) (*Positivity*), even (*Symmetric property*) and decays monotonically as the relative distance (*R*) augments (*Decay property*). In addition, owing to the simultaneous presence of the Gaussian ($Exp(\frac{-R^2}{\pi})$) and cosine ($\cos^{3.5}(\frac{\pi R}{6})$) functions, it is outstandingly continuous with the compact support of $R = 3$ even for higher derivatives of kernel function ($\nabla^3 W_{ij}$, *Smoothness criteria*). The new kernel also fulfills the Dirac delta function condition when its support domain approaches zero ($\lim_{h \to 0} W_{ij}(h, R) = \delta$, *Delta function property*) [52]. The performance and consistency of proposed kernel function are also demonstrated via numerical modeling of 1D Sod shock tube problem where two following well-known kernels (i.e. Wendland [53] and quintic spline [52]) are used for comparison purposes. The predicted results in terms of gas velocity, density, internal energy and pressure profiles at time t=0.2s are plotted in Fig. 7-3. The comparison with reference exact solution reveals that, the proposed kernel function is stable and reproduces much more accurate solutions than the Wendland and quintic spline kernels in the area of rarefaction wave ($-0.3 < x < 0$), contact discontinuities ($0.1 < x < 0.15$) and shock wave ($x = 0.3$). It is evident that, the variations of density, pressure and velocity across the contact surface and expansion wave are continuous and the shock position is captured with no smearing or overshoots while large amplitudes of oscillations take place in the results obtained using two other kernels.

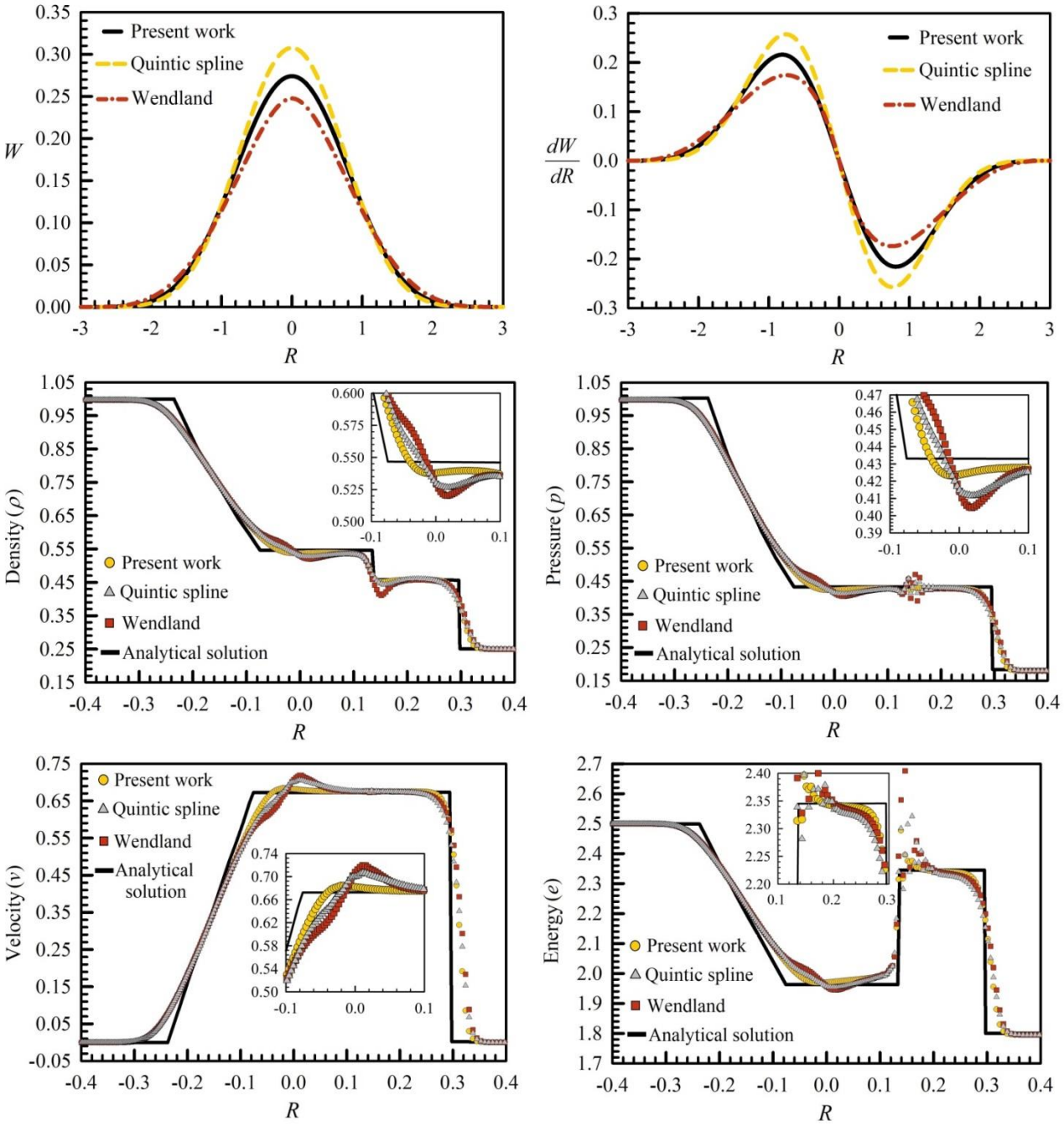

Figure 7-3 The effects of the kernel type on the spatial variation of density, pressure, velocity and internal energy along the shock tube at t=0.2s .

$$W_{ij} = \alpha \begin{cases} (1-R/2)^4(2R+1) & 0 \le R < 2 \\ 0 & 2 \le R \end{cases}$$
$$\alpha_{1D} = \frac{3}{4h},\ \alpha_{2D} = \frac{7}{4\pi h^2},\ \alpha_{3D} = \frac{21}{16\pi h^3}, \tag{7-23}$$

$$W_{ij} = \alpha \begin{cases} (3-R)^5 - 6(2-R)^5 + 15(1-R)^5 & 0 \le R \le 1 \\ (3-R)^5 - 6(2-R)^5 & 1 < R \le 2 \\ (3-R)^5 & 2 < R \le 3 \\ 0 & R > 3 \end{cases}$$
$$\alpha_{1D} = \frac{1}{120h},\ \alpha_{2D} = \frac{7}{478\pi h^2},\ \alpha_{3D} = \frac{1}{120\pi h^3}, \tag{7-24}$$

A more detailed description of the underlying methodology and discretization process can be found in appendix B.

7.4.1 Discretization of governing equations and solution methodology

The non-linear governing equations (7-1)-(7-5) with associated boundary conditions (Eqs. (7-18) and (7-19)) are discretized over a set of mobile particles in the context of the Moving Particle Semi-implicit (MPS) method where the contribution of each neighboring particle is approximated by the use of the newly proposed smoothing kernel (Eq. (7-22)). In the current work, the combination of the third-order TVD Runge-kutta scheme [54] and classical two-step projection method [55] has been employed for the treatment of the velocity-pressure coupling and transient terms. The aforementioned algorithm separates calculations into three distinct stages (i.e. explicit, implicit and explicit) at each intermediate step of the Runge–Kutta scheme (TVD-RK3). In the first explicit stage, an auxiliary velocity is estimated through Navier-Stokes equations without the pressure term as follows:

$$\mathbf{u}^* = \mathbf{u}^n + (\upsilon \nabla^2 \mathbf{u}^n + \mathbf{F}_B / \rho)\Delta t \tag{7-25}$$

In the implicit stage, pressure is evaluated through PPE by taking into consideration the fluid incompressible condition ($\nabla \cdot u^1 = 0$) as:

$$\nabla^2 p^1 = \frac{\rho \nabla \cdot \mathbf{u}^*}{\Delta t} \tag{7-26}$$

The superscript (^{1}) denotes the first step of the TVD-RK3. The above equation is discretized using the proposed Laplacian and gradient operators as follows (see also Eqs. (7-A10) and (7-A15) in appendix A):

$$\frac{\frac{1}{2}\sum_{j=1}^{N}(p_j - p_i)W_{ij}dV - p_{i,x}\sum_{j=1}^{N}x_{ij}W_{ij}dV}{\sum_{j=1}^{N}\frac{1}{2}x_{ij}^2W_{ij}dV} + \frac{\frac{1}{2}\sum_{j=1}^{N}(p_j - p_i)W_{ij}dV - p_{i,y}\sum_{j=1}^{N}y_{ij}W_{ij}dV}{\sum_{j=1}^{N}\frac{1}{2}y_{ij}^2W_{ij}dV} = \frac{\rho_s}{\Delta t}\sum_{j=1}^{N}\frac{(\mathbf{u}_j^* - \mathbf{u}_i^*)\cdot\mathbf{r}_{ij}}{|\mathbf{r}_{ij}|}(L)W_{ij}dV \tag{7-27}$$

where L is the corrective matrix and $p_{i,x}$ and $p_{i,y}$ denote pressure gradients which should be calculated via Eq. (7-36). In the last explicit stage, the material derivatives of velocity ($D\mathbf{u}/Dt$) and energy (DT/Dt) are computed through Eqs. (7-2) to (7-4) as follows:

$$\frac{D\mathbf{u}^n}{Dt} = -\frac{\nabla p^1}{\rho} + \frac{\mu}{\rho}\nabla^2\mathbf{u}^n + \frac{\mathbf{F}_B}{\rho} \tag{7-28}$$

$$\frac{DT^n}{Dt} = \frac{k}{\rho C_p}\nabla^2 T^n \tag{7-29}$$

After solving equations (7-28) and (7-29), the first step of the Runge-Kutta scheme can be accomplished as follows:

$$\begin{aligned}\mathbf{u}^{(1)} &= \mathbf{u}^{(n)} + \Delta t\frac{D\mathbf{u}^{(n)}}{Dt}\\ \mathbf{r}^{(1)} &= \mathbf{r}^{(n)} + \Delta t\,\mathbf{u}^{(1)}\\ \theta^{(1)} &= \theta^{(n)} + \Delta t\frac{D\theta^{(n)}}{Dt}\end{aligned} \tag{7-30}$$

By repeating the above procedure with updated values of $\mathbf{u}^{(1)}$, $\mathbf{r}^{(1)}$ and $\theta^{(1)}$ (instead of the $\mathbf{u}^n$, $\mathbf{r}^n$ and θ^n), the second step of the TVD-RK3 scheme can be fulfilled as below:

$$\mathbf{u}^{(2)} = \frac{3}{4}\mathbf{u}^{(n)} + \frac{1}{4}\mathbf{u}^{(1)} + \frac{1}{4}\Delta t \frac{D\mathbf{u}^{(1)}}{Dt}$$
$$\mathbf{r}^{(2)} = \frac{3}{4}\mathbf{r}^{(n)} + \frac{1}{4}\mathbf{r}^{(1)} + \frac{1}{4}\Delta t\, \mathbf{u}^{(2)} \qquad (7\text{-}31)$$
$$\theta^{(2)} = \frac{3}{4}\theta^{(n)} + \frac{1}{4}\theta^{(1)} + \frac{1}{4}\Delta t \frac{D\theta^{(1)}}{Dt}$$

This trend is continued for the third (last) step where particles are advected to the new positions ($\mathbf{r}^{(n+1)}$) with the modified velocity ($\mathbf{u}^{(n+1)}$) and temperature ($\theta^{(n+1)}$) as follows:

$$\mathbf{u}^{(n+1)} = \frac{1}{3}\mathbf{u}^{(n)} + \frac{2}{3}\mathbf{u}^{(2)} + \frac{2}{3}\Delta t \frac{D\mathbf{u}^{(2)}}{Dt}$$
$$\mathbf{r}^{(n+1)} = \frac{1}{3}\mathbf{r}^{(n)} + \frac{2}{3}\mathbf{r}^{(2)} + \frac{2}{3}\Delta t\, \mathbf{u}^{(n+1)} \qquad (7\text{-}32)$$
$$\theta^{(n+1)} = \frac{1}{3}\theta^{(n)} + \frac{2}{3}\theta^{(2)} + \frac{2}{3}\Delta t \frac{D\theta^{(2)}}{Dt}$$

where $D\mathbf{u}^{(2)}/Dt$ and $D\theta^{(2)}/Dt$ are updated substantial derivatives of velocity components and temperature field. As stated earlier, particles in Lagrangian framework have a natural tendency to migrate along the streamline, leading to the formation of either empty space or the occurrence of the particle clumping within the computational domain. Therefore, to preclude particle bunching and circumvent the instability introduced by ill-distributed particles, the Optimized Particle Shifting (OPS) technique [56] in the context of the MPS [29] is applied on the particle positions as follows:

$$\mathbf{r}_i^{(n+1)*} = \mathbf{r}_i^{(n+1)} + \delta\mathbf{r}_{i,PS}^{(n+1)} \quad \text{for inner particles}$$
$$\mathbf{r}_{i,t}^{(n+1)*} = \mathbf{r}_i^{(n+1)} + \delta\mathbf{r}_{i,OPS}^{(n+1)} \quad \text{for surface and vicinity particles} \qquad (7\text{-}33)$$

$\delta\mathbf{r}_{i,PS}^{(n+1)}$ and $\delta\mathbf{r}_{i,OPS}^{(n+1)}$ are particle shifting displacement which can be computed as follows:

$$\nabla C_{i,x} = \frac{2}{\lambda}\sum_{j=1}^{N} x_{ij} W_{ij} \frac{m_j}{\rho_j} \qquad \nabla C_{i,y} = \frac{2}{\lambda}\sum_{j=1}^{N} y_{ij} W_{ij} \frac{m_j}{\rho_j} \qquad \lambda = \sum_{j=1}^{N} r_{ij}^2 W_{ij} \frac{m_j}{\rho_j}$$
$$\delta\mathbf{r}_{i,PS}^{(n+1)} = -D \times \nabla C_i \qquad \delta\mathbf{r}_{i,OPS}^{(n+1)} = -D \times (I - n_i \otimes n_i) \cdot \nabla C_i \qquad D = 0.5\alpha h^2 \qquad (7\text{-}34)$$

Table 7.1 List of the operators used for discretization of diffusion and gradient terms.

Operator	Equation used
Divergence (for velocity) ($\mathbf{u}_x^{'}, \mathbf{u}_y^{'}$) Gradient (for temperature) ($\theta_x^{'}, \theta_y^{'}$)	Eq. (7-A10) is implemented in the present study whereas Eq. (7-A3), (7-A5), (7-A8), (7-A9) or (7-A11) can also be used.
Gradient (for pressure) ($p_x^{'}, p_y^{'}$)	Revised form of the Eq. (7-A10) is applied in the current work where $\chi = 1$ and $\chi = -1$ are used for inner and surface particles, respectively. (see also Eq. (7-36))
Particle Shifting Technique (PST)	Eqs. (7-33), (7-34) and (7-35) are used as a particles regularization scheme.
Kernel function	Eq. (7-22) is used for all simulations (cases A1 to B4)
Free-surface detection technique	Combination of the Particle Number Density (PND) and divergence of the displacement is used (see also our previous work [29])
Buoyancy force in natural convection (θ_i) Density smoothing process in Rayleigh Taylor instability ($\rho_{\text{interface}}$)	Eq. (7-A2) is used to calculate field functions (θ_i and $\rho_{\text{interface}}$).
Pressure on the solid walls (p_i) Temperature on the insulated walls (θ_i)	Eq. (7-A2) is applied to calculate field functions on the solid walls (p_i and θ_i)
Laplacian (for pressure $\nabla^2 P$ and diffusion $\nabla^2 \mathbf{u}, \nabla^2 \theta$)	Eq. (7-A15) is applied in the present work whereas Eqs. (7-A16) or (7-A18) can also be used.

The terms $\nabla C_{i,x}$ and $\nabla C_{i,y}$ are gradients of concentration (C) which encourage particles to travel out from high concentration area to the lower one. The parameter λ represents a normalisation coefficient which should be computed at the initial position of particles (initial time step, t=0) where kernel has a fully compact support (interior particles). α is the problem-dependent parameter which controls the magnitude of the shifting displacement (D) in the interests of retaining numerical consistency. In the present work, it is taken as $\alpha = 0.08$. n_i denotes corrective matrix which is given by:

$$n_i = \begin{bmatrix} \sum_{j=1}^{N} x_{ij}^2 W_{ij} dV & \sum_{j=1}^{N} x_{ij} y_{ij} W_{ij} dV \\ \sum_{j=1}^{N} x_{ij} y_{ij} W_{ij} dV & \sum_{j=1}^{N} y_{ij}^2 W_{ij} dV \end{bmatrix}^{-1} \tag{7-35}$$

From the above discussion, one may deduce that, prior to implementing Particle Shifting Technique, the specific particle labeling algorithm is required to identify the role of the each particle (inner, vicinity or surface particle) and position of the interface. In the present study, the combination of the Particle Number Density (PND) and divergence of the displacement is used to determine the position of the interface. For more details see our previous work [29]. At the end of the process, two other useful quantities such as average Nusselt number ($\overline{Nu}$) and overall entropy generation ($\overline{S}_{tot}$) can be determined via Eqs. (7-15) to (7-17) particularly for the case of natural convection heat transfer. Before closing this section, it should be noted that, the proposed higher-order Laplacian operator (Eq. (7-A15)) has been utilized for estimating diffusion terms ($\nabla^2\mathbf{u}, \nabla^2 T$) and PPE ($\nabla^2 p$) whereas Eq. (7-A10) is applied to predict temperature gradient (∇T, $\nabla\theta$) and divergence of velocity components ($\nabla\cdot\mathbf{u}$). Meanwhile, Eq. (7-A2) is used as a smoothing operator to estimate temperature (T) in the buoyancy force ($F_b = -\rho g\,\beta(T - T_c)$) or density of the interface ($\rho_{\text{interface}}$) in buoyancy-driven and multiphase flows problems, respectively. However, for predicting the pressure gradient (∇p), another strategy should be adopted to deal with topological inconsistency caused by truncated kernel error adjacent to the free-surface area. To rectify this shortcoming, Eq. (7-A10) is revised based on *Tensile Instability Control* (TIC) suggested by Sun et al. [27], [57] as follows:

$$\begin{bmatrix} \frac{\partial p}{\partial x} \\ \frac{\partial p}{\partial y} \end{bmatrix} = L \begin{bmatrix} \sum_{j=1}^{N} \frac{(p_j - \chi p_i) x_{ij} W_{ij}}{|r_{ij}|} dV \\ \sum_{j=1}^{N} \frac{(p_j - \chi p_i) y_{ij} W_{ij}}{|r_{ij}|} dV \end{bmatrix} \qquad L = \begin{bmatrix} \sum_{j=1}^{N} \frac{x_{ij}^2 W_{ij}}{|r_{ij}|} dV & \sum_{j=1}^{N} \frac{x_{ij} y_{ij} W_{ij}}{|r_{ij}|} dV \\ \sum_{j=1}^{N} \frac{x_{ij} y_{ij} W_{ij}}{|r_{ij}|} dV & \sum_{j=1}^{N} \frac{y_{ij}^2 W_{ij}}{|r_{ij}|} dV \end{bmatrix}^{-1} \tag{7-36}$$

χ is an integer variable which alters between 1 and -1 for interior and surface particles, respectively. More precisely, in this switching technique, the conservative form ($\chi = -1$) of the Navier-stocks equations ($p_j + p_i$) is implemented on the free-surface area and its vicinity particles whereas the non-conservative form ($\chi = 1$) with first-order accuracy is applied on the

inner particles ($p_j - p_i$). In this way, Eq. (7-36) is able to take advantage of simultaneous momentum conservation and first-order accuracy. Eq. (7-36) will henceforth be referred to as a *Revised Pressure Gradient* operator. The summary of equations outlined in the present study is tabulated in table 7-1. The detailed description of the derivation of the discrete differential operators is also provided in appendix A.

7.5 Validation

The robustness and validity of proposed modifications in handling negative pressure field and violent free-surface flow with wave impact are ascertained in this section through numerical simulation of four well-known benchmark cases namely: the hydrodynamic evolution of classical dam break over the dry bed (case A1), rotation of a square patch of fluid (case A2), two-phase Rayleigh-Taylor instability (case A3) and oscillating concentric circular drop (case A4). For all runs, the ratio of smoothing length over the particle spacing is taken as a unity ($h/\Delta x = h/\Delta y = 1$) while the time step follows the Courant number (CFL) conditions based on the acoustic and diffusion constraints:

$$\Delta t_{convection} = CFL \frac{\Delta x}{|\mathbf{u}_{\max}|}$$
$$\Delta t_{viscous} = CFL \frac{\Delta x^2}{\nu} \qquad (7\text{-}37)$$
$$\Delta t = \min(\Delta t_{convection}, \Delta t_{viscous})$$

In the present work, minimum and maximum values of Courant number are chosen as $\mathrm{CFL}_{\min} = 0.05$ and $\mathrm{CFL}_{\max} = 0.15$ for the cases dam break and Rayleigh-Taylor instability, respectively. The numerical methodology was coded in the Intel® Visual FORTRAN Compiler.

7.5.1 Dam break (case A1)

Dam failure problem is a well-known benchmark test case which has been widely used to verify the performance of different Euilerian/Lagrangian numerical methods. Probably because it involves severe deformation and topological changes such as: water re-entry, impact pressure, splashing and wave breaking which are crucial physical phenomena in ocean engineering. The initial setup of the problem is similar to the numerical and experimental investigations conducted by Zhang et al. [58] and Lobovský et al. [59] where a rectangular water column ($\rho = 997\, Kgm^{-3}$

and $\mu = 855\times10^{-6}\ Kgm^{-1}s^{-1}$) with the initial height and width denoted as $H = 0.3m$ and $W = 0.6m$ is stored on the LHS of a reservoir ($D = 1.61m, L = 0.8m$). As shown in Fig. 7-1, the time histories of pressure variations and water level height are monitored at three different sampling points ($h_1 = 0.003m,\ h_2 = 0.03m,\ h_3 = 0.08m$) and sections ($l_1 = 0.3m,\ l_2 = 1.14m$ and , $l_3 = 1.362m$). Fig. 7-4 illustrates snapshots of the flow evolution together with the effects of the Particle Shifting Technique (PST) on the particle configurations and pressure filed at different time instants. Generally, once the virtual gate is removed, under the effects of gravity force, the water column collapses and moves horizontally along the dry bed while its level of kinetic energy increases. During this period $0 \le t\sqrt{g/H} \le 2.5$, the pressure distribution within the fluid deviates considerably from hydrostatic such that maximum pressure is dropped to approximately half of its initial value, indicating rapid exchanges between potential and kinetic energies. The surge front eventually hits the downstream wall, producing the first impact pressure at $t^* = t\sqrt{g/H} = 2.531$. This stage is accompanied by an irreversible conversion of kinetic energy into shock pressure and rapid formation of the stagnation point on the corner of the enclosure. Since, the right wall is rigid and impermeable, the fluid starts to deviate upwards, resulting in a formation of ascending jet along the vertical wall. As time progresses, due to the restoring action of gravity force, the fluid acceleration declines and consequently upward movement of the water jet slows down. In this circumstance, the thickness of the water jet augments and its crest starts

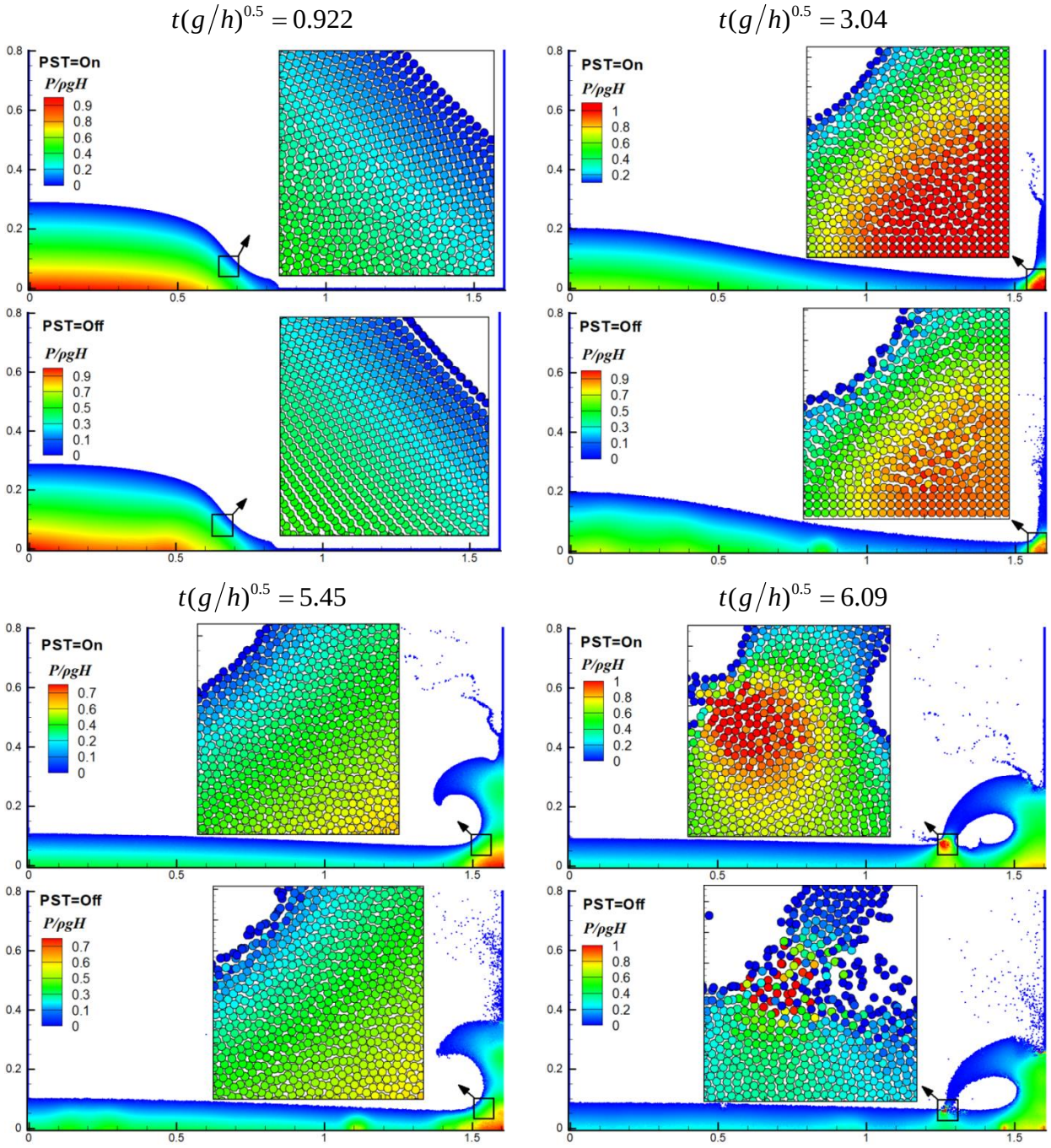

Figure 7-4 The effects of the Particle Shifting Technique (PST) on the particle distributions and pressure field for problem of dam failure (case A1) at four different time instants.

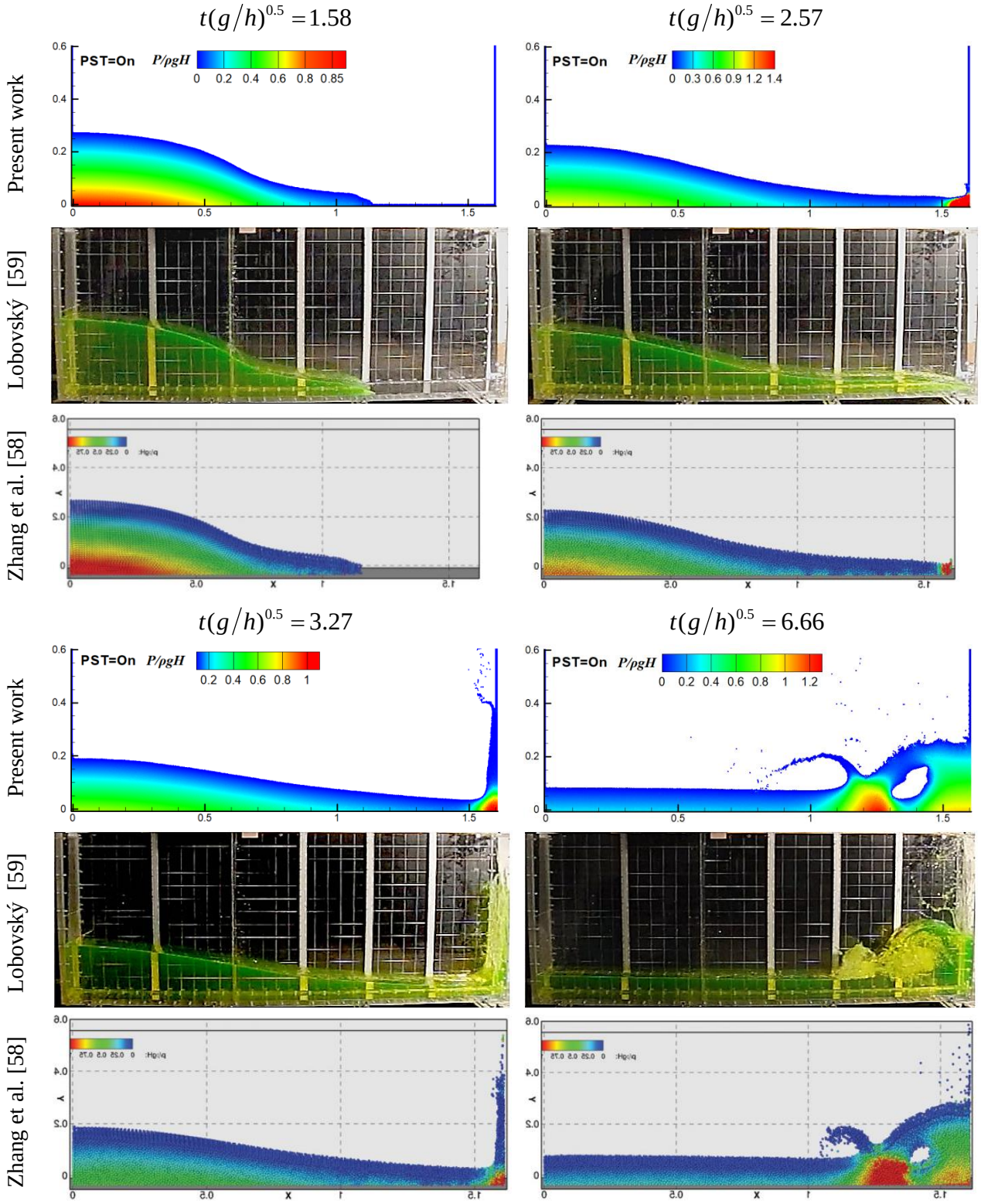

Figure 7-5 Qualitative comparison of predicted results with experimental measurements and numerical simulations of Lobovský [59] and Zhang et al. [58] for case A1.

losing its kinetic energy, while the underling fluid is still moving rightwards, leading to the creation of the rolling wave at $t^* = 4.75$. As time goes on, the magnitude of the pressure inside the plunging wave gradually augments such that distribution of the lateral pressure becomes nearly quasi-hydrostatic as depicted in Fig. 7-4. This phenomenon is more prominent adjacent to the right wall where stagnation point gets extended to the middle portion of the rolling wave. Finally, due to the oncoming flow, the plunging jet ultimately falls back onto the moving wet bed at $t^* = 6.33$ where the second splash-up scenario and sudden rise in pressure time history ($P^* = 0.976$) occur. Close-up views of particles position during the flow evolution in Fig. 7-4 reveal that, the use of Particle Shifting Technique (PST=On) can efficiently suppress spurious pressure fluctuations and singular pressure impulse via enhancing the uniformity of particles distribution. On the contrary, it can be seen that in the absence of PST, due to Lagrangian nature of the method, particles begin to follow the pattern of streamlines such that the occurrence of the particle clustering and its undesirable consequences (unphysical particle splashing and void formation) are inevitable. As highlighted before, the development of the particle stratification (line structures) and anisotropic distributions can trigger tension-instability problem which leads to the density error accumulation and degradation of the interpolation procedure. A closer inspection of Fig. 7-4 shows that at $t^* = 0.922$, when PST is turned off, particles are deployed obliquely and a moderate pressure oscillation takes place near the bottom wall, presumably because of non-physical particles distortion in that area. This behavior persists or even gets worse, resulting in the formation of check-board pressure filed and spurious interface fragmentation at the moment of second impact pressure ($t^* = 6.09$) induced by backward plunging water front. Comparison of calculated pressure signals at three different probes with experimental data is presented in Figs. 7-5 and 7-6. Satisfactory agreement with previously published works in Figs. 7-5 and 7-6 vividly confirms the applicability of the proposed models in handling positive pressure field involving shock waves. It is also evident that, the predicted results using the improved MPS model in terms of pressure time histories and water level heights are quite smooth and noise-free while there are visible differences between the experimental measurements [59] and those obtained by original WCSPH method [58].

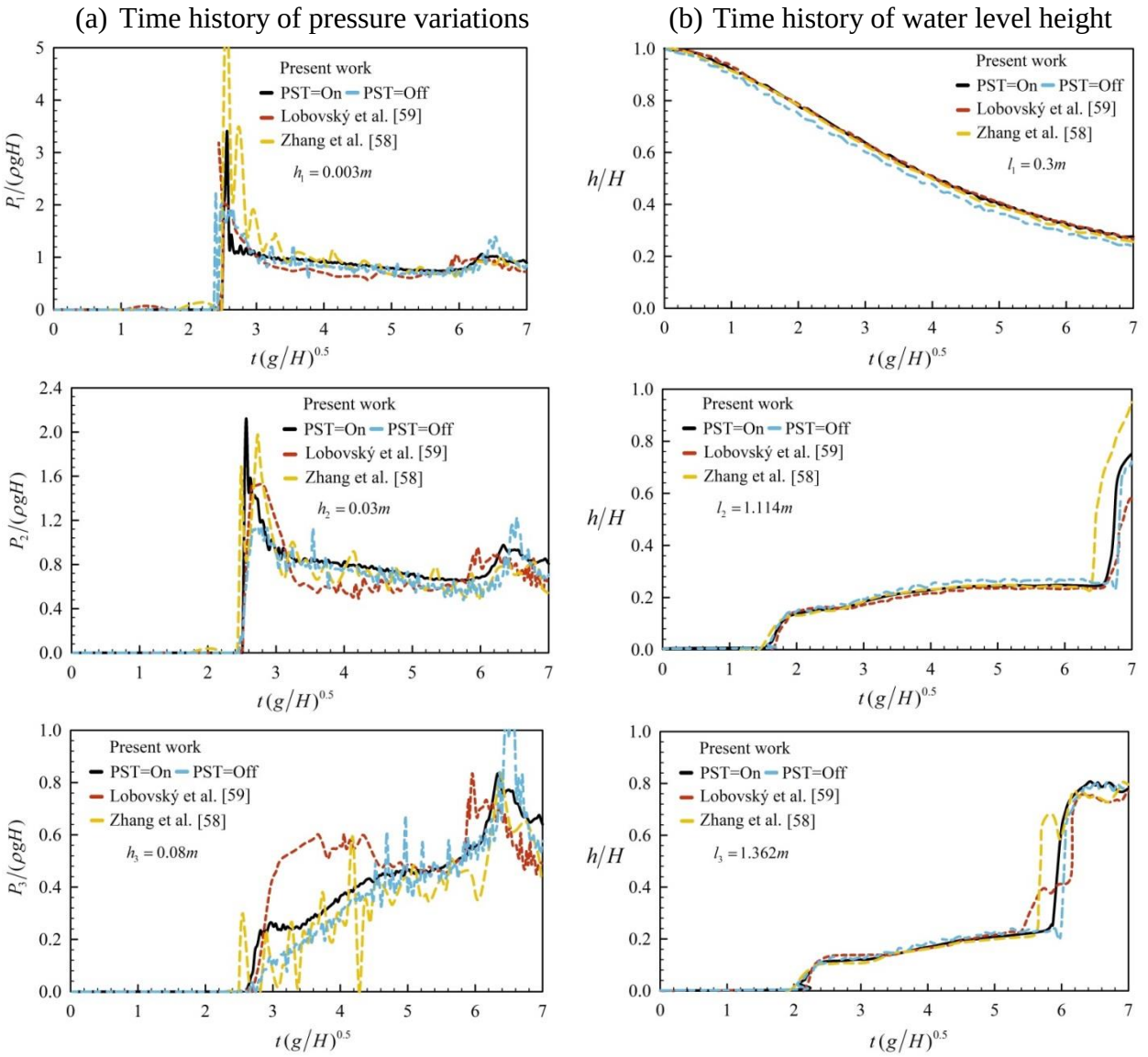

Figure 7-6 Quantitative comparison of calculated results in terms of the pressure variations on the right wall and water level height at three different sample points with experimental measurements and numerical simulations of Lobovský [59] and Zhang et al. [58].

The first reason for such a discrepancy can be attributed to the large truncation error associated with traditional SPH formulations which can deteriorate the overall quality of the simulation in terms of smoothness, consistency and precision especially in the case of irregular particle distributions. Similar findings were reported by Quinlan et al. [60] and Oger et al. [31] who numerically confirmed that the classical SPH operators are only valid for homogeneous particles

distribution so that the existence of any anisotropic or coherent particle structures can seriously jeopardize the reliability of numerical solutions. However, since the enhanced MPS model benefits from high level of accuracy through implementing higher-order gradient, divergence and Laplacian operators, the pressure oscillations at the time domain are totally trivial. The second reason for such inconsistency can be traced back to the discretization of the pressure gradient terms. Thanks to the *Tensile Instability Control* (TIC) proposed by Sun et al. [27], [28], the improved MPS model in the present work takes advantages of simultaneous momentum conservation and first-order accuracy (see Eq. (7-36)) while conventional WCSPH model [58] used conservative form of pressure gradient operator ($p_j + p_i$) so-called *Purely repulsive pressure gradient* [61] across the entire fluid domain to overcome the tensile instability problem at the expense of losing accuracy. As mentioned earlier, type of the kernel function and implementation of the particle regularization technique are also two other major factors which can immensely influence the stability and accuracy of the method. In more details, Zhang et al. [58] applied 5th-order Wendland kernel function whereas the results of the current work have clearly shown that Wendland kernel fails to accurately predict the flow characteristics of 1D Sod shock tube problem (see section 4). Heterogeneity in the particle distribution in the absence of an efficient Particle Shifting Technique is another source of inaccuracy and oscillatory behaviors in [58].

7.5.2 Rotation of a square patch of fluid (case A2)

The evolution of rotating square patch of fluid is examined in this subsection as a second benchmark problem to demonstrate the efficiency and performance of the improved MPS model in dealing with negative pressure field. This canonical test case was originally introduced by Colagrossi [62] to investigate detrimental effects of tensile-instability on the particles behavior. The initial conditions of the velocity and pressure are given by [63] as follows:

$$\begin{aligned} &u_0(x,y) = +y\,\omega \qquad -L/2 \le y \le L/2 \\ &v_0(x,y) = -x\omega \qquad -L/2 \le x \le L/2 \\ &p_0(x,y) = 0 \\ &g(x,y,t) = 0 \end{aligned} \tag{7-38}$$

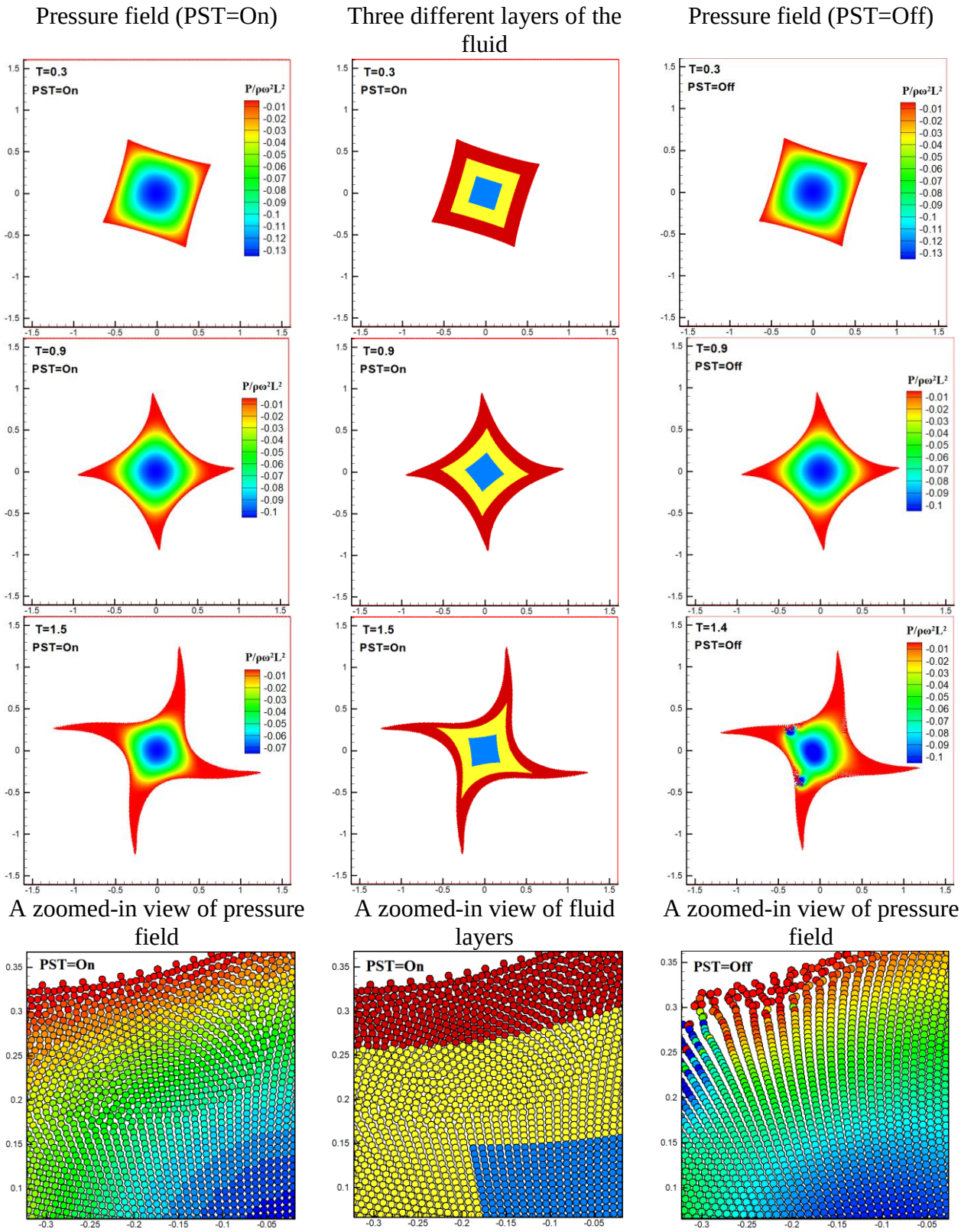

Figure 7-7 The effects of PST on the particle distributions and pressure field for case A2.

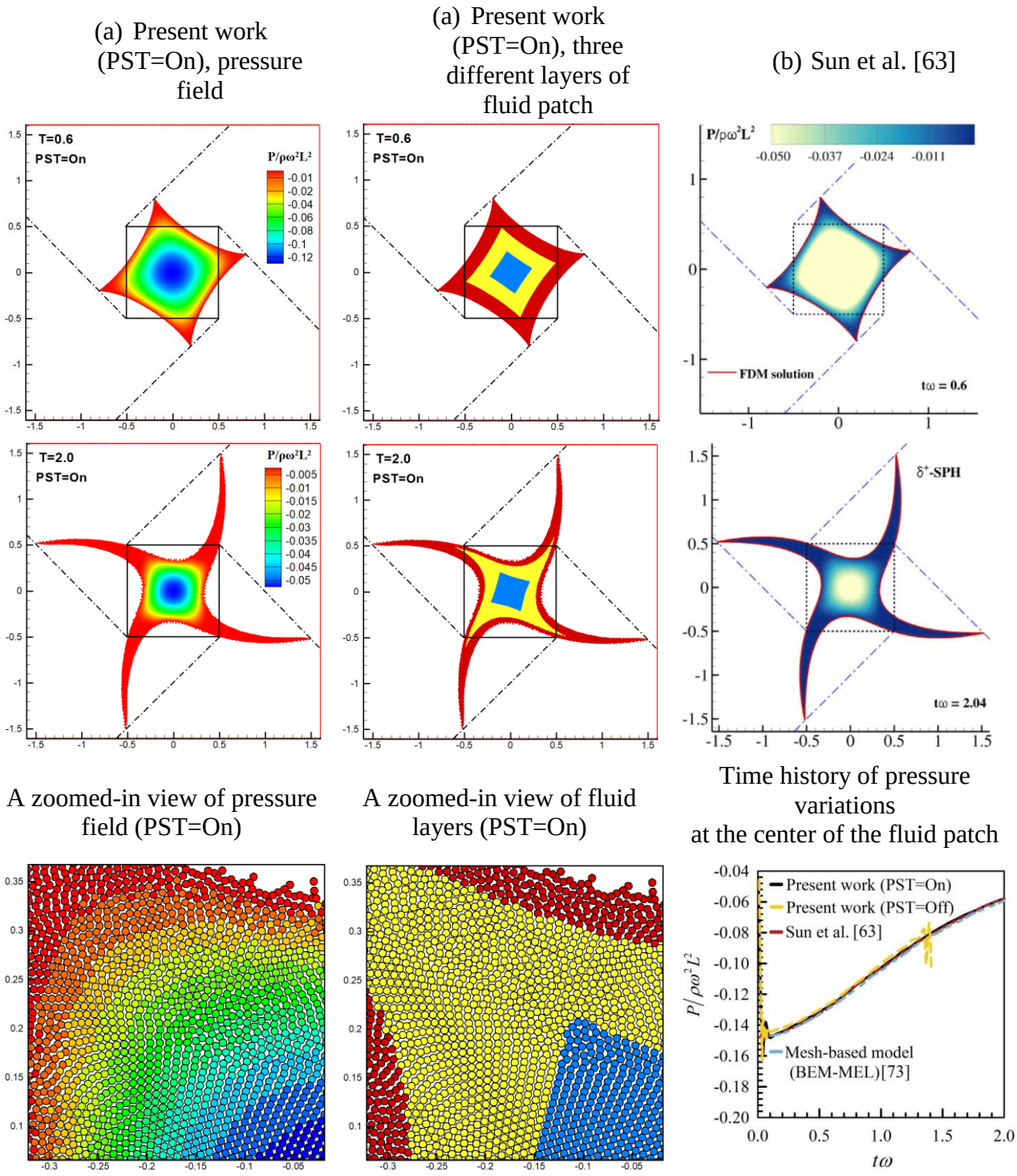

Figure 7-8 Qualitative and quantitative comparison of simulated results with numerical work of Sun et al. [63] for the case of rotating square patch of fluid (case A2, $\rho = 10^3\, Kgm^{-3}$).

where $\omega = 1 s^{-1}$ and $L = 1$ denote angular velocity and length of the fluid patch, respectively. Generally, unlike the previous case, due to the existence of the centrifugal force, the flow field is characterized by negative pressure field which causes sides of the element to shrink inward towards the center of the vortex while corners of the patch extend radially outward to satisfy continuity requirements. This mechanism results in the formation of star-shaped structure within the fluid domain. Fig. 7-7 reveals that, because of very high strain rates and pressure gradient adjacent to the free-surface area, the outer layer (highlighted in red) undergoes large deformation while the interior one (highlighted in blue) remains nearly unaltered which indicates that the surface area is more prone to fragmentations and crack propagation. The close-up snapshots in Fig. 7-7 illustrate that, the utilization of PST has made a significant contribution to establish smoother surfaces and uniform particles distribution via eliminating non-physical gap and overlapping. However, similar to previous case, when the Particle Shifting Technique is turned off (PST=Off), due to rapid distortion of the boundary and excessive migration of particles towards the central portion, the unfavorable branch-like structures and particles stratification start to develop within the fluid domain. As expected, the growth of these line structures and irregularities in particle arrangements eventually corrupt the quality of kernel approximations, leading to a total failure of the calculation at $T = t\omega = 1.4$. Comparison of predicted results with existing numerical solutions in the literature [63] in terms of the pressure time histories at the center of the patch together with free surface profile is presented in Fig. 7-8. It is evident that, the tips of the four arms are exactly matched with the trajectories arising from straight lines reported in work of Sun et al. [63] and good agreement is found with the reference Boundary Element Method (Eulerian model).

7.5.3 Two-phase Rayleigh-Taylor instability (cases A3)

To further assess the performance and applicability of the proposed modifications in handling multifluid flows, the classical Rayleigh-Taylor instability (RTI) problem enclosed in a rectangular cavity [1m, 2m] is investigated in this subsection as a third benchmark test problem. As schematically shown in Fig. 7-1, the computational domain initially consists of two immiscible fluids with density ratio of $\rho_R = \rho_H / \rho_L = 1.8$ where the denser fluid with physical properties of $\rho_H = 180\, Kg/m^3$ and $\mu_H = 0.9\, Pa.s$ is located above the lighter fluid

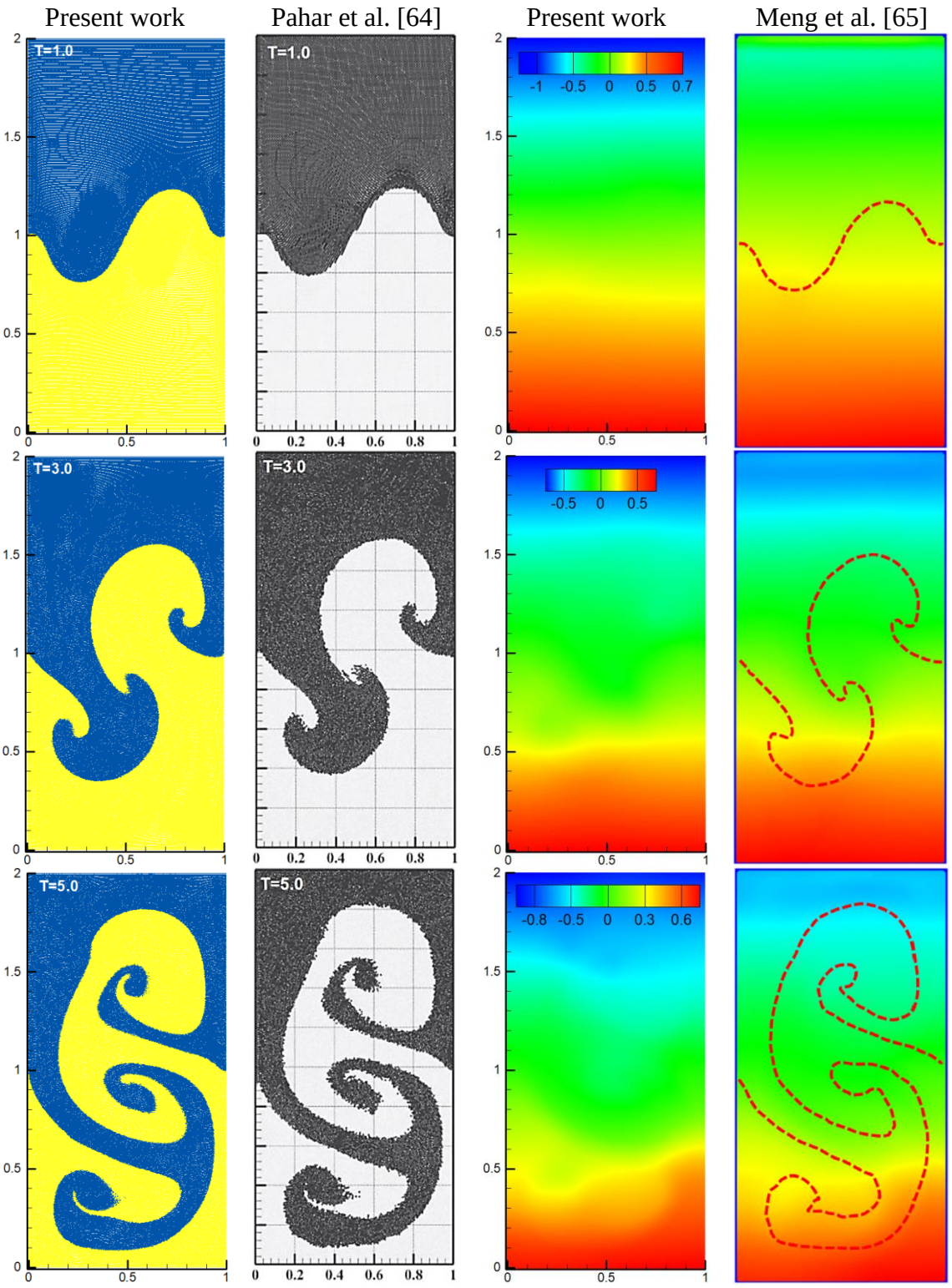

Figure 7-9 Comparison of the obtained results with numerical data of Pahar et al. [64] and Meng et al. [65] two-phase Rayleigh-Taylor instability (case A3).

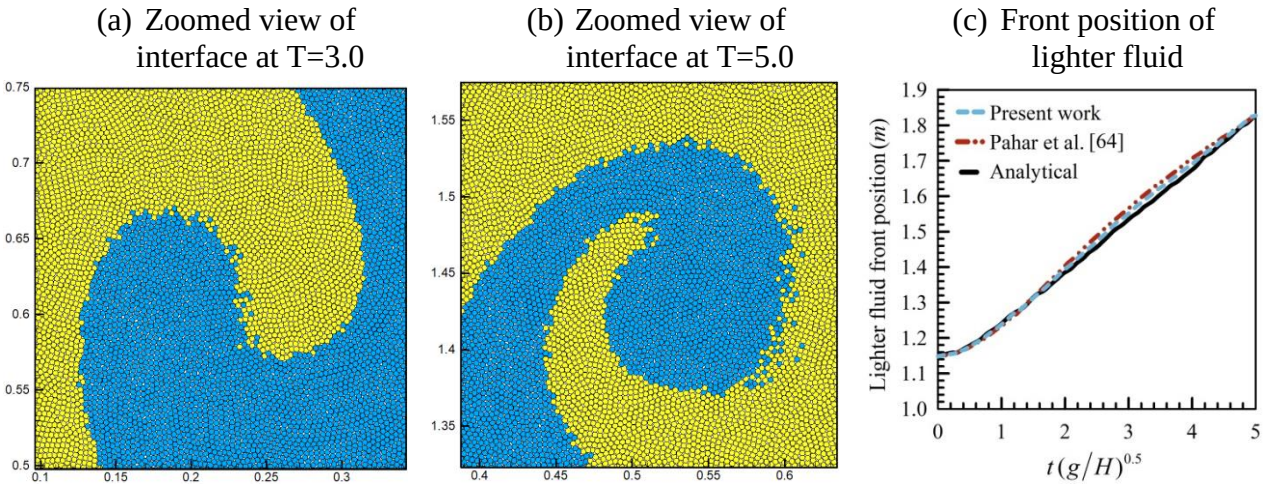

Figure 7-10 Quantitative comparison of the present MPS predictions against the numerical and analytical results of Pahar et al. [64]; (a) and (b) zoomed-in views of material interface obtained from the present model; (c) time history of front position of lighter fluid.

($\rho_L = 100\,Kg/m^3$ and $\mu_L = 0.5\,Pa.s$) and the system is subject to a gravitational field ($\mathbf{g} = 4.41 ms^{-2}$). The instability is characterized by the Reynolds number of $\mathrm{Re} = \rho_H H\sqrt{H\mathbf{g}}/\mu_H$ where $H = 1m$ is width of the enclosure and $\sqrt{H\mathbf{g}}$ is the characteristic velocity with $\mathbf{g}$ being the gravitational acceleration. The Atwood number is defined as $At = (\rho_R - 1)/(\rho_R + 1) = 2/7$ which represents the density contrast between two fluids. The initial position of the perturbed interface between two fluids is defined by a sinusoidal function ($y = 1 - 0.15 \times \sin(2\pi x)$) and the mirror velocity technique described in section 3 is employed to enforce no-slip boundary condition on all rigid walls. The simulation is carried out on medium resolution of 250×500 fluid particles. It should be noted that, in order to circumvent the physical discontinuities at the multi-fluid interface, the proposed smoothing operator (Eq. (7-A2)) is utilized for the treatment of the density and viscosity. The temporal evolution of interface together with the corresponding pressure distribution at three different dimensionless times ($T = t\sqrt{\mathbf{g}/H}$) are presented in Fig. 7-9. Generally, due to buoyancy force and initial interface distortion, the denser fluid is directed downward as a spike while the lighter fluid rises up along the right wall as a bubble to satisfy the need for the mass conservation. Inspection of Fig. 7-9 reveals that during the early stages of the

interface evolution ($T \leq 1$), the position of the tip of the rising and falling fluids remains symmetrical with respect to center of the enclosure which indicates that the fluid flow is governed by the viscous force. As the heavy fluid penetrates further into the light fluid ($1 \leq T \leq 3$), the strength of the fluid flow enhances and consequently the surface force due to the shear stresses (shear velocity) is intensified, resulting in the appearance of the dynamic bubble-spike structure within the enclosure. In fact, the formation of the mushroom-like structure is a strong indication of the development of Kelvin-Helmholtz instability (KHI) which causes the heavy fluid to roll up into two counter-rotating vortices. As the time further proceeds, more and more secondary vortexes are appeared along the side spikes and subsequently the interface becomes highly twisted and distorted within the container which implies that KHI is still dominant over the RTI. Fig. 7-9 illustrates that the predicted results in terms of the particle distributions and pressure contours are qualitatively in a satisfactory agreement with the numerical data of Pahar et al. [64] and Meng et al. [65]. It can be seen that, the pressure field is smoothed and the interface is free from unphysical mixing of phases which confirms the overall consistency and accuracy of the developed model in capturing primary and secondary recirculation zones generated at the material discontinuities. Finally, in Fig. 7-10, the time history of the front position of ascending lighter fluid is compared with the analytical and numerical results of Pahar et al. [64] and a good agreement is found.

7.5.4 Oscillating concentric circular drop (case A4)

The evolution of a weightless ($\mathbf{g} = 0$) oscillating concentric circular drop subjected to an external body force ($F_{ext} = -\Omega^2 \mathbf{r}$ with $\mathbf{r} = xi + yj$ being the distance from the center of the drop) is considered in this subsection to demonstrate the capability of the proposed modifications in handling multiphase flow problems with high density contrast. This canonical test case was originally introduced by Monaghan and Rafiee [66] and was then successfully reproduced by Meng et al. [65] and Lind et al. [67]. As schematically portrayed in Fig. 7-1, the computational domain consists of two immiscible inviscid fluids ($\mu_H = \mu_L = 0$) with physical density ratio of $\rho_R = \rho_H / \rho_L = 1000$ where the heavy fluid ($\rho_H = 1000\, Kg/m^3$) with radius of $R_1 = 0.5\, m$

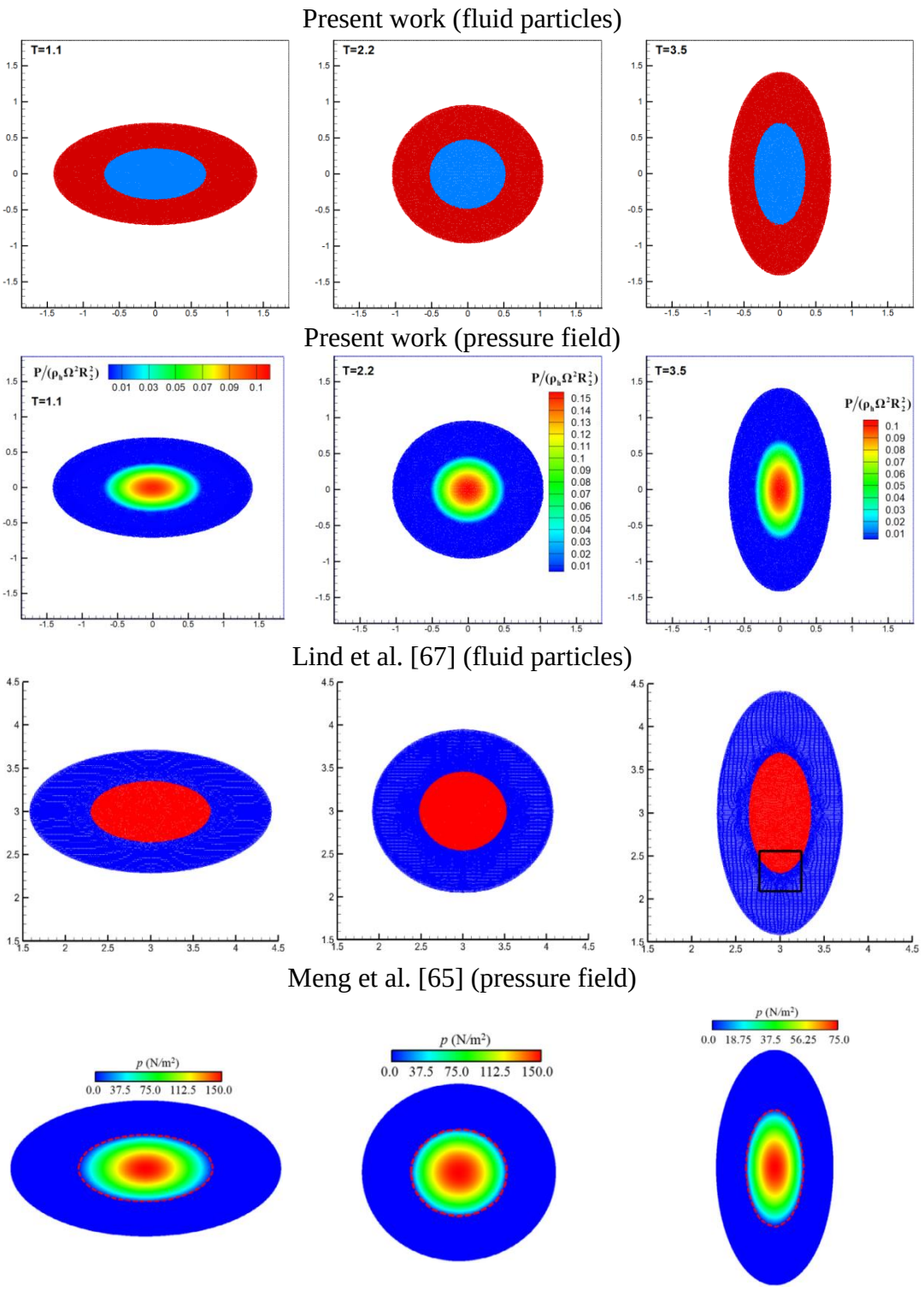

Figure 7-11 Qualitative comparison of the predicted results from the current work with numerical data of Lind et al. [67] and Meng et al. [65] in terms of the phase distribution and pressure field for case A4.

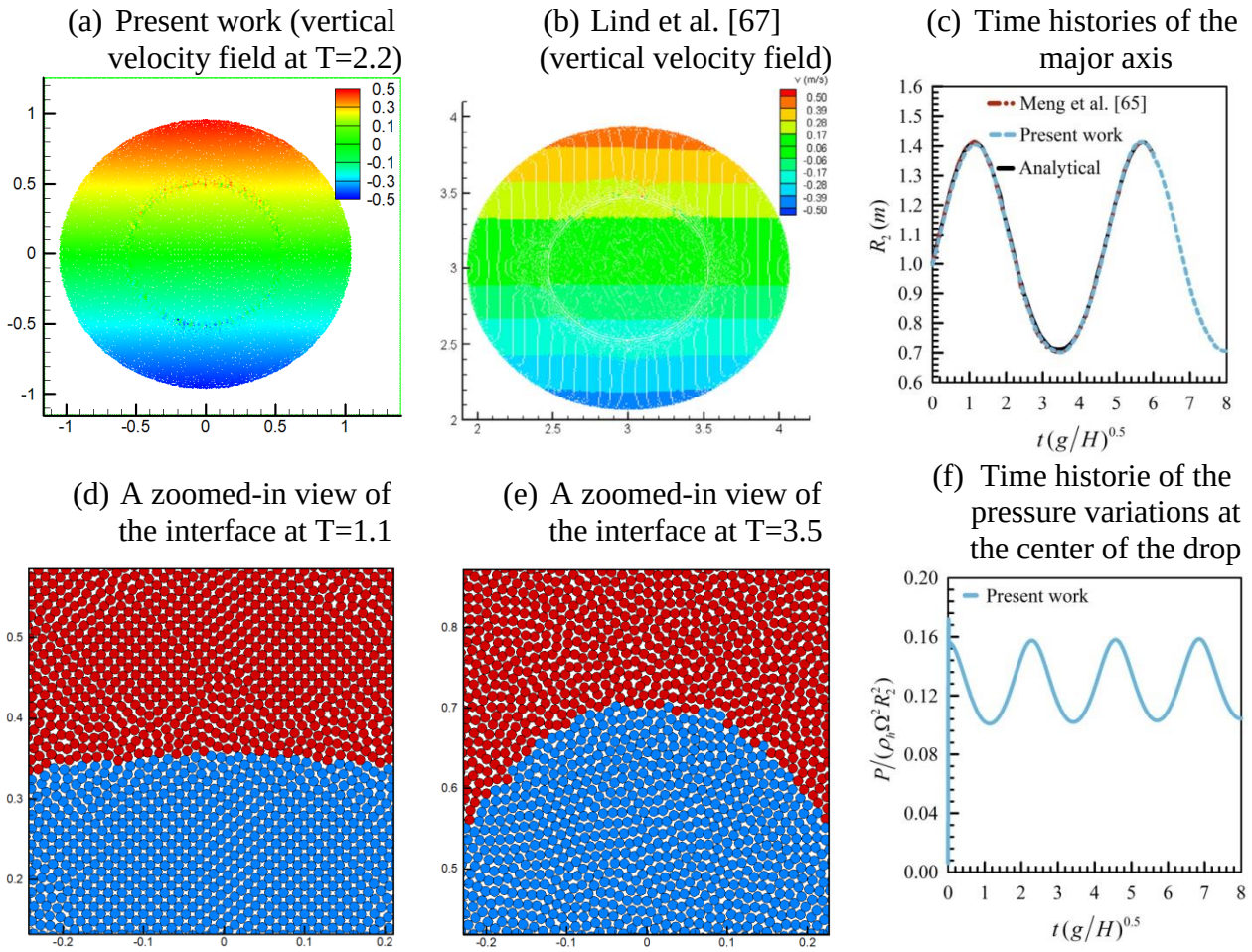

Figure 7-12 Quantitative comparison of the present MPS predictions against the numerical and analytical results of Meng et al. [65] and Lind et al. [67] for case A4 (oscillating concentric circular drop with density ratio of $\rho_R = \rho_H / \rho_L = 1000$); (a) and (b) vertical velocity contours, (c) time history of variation of the outer major axis; (d) and (e) zoomed-in views of material interface obtained from the proposed model; (c) time history of pressure variations at the center of the drop.

is surrounded by a lighter fluid ($\rho_L = 1 Kg/m^3$) whose initial radius is $R_2 = 1m$. The initial pressure and velocity fields are given by:

$$u_0(x,y) = Ax$$
$$v_0(x,y) = -Ay \qquad (7\text{-}39)$$
$$p_0(x,y) = 0$$

Similar to [65]–[67], the ratio A/Ω is set equal to 0.5where A and Ω are taken as 0.5 and 1.0, respectively. Fig. 7-11 illustrates a series of snapshots of particle distributions and pressure contours at various time instants. Generally, hydrodynamic behavior of the oscillating circular drop under the influence of the negative external force and irrotational velocity field ($\mathbf{u} = 0.5\hat{i} - 0.5\, j$) is characterized by the isotropic elongation of the circular patch where top and bottom portions of the medium starts to shrink in the longitudinal direction while left and right sides stretch transversally. This mechanism leads to the development of the positive pressure field. However, as time goes on, the magnitude of the external force induced by the particles position ($F_{ext} = -\Omega^2 \mathbf{r}$) augments and begins to overcome the fluid momentum. In this circumstance, the side parts of the patch start to move towards the center of the drop while upper and lower portions elongate vertically, leading to the drop oscillations with period of $T = \pi\sqrt{2}/\Omega \approx 4.44$. Comparison with previously published numerical SPH results in Fig. 7-11 vividly demonstrates that, the complex interface evolutions are accurately captured by the enhanced model with no additional unphysical behavior. To confirm the absence of any nonphysical particle clustering and tensile instability, two zoomed-in views of the interface at $T = 1.1$ and $T = 3.5$ are presented in Fig. 7-12. It is evident that, particles are regularly distributed across the material interface and the corresponding pressure fields are smooth without the remarkable unphysical noise (see also Fig. 7-11), supporting the effectiveness of the interface treatment and density smoothing (see Eq. (7-A2)). However, there are small numerical noises in the vertical velocity field in the close vicinity of the material discontinuity which can be attributed to the implementation of the Particle Shifting Technique [68]. Finally, comparison of the time histories of the major axis of outer ellipse with previously analytical and numerical solutions [65] in Fig. 7-12 clearly proves the performance and validity of the enhanced MPS model.

7.6 Results and discussion

Previous section vividly verified the capability and feasibility of the proposed modifications in predicting the dynamics of free-surface and multiphase flow problems. Thus, in this section, the improved MPS model will be employed to simulate three-phase Rayleigh-Taylor instability

(cases B1 and B2) and entropy generation due to transient natural convection heat transfer in square cavity (cases B3 and B4).

7.6.1 Three-phase Rayleigh-Taylor instability (cases B3 and B4)

To demonstrate the ability of the enhanced model in capturing large interface deformations in the multi-component problems with density contrast, the development of three-phase Rayleigh-Taylor instability (RTI) in two different systems with double-mode perturbations is examined in this subsection. The specifications of the instability with associated initial and boundary conditions are presented in Fig. 7-1. As portrayed in Fig. 7-1 the computations are performed in a rectangular enclosure with dimensions of $1m \times 3m$ (width×height) where three immiscible incompressible Newtonian fluids with densities of $\rho_H = 4$, $\rho_M = 2$ and $\rho_L = 1$ are confined in the upper, middle and lower portions of the enclosure, respectively. The dynamic viscosities are set to $\mu_H = 0.04$, $\mu_M = 0.02$ and $\mu_L = 0.01$ which causes the fluids to have an identical kinematic viscosity ($\upsilon_H = \upsilon_M = \upsilon_L = 0.01$). It can be seen from the figure that, the lower and middle phases are segregated by the interface located at $y = 1 + 0.1 \times \cos(2\pi x)$ while the interfaces between middle and upper phases are defined as $y = 2 + 0.1 \times \cos(2\pi x)$ and $y = 2 - 0.1 \times \cos(2\pi x)$ in cases B1 and B2, respectively. Non-slip boundary condition is imposed on all rigid walls using mirror particle velocity technique [48]. The instability in both cases is governed by non-dimensional Reynolds and Atwood numbers defined as $\mathrm{Re} = H\sqrt{Hg}\,/\upsilon = 420$ and $At = (\rho_{\max} - \rho_{\min})/(\rho_{\max} + \rho_{\min}) = 0.6$ where $\mathbf{g} = 17.64$, $\rho_{\max} = \rho_H$ and $\rho_{\min} = \rho_L$ represent gravitational acceleration , maximum and minimum values of densities within the computational domain. All parameters are defined in the International System of Units (SI). It should be noted that, in order to avoid the excessive smearing of contact discontinuities and keep a sharp and non-oscillatory interface, Eq. (7-A2) has been used for treatment of the solution near the material interfaces as follows:

$$\begin{bmatrix} \rho_s \\ \rho_{s,x} \\ \rho_{s,y} \end{bmatrix} = L \begin{bmatrix} \sum_{j=1}^{N} \frac{\rho_j W_{ij}}{|r_{ij}|} dV \\ \sum_{j=1}^{N} \frac{\rho_j x_{ij} W_{ij}}{|r_{ij}|} dV \\ \sum_{j=1}^{N} \frac{\rho_j y_{ij} W_{ij}}{|r_{ij}|} dV \end{bmatrix} \qquad \begin{bmatrix} \mu_s \\ \mu_{s,x} \\ \mu_{s,y} \end{bmatrix} = L \begin{bmatrix} \sum_{j=1}^{N} \frac{\mu_j W_{ij}}{|r_{ij}|} dV \\ \sum_{j=1}^{N} \frac{\mu_j x_{ij} W_{ij}}{|r_{ij}|} dV \\ \sum_{j=1}^{N} \frac{\mu_j y_{ij} W_{ij}}{|r_{ij}|} dV \end{bmatrix} \tag{7-40}$$

In the above equation, ρ_s and μ_s denote smoothing density and viscosity, respectively. The evolution of the interfaces together with the corresponding contours of velocity in the *x* and *y*-directions are shown in Figs. 7-13 to 7-15 at different dimensionless times ($T = t(g/H)^{0.5}$). Generally, due to the existence of density gradient between two adjacent fluids, the hydrodynamic behavior of the Rayleigh-Taylor instability is characterized by upward movement of the lighter fluid and downward motion of the denser one, leading to the formation of the ascending bubbles and descending spikes within the computational domain. It can be seen from Fig. 7-13 that during the early stages ($T \le 1.0$), the growth and amplitude of bubbles and spikes remain nearly symmetrical with respect to their initial planar interfaces defined by $y = 1.0\,m$ and $y = 2.0\,m$. However, starting from $T = 2.0$, due to the presence of the shear force at the moving interfaces, the spikes of heavier and medium fluids begin to roll up and consequently four secondary counter-rotating vortices are established within the enclosure. It is evident that, as the times goes on ($2.875 \le T \le 3.890$), the upper spike keeps descending downward while two main bubbles driven by the up-moving lighter fluid ($\rho_L = 1$) rise up at both sides of the domain and ultimately outpace the primary spike at $T = 3.890$. At this stage, the upcoming spike becomes totally surrounded by rising bubble, leading to the appearance of a tulip-shaped structure (or reverse arrow-shaped structure). Inspection of Fig. 7-14 also reveals that as the top fluid ($\rho_H = 4$) penetrates into the light one ($\rho_L = 1$), the medium phase ($\rho_M = 2$) gets more and more squeezed between them and consequently magnitude of the velocity components intensifies steadily. In fact, the constant increase in the flow strength can be attributed to the variation of the local Atwood number during the evolution of the three-phase Rayleigh-Taylor instability.

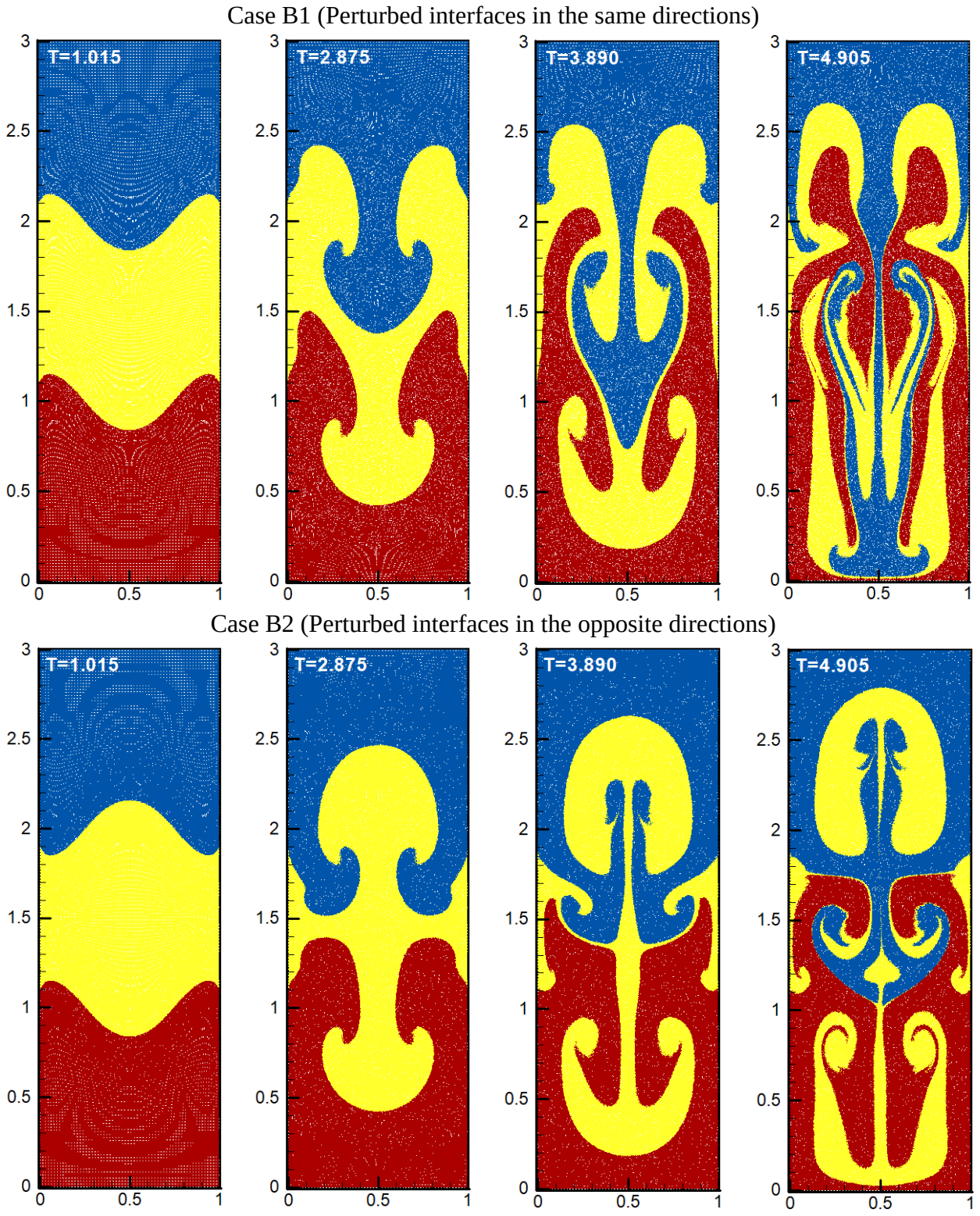

Figure 7-13 Fluid interface evolution of three-phase Rayleigh-Taylor instability problem.

More precisely, in the three-phase RTI, the Atwood number ($At=(\rho_2-\rho_1)/(\rho_2+\rho_1)$) can be defined between any arbitrary pair of working fluids namely: Heavy and Medium fluids ($At_{H,M}=0.33\bar{3}$), Medium and Lighter fluids ($At_{M,L}=0.33\bar{3}$) or between Heavier and Lighter ones ($At_{H,L}=0.6$). It is apparent that as the denser fluid approaches the lighter one, the local Atwood number and density contrast between them increase and consequently the RTI evolution begins to deviate from the Kelvin-Helmholtz instability (KHI). Since, the deviation from the KHI is responsible for considerable enhancement in the flow acceleration, the upper spike undergoes a rapid displacement toward the bottom wall under the effects of the gravity force. Similar observations were also reported by He et al. [69], Tryggvason [70] and Nabavizadeh et al. [71] who investigated the effects of the Atwood number on the RTI. Finally, it can be seen that as time progresses, the interfaces of spikes and bubbles are elongated along the *y*-axis direction and eventually evolved into very complicated shapes where a significant amount of vertical mixing takes place. However, Fig. 7-13 shows that by changing the direction of the upper cosinusoidal perturbation from $y=2+0.1\times\cos(2\pi x)$ to $y=2-0.1\times\cos(2\pi x)$, a different scenario occurs within the enclosure. It can be seen that in case B2, at the early start-up and transitional stages ($0\le T\le 1.0$), the heavier and lighter phases behave identically such that the distributions of velocity components and the growth of interfaces remain symmetrical with respect to both horizontal and vertical centerline of the enclosure ($X=0.5m, Y=1.5m$). These features remain to be the case during $1\le T\le 2.8$ where the initial perturbations near the vertical walls move towards the central region while the medium fluid starts to propagate in the *y*-direction, leading to the formation of ascending bubble and descending spike in the heavier and lighter fluids, respectively. It is worth to mention that at this stage, owing to the small density difference across the interfaces ($At_{H,M}=At_{M,L}=0.33\bar{3}$), the flow field is characterized by the appearance of Kelvin-Helmholtz shear instability (KHI) which causes the sides of the medium phase to roll-up/fold-up into two vortex rings. Note that, these vortex shedding process and shear instability of the rolls are somewhat analogous to the semi-von-Karman vortex streets observed by Meng et al. [72] and Hicks [73].

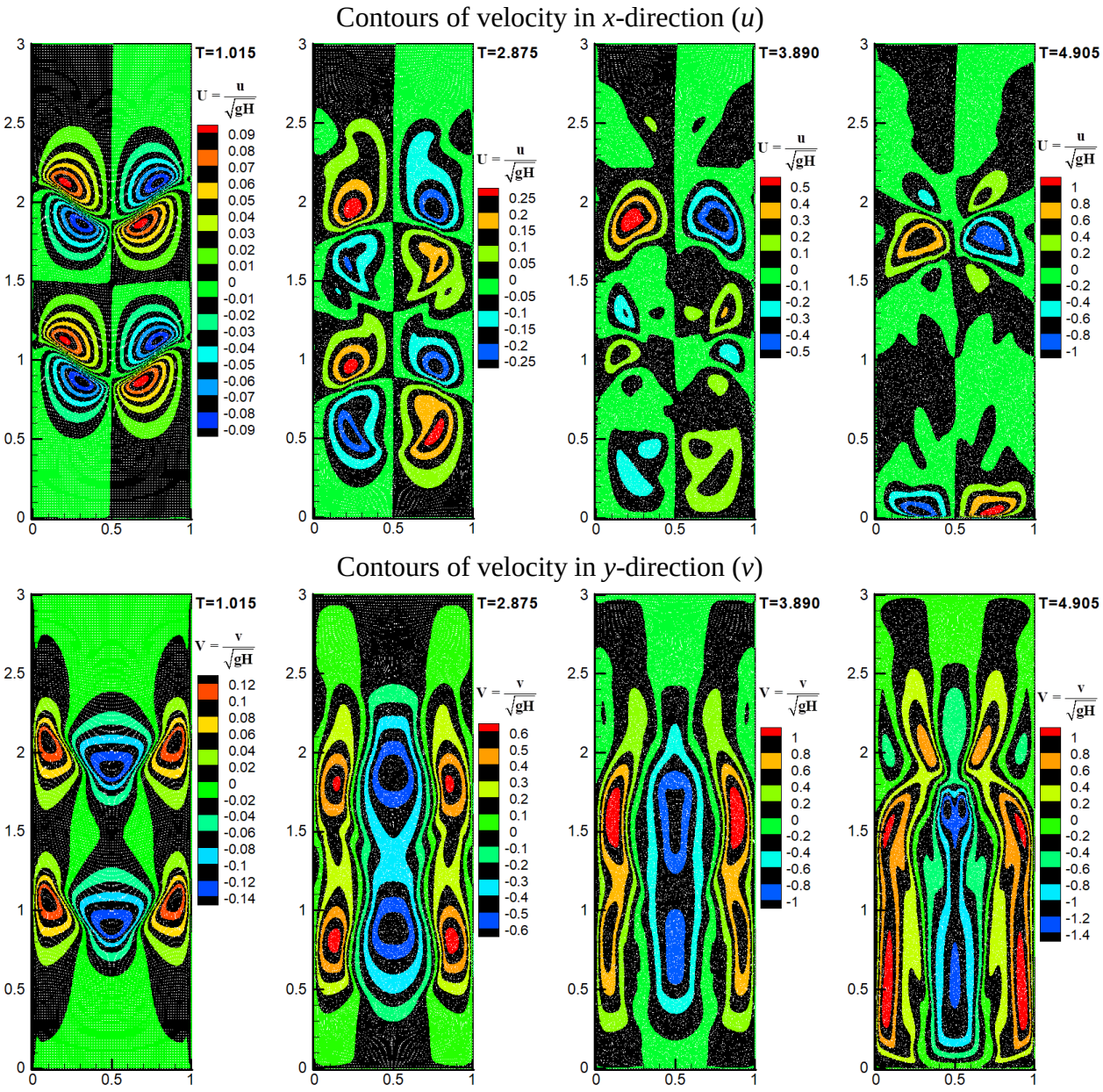

Figure 7-14 Contours of velocity in the x and y-directions (u,v) for three-phase Rayleigh-Taylor instability problem. Case B1 (perturbed interfaces in the same directions). $N_p = 250 \times 750$.

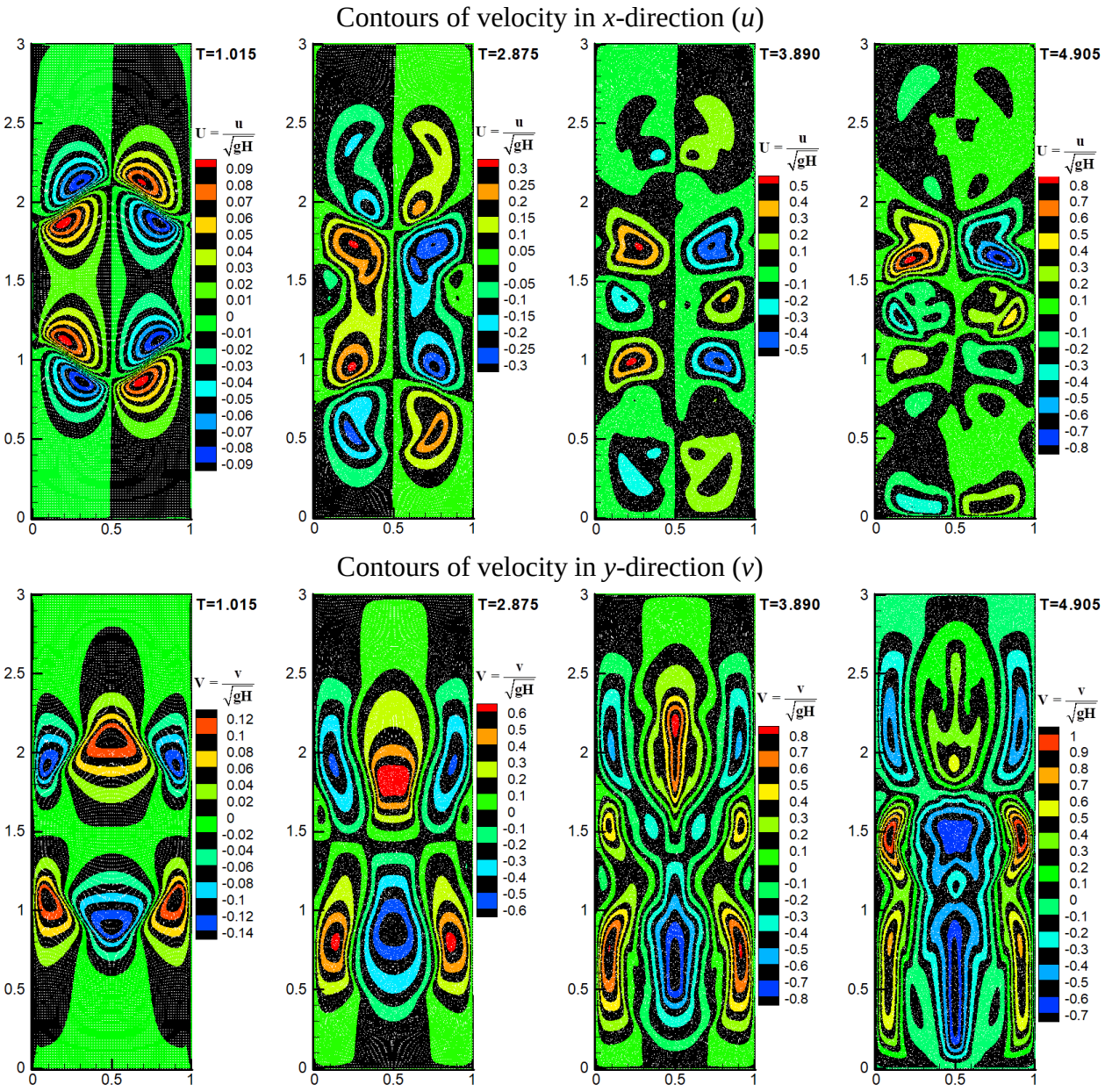

Figure 7-15 Contours of velocity in the x and y-directions (u,v) for three-phase Rayleigh-Taylor instability problem. Case B2 (perturbed interfaces in the opposite directions). $N_p = 250 \times 750$.

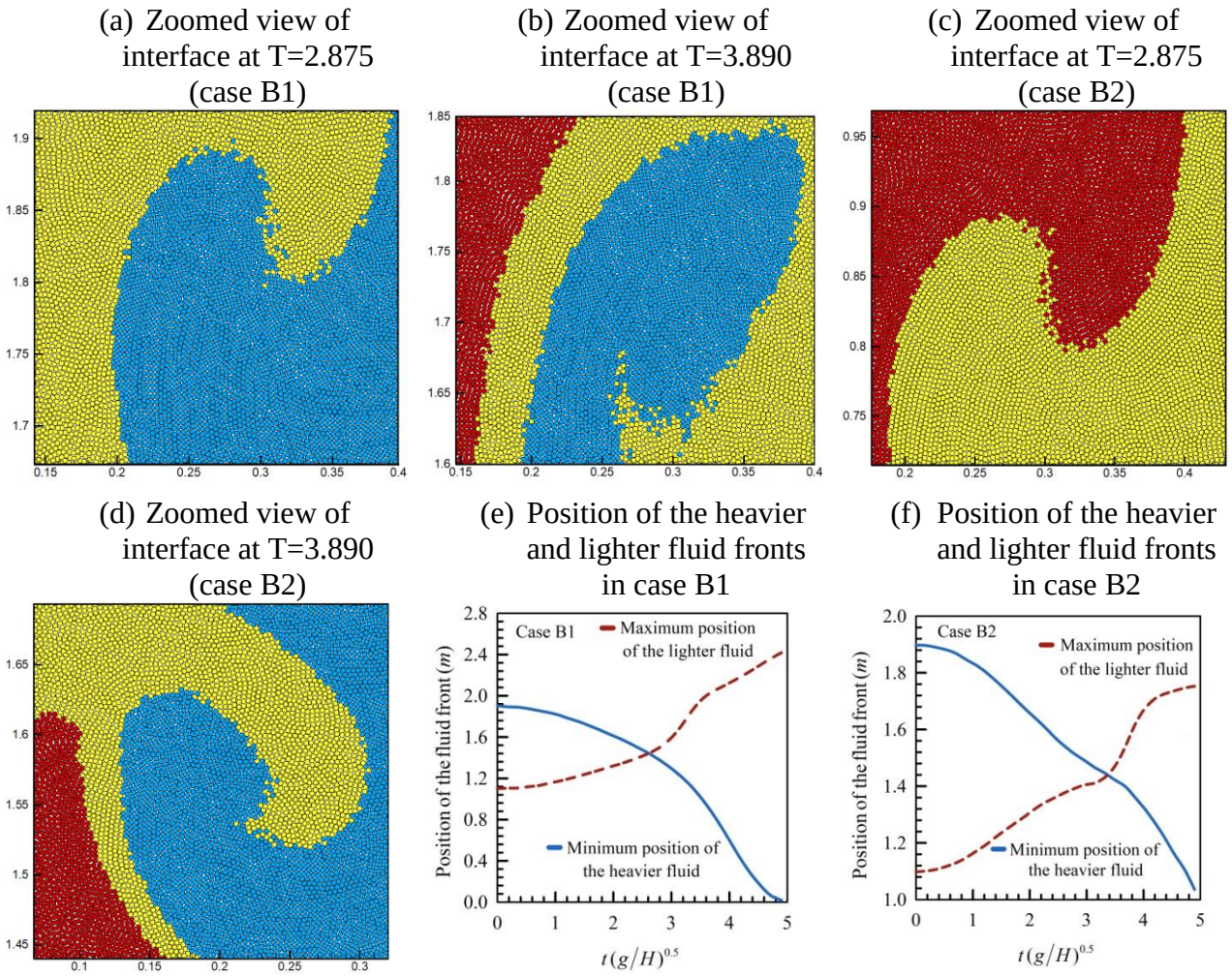

Figure 7-16 (a)-(d) four different zoomed-in view of fluid interfaces in cases B1 and B2. (e) and (f) time evolution of the heavier and lighter fluid fronts in cases B1 and B2. $\rho_L = 1.0$, $\rho_M = 2.0$, $\rho_H = 4.0$.

The corresponding velocity contours in Fig. 7-15 also reveal that with an increase in time ($2.8 \le T \le 3.8$), the intensity of the recirculation augments and consequently some secondary eddies are generated inside the enclosure as a consequence of extreme interfaces deformation and stretching. However, this trend starts to weaken as the medium fluid penetrates further into to the lower and upper portions of the enclosure ($3.8 \le T \le 4.9$). It can be seen that unlike the case B1, due to blockage and deterrent effects of the ascending fluid ($\rho_L = 1$), the effective momentum transfer and flow acceleration attenuate slowly, and consequently the falling fluid gets stuck

within the rising lighter fluid. Fig. 7-13 vividly illustrates that at this circumstance, the rising sheet plumes begin to swallow the heavier fluid, leading to the significant deflection of the lighter fluid in the central zone of the enclosure. In fact, the development of the stationary mushroom-shaped structure and its rapid expansion to the sidewalls are strong indications of the flow deceleration and its subsequent fluid trapping in that area.

Fig. 7-16 shows the spike tip and bubble front locations versus time in both cases together with four close-up snapshots of interfaces at different time instants. The enlarged views of the domain clearly demonstrate the applicability of the proposed smoothing operator (Eq. (7-A2)) in retaining the sharpness of the interface without the need to use extra repulsive force [74] to suppress spurious particle interpenetration on the two sides of the interface. In addition to the smoothness of the interfaces, it is evident that particles are uniformly distributed across the interfaces without unphysical void formation or cavitation which clearly highlights the effectiveness and robustness of previously proposed Particle Regularization Technique. Finally, as expected, the lowest vertical displacement rates of the heavier ($\Delta Y = 0.865m$) and lighter ($\Delta Y = 0.646m$) fluids during the simulations ($0 \le T \le 4.9$) take place in case B2 which can be attributed to the aforementioned fluids trapping phenomena in this case. Take as an illustration, in case B1 the heavier and lighter fluids reach the same height at $T = 2.61 (Y = 1.44m)$ while this event occurs at $T = 3.36 (Y = 1.43m)$ in case B2.

7.6.2 Entropy generation due to natural convection heat transfer (cases B3 and B4)

The analysis of transient entropy generation due to natural convection heat transfer in two well-known benchmark cases namely: Differentially Heated Cavity (cases B3) and Rayleigh-Bénard convection (case B4) containing an adiabatic obstacle ($L = 0.3H$) is adopted here to verify the reliability and performance of the improved MPS model in handling particulate flows with thermal convection. The schematic diagrams of two considered configurations with associated boundary conditions are presented in Fig. 7-1. In case B3, the vertical walls are maintained at two different temperatures ($T_c < T_h$) while horizontal walls are thermally adiabatic. However, contrary to case B3, the Rayleigh-Bénard convection in case B4 is induced by differentially heated horizontal walls and insulated vertical walls. The enclosures are filled with air ($\mathrm{Pr} = 0.71$) and

Boussinesq approximation is used to estimate density variations. It is worth noting that, in order to eliminate the unphysical temperature fluctuations from the computational domain, the proposed smoothing operator (Eq. (7-A2)) is employed to calculate the temperature value (T) in the buoyancy force term ($F_b = -\rho g \beta (T - T_c)$) as follows:

$$\begin{bmatrix} T_i \\ T_{i,x} \\ T_{i,y} \end{bmatrix} = L \begin{bmatrix} \sum_{j=1}^{N} \frac{T_j W_{ij}}{|r_{ij}|} dV \\ \sum_{j=1}^{N} \frac{T_j x_{ij} W_{ij}}{|r_{ij}|} dV \\ \sum_{j=1}^{N} \frac{T_j y_{ij} W_{ij}}{|r_{ij}|} dV \end{bmatrix} \qquad L = \begin{bmatrix} \sum_{j=1}^{N} \frac{W_{ij}}{|r_{ij}|} dV & \sum_{j=1}^{N} \frac{x_{ij} W_{ij}}{|r_{ij}|} dV & \sum_{j=1}^{N} \frac{y_{ij} W_{ij}}{|r_{ij}|} dV \\ \sum_{j=1}^{N} \frac{x_{ij} W_{ij}}{|r_{ij}|} dV & \sum_{j=1}^{N} \frac{x_{ij}^2 W_{ij}}{|r_{ij}|} dV & \sum_{j=1}^{N} \frac{x_{ij} y_{ij} W_{ij}}{|r_{ij}|} dV \\ \sum_{j=1}^{N} \frac{y_{ij} W_{ij}}{|r_{ij}|} dV & \sum_{j=1}^{N} \frac{x_{ij} y_{ij} W_{ij}}{|r_{ij}|} dV & \sum_{j=1}^{N} \frac{y_{ij}^2 W_{ij}}{|r_{ij}|} dV \end{bmatrix}^{-1} \qquad (7\text{-}41)$$

Figs. 7-17 to 7-20 illustrate transient variations of streamlines, isotherms, local Bejan number and entropy generation due to heat transfer irreversibility at different Rayleigh number in case B3. It should be mentioned that for the sake of brevity, the contour of velocity in the *y*-direction (*v*) is provided as a supplementary material.

Generally, the hydrodynamic and thermal behaviors of natural convection heat transfer in differentially heated cavity are characterized by upward movement of the heated fluid in close proximity of hot surfaces and downward motion of the denser fluid near the cold surfaces, leading to the establishment of mono- and/or multi-cellular flow pattern inside the enclosure. It can be seen from Figs. 7-17 and 7-18 that the overall features of the flow structures and temperature distributions in case B3 are very similar to those observed in the classical buoyancy-driven cavity [45] where due to thermally-induced buoyant force, the clockwise circulating cell is established and occupies the entire enclosure. Visual examination of the velocity magnitude in Fig. 7-18 reveals that, owing to the weak buoyancy force at $Ra=10^3$, there is no disturbance and significant perturbation in the flow structure, signifying the predominance of heat conduction. The corresponding isotherms in Fig. 7-17 demonstrate the benchmark temperature pattern for the given Rayleigh number since they are nearly parallel to each other and evenly scattered.

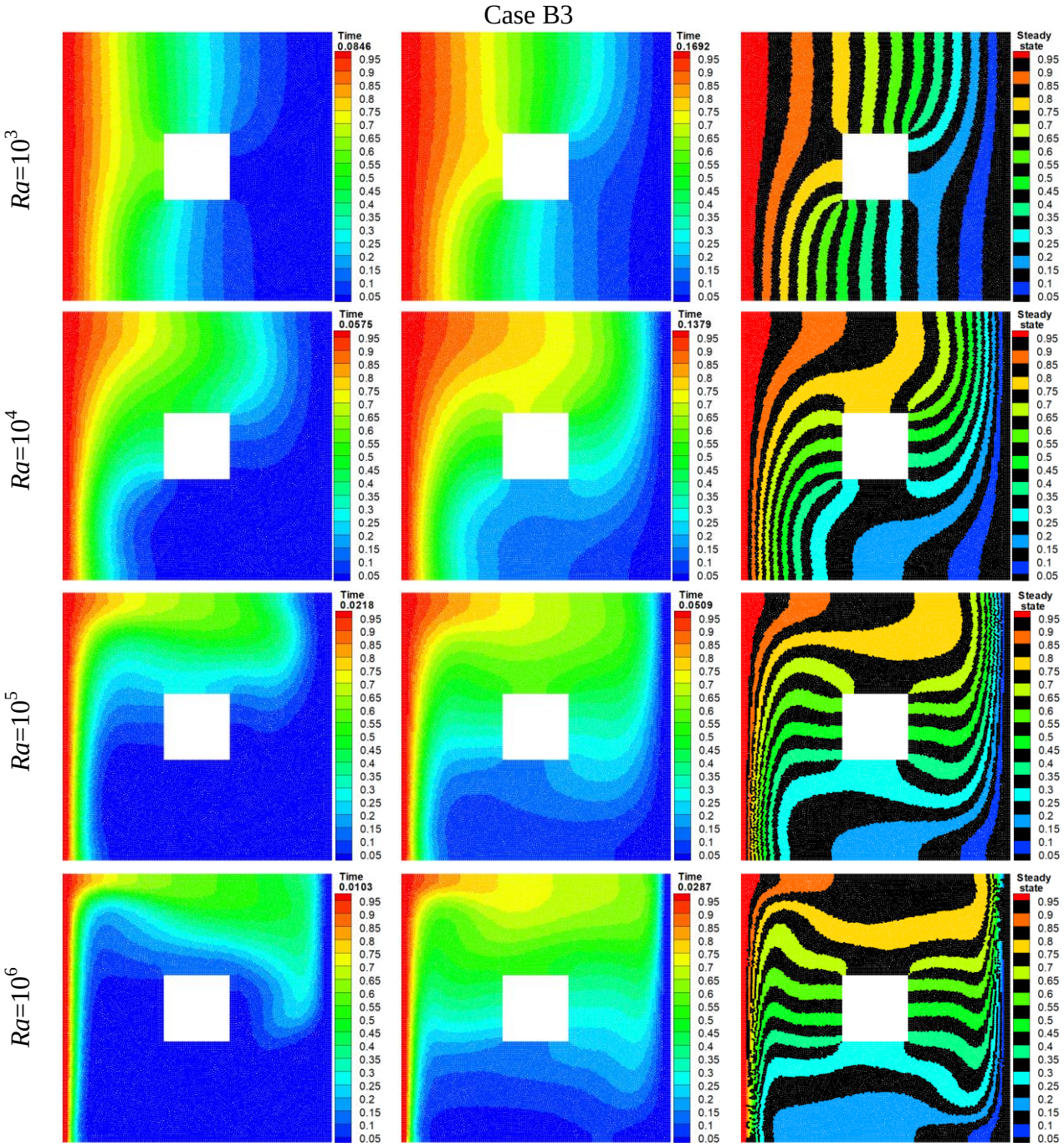

Figure 7-17 Transient variations of temperature field (isotherms) as a function of the non-dimensional time at different Rayleigh numbers for case B3.

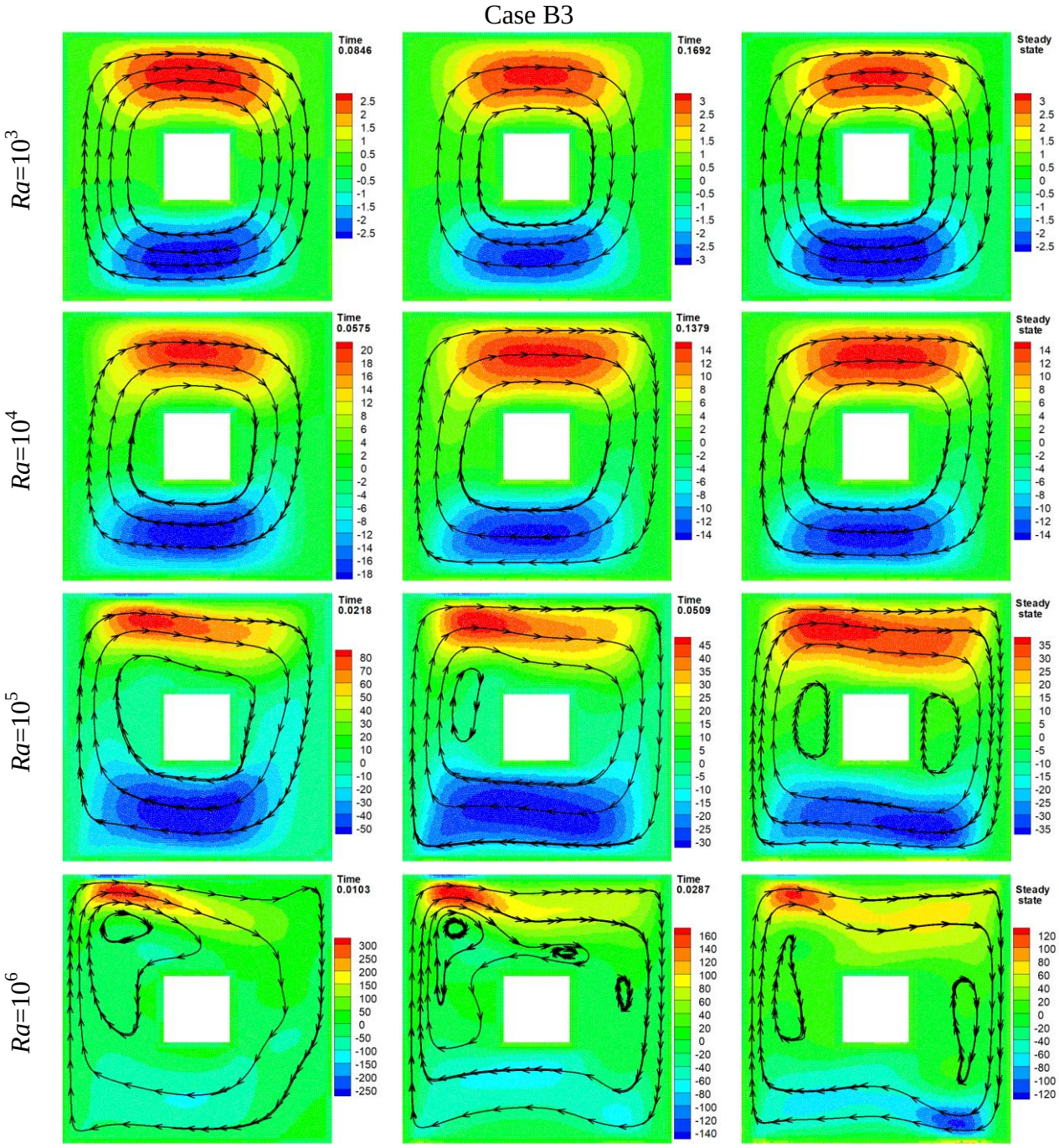

Figure 7-18 Transient variations of velocity field in the x-direction with associated streamlines as a function of the non-dimensional time at different Rayleigh numbers for case B3.

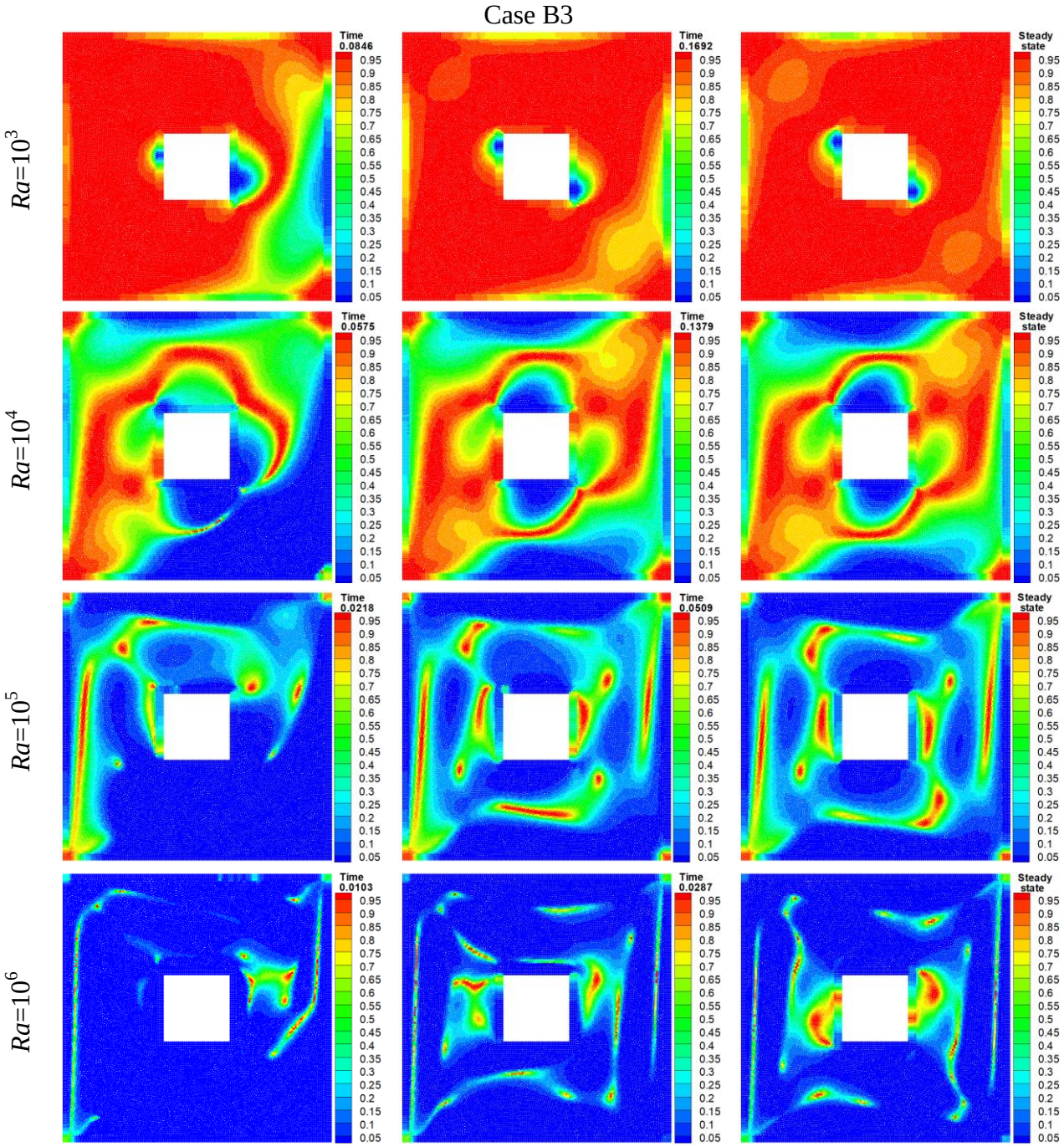

Figure 7-19 Transient variations of the local Bejan number (*Be*) as a function of the non-dimensional time at different Rayleigh numbers for case B3.

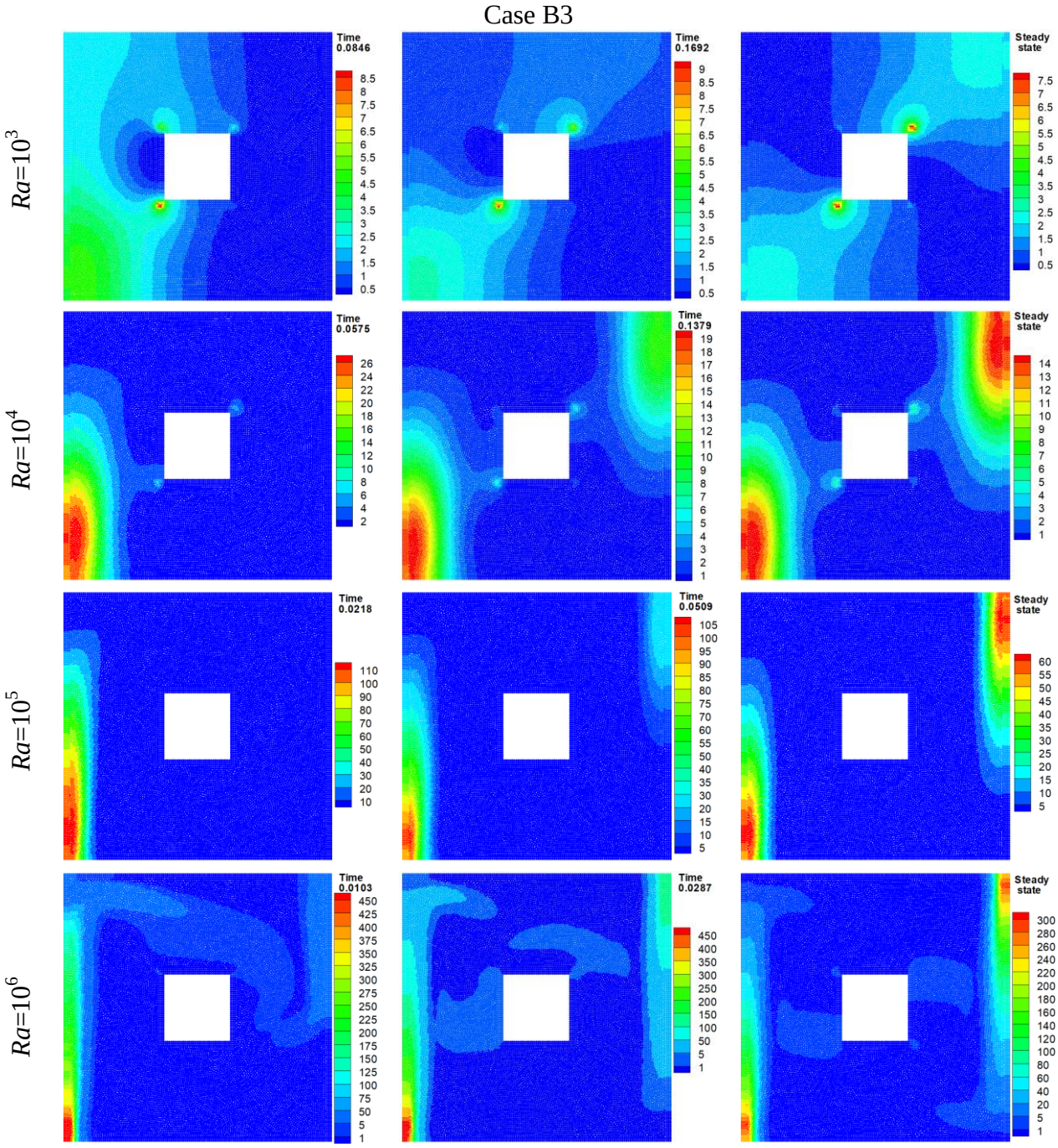

Figure 7-20 Transient variations of the local entropy generation due to heat transfer irreversibility (S_T) as a function of the non-dimensional time at different Rayleigh numbers for case B3.

By increasing Rayleigh number up to 10^4, the vortex strength enhances and isotherms begin to follow the patterns of the streamlines. It should be noted that, the deviation of isotherms from their parallel state vividly implies that the transition point from conduction to convection mode takes place at this stage (quasi-conduction regime). With further increase in the value of Rayleigh number (Ra=10^5), the strength of the convective flow enhances and two secondary circulation cells are developed in the left and right sides of the inner block, reflecting the flow separation in those regions. These flow separation and significant twisting of the isotherms are completely consistent with numerical findings reported by Mahapatra et al. [75] who investigated the effects of the aspect ratio of adiabatic block on the entropy generation and hydrodynamic characteristics of the Differentially Heated Cavity (DHC). Note that, their work at $L = 0.3H$ can be regarded as an extra validation for the current work. However, it can be seen that due to enhanced effects of natural convection at Ra=10^6, the intensity of fluid motion and thermal mixing increases and consequently velocity contour and streamlines are stretched dramatically which support the dominance of the convective mode. Figs. 7-19 and 7-20 show corresponding variations of transient local Bejan number and entropy generation due to heat transfer irreversibility in case B3. As expected, at low Rayleigh number (Ra=10^3) due to domination of conduction mode of heat transfer and weak buoyancy force, the local Bejan number values approach unity which indicates that most of the exergy destruction occurs as a results of the thermal dissipation. Table 7-2 reveals that as the Ra intensifies, the average Nusselt number ($\overline{Nu}$) and maximum absolute values of velocity components ($|U_{\max}|$, $|V_{\max}|$) increase. Since, according to Eqs. (7-12) and (7-13), the enhancement in the heat transfer rate and flow intensity causes temperature and velocity gradients to increase, the entropy generation due to both factors ($\overline{S}_T$, $\overline{S}_F$) augments dramatically. However, since the increment in the viscous dissipation (S_F) is significantly higher than that of the heat transfer irreversibility (S_T), the local and average Bejan number decline. This assertion is well reflected in the contours of the local Bejan number in Fig. 7-19 where entropy generation due to thermal dissipation is only restricted to certain regions between inner cylinder and outer enclosure. As it can be seen in Fig. 7-20 the maximum entropy generation due to heat transfer irreversibility (S_T) is concentrated in the lower-left and upper-right corners of the enclosure, where the contour plots of isotherms are congested and temperature gradients are more intense.

Table 7.2 The effects of the Rayleigh number on the maximum velocity components, average Nusselt number and entropy generation for case B3 and B4 (steady-state condition).

Case B3 (Differentially Heated Cavity)							
Ra	$\overline{Nu}$	$\lvert U_{\max}\rvert$	$\lvert V_{\max}\rvert$	$\overline{Be}$	$\overline{S}_{tot}$	$\overline{S}_T$	$\overline{S}_F$
10^3	0.93560	2.9814	2.9311	0.9566	1.0869	1.0519	0.03496
10^4	2.2424	14.9702	17.4082	0.5809	3.6110	2.4641	1.1468
10^5	4.6517	39.9061	68.1099	0.2373	25.3720	5.0348	20.3372
10^6	9.0540	118.2826	220.4287	0.1148	365.8094	9.6360	356.1734
Case B4 (Rayleigh-Bénard convection)							
Ra	$\overline{Nu}$	$\lvert U_{\max}\rvert$	$\lvert V_{\max}\rvert$	$\overline{Be}$	$\overline{S}_{tot}$	$\overline{S}_T$	$\overline{S}_F$
10^3	0.8130	0.0670	0.05425	0.9907	0.9207	0.9206	3.72×10^{-5}
10^4	2.3169	19.4668	19.1151	0.5415	3.9731	2.5373	1.4358
10^5	3.8763	78.0790	90.4418	0.1999	33.5765	4.1557	29.4208
10^6	6.6802	276.804	322.0081	0.02462	535.9981	6.7532	529.2449

As Ra increases to 10^5, the buoyancy force becomes more prominent and the thickness of the thermal boundary layer decreases. However, as expected, due to small increase in S_T compared to S_F, the magnitude of local and average Bejan number decrease which indicates that entropy generation due to viscous dissipation is coming in to the picture. This trend is maintained or even accentuated as the convective transport strengthens. It can be seen from table 7-2 and Fig. 7-19 that at Ra=10^6, due to faster rotation of clockwise vortex in the enclosure and higher velocity gradients, the average Bejan number decreases and becomes less than half ($\overline{Be} = 0.114$) which implies that contribution of thermal dissipation on total entropy generation ($S_F \approx S_{tot}$) is trivial at this stage. The time-evolution of Rayleigh-Bénard (RB) convection in the square enclosure with heating from below and cooled from above (case B4) is presented in Figs. 7-21 to 7-24 at different Rayleigh number.

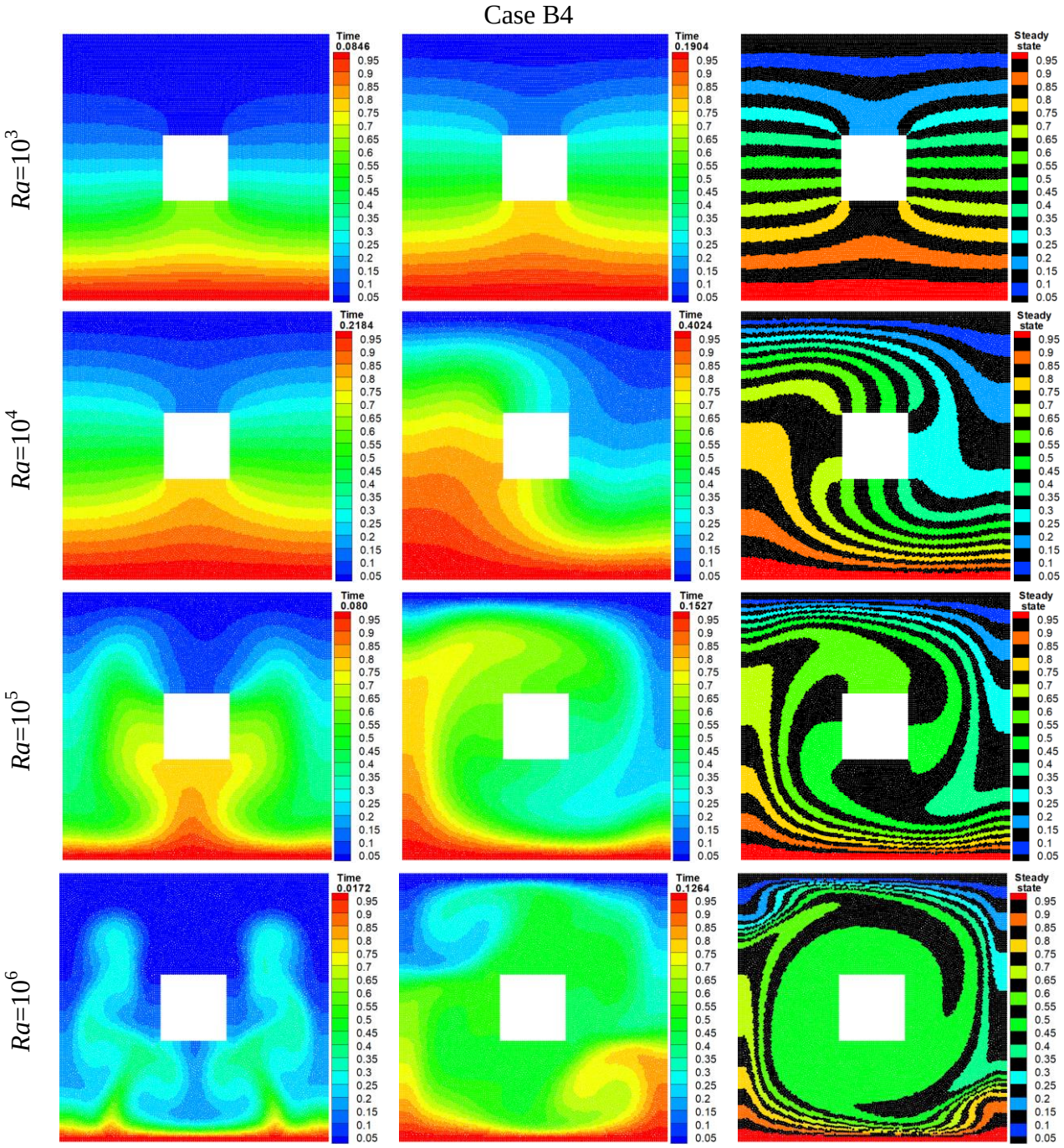

Figure 7-21 Transient variations of temperature field (isotherms) as a function of the non-dimensional time at different Rayleigh numbers for case B4.

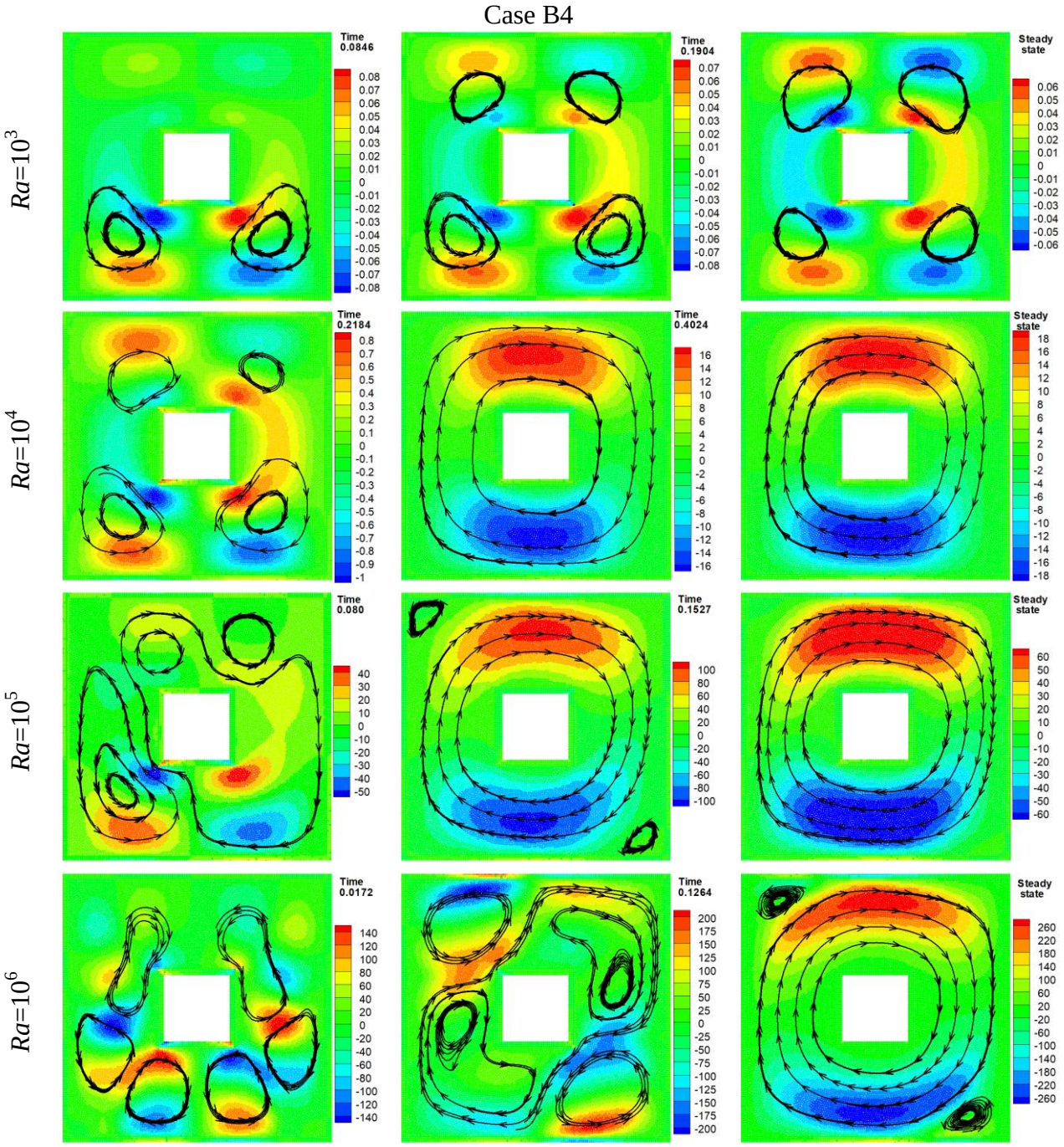

Figure 7-22 Transient variations of velocity field in the *x*-direction with associated streamlines as a function of the non-dimensional time at different Rayleigh numbers for case B4.

Generally, according to linear stability theory [76], [77], the hydrodynamic development of the RB convection can be divided into two distinct stages: (a) conduction dominant regime where at low Rayleigh number ($Ra < Ra_c = 1708$) due to weak buoyancy force, the fluid flow is almost stagnant in the bulk of the enclosure and isotherms are horizontally oriented and (b) convection dominant regime ($Ra_c = 1708 < Ra$) where the flow field is dynamically characterized by the formation of the clockwise Bénard cell. As visualized by low magnitude of velocity field in Fig. 7-22 at Ra=10^3, one can infer that because of high hydraulic resistance and viscous effects, the fluid motion inside the enclosure is weak and has a negligible influence on the temperature field. In this circumstance, isotherms are horizontally stratified and four symmetric rotating eddies of almost same size are established within the enclosure which indicates that heat transfer occurs primarily as the result of conduction mode. As expected, Fig. 7-23 and table 7-2 show that the corresponding local and average Bejan numbers are very close to unity ($\overline{Be} = 0.99$) which indicates that a significant contribution on the total entropy generation comes from thermal dissipation ($\overline{S}_{tot} = \overline{S}_T$, $\overline{S}_F \approx 0$). It can be seen from Fig. 7-24 that, the local entropy generation due to heat transfer irreversibility is completely symmetric with respect to vertical centerline at X=0.5 and maximum S_T is found to occur on the corners of the adiabatic obstacle similar to work of Pandit [78]. A close inspection of table 7-2 and Fig. 7-22 reveal that when Rayleigh number exceeds the critical value ($Ra_c = 1708 < Ra = 10^4$), convective motion of the fluid ($|U_{\max}|, |V_{\max}|$) increases dramatically and thermal stratification becomes unstable which is an indication of the onset of the Bénard instability. It can be seen from Figs. 7-21 and 7-22 that, with the passage of time, the axial symmetry feature starts to vanish gradually and the clockwise recirculation roll is ultimately emerged within the enclosure. As a consequence of stronger thermal mixing, distinct thermal boundary layers are developed near the top-left and bottom-right parts of the horizontal walls which results in active sites of S_T in those regions where due to immediate contact of working fluid with isothermal walls, the higher temperature gradient exists. It is interesting to note that, the formation of the Bénard cell is also accompanied by substantial increase in the intensity of fluid flow which in turn leads to the higher velocity gradient and entropy generation due to fluid friction irreversibility.

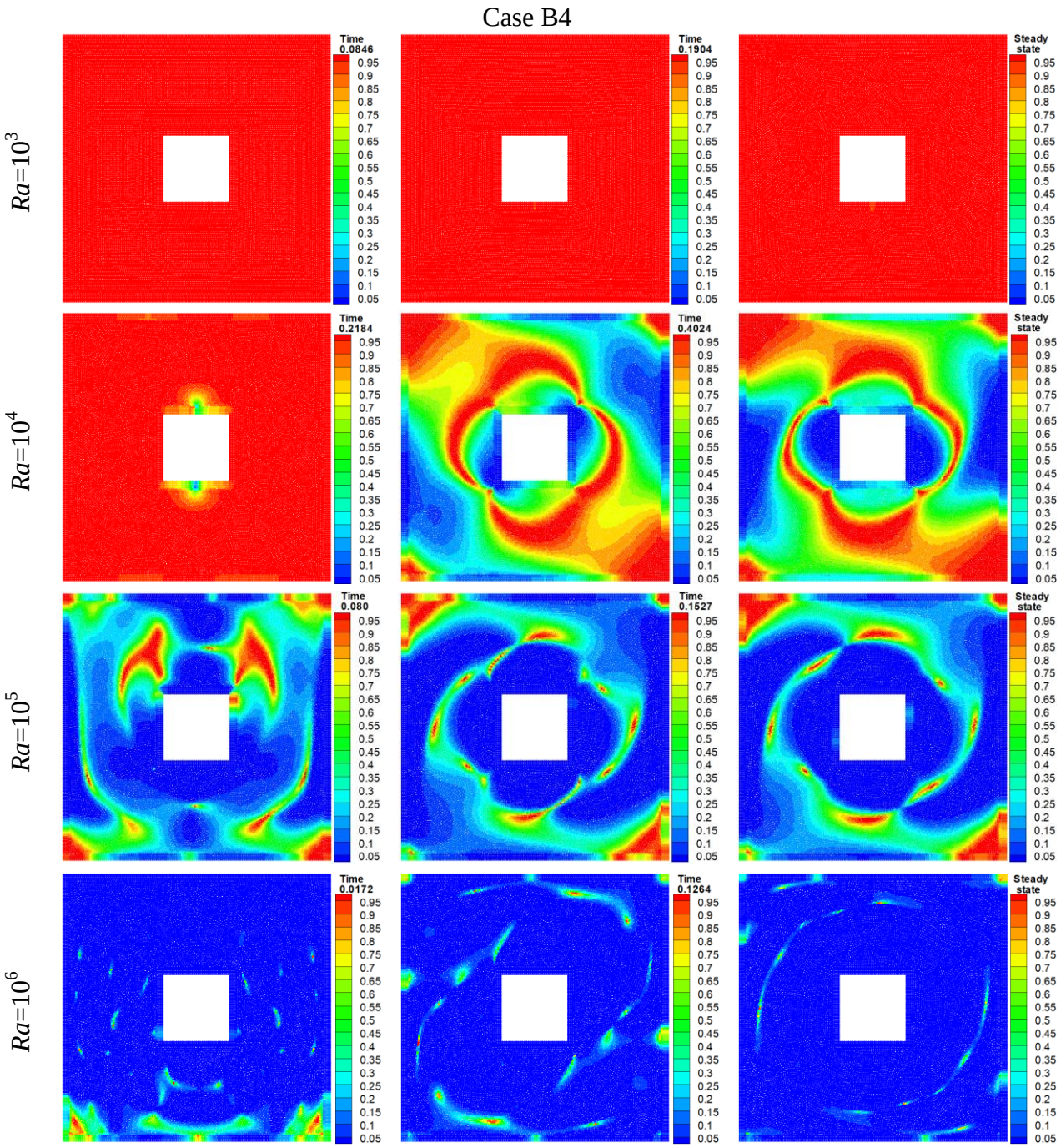

Figure 7-23 Transient variations of the local Bejan number (*Be*) as a function of the non-dimensional time at different Rayleigh numbers for case B4.

As discussed before, since the increase in velocity gradient at $Ra=10^4$ is remarkably greater than that of the temperature gradient, the average Bejan number declines rapidly and becomes equal to

$\overline{Be} = 0.54$ which indicates that both S_F and S_T have a same contribution to overall entropy generation. With further increase in the Rayleigh number (Ra=10^5), the strength of the Bénard cell evidently augments and consequently isotherms in the fluid region get more oriented towards the flow direction and thickness of thermal boundary layer decreases, indicating the establishment of the convective mode. The corresponding local Bejan number in Fig. 7-23 reveals that, owning to intense fluid flow and as a consequence of implementation of no-slip boundary conditions, all walls of the enclosure act as strong active zones of S_F where steeper velocity gradients occur. Finally, it can be seen from table 7-2 and Fig. 7-23 that at Ra=10^6, due to remarkable enhancement in the convection effects, the magnitude of S_F increases considerably and subsequently the average Bejan number becomes less than 0.024. This observation signifies that in the convection dominant region ($Ra \geq 10^6$), the considerable amount of available work might be exploited to overcome the irreversibility due to viscous dissipation. Finally, it can be seen from Fig. 7-22 that, when the system reaches the steady-state condition, the primary clockwise eddy together with a pair of secondary CCW vortices are appeared within the enclosure. These flow structure and temperature pattern together with their associated numbers of vortices are in accordance with numerical observations of Ouertatani et al. [79].

To get more insights into the performance of thermal systems in cases B3 and B4, the transient variations of average Nusselt number ($\overline{Nu}$) on the isothermal walls, total entropy generation ($\overline{S}_{tot}$) due to thermal ($\overline{S}_T$) and viscous dissipations ($\overline{S}_F$) and average Bejan number ($\overline{Be}$) at different Rayleigh number ($10^3 \leq Ra \leq 10^6$) are plotted in Fig. 7-25. The general trend of results shows that as the Rayleigh number intensifies, the heat transfer rate and entropy generation due to both factors ($\overline{S}_T$, $\overline{S}_F$) augment whereas a downward trend is observed in the values of average Bejan number. Again, as it was previously described, the rapid decreasing trend of $\overline{Be}$ can be attributed to the significant enhancement in the values of $\overline{S}_F$ compared to $\overline{S}_T$ with the augmentation of Ra. As expected, due to static condition and weak fluid flow at Ra=10^3, the values of $\overline{S}_F$ is significantly lower than that of the $\overline{S}_T$ (especially in case B4).

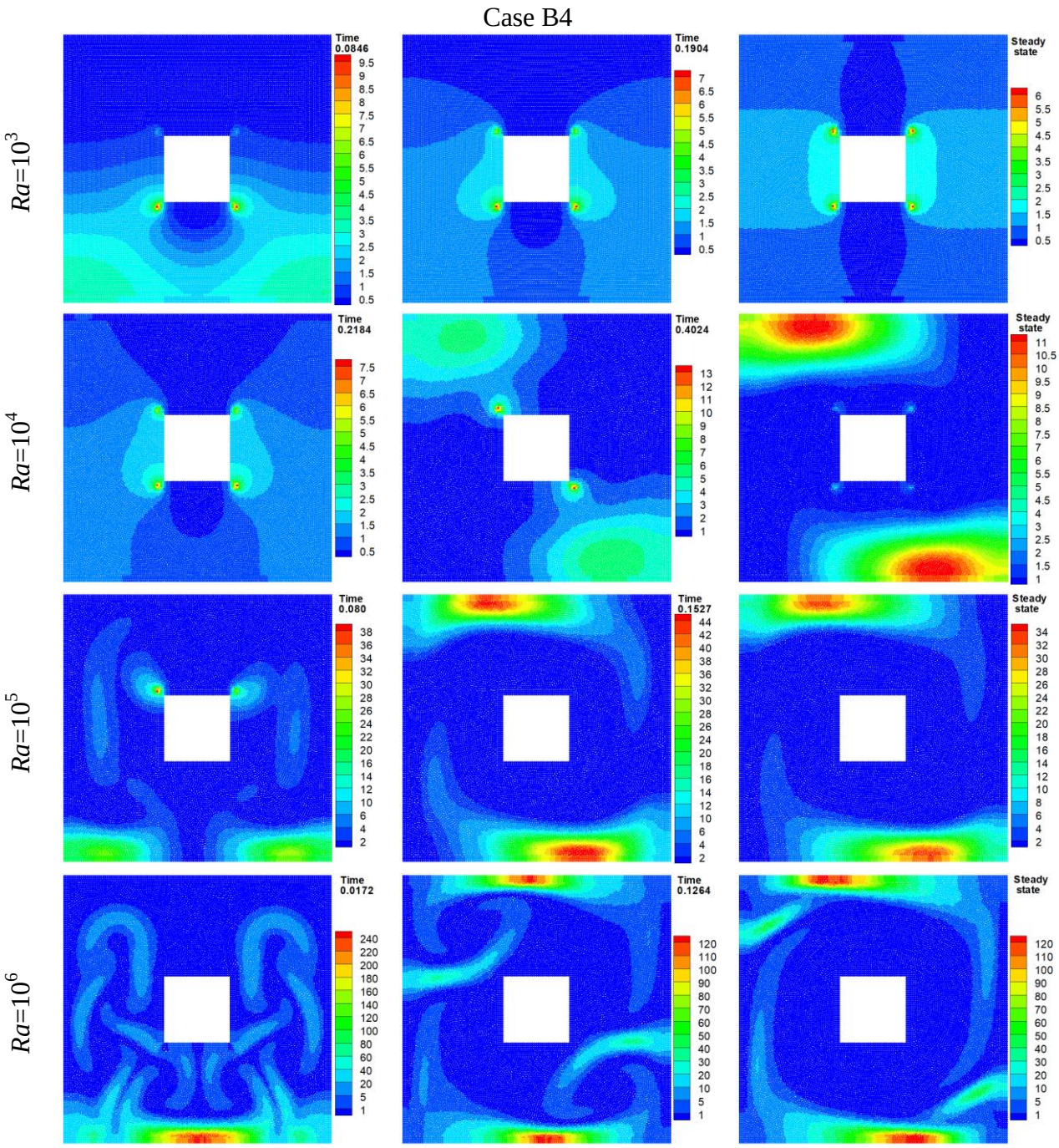

Figure 7-24 Transient variations of the local entropy generation due to heat transfer irreversibility (ST) as a function of the non-dimensional time at different Rayleigh numbers for case B4.

This observation again verifies the earlier assertion that, at conduction-dominated regime only a small amount of available work is used to overcome irreversibilities due to viscous dissipation.

Thus, it is not surprising that the overall behavior of total entropy generation becomes very similar to the thermal dissipation profile ($\overline{S}_{tot} \approx \overline{S}_T$) at low *Ra*. Furthermore, the smooth time variations of $\overline{Nu}$, $\overline{S}_{tot}$, $\overline{S}_T$, $\overline{S}_F$ and $\overline{Be}$ vividly demonstrates that since at low Rayleigh number ($Ra = 10^3$), the thermal system in both cases is very close to the equilibrium state [80], the aforementioned pertinent parameters reach the steady state condition asymptotically without passing through the fluctuation period. However, by increasing the *Ra* up to 10^4, deviation from equilibrium state increases and consequently oscillatory behavior starts to appear within the computational domain especially in case B4 where flow and temperature fields are inherently more prone to instability. Note that, such a behavior can readily be seen in Fig. 7-22 where due to drastic changes in the flow patterns including the merging of rolls or exchange of mass between them, the streamlines undergo complex structural changes over a period range of $0 \le t^* \le 0.402$. For example, the detailed analysis of time-variations of heat transfer rate in case B4 illustrates that at *Ra*=10^4, the mean Nusselt number on the top wall decreases rapidly to reach minimum value ($\overline{Nu}_{\min} = 0.88$) at $t^* = 0.322$ and then increases and attains a maximum value ($\overline{Nu}_{\max} = 2.69$) at $t^* = 0.46$. This extreme oscillating behavior may be ascribed to the formation and destruction of the first bifurcation phenomena which occurred at the onset of the instability. It can be also seen that due to quasi-conduction dominant regime, this course of the event also occurs in the time-histories of $\overline{S}_{tot}$ and $\overline{S}_T$ but with different values. With further increase in the values of *Ra*, intensity of buoyancy force is invigorated and subsequently the frequency and amplitude of the oscillations increase [81]. From a thermodynamics view point, the oscillatory behavior of the entropy generation at high Rayleigh numbers can be attributed to the irreversible generation of internal waves and thermal jump in the velocity and temperature fields [82]. Moreover, from the viewpoint of optimization theory and energy efficiency, it is evident that case B3 exhibits higher heat transfer rate and lower $\overline{S}_{tot}$. Take as an illustration, in case B3 the ratios of average Nusselt number to total entropy generation ($\overline{Nu}/\overline{S}_{tot}$) at *Ra*=$10^3$, 10^4, 10^5 and 10^6 are approximately 0.86, 0.615, 0.183 and 0.024 while these values are respectively equal to 0.88, 0.583, 0.115 and 0.012 in case B4.

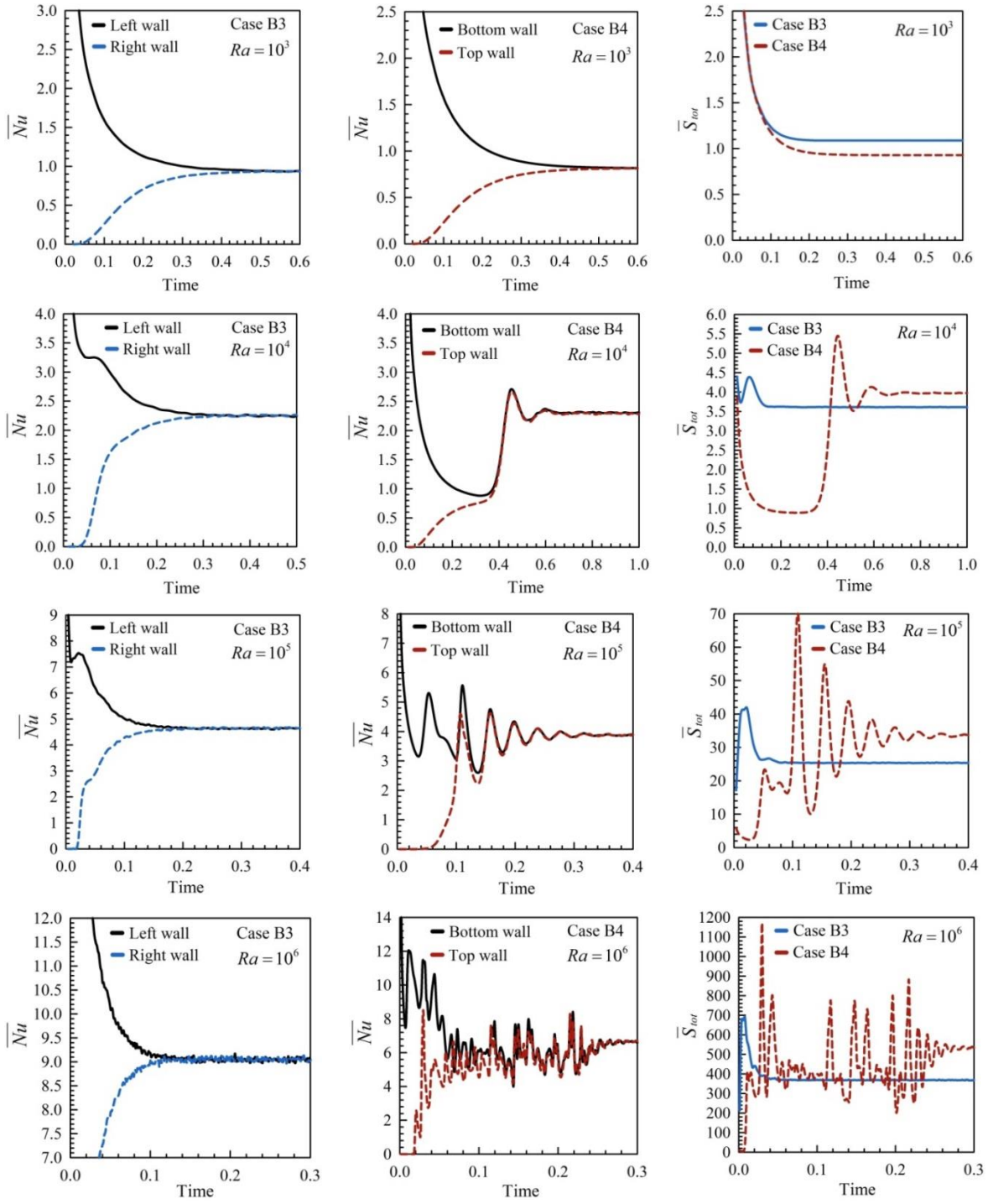

Figure 7-25 Transient variations of average Nusselt number ($\overline{Nu}$), average Bejan number ($\overline{Be}$), total entropy generation ($\overline{S}_{tot}$), average entropy generation due to thermal ($\overline{S}_T$) and viscous ($\overline{S}_F$) dissipations as a function of the non-dimensional time for cases B3 and B4 at different Rayleigh number. Pr=0.71, L=0.3H.

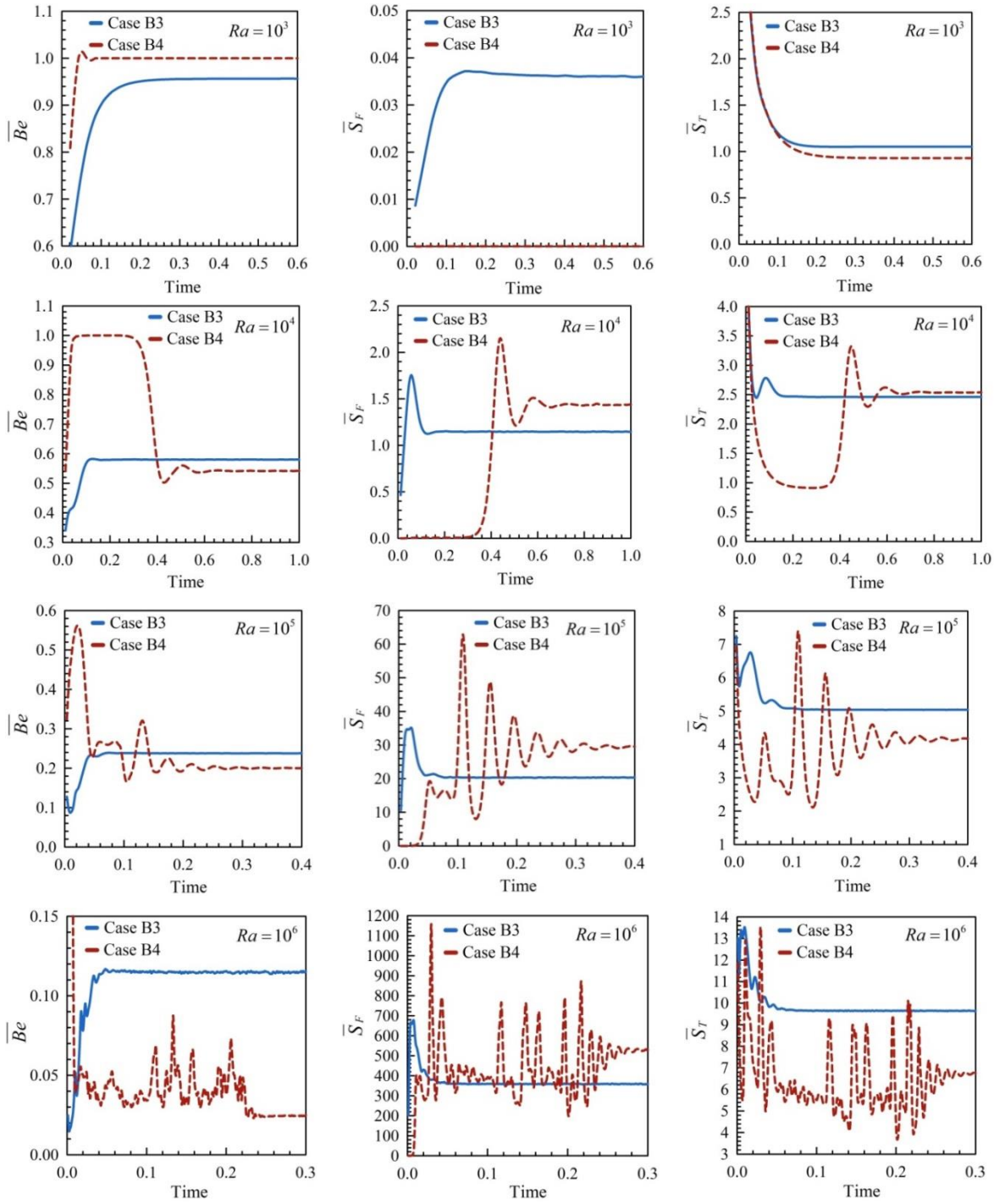

Figure 7-26 Transient variations of average Nusselt number ($\overline{Nu}$), average Bejan number ($\overline{Be}$), total entropy generation ($\overline{S}_{tot}$), average entropy generation due to thermal ($\overline{S}_T$) and viscous ($\overline{S}_F$) dissipations as a function of the non-dimensional time for cases B3 and B4 at different Rayleigh number. Pr=0.71, L=0.3H. (cont'd).

Based on the above analysis, it can be concluded that the Differentially Heated Cavity (case B3) appears to be an energy-efficient compared to the Rayleigh-Benard convection especially at the onset of the convection. Similar findings were also documented by Anandalakshmi et al. [83] who investigated the entropy generation due to natural convection in rhombic enclosures with isothermally heated walls. Finally, similar to previous benchmark test cases, it is apparent that, particles in case B3 and B4 are regularly distributed throughout the simulations without any unphysical gap and void formation which in turn demonstrate the robustness and applicability of proposed models in handling particulate flows with thermal convection.

7.7 Conclusions

This paper introduced a new kernel function and two novel high-order gradient and Laplacian operators in the context of the Lagrangian mesh-free particle method (particularly MPS) for simulation of free-surface flows and exergy analysis of convection heat transfer problems. The numerical examples vividly confirm the effectiveness and applicability of currently enhanced MPS model in solving real-life and academic problems ranging from free-surface flows to convection heat transfer. The important findings of this study can be highlighted as follows:

- The results shown that, the newly constructed kernel function remarkably outperformed the existing smoothing kernels (i.e. quintic spline and Wendland) in capturing/resolving shocks discontinuities and rarefaction wave region.
- It was also found that, the proposed kernel function produces more reliable and stable results than the quintic spline and Wendland functions in modeling of free-surface problems and multiphase flows.
- It was found that, the proposed *Revised Pressure Gradient* operator (switching model) can efficiently eliminate tensile instability problem from the free-surface area and subsequently provide more accurate and smoother pressure field than the traditional conservative form of the MPS operator.
- The results show that, particles in Lagrangian framework have a natural tendency to migrate along the streamline, leading to the formation of empty space and the particles clumping/stratification within the computational domain.
- The results show that, Particle Shifting Technique (PST) has a notable impact on the accuracy and efficiency of the Lagrangian particle methods.

- The results reveal that, the proposed smoothing operator (Eq. (7-A2)) can efficiently handle sharp density discontinuities adjacent to the material interfaces.
- The results illustrate that, the proposed novel higher-order gradient and Laplacian operators for discretization of Pressure-Poisson equation and divergence of velocity can effectively eliminate spurious pressure fluctuation and density error accumulation from the fluid domain.

7.8 Appendix A (gradient, Laplacian and divergence operators)

Along this appendix two new gradient and Laplacian operators are systematically derived based on Taylor series expansion. Generally, for 2D space, by multiplying both sides of Eq. (7-A1) first by $W_{ij}, x_{ij}W_{ij}/|r_{ij}|$, $y_{ij}W_{ij}/|r_{ij}|$ and then summing it over every detected neighbor particle *j*, the shape function for any arbitrarily variable (f_i) can be obtained as follows:

$$f_j = f_i + f_{i,x}x_{ij} + f_{i,y}y_{ij} + \frac{1}{2}f_{i,xx}x_{ij}^2 + \frac{1}{2}f_{i,yy}y_{ij}^2 + f_{i,xy}x_{ij}y_{ij} + O(h^3) \tag{7-A1}$$

$$\begin{bmatrix} f_i \\ f_{i,x} \\ f_{i,y} \end{bmatrix} = L \begin{bmatrix} \sum_{j=1}^{N} \frac{f_j W_{ij}}{|r_{ij}|} dV \\ \sum_{j=1}^{N} \frac{f_j x_{ij} W_{ij}}{|r_{ij}|} dV \\ \sum_{j=1}^{N} \frac{f_j y_{ij} W_{ij}}{|r_{ij}|} dV \end{bmatrix} \qquad L = \begin{bmatrix} \sum_{j=1}^{N} \frac{W_{ij}}{|r_{ij}|} dV & \sum_{j=1}^{N} \frac{x_{ij} W_{ij}}{|r_{ij}|} dV & \sum_{j=1}^{N} \frac{y_{ij} W_{ij}}{|r_{ij}|} dV \\ \sum_{j=1}^{N} \frac{x_{ij} W_{ij}}{|r_{ij}|} dV & \sum_{j=1}^{N} \frac{x_{ij}^2 W_{ij}}{|r_{ij}|} dV & \sum_{j=1}^{N} \frac{x_{ij} y_{ij} W_{ij}}{|r_{ij}|} dV \\ \sum_{j=1}^{N} \frac{y_{ij} W_{ij}}{|r_{ij}|} dV & \sum_{j=1}^{N} \frac{x_{ij} y_{ij} W_{ij}}{|r_{ij}|} dV & \sum_{j=1}^{N} \frac{y_{ij}^2 W_{ij}}{|r_{ij}|} dV \end{bmatrix}^{-1} \tag{7-A2}$$

In above equations, W_{ij} and $dV = m_j/\rho_j$ denote kernel function and volume of the particle while $x_{ij} = x_j - x_i$ and $y_{ij} = y_j - y_i$ represent the distance between candidate particle *i* and its neighboring particle *j*, respectively. *L* is a corrective matrix which guarantees first-order completeness in kernel approximations. It is worth to mention that, Eq. (7-A2) is analogous to the MLS approximation pioneered by Nayroles et al. [84].

By subtracting f_i from both sides of Eq. (7-A1) and multiplying it by $x_{ij}W_{ij}/r_{ij}^2$ and $y_{ij}W_{ij}/r_{ij}^2$, the first derivatives of field function (gradient operator) can be obtained as follow:

$$\begin{bmatrix} f_{i,x} \\ f_{i,y} \end{bmatrix} = L \begin{bmatrix} \sum_{j=1}^{N} \frac{(f_j - f_i)x_{ij}W_{ij}}{r_{ij}^2} dV \\ \sum_{j=1}^{N} \frac{(f_j - f_i)y_{ij}W_{ij}}{r_{ij}^2} dV \end{bmatrix} \qquad L = \begin{bmatrix} \sum_{j=1}^{N} \frac{x_{ij}^2 W_{ij}}{r_{ij}^2} dV & \sum_{j=1}^{N} \frac{x_{ij}y_{ij}W_{ij}}{r_{ij}^2} dV \\ \sum_{j=1}^{N} \frac{x_{ij}y_{ij}W_{ij}}{r_{ij}^2} dV & \sum_{j=1}^{N} \frac{y_{ij}^2 W_{ij}}{r_{ij}^2} dV \end{bmatrix}^{-1} \tag{7-A3}$$

Eq. (7-A3) was originally introduced by Khayyer et al. [24] and then was extended and utilized by [25], [85] for simulation of multiphase flow problems. However, when the kernel function has a compact support, all off-diagonal entries of L matrix vanish, thereby producing the symmetric diagonal corrective matrix ($\sum_{j=1}^{N} x_{ij}y_{ij}W_{ij}/r_{ij}^2\, dV = \sum_{j=1}^{N} x_{ij}y_{ij}W_{ij}/r_{ij}^2\, dV = 0$) as follows:

$$L = \begin{bmatrix} \sum_{j=1}^{N} \frac{x_{ij}^2 W_{ij}}{r_{ij}^2} dV & 0 \\ 0 & \sum_{j=1}^{N} \frac{y_{ij}^2 W_{ij}}{r_{ij}^2} dV \end{bmatrix}^{-1} \tag{7-A4}$$

In this condition, the corrective matrix L acts like a normalization factor in the traditional MPS approximations such that gradient operator can be calculated with less computational cost as:

$$f_{i,x} = \frac{\partial f}{\partial x} = \frac{\sum_{j=1}^{N} \frac{(f_j - f_i)x_{ij}W_{ij}}{r_{ij}^2} dV}{\sum_{j=1}^{N} \frac{x_{ij}^2 W_{ij}}{r_{ij}^2} dV}, \qquad f_{i,y} = \frac{\partial f}{\partial y} = \frac{\sum_{j=1}^{N} \frac{(f_j - f_i)y_{ij}W_{ij}}{r_{ij}^2} dV}{\sum_{j=1}^{N} \frac{y_{ij}^2 W_{ij}}{r_{ij}^2} dV} \tag{7-A5}$$

Based on the above formulations, divergence operator for the regular particle distribution can be calculated as follows:

$$\nabla \cdot \mathbf{f} = \frac{\sum_{j=1}^{N} \frac{(\mathbf{f}_j - \mathbf{f}_i) \cdot \mathbf{x}_{ij}}{\mathbf{r}_{ij}^2} W_{ij} dV}{\sum_{j=1}^{N} \frac{\mathbf{x}_{ij}^2 W_{ij}}{\mathbf{r}_{ij}^2} dV} \tag{7-A6}$$

where $\mathbf{x}_{ij}$ is spatial distance in x ($x_{ij} = x_j - x_i$) or y-direction ($y_{ij} = y_j - y_i$). However, as stated previously, in the case of irregular particles distribution, Eq. (7-A3) should be used to calculate divergence of field function. For instance, for calculating divergence of the velocity in two-dimensional system, Eq. (7-A3) must be solved twice, where sum of the velocity gradients in x ($\partial u/\partial x$) and y ($\partial v/\partial y$) directions can provide $\nabla \cdot \mathbf{u}$.

It should be note that, Eq. (7-A5) can be further simplified by solving $\sum_{j=1}^{N}\frac{x_{ij}^2 W_{ij}}{r_{ij}^2}dV$ and $\sum_{j=1}^{N}\frac{y_{ij}^2 W_{ij}}{r_{ij}^2}dV$ in a polar coordinate system ($x_{ij}=r_{ij}\cos(\theta),\ y_{ij}=r_{ij}\sin(\theta)$) as follows:

$$\sum_{j=1}^{N}\frac{x_{ij}^2}{r_{ij}^2}W_{ij}dV=\sum_{j=1}^{N}\frac{y_{ij}^2}{r_{ij}^2}W_{ij}dV=\frac{1}{2}(\sum_{j=1}^{N}\frac{x_{ij}^2}{r_{ij}^2}W_{ij}dV+\sum_{j=1}^{N}\frac{y_{ij}^2}{r_{ij}^2}W_{ij}dV)=\frac{1}{2}(\sum_{j=1}^{N}W_{ij}dV)$$
$$\frac{1}{3}(\sum_{j=1}^{N}\frac{x_{ij}^2}{r_{ij}^2}W_{ij}dV+\sum_{j=1}^{N}\frac{y_{ij}^2}{r_{ij}^2}W_{ij}dV+\sum_{j=1}^{N}\frac{z_{ij}^2}{r_{ij}^2}W_{ij}dV)=\frac{1}{D_0}\sum_{j=1}^{N}W_{ij}dV,\quad \text{where}\quad x_{ij}^2+y_{ij}^2=r_{ij}^2 \tag{7-A7}$$

$$\nabla f=\frac{D_0\sum_{j=1}^{N}\frac{\mathbf{r}_{ij}(f_j-f_i)}{r_{ij}^2}W_{ij}dV}{\sum_{j=1}^{N}W_{ij}dV} \tag{7-A8}$$

$$\nabla\cdot\mathbf{f}=\frac{D_0\sum_{j=1}^{N}\frac{\mathbf{r}_{ij}\cdot(\mathbf{f}_j-\mathbf{f}_i)W_{ij}}{r_{ij}^2}dV}{\sum_{j=1}^{N}W_{ij}dV} \tag{7-A9}$$

where D_0 is spatial dimension. Eqs. (7-A8) and (7-A9) were initially proposed by Koshizuka et al. [86] in the context of the MPS description and then employed by Tanaka et al. [4] and Liang et al. [87] to calculate the gradient and divergence of arbitrary scalar or vector functions. However, It is also possible to derive the second gradient operator by subtracting f_i from both sides of Eq. (7-A1) and multiplying it by $x_{ij}W_{ij}/|r_{ij}|$ and $y_{ij}W_{ij}/|r_{ij}|$ instead of $x_{ij}W_{ij}/r_{ij}^2$ and $y_{ij}W_{ij}/r_{ij}^2$. This gives:

$$\begin{bmatrix} f_{i,x} \\ f_{i,y} \end{bmatrix}=L\begin{bmatrix} \sum_{j=1}^{N}\frac{(f_j-f_i)x_{ij}W_{ij}}{|r_{ij}|}dV \\ \sum_{j=1}^{N}\frac{(f_j-f_i)y_{ij}W_{ij}}{|r_{ij}|}dV \end{bmatrix}\qquad L=\begin{bmatrix} \sum_{j=1}^{N}\frac{x_{ij}^2W_{ij}}{|r_{ij}|}dV & \sum_{j=1}^{N}\frac{x_{ij}y_{ij}W_{ij}}{|r_{ij}|}dV \\ \sum_{j=1}^{N}\frac{x_{ij}y_{ij}W_{ij}}{|r_{ij}|}dV & \sum_{j=1}^{N}\frac{y_{ij}^2W_{ij}}{|r_{ij}|}dV \end{bmatrix}^{-1} \tag{7-A10}$$

By comparing Eqs. (7-A3) and (7-A10), one can deduce that, the power of r_{ij}^n in Eq. (7-A3) is reduced from $n=2\,\text{to}\,n=1$ in Eq. (7-A10). At this stage, it is worth to mention that, although Eqs. (7-A3) and (7-A10) are very similar to each other, but they have different stability

characteristics in dealing with the tensile stability and particle clustering. With further reduction in the power of the variable r_{ij}^{n} from $n=1$ to $n=0$, the third form of gradient operator with first-order of accuracy can be obtained as:

$$\begin{bmatrix} f_{i,x} \\ f_{i,y} \end{bmatrix} = L \begin{bmatrix} \sum_{j=1}^{N} (f_j - f_i) x_{ij} W_{ij} dV \\ \sum_{j=1}^{N} (f_j - f_i) y_{ij} W_{ij} dV \end{bmatrix} \qquad L = \begin{bmatrix} \sum_{j=1}^{N} x_{ij}^2 W_{ij} dV & \sum_{j=1}^{N} x_{ij} y_{ij} W_{ij} dV \\ \sum_{j=1}^{N} x_{ij} y_{ij} W_{ij} dV & \sum_{j=1}^{N} y_{ij}^2 W_{ij} dV \end{bmatrix}^{-1} \tag{7-A11}$$

Eq. (7-A11) is known as a *mixed symmetric correction of kernel gradient* which was initially proposed by Xu et al. [26] in the context of the MPS description.

By ignoring the term $f_{i,xy}\, x_{ij} y_{ij}$ in Eq. (7-A1) and subtracting f_i from both sides of the equation, and multiplying it by W_{ij}, the MPS stencil for the Laplacian operator can be achieved as:

$$\begin{aligned} \sum_{j=1}^{N} (f_j - f_i) W_{ij} dV &= f_{i,x} \sum_{j=1}^{N} x_{ij} W_{ij} dV + f_{i,y} \sum_{j=1}^{N} y_{ij} W_{ij} dV \\ &+ f_{i,xx} \sum_{j=1}^{N} \frac{1}{2} x_{ij}^2 W_{ij} dV + f_{i,yy} \sum_{j=1}^{N} \frac{1}{2} y_{ij}^2 W_{ij} dV, \end{aligned} \tag{7-A12}$$

Similar to work of Schwaiger et al. [30], in order to derive $\nabla^2 f = f_{i,xx} + f_{i,yy}$, one can assume that $\sum_{j=1}^{N} \frac{1}{2} x_{ij}^2 W_{ij} dV$ is equal to $\sum_{j=1}^{N} \frac{1}{2} y_{ij}^2 W_{ij} dV$ for uniform particles distribution. Under the aforementioned hypothesis, the Laplacian operator can be obtained as follows:

$$\nabla^2 f = f_{i,xx} + f_{i,yy} = \frac{\sum_{j=1}^{N} (f_j - f_i) W_{ij} dV - f_{i,x} \sum_{j=1}^{N} x_{ij} W_{ij} dV - f_{i,y} \sum_{j=1}^{N} y_{ij} W_{ij} dV}{\sum_{j=1}^{N} \frac{1}{2} x_{ij}^2 W_{ij} dV} \tag{7-A13}$$

By decomposing the first term in the right-hand side of the Eq. (7-A13) into two separate parts ($\sum_{j=1}^{N} (f_j - f_i) W_{ij} dV = 0.5 \times \sum_{j=1}^{N} (f_j - f_i) W_{ij} dV + 0.5 \times \sum_{j=1}^{N} (f_j - f_i) W_{ij} dV$), the above equation may be rewritten as:

$$\nabla^2 f = \frac{\frac{1}{2}\sum_{j=1}^{N}(f_j - f_i)W_{ij}dV + \frac{1}{2}\sum_{j=1}^{N}(f_j - f_i)W_{ij}dV - f_{i,x}\sum_{j=1}^{N}x_{ij}W_{ij}dV - f_{i,y}\sum_{j=1}^{N}y_{ij}W_{ij}dV}{\sum_{j=1}^{N}\frac{1}{2}x_{ij}^2 W_{ij}dV} \tag{7-A14}$$

Finally, the above equation can be rearranged into two separate and distinct terms as follows:

$$\nabla^2 f = f_{i,xx} + f_{i,yy} = \frac{\frac{1}{2}\sum_{j=1}^{N}(f_j - f_i)W_{ij}dV - f_{i,x}\sum_{j=1}^{N}x_{ij}W_{ij}dV}{\sum_{j=1}^{N}\frac{1}{2}x_{ij}^2 W_{ij}dV} + \frac{\frac{1}{2}\sum_{j=1}^{N}(f_j - f_i)W_{ij}dV - f_{i,y}\sum_{j=1}^{N}y_{ij}W_{ij}dV}{\sum_{j=1}^{N}\frac{1}{2}y_{ij}^2 W_{ij}dV} \tag{7-A15}$$

where the term $\sum_{j=1}^{N}\frac{1}{2}x_{ij}^2 W_{ij}dV$ is replaced by $\sum_{j=1}^{N}\frac{1}{2}y_{ij}^2 W_{ij}dV$ in the second term of the above equation. However, similar to gradient operator, by eliminating the first derivative of the field function from the Eq. (7-A15) ($\sum_{j=1}^{N}x_{ij}W_{ij}dV = \sum_{j=1}^{N}y_{ij}W_{ij}dV = 0$), the Laplacian operator for uniform particles distribution can be expressed in a relatively simpler form as follows:

$$\nabla^2 f = f_{i,xx} + f_{i,yy} = \frac{\sum_{j=1}^{N}\frac{1}{2}(f_j - f_i)W_{ij}dV}{\sum_{j=1}^{N}\frac{1}{2}x_{ij}^2 W_{ij}dV} + \frac{\sum_{j=1}^{N}\frac{1}{2}(f_j - f_i)W_{ij}dV}{\sum_{j=1}^{N}\frac{1}{2}y_{ij}^2 W_{ij}dV} \tag{7-A16}$$

By solving $\int\frac{1}{2}x_{ij}^2 W_{ij}dV$ and $\int\frac{1}{2}y_{ij}^2 W_{ij}dV$ in a polar coordinate system ($x_{ij} = r_{ij}\cos\varphi$, $y_{ij} = r_{ij}\sin\varphi$), Eq. (7-A16) can be re-written in the general form as follows:

$$\sum_{j=1}^{N}\frac{1}{2}x_{ij}^2 W_{ij}dV = \sum_{j=1}^{N}\frac{1}{2}y_{ij}^2 W_{ij}dV = \frac{1}{2}(\sum_{j=1}^{N}\frac{1}{2}x_{ij}^2 W_{ij}dV + \sum_{j=1}^{N}\frac{1}{2}y_{ij}^2 W_{ij}dV) = \frac{1}{2}\times\frac{1}{2}(\sum_{j=1}^{N}r_{ij}^2 W_{ij}dV)$$
$$\frac{1}{3}(\sum_{j=1}^{N}\frac{1}{2}x_{ij}^2 W_{ij}dV + \sum_{j=1}^{N}\frac{1}{2}y_{ij}^2 W_{ij}dV + \sum_{j=1}^{N}\frac{1}{2}z_{ij}^2 W_{ij}dV) = \frac{1}{2D_0}\sum_{j=1}^{N}r_{ij}^2 W_{ij}dV, \quad \text{where} \quad x_{ij}^2 + y_{ij}^2 = r_{ij}^2 \tag{7-A17}$$

$$\nabla^2 f = f_{i,xx} + f_{i,yy} = \frac{2D_0 \sum_{j=1}^{N} (f_j - f_i) W_{ij} dV}{n_0^* \lambda} \tag{7-A18}$$

In the above equation, the terms n_0^*, D_0 and λ signify the Particle Number Density (PND), the number of space dimensions and coefficient in the Laplacian model which are defined as:

$$\begin{aligned} n_0^* &= \sum_{j=1}^{N} W_{ij} dV \\ \lambda &= \sum_{j=1}^{N} r_{ij}^2 W_{ij} dV \Big/ \sum_{j=1}^{N} W_{ij} dV \end{aligned} \tag{7-A19}$$

Eq. (7-A18) was originally proposed by Koshizuka et al. [1] for discretization of Pressure Poisson Equation (PPE) and then was used by Sub et al. [10], Sasaki et al. [88], Liu et al. [23] and Sun et al. [89] for simulation of violent free-surface flows.

7.9 Appendix B (1D shock tube problem)

The discretization procedure with associated classical governing equations for analysis of 1D Sod shock tube problem in a Lagrangian particle description are presented along this appendix [52].

$$\frac{D\mathbf{u}}{Dt} = -\sum_{J=1}^{N} m_j \left(\frac{p_i + p_j}{\rho_i \rho_j} + \Pi_{ij}\right) \nabla W_{ij} \tag{7-B1}$$

$$\frac{De}{Dt} = -\frac{1}{2} \sum_{J=1}^{N} m_j \left(\frac{p_i}{\rho_i^2} + \frac{p_j}{\rho_j^2}\right) (\mathbf{u}_{ij} \cdot \nabla W_{ij}) \tag{7-B2}$$

$$\rho = \sum_{J=1}^{N} m_j W_{ij} \tag{7-B3}$$

$$\begin{aligned} \mathbf{u}^{(n+1)} &= \mathbf{u}^{(n)} + \Delta t \frac{D\mathbf{u}^{(n)}}{Dt} \\ e^{(n+1)} &= e^{(n)} + \Delta t \frac{De^{(n)}}{Dt} \\ \mathbf{r}^{(n+1)} &= \mathbf{r}^{(n)} + \Delta t\, \mathbf{u}^{(n+1)} \end{aligned} \tag{7-B4}$$

$$p = \rho(\gamma - 1)e, \quad c = \sqrt{\frac{\gamma p}{\rho}}, \tag{7-B5}$$

In above equations, e , p , ρ and u are internal energy, pressure, density and velocity of the gas, respectively. c denotes the speed of sound in lattice particle and $\gamma = 1.4$ is heat capacity ratio. Similar to work of Liu et al. [52], simulation has been performed for 40 time step ($\Delta t = 0.005 s$) where 320 particles with high level of pressure and density are located in the *driven section* of the tube $[-0.6, 0]$ while 80 particles with low level of energy are uniformly deployed in the *working section* $[0, 0.6]$.

$$\begin{array}{llllll} x \le 0, & \rho = 1, & u = 0, & e = 2.5, & p = 1, & \Delta x = 0.001875, \quad m = 0.001875 \\ x > 0, & \rho = 0.25, & u = 0, & e = 1.795, & p = 0.1795, & \Delta x = 0.0075, \quad m = 0.001875 \end{array} \tag{7-B6}$$

As is clear from Eqs. (7-B1) to (7-B5), sequence and solution structure of shock tube problem consists of three stages: (a) first material derivatives of velocity ($D\mathbf{u}/Dt$) and energy (De/Dt) as well as density (ρ) are calculated through Eqs. (7-B1) to (7-B3). In the second stage particles are shifted to the new position ($\mathbf{r}^{(n+1)}$) with updated velocity ($\mathbf{u}^{(n+1)}$) and internal energy ($e^{(n+1)}$) according to first-order explicit (forward time) Euler scheme. In the last stage, pressure and sound speed for each particle will be updated based on the equation of state (EOS) and isentropic condition (Eq. (7-B5)). To suppress unphysical pressure oscillation near the shock region, the artificial viscosity (Π_{ij}) suggested by Monaghan [90] is frequently employed as follows:

$$\begin{aligned} \Pi_{ij} &= \begin{cases} \dfrac{-\alpha \bar{c}_{ij} \phi_{ij} + \beta \phi_{ij}^2}{\bar{\rho}_{ij}} & \mathbf{u}_{ij} \cdot \mathbf{r}_{ij} < 0 \\ 0 & \mathbf{u}_{ij} \cdot \mathbf{r}_{ij} > 0 \end{cases} \\ \phi_{ij} &= \frac{h_{ij} (\mathbf{u}_{ij} \cdot \mathbf{r}_{ij})}{\left| r_{ij} \right|^2 + \varphi^2} \\ \bar{c}_{ij} &= \frac{c_i + c_j}{2}, \ \bar{\rho}_{ij} = \frac{\rho_i + \rho_j}{2}, \ \varphi = 0.01 h_{ij}, \ \alpha = \beta = 1 \end{aligned} \tag{7-B7}$$

where α and β are constant parameters which control the strength of the artificial viscosity.

7.10 References

[1] S. Koshizuka and Y. Oka, “Moving-particle semi-implicit method for fragmentation of incompressible fluid,” Nucl. Sci. Eng., vol. 123, no. 3, pp. 421–434, 1996.

[2] C. W. Hirt and B. D. Nichols, “Volume of fluid (VOF) method for the dynamics of free boundaries,” J. Comput. Phys., vol. 39, no. 1, pp. 201–225, 1981.

[3] J. A. Sethian, Level set methods and fast marching methods: evolving interfaces in computational geometry, fluid mechanics, computer vision, and materials science, vol. 3. Cambridge university press, 1999.

[4] M. Tanaka, R. Cardoso, and H. Bahai, “Multi-resolution MPS method,” J. Comput. Phys., vol. 359, pp. 106–136, 2018.

[5] Z. Sun, K. Djidjeli, and J. T. Xing, “The weak coupling between MPS and BEM for wave structure interaction simulation,” Eng. Anal. Bound. Elem., vol. 82, pp. 111–118, 2017.

[6] K. C. Ng, Y. L. Ng, T. W. H. Sheu, and A. Alexiadis, “Assessment of Smoothed Particle Hydrodynamics (SPH) models for predicting wall heat transfer rate at complex boundary,” Eng. Anal. Bound. Elem., vol. 111, pp. 195–205, 2020.

[7] S. Saso, M. Mouri, M. Tanaka, and S. Koshizuka, “Numerical analysis of two-dimensional welding process using particle method,” Weld. World, vol. 60, no. 1, pp. 127–136, 2016.

[8] G. Duan, A. Yamaji, and S. Koshizuka, “A novel multiphase MPS algorithm for modeling crust formation by highly viscous fluid for simulating corium spreading,” Nucl. Eng. Des., vol. 343, pp. 218–231, 2019.

[9] M. Tajnesaie, A. Shakibaeinia, and K. Hosseini, “Meshfree particle numerical modelling of sub-aerial and submerged landslides,” Comput. Fluids, vol. 172, pp. 109–121, 2018.

[10] C. Sun, Z. Shen, and M. Zhang, “Surface treatment technique of MPS method for free surface flows,” Eng. Anal. Bound. Elem., vol. 102, pp. 60–72, 2019.

[11] J. Wang and X. Zhang, “Improved Moving Particle Semi-implicit method for multiphase flow with discontinuity,” Comput. Methods Appl. Mech. Eng., vol. 346, pp. 312–331, 2019.

[12] E. J. Nodoushan, A. Shakibaeinia, and K. Hosseini, “A multiphase meshfree particle method for continuum-based modeling of dry and submerged granular flows,” Powder Technol., vol. 335, pp. 258–274, 2018.

[13] A. Alexiadis, S. Ghraybeh, and G. Qiao, “Natural convection and solidification of phase-change materials in circular pipes: A SPH approach,” Comput. Mater. Sci., vol. 150, pp. 475–483, 2018.

[14] T. Matsunaga, S. Koshizuka, T. Hosaka, and E. Ishii, “Moving surface mesh-incorporated particle method for numerical simulation of a liquid droplet,” J. Comput. Phys., vol. 409, p. 109349, 2020.

[15] G. Li, M. Liu, G. Duan, D. Chong, and J. Yan, “Numerical investigation of erosion and heat transfer characteristics of molten jet impinging onto solid plate with MPS–LES method,” Int. J. Heat Mass Transf., vol. 99, pp. 44–52, 2016.

[16] Z.-B. Wang, R. Chen, H. Wang, Q. Liao, X. Zhu, and S.-Z. Li, “An overview of smoothed particle hydrodynamics for simulating multiphase flow,” Appl. Math. Model., vol. 40, no. 23–24, pp. 9625–9655, 2016.

[17] M. S. Shadloo, G. Oger, and D. Le Touzé, “Smoothed particle hydrodynamics method for fluid flows, towards industrial applications: Motivations, current state, and challenges,” Comput. Fluids, vol. 136, pp. 11–34, 2016.

[18] R. Xu, P. Stansby, and D. Laurence, “Accuracy and stability in incompressible SPH (ISPH) based on the projection method and a new approach,” J. Comput. Phys., vol. 228, no. 18, pp. 6703–6725, 2009.

[19] M. S. Shadloo, A. Zainali, and M. Yildiz, “Simulation of single mode Rayleigh–Taylor instability by SPH method,” Comput. Mech., vol. 51, no. 5, pp. 699–715, 2013.

[20] A. Khayyer, H. Gotoh, and Y. Shimizu, “Comparative study on accuracy and conservation properties of two particle regularization schemes and proposal of an optimized particle shifting scheme in ISPH context,” J. Comput. Phys., vol. 332, pp. 236–256, 2017.

[21] S. J. Lind, R. Xu, P. K. Stansby, and B. D. Rogers, “Incompressible smoothed particle hydrodynamics for free-surface flows: A generalised diffusion-based algorithm for stability and validations for impulsive flows and propagating waves,” J. Comput. Phys., vol. 231, no. 4, pp. 1499–1523, 2012.

[22] G. Oger, M. Doring, B. Alessandrini, and P. Ferrant, “An improved SPH method: Towards higher order convergence,” J. Comput. Phys., vol. 225, no. 2, pp. 1472–1492, 2007.

[23] X. Liu, K. Morita, and S. Zhang, “A stable moving particle semi-implicit method with renormalized Laplacian model improved for incompressible free-surface flows,” Comput. Methods Appl. Mech. Eng., vol. 356, pp. 199–219, 2019.

[24] A. Khayyer and H. Gotoh, “Enhancement of stability and accuracy of the moving particle semi-implicit method,” J. Comput. Phys., vol. 230, no. 8, pp. 3093–3118, 2011.

[25] G. Duan, S. Koshizuka, A. Yamaji, B. Chen, X. Li, and T. Tamai, “An accurate and stable multiphase moving particle semi-implicit method based on a corrective matrix for all particle interaction models,” Int. J. Numer. Methods Eng., vol. 115, no. 10, pp. 1287–1314, 2018.

[26] X. Xu and X.-L. Deng, “An improved weakly compressible SPH method for simulating free surface flows of viscous and viscoelastic fluids,” Comput. Phys. Commun., vol. 201, pp. 43–62, 2016.

[27] P. N. Sun, D. Le Touzé, and A.-M. Zhang, “Study of a complex fluid-structure dam-breaking benchmark problem using a multi-phase SPH method with APR,” Eng. Anal. Bound. Elem., vol. 104, pp. 240–258, 2019.

[28] P. N. Sun, A. Colagrossi, D. Le Touzé, and A.-M. Zhang, “Extension of the δ-plus-SPH model for simulating vortex-induced-vibration problems,” J. Fluids Struct., vol. 90, pp. 19–42, 2019.

[29] F. Garoosi and A. Shakibaeinia, “Numerical simulation of entropy generation due to natural convection heat transfer using Kernel Derivative-Free (KDF) Incompressible Smoothed Particle Hydrodynamics (ISPH) model,” Int. J. Heat Mass Transf., vol. 150, p. 119377, 2020.

[30] H. F. Schwaiger, “An implicit corrected SPH formulation for thermal diffusion with linear free surface boundary conditions,” Int. J. Numer. Methods Eng., vol. 75, no. 6, pp. 647–671, 2008.

[31] G. Oger, S. Marrone, D. Le Touzé, and M. De Leffe, “SPH accuracy improvement through the combination of a quasi-Lagrangian shifting transport velocity and consistent ALE formalisms,” J. Comput. Phys., vol. 313, pp. 76–98, 2016.

[32] S. J. Cummins and M. Rudman, “An SPH projection method,” J. Comput. Phys., vol. 152, no. 2, pp. 584–607, 1999.

[33] X. Y. Cao, F. R. Ming, and A. M. Zhang, “Sloshing in a rectangular tank based on SPH simulation,” Appl. Ocean Res., vol. 47, pp. 241–254, 2014.

[34] J. Hongbin and D. Xin, “On criterions for smoothed particle hydrodynamics kernels in stable field,” J. Comput. Phys., vol. 202, no. 2, pp. 699–709, 2005.

[35] M. B. Liu, G. R. Liu, and K. Y. Lam, “Constructing smoothing functions in smoothed particle hydrodynamics with applications,” J. Comput. Appl. Math., vol. 155, no. 2, pp. 263–284, 2003.

[36] X. F. Yang, S. L. Peng, and M. B. Liu, “A new kernel function for SPH with applications to free surface flows,” Appl. Math. Model., vol. 38, no. 15–16, pp. 3822–3833, 2014.

[37] X. Yang, M. Liu, and S. Peng, “Smoothed particle hydrodynamics modeling of viscous liquid drop without tensile instability,” Comput. Fluids, vol. 92, pp. 199–208, 2014.

[38] Y. Gao, D. Hong, H. Lu, Y. Cheng, L. Wang, and X. Li, “Gas holdup and liquid velocity distributions in the up flow jet-loop reactor,” Chem. Eng. Res. Des., vol. 136, pp. 94–104, 2018.

[39] J. M. Cadou, Y. Guevel, and G. Girault, “Numerical tools for the stability analysis of 2D flows: Application to the two- and four-sided lid-driven cavity,” Fluid Dyn. Res., vol. 44, no. 3, pp. 0–12, 2012.

[40] L. D. G. Sigalotti, O. Rendón, J. Klapp, C. A. Vargas, and F. Cruz, “A new insight into the consistency of the SPH interpolation formula,” Appl. Math. Comput., vol. 356, pp. 50–73, 2019.

[41] A. M. Aly and S. E. Ahmed, “ISPH simulations for a variable magneto-convective flow of a ferrofluid in a closed space includes open circular pipes,” Int. Commun. Heat Mass Transf., vol. 110, p. 104412, 2020.

[42] A. Bejan, Entropy generation through heat and fluid flow. Wiley, 1982.

[43] P. Biswal and T. Basak, “Bejan’s heatlines and numerical visualization of convective heat flow in differentially heated enclosures with concave/convex side walls,” Energy, vol. 64, pp. 69–94, 2014.

[44] S. Bhardwaj, A. Dalal, and S. Pati, “Influence of wavy wall and non-uniform heating on natural convection heat transfer and entropy generation inside porous complex enclosure,” Energy, vol. 79, pp. 467–481, 2015.

[45] G. G. Ilis, M. Mobedi, and B. Sunden, “Effect of aspect ratio on entropy generation in a rectangular cavity with differentially heated vertical walls,” Int. Commun. Heat Mass Transf., vol. 35, no. 6, pp. 696–703, 2008.

[46] P. Biswal and T. Basak, “Entropy generation based approach on natural convection in enclosures with concave/convex side walls,” Int. J. Heat Mass Transf., vol. 82, pp. 213–235, 2015.

[47] G. H. R. Kefayati, “Simulation of double diffusive MHD (magnetohydrodynamic) natural convection and entropy generation in an open cavity filled with power-law fluids in the presence of Soret and Dufour effects (part II: entropy generation),” Energy, vol. 107, pp. 917–959, 2016.

[48] S. Marrone, M. Antuono, A. Colagrossi, G. Colicchio, D. Le Touzé, and G. Graziani, “δ-SPH model for simulating violent impact flows,” Comput. Methods Appl. Mech. Eng., vol. 200, no. 13–16, pp. 1526–1542, 2011.

[49] T. Matsunaga, A. Södersten, K. Shibata, and S. Koshizuka, “Improved treatment of wall boundary conditions for a particle method with consistent spatial discretization,” Comput. Methods Appl. Mech. Eng., vol. 358, p. 112624, 2020.

[50] G. Duan, T. Matsunaga, A. Yamaji, S. Koshizuka, and M. Sakai, “Imposing accurate wall boundary conditions in corrective-matrix-based moving particle semi-implicit method for free surface flow,” Int. J. Numer. Methods Fluids, 2020.

[51] J. Hongbin and D. Xin, “On criterions for smoothed particle hydrodynamics kernels in stable field,” J. Comput. Phys., vol. 202, no. 2, pp. 699–709, 2005.

[52] G.-R. Liu and M. B. Liu, Smoothed particle hydrodynamics: a meshfree particle method. World Scientific, 2003.

[53] H. Wendland, “Piecewise polynomial, positive definite and compactly supported radial functions of minimal degree,” Adv. Comput. Math., vol. 4, no. 1, pp. 389–396, 1995.

[54] C.-W. Shu and S. Osher, “Efficient implementation of essentially non-oscillatory shock-capturing schemes,” J. Comput. Phys., vol. 77, no. 2, pp. 439–471, 1988.

[55] A. J. Chorin, “Numerical solution of the Navier-Stokes equations,” Math. Comput., vol. 22, no. 104, pp. 745–762, 1968.

[56] A. Khayyer, H. Gotoh, and Y. Shimizu, “Comparative study on accuracy and conservation properties of two particle regularization schemes and proposal of an optimized particle shifting scheme in ISPH context,” J. Comput. Phys., vol. 332, pp. 236–256, 2017.

[57] P. N. Sun, A. Colagrossi, S. Marrone, M. Antuono, and A. M. Zhang, “Multi-resolution Delta-plus-SPH with tensile instability control: Towards high Reynolds number flows,” Comput. Phys. Commun., vol. 224, pp. 63–80, 2018.

[58] C. Zhang, X. Y. Hu, and N. A. Adams, “A weakly compressible SPH method based on a low-dissipation Riemann solver,” J. Comput. Phys., vol. 335, pp. 605–620, 2017.

[59] L. Lobovský, E. Botia-Vera, F. Castellana, J. Mas-Soler, and A. Souto-Iglesias, “Experimental investigation of dynamic pressure loads during dam break,” J. Fluids Struct., vol. 48, pp. 407–434, 2014.

[60] N. J. Quinlan, M. Basa, and M. Lastiwka, “Truncation error in mesh-free particle methods,” Int. J. Numer. Methods Eng., vol. 66, no. 13, pp. 2064–2085, 2006.

[61] X. Liu, K. Morita, and S. Zhang, “An advanced moving particle semi-implicit method for accurate and stable simulation of incompressible flows,” Comput. Methods Appl. Mech. Eng., vol. 339, pp. 467–487, 2018.

[62] A. Colagrossi, “A meshless Lagrangian method for free-surface and interface flows with fragmentation,” These, Univ. di Roma, 2005.

[63] P. N. Sun, A. Colagrossi, S. Marrone, and A. M. Zhang, “The δplus-SPH model: simple procedures for a further improvement of the SPH scheme,” Comput. Methods Appl. Mech. Eng., vol. 315, pp. 25–49, 2017.

[64] G. Pahar and A. Dhar, “Mixed miscible-immiscible fluid flow modelling with incompressible SPH framework,” Eng. Anal. Bound. Elem., vol. 73, pp. 50–60, 2016.

[65] Z.-F. Meng, P.-P. Wang, A.-M. Zhang, F.-R. Ming, and P.-N. Sun, “A multiphase SPH model based on Roe’s approximate Riemann solver for hydraulic flows with complex interface,” Comput. Methods Appl. Mech. Eng., vol. 365, p. 112999, 2020.

[66] J. J. Monaghan and A. Rafiee, “A simple SPH algorithm for multi-fluid flow with high density ratios,” Int. J. Numer. Methods Fluids, vol. 71, no. 5, pp. 537–561, 2013.

[67] S. J. Lind, P. K. Stansby, and B. D. Rogers, “Incompressible–compressible flows with a transient discontinuous interface using smoothed particle hydrodynamics (SPH),” J. Comput. Phys., vol. 309, pp. 129–147, 2016.

[68] A. Khayyer, H. Gotoh, and Y. Shimizu, “A projection-based particle method with optimized particle shifting for multiphase flows with large density ratios and discontinuous density fields,” Comput. Fluids, vol. 179, pp. 356–371, 2019.

[69] X. He, S. Chen, and R. Zhang, “A lattice Boltzmann scheme for incompressible multiphase flow and its application in simulation of Rayleigh–Taylor instability,” J. Comput. Phys., vol. 152, no. 2, pp. 642–663, 1999.

[70] G. Tryggvason, “Numerical simulations of the Rayleigh-Taylor instability,” J. Comput. Phys., vol. 75, no. 2, pp. 253–282, 1988.

[71] S. A. Nabavizadeh, M. Eshraghi, S. D. Felicelli, S. N. Tewari, and R. N. Grugel, “Effect of bubble-induced Marangoni convection on dendritic solidification,” Int. J. Multiph. Flow, vol. 116, pp. 137–152, 2019.

[72] J. C. S. Meng and J. A. L. Thomson, “Numerical studies of some nonlinear hydrodynamic problems by discrete vortex element methods,” J. Fluid Mech., vol. 84, no. 3, pp. 433–453, 1978.

[73] E. P. Hicks, “A shear instability mechanism for the pulsations of Rayleigh–Taylor unstable model flames,” J. Fluid Mech., vol. 748, pp. 618–640, 2014.

[74] K. Szewc, J. Pozorski, and J. Minier, “Spurious interface fragmentation in multiphase SPH,” Int. J. Numer. Methods Eng., vol. 103, no. 9, pp. 625–649, 2015.

[75] P. S. Mahapatra, S. De, K. Ghosh, N. K. Manna, and A. Mukhopadhyay, “Heat transfer enhancement and entropy generation in a square enclosure in the presence of adiabatic and isothermal blocks,” Numer. Heat Transf. Part A Appl., vol. 64, no. 7, pp. 577–596, 2013.

[76] M. Eslamian, M. Ahmed, M. F. El-Dosoky, and M. Z. Saghir, “Effect of thermophoresis on natural convection in a Rayleigh–Benard cell filled with a nanofluid,” Int. J. Heat Mass Transf., vol. 81, pp. 142–156, 2015.

[77] P.-H. Kao and R.-J. Yang, “Simulating oscillatory flows in Rayleigh–Benard convection using the lattice Boltzmann method,” Int. J. Heat Mass Transf., vol. 50, no. 17–18, pp. 3315–3328, 2007.

[78] S. K. Pandit, “Numerical Simulations of Natural Convection and Entropy Generation in a Square Cavity with an Adiabatic Body,” in Applied Mathematics, Springer, 2015, pp. 271–276.

[79] N. Ouertatani, N. Ben Cheikh, B. Ben Beya, and T. Lili, “Numerical simulation of two-dimensional Rayleigh–Bénard convection in an enclosure,” Comptes Rendus Mécanique, vol. 336, no. 5, pp. 464–470, 2008.

[80] R. D. C. Oliveski, M. H. Macagnan, and J. B. Copetti, “Entropy generation and natural convection in rectangular cavities,” Appl. Therm. Eng., vol. 29, no. 8–9, pp. 1417–1425, 2009.

[81] M. C. D’Orazio, C. Cianfrini, and M. Corcione, “Rayleigh–Bénard convection in tall rectangular enclosures,” Int. J. Therm. Sci., vol. 43, no. 2, pp. 135–144, 2004.

[82] M. Magherbi, H. Abbassi, and A. Ben Brahim, “Entropy generation at the onset of natural convection,” Int. J. Heat Mass Transf., vol. 46, no. 18, pp. 3441–3450, 2003.

[83] R. Anandalakshmi and T. Basak, “Natural convection in rhombic enclosures with isothermally heated side or bottom wall: entropy generation analysis,” Eur. J. Mech., vol. 54, pp. 27–44, 2015.

[84] B. Nayroles, G. Touzot, and P. Villon, “Generalizing the finite element method: diffuse approximation and diffuse elements,” Comput. Mech., vol. 10, no. 5, pp. 307–318, 1992.

[85] G. Duan, B. Chen, X. Zhang, and Y. Wang, “A multiphase MPS solver for modeling multi-fluid interaction with free surface and its application in oil spill,” Comput. Methods Appl. Mech. Eng., vol. 320, pp. 133–161, 2017.

[86] S. Koshizuka, Y. Oka, and H. Tamako, “A particle method for calculating splashing of incompressible viscous fluid,” American Nuclear Society, Inc., La Grange Park, IL (United States), 1995.

[87] Y. Liang, Z. Sun, G. Xi, and L. Liu, “Numerical models for heat conduction and natural convection with symmetry boundary condition based on particle method,” Int. J. Heat Mass Transf., vol. 88, pp. 433–444, 2015.

[88] Y. Sasaki, Y. Sato, T. Yamada, K. Izui, and S. Nishiwaki, “Topology optimization for fluid flows using the MPS method incorporating the level set method,” Comput. Fluids, vol. 188, pp. 86–101, 2019.

[89] Z. Sun, X. Chen, G. Xi, L. Liu, and X. Chen, “Mass transfer mechanisms of rotary atomization: A numerical study using the moving particle semi-implicit method,” Int. J. Heat Mass Transf., vol. 105, pp. 90–101, 2017.

[90] J. J. Monaghan, “Smoothed particle hydrodynamics,” Annu. Rev. Astron. Astrophys., vol. 30, no. 1, pp. 543–574, 1992.

Chapter 8 SUMMARY AND GENERAL DISCUSSION

In this chapter, the main findings from the current thesis is summarized and discussed in details. As outlined before, the global objectives of the present research study were to introduce some possible modifications to increase the accuracy and efficiency of the existing SPH and MPS models in handling multiphase and free-surface flows through addressing eight common drawbacks namely: (1) uncertainty in the selection of appropriate kernel function, (2) low-order space and time discretization schemes used for calculating gradient, divergence and Laplacian operators, (3) non-conservative form of pressure gradient operator, (4) unphysical pressure fluctuations associated with Weakly Compressible version of the SPH, (5) false detection of interfacial particles in free-surface flows, (6) Low-order boundary treatment, (7) penetration of fluid particles into the boundaries walls and (8) tensile instability caused by particle clustering. In order to accomplish this, a number of modifications have been proposed and applied on SPH and MPS models as follows:

8.1 Kernel function

As illustrated in table 8-1, in order to address the first issue, four new kernel functions were constructed and successfully applied to the simulation of 1D Sod shock tube problem. The comparison of obtained results with the analytical solution in Fig. 8-1 clearly demonstrates that, the newly developed kernel functions can efficiently identify and resolve the locations of the shock wave ($x = 0.3$), contact discontinuity ($x = 0.135$) and internal energy profiles of the rarefaction wave ($-0.25 \le x \le 0$) with minimal oscillation and consequently outperformed the existing kernel functions (i.e. Cubic, quintic spline and Wendland) in handeling shock wave with physical discontinuities. In addition to that, it can be seen that the cubic kernel function considerably failed to capture density discontinuity whereas the results of Wendland and quintic kernels in terms of density, energy, pressure and velocity profiles are more compatible with predicted results from kernels A to D. Finally, it should be noted that, although the obtained results in Fig. 8-1 clearly prove the superiority of the newly developed kernels over the exsiting kernel functions, the comparison of the developed kernels A to D shows similar results in capturing shock area and material discountinuety which indicates that they can be used interchangeably and consequently one cannot recommend one kernel over the others.

Table 8.1 The summary of the four newly developed kernel functions used for the interpolation and particle approximation.

Kernel A (see article 1)

$$W_{ij}=\alpha_D\begin{cases}\dfrac{\cos^3(\pi R/6)}{25+13R^2} & 0\le R\le 3\\ 0 & R>3\end{cases}$$

$$\alpha_1=\frac{12.9371393}{h},\ \alpha_2=\frac{6.6067745}{h^2},\ \alpha_3=\frac{3.3694114}{h^3},$$

Kernel B (see article 2)

$$W_{ij}=\alpha_D\begin{cases}\cos^{2.25}(\pi R/6)(3-R)^3(1+R) & 0\le R\le 3\\ 0 & R>3\end{cases}$$

$$\alpha_{1D}=\frac{0.019505894}{h},\ \alpha_{2D}=\frac{0.010373313}{h^2},\ \alpha_{3D}=\frac{0.005612838}{h^3},$$

Kernel C (see article 3)

$$W_{ij}=\alpha_D\begin{cases}e^{\left(\frac{-R^2}{1.125\sqrt{\pi}}\right)}(9-R^2)^3 & 0\le R\le 3\\ 0 & R>3\end{cases}$$

$$\alpha_{1D}=\frac{0.723176\times10^{-3}}{h},\ \alpha_{2D}=\frac{0.38735\times10^{-3}}{h^2},\ \alpha_{3D}=\frac{0.210907\times10^{-3}}{h^3},$$

Kernel D (see article 4)

$$W_{ij}=\alpha_D\begin{cases}\cos^{3.5}\left(\dfrac{\pi R}{6}\right)\times e^{\left(\frac{-R^2}{\pi}\right)} & 0\le R\le 3\\ 0 & R>3\end{cases}$$

$$\alpha_{1D}=\frac{0.518442932}{h},\ \alpha_{2D}=\frac{0.274031624}{h^2},\ \alpha_{3D}=\frac{0.147708163}{h^3},$$

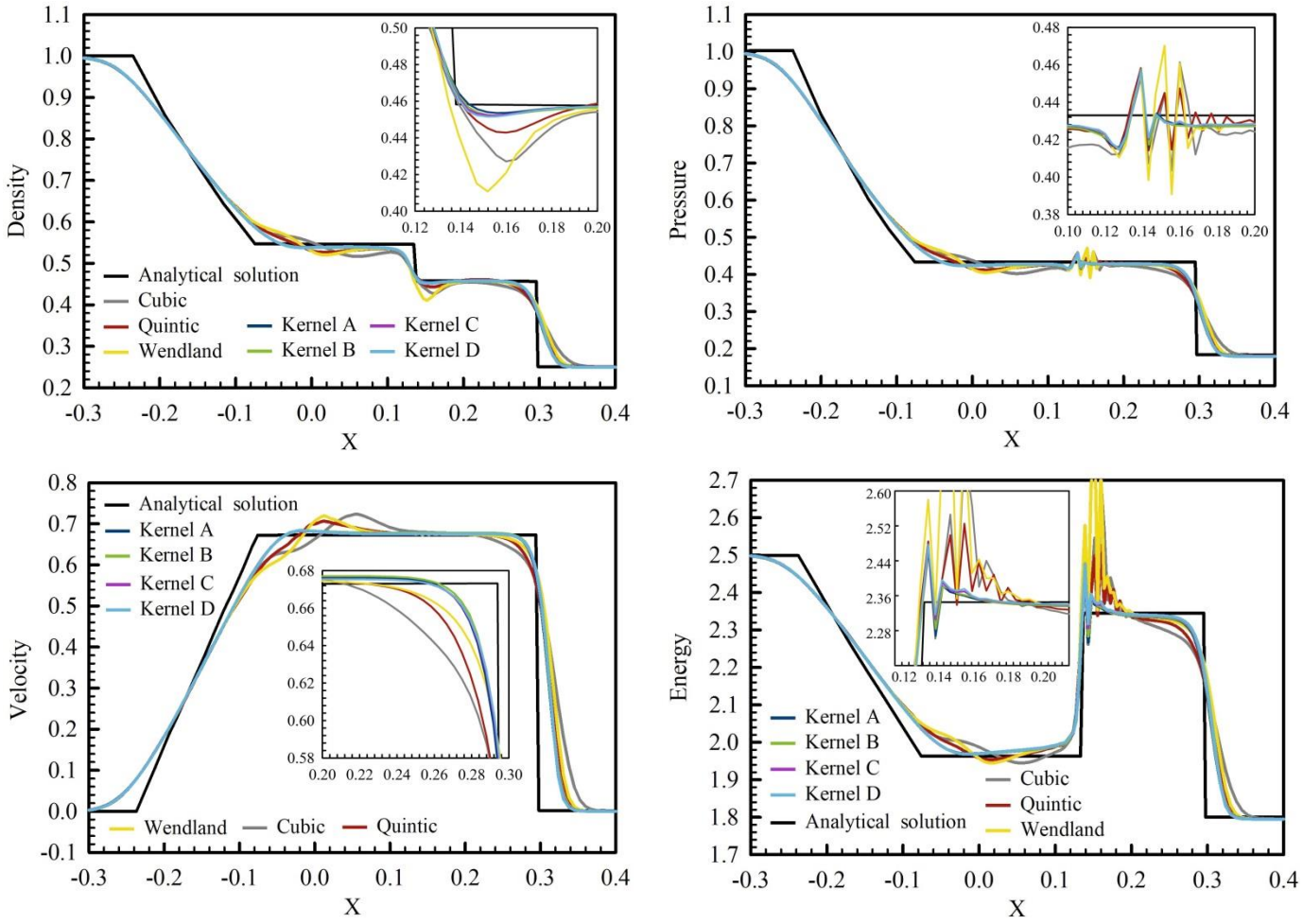

Figure 8-1 Comparison between calculated results from the four newly constructed kernel function with the analytical solution and existing kernels in modelling of shock tube problem.

8.2 Gradient, Laplacian and smoothing operators

To tackle the shortcoming of non-conservative form of pressure gradient operator and to solve the problems of low-order spatial discretization schemes used for calculating gradient, divergence and Laplacian operators in the governing equations, a set of high-order discretization formulations were proposed based on the Taylor series expantion. More precisely, in order to circumvent the problem of density/viscosity discontinuity in the multiphase flows or to approximate the values of field function (i.e. pressure, temperature) on the rigid walls, the following smoothing operators have been proposed and implemented (Eqs (8-1 to 8-4)):

Smoothing operator (model A)

$$\begin{bmatrix} f_i \\ f_x^{'} \\ f_y^{'} \end{bmatrix} = L \begin{bmatrix} \sum_{j=1}^{N} f_j W_{ij} dV \\ \sum_{j=1}^{N} x_{ij} f_j W_{ij} dV \\ \sum_{j=1}^{N} y_{ij} f_j W_{ij} dV \end{bmatrix} \qquad L = \begin{bmatrix} \sum_{j=1}^{N} W_{ij} dV & \sum_{j=1}^{N} x_{ij} W_{ij} dV & \sum_{j=1}^{N} y_{ij} W_{ij} dV \\ \sum_{j=1}^{N} x_{ij} W_{ij} dV & \sum_{j=1}^{N} x_{ij}^2 W_{ij} dV & \sum_{j=1}^{N} x_{ij} y_{ij} W_{ij} dV \\ \sum_{j=1}^{N} y_{ij} W_{ij} dV & \sum_{j=1}^{N} x_{ij} y_{ij} W_{ij} dV & \sum_{j=1}^{N} y_{ij}^2 W_{ij} dV \end{bmatrix}^{-1} \tag{8-1}$$

Smoothing operator (model B)

$$\begin{bmatrix} f_i \\ f_{i,x}^{'} \\ f_{i,y}^{'} \end{bmatrix} = L \begin{bmatrix} \sum_{j=1}^{N} \frac{f_j W_{ij}}{r_{ij}^2} dV \\ \sum_{j=1}^{N} \frac{x_{ij} f_j W_{ij}}{r_{ij}^2} dV \\ \sum_{j=1}^{N} \frac{y_{ij} f_j W_{ij}}{r_{ij}^2} dV \end{bmatrix} \qquad L = \begin{bmatrix} \sum_{j=1}^{N} \frac{W_{ij}}{r_{ij}^2} dV & \sum_{j=1}^{N} \frac{x_{ij} W_{ij}}{r_{ij}^2} dV & \sum_{j=1}^{N} \frac{y_{ij} W_{ij}}{r_{ij}^2} dV \\ \sum_{j=1}^{N} \frac{x_{ij} W_{ij}}{r_{ij}^2} dV & \sum_{j=1}^{N} \frac{x_{ij}^2 W_{ij}}{r_{ij}^2} dV & \sum_{j=1}^{N} \frac{x_{ij} y_{ij} W_{ij}}{r_{ij}^2} dV \\ \sum_{j=1}^{N} \frac{y_{ij} W_{ij}}{r_{ij}^2} dV & \sum_{j=1}^{N} \frac{x_{ij} y_{ij} W_{ij}}{r_{ij}^2} dV & \sum_{j=1}^{N} \frac{y_{ij}^2 W_{ij}}{r_{ij}^2} dV \end{bmatrix}^{-1} \tag{8-2}$$

Smoothing operator (model C)

$$\begin{bmatrix} f_i \\ f_x^{'} \\ f_y^{'} \end{bmatrix} = L \begin{bmatrix} \sum_{j=1}^{N} f_j W_{ij} dV \\ \sum_{j=1}^{N} f_j \nabla W_{ij,x} dV \\ \sum_{j=1}^{N} f_j \nabla W_{ij,y} dV \end{bmatrix} \qquad L = \begin{bmatrix} \sum_{j=1}^{N} W_{ij} dV & \sum_{j=1}^{N} x_{ij} W_{ij} dV & \sum_{j=1}^{N} y_{ij} W_{ij} dV \\ \sum_{j=1}^{N} \nabla W_{ij,x} dV & \sum_{j=1}^{N} x_{ij} \nabla W_{ij,x} dV & \sum_{j=1}^{N} y_{ij} \nabla W_{ij,x} dV \\ \sum_{j=1}^{N} \nabla W_{ij,y} dV & \sum_{j=1}^{N} x_{ij} \nabla W_{ij,y} dV & \sum_{j=1}^{N} y_{ij} \nabla W_{ij,y} dV \end{bmatrix}^{-1} \tag{8-3}$$

Smoothing operator (model D)

$$\begin{bmatrix} f_i \\ f_{i,x} \\ f_{i,y} \end{bmatrix} = L \begin{bmatrix} \sum_{j=1}^{N} \frac{f_j W_{ij}}{|r_{ij}|} dV \\ \sum_{j=1}^{N} \frac{f_j x_{ij} W_{ij}}{|r_{ij}|} dV \\ \sum_{j=1}^{N} \frac{f_j y_{ij} W_{ij}}{|r_{ij}|} dV \end{bmatrix} \qquad L = \begin{bmatrix} \sum_{j=1}^{N} \frac{W_{ij}}{|r_{ij}|} dV & \sum_{j=1}^{N} \frac{x_{ij} W_{ij}}{|r_{ij}|} dV & \sum_{j=1}^{N} \frac{y_{ij} W_{ij}}{|r_{ij}|} dV \\ \sum_{j=1}^{N} \frac{x_{ij} W_{ij}}{|r_{ij}|} dV & \sum_{j=1}^{N} \frac{x_{ij}^2 W_{ij}}{|r_{ij}|} dV & \sum_{j=1}^{N} \frac{x_{ij} y_{ij} W_{ij}}{|r_{ij}|} dV \\ \sum_{j=1}^{N} \frac{y_{ij} W_{ij}}{|r_{ij}|} dV & \sum_{j=1}^{N} \frac{x_{ij} y_{ij} W_{ij}}{|r_{ij}|} dV & \sum_{j=1}^{N} \frac{y_{ij}^2 W_{ij}}{|r_{ij}|} dV \end{bmatrix}^{-1} \tag{8-4}$$

In the above equations, the model A is known as Moving Least Squares (MLS) method which was originally proposed by Colagrossi et al. (Colagrossi and Landrini, 2003) for the simulation of bubble rising and dam break problems. The second model (Eq. (8-2)) is the MPS version of the MLS model which has been proposed in the current study to calculate the temperature field in buoyancy term in natural convection heat transfer problem (see also article 2). The third model (Eq. (8-3)) is known as MLSPH model which is the SPH version of the MLS technique. This model was initially pioneered by Nayroles et al. (Nayroles, Touzot, (1992)) and was then successfully employed by Huang et al. (Huang, Lei, and Peng, 2016) for modelling the lid-driven cavity flow. Motivated by work of Ng et al. (Ng, Hwang, and Sheu, 2014), the second version of the MLS in the context of the MPS model was proposed in the current study through decreasing the power of r (r^n) in Eqs. (8-2) from n=2 to n=1 in Eq. (8-4). At this stage, it worthwhile to mention that, the presence of corrective matrix L, can efficiently guarantee the first-order completeness condition for the kernel function as mathematically showed by Belytschko et al. (Belytschko, Ted, Krongauz, 1998). The calculated results revealed that, the proposed smoothing operators can efficiently handle sharp density discontinuities adjacent to the material interfaces.

To enhance the order of accuracy of the gradient operator, the similar procedure has been adopted in the current. The summary of proposed gradient operators used in the current study is given by Eqs. (8-5 to 8-9):

Gradient operator (Model A)

$$\begin{bmatrix} f_x^{'} \\ f_y^{'} \end{bmatrix} = L \begin{bmatrix} \sum_{j=1}^{N} x_{ij}(f_j - f_i) W_{ij} dV \\ \sum_{j=1}^{N} y_{ij}(f_j - f_i) W_{ij} dV \end{bmatrix} \qquad L = \begin{bmatrix} \sum_{j=1}^{N} x_{ij}^2 W_{ij} dV & \sum_{j=1}^{N} x_{ij} y_{ij} W_{ij} dV \\ \sum_{j=1}^{N} x_{ij} y_{ij} W_{ij} dV & \sum_{j=1}^{N} y_{ij}^2 W_{ij} dV \end{bmatrix}^{-1} \tag{8-5}$$

Gradient operator (Model B)

$$\begin{bmatrix} f_x^{'} \\ f_y^{'} \end{bmatrix} = L \begin{bmatrix} \sum_{j=1}^{N} \frac{x_{ij}(f_j - f_i)}{r_{ij}^2} W_{ij} dV \\ \sum_{j=1}^{N} \frac{y_{ij}(f_j - f_i)}{r_{ij}^2} W_{ij} dV \end{bmatrix} \qquad L = \begin{bmatrix} \sum_{j=1}^{N} \frac{x_{ij}^2 W_{ij}}{r_{ij}^2} dV & \sum_{j=1}^{N} \frac{x_{ij} y_{ij} W_{ij}}{r_{ij}^2} dV \\ \sum_{j=1}^{N} \frac{x_{ij} y_{ij} W_{ij}}{r_{ij}^2} dV & \sum_{j=1}^{N} \frac{y_{ij}^2 W_{ij}}{r_{ij}^2} dV \end{bmatrix}^{-1} \tag{8-6}$$

Gradient operator (Model C)

$$\begin{bmatrix} f_x^{'} \\ f_y^{'} \end{bmatrix} = L \begin{bmatrix} \sum_{j=1}^{N} (f_j - f_i) \nabla W_{ij,x} dV \\ \sum_{j=1}^{N} (f_j - f_i) \nabla W_{ij,y} dV \end{bmatrix} \qquad L = \begin{bmatrix} \sum_{j=1}^{N} x_{ij} \nabla W_{ij,x} dV & \sum_{j=1}^{N} y_{ij} \nabla W_{ij,x} dV \\ \sum_{j=1}^{N} x_{ij} \nabla W_{ij,y} dV & \sum_{j=1}^{N} y_{ij} \nabla W_{ij,y} dV \end{bmatrix}^{-1} \tag{8-7}$$

Gradient operator (Model D)

$$\begin{bmatrix} f_x^{'} \\ f_y^{'} \end{bmatrix} = L \begin{bmatrix} \sum_{j=1}^{N} \frac{(f_j - f_i)}{r_{ij}^2} \nabla W_{ij,x} dV \\ \sum_{j=1}^{N} \frac{(f_j - f_i)}{r_{ij}^2} \nabla W_{ij,y} dV \end{bmatrix} \qquad L = \begin{bmatrix} \sum_{j=1}^{N} \frac{x_{ij} \nabla W_{ij,x}}{r_{ij}^2} dV & \sum_{j=1}^{N} \frac{y_{ij} \nabla W_{ij,x}}{r_{ij}^2} dV \\ \sum_{j=1}^{N} \frac{x_{ij} \nabla W_{ij,y}}{r_{ij}^2} dV & \sum_{j=1}^{N} \frac{y_{ij} \nabla W_{ij,y}}{r_{ij}^2} dV \end{bmatrix}^{-1} \tag{8-8}$$

Gradient operator (Model E)

$$\begin{bmatrix} f_{i,x} \\ f_{i,y} \end{bmatrix} = L \begin{bmatrix} \sum_{j=1}^{N} \frac{(f_j - f_i) x_{ij} W_{ij}}{|r_{ij}|} dV \\ \sum_{j=1}^{N} \frac{(f_j - f_i) y_{ij} W_{ij}}{|r_{ij}|} dV \end{bmatrix} \qquad L = \begin{bmatrix} \sum_{j=1}^{N} \frac{x_{ij}^2 W_{ij}}{|r_{ij}|} dV & \sum_{j=1}^{N} \frac{x_{ij} y_{ij} W_{ij}}{|r_{ij}|} dV \\ \sum_{j=1}^{N} \frac{x_{ij} y_{ij} W_{ij}}{|r_{ij}|} dV & \sum_{j=1}^{N} \frac{y_{ij}^2 W_{ij}}{|r_{ij}|} dV \end{bmatrix}^{-1} \tag{8-9}$$

In the above equation, the model A (Eq. (8-5)) was initially introduced by Xu et al. (Xu, & Deng, (2016)) in the context of MLS model for the simulation of the 2D dam break problem. Model B was originally introduced by Khayyer et al. (Khayyer and Gotoh, 2011) and known as a corrected gradient model of original MPS method. Model C as the one of the classical gradient operators in the context of the SPH description was orginally proposed by Krongauz et al. (Y. Krongauz, Belytschko, 1997) and was then successfully implemented by Oger et al. (Oger, Doring, Alessandrini, Ferrant, 2007) to solve the problem of free-surface flow. Following the idea of Khayyer et al. (Khayyer and Gotoh, 2011) and Xu et al. (Xu, & Deng, (2016)), the terms $x_{ij}W_{ij}$ and $y_{ij}W_{ij}$ in Eq. (8-6) were replaced by $\nabla W_{ij,x}$ and $\nabla W_{ij,y}$ in Eq. (8-7) and subsequently the model D was developed in the current work (see also article 3). This operator (Eq. (8-8)) was then

utilized to simulate the problems of free-surface flow, natural convection heat transfer and two-phase Rayleigh-Taylor Instability. The second version of the gradient operator in the context of the MPS model was also proposed through decreasing the power of r (r^n) in Eqs. (8-6) from n=2 to n=1 in Eq. (8-9). This model has been employed to simulate the three-phase Rayleigh-Taylor Instability, dam break flow, natural convection heat transfer in differentially heated cavity, Rayleigh-Bénard convection and oscillating concentric circular drop with high density ratio. The proposed gradient operators have been utilized to calculate the divergence of velocity, gradient of temperature and pressure in Navier-Stokes and energy equations. Finally, it should be noted that, similar to the smoothing operator, the presence of the corrective matrix L in the above equations can ensure the first order completeness of the gradient models in the discretization process (for more details see works of Oger et al. (Oger, Doring, Alessandrini, Ferrant, 2007) and Khayyer et al. (Khayyer and Gotoh, 2011) and Yun, Sang-Moon, Park, Khayyer, and Jeong, 2018).

Following the idea of Schwaiger (Schwaiger, (2008)), in order to further improve the accuracy of the numerical simulations, a set of high-order Laplacian operators were derived based on the Taylor series expansion and were applied for the discretization of Pressure Poisson Equation (PPE) and diffusion terms in Navier-Stokes and energy equations. The summary of proposed Laplacian operators used in the current study is given by Eqs. (8-10 to 8-13):

Laplacian operator (Model A)

$$\nabla^2 f = \frac{2D_0 \left[\sum_{j=1}^{N}(f_j - f_i)W_{ij}dV - f_x^{'}\sum_{j=1}^{N}x_{ij}W_{ij}dV - f_y^{'}\sum_{j=1}^{N}y_{ij}W_{ij}dV\right]}{\sum_{j=1}^{N}r_{ij}^2 W_{ij}dV} \tag{8-10}$$

Laplacian operator (Model B)

$$\nabla^2 f = \frac{2D_0 \left[\sum_{j=1}^{N}\frac{(f_j - f_i)W_{ij}}{r_{ij}^2}dV - f_x^{'}\sum_{j=1}^{N}\frac{x_{ij}W_{ij}}{r_{ij}^2}dV - f_y^{'}\sum_{j=1}^{N}\frac{y_{ij}W_{ij}}{r_{ij}^2}dV\right]}{\sum_{j=1}^{N}W_{ij}dV} \tag{8-11}$$

Laplacian operator (Model C)

$$\nabla^2 f = f''_{xx} + f''_{yy} = \frac{\sum_{j=1}^{N} \frac{1}{2}(f_j - f_i)\, x_{ij} \nabla W_{ij,x} dV - f'_x \sum_{j=1}^{N} x_{ij}^2 \nabla W_{ij,x} dV}{\sum_{j=1}^{N} \frac{1}{2} x_{ij}^3 \nabla W_{ij,x} dV} + \frac{\sum_{j=1}^{N} \frac{1}{2}(f_j - f_i)\, y_{ij} \nabla W_{ij,y} dV - f'_y \sum_{j=1}^{N} y_{ij}^2 \nabla W_{ij,y} dV}{\sum_{j=1}^{N} \frac{1}{2} y_{ij}^3 \nabla W_{ij,y} dV} \tag{8-12}$$

Laplacian operator (Model D)

$$\nabla^2 f = f_{i,xx} + f_{i,yy} = \frac{\frac{1}{2}\sum_{j=1}^{N}(f_j - f_i) W_{ij} dV - f_{i,x} \sum_{j=1}^{N} x_{ij} W_{ij} dV}{\sum_{j=1}^{N} \frac{1}{2} x_{ij}^2 W_{ij} dV} + \frac{\frac{1}{2}\sum_{j=1}^{N}(f_j - f_i) W_{ij} dV - f_{i,y} \sum_{j=1}^{N} y_{ij} W_{ij} dV}{\sum_{j=1}^{N} \frac{1}{2} y_{ij}^2 W_{ij} dV} \tag{8-13}$$

As expected, the models A, B, C and D are respectively, MLS, MPS, SPH and FDM-MPS versions of the Laplacian operator which have been derived in the Lagrangian framework. Due to the presence of the first derivatives of the field function ($f_{i,x}$ and $f_{i,y}$), it is not difficult to deduce that, the proposed models are very analogous to the orginal high-order Laplacian operator introduced by Schwaiger (Schwaiger, (2008)) as:

$$\nabla^2 f = \frac{\Gamma^{-1}_{\beta\beta}}{n} \left\{ 2\sum_{j=1}^{N} (f_j - f_i) \frac{(\mathbf{r}_{ij})_\alpha W_{ij,\alpha}}{|r_{ij}|^2} dV - 2 f_{i,\alpha} \cdot \left(\sum_{j=1}^{N} W_{ij,\alpha} dV \right) \right\} \tag{8-14}$$

where n is the number of dimensions and Γ is a tensor which is defined as;

$$\Gamma_{\beta\gamma} = \int_{\Omega} \frac{(\Delta x)_\alpha W_{ij,\alpha}}{|\Delta x|^2} (\Delta x)_\beta (\Delta x)_\gamma dx \tag{8-15}$$

As highlighted by Schwaiger (Schwaiger, (2008)), the existence of the second term on the RHS of Eq. (8-14) is the correction which can provide a modest improvement over just the first term. Moreover, he found that, for regularly spaced arrays, the second-order convergence can be achieaved via the implementation of Eq. (8-14).

Finally, the results obtained from the modeling of dam break problem, two-phase and three-phase Rayleigh-Taylor instability (RTI) in the present work clearly demonstrated that, implementing high-order discretization schemes can immensely improve the stability and performance of the classical ISPH and IMPS models. Furthermore, it was found that, the implementation of the high-order discretization scheme for the treatment of the Laplacian and gradient operators can efficiently remove an unphysical pressure fluctuations from the computational domain which is a common problem in Lagrangian particle methods.

8.3 Particle Shifting Technique (PST)

As heighlited in the previous section, the order of accuracy of the proposed operators is strongly dependent on the regularity of the particles distribution such that the occurrence of tensile instability caused by particle clustering can significantly damage the interpolation accuracy or even lead to the unwanted termination of the calculations. To address the issue of particle clustering and prevent the inception of the tensile-instability, in a pioneering work, Xu et al. (Xu, Stansby, Laurence, (2009)) introduced the concept of the Particle Shifting Technique (PST) in which particles are encouraged to migrate from region of high concentration to the lower one, leading to the more uniform particle arrangement within the computational domain. Following the idea of Xu et al. (Xu, Stansby, Laurence, (2009)), a novel MLS version of the PST has been proposed in the current work as follows:

$$\delta r_{i,x,PST} = \frac{-\beta}{\lambda}\sum_{j=1}^{N} x_{ij} W_{ij} dV \qquad \delta r_{i,y,PST} = \frac{-\beta}{\lambda}\sum_{j=1}^{N} y_{ij} W_{ij} dV \tag{8-16}$$

where $\beta = 0.5\alpha h^2$ is a shifting coefficient which controls the magnitude of particle displacement with $0 \le \alpha \le 1$ (for more details see articles 1 to 3). The obtained results clearly demonstrated that, the newly developed PST could efficiently remove the tensile instability from the computational domain, leading to a more uniform particle distribution. However, this technique

was then further improved by incorporating the concept of the particle collision (Discrete Element Method (DEM)) for the treatment of the free-surface flows as:

$$\delta_{n,xij} = (R_j + R_i - \left|\vec{r}_j - \vec{r}_i\right|)\vec{n}_x \qquad \vec{n}_x = (\vec{x}_j - \vec{x}_i)\Big/\left|\vec{r}_{ij}\right| \tag{8-17}$$

$$\delta_{n,yij} = (R_j + R_i - \left|\vec{r}_j - \vec{r}_i\right|)\vec{n}_y \qquad \vec{n}_y = (\vec{y}_j - \vec{y}_i)\Big/\left|\vec{r}_{ij}\right| \tag{8-18}$$

$$f_{i,x} = -\sum_{j=1}^{N}(k_n\delta_{n,xij} + \gamma_n v_{n,xij}) \qquad \delta r_{i,x,DEM} = (dt)^2\ f_{i,x}/m_i \tag{8-19}$$

$$f_{i,y} = -\sum_{j=1}^{N}(k_n\delta_{n,yij} + \gamma_n v_{n,yij}) \qquad \delta r_{i,y,DEM} = (dt)^2\ f_{i,y}/m_i \tag{8-20}$$

In this technique, the previous PST model was applied only to the interior particles whereas the collision model was used for treatment of the interface and its nearby particles as:

$$\begin{aligned} \mathbf{r}_i^{(n+1)*} &= \mathbf{r}_i^{(n+1)} + \delta\mathbf{r}_{i,PST}^{(n+1)} \quad \text{for inner particles} \\ \mathbf{r}_{i,t}^{(n+1)*} &= \mathbf{r}_i^{(n+1)} + \delta\mathbf{r}_{i,DEM}^{(n+1)} \quad \text{for surface and vicinity particles} \end{aligned} \tag{8-21}$$

The validity and applicability of the proposed scheme were demonstrated against the several challenging benchmark cases including: dam-break flows with/without an obstacle, stretching water drop and rotating square patch of fluid. It was found that, implementing an efficient particle regularization technique (HPST) can considerably increase the accuracy and stability of the numerical solution.

8.4 Free-surface detection technique

As mentioned in the introduction section, Dirichlet pressure condition (p=0) must be applied on the free-surface region when single-phase model is employed for simulation of the free-surface flows such dam break problem. This highlights the need of proper identification of the interface position and its vicinity particles. Thus, a novel Hybrid Free-surface Detection (HFD) technique was developed based on the first and second derivatives of kernel function as:

$$\Phi_1 = \sum_{j=1}^{N} W_{ij}\frac{m_j}{\rho_j}, \tag{8-22}$$

$$\Phi_2 = \nabla\cdot\mathbf{r} = \sum_{j=1}^{N} x_{ij}\nabla W_{ij,x}\frac{m_j}{\rho_j} + \sum_{j=1}^{N} y_{ij}\nabla W_{ij,y}\frac{m_j}{\rho_j} \tag{8-23}$$

$$\Phi_3 = \nabla^2 \mathbf{r} = \frac{1}{2}\sum_{j=1}^{N} x_{ij}^2 \nabla^2 W_{ij,xx} \frac{m_j}{\rho_j} + \frac{1}{2}\sum_{j=1}^{N} y_{ij}^2 \nabla^2 W_{ij,yy} \frac{m_j}{\rho_j} \tag{8-24}$$

$$\Phi_4 = \sum_{j=1}^{N} x_{ij} y_{ij} \nabla^2 W_{ij,xy} \frac{m_j}{\rho_j} \tag{8-25}$$

The variables Φ_1 and Φ_2 in the above equations are known as a Particle Number Density (PND) (Koshizuka, & Oka, (1996)) and divergence of particle displacement (Lee, Moulinec, Xu, Violeau, Laurence, & Stansby, (2008)) while Φ_3 and Φ_4 are two new complementary conditions which can be simply referred to as Laplacian of particle displacement and mixed partial derivative of kernel function, respectively. The results showed that, the newly developed scheme can efficiently identify the position of interface and its nearby particles.

8.5 Density error accumulation

Motivated by work of Antuono et al. (Antuono, M., Colagrossi, A., Marrone, S., & Molteni, D. (2010)), in order to tackle the problems of unphysical pressure oscillation and density error accumulation associated with the standard WCSPH model, a novel high-order artificial diffusion term was derived based on the Taylor series expansion and then added into the continuity equation as:

$$\frac{D\rho^{(n)}}{Dt} = -\rho^{(n)} \nabla \cdot \mathbf{u}^* + \psi \tag{8-26}$$

The second term ($\psi = \lambda \Delta t \, c_0^2 \nabla^2 \rho$) in the right-hand side of the above equation is the additional diffusive term. One of the most notable features of Eq. (8-26) is that unlike the conventional δ-WCSPH (Antuono, Colagrossi, Marrone, & Molteni, (2010)), the present model does not contain any tunable parameter to control the density diffusive term (ψ). The performance and robustness of the proposed modification was verified against a series of challenging benchmark cases such as dam break, stretching of a circular water drop, rotating square patch of fluid and natural convection heat transfer in a square enclosure. The obtained results showed that, inserting additional diffusive term into the continuity equation can efficiently remove high-frequency oscillations noise from the pressure field (unfavorable check-board pressure field), leading to a more accurate and stable results as compared to conventional WCSPH (for more details see article 2).

8.6 Treatment of the boundary conditions

As highlighted before, unlike the conventional Eulerian mesh-based methods, addressing the influence of the solid walls in the purely Lagrangian mesh-free models such as MPS and SPH is not often as straightforward as it seemed. To overcome this shortcoming, the dynamic ghost particle technique suggested by Marrone et al. (Marrone, Antuono, Colagrossi, Colicchio, Le Touzé, & Graziani, (2011)) is adopted in the current work to enforce no-slip and no-penetration conditions on the rigid walls. As portrayed in Fig. 8-2, in this technique, both tangential and normal component of fluid velocity with opposite sign (no-slip) is extrapolated on the corresponding wall particles outside of the flow domain. However, to impose the Neumann boundary condition, the target variable (i.e. pressure (p_i) or temperature (θ_i) on the isolated walls) is first computed on the solid boundary line using one of the smoothing operators presented in section 8-2 (Eqs. (8-1) to (8-4)), and then the predicted values are assigned to the corresponding ghost particles in the same row, column or corner. Note that, as schematically shown in Fig. 8-2, only the fluid particles in the support domain of the kernel function are used to approximate the pressure or temperature on the fixed ghost particles. The obtained results showed that, the implementing the mirror velocity technique can successfully mitigate the undesirable problem of penetration of fluid particles into the boundaries walls.

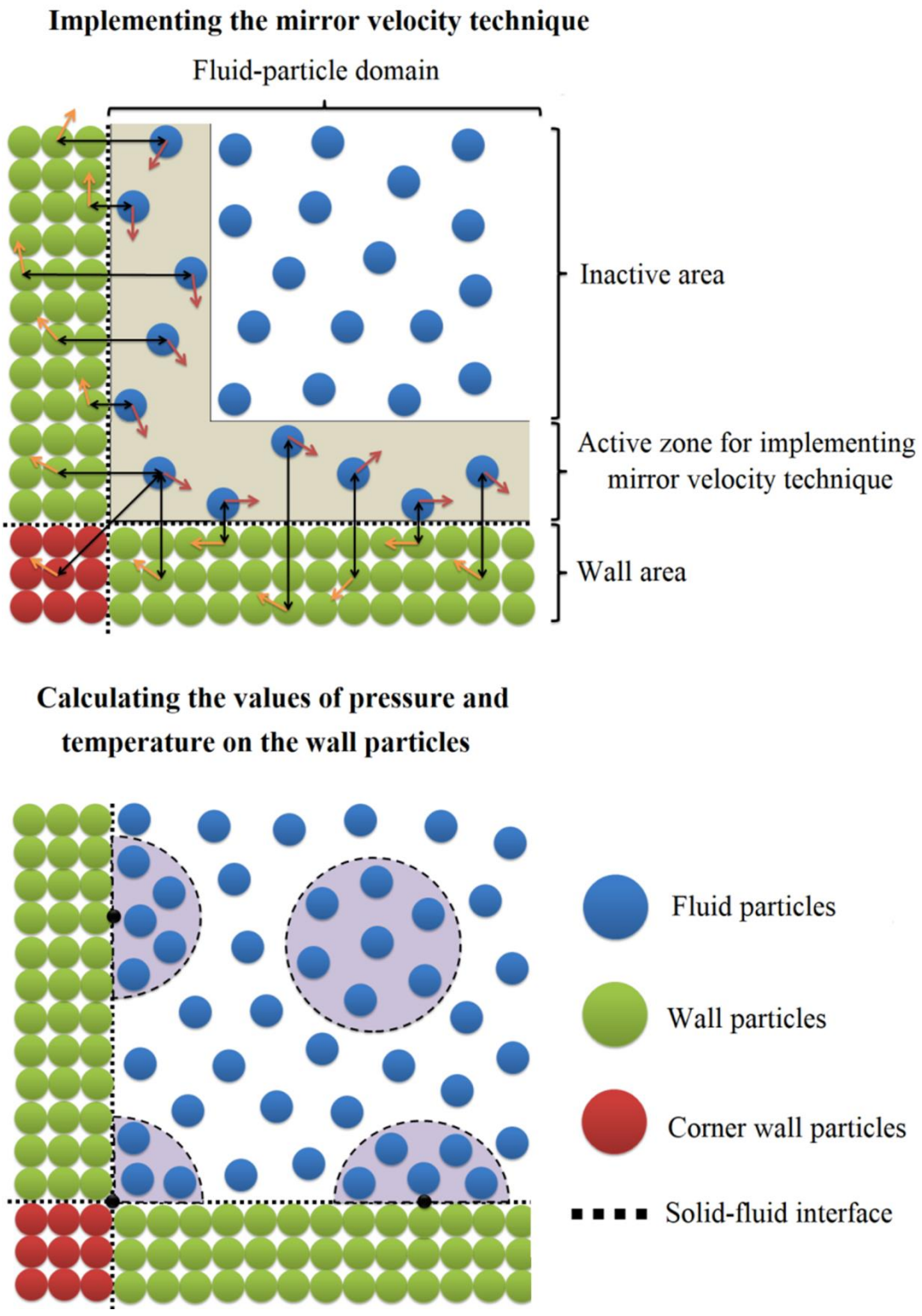

Figure 8-2 The conceptual illustrations of implementing Neumannand and Dirichlet (mirror velocity technique) boundary conditions in the context of the Lagrangian particle method.

Chapter 9 CONCLUSION AND RECOMMENDATIONS

9.1 Conclusions

Based on the results obtained from the present thesis, the following major conclusions may be drawn:

1. The results showed that, the type of the kernel function has a remarkable impact on the accuracy and stability of the particle methods,
2. The results show that, four newly developed smoothing kernel (W_{ij}) considerably outperformed the existing kernel functions (i.e. Cubic, Wendland, quintic spline) in modeling of shockwave propagation and multiphase flow with physical discontinuities.
3. It was found that, the order of accuracy of governing operators (i.e. gradient, Laplacian and divergence of velocity) has a significant impact on the regularity of particle distributions and stability of the numerical solution
4. The results showed that the newly proposed Laplacian operators could provide more accurate, stable and reliable results compared to the traditional operators used in WCSPH, ISPH and MPS methods, in modeling breaking dam flow, stretching of circular water drop, rotating square patch of fluid and natural convection heat transfer in a square enclosure.
5. The results showed that the newly proposed high-order gradient operators could successfully eliminate the non-physical pressure fluctuations from the computational domain, leading to a more stable and robust numerical model,
6. The results showed that the newly proposed free-surface detection technique could accurately identify the position of the free-surface and its vicinity particles,
7. The results show that, particles in Lagrangian framework have a natural tendency to cluster along the streamline, leading to the significant void formation and density error accumulation.
8. It was found that the implementation of the Particle Shifting Technique (PST) has a notable impact on the stability and accuracy of the mesh-free particle methods,

9. It was found that, the proposed Hybrid Particle Shifting Technique (HPST) could efficiently eliminate spurious pressure fluctuation caused by tensile instability (particle clustering) from the computational domain,
10. The obtained results vividly confirmed the broad applicability of proposed modifications in handling free-surface flows and particulate flows with thermal convection.
11. The results showed that, the proposed Modified Pressure Gradient operator (MPG) could effectively resolve the problem of particle clumping on the interface while retaining the conservation properties of momentum,
12. It was found that inserting additional diffusive term into the continuity equation can successfully remove high-frequency oscillations noise from the pressure field (undesirable check-board pressure field), leading to more accurate results as compared to conventional WCSPH model.
13. It was found that, the newly proposed smoothing operators can accurately interpolate values of the field function and circumvent the problem of density discontinuity in the multiphase flows,
14. It was found that traditional formulations of SPH model are prone to tensile instability and characterized by noisy pressure field whereas the proposed KDF-WCSPH model benefit from high level of accuracy and consistency,

9.2 Recommendations for Future Works

As a future investigation, the proposed models can be employed to explore multiphase flows with high-density ratio such as bubble rising and water droplet falling in air where undesirable particle scattering/clustering is likely to occur on the interface. It would be a future challenge to investigate turbulent natural convection heat transfer in porous enclosure, which has many important applications ranging from electronic packaging to solar collector technology.

Moreover, although the sensitivity of the models to the particle size was eventuated for a few benchmark cases (natural convection heat transfer), a detailed particle convergence study is re-commented for the future work to (1) determine the particle size which ensures the interdependency of results to the particle size, and (2) qualify the order of spatial convergence.

To further enhance the capability and robustness of the proposed models in solving real-life large-scale moving interface problems involving breaking and spray formation, the existing mesh-free Lagrangian particle methods can be combined with the classical grid-based Eulerian models. In this technique, the mesh-free particle method can be employed to capture details of the free-surface area whereas the mesh-based model can be applied to resolve the bulk flow.

To further improve the versatility and consistency of the newly developed SPH and MPS models in handling multiphase flows with high-density contrast, the particle refinement scheme (Multi-resolution technique) introduced by Tanaka et al. (Tanaka et al., 2018b) will be incorporated into the models.

BIBLIOGRAPHY

Antuono, M., Colagrossi, A., Marrone, S., & Molteni, D. (2010). Free-surface flows solved by means of SPH schemes with numerical diffusive terms. *Computer Physics Communications*, *181*(3), 532–549.

A. Colagrossi, M. Landrini, Numerical simulation of interfacial flows by smoothed particle hydrodynamics, J. Comput. Phys. 191 (2003) 448–475.

Belytschko, Ted, Yury Krongauz, John Dolbow, and C. Gerlach. "On the completeness of meshfree particle methods." International Journal for Numerical Methods in Engineering 43, no. 5 (1998): 785-819.

B. Nayroles, G. Touzot, P. Villon, Generalizing the finite element method: diffuse approximation and diffuse elements, Comput. Mech. 10 (1992) 307–318.

Chaves, I. L., Duarte, L. C., Coltro, W. K. T., & Santos, D. A. (2020). Droplet length and generation rate investigation inside microfluidic devices by means of CFD simulations and experiments. *Chemical Engineering Research and Design*, *161*, 260–270.

Chow, A. D., Rogers, B. D., Lind, S. J., & Stansby, P. K. (2018). Incompressible SPH (ISPH) with fast Poisson solver on a GPU. *Computer Physics Communications*, *226*, 81–103.

Daly, E., Grimaldi, S., & Bui, H. H. (2016a). Explicit incompressible SPH algorithm for free-surface flow modelling : A comparison with weakly compressible schemes. *Advances in Water Resources*, *97*, 156–167. https://doi.org/10.1016/j.advwatres.2016.09.008

Daly, E., Grimaldi, S., & Bui, H. H. (2016b). Explicit incompressible SPH algorithm for free-surface flow modelling: A comparison with weakly compressible schemes. *Advances in Water Resources*, *97*, 156–167.

Deng, L., Liu, Y., Wang, W., Ge, W., & Li, J. (2013). A two-fluid smoothed particle hydrodynamics (TF-SPH) method for gas–solid fluidization. *Chemical Engineering Science*, *99*, 89–101.

Dou, Y., Luo, J., Qi, L., Lian, H., & Hou, X. (2021). Generation mechanism and suppression method of landing error of two successively deposited metal droplets caused by coalescence and solidification. *International Journal of Heat and Mass Transfer*, *172*, 121100.

Gibou, F., Fedkiw, R., & Osher, S. (2018). A review of level-set methods and some recent applications. *Journal of Computational Physics*, *353*, 82–109.

Gingold, R. A., & Monaghan, J. J. (1977). Smoothed particle hydrodynamics: theory and application to non-spherical stars. *Monthly Notices of the Royal Astronomical Society*, *181*(3), 375–389.

Ha, J., & Cleary, P. W. (2000). Comparison of SPH simulations of high pressure die casting with the experiments and VOF simulations of Schmid and Klein. *International Journal of Cast Metals Research*, *12*(6), 409–418.

Hammani, I., Marrone, S., Colagrossi, A., Oger, G., & Le Touzé, D. (2020). Detailed study on the extension of the δ-SPH model to multi-phase flow. *Computer Methods in Applied Mechanics and Engineering*, *368*, 113189.

Haque, A., & Dilts, G. A. (2007). Three-dimensional boundary detection for particle methods. *Journal of Computational Physics*, *226*(2), 1710–1730.

Hirt, C. W., & Nichols, B. D. (1981). Volume of fluid (VOF) method for the dynamics of free boundaries. *Journal of Computational Physics*, *39*(1), 201–225.

Hongbin, J., & Xin, D. (2005). On criterions for smoothed particle hydrodynamics kernels in stable field. *Journal of Computational Physics*, *202*(2), 699–709.

Hosain, M. L., Domínguez, J. M., Fdhila, R. B., & Kyprianidis, K. (2019). Smoothed particle hydrodynamics modeling of industrial processes involving heat transfer. *Applied Energy*, *252*, 113441.

Hosseini, K., Omidvar, P., Kheirkhahan, M., & Farzin, S. (2019). Smoothed particle hydrodynamics for the interaction of Newtonian and non-Newtonian fluids using the μ (I) model. *Powder Technology*, *351*, 325–337.

Huang, C., J. M. Lei, M. B. Liu, and X. Y. Peng. "An improved KGF-SPH with a novel discrete scheme of Laplacian operator for viscous incompressible fluid flows." International Journal for Numerical Methods in Fluids 81, no. 6 (2016): 377-396.

Ishii, M., & Hibiki, T. (2010). *Thermo-fluid dynamics of two-phase flow*. Springer Science & Business Media.

Jandaghian, M., & Shakibaeinia, A. (2020). An enhanced weakly-compressible MPS method for free-surface flows. *Computer Methods in Applied Mechanics and Engineering*, *360*, 112771.

Khayyer, A., Gotoh, H., Falahaty, H., & Shimizu, Y. (2018). Towards development of enhanced fully-Lagrangian mesh-free computational methods for fluid-structure interaction. *Journal of Hydrodynamics*, *30*(1), 49–61.

Khayyer, A., Gotoh, H., & Shimizu, Y. (2017). Comparative study on accuracy and conservation properties of two particle regularization schemes and proposal of an optimized particle shifting scheme in ISPH context. *Journal of Computational Physics*, *332*, 236–256. https://doi.org/10.1016/j.jcp.2016.12.005

A. Khayyer and H. Gotoh, “Enhancement of stability and accuracy of the moving particle semi-implicit method,” J. Comput. Phys., vol. 230, no. 8, pp. 3093–3118, 2011.

Y. Krongauz, T. Belytschko, Consistent pseudo-derivatives in meshless methods, Comput. Methods Appl. Mech. Eng. 146 (1997) 371–386.

Koshizuka, S., & Oka, Y. (1996). Moving-particle semi-implicit method for fragmentation of incompressible fluid. *Nuclear Science and Engineering*, *123*(3), 421–434.

Kurowski, M.-P., & Spliethoff, H. (2016). Deposition and slagging in an entrained-flow gasifier

with focus on heat transfer, reactor design and flow dynamics with SPH. *Fuel Processing Technology*, *152*, 147–155.

Lee, E., Moulinec, C., Xu, R., Violeau, D., Laurence, D., & Stansby, P. (2008). Comparisons of weakly compressible and truly incompressible algorithms for the SPH mesh free particle method. *Journal of Computational Physics*, *227*, 8417–8436. https://doi.org/10.1016/j.jcp.2008.06.005

Li, G., Gao, J., Wen, P., Zhao, Q., Wang, J., Yan, J., & Yamaji, A. (2020). A review on MPS method developments and applications in nuclear engineering. *Computer Methods in Applied Mechanics and Engineering*, *367*, 113166.

Li, G., Liu, M., Duan, G., Chong, D., & Yan, J. (2016). Numerical investigation of erosion and heat transfer characteristics of molten jet impinging onto solid plate with MPS–LES method. *International Journal of Heat and Mass Transfer*, *99*, 44–52.

Lind, S. J., Stansby, P. K., & Rogers, B. D. (2016). Incompressible–compressible flows with a transient discontinuous interface using smoothed particle hydrodynamics (SPH). *Journal of Computational Physics*, *309*, 129–147.

Lind, S. J., Xu, R., Stansby, P. K., & Rogers, B. D. (2012). Incompressible smoothed particle hydrodynamics for free-surface flows: A generalised diffusion-based algorithm for stability and validations for impulsive flows and propagating waves. *Journal of Computational Physics*, *231*(4), 1499–1523.

Liu, Y., Luo, Y., Chu, G.-W., Larachi, F., Zou, H.-K., & Chen, J.-F. (2020). Liquid microflow inside the packing of a rotating packed bed reactor: Computational, observational and experimental studies. *Chemical Engineering Journal*, *386*, 121134.

Lucy, L. B. (1977). A numerical approach to the testing of the fission hypothesis. *The Astronomical Journal*, *82*, 1013–1024.

Marrone, S., Antuono, M., Colagrossi, A., Colicchio, G., Le Touzé, D., & Graziani, G. (2011). δ-SPH model for simulating violent impact flows. *Computer Methods in Applied Mechanics and Engineering*, *200*(13), 1526–1542.

Marrone, S., Colagrossi, A., Le Touzé, D., & Graziani, G. (2010). Fast free-surface detection and level-set function definition in SPH solvers. *Journal of Computational Physics*, *229*(10), 3652–3663.

Martinsson, P.-G., & Rokhlin, V. (2005). A fast direct solver for boundary integral equations in two dimensions. *Journal of Computational Physics*, *205*(1), 1–23.

Masterov, M. V, Baltussen, M. W., & Kuipers, J. A. M. (2020). Influence of the free surface on hydrodynamics in a bubble column. *Chemical Engineering Science: X*, *8*, 100077.

Molteni, D., & Colagrossi, A. (2009). A simple procedure to improve the pressure evaluation in hydrodynamic context using the SPH. *Computer Physics Communications*, *180*(6), 861–872.

Ng, K. C., Y. H. Hwang, and Tony WH Sheu. "On the accuracy assessment of Laplacian models in MPS." Computer Physics Communications 185, no. 10 (2014): 2412-2426.

Oger, G., Doring, M., Alessandrini, B., & Ferrant, P. (2007). An improved SPH method: Towards higher order convergence. *Journal of Computational Physics*, *225*(2), 1472–1492.

Piscaglia, F., Giussani, F., Hèlie, J., Lamarque, N., & Aithal, S. M. (2021). Vortex Flow and Cavitation in Liquid Injection: a Comparison between High-Fidelity CFD Simulations and Experimental Visualizations on Transparent Nozzle Replicas. *International Journal of Multiphase Flow*, 103605.

Rebouillat, S., & Liksonov, D. (2010). Fluid–structure interaction in partially filled liquid containers: a comparative review of numerical approaches. *Computers & Fluids*, *39*(5), 739–746.

Samulyak, R., Wang, X., & Chen, H.-C. (2018). Lagrangian particle method for compressible fluid dynamics. *Journal of Computational Physics*, *362*, 1–19.

Schwaiger, H. F. (2008). An implicit corrected SPH formulation for thermal diffusion with linear free surface boundary conditions. *International Journal for Numerical Methods in Engineering*, *75*(6), 647–671.

Shadloo, M. S., Oger, G., & Le Touzé, D. (2016). Smoothed particle hydrodynamics method for fluid flows, towards industrial applications: Motivations, current state, and challenges. *Computers & Fluids*, *136*, 11–34.

Shakibaeinia, A., & Jin, Y.-C. (2012). MPS mesh-free particle method for multiphase flows. *Computer Methods in Applied Mechanics and Engineering*, *229*, 13–26.

Sun, P. N., Colagrossi, A., Marrone, S., Antuono, M., & Zhang, A.-M. (2019). A consistent approach to particle shifting in the δ-Plus-SPH model. *Computer Methods in Applied Mechanics and Engineering*, *348*, 912–934.

Sun, P. N., Colagrossi, A., Marrone, S., Antuono, M., & Zhang, A. M. (2018). Multi-resolution Delta-plus-SPH with tensile instability control: Towards high Reynolds number flows. *Computer Physics Communications*, *224*, 63–80.

Sussman, M., Smereka, P., & Osher, S. (1994). A level set approach for computing solutions to incompressible two-phase flow. *Journal of Computational Physics*, *114*(1), 146–159.

Tan, H., & Chen, S. (2017). A hybrid DEM-SPH model for deformable landslide and its generated surge waves. *Advances in Water Resources*, *108*, 256–276.

Tanaka, M., Cardoso, R., & Bahai, H. (2018a). Multi-resolution MPS method. *Journal of Computational Physics*, *359*, 106–136.

Tanaka, M., Cardoso, R., & Bahai, H. (2018b). Multi-resolution MPS method. *Journal of Computational Physics*.

Tryggvason, G., Scardovelli, R., & Zaleski, S. (2011). *Direct numerical simulations of gas–liquid*

multiphase flows. Cambridge University Press.

Wang, W., Chen, G., Zhang, Y., Zheng, L., & Zhang, H. (2017). Dynamic simulation of landslide dam behavior considering kinematic characteristics using a coupled DDA-SPH method. *Engineering Analysis with Boundary Elements*, *80*, 172–183.

Wang, W., Yin, K., Chen, G., Chai, B., Han, Z., & Zhou, J. (2019). Practical application of the coupled DDA-SPH method in dynamic modeling for the formation of landslide dam. *Landslides*, *16*(5), 1021–1032.

Wang, Z.-B., Chen, R., Wang, H., Liao, Q., Zhu, X., & Li, S.-Z. (2016). An overview of smoothed particle hydrodynamics for simulating multiphase flow. *Applied Mathematical Modelling*, *40*(23–24), 9625–9655.

Wu, B., Firouzi, M., Mitchell, T., Rufford, T. E., Leonardi, C., & Towler, B. (2017). A critical review of flow maps for gas-liquid flows in vertical pipes and annuli. *Chemical Engineering Journal*, *326*, 350–377.

Xu, R., Stansby, P., & Laurence, D. (2009). Accuracy and stability in incompressible SPH (ISPH) based on the projection method and a new approach. *Journal of Computational Physics*, *228*(18), 6703–6725.

Xu, X., & Deng, X.-L. (2016). An improved weakly compressible SPH method for simulating free surface flows of viscous and viscoelastic fluids. *Computer Physics Communications*, *201*, 43–62.

Xu, X., & Yu, P. (2019). Extension of SPH to simulate non-isothermal free surface flows during the injection molding process. *Applied Mathematical Modelling*.

Xue, Q., Battistoni, M., Powell, C. F., Longman, D. E., Quan, S. P., Pomraning, E., … Som, S. (2015). An Eulerian CFD model and X-ray radiography for coupled nozzle flow and spray in internal combustion engines. *International Journal of Multiphase Flow*, *70*, 77–88.

Yan, K., & Che, D. (2010). A coupled model for simulation of the gas–liquid two-phase flow with complex flow patterns. *International Journal of Multiphase Flow*, *36*(4), 333–348.

Yang, X. F., Peng, S. L., & Liu, M. B. (2014). A new kernel function for SPH with applications to free surface flows. *Applied Mathematical Modelling*, *38*(15–16), 3822–3833.

Yang, X., Liu, M., & Peng, S. (2014). Smoothed particle hydrodynamics modeling of viscous liquid drop without tensile instability. *Computers & Fluids*, *92*, 199–208.

Yun, Sang-Moon, Jong-Chun Park, Abbas Khayyer, and Se-Min Jeong. "Two-Phase Particle Simulation of Violent Sloshing Flows with Large Density Ratios." In The 28th International Ocean and Polar Engineering Conference. International Society of Offshore and Polar Engineers, 2018.

Zhang, C., Hu, X. Y., & Adams, N. A. (2017). A weakly compressible SPH method based on a

low-dissipation Riemann solver. *Journal of Computational Physics, 335*, 605–620.

Zheng, B. X., Sun, L., & Yu, P. (n.d.). A novel interface method for two-dimensional multiphase SPH: Interface detection and surface tension formulation. *Journal of Computational Physics*, 110119